The response of Antarctic ice volume, global sea-level and southwest Pacific Ocean circulation to orbital variations during the Pliocene to Early Pleistocene

by

Molly O’Rourke Patterson

A thesis

Submitted to Victoria University of Wellington

In fulfilment of the requirements for the degree of

Doctor of Philosophy

In Geology

Victoria University of Wellington

2014

ABSTRACT

This thesis investigates orbitally-paced variations in the extent of East Antarctic Ice Sheet (EAIS), and the "downstream" influence of these ice sheet variations on ocean circulation and sea level variability during the Pliocene and Early Pleistocene - a time period characterised by a major global cooling step that culminated in the development of a bipolar glaciated world. Three unique records are examined from (1) the Antarctic margin, (2) the southwest Pacific Ocean, and (3) shallow-marine sedimentary strata exposed in Wangnaui Basin, New Zealand.

The Integrated Ocean Drilling Program (IODP) Site U1361 recovered a continuous sedimentary Early Pliocene to Early Pleistocene (4.3 to 2.0 Ma) record from the lowermost continental rise on the Wilkes Land margin offshore of the EAIS. A facies model and stratigraphic framework were developed that allowed for the identification of glacial advances (massive and laminated mudstones) and retreats (diatom-rich mudstones) across the continental shelf, with evidence for prolonged retreats spanning several glacial to interglacial cycles throughout the Pliocene. These cycles are followed by an extensive Early Pleistocene interval (~2.6 Ma) of diatom-rich mudstone with evidence for reworking by bottom currents, interpreted to be the consequence of downslope density currents associated with increased sea ice production after 2.6 Ma. Frequency analysis on Iceberg Rafted Debris (IBRD) from Site U1361 reveals that under an Early Pliocene warm climate state (4.3 to 3.3 Ma), that ice discharge off the EAIS occurred in response to climate change paced by the 40-kyr cycles of obliquity. Whereas, the colder climate state of Late Pliocene to Early Pleistocene (3.3 to 2.0 Ma) resulted in a transferral of orbital variance to 20-kyr-duration, precession-dominated variability in IBRD preceding the development of a more stable marine-based margin of the EAIS at ~2.6 Ma, which is hypothesized to reflect the declining influence of oceanic forcing as the high-latitude Southern Ocean cooled thereby increasing the seasonal duration and extent of sea-ice. The precession-paced influence on IBRD and ice volume variability of the EAIS was strongly modulated by 100-kyr-eccentricity, which is expressed lithologically in cycles of two alternating lithofacies 1) diatom-rich mudstones and 2) massive and laminted mudstones in the Site U1361 record.

A compilation of benthic stable isotope records from Ocean Drilling Program (ODP) Site 1123 in the southwest Pacific Ocean was also developed. The $\delta^{18}O$ record identified a 40-kyr

obliquity pacing, consistent with other benthic $\delta^{18}O$ records globally for this time period, thus allowing for an orbitally-tuned timescale to be developed for this site. Long-term trends in both the $\delta^{18}O$ and $\delta^{13}C$ records at ODP Site 1123 coincide with major developments of the Antarctic Ice Sheet and Northern Hemisphere glaciation at 3.33 Ma and ~2.6 Ma respectively. A gradual reduction in the deep water $\delta^{13}C$ gradient between the southwest Pacific (ODP Site 1123) and equatorial Pacific (ODP Site 849) between 3.33 and 2.6 Ma coincides with expansion of the Antarctic Ice Sheet, enhanced Antarctic Bottom Water (AABW) production, invigorated atmospheric zonal circulation in the southern hemisphere mid-latitudes, and increased meridional sea surface temperature (SST) gradients in the Pacific Ocean.

Finally, a shallow-marine, continental margin stratigraphic section from the Turakina River Valley in the Wanganui Basin, New Zealand, was used to record local sea-level changes, dominated by orbitally-driven, global glacio-eustasy, during the mid-Pliocene interval (3.2 to 3.0 Ma). This interval was selected as it precedes the build-up of significant Northern Hemisphere Ice Sheet, thus allowing for an independent assessment of the orbtial-scale variability of Antarctic Ice Sheet volume. Grain size based proxy of percent mud was employed to reconstruct paleobathymetric changes, which displayed 100-kyr cycles consistent with ~20 m variations in local water depths during the mid-Pliocene. Combined with IBRD record from Site U1361, this reconstruction suggests that the marine margins of East Antarctica varied at orbital timescale, and provided a significant contribution to global eustatic sea-level variations during the mid Pliocene (consistent with global mean sea-level estimates of up to ~+20 m above present from related studies).

ACKNOWLEDGEMENTS

First and foremost, I would like to thank Rob McKay and Tim Naish for supervising this project. You two have been nothing but supportive, encouraging and entertaining throughout this process. Rob, you really know how to bring the rigor (fist pump).

Thanks to all the staff and students in the Antarctic Research Centre. In particularly, Gavin Dunbar for his helpful insight towards lab and field work that aided in the development of data sets presented in Chapters 4 and 5 of this thesis. I would also like to thank Lionel Carter for his useful conversations and insight. Thanks to Lana Cohen for her field assistance.

I am also thankful to the scientist I have interacted with during aspects of work presented in this thesis as well as towards my professional development over these past few years; Amy Leventer (Colgate University), Scott Ishman (Southern Illinois University of Carbondale), Gillian Turner (VUW), Helen Bosotock (NIWA) and Mark Fenwick (NIWA). A special thanks to Carlota Escutia (Universidad de Granada) for her assistance towards interpretation of the sediment model presented in Chapter 2, Steven Meyers (University of Wisconsin) for his enthusiasm and advanced statistical analysis towards data sets discussed in this thesis, Maureen Raymo (Lamont-Doherty Earth Observatory, Columbia University) for challenging me intellectually, and Gary Wilson (University of Otago) for the use of the age model presented in Chapter 4.

This thesis presents large data sets which have only been made possible through a combination of lab assistance and support from Jennifer Staffenberg, Jane Chewings and Ashley Pocock. I am especially grateful to Rob Dunbar, Dave Mucciarone and their students for their hospitality as well as assistance during my visit to Stanford University. Furthermore, I would like to thank shipboard scientist of Ocean Drilling Program Leg 181 and the Integrated Ocean Drilling Program Expedition 318 for their successful recovery and data sets from the marine sediment records presented in this thesis.

Thanks to all my family and friends for their constant support and encouragement throughout the years. I have particularly appreciated the photos of “the little ones” and packages of wine. Finally, I want to give a special thanks to Cal. The most *SUPPORTIVE* and *PATIENT* special man-friend any special woman-friend could ever ask for.

Financial support for this thesis comes from the Victoria PhD Scholarship and Marsden Funds.

TABLE OF CONTENTS

LIST OF FIGURES

LIST OF TABLES

INTRODUCTION

Geological records of Southern Hemisphere ice sheet and paleoceanograhpic changes through the global climatic transition associated with the onset of the bipolar glaciated world at 2.7 Ma, are investigated in this thesis in order to better understand Earth system feedbacks. This transition has been the focus of intensive prior study, through both proxy records and modelling experiments – although detailed Southern Ocean and Antarctic records remain under sampled. However, the recent ANDRILL-1B record indicates that important climatic transition occurred in southern high latitudes with increased extent and duration of Antarctic sea ice, with the marine-based sectors of the West Antarctic Ice Sheet (WAIS) becoming a more permanent feature (post-marine isotope event M2 at ~3.3 Ma; McKay et al., 2012) prior to the onset of major Northern Hemisphere glaciation (~2.7 Ma; Shackleton and Opdyke, 1973; Ravelo et al., 2004).

The Early to mid-Pliocene (5.3 to ~3 Ma) is heavily studied as a potential analogue for Earth's future climate conditions near the end of the century and beyond (e.g., Hansen et al., 2006; Bonham et al., 2008; Dwyer and Chandler, 2008; Salzmann et al., 2008; Dowsett et al., 2012; Masson-Delmotte et al., 2013). Geological proxies indicate that this is the last time in Earth's history that atmospheric CO_2 concentrations were similar to present-day level (~400 ppm; Pagani et al., 2010; Seki et al., 2010; Bartoli et al., 2011) and globally averaged surface temperatures were 2-3°C warmer than present day, with amplified warming at the high latitudes (Figure 1) (Chandler et al., 1994; Sloan et al., 1996; Dowsett et al., 2012; Haywood et al., 2013).

The Pliocene is ideal for studying climate system questions in a fully-equilibrated state as boundary conditions such as land-sea (i.e., tectonic) configuration, ocean bathymetry, fauna and flora, and polar ice sheet configuration were effectively the same as present (e.g., Salzmann et al., 2008; Salzmann et al., 2011). Furthermore, geological evidence from paleo-shorelines suggest eustatic sea levels were very likely (95% confidence) up to ~20±10 m higher, a value that is more or less consistent with ice volume changes inferred from deep sea oxygen isotope records (Dowsett and Cronin, 1990; Cronin et al., 1994; Lisiecki and Raymo, 2005; Naish and Wilson, 2009; Miller et al., 2012) and reconstructions of polar ice sheets from models (Lunt et al., 2009; Pollard and DeConto, 2009; Hill et al., 2010; Dolan et al., 2011; Raymo et al., 2011). The Pliocene offers the most accessible recent period in Earth's history during which to assess the response of fast feedbacks such as sea ice extent, ocean heat transport, and the carbon cycle, as well as slow feedbacks such as polar ice sheets variability, under scenarios of global surface temperatures and sea-level predictions in the next 100 years and beyond. While many boundary conditions were similar to modern, a caveat is that the natural variability of the Pliocene ice age cycles appears to respond to 40-kyr cycles related to obliquity, with less influence from ~20-kyr cycles of precession and its 100-kyr modulating effect of eccentricity which has driven the climate system for the last 800,000 years (e.g., Raymo and Huybers, 2008). However, this observation is based largely on globally integrated records of ice sheet variability (e.g. sea level and oxygen isotope records), and the exact response of ice sheets in either hemisphere to orbital-paced variations in solar insolation remains unconstrained.

The over-arching aim of this thesis is to investigate the response of the East Antarctic Ice Sheet (EAIS) to orbital pacing as the world transitioned from a unipolar to bipolar world at 2.7 Ma.

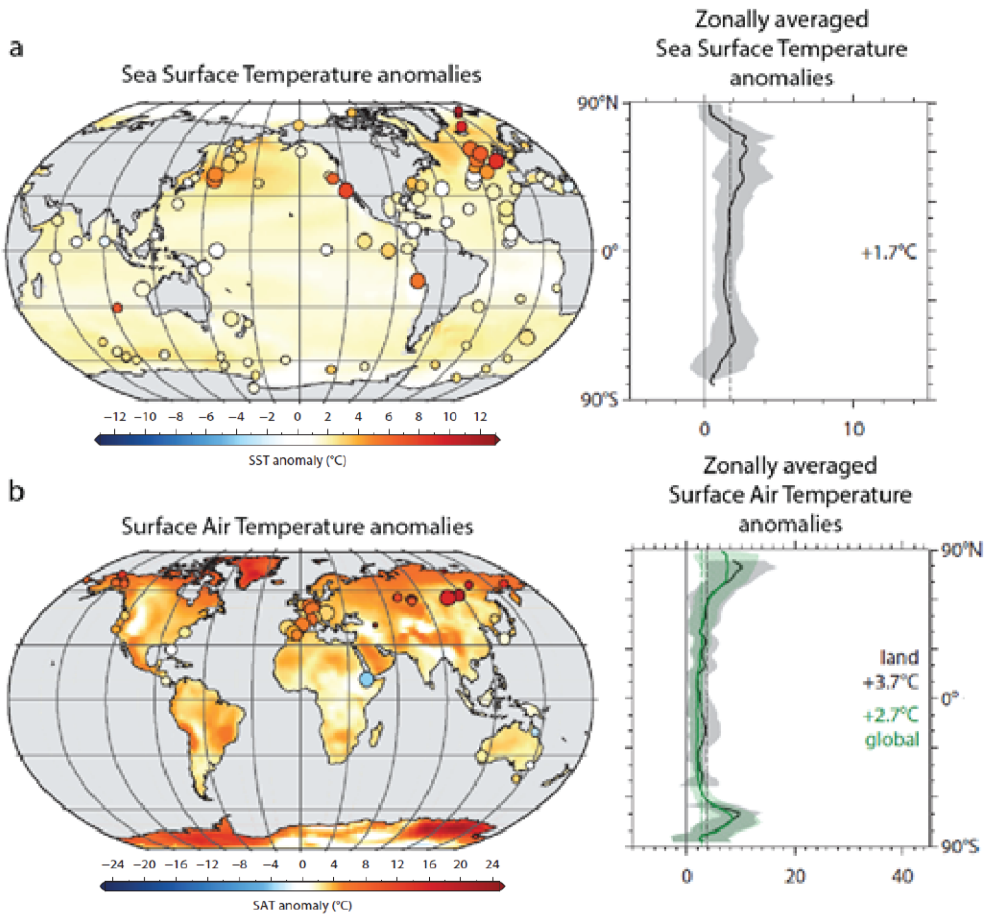

Figure 1. Reconstruction of mid-Pliocene (3.3 to 3.0 Ma) (a) Sea Surface Temperature anomalies with zonal averages and (b) land Surface Air Temperature anomalies with zonal averages for both global (green) and land (grey) (from Masson-Delmotte et al., 2013).

To achive this overarching aim, the approach in this thesis is three objectives:

1. *Interpret the sedimentological processes operating at the oceanic margin of the largest marine-based sector (i.e. Wilkes Land subglacial basin) of the EAIS during the Pliocene. Iceberg rafting, turbidity current activity and changes in biological productivity are investigated to assess EAIS variability at orbital timescale from a marine sediment core recovered by the Integrated Ocean Drilling Program (IODP) Expedition 318 (Site U1361).*

2. *Assess the variation in cold dense bottom water entering the southwest Pacific Ocean and how this relates to direct records of Antarctic ice volume variability observed along the Wilkes Land margin (i.e. objective 1) and the Ross Sea from previous drilling (e.g. ANDRILL records). To achieved this, stable isotope and sedimentological analyses are conducted on a marine sediment core recovered by Ocean Drilling Program (ODP) Leg 181 Site 1123.*

3. *Examine a high-resolution record of local sea-level change exposed in mid-Pliocene (3.2 to 3.0 Ma) shallow-marine sedimentary strata in Wanganui Basin, New Zealand that will enable the eventual assessment of eustatic sea-level change. Furthermore, this objective will offer the ability to assess, at orbital resolution, how the variability of Antarctic ice volume is expressed in sea-level records, prior to the development of significant Northern Hemisphere ice sheets.*

This thesis is organized into six chapters in which Chapters 2-5 are written as quasi papers. Due to this structuring there may be some unavoidable repetitiveness between these chapters. Chapter 1 provides an overview on orbital scale variability of the climate system and a discussion of paleoclimatic/oceanographic records through key climatic events of the past ~5.3 Ma, specifically the warmer-than-present Early Pliocene, high-latitude Southern Hemisphere cooling following Marine Oxygen Isotope Stage (MIS) M2 (3.3. Ma), and the onset of Northern Hemisphere glaciation at ~2.7 Ma.

Chapter 2 develops a sedimentary model for the Early Pliocene-Early Pleistocene record of Site U1361. Sedimentary lithofacies are defined on the basis of previously established models from deep-sea low- and high-latitude margins and are used to identify glacial to interglacial sedimentary processes in a stratigraphic framework. I performed all grain size analysis and semi-quantitatively developed a biogenic opal weight percent curve as an independent proxy for productivity. This chapter builds on the facies scheme developed in the initial sedimentological report (including visual core descriptions) by the shipboard sedimentological team members from IODP Exp. 318 (Escutia et al., 2011). I characterised the high-resoultion facies distribution throughout the Site U1361 core (this was conducted by Escutia et al., 2011). Francisco Jiménez-Espejo provided XRF Ba/Al data, which are used as an additional productivity indicator. Seismic data sets are included in the overall sediment model interpretations, and these data are supplied by Carlota Escutia (Co-Chief Scientist IODP Exp. 318), who assisted me in integrating these data into the sedimentation model. The majority of this Chapter (~90%) has been applied to the supplementary information of a recent publication accepted by *Nature Geoscience*.

Chapter 3 further develops the sedimentary model from Chapter 2 and evaluates it within a cyclo-chronostratigraphic framework. The Ice-Berg Rafted Debris Mass Accumulation Rate (IBRD MAR) and biogenic opal weight percent records developed in Chapter 2 were analysed using spectral analysis to determine the orbital (frequency) response of a marine based sector of the EAIS. Findings from this chapter demonstrate a shift in orbital forcing (via the IBRD MAR) of the EAIS from obliquity during the warm Early Pliocene to precession-dominated forcing during the Late Pliocene-Early Pleistocene cooling. The results of this Chapter highlight the importance the overall climate state has in determining the orbital variability of ice sheets. I have carried out the frequency analysis presented in this thesis, but have subsequently also consulted a time series analyis expert (Steven Meyers (co-author on Patterson et al., *Nature Geoscience* accepted) to run more advanced statistical analysis and testing which confirms the results of this chapter. Additional co-authors associated with the publication based on the chapter currently accepted by *Nature Geoscience* include Rob McKay and Tim Naish (my PhD supervisors), Carlota Escutia (seismic data and co-chief scientist on IODP Expedition 318), Francisco Jiménez-Espejo (XRF data), Maureen Raymo (advice on orbital theory of the ice ages), Lisa Tauxe (Paleomagnetic age model), and Henk Brinkhuis (co-chief scientist on IODP Expedition 318). I estimate that 90% of this chapter represents my primary data set and intellectual input, with the additional, but subordinate, data sets represent the combined efforts of many of the Expedition 318 scientific party.

Chapter 4 assesses the paleooceanographic response to major phase of Antarctic Ice Sheet development documented in Chater 3. This chapter provides a compilation of benthic $\delta^{18}O$ and $\delta^{13}C$ stable isotope data from ODP Site 1123 extending from the Early Pliocene (~4.6 Ma) to the Early Pleistocene (1.24 Ma). Stable isotope data from ODP Site 1123 are compared to previously established records from the North Atlantic (ODP Site 607), South Atlantic (ODP Site 704/1090), equatorial Pacific (ODP Site 849) and the South Pacific (MV0502-AJC). Grain size data for the Early to mid Pliocene is used as a proxy for paleocurrent intensity. A new age model for ODP Site 1123 is employed (personal communications G. Wilson, University of Otago). This chapter will comprise the basis of a paper that will focus on the role that the Antarctic Ice Sheet and Southern Ocean have played in pre-conditioning the onset of major Northern Hemisphere glaciation. I developed the benthic $\delta^{18}O$ and $\delta^{13}C$ record from ODP Site 1123 extending from 4.6 to 3.0 Ma. 20% of the work towards the stable isotope data set was carried out by lab assistents whereas I carried out 80%. This record was combined with stable isotope data of Harris (2002) from 3.0 to 1.24 Ma in which I applied the new age model. Additionally, I analysed 529 sampled intervals for grain size data from ODP Site 1123 in this thesis. When considering sample preperations, I contributed up to 70% of the lab work that aided in the development of the stable isotope data extending from 4.3 to 3.0 Ma and all the grain size data presented in this chapter.

Chapter 5 provides initial sedimentological and cyclostratigraphic interpretation of a mid-Pliocene shallow marine sediment record from Wanganui Basin, New Zealand that has a local expression of sea level changes in response to global sea-level variability. Percent mud highlights cyclical paleo-water depth cycles extending from an inner to out-shelf setting. Magnetostratigraphy developed by Turner et al., (2005) is used to constrain paleo-water depth cycles and access cycles in an orbital context. I participated in field work, sampling, described out crop exposures and performed grain size analysis. Benthic foraminifera analysis will serve as an additional proxy for paleo-water depth but is currently being carried out by Hugh Morgans (GNS Science). A more detailed assessment of the magentrostratigraphy, aimed at improving the stratigraphic precision of key paleomagnetic transitions, is currently being carried out by Gillian Turner.

Chapter 6 summarizes the main results of this thesis while incorporating other geological records in order to assess and discuss climate system feedbacks in relation to major reorganisiations (3.3 Ma and ~2.5 Ma) in Antarctic ice volume, deep ocean circulation, Southern Ocean ventilation and atmospheric CO_2 concentrations.

CHAPTER 1

ORBITAL CLIMATE FORCING AND THE PLIOCENE-EARLY PLEISTOCENE

1.1. ORBITALLY DRIVEN CLIMATE FORCING

1.1.1. Introduction

Earth's orbital configuration on time scales over tens of thousands of years has been central to pacing of glacial to interglacial variability, in particular the influence cyclic changes in the orbits have on the amount and seasonal timing of radiation received by the sun at a given latitude (e.g., Croll, 1867; Milanković, 1941; Hays et al., 1976; Raymo and Huybers, 2008; Palliard, 2010). Orbital parameters such as eccentricity, precession and obliquity effect the distribution of incoming solar radiation (insolation), which directly influence Earth's climate in several ways (Figure 1.1). Eccentricity (e) defines the size parameter of Earth's elliptical orbit and is defined by the ratio between the center of the ellipse (c) with respect to the semi-major axis (a) (Figure 1.2),

$$e = c/a$$

Where,

c = distance between focus and center of ellipse

a = semi-major axis

Directly, the 100-kyr, 400-kyr and 2-myr cycles of eccentricity have a minor effect on the climate system, as maxima in eccentricity provide only a 0.18% increase in energy received by the Sun relative to the minima states (Paillard, 2010). However, as discussed below, eccentricity modulates the precession of the equinoxes (herein termed "precession") which exerts a strong control on changes in seasonality.

Precessional changes of Earth's orbit influence the timing of the year in which Earth reaches perihelion (when Earth is closest to the Sun) and is defined by,

$$\text{precession} = e \sin \omega$$

The vernal point (defined by the location of the sun at the March equinox; NH spring) and location of seasons on the Earth orbit moves with precession of equinoxes, the time of the year defined by the intersection of the equatorial plane and the orbital plane (days and nights of equal length). Since the orbit is elliptic, seasons also occur depending on their position relative to perihelion (nearest to the Sun) and aphelion (farthest from the Sun) which is in opposite motion to that of the precession of equinoxes (Figure 1.2; ω). The combined yet opposing motions of the positioning of the vernal point (precession of equinoxes) moving around the sky at 25,700 years cycles and perihelion at 112,000 year frequencies combine into a mean climatic precessional cycle of 21,000 years (Paillard, 2010). The larger the eccentricity, the climatic effects associated with precession are stronger and vice versa. However, the periodicity of precession detected in oceanic and paleoclimatic records is often associated with the 23-kyr and 19-kyr, as they have a mean of 21,000 years (Paillard, 2010). The effect of climatic precession amplifies or decreases the local seasonal variance and is out-of-phase between hemispheres.

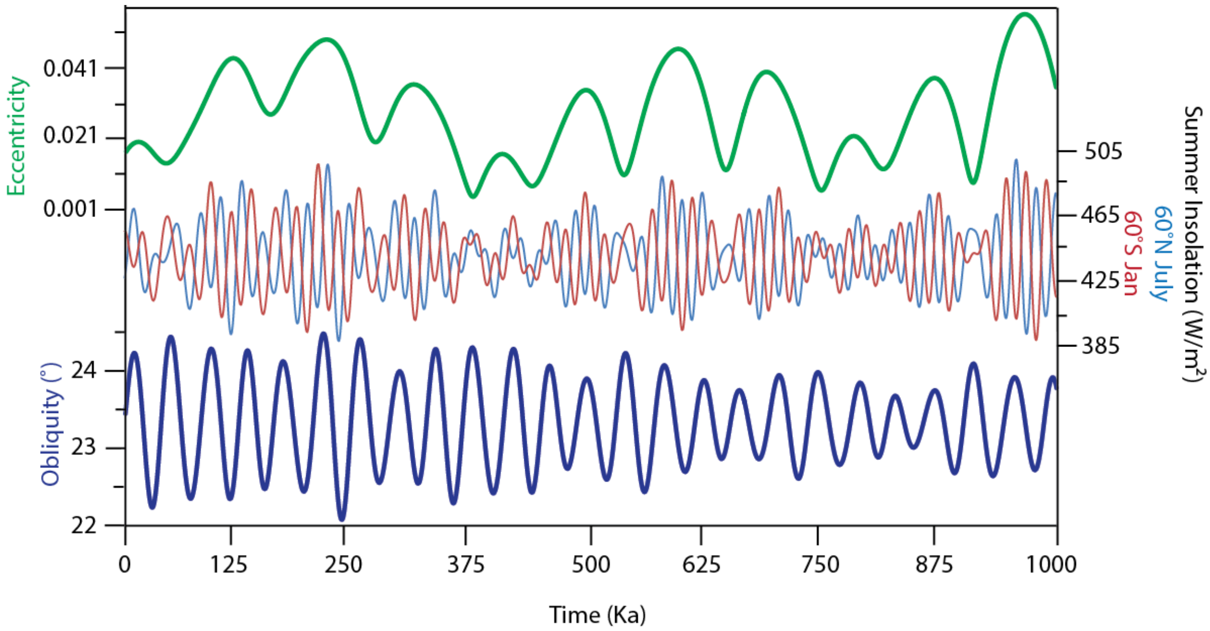

Figure 1.1. Time series of eccentricity, precession (summer insolation) and obliquity for the last million years.

Obliquity (ϵ) is the tilt of Earth's axis compared to the ecliptic or orbital plane. The effects of obliquity include the latitudinal location of the tropics and polar circles, as well as meridional distribution of heat with greatest effect in high latitudes. Today, obliquity is ϵ = 23.44° but can vary from 21.9° and 24.5° at a periodicity of 40-kyr (Figure 1.2).

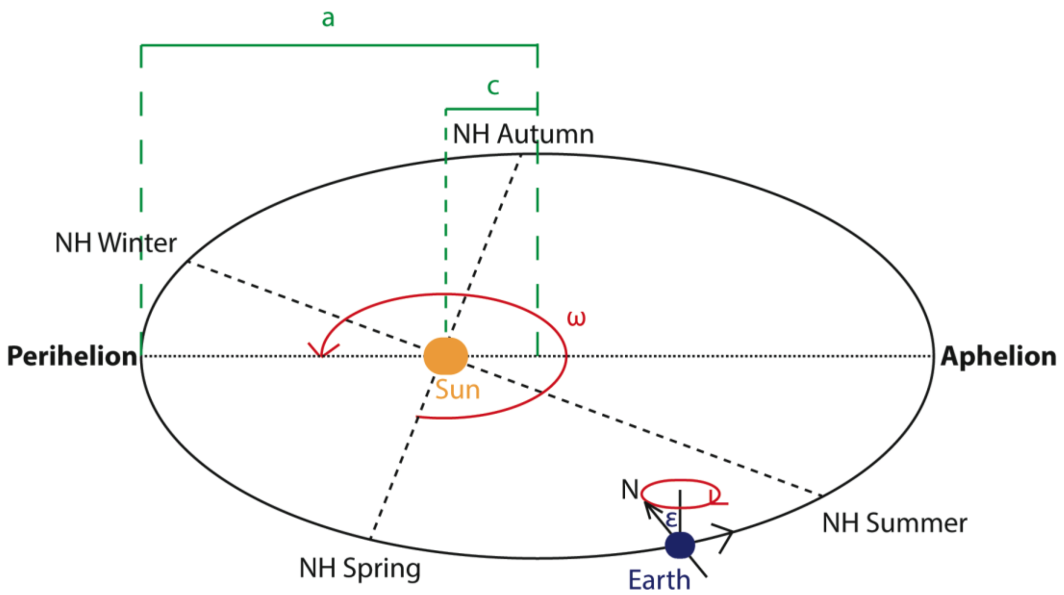

Figure 1.2. Schematic diagram of Earth's orbital configuration used in the calculation of parameters (eccentricity/green = c/a; obliquity/blue = ε; precession/red = ω) (after Paillard, 2010).

For more than 150 years, Earth scientists have used orbital parameters to explain the periodicities of glaciations. Joseph Adhémar proposed in 1842 that glaciations occur when winters align with aphelion, making them relatively longer in duration. However, in 1860 James Croll argued that glaciations occurred when winters coincided with aphelion (farthest point from the sun) not because they are longer in duration but rather the intensity of insolation is weaker (Imbrie and Imbrie, 1980; Raymo and Huybers, 2008). Following Croll, Milutin Milankovitch in the 1930's theorized that summers experiencing weak insolation intensity at high Northern latitudes result in glaciation (Milanković, 1941; Imbrie and Imbrie, 1980). More specifically, glaciation occurs when Earth's spin axis is tilted at a low angle relative to the orbital plane (low obliquity) and when Northern Hemisphere summer occurs during aphelion allowing for snow and ice to persist through the melting season. Based on geological evidence, Milankovitch's theory has become adopted in order to explain the pacing of ice ages (e.g., Hays et al., 1976 and others).

Although long-term, high-resolution geological records are often complicated by sedimentation rates, erosional events and bioturbation, the study of Hays et al., (1976) directly linked for the first time the orbital pacing in geological records to glacial-interglacial variability. Evidence of such forcing in paleoclimate records is widespread and includes (1) ice core records that provide evidence for atmospheric gas composition changes (Jouzel et al., 2007; WAIS Divide Project Members, 2013); (2) continental dust record that imply changes in atmospheric circulation (Tiedemann et al., 1994; Ding et al., 2002; Martínez-Garcia et al., 2011; Naafs et al., 2012); (3) deep sea proxies recording variability in ocean circulation and temperature (Dwyer et al., 1995; Hall et al., 2001; Crundwell et al., 2008; Lisiecki et al., 2008; Lisiecki, 2010; Lourens et al., 2010; Meyers and Hinnov, 2010); (4) sediment records recovered from the Antarctic margin and North Atlantic records demonstrating ice sheet variability and sensitivity (Shackleton et al., 1984; Naish et al., 2009); (5) shallow-marine continental margin records inferring sea level fluctuations (Dowsett and Cronin, 1990; Cronin et al., 1994; Naish, 2007; Naish and Wilson, 2009); and (6) lake deposits from high Northern latitudes (Melles et al., 2012; Bringham-Grette et al., 2013). A significant feature of Quaternary climate is the transition in the orbital pacing of glacial cycles (i.e., The mid-Pleistocene Transition (MPT)) at ~800-kyr ago which marks a switch from 40-kyr obliquity pacing to the most recent 100-kyr eccentricity modulated but precession-paced glacial cycles (Figure 1.3).

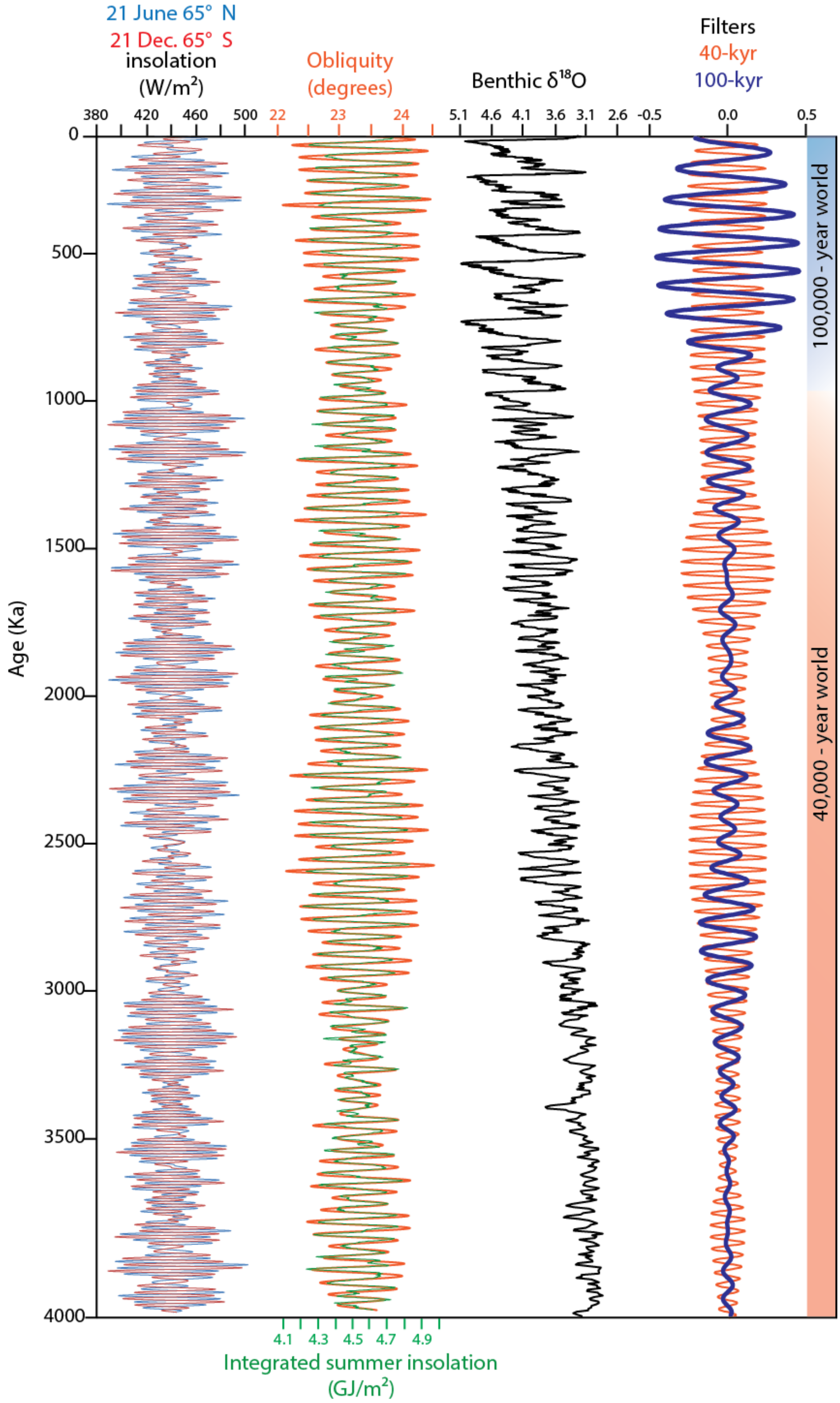

Figure 1.3. Orbital parameters, the deep sea benthic $\delta^{18}O$ stack (Lisiecki and Raymo, 2005) recording ice volume changes for the last 4 million years, and Gaussian band-pass filters isolating the variance associated with 100-kyr (blue) and 40-kyr (orange) cycles in the benthic $\delta^{18}O$ stack. The 100-kyr filter has a central frequency = 0.01 and bandwidth = 0.002; the 40-kyr central frequency = 0.025 and bandwidth = 0.003. Filters demonstrate a switch from 40-kyr to 100-kyr dominance after 600,000 Ka.

1.1.2. Identifying the 100,000 year ice age cycles since the Mid-Pleistocene Transition (MPT) (~800,000 years ago)

Although previous studies had suggested a relationship between ice ages and orbital cycles (e.g. Emiliani, 1966), Hays et al., (1976) provided the first compelling spectral analysis of geological evidence to test Milankovitch's orbital hypothesis. They used two deep-sea sediment cores recording the variability of $\delta^{18}O$ in planktonic foraminifera to estimate summer (SST) of the last 500 kyr in order to demonstrate the frequency of glacial to interglacial variability. While the 40-kyr and 20-kyr years cycles of obliquity and precession pacing were identified in their spectral analysis, an unexpected result was the dominance of the 100-kyr long eccentricity-paced cycles, indicating a strong non-linearity of the climate system response to eccentricity forcing (Figure 1.4). Hays et al. (1976) reasoned that because of the non-linear nature of the ice sheet growth (90 kyr) and decay (10 kyr) and the small effect that eccentricity has on insolation, they recognized the 100-kyr signal in the geological record is related to the 23- and 19-kyr cycles of precession as a result of the modulating effect of eccentricity on precession. However, studies have called into question the assumption in which Earth's climate responds to direct linkages between seasonality (eccentricity modulated changes in precession) and ice-sheet size with consequences at lower latitude climate (e.g., Broecker and Denton, 1989). Broecker and Denton (1989) used a generalized ocean circulation model to suggest that the 100-kyr glacial variability is not a direct consequence of eccentricity, but rather involves a massive reorganization in a non-linear manner to self-sustained internal oscillations between the oceans and atmosphere.

The Vostok ice core record of the EAIS spanning the last 420 kyr highlights the role greenhouse gases (i.e., CH_4 and CO_2) and the carbon cycle (Petit et al., 1999; Shackleton, 2000) have in amplifying orbital forcing. This is highlighted by termination events of each 100-kyr-paced glaciation, which are characterised by a systematic sequence, whereby an increase in temperature (initiated by the orbital influence on insolation) is followed by a decrease in dust input, and rapid increase of both CH_4 and $CO_{2.}$ Such a sequence is a consequence of the role deep-ocean circulation and Southern Ocean sea ice extent have on deep ocean ventilation and dust input over East Antarctica (e.g., Martin, 1990). This is then followed by an additional increase in CH_4 and decrease in $\delta^{18}O$(atm) which are thought to be the consequence of Northern Hemisphere deglaciation (Petit et al., 1999). The European Project for Ice Coring (EPICA) recovered an ice core from the EAIS spanning the last 800 kyr, including eight glacial cycles back to MIS 20. This record infers long-term changes as a result from interplay between Northern Hemisphere insolation and obliquity cycles, whereas millennial scale changes within the climate system are induced by variability in the production of NADW potentially through the thermal bipolar sea-saw (Jouzel et al., 2007).

Southern Hemisphere climate proxy records imply a near in-phase relationship between Antarctic ice volume and Northern Hemisphere insolation (Masson et al., 2000; Jouzel et al., 2007; Kawamura et al., 2007), using atmospheric temperature anomaly estimates and $\delta O_2/N_2$ from Dome F (high plateau of the EAIS) for the last 350 kyr. Huybers and Denton (2008) modelled an Antarctic response to Southern Hemisphere insolation. Their findings support a hypothesis in which interhemispheric changes during the Late Pleistocene depended on Northern Hemisphere climate responding primarily to summer intensity (Northern Hemisphere insolation) and Southern Hemisphere climate responded primarily to the duration of summer and winter seasons. Such a situation promotes long Antarctic summers (Southern Hemisphere summer solstice coinciding with aphelion), thereby inferred to decrease the extent of sea ice, and promoting the outgassing of CO_2 from the Southern Ocean. When combined with the combination of short intense Northern Hemisphere summers and large unstable Northern Hemisphere ice sheets, this is hypthosized to have led to the collapse of Northern Hemisphere ice sheets (Huybers and Denton, 2008). The recent West Antarctic Ice Sheet (WAIS) Divide ice core documents that during the last deglaciation, marine based sectors warmed 2000 years prior to the Antarctic interior regions (18,000 years ago). This was inferred to be the consequence of changes in local insolation for reasons hypothesized by Huybers and Denton (2008), rather than Northern Hemisphere summer insolation intensity (WAIS Divide Project Members; 2013).

While understanding internal mechanisms and feedbacks within the overall climate system (e.g., oceans and atmosphere) is essential, much has been discussed on the role of orbital configurations responsible for triggering and or pacing such internal oscillations during the Late Pleistocene (e.g., Huybers, 2007; Lisiecki, 2010; Huybers, 2011; Rial et al., 2013). Using non-orbitally tuned age models from 17 marine sediment cores, Huybers (2007) provided statistical evidence, based on $\delta^{18}O$ records, in which for the last 2 Ma the Early Pleistocene deglaciation events occurred every 40-kyr obliquity cycle in which obliquity was largest (high degree of tilt). However, the Late Pleistocene deglaciations may be the consequece of a glacial cycle skipped one or two obliquity beats, - i.e. they correspond to 80 or 120 Ka cycle, which average out to 100 ka. Thus, in that study, it was inferred that the orbital pacing of glacial-interglacial cycles could be simplified to obliquity beat skipping, rather than long-period variability of the 100-kyr eccentricity cycle modulating ~20-kyr precession cycles (Raymo, 1997b; Huybers, 2007).

Huybers (2011) subsequently used statistical modelling techniques to test whether anomalously large combinations of precession and obliquity forcing combine to determine the pacing of Late Pleistocene deglaciations. By correlating the timing of terminations using a composite $\delta^{18}O$ record independent of orbital tuning to that of an insolation forcing function derived from equal amounts of obliquity and climatic precession. Huybers (2011) demonstrated that while precession determines the precise timing of deglaciation events obliquity fundamentally governs the time between deglaciations. However, more recently using spectral analyses aided by a numerical modelling Rial et al., (2013) demonstrated the 100-kyr cycles arising since the MPT can be explained by the synchronization of nonlinear transfer from long-period 400-kyr eccentricity, which is apparent since 3.6 Ma (Rial et al., 2013; Figure 4), to the 100-kyr component starting at about 1.2 Ma. According to Rial et al., (2013), synchronization allowed energy from the sun to be transferred in and out of the climate system at the same time as internal ocean and atmosphere feedbacks were warming and cooling the climate. Thus, synchronization between the overriding orbital influence controlling insolation variability with that of internal climate system feedbacks allowed for large fluctuations in the climate system transferring power to the 100-kyr Late Pleistocene cycles. Such a scenario supports previous studies that favour the hypothesis that internally driven climate feedbacks are the source of the 100-kyr climate variation for the last 5 myr (Nie et al., 2008; Lisiecki et al., 2010; Meyers and Hinnov, 2010). Elderfield et al., (2012) recently suggested the rise of the 100-kyr glacial cycles was initiated by an abrupt increase in Antarctic ice volume. By separating the effects of temperature and global ice volume from oxygen isotope records, Elderfield et al., (2012) examined sea-level fluctuations across the MPT. They argued an abrupt increase in continental ice volume, coinciding with anomalously low Southern Hemisphere summer insolation, suppressed ice sheet melting and allowed larger ice-sheet growth in Antarctica and promoted the first prolonged 100-ky glacial cycle.

Because the 100-kyr cycles since the MPT are influenced by numerous and complex internal climate system feedbacks, researchers have been looking towards understanding the shorter, lower amplitude 40-kyr cycles of the Pliocene and Early Pleistocene. This time interval offers advantages when considering ice sheet response to orbitally-driven climate forcing, as well as the changing climatic response through the transition into a bipolar glacial world after 2.7 Ma.

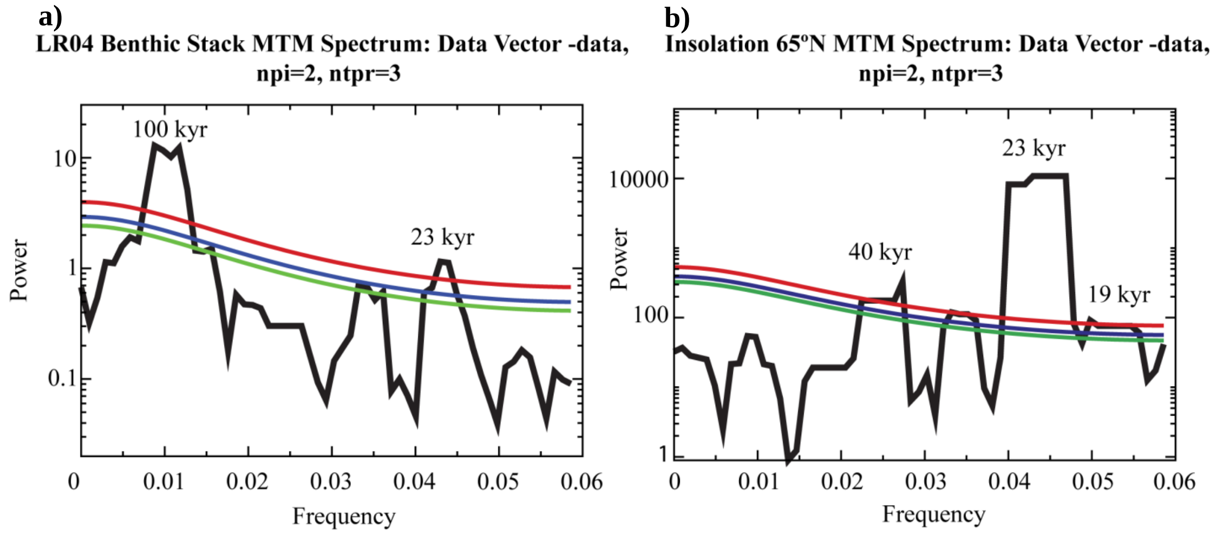

Figure 1.4. Power spectra analysis using the Multi-Taper Method (MTM) of the LR04 benthic $\delta^{18}O$ stack (a) and insolation at 65°N (b) for the last 800,000 years. Statistical significance of spectral peaks was tested to a null hypothesis of a red noise background (Ghil et al., 2002) with green = 90%, blue = 95% and red = 99% confidence. (a) Highlights the dominance of the 100-kyr cycles of eccentricity over ice volume changes, while (b) demonstrates the lack of eccentricity power (100-kyr) and the significance of the 23-kyr and 40-kyr cycles of precession and obliquity, respectively.

1.1.3. The Pliocene and Early Pleistocene 40,000 year debate

If the ice ages of the last ~800-kyr follow Milankovitch's hypothesis that weak insolation forcing at high Northern latitudes (65°N) is driven by precession, than why do the 40-kyr cycles of obliquity, which is in phase between hemispheres, dominate the Pliocene and Early Pleistocene records? Geological records prior to ~800 kyr ago are dominated by strong 40-kyr variability and near absence to weak ~20-kyr precession variability (e.g., Shackleton et al., 1984; Ding et al., 2002; Naish, 2007; Naish et al., 2009; Naafs et al., 2012), whereas, modelling experiments have struggled to reproduce growth and decay of ice sheets without a significant precessional influence (e.g., Berger et al., 1999).

Recent debate has surrounded the role local summer insolation has on the Antarctic Ice Sheet. Raymo et al., (2006) used a non-dimensional ice sheet-climate model with the assumption that surface ablation is dependent on summer insolation intensity in both hemispheres. Such a model requires a dynamic Antarctic Ice Sheet with a terrestrial-based (i.e. surface) ablation margin in order to infer precession-based insolation forcing for ice growth and decay in both hemispheres. They suggested the out-of-phase relationship of precession between hemispheres results in the 23- and 19-kyr changes of ice volume in each hemisphere cancelling each other out in the globally integrated proxies such as benthic foraminiferal $\delta^{18}O$ and eustatic sea level records. This, results in leaving behind the residual obliquity component of insolation, which is in-phase globally, to dominate these records. They reasoned, due to the differences in the oxygen isotopic ratios between Northern and Southern hemisphere ice sheets, a relatively small change in the isotopically lighter EAIS could effectively cancel out the volumetrically larger and the isotopically-heavier Northern hemisphere changes (Raymo et al., 2006). Scherer et al., (2008) used geological records recovered from the Antarctic continental margin and Southern Ocean to demonstrate that a retreat of the marine-based WAIS occurred during Southern Hemisphere insolation maximum surrounding the MIS-31, supporting the notion that local insolation (including the precession component) influences Antarctic Ice Sheet volume, at least during periods of very high precession values.

However, Huybers (2006) provided an alternative hypothesis where the direct influence of precession on ice sheet mass balance is negligible under certain boundary conditions. To explain his hypothesis, Kepler's second law of planetary motion is invoked, such that when the Earth is at perihelion it is traveling faster than when it is at aphelion. This results in intense short summers being inversely balanced out by longer cold winters (Figure 1.5). Thus, ice sheets become more sensitive to the overall duration of the summer melt season via mean annual insolation which is controlled by obliquity. Huybers (2006) infers that given a certain melt threshold of ice sheets, the duration of the summer melt season becomes more sensitive to either obliquity or precession forcing. For example, in a higher CO_2 world (~400 ppm) during the Pliocene (Pagani et al., 2009; Seki et al., 2010; Bartoli et al., 2011) the insolation threshold required to achieve positive degree days at high latitudes would have been lower than today (e.g., Figure 1.5; W/m^2 = 200) due to enhanced radiative forcing. This scenario would extend the melt season and leave obliquity to dominate the total integrated summer insolation at latitudes greater than 60°, as the influence of Northern Hemisphere summer insolation would have been counter balanced by long cold winters. However, as a melt thresholds increase through time, as the world cools (Figure 1.5; W/m2 = 400), the influence of precession becomes the dominant control on the duration of the summer melt season (Figure 1.5).

Expanding on the hypothesis of Huybers (2006), Huybers and Tziperman (2008) used a coupled ice-sheet/energy-balance model to simulate glacial response to obliquity under set boundary conditions. They found that when relatively thin ice sheets reside northward of 60°N, their model generated almost exclusively obliquity period glacial variability (Huybers and Tziperman, 2008). An additional boundary condition is that the ablation season must be long enough for precession's opposing influences on summer and fall insolation intensity to counterbalance one another (Huybers and Tziperman, 2008). However, these assumptions are contradicted by several tills deposited by the North American Laurentide Ice Sheet prior to 1.97 Ma. These tills indicate that while the ice sheet was volumetrically one half to two thirds as large as Late Pleistocene ice sheets, it's southern boundary extended much farther south (~40°N) than during the Last Glacial Maximum (LGM) (Clark and Pollard, 1998; Balco and Rovey, 2010).

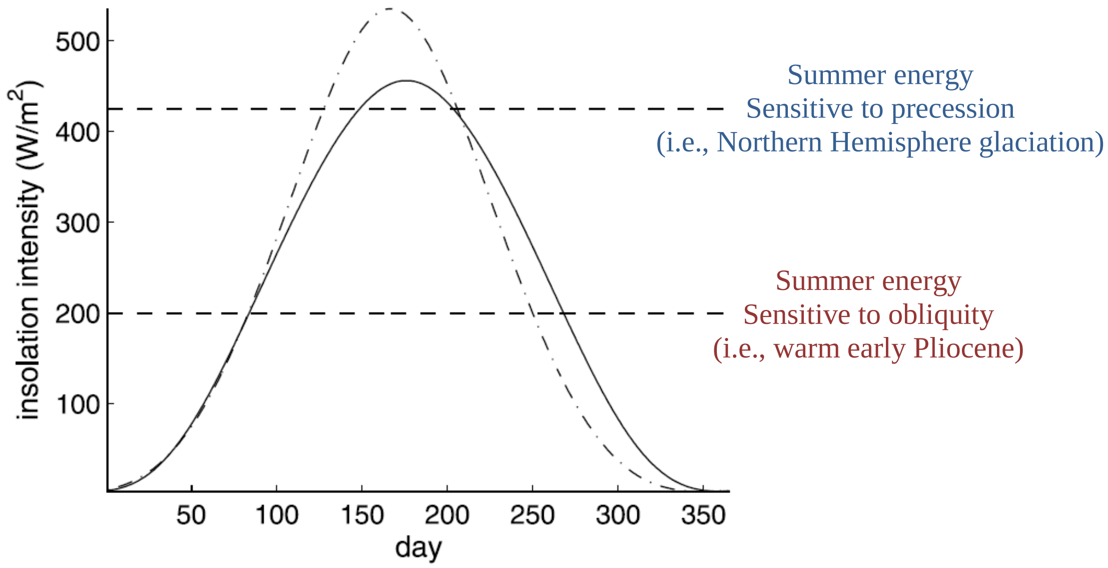

Figure 1.5. The seasonal cycle as represented by daily average intensity at 65°N in which perihelion occurs during Northern Hemisphere winter solstice (solid line) and summer solstice (dotted line). The switch between obliquity and precession driven variability occurs at a threshold around 350 W/m^2. For a lower threshold (i.e., 200 W/m^2), the duration of summer is longer, and thus summer melt season (i.e. area integrated under the curves above W/m^2 = 200) is more influenced by the mean annual insolation signal – i.e. these latitudes receive majority of annual insolation during summer months (due to greatly reduced daylight hours in winter). However, at higher threshold (i.e., 400 W/m^2), Northern Hemisphere summer when the Earth is at perihelion causes an increase the intensity of insolation yet a significant decrease in the summer melt season (sum of positive degree days), and thus the influence of peak summer insolation controlled by precession has more of an influence (after Huybers and Tziperman, 2008)

1.2 THE ONSET OF LATE PLIOCENE GLOBAL COOLING AND NORTHERN HEMISPHERE GLACIATION

1.2.1. Small scale Northern Hemisphere glaciations prior to the Early Pliocene

While the onset of "major" Northern Hemisphere glaciation did not take place until the Late Pliocene (~3.0 to 2.5 Ma) (i.e., Shackleton et al., 1984; Raymo, 1994; Jansen et al., 1996; Zachos et al., 2001; Ravelo and Wara., 2004; Haug et al., 2005), small scale glaciations are believed to have occurred in Northern high latitudes since the late Miocene (~7.3 to 6.0 Ma) and onset as far back as the middle Eocene (44.5 to 44.7 Ma) (Fronval and Jansen, 1996; St. John, 2008). Although Ice Rafted Debris (IRD) (IRD - detrial material transported by ice sheets, ice shelves and or sea ice) records from Miocene and older records are low in resolution, and limited spatially compared to the Late Pleistocene, drill cores from the Norwegian-Greenland Sea suggest glaciers reached sea level as early as ~7.3 Ma (Figure 1.6) (Larsen et al., 1994; St. John and Krissek, 2002). The gradual intensification of Northern Hemisphere glaciation starting in the Miocene is also recorded in ice-born deposits from the VØring Plateau near Iceland (Fronval and Jansen, 1996), as well as the IRD records recovered from the central Arctic Ocean (St. John, 2008). Furthermore, based on a rapid increase of terrigenous material into the Gulf of Alaska, alpine glaciation in southeastern Alaska is suggested to have started in the late Miocene between 5.91 and 5.50 Ma and continued into the Pliocene (Rea and Snoeckx, 1995; Rea et al., 1998). IRD Mass Accumulation Rates (MAR) records, as well as massive amounts of glaciomarine diamictites from the northern Pacific Ocean indicates the presence of tidewater glaciers as early as ~6 to 4.2 Ma (Krissek, 1995; Lagoe and Zellers, 1996). Glacial advance across the Greenland shelf has been recorded in sediment cores (ODP Site 918) recovered off southeastern Greenland since ~7 Ma (Solheim et al., 1998). Finally, while the record of sea ice recovered from the central Arctic Ocean extends back to the relatively warmer Eocene and middle Miocene (St. John, 2008; Stickley et al., 2009), the spatial extent of sea ice since this time until the Pliocene is debated (Cronin et al., 1993; Butt et al., 2002; Dowsett, 2007; Darby, 2008; Haley et al., 2008; Krylov et al., 2008; St. John, 2008).

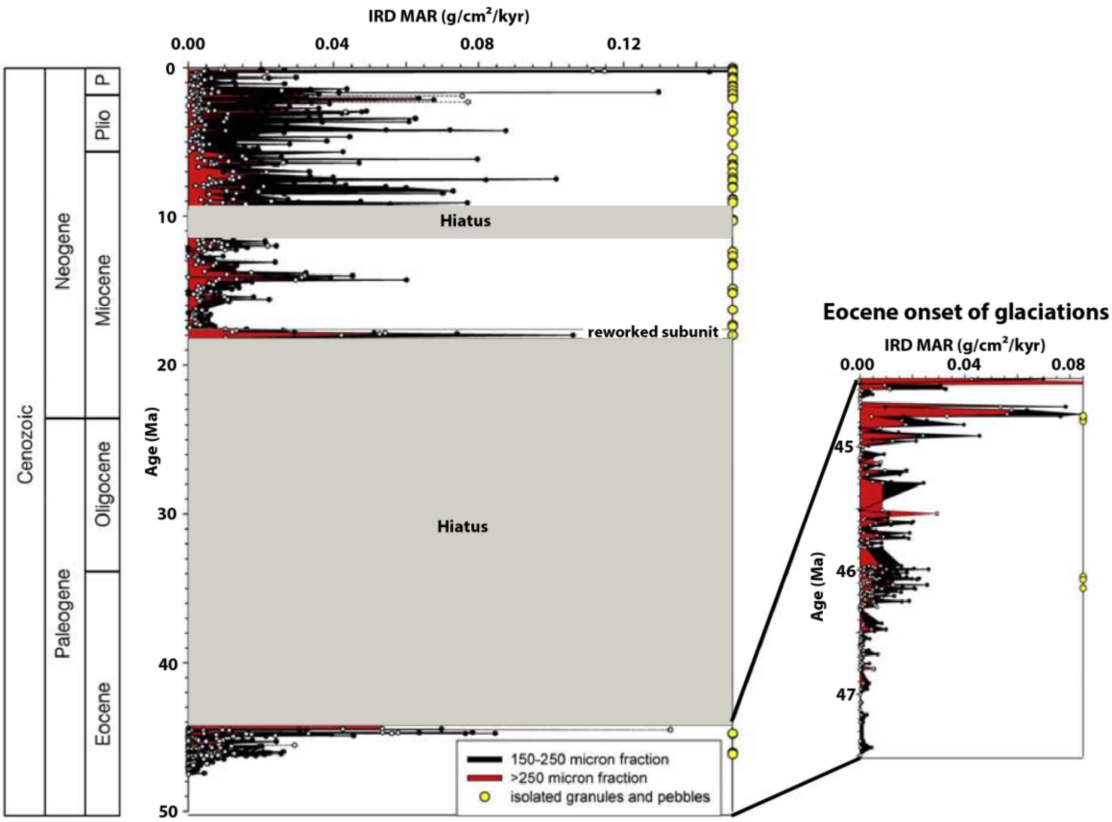

Figure 1.6. Ice-rafted debris mass accumulation rate record from the Integrated Ocean IODP Site 302 in the central Arctic (after St. John, 2008).

1.2.2. Amplified warming in the Northern high latitudes during the Pliocene

The United States Geological Survey's Pliocene Interpretation and Synoptic Mapping (PRISM) Sea Surface Temperatures (SST) reconstruction PRISM3 based on a large data set of temperature proxy estimates displays little differences in low latitude SST compared to present day (Figure 1) (Dowsett et al., 2011; Dowsett et al., 2012). However, temperature anomalies appear to increase with latitude (Dowsett et al., 2011; Dowsett et al., 2012; Naish and Zwartz; 2012). Amplification in temperature during the Pliocene, based on SST reconstructions (PRISM3), is supported by a similar trend in the distribution of land plants (Ballantyne et al., 2010; Salzmann et al., 2011; Brigham-Grette et al., 2013).

Multi-proxy SST and terrestrial paleotemperature data sets from the Canadian high Arctic demonstrate good agreement and estimate land temperatures were warmer than modern during the Pliocene with a perennially ice-free Arctic Ocean (Ballantyne et al., 2010; Dowsett et al., 2012; Ballantyne et al., 2013). The zonal distribution of vegetation in the Arctic and sub-Arctic latitudes demonstrates one of the most prominent responses to mid-Pliocene warmth (Salzmann et al., 2011). The modern tundra vegetation that dominates the Northern high latitudes at present was replaced by taiga forests dominated by *Picea* and *Pinus* inferring temperatures approximately 19°C warmer than modern (Salzmann et al., 2011). A 30% reduction in the Greenland Ice Sheet (GIS) (Dolan et al., 2011) allowed for taiga forest to reach as far north as 82°N during the Late Pliocene (3.6-2.58 Ma) (Salzmann et al., 2011). Furthmore, pollen and biogenic silica records from Lake El'gygytgyn in northeastern Arctic Russia suggest summer temperatures were ~8°C warmer and ~400mm/year wetter with greater seasonal productivity from 3.6 to 3.4 myr ago compared to modern (Figure 1.7) (Brigham-Grette et al., 2013).

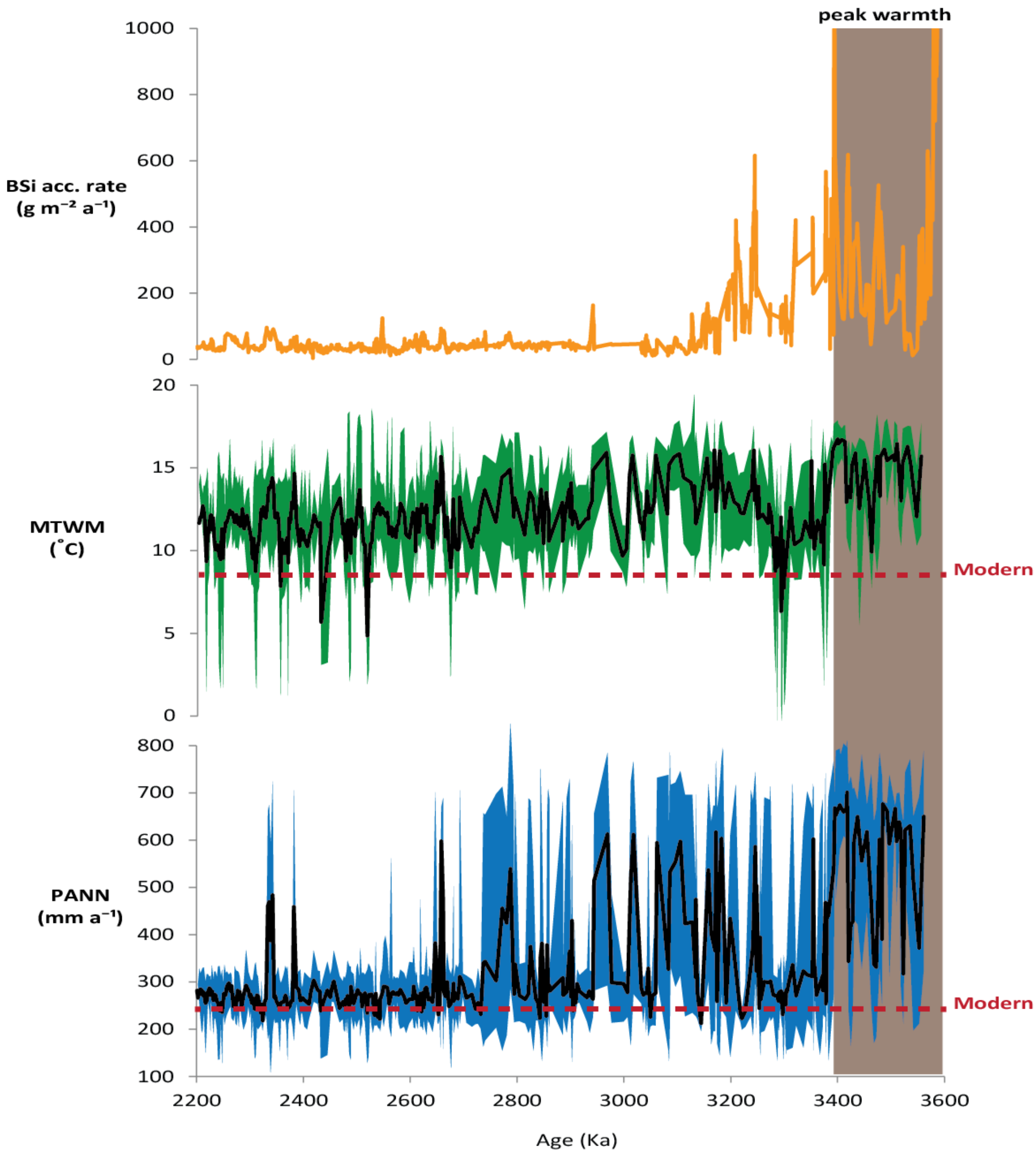

Figure 1.7. Lake El'gygytgyn biogenic silica accumulation rate (BSi acc. rate), reconstructions of mean temperature of the warmest month (MTWM) and annual

precipitation (PANN) based on pollen data (Brigham-Grette et al., 2013). Peak warmth is highlighted in grey/brown.

1.2.3. North Atlantic Ocean circulation

The Arctic and high Northern Hemisphere oceans are considered to play a critical role in the global climate system evolution of the Pliocene-Pleistocene. Large-scale overturning ocean circulation in the North Atlantic during the Pliocene is considered to have been similar to modern, although several key tectonic and sea level shifts are suggested to have important consequences for ocean circulation and moisture transport (Matthiesen et al., 2008). The initial opening of the Bering Strait during the late Miocene (5.5 to 5.4 Ma), partial closing of the Indonesian Seaway (~5.2 to 3.8 Ma) and shallowing of the Central American Seaway (CAS) (~4.6 Ma) all potentially impacted the heat and salinity gradients between the Pacific, Atlantic and Arctic Ocean Basins. This would have impacted water mass transport from the equatorial Atlantic into the North Atlantic potentially enhancing the formation of Northern Component Water (NCW), the precursor to NADW (Srinivasan and Sinha, 1998; Haug and Tiedemann, 1998; Cane and Monlar, 2001; Haug et al., 2001; Gladenkov, 2006; Steph et al., 2010).

According to ice volume reconstructions (Lisiecki and Raymo, 2005), sea level during the Early Pliocene was higher than modern, negating some of the changing physical bathymetric barriers for water mass exchange between the Arctic Ocean Basin and the North Atlantic (Poore et al., 2006; Haley et al., 2008; Matthiessen et al., 2009). However, the bathymetry along the Greenland-Scotland Ridge during the Pliocene has been estimated to be several hundreds of meters lower than its modern elevation due to isostatic effects related to mantle dynamics, specifically in relationship to temperatures associated with the Icelandic hotspot (Wright and Miller, 1996; Poore et al., 2006; Robinson et al., 2011). Combined with sea level highstands, a deeper bathymetry along the Greenland-Scotland Ridge would allow for greater deep water overflow from the Nordic Seas into the North Atlantic, consequently increasing NADW formation rates (ie. Enhanced North Atlantic overturing) and more northward penetration of warm saline North Atlantic surface waters to deliver moisture into the Arctic Ocean. This process in turn would have enhanced heat flow and ultimately moisture supply to the area (Henrich et al., 1989; Poore et al., 2006; Haley et al., 2008). Additional deepening of the Iceland-Faroe Ridge resulted in an increase in the strength and northward extension of surface currents bringing warm surface water into the Arctic Ocean as well as increasing the production in addition to the export of warmer deep water (Robinson et al., 2011).

The North Atlantic benthic oxygen isotope record recovered from VØring Plateau, while discontinuous, reflects distinct glacial excursions in the past 6.5 Ma indicating large ice volume fluxes and/or variation in bottom water temperatures (Fronval and Jansen, 1996). Continuous and strong outflow of NADW is documented to have taken place prior to 3.0 Ma from both benthic $\delta^{13}C$ records (i.e., Billups et al., 1997; Kwiek and Ravelo, 1999; Ravelo and Andreasen, 2000), Nd and Pb isotopes in ferromanganese nodule records (Frank et al., 2002), and percent $CaCO_3$ inferring a significant lowering of the calcite-lyscocline in the western equatorial Atlantic (Figure 1.7a) (King et al., 1997). A reduction of outflow and shift to shallower depths are suggested to have taken place after 3.0 Ma, in particular at 2.7 Ma, coinciding with the build-up of the Northern Hemipshere ice sheets as a result of enhanced production of the analogous Glacial North Atlantic Intermediate Water (GNAIW) (Figure 1.8b) (Boyle and Keigwin, 1987; de Menocal et al., 1993; Oppo and Lehman, 1995; Billups et al., 1997; Oppo et al., 1997; Marchitto et al., 1998; Oppo and Horowitz, 2000; Ravelo and Andreasen, 2000; Frank et al., 2002).

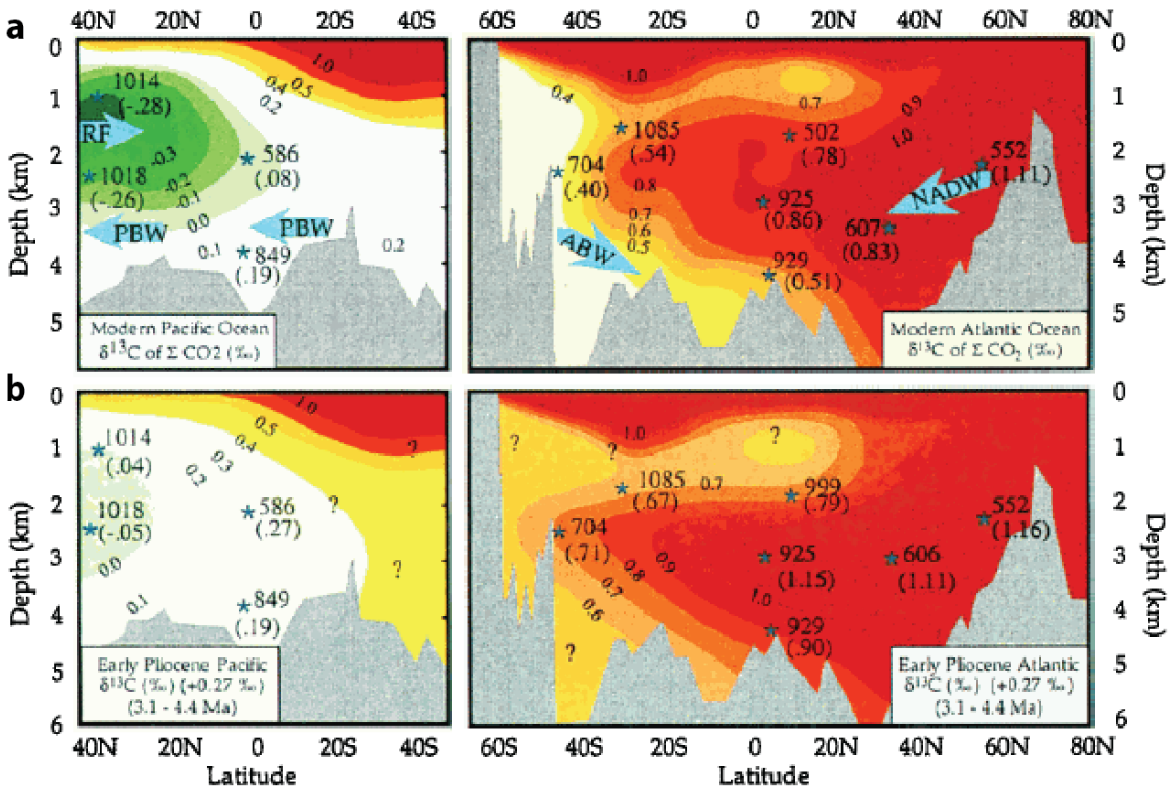

Figure 1.8. Contours demonstrating enhanced NADW export during the Pliocene compared to modern. The distribution of modern $\delta^{13}C_{DIC}$ and interglacial values of $\delta^{13}C_{CALCITE}$ for the last 0.5 Ma (a) as well as contours of discrete average $\delta^{13}C_{CALCITE}$ values for the Early Pliocene (b) (from Ravelo and Andreasen, 2000). ABW = Antarctic Bottom Water, PBW = Pacific Bottom Water and RF = return flow a mixture of PBW and ventilated North Pacific Intermediate Waters.

1.2.4. The equatorial Pacific warm pool and proposed mechanisms

While the global climate during the Pliocene was relatively warmer than today, it was also wetter, and is reflected in the vegetation of Australia and Africa during that time (Salzmann et al., 2011; Zhang et al., 2013). Areas currently occupying deserts today consisted of expanded temperate and boreal zones as well as tropical forest and savannas (Salzmann et al., 2011) Global circulation models predict an enhanced hydrological cycle with implications for monsoon systems (i.e., East Asian Summer Monsoon) (Haywood et al., 2013). However, these models contain reasonable large inter-model variability (Haywood et al., 2013). A shift to more arid conditions similar to modern day (i.e., Australia and Africa) is thought to be associated with the evolution of oceanic-atmospheric circulation during the Pliocene (Salzman et al., 2011; Fedorov et al., 2010; 2013).

Fedorov et al., (2013) used SST proxies (Mg/Ca and the alkenones; U^{K}_{37}) to infer the Atlantic, Pacific and Indian tropical ocean temperatures were similar to modern at ~29°C. However, these data also point towards two prominent differences of Early Pliocene climate relative to today: 1) a reduced equator-to-pole temperature gradient; and 2) a reduced zonal (east-west) SST gradient along the equator (~1°C or less) (Figure 1.9) (Fedorov et al., 2013), both in the eastern Atlantic (Dekens et al., 2007; Marlow et al., 2000), and Pacific oceans (Wara et al., 2005; Robinson et al., 2011). The reduced zonal SST gradient of the Pacific has been referred to as a “permanent El Niño like” state (Wara et al., 2005). Understanding the mechanisms driving such a situation is imperative as it has implications for meridional heat transport as well as for testing climate sensitivity in a higher atmospheric CO_2 world (Fedorov et al., 2013). However, debate has ensued mostly on mechanisms driving such a scenario (Fedorov et al., 2013). Proposed mechanisms for the Pacific warm pool as well as the transition into the modern eastern equatorial cold pool setting with a shallow thermocline includes tectonic configurations, atmospheric CO_2 concentrations, atmospheric circulation as well as ocean circulating and mixing (i.e., Raymo, 1994; Crowley, 1996; Monler, 2008; Steph et al., 2010; Fedorov et al., 2010).

The North American Cordillera, South American Andes and Tibetan Plateau had developed into their near modern state by the Early Pliocene (Harrison et al., 1992; Molnar et al., 1993; Cane and Molnar, 2001; Hartley, 2003; Dickinson, 2004; Dowsett et al., 2011). The establishment of these topographic highs, particularly the Tibetan Plateau, is important as they have roles in regional climate systems such as, influencing atmospheric circulation patterns and differential heating between the ocean and atmosphere. These regional climate systems have a strong effect locally and far field (i.e., Asian Monsoon). However, since these topographic highs had already achieved their basic modern configuration by the start of the Pliocene, they alone cannot account for the large-scale stable trends observed in the equatorial Pacific. That said, two prominent tectonic events, that occurred during the Pliocene and suggested to have influenced the climate system through re-routing ocean-atmosphere circulation, were the closures of the CAS (4.7 to 4.2 Ma) and constriction of the Indonesian seaway (4.0 to 3.0 Ma) (Haug et al., 2001; Cane and Monler, 2001; Steph et al., 2010).

Molnar (2008) summarized evidence surrounding the exact timing of the closing of the CAS in order to assess its role in enabling continental ice sheets to develop over North America and Fennoscandia. While geological evidence of crustal thickening infers deep water circulation between the Caribbean and Pacific Oceans vanished by ~7 Ma, the "Great American Exchange" commonly used to constrain the timing of final closure, did not occur until 2.7 to 2.6 Ma. However, Molnar (2008) argues that climate change enabled this migration with expansion of North Hemisphere ice sheets being a requirement as aridification of Central America and episodes of lower sea level allowed for savannah-dwelling vertebrates to pass through that region. Furthermore, paleoclimatic evidence from benthic and planktonic fossil assemblages as well as isotope ($\delta^{18}O$ and $\delta^{13}C$) data infer cooling before 2.7 Ma. Thus, while the exact timing of the closure of the CAS is not defined, all paleoenvironmental change can be attributed to climatic events rather than the closure itself (Molnar, 2008).

Steph et al., (2010) interpreted from planktonic foraminiferal $\delta^{18}O$ and Mg/Ca-derived temperatures, alkenone SSTs estimates, opal accumulation rates, and benthic foraminiferal $\delta^{18}O$, that closure of the CAS initiated an increase in meridional overturning circulation as a result of increased production of warm saline waters in the Caribbean with shoaling of the thermocline in the eastern tropical Pacific between 4.8 to 4.0 Ma, i.e. more than a million years prior to the intensification of North American glaciation. Additional feedbacks involving orbital nodes (i.e., low astronomical forcing) have been proposed to help maintain shoaling of the thermocline until reaching the modern persistent appearance of the eastern equatorial cold tongue (Maslin et al., 1998; Steph et al., 2010). This age estimate is in good agreement with previous studies inferring the Caribbean and eastern tropical Pacific became sensitive to an obstructed seaway prior to 2.7 Ma (e.g., Keigwin, 1978, 1982; Keller et al., 1989; Haug and Tiedemann, 1998; Marlow et al., 2000; Mudelsee and Raymo, 2005; Wara et al., 2005; Groeneveld et al., 2006; Dekens et al., 2007; Lawrence et al., 2006; Steph et al., 2006).

The restriction of the Indonesian seaway, with a northward shift of New Guinea, may have switched the source of flow through the seaway from warm south Pacific to relatively cold north Pacific waters (Cane and Monlar, 2001). Such a situation is considered to have led to the aridity of east Africa through a decrease in SST in the equatorial Pacific acting to reduce meridional atmospheric heat transport and fuelling global cooling (Cane and Monlar, 2001).

Investigating the relative importance of tectonic, oceanographic and atmospheric forcing, Lunt et al., (2009) highlight that declining atmospheric CO_2 concentration was the primary forcing for Late Pliocene cooling and initiating growth of the GIS. To simulate mechanisms for the warm Pliocene state, Lunt et al., (2010) used a coupled atmosphere-ocean general circulation model with a prescribed 400 ppm atmospheric CO_2 concentrations using PRISM3 land surface boundary conditions. While output displayed a change in global mean temperatures around 3°C, approximately half of the warming was driven by CO_2, with lower orography (i.e., North American Cordillera) and reduced land albedo (i.e., a smaller GIS) accounting for the rest. Notably, their model did not reproduce the permanent El Niño concept for the equatorial pacific region.

Through positive feedbacks relating to tropical cyclones vigorously mixing the upper ocean, modelling experiments demonstrate how such a mechanism could result in permanent El Niño-like conditions (Fedorov et al., 2010). A polaward expansion of the equatoral warm pool is inferred to have enhanced hurricane activity throughout the subtropical Pacific (Fedorov et al., 2010). Tropical storms can suppress the ocean mixed layer to as deep as 120-200 meters (Jacobs et al., 2000; D’Asaro, 2003; Korty et al., 2008). Such strong vertical mixing leads to further warming of the eastern equatorial Pacific and deepening of the tropical thermocline which only invigorates the process more (Fedorov et al., 2010). Earth system model experiments, Fedorov et al., (2013) highlighted not only the importance of feedbacks related to ocean mixing, but also extratropical processes such as the distribution of less reflective (low cloud albedo) low lying clouds (e.g., Barreiro and Philander, 2008) to be integrated into any explanation of Pliocene warmth.

Extratropical processes through oceanic and atmospheric circulation are also suggested to have had a strong influence on the equatorial Pacific warm pool and the emergence of the modern cold tongue (Chiang and Bitz 2005; Lee and Poulsen, 2006; Barreiro and Philander, 2008; Martínez-Garcia et al., 2010; McKay et al., 2012). It has been proposed a reduction in cloud cover south of 35°S can reduce albebo and promote local deepening of the thermocline (Barreiro and Philander, 2008). In other words, the increase in short wave energy due to a reduced albedo decreases the heat loss in the high latitudes by decreasing the loss of sensible heat flux from the ocean. The equatorial thermocline deepens in order to recover and balance the heat budget (Barreiro and Philander, 2008). Southern Hemisphere cooling with the development of extended sea ice fields lasting longer seasonally, and the role this process has on the formation of dense cold bottom and deep water (i.e., AABW) as well as atmospheric circulation, such as the displacement of the Intertropical Convergence Zone (ITCZ), near the end of the Pliocene has been suggested to help drive the equatorial pacific into the emergence of the modern cold tongue (Chiang and Bitz, 2005; Lee and Poulse, 2006; Barreiro and Philander, 2008; Martínez-Garcia et al., 2010; McKay et al., 2012).

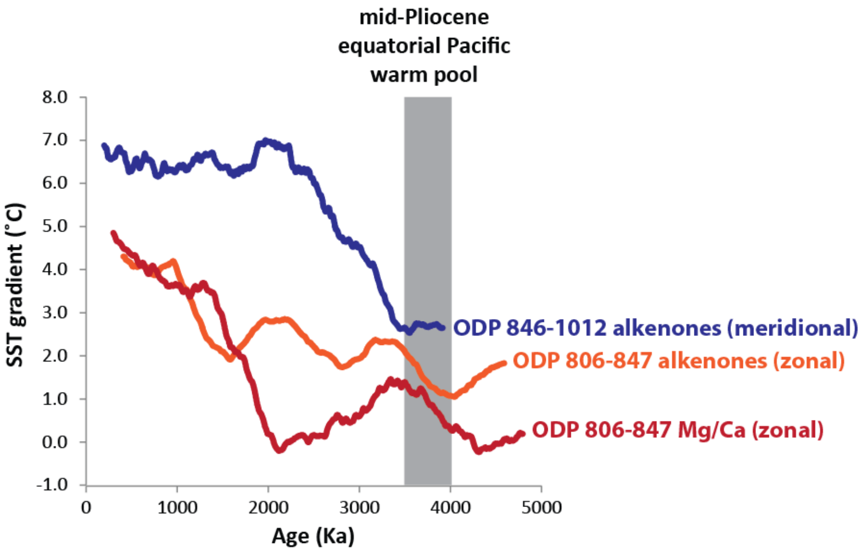

Figure 1.9. Proxy records inferring reduced meridional and zonal Sea Surface Temperatures gradients in the equatorial Pacific during the mid-Pliocene (Fedorov et al., 2013). ODP sites 846 (3°S 90°W) and 847 (0° 95°W) located in the eastern equatorial Pacific Ocean; ODP Site

1012 (32°N 118°W), off the western coast of North America; and ODP Site 806 (0°N 159°E), western equatorial Pacific Ocean.

1.2.5. East Antarctica and the Southern Ocean during the warm Pliocene (5.332 to 3.330 Ma)

While the benthic oxygen isotope-based ice volume record suggests rapid cooling and expansion in the form of permanent ice sheets since the earliest Oligocene, an increase of ~1‰ during the Miocene at ~14 Ma is associated with the transition of a more stable EAIS (Zachos et al., 2001; Miller et al., 2005). The expansion of the EAIS and growth of marine based ice sheets to a more persistent state at ~14 Ma is supported in Southern Ocean surface temperatures proxies indicating a 7°C cooling (Shevenell et al., 2004). However, the extent of the EAIS during the Early to mid-Pliocene (5.3 to 3.0 Ma) has been heavily debated for over three decades. Whatever the exact extent was, interglacials of the warm Pliocene likely contained a marine-based ice sheet margin that was farther south than modern with a reduced sea ice field (Hambrey and Mckelvey, 2000, Whitehead et al., 2005 Quilty et al., 2000). Whereas during glacial periods, the ice sheet margin extended northward although it remains uncertain if any of these advances approached LGM ice volume.

The existence of a trans-Antarctic seaway extending through the Wilkes and Pensacola basins, now covered by the EAIS, was argued due to the presence of reworked Pliocene aged open-marine diatom assemblages in the Sirius Formation (presently referred to as the Sirius Group; McKelvey et al., 1981) that crop out in the Transantarctic Mountains (TAM) (Figure 1.10a) (Harwood, 1983; Webb et al., 1984). These diatoms were hypothesized to have been deposited initially in an open marine environment. Subsequent ice sheet expansion during Pliocene eroded and transported these diatoms into glacial sediments deposited at high elevations within the TAM (Webb et al., 1984). According to the original hypothesis of Webb et al., (1984), such a reduction of the Antarctic ice sheet is consistent with Shackleton and Cita (1979)'s benthic oxygen isotope record from Deep Sea Drilling Project (DSDP) Site 397 inferring deep ocean temperatures were 1°C warmer than modern as a result of ice sheet reduction up to at least half of its modern size. The presence of fossilized wood and leaves of *Nothofagus beardmorensis* (Figure 1.10b) with a prostrate shrub habit within the Sirius Group is indicative of summer growing season temperatures in the range of 5°C, but with a mean annual temperature in the range of -12°C (Francis and Hill, 1996). Glaciolacustrine as well as glaciomarine sediments recovered from low lying margins of the EAIS in the Western

Ross Sea and in the Prydz Bay region highlight episodes of deglaciation with marine incursions into fjords, indicating that at the very least, there was some retreat of the marine-based margins of the EAIS relative to the present day (Barrett and Hambrey, 1992; Ishman and Reick, 1992; Hambrey and McKelvey, 2000).

A widespread deglaciation of the EAIS inferred by the Sirius Group interpretations of Webb et al. (1984) is contradicted by separate studies of terrestrial glacial deposits and geomorphology studies conducted in TAM, and by far-field proxy data. Oxygen and carbon isotope data recovered from the Subantarctic region by Kennett and Hodell (1993) challenge Shackleton and Cita (1979)'s record by indicating seasurface temperature during the warmest interval of the Pliocene increased by no more than ~3°C in which sea-level high stands were no more than 25 m above present. Landscape evolution of surficial sediment infers there was no EAIS overriding of the Dry Valley glacier system during the Pliocene as required by the Webb et al., (1984) mechanism to emplace marine diatoms in high elevated areas in which the Sirius Group crops out (Denton et al., 1993). Additionally, TAM geological outcrops indicate a permanent transition from wet-based to dry-based glacial deposition (Lewis et al., 2007), the extinction of the Antarctic tundra in the Transantarctic Mountains (Lewis et al., 2008), and the development of a hyperarid polar environment at this time (Marchant et al., 1996). However, while there is no evidence of large subglacial meltwater outburst floods at high elevation in the Transantarctic Mountains after 14 Ma (Lewis et al., 2006), late Miocene sedimentary sequences in Ross Sea drill cores (McKay et al. 2009), and outcrops in Prydz Bay contain glacimarine facies that indicate that significant discharge of sediment-laden subglacial meltwater from the low-elevation, marine termini of EAIS outlet glaciers persisted well into the late Miocene (11.6 to 5.3 Ma; Hambrey and Mckelvey 2000). Following work done by Stroeven et al., (1996), McKay et al., (2008) demonstrated the ability of katabatic winds to deposit diatoms through atmospheric transport as a potential mechanism of deposition for the Sirius Group diatoms, and thus can not be used as biostratigrahpic constraints. Furthermore, modelling exercises constrained by geological records do not support a largely deglaciated EAIS (Figure 1.10c) (Hill et al., 2007; Pollard and DeConto, 2009).

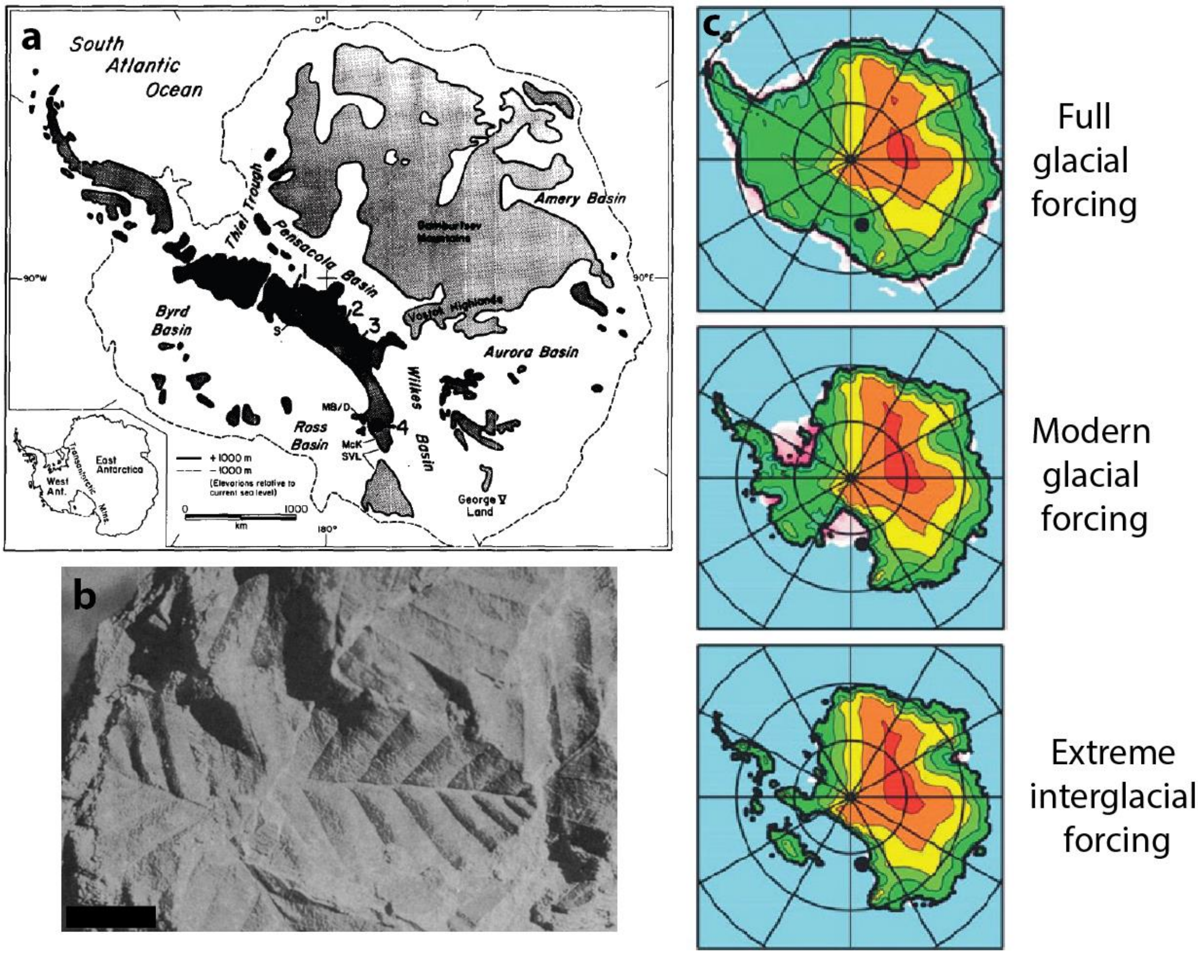

Figure 1.10. (a) Original map from Webb et al., (1984) showing topography of Antarctica with all ice removed and subsequent isostatic uplift (shaded areas indicate 1000 meters above and below present sea level) (after Drewry, 1983). The source of sediment for the Sirius Formation was inferred to lie within the Wilkes and Pensacola basins. Locations of Sirius Formation sediment: 1 = Wisconsin Plateau, Metavolcanic Mountain, Tillite Spur, quartz Hills, Reedy Glacier; 2 = Beardmore Glacier, Plunket Point, Dominion Range; 3 = Mt. Sirius; 4 = Mt. Feather, Table Mountain, Ferrar Glacier. (b) Fossil *Nothofagus* from the Sirius Group at Beardmore Glacier indicating a summer growing season in the range of 5°C (after Francis and Hill, 1996). Black scale bar equals 1 cm. (c) Range of ice sheet configurations over the last 5 million years using a coupled atmosphere-ice sheet model (from Pollard and DeConto, 2009). Black dot indicated the location of the ANDRILL AND-1B drill core site.

While the relative stability of the EAIS is still debated (summarized in Barrett, 2013), shipboard and shorebased drilling around the margin is helping to constrain the extent of the ice sheet as well as oceangraphic variations in the Southern Ocean. Phytoplankton records of silicoflagellate genera *Dictyocha* and *Distephanus* from ODP holes 748B and 751A on the southern Kerguelen Plateau suggest the Polar Front Zone (PFZ) was 900 km south of its present location with surface water warming of at least 4°C (Bohaty and Harwood, 1998). However, it should be noted that the complex bathymetry surrounding the Kerguelen Plateau potentially exaggerates the extent of latitudinal migrations of Southern Ocean frontal systems compared to other sectors of the Southern Ocean. Sediment records from ODP sites 1165 and 1166 from the Prydz Bay margin suggest latitudinal migrations of frontal systmes was associated with a 45% reduction in sea ice extent during the Early Pliocene and SST up to 5.5°C (Figure 1.11) (Whitehead and Bohaty, 2003; Whitehead et al., 2005). In the Wilkes Land sector of the East Antarctic margin, Escutia et al., (2009) indicated that relatively warm oceanic conditions prevailed to about 3.5 Ma. This inference is based on the increase in terrigenous sediment supply and silicoflagellate data that suggest warmer SSTs in the range of >5.6°C to 2.5°C reflecting reduced or no summer sea-ice with a retreated ice sheet margin during interglacials (Escutia et al., 2009).

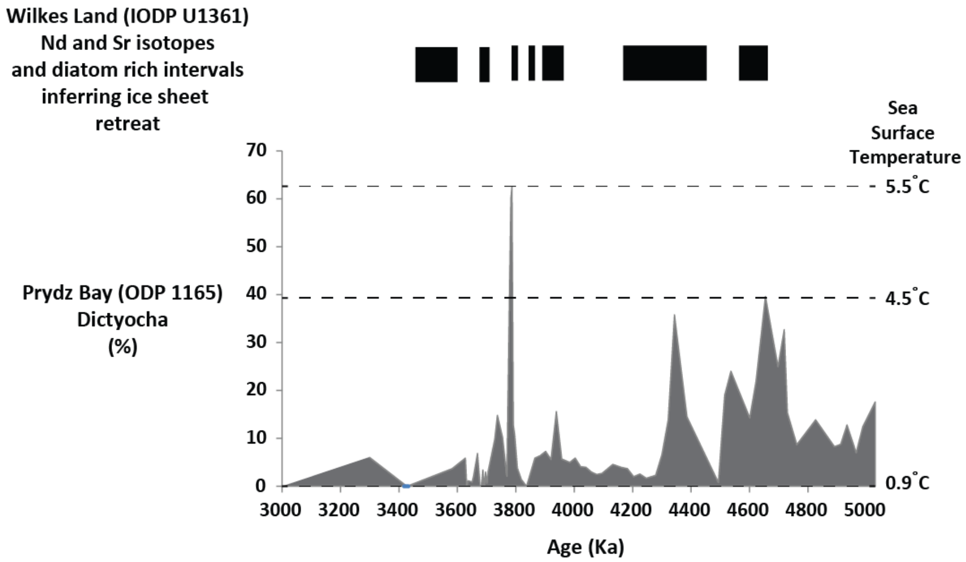

Figure 1.11. Provenence and productivity records inferring ice sheet retreats hundreds of kilometres inland (Cook et al., 2013) and the *Dictyocha* percent (unicellular marine phytoplankton) from Site 1165 in the Prydz Bay region of Antarctica (Whitehead and Bohaty, 2003) with interpreted sea surface temperature estimates based on Ciesielski and Weaver (1974).

Geochemical provenance data derived from IRD recovered at IODP Site U1361 highlights the potential for a dynamic response of the EAIS under varying Pliocene climatic conditions (Cook et al., 2013). Using radiogenic isotope compositions of neodymium and ($^{143}Nd/^{144}Nd$) and strontium ($^{87}Sr/^{86}Sr$), both of which vary compositionally in continental rocks on the basis of age and lithology, Cook et al., (2013) identified provenance signatures of two Pliocene sedimentary types. Sediments deposited within diatom-rich and highly productive intervals (warm intervals) resembled a compositional make-up associated with abundant Jurassic to Cretaceous intrusive sills (the Ferrar Large Igneous Province; FLIP). This provenance data, in conjunction with aerogeophysical data, infer the central portion of the

Wilkes Land Basin contains unconsolidated sediments of similar compositional make-up, suggesting sediment was sourced during multiple erosional events in which the current ice margin retreated, potentially 100's of kilometres inland (Figure 1.11) (Ferraccioli et al., 2009; Cook et al., 2013).

1.2.6. West Antarctic and Ross Sea variability during the Pliocene

The Antarctic Geological DRILLing program (ANDRILL) recovered a sediment core, AND-1B, in the western Ross Sea region of the McMurdo Sound. The core has a climate and glacial/marine history of the last 13 Ma that is paced by obliquity (40-kyr cycles) (Naish et al., 2009). The late Miocene and Early Pliocene glacial cycles of AND-1B contain subglacial diamictities interstratified with terrigenous-rich glacimarine mudstones, that pass upsection into an Early Pliocene sequence of diamictites alternating with open-marine diatomites with a progressively decreasing terrigenous component into the Late Pliocene. This decreasing terrigenous composition of interglacial sediment was interpreted by McKay et al., (2009) as representing a gradual cooling from a subpolar glacial regime (i.e. ablation dominated by meltwater processes) to a sediment-starved polar glacial regime (i.e. ablation dominated iceberg claving) (McKay et al., 2009). A 60-m thick diatomite deposited during the mid-Pliocene (3.6 to 3.4 Ma) contains reduced sea ice associated diatoms with a coevel occurance of subantarctic-subtropical diatoms. Additioanlly, sea surface temperature reconstructions based on TEX_{86} (tetraether index of lipids consisting of 86 carbon atoms) from this diatomite implies warmer oceanic and atmospheric conditions compared to modern during the Early Pliocene with a much reduced WAIS and coastal sea ice for multiple glacial to interglacial cycles paced by obliquity (Naish et al., 2009; McKay et al., 2012).

Foraminifera assemblages identified by the Dry Valley Drilling Project (DVDP) -10 and -11 indicate the Taylor Valley was at times an open marine fjord ranging from 300-900 meters water depth (Ishman and Reick, 1992). Lithofacies consisting of mudstone, sandy mudstone, fine sandstone, pebble conglomerate and minor diamictit suggest a glacial-marine environment distal to the grounding line (Powell, 1981; McKelvey, 1982). Furthermore, sedimentological evidence suggests Taylor Glacier did not advance to the mouth of Taylor Valley and sedimentation was influenced by local alpine glaciers during glacial minima (Levy et al., 2012). However, ice sheet advance across the Ross Sea in Taylor Valley occurred during peak glacial periods (McKelvey, 1982; Levy et al., 2012). Webb (1974) identified the Prospect Mesa Gravels in Wright Valley to contain abundant calcareous foraminifera and the extinct pectinid *Chlamys tuftensis* suggesting a fjord environment with bottom water temperatures between -2 to 5°C. From a sea-ice platform near the middle of Ferrar Fjord, the Cenozoic Investigation in the Western Ross Sea-2 (CIROS-2) drillcore recovered mudstone sediments rich with *in situ* diatoms indicating open marine conditions (Barrett and Hambrey, 1992). These sediments are overlain by glacier till with provenance indicating glacier flow from the Ross Sea suggesting expansion of marine based ice sheets in the Ross Sea occurred during glacial maximum in the Pleistocene (Barrett and Hambrey, 1992; Sandroni and Talarico, 2006).

Similar to the Prydz Bay and Ross Sea records, ODP Site 1095 from the Antarctic Peninsula region identifies warm episodes during the Early to mid-Pliocene (4 to 3.5 Ma) containing high concentration of siliceous microfossils with assemblages indicative of reduced sea ice field compared to modern (Escutia et al., 2009). While cold glacier periods are identified from laminated and structureless muds with silt mottles. The absence of bioturbation and the presence of undisturbed continous lateral laminations highlights the lack of benthic activity during these glacial periods. Additionally, structureless muds which lack of laminations indicates little to no shear stress at the sea floor bottom by either little influence gravity flows triggered by ice sheet advances across the shelf or weak bottom currents (e.g., weak AABW production) (Escutia et al., 2009). Overall, these glacial sediments are suggested to be warmer in character compared to late Quaternary sedimentary sequences identified by Pudsey and Camerlenghi (1998), Pudsey (2000), Lucchi et al., (2002), and Lucchi and Rebesco (2007). Furthermore, siliceous microfossil assemblages which indicate biogeographic constraints in Weddell Sea cores, is associated with widespread upwelling with reduced and less well developed local latitudinal gradient than those of today (Abelman et al., 1990).

Reconstructions of Pliocene sea-level based on far-field geological evidence suggest mean sea-level was up to 22+/-10 m higher than present (Miller et al., 2012) during the warmest interglacial highstands. Studies accounting for some degree of glacio-hydro isostatic contamination suggest polar region sea level estimates range between +5-25 m (Raymo et al., 2011) and imply not only a deglaciated GIS (Dolan et al., 2011) and WAIS (Naish et al., 2009; Pollard and DeConto, 2009), but also a significant meltwater contribution from the EAIS. Under the warmest Pliocene conditions this would consist of a GIS contribution of +7 m sea level-equivalent (SLE), a WAIS +3 m SLE and between +2-15 m SLE from the marine margins of the EAIS (Miller et al., 2012; Cook et al., 2013).

1.2.7. Expansion of the Antarctic Ice Sheet and Northern Hemisphere ice sheets during the Late Pliocene to Early Pleistocene cooling (~3.33 to ~2.0 Ma)

Sediment cores recovered around the Antarctic margin and Southern Ocean show a distinct step wise climatic and oceanographic shift that coincides with MIS M2 at ~3.33 Ma, and at ~2.7 Ma during the onset of Northern Hemisphere glaciation (Figure 1.12) (Lisiecki and Raymo, 2005). This step appears to be assoicted with a shift in the seismic stratigraphic architecture from the Antarctic Peninsula, Prydz Bay, Wilkes Land, Weddell Sea, Eastern and Western Ross Sea interpreted to reflect the coeval erosional events followed by progradation of the continental shelf and the development of sedimentary wedges at the mouth of ice troughs (Rebesco and Camerlenghi, 2008), although the age control on many of the cores used to constrain this event remains insufficient to determine if this event was truly coeval around the margin (e.g., Larter and Barker 2009). Various sediment cores highlight both a diachronous and gradual decrease in biogenic silica between 3.3 and 2.3 Ma as a result of an expansion of winter sea ice fields around the margin (Figure 1.12b) (Hillenbrand and Cortese, 2006). Modelling experiments demonstrate the need of a stable grounded ice sheet prior to development of sea ice (DeConto et al., 2007).

Sediment drift deposits on the continental rise at ODP sites 1101, 1096 and 1095 record glacial to interglacial cyclicity on the western Antarctic Peninsula. This suggests of small polythermal glaciers with calving of debris rich icebergs, abundant supraglacial debris, and melt water plumes occupied the margin between 3.1-2.2 Ma (Hepp et al., 2006; Cowan et al., 2008; Smellie et al., 2009). A significant change in sedimentation rates occurs after 3.0 Ma with higher Early Pliocene values of ~180 m/Ma reducing to ~80 m/Ma in the Late Pliocene and Pleistocene increasing sediment starvation in a cooling glacial environment (Hepp et al., 2006). Furthermore, a large mass wasting event, continental shelf erosion and the onset of a downlap surface at the base of the continental slope corresponding to the base of a seismic unit has been used to infer a regime shift with reduced subglacial meltwater discharge after 3.0 Ma (Rebesco and Camerlenghi, 2008). Sedimentological evidence suggests localized glacial advances to the shelf edge did not occur until 2.2 Ma (Cowan et al., 2008). However, it was not until 1.35 Ma in which glacials persistently reached the shelf edge which coincided with extended sea ice coverage (Cowan et al., 2008). Siliceous microfossils recovered from

ODP sites 1101, 1096 and 1095 further highlight the latitudinal expansion of the sea-ice field between 3.1 and 1.8 Ma (Hillenbrand and Futterer, 2002).

In the Weddell Sea, the prograding sedimentary wedge of the Crary Trough-Mouth Fan overlies a major seismic unconformity, that is overlain by downlapping strata at the base of the continental slope (Bart et al., 1999; Rebesco and Camerlenghi, 2008), and is believed to be associated with periodic glacial advance to the shelf edge in the Weddell Sea region (Rebesco and Camerlenghi, 2008). Large mass wasting events from slope failures as a result of glacial advances across the shelf, decreases in regional sedimentation rates as the depocenter for sedimention migrates towards the inner shelf due to the reverse slope shelf geometry formed in response to glacial advances, as well as in diatom abundance derived from ODP Site 693 coolectively suggests the onset of polar-style ice sheet expansion to the shelf edge at about 3.0 Ma (Kennett and Barker, 1990; Bart et al., 1999; Rebesco and Camerlenghi, 2008). Siliceous microfossils from sediment cores recovered along a north – south transect between Atlantic sector of the Agulhas Basin and the Antarctic continent as well as widespread disconformitites indicate drastic changes in ocean circulation patterns in response to Late Pliocene cooling at ~2.6 Ma (Abelmann et al., 1990). Responses to cooling include the steepening of latitudinal gradients and the formation of oceanic frontal systems (Abelmann et al., 1990).

Coincident with Southern Ocean cooling at ~3.6 to 3.3 Ma were ice advances in the Lambert Glacier-Amery Ice stream system resulting in the Prydz Channel Trough-Mouth Fan, as recorded from Prydz Bay ODP Site 1165 (Whitehead and Bohaty, 2003; Cooper and O’Brien, 2004; Rebesco and Camerlenghi, 2008; Passchier et al., 2011). During the Late Pliocene-Early Pleistocene, the Lambert Graben-Prydz Bay transitioned from an environment with marine glaciers (lacking ice shelves) with ice cliff termini and high release of terrigenous sediment into the marine environment (3.86 cm/kyr), into a similar ice shelf configuration as present day with a lower rate of terrigenous deposition (1.28 cm/kyr). Currently, the Lambert Graben is fully covered by the Amery Ice Shelf, which is fed by numerious tributary glaciers draining 13% of the EAIS (Whitehead et al., 2006; Rebesco and Camerlenghi, 2008; Passchier, 2011). Ice advances to the shelf edge and progressive deepening of the inner shelf continued into the middle to Late Pleistocene (Hambrey et al., 1991; Theissen et al., 2003; O’Brien et al., 2007).

Drilling in the McMurdo Sound region of the Ross Sea also highlights a significant environmental change at ~3.4 Ma in the Ross Embayment (Levy et al., 2012). Based on the chronology of glacier moraines (Staiger et al., 2006) and provenance data in CIROS-2 (Sandroni and Talarico, 2006), Levy et al., (2012) suggest outlet glaciers from the EAIS did not flow down Ferrar Valley until 3.4 Ma as a result of climatic cooling and ice sheet expansion. A lithofacies change in DVDP -10 and -11 cores at 3.4 Ma infers a shift in depositional environments (McKelvey, 1981; Powell, 1981). Prior to 3.4 Ma, lithofacies contain sandy mud, pebble gravel and breccia inferring distal glacial conditions with icebergs and floating tongues (McKelvey, 1981; Powell, 1981). Whereas, after 3.4 Ma, lithofacies consists of coarse clastic facies with pebble diamicitie, interbedded pebble gravel and breccia suggesting a proximal glacial setting with periodic grounded ice over the drill site (McKelvey, 1981; Powell, 1981). Furthermore, a shift in foraminifera faunal asssemblages indicates a shallowing in water depth during the Late Pliocene (Ishman and Reick, 1992). The deeper water, offshore record of AND-1B from the McMurdo Sound region, contains a transition in facies successions that suggest a distinct change in glacial regime after the M2 glaciation at 3.33 Ma (McKay et al., 2009). The progressive up-section thinning of outwash facies marking the transition between subglacial to open-marine conditions suggests a decrease in meltwater influence as a result of a transition towards an increasinlgy sediment-starved polar glacial thermal regime, that by ~2.6 Ma ultimately culminating in extensive summerl sea ice, and after ~1.0 Ma the Ross Ice shelf persisting through most interglacial periods (Figure 1.12a) (McKay et al., 2009; McKay 2012b).

Antarctic ice sheet growth and Southern Ocean cooling during the Late Pliocene is suggested to play an important role in the development of the bipolar world (McKay et al., 2012). Major cooling in the Ross Sea at ~3.3 Ma (McKay et al., 2009; Naish et al., 2009; Levy et al., 2012) also coincides with oceanic cooling and glacial expansion in the Prydz Bay, Antarctic Peninsula and Weddell Sea regions (i.e., Abelmann et al., 1990; Rebesco and Camerlenghi, 2008; Escutia et al., 2009). This coeval cooling of the ice sheet and a stepwise expansion of the sea ice field around the margin to enhance AABW formation from 3.3 to 2.5 Ma (Hillenbrand and Cortese, 2006; McKay et al., 2012), has been postulated to increase the upwelling of colder waters in lower latitudes (i.e., eastern equatorial Pacific) and reduce heat transport to the Northern Hemipshere (Lawrence et al., 2006; McKay et al., 2012). Stable isotope records ($\delta^{13}C$, $\delta^{18}O$) from the Ceara Rise ODP sites 925 and 929 are interpreted to represent a reduction in the formation of warm saline NCW and extension of colder Southern

Component Water (SCW) (AABW precursor) after ~3.4 Ma (Billups et al., 1997). Convergence of Southern Ocean interbasinal $\delta^{13}C$ gradients to more enriched values (negative) (Figure 1.12c), coinciding with increased sea ice cover around the margin (Figure 1.12b), acting to lower preformed $\delta^{13}C$ values in the Ross Sea due to less exposure time at the surface is consistent with polynya style mixing and the formation of AABW (McKay et al., 2012) at ~2.7 Ma. This infers enhanced surface water stratification in response to sea ice formation around the margin acts to decrease upwelling and ventilation of deep waters in the Southern Ocean (Hodell and Venz-Curtis, 2006). Ultimately this scenario would have acted as a positive feedback in reducing atmospheric CO_2 concentrations and heat transport preconditioning the high Northern latitudes for the onset of major glaciation at ~2.7 (Raymo, 1994; Haug et al., 2005; Hodell and Venz-Curtis, 2006; Lawrence et al., 2006; McKay et al., 2012).

Expansion of the Northern Hemisphere ice sheets at ~2.7 Ma is reflected in the widespread appearance of IRD in the North Atlantic/Baltic Sea (Figure 1.12d) (Jansen et al., 1996; Kleiven et al., 2002; Knies et al., 2009), significant cooling of the subarctic Pacific Ocean (Haug et al., 2005), IRD sourced from Northeast America (after 2.64 Ma) (Bailey et al., 2013), and glacial outwash plains in North America (Naafs et al., 2012). Sediment records from northeastern Russian Arctic demonstrate a step wise cooling with the first cold “glacial” facies at ~2.6 Ma with perennial summer lake ice becoming common after 2.3 Ma (Brigham-Grette et al., 2013).

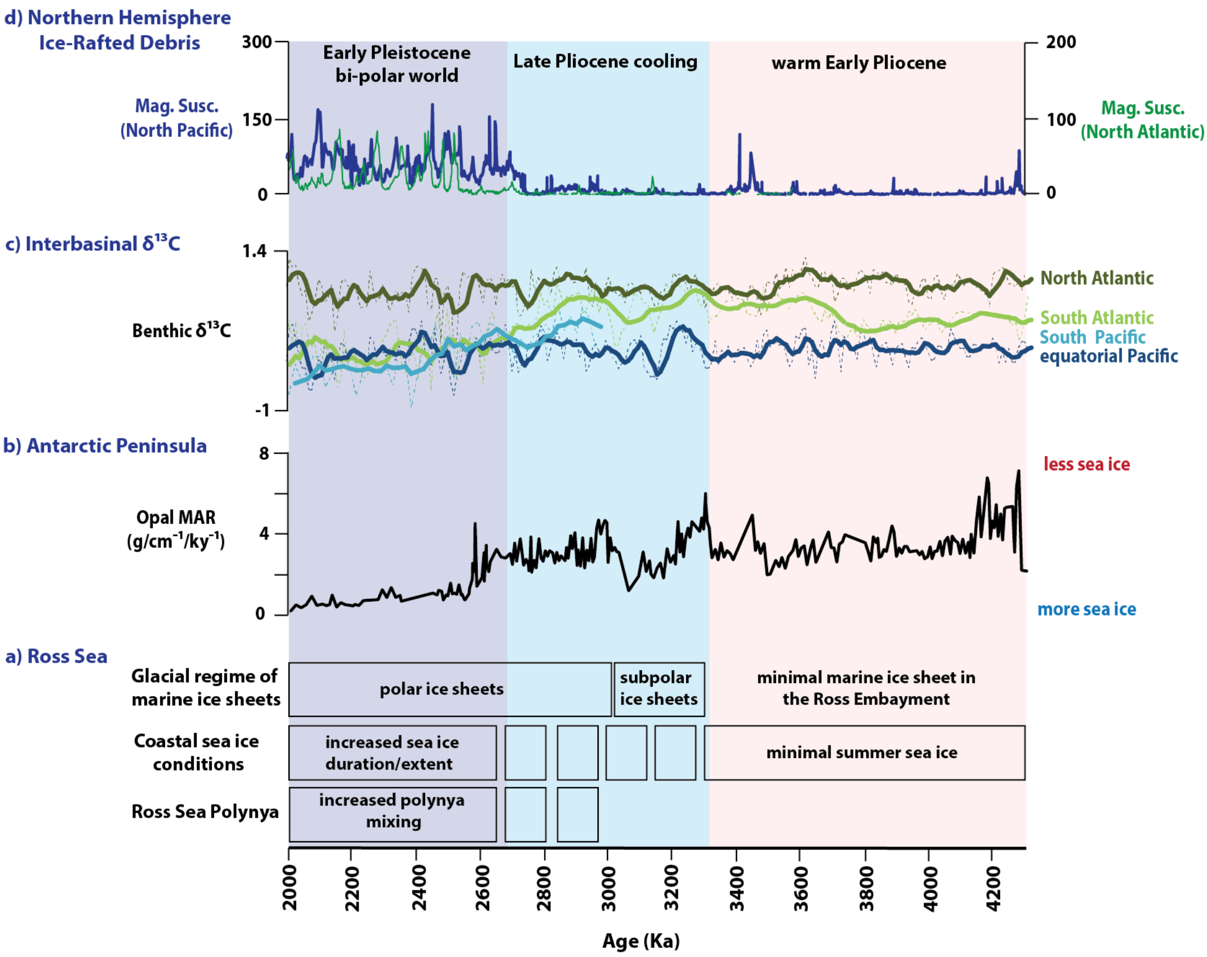

Figure 1.12. Step wise Late Pliocene cooling into the Early Pleistocene bi-polar world. (a) Thermal regime of the WAIS as inferred from the AND-1B sediment record (McKay et al., 2012). (b) Opal MAR from the Antarctic Peninsula region (Hillenbrand and Cortese, 2006). (c) Interbasinal $\delta^{13}C$ gradients (Hodell and Venz-Curtis, 2006; Waddell et al., 2009). (d) North Atlantic (Jansen et al., 1996) and North Pacific (Haug et al., 2005) IRD records.

CHAPTER 2

PLIOCENE-EARLY PLEISTOCENE SEDIMENTATION PROCESSES AND STRATIGRAPHY FOR IODP SITE U1361 DRILL CORE RECOVERED OFF THE WILKES LAND MARGIN, EAST ANTARCTICA

This chapter presents a sedimentation model for the Pliocene to Early Pleistocene (4.3 to ~2.0 Ma) interval of a continental rise drill core (Site U1361) that was recovered off the Wilkes Land margin of the East Antarctic Ice Sheet during IODP Expedition 318. The Pliocene record contains 14 lithological cycles consisting of interbeds of two lithofacies: 1) diatom-rich/bearing mudstones; and 2) massive and laminated mudstones. These lithofacies are consistent with pre-existing sedimentation models in distal channel-levee systems and infer glacial advances and retreat across the continental shelf occurring over multiple glacial to interglacial cycles throughout the Pliocene. Glacial minima are associated with diatom-rich/bearing mudstones that are the result of increased productivity over the drill site with a homogenization of sediment texture due to the interplay of bioturbation and downslope currents. Massive and laminated mudstones infer glacial maxima events in which non-erosive low-density turbidites are deposited as a result of slope failures triggered from over steepend foreset strata on the continental shelf during glacial advances. Early Pleistocene lithological cycles become difficult to distinguish and generally consist of diatom-rich/bearing mudstones with reduced iceberg rafted debris compared to underlying strata, while silt lenses and mottles are more discontinuous suggesting enhanced bottom current reworking associated with ice sheet stabilization and increased delivery of highly oxygenated waters formed in the Mertz Polynya.

2.1. INTRODUCTION

Due to Antarctica's extended ice cover for the last 34 Ma, much of the late Cenozoic ice volume history is poorly understood. However, the integration of benthic $\delta^{18}O$ global ice volume records (e.g., Zachos et al., 2001; Lisiecki and Raymo, 2005) with seismic data profiles (e.g., Rebesco and Camerlenghi, 2008) in addition to land-based and ship-based geological drilling recovering sediment cores along the margin (e.g., Levy et al., 2012) have provided direct evidence of ice sheet development and oscillations in response to long-term trends in global climate occurring over millions of years (Zachos et al., 2001) as well as orbital timescales (Naish et al., 2001; Naish et al., 2009; McKay et al., 2012). However, direct records of Neogene and Quaternary Antarctic ice sheet variablity are sparse. Semi-continous drill core records are largely confined to the McMurdo Sound region in the Ross Sea (e.g., Barrett, 1989; McKay et al., 2009; Levy et al., 2012), Prydz Bay (e.g., Shipboard Scientific Party, 2001) and the Antarctic Peninsula (e.g., Barker and Camerlenghi, 2002; Cowan et al., 2008) leaving many unanswered questions concerning the relative stability of the marine-based sectors of EAIS during Pliocene (summarized in Barrett, 2013 and in Chapter 1 of this thesis).

At present, the EAIS is considered stable in terms of mass balance (Rignot et al., 2013), however, new bedrock topography data (Pritchard et al., 2012: Fretwell et al., 2012) reveal extensive margins grounded below sea level with landward deepening reverse slope troughs, which may be vulnerable to processes similar to that of the largely marine-based WAIS (Scherer et al., 2008; Naish et al., 2009; Pollard and Deconto, 2009; Pritchard et al., 2012; Rignot et al., 2013). While debate still surrounds the stability of the EAIS during the Pliocene, recent geochemical provenance of detrital material recovered off-shore of the Wilkes Land margin (IODP Site U1361), suggests the EAIS may have retreated several hundred kilometres inland between ~70°-74°S during the warmest Early Pliocene episodes between 5.3 to 3.3 Ma (Cook et al., 2013). Furthermore, proximal sedimentary records from the Ross Sea region show a periodic deglaciated WAIS paced by the 40-kyr cycles of obliquity (Naish et al., 2009). Far-field geological evidence suggests that during the warmest interglacial highstands mean sea level was ~20 m higher than present (Miller et al., 2012) and while containing some degree of glacio-isostatic contamination (Raymo et al., 2011), global mean sea-level estimates imply not only deglaciated Greenland Ice Sheet (GIS) and WAIS but also a significant meltwater contribution from the EAIS.

The Wilkes Land Subglacial Basin has been identified from airborne geophysical data (Pritchard et al., 2012) as well as through ice sheet simulations (Pollard and DeConto, 2009) to be sensitive to processes such as ocean induced warming, as it is grounded below sea level with a landward dipping reverse slope behind the present grounding line (Ross et al., 2012), and sea-level potential associated with marine-based sectors of the EAIS as a whole totals 19.2m (Fretwell et al., 2012). The IODP Expedition 318 to the Wilkes Land margin of the EAIS recovered a well-dated continuous continental rise sediment record spanning the Pliocene-Early Pleistocene from Site U1361. This record provides an opportunity to assess ice sheet sensitivity during the last time in Earth's history when atmospheric CO_2 concentrations were in the range of modern values (Jansen et al., 2007: Pagani et al., 2009; Seki et al., 2010). Furthermore, this time also experienced a relatively small increase in average global surface temperatures(+2-3°C) followed by global cooling and onset of Northern Hemisphere glaciation. Lithofacies associations and stratigraphy with proxy data time series have been used to reconstruct fluctuations during the Early Pliocene (~4.3 Ma) through the Early Pleistocene (~2.0 Ma). By integrating these data sets, interpretations have been made in regards to (1) a depositional model demonstrating extended periods of ice sheet retreat and advance across the shelf that highlight Southern Ocean boundary front migrations related to processing ice extent etc. (i.e., winds), and (2) provide evidence for a EAIS regime shift during Late Pliocene-Early Pleistocene cooling trend coincident with a 100 ppm drawdown in atmospheric CO_2 and 5°C cooling in the southern high latitudes (Pagani et al., 2009; Seki et al., 2010; McKay et al., 2012).

2.1.1. Setting and general depositional processes

IODP Site U1361 (64°24.5°S 143°53.1°E) is located on the lowermost continental rise of the Wilkes Land margin of East Antarctica and positioned on the east levee of the Jussieau submarine channel (Figure 2.1). The modern-day Wilkes Land margin of the EAIS is characterised by 20-30 m high marine-terminating ice cliffs and two major EAIS outlet glaciers, the Mertz and Ninnis. Sparse outcrop exposures along the coast reveal Precambrian igneous and metamorphic, and Mesozoic sedimentary, as well as intrusive rocks of Beacon (Devonian to Jurassic) and Ferrar (Jurassic) Groups (Anderson et al., 1980; Domack, 1982; Drewry 1983; Peucat et al., 1999; Escutia et al., 2011). At present Site U1361 sits ~2° of latitude (over 200 kms) south of the Antarctic Circumpolar Current (ACC) southern boundary, where Upper Circumpolar Deep Water (UCDW) upwells to the surface creating a zone of highly productive surface waters around the Antarctic margin (Bindoff et al., 2000). While under the influence of the westward flowing Antarctic Slope current, Site U1361 also lies immediately north of the Mertz Polynya, a region where the formation of up to 24% of the total Antarctic Bottom Water (AABW) around Antarctica occurs (Orsi et al., 1999; Bindoff et al., 2000; Williams and Bindoff, 2003; McCartney and Donohue, 2007; Williams et al., 2008). Brine rejection from sea ice growth in the Mertz Polynya results in the formation of High Salinity Shelf Water (HSSW), which ultimately passes down the continental slope in the form of plumes of cold and dense water over Site U1361, to form AABW, albeit with some mixing with overlying Modified Circumpolar Deep Water (MCDW) (Rintoul 1998). This process is discussed in detail in section 2.1.2.

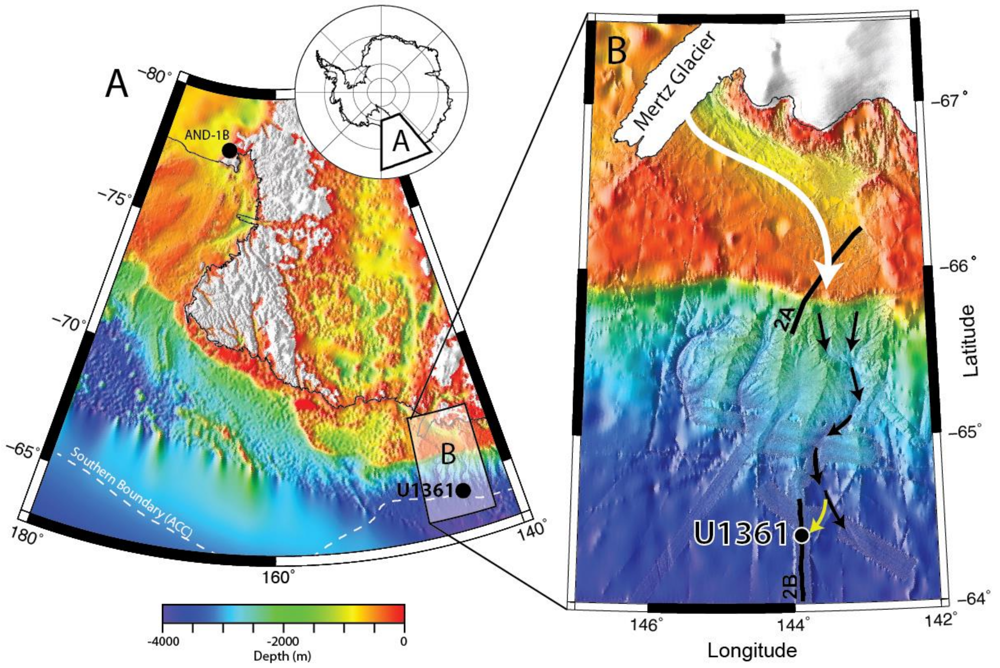

Figure 2.1. Location and bathymetry of the Wilkes Land margin (a) as well as Site U1361 (A-B). Also shown is the location of ANDRILL's Miocene-Pleistocene AND-1B core in the northwestern corner of the Ross ice shelf and the southern boundary of the ACC (a). The Mertz glacier tongue (prior to break up in 2009) and drainage path extending from the shelf to rise (B). Seismic reflection profile path 2A and 2B are represented with black solid line (B).

An integration of seismic surveys (1981-2000) and sediment cores (1975-2003) collected from the Wilkes Land margin has provided a foundation of Cenozoic ice sheet and sedimentation history (Figure 2.2) (Hayes and Frakes, 1975; Payne and Conolly, 1972; Domack, 1982; Eittreim et al., 1995; Escutia et al., 2000; De Santis et al., 2003; Donda et al., 2003; Escutia et al., 2003; Escutia et al., 2005; Caburlotto et al., 2010). These findings highlight continental shelf and rise linkages that consist of an interplay between downslope failures of mass wasting events (e.g., turbidity currents), downslope bottom current influences (deep water discharge) and Coriolis forcing (Escutia et al., 2005). Continental slope canyons act as the main conduit for turbidity currents transporting sediment from the outer shelf and slope to the continental rise, resulting in a complex network of tributary like channels (Eittreim et al., 1995; Escutia et al., 2000; Donda et al., 2003; Escutia et al., 2005). The fine-grained component of turbidity flow gets entrained by the westward flowing coastal current (or slope current) and deposits sediment on the eastern gentle slope of the ridges.

The position of Site U1361 on the east levee of the Jussieau submarine channel and on the lowermost continental rise allows for the preservation of low-density turbidite deposition, as the fine-grained material creates a non-erosive hemipelagic drape from inter and overflow processes, as erosion occurs mostly within the canyon system itself, as well as within and on ridges that are in higher reaches of this canyon (continental slope and upper continental rise) (Escutia et al., 2005; Escutia et al., 2011).

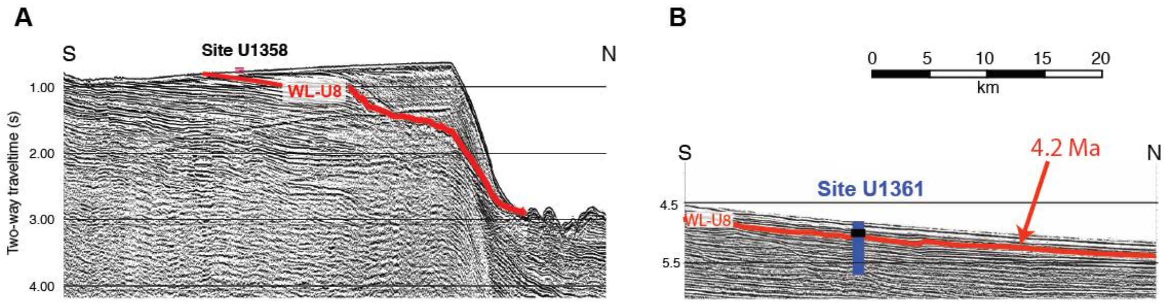

Figure 2.2. Seismic reflection profiles of the Wilkes Land continental shelf (A) and rise (B). Seismic unconformity WL-U8 is marked in red with IODP Exp. 318 shelf Site U1358 highlighted in red and rise Site U1361 highlighted in blue (after Escutia et al., 2011). See Fig. 2.1 for profile locations.

2.1.2. Adelie Land Bottom Water (ALBW) formation along the Wilkes Land margin, Antarctica

Site U1361 (64°24.5°S 143°53.1°E) at present sits south (~2° Latitudinally) of the southern boundary of the ACC where CDW upwells to the surface creating highly productive areas around the Antarctic margin (Bindoff et al., 2000). While under the influence of the westward Antarctic Slope current, Site U1361 lies north of the Adélie depression which is one of three major locations (Ross Sea and Weddell Sea) around Antarctica where AABW forms (Orsi et al., 1999; Bindoff et al., 2000; Williams and Bindoff, 2003; McCartney and Donohue, 2007; Williams et al., 2008). Adélie Land Bottom Water (ALBW) as well as the other two subsets of AABW, Ross Sea Bottom Water (RSBW) and Weddell Sea Bottom Water (WSBW), forms from atmospheric cooling, brine rejection from sea ice growth (i.e., polynyas), and ocean/ice shelf interactions. The cold high salinity density flows from the formation ALBW is significant in that they have potential to triger turbidity currents and post depositional processes such as sediment winnowing at Site U1361 (i.e, Baines and Condie, 1998).

In general, within the Adélie Depression is a broad clockwise circulation of Modified Circumpolar Deep Water (MCDW) flowing southward (144° E) along the Mertz Glacier Tongue and continues with a return westward flow along the coast with shelf waters exiting through the sill (143° E). The relatively warmer and fresher MCDW intrudes into the Adélie Depression in two places, the western section of the shelf break and to a lesser extent around the grounded icebergs north of the Mertz Glacier Tongue (Williams and Bindoff, 2003). Brine rejection occurs beneath the Mertz Glacier Polynya along the Mertz Glacier Tongue and in the coastal bays (e.g., Commonwealth, Watt and Buchanan) polynya regions. Due to brine rejection from sea ice growth (most dominant during April-September) in the polynyas, salinity and density increases (manily as a function of temperature) and erodes the MCDW signature in Adélie Depression (Bindoff et al., 2000; Williams et al., 2008). Through this process the formation of HSSW occurs. The contact of the densest HSSW with the base of the Mertz Glacier Tongue produces Ice Shelf Water (ISW) that ascends and provides a cold, freshwater signal in the upper shelf waters. Shelf waters (ISW and HSSW) at intermediate depths flow out of the Adélie Depression through the Adélie Sill. Williams et al., (2008) recorded the densest waters observed over the sill region and related it to the influence of additional brine rejection in the Commonwealth Bay polynya. This shelf water export results in the downslope transport of cold high salinity water masses resulting in bottom water production of AABW which as it flows westward along the Antarctic Slope Current, erodes the RSBW signal (Williams et al., 2008). The motion of high salinity density currents down the slope is suggested to be linked to an irregular motion and turbulence of bottom water resulting in a nepheloid layer with a maximum thickness of about 600m and 100km across in water depths of 3100 m (i.e., the continental rise) (Escutia et al., 2005).

The production of ALBW, while important to the understanding of the depositional processes at Site U1361, also has the potential to have a downstream affect related to the intensity and variability of AABW inflow into the southwest Pacific. ALBW flows along with the Antarctic Slope Current until it reaches the Kerguelen Plateau, it either continues westward, south of the Plateau, or flows north along the eastern margin. In the latter case, ALBW joins the path of the Australian-Antarctic Basin's cyclonic gyre, which is referred to as the Wilkes Land Gyre. After the ALBW merges with the Wilkes Land Gyre, the northern limb flows eastward, in which case in merges with the ACC (Figure 2.3). The ACC is responsible for delivery of AABW into the southwest Pacific Basin via the lateral mixing of water masses (i.e., AABW and LCDW) (Orsi et al., 1999; McCartney and Donohue, 2007; Williams et al., 2008).

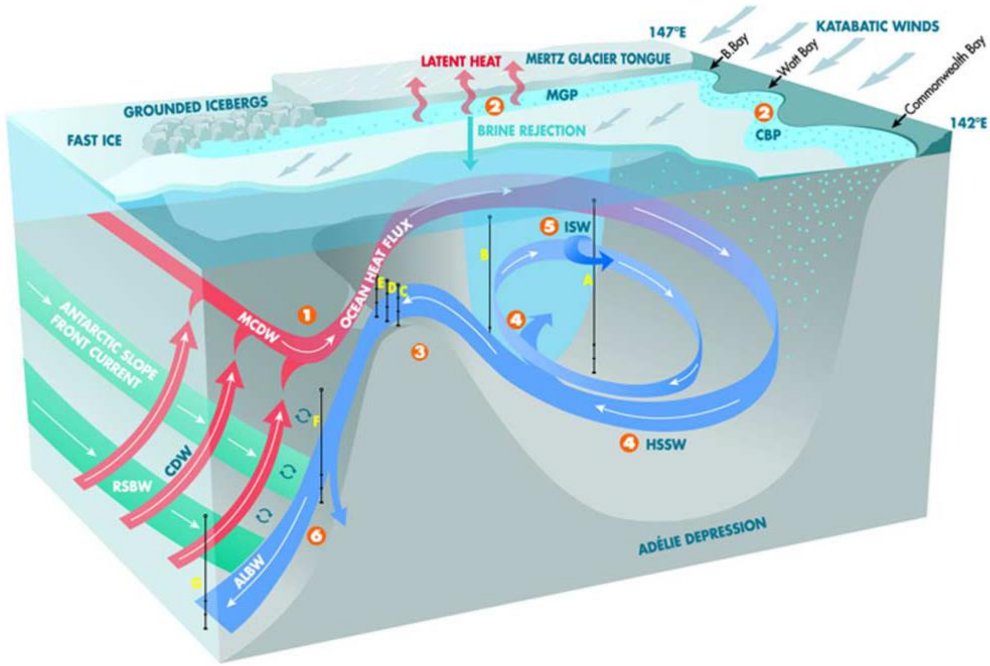

Figure 2.3. Adélie Land depression ocean circulation and the processes involved in the formation, as well as transportation of ALBW down the Antarctic slope (from Williams et al., 2008 Figure 3). Important to note the presence of the Mertz glacier tongue in this figure, as it has since broken away from the margin. 1 = inflow of MCDW into the Adélie Land depression, 2 = super cooling of MCDWand brine rejection of sea ice, 4 = formation of HSSW as a result of super cooling below the ice shelf and brine rection, 5 = formation of ISW, 3 = outflow ALBW over the sill and 6 = ALBW entrained into the Antarctic Slope Current and mixing/replacing RSBW.

2.1.3. IODP Site U1361 Chronology

The age model for the Site U1361 record was developed through an integration of biostratigraphic indicators (diatom, radiolarian, calcareous nannofossils and dinoflagellate cysts and magnetostratigraphy, and allowed the Gradstein et al., (2004) geological time scale (Table 2.1) (Tauxe et al., 2012). The age model of Site U1361 also highlights the continuous nature of the Plio-Pleistocene interval in Site U1361 (Figure 2.4) with long term sedimentation rates of ~30 m/m.y., and no major gaps. However, a single condensed interval is identified centred on 3.3 Ma. The Early Pliocene at ~4.2 Ma to Early Pleistocene at ~2.0 Ma contains no major core disturbances with only one major core gap extending between ~3.6 to ~3.33 Ma. The continuous and uniform nature of the Plio-Pleistocene sedimentation rates at Site U1361, combined with the detailed grain size analysis discussed in this chapter (see section 2.2.4) indicates that winnowing is not a major influence on sedimentation at this site. While many Antarctic records, even the more distal sites, are hindered by hiatuses and variable sedimentation rates, the continuous nature of Site U1361's age model is unprecedented when considering Antarctic marginal records and is more comparable to that of the orbitally-tuned bench mark studies from the equatorial Pacific records of ODP sites 846 and 849, than those from the Antarctic margin (e.g. Figure 2.4; Shackleton et al., 1995; Shackleton et al., 1995b, Florindo et al., 2003).

Table 2.1. Age model from Tauxe et al., (2012) based on magnetic polarity stratigraphy and is constrained by first (FO) and last (LO) occurrence of biostratigraphic indicators (diatoms, radiolarian, calcareous nannofossils and dinoflagellate cyst).

LO/FO	**Event**	**Average Age (Ma) GTS 2004**	**Upper Depth (mbsf)**	**Lower Depth (mbsf)**	**Median Depth (mbsf)**	**Depth uncertainity (m)**
	C2n (o)	**1.945**	**34.85**	**34.85**	**34.85**	**0.00**
	C2An.1n (y)	**2.581**	**49.70**	**49.75**	**49.73**	**0.02**
LO	*Thalassiosira insigna*	2.475	47.42	56.72	52.07	4.65
LO	*Thalassiosira inura*	2.54	47.42	56.72	52.07	4.65
FO	*Thalassiosira vulnifica*	3.15	65.02	66.15	65.59	0.57
FO	*Thalassiosira insigna*	3.25	64.52	66.15	65.34	0.82
LO	*Fragilariopsis weaveri*	2.49	56.72	64.04	60.38	3.66
	C2An.1n (o)	**3.032**	**64.55**	**64.60**	**64.58**	**0.02**
	C2An.2n (y)	**3.116**	**66.70**	**66.70**	**66.70**	**0.00**
FO	*Fragilariopsis weaveri*	3.53	72.54	75.12	73.83	1.29
	C2An.2n (o)	**3.207**	**71.67**	**71.72**	**71.70**	**0.02**
	C2An.3n (y)	**3.33**	**74.52**	**75.90**	**75.21**	**0.69**
	C2An.3n (o)	**3.596**	**77.45**	**77.50**	**77.48**	**0.02**
LO	*Eucyrtidium pseudoninflatum*	4.2	94.99	104.26	99.63	4.64
	C3n.1n (y)	**4.187**	**99.99**	**99.99**	**99.99**	**0.00**
	C3n.2n (o)	**4.631**	**109.68**	**109.68**	**109.68**	**0.00**

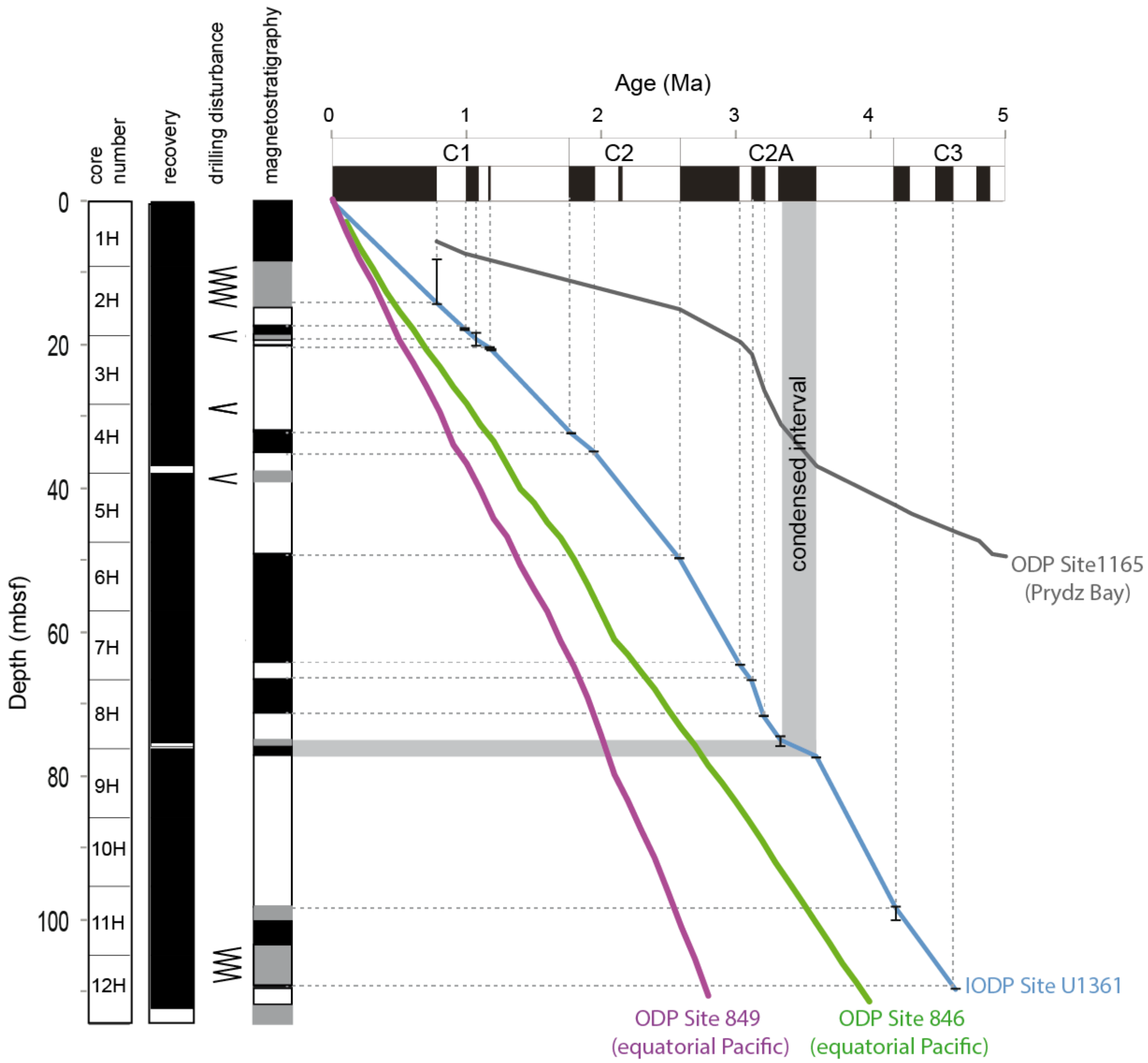

Figure. 2.4. Site U1361 magnetostratigraphic tie points, with error bars, following Tauxe et al., (2012), demonstrate the near continuous sedimentation for the Pliocene and Pleistocene Site U1361 record (blue). A condensed interval around ~3.3 Ma is highlighted. Core recovery and drilling disturbance are also displayed. The age model for Site U1361 is compared to other distal Antarctic records, with ODP Site 1165 used an example as it is generally considered to have the best Neogene record from the Antarctic Margin prior to drilling of Site U1361 (grey), as well as bench mark sites 846 (green) and 849 (purple).

2.1.4. Previous high latitude deep-sea channel levee/ridge depositional models

The interpretations of past glacial extent made in this chapter are established from sediment characteristics based on low-latitude model of deep-water fine-grained sediment facies types as well as previously published model of high latitude deep-sea glacimarine sediment models. Seismic survey studies along the Wilkes Land margin highlight sediment deposition under the influence of pelagic settling, turbidity and bottom currents (e.g., Escutia et al., 2005). In high latitudes, processes occurring on the continental shelf as a direct result of glacial to interglacial cycles (e.g., glacial extent) are responsible for sediment deposition on the more distal continental rise (e.g., Gilbert et al., 1998; Lucchi et al., 2002; Cowan et al., 2008). Thus, examining sediment characteristics in a stratigraphic framework allows for interpretations to be made in regards to both glacial and oceanographic processes at the time of deposition.

The main depositional processes reflected in deep-water continental margin settings are summarized by Stow and Piper (1984) and represent a continuum between turbidity currents, bottom currents and pelagic/hemipelagic settling. While there is a continuum between these processes, Stow and Piper (1984) defined three main facies depositional models (turbidites, contourites and pelagites/hemipelagites) that can be identified on the basis of distinct characteristic sedimentary structures, textures and composition that then allow for the interpretation of past depositional environments. Fine grainded turbidites are difficult to identify in the field and are commonly identified as mudstones with very thin mm-scale (laminae) to thick cm-scale (beds) that are a result of re-sedimentation events. However, Stow and Piper (1984) identify several distinct facies models, consisting of silt turbidites, mud turbidites, biogenic turbidites and disorganized turbidites. Each of these models are distinct from other facies assemblages as they consist of: (1) a regular vertical sequence of sedimentary structures commonly associated with a positive grading; (2) the presence of sedimentary structures indicating rapid deposition with bioturbation restricted to the tops of beds; and (3) compositional, textural or other features which show they are exotic to their depositional environment (Stow and Piper, 1984). While an idealised turbidite sequence consists of an up-sequence succession from graded laminated turbidite mud, graded turbidite mud, ungraded turbidite mud, and pelagite/hemipelagite the complete set of divisions is rarely preserved. In that case only tops middles, and bottoms of sequences occur in the sediment record (Figure 2.5a) (Stow and Piper, 1984).

Contourites are the result of deposition controlled by the reworking of sediments by bottom currents that flow parallel to bathymetric contours (e.g. alongslope, contour or boundary currents), although similar/identical deposits could be form by other bottom currents (e.g. downslope) that are persistent through time (Stow and Piper et al., 1984) and herein the term "bottom current deposit" is used to described such deposits. Bottom current deposits are distinguishable by (1) an irregular vertical arrangement of facies types and structures with both negative and positive grading, but no regular structural sequence; (2) evidence for more or less continuous bioturbation that has kept pace with deposition, but with the relic of current-induced structures remaining; and (3) compositional, textural or other features that indicate a combined *in situ* and exotic origin (Stow and Piper, 1984). Bottom current deposits commonly occur in areas of higher velocity current flow, particularly along western margins of basins, restricted passageways as well as occurring as isolated mounds parallel to the continental rise (Stow and Piper, 1984). Pelagite and hemipelagite sediments primarily are deposited by slow settling through the water column and not under the influence of any significant bottom current reworking (Stow and Piper, 1984). Pelagite/hemipelagite lithological characterisitics are (1) evidence for low-energy, low-sedimentation rates and continuous bioturbation; (2) a lack of primary sediment structures or other evidence of current controlled deposition; (3) uniform composition within any one succession that are often interbedded to a varying degree to reflect changes in climate state; and (4) variable biogenic component mainly of planktonic tests (pelagic) that is often associated with a terrigenous component (hemipelagic) and significant authigenic component. Pelagites are mostly restricted to some of the deepest parts of the ocean basin with carbonate pelagites being restricted to depths shallower than the carbonate compensation depth (~4500 meters below sea leve), whereas, hemipelagites occur more near the continental margin (Stow and Piper, 1984).

While not considered within the Stow and Piper (1984) lithofacies scheme, in high latitudes turbid surface plumes supplied from meltwater result in sedimentary sequences referred to as "plumites". Such events, in addition to mass flows (e.g., turbidity currents), are responsible for the delivery of terrigenous sediment to the more distal continental slope along glacimarine margins through the suspension settling of inter and overflow fine grained sediment (Hesse et al., 1997). Hesse et al., (1997) identified plumite sedimentary sequences along the Labrador slope that consist of 1 to 2-cm-thick repeated alternations of fine sandy silt/coarse silt interlayerd with laminated and burrowed clayey silt and silty clay. Hesse et al., (1997) note the seaward limit of plumite deposition is restricted to tens of kilometres from the ice front.

Caburlotto et al., (2010) recovered four sediment cores spanning the mid-Late Pleistocene from the WEGA channel along the Wilkes Land margin of Antarctica. Their findings suggest distinct depositional processes occur at crest ridges versus the channel and along the western gentle sloping side of ridges. Proximal to the crest, settling from sediment-laden water plumes and ice-rafted debris is reflected in bioturbated iceberg-rafted debris (IBRD) rich sediments. In areas distal to ridge crests, the interplay of turbidity currents, along slope and downslope bottom currents are reflected in the sediment architecture. The authors associated higher energy depositional process with turbidite sequences displaying no bioturbation, thick and well defined laminations, no IBRD with sharp to irregular bases. While erosion within the channel thalweg is interpreted to be the result of these turbidity current events, low density cm-thick fine-grained laminated turbidites suggest depositional processes dominated over erosion processes in the more distal channel setting (Figure 2.5b). Following mass flow events (e.g., turbidites) along-slope and down-slope bottom currents may rework fine-grain sediments and are distinguishable by their pervasive weak laminations, bioturbation and scattered IRD. Downslope currents, in response to plumes of cold dense HSSW flowing downslope, contribute to suspended sediment loads to the bottom nepheloid layer within the channel system.

Similar depositional processes identified by Caburlotto et al., (2010) have also been noted from other continental slope and rise cores recovered around the Antarctic Peninsula (Gilbert et al.,1998; Pudsey and Camerlenghi, 1998; Pudsey, 2000; Lucchi et al., 2002; Hepp et al., 2006; Lucchi and Rebesco, 2007; Cowan et al., 2008). Sedimentary facies analysis of cores collected along the Antarctic Peninsular margin led Lucchi et al. (2002) to place these glacimarine sedimentary processes in context to glacial and interglacial climate states that reflect one of several depositional processes occurring. They defined four sediment types associated with glacial advance, glacial maxima, deglacation and interglacial processes.

Glacial advance sediments are represented by massive muds with rare to sparse IRD and low biogenic content, with sedimentation inferred to be the result of sediment-laden meltwater turbid plumes eminating from the margin of an advancing ice sheet, with wind/ice-rafted debris and pelagic sedimentation restricted to polynyas. However, these glacial mud facies are interpreted as being the probable result of various processes, and contain a number of subfacies; (1) laminated mud with silty layers, laminae and lenses, (2) cross stratified mud, (3) laminated mud including IRD layers, (4) slump deposits of graded gravel and sand forming elongated deep sea fans and (5) sand and gravelly-grained turbidites. While continuous intervals of well-defined, finely-laminated muds containing IRD suggest bottom-current deposition, mass flow deposits are characterised by more traditional turbidite facies models. These turbidites facies models are interperted as being the result of an expanded ice sheet margin delivering large amounts of glacially derived unconsolidated sediment to the continental shelf with turbid meltwater plumes restricted to topographic highs. Turbidity current spillout onto the channel levees is reflected through silty layers, laminae and lenses. An important caveat to Lucchi et al., (2002) glacial facies is the distinct differences between glacial bottom current deposits observed around the Antarctic margin. In areas in where polynyas are present, glacial bottom current deposits do not necessarily have a well-laminated appearance. This is potentially due to the delivery of highly oxygenated water down slope, promoting productivity and bioturbation, therefore, reworking primary sediment features and aiding in sediment remobilization by currents (Caburlotto et al., 2010). Thus, such glacial bottom currents can actually serve as a proxy to define temporal and spatial extension of Antarctic sea-ice (Lucchi and Rebesco, 2007). However, Weber et al., (2011) suggest that while glacial maxima polynya style deposition is consistent with broad continental slope channels transporting voluminous flows of highly oxygenated water, their model differs from that of Lucchi and Rebesco (2007). Lucchi and Rebesco (2007) suggest that sediment gets rapidly deposited adjacent to contourite ridges (drift deposits) as fine grain siliciclastic varves when the polynyas are most active. When inactive bioturbated hemipelagic mud deposits prevail.

Deglaciation events with a disintegrating and retreating ice sheet are characterized by hemipelagic bioturbated structureless muds with distinct IRD layers. Highly productive interglacial periods are reflected in strongly bioturbated mud with a high biogenic content, sparse IRD and abundant aeolian sediment input (Lucchi et al., 2002). Table 2.2 summarizes lithofacies characteristics with glacimarine sedimentary processes based on previous high latitude studies in reference to climate state that are used in this study.

The lithofacies scheme and depositional model defined in this study will help further enhance stratigraphic models recovered from continental rise settings around the Antarctic margin. While much focus has been on creating depositional models for processes occurring in high-latitude continental shelf settings, these records are commonly hindered by hiatuses from glacial erosion (e.g. Naish et al., 2001; 2009). Drilling of continental rise sediments provides the opportunity to access more complete records at orbital resolution to allow for a cyclostratigraphic framework of late Cenozoic ice sheet responses to climate system feedbacks. As discussed above, the lithofacies associations are likely to represent a continuum of processes related to glacial extent and oceanography along the Wilkes Land margin. The lithofacies assembalges thus highlights extended periods of time consisting of both ice advance and retreat, in addition to, regional controls that sea ice development has on the intensity of bottom water circulation and ice sheet stability.

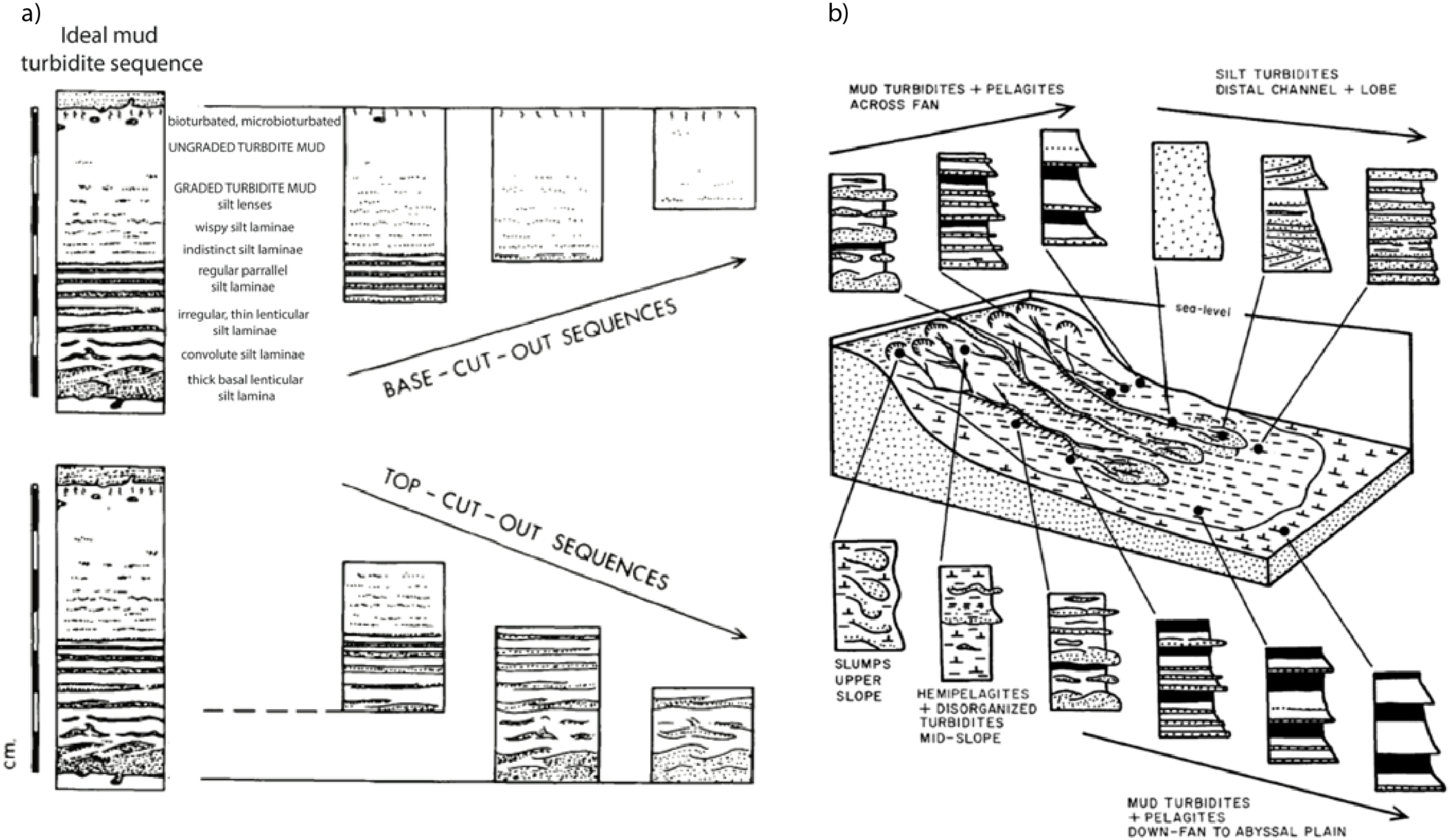

a)
Ideal mud turbidite sequence
bioturbated, microbioturbated
UNGRADED TURBDITE MUD
GRADED TURBDITE MUD
silt lenses
wispy silt laminae
indistinct silt laminae
regular parrallel silt laminae
irregular, thin lenticular silt laminae
convolute silt laminae
thick basal lenticular silt lamina
cm.
BASE - CUT - OUT SEQUENCES
TOP - CUT - OUT SEQUENCES
b)
MUD TURBIDITES + PELAGITES ACROSS FAN
SILT TURBIDITES DISTAL CHANNEL + LOBE
sea-level
SLUMPS UPPER SLOPE
HEMIPELAGITES + DISORGANIZED TURBIDITES MID-SLOPE
MUD TURBIDITES + PELAGITES DOWN-FAN TO ABYSSAL PLAIN

Figure 2.5. Schematic diagram of turbidite facies sequences (a) and depositional setting (b) (from Stow and Pipers, 1984).

Table 2.2. Continental slope and rise lithofacies characteristics and glacimarine sedimentary processes related to climate state (Hesse et al., 1997; Gilbert et al., 1998; Pudsey and Camerlenghi, 1998; Pudsey, 2000; Lucchi et al., 2002; Busetti et al., 2003; Hepp et al., 2006; Lucchi and Rebesco, 2007; Caburlotto et al., 2010).

Climate State	Lithofacies characteristics	Characteristic continental slope and rise glacimarine sedimentary processes
Interglacial	- hemipelagic mud - strong and pervasive bioturbation - sparse IRD - no laminations	- Low energy not preventing benthic activity with sediment accumulation rates on the order of 2-3.5 cm/k.y. - Settling of planktonic organisms, ice rafted debri and wind transport of debri. -Meltwater plumes "plumites" confined to the shelf.
Glacial to Interglacial Transition	- hemipelagic mud - slight bioturbation with gravelly mud layers - distinct IRD layers at the base of lithofacies	- Initial warming phase with discrete events of iceberg calving accompained with the disintegration of the ice shelf, ice sheet that was grounded at the continental shelf.
Glacial	- hemipelagic laminated to massive grey mud - poorly sorted - low biogenic content (very rare diatoms) TURBIDITE FACIES - no IRD - terrigenous sediment - silty layers, laminae and lenses - cross-stratified mud and slumps - sand/gravelly-grained laminations - sharp erosive to non-erosive boundaries CONTOURITE FACIES - well defined laminations - bioturbated to no bioturbation - IRD layers and sparse pebbles - occasional wispy layers indicating weak but steady bottom currents	- Sedimentation rate proximal to the channel system 11.5 cm/k.y. to top of drifts 7-5 cm/k.y. and 1.6 cm/k.y. oceanwards. - Large amounts of sediment delivered to the continental rise by down slope mass flows processes and meltwater turbid plumes from a grounded ice sheet at the shelf edge. - Sediment laden plumes inject a significant amount of fine sediments to the upper rise. - Non erosive low density spill-out of turbidites (silty layers, laminae and lenses with no IRD). - Extended sea ice cover with biological activity restricted to polynyas - Contour currents. -Nepheloid layers.
Interglacial to Glacial Transition	- structurelss hemipelagic mud - rarer to sparse IRD - low biogenic content	- Ice sheet with advancing grounding line toward the continental shelf edge. - Sediment laden plumes inject a significant amount of fine sediments to the upper rise. - Extended sea ice cover with biological activity restricted to polynyas

2.2. METHODS

The Pliocene-Early Plesitocene record of Site U1361 was recovered using the advanced piston coring system aboard the JOIDES Resolution with 103% core recovery. Initial lithofacies descriptions, which included the evaluation of smear slides, was carried out on board the JOIDES Resolution. Initial scientific results can be found in Escutia et al., (2011).

IRD can be deposited via processes associated with (1) ice shelves, (2) icebergs and (3) sea ice. Powell (1984) suggested using the general term IRD when there was uncertainty in the source of rafted material. However, if the style of rafting can be inferred it is best to specify the form of rafting by using terms such as ice shelf-rafted debris (ISRD), iceberg-rafted debris (IBRD) and sea ice-rafted debris (SIRD). Therefore, when referring to this study the term IBRD will be used while IRD will be used when referring to previous studies.

2.2.1. Iceberg Rafted Debris Mass Accumulation Rate calculation

On the basis of other Arctic and Antarctic studies, the 250 μm to 2 mm fraction of coarse sand was used to indicate IBRD (e.g., Krissek, 1995; Cowan et al., 2008). The calculation of an IBRD Mass Accumulation Rate (MAR) followed the methodology used by Krissek (1995). However, on the basis of Krissek's (1995) discussion concerning IRD MAR and following the examination of the dried coarse fraction after wet sieving at 150 μm under binocular microscope, the >150 μm fraction was dissolved of biogenics using NaOH. This step was used to remove "diatomaceous fuzz" in diatom-rich/bearing sediments that appeared to trap finer grains into the coarse sand fraction, further biasing sample weights, particularly if the percent of biogenics was greater than 10% (based on visual estimation). Dissolution of biogenic components also corrected for an underestimate of the mass contribution from IBRD (Krissek, 1995), a quantity that has been visually estimated in previous studies. After biogenic opal was dissolved, samples were then dry sieved at 250 μm to 2 mm grain-size. Each sample was then examined under binocular microscope for volcanic ash residue as well as authigenic material, which would also result in an overestimation of the IBRD MAR component. Only one sample was observed to have either of these and was excluded from the data set. The MAR of the coarse sand fraction was then estimated using the following equation:

$$\text{IBRD MAR} = \text{CS\%} * \text{DBD} * \text{LSR}$$

where IBRD MAR is the mass accumulation rate (g/cm^2/k.y.), CS% is the coarse-sand weight percent, DBD is the dry-bulk density of the nearest value (g/cm^3) and LSR is the interval average linear sedimentation rate (cm/k.y.). Although the orignal Krissek (1995) equation requires an estimation of IRD volume percent, this is redundant in this study, as biogenic material was dissolved, and authigenic or volcanic material was absent in all but one sample, thus the entire CS% in these data is interpreted as being IBRD. Appendix A provides the values for each of these variables.

2.2.2. Grain size distribution of the fine grain (<150 um) material

The fine grain fraction was recovered by wet sieving at 150 μm followed by the removal of organic material using 27% H_2O_2 and biogenic opal using 2M NaOH. Biogenic opal weight percent was obtained from dried weights before and after NaOH treatments. Sampled intervals were analysed for grain size fractions using a LS 13 320 Laser Diffraction Particle Size Analyzer. While caution was exercised in controlling sediment cohesiveness (Calgon, sonication and stirring), it is acknowledged the Laser method under estimates mud percentages in highly cohesive sediments (i.e., Sperazza et al., 2004; McCave et al.,, 2006). In this study, while the traditional boundary for clay-silt is 4 μm our output data may actually reflect clay percentages up to 8 μm due to the variation in grain size absorption values (i.e., Sperazza et al., 2004). Finally, the medium sand fraction (150 to 250 μm) was obtained following wet sieving at 150 μm and dry sieving at 250 μm with biogenic components removed. Statistical analysis of fine grain material was carried out with GRADISTAT (Blott and Pye, 2001). See Appendix A for results.

2.2.3. Productivity indicators

Biogenic opal weight percent (Appendix A) was obtained from dried weights before and after NaOH dissolution. This method of opal wt% data carries a high degree of analytical uncertainty, as the alkali treatment may also leach clay minerals and volcanic glass. However, comparison to the facies (based on smear slides) and to low-resolution quantitative opal data (Cook et al., 2013) show identical G/I cyclicity, albeit with an overestimation (10-20%). However, there is strong covariance between the opal wt% and the Ba/Al, with any scatter or outliers potentially due to some of opal being the deposited in the turbidites (some of the silt laminae were diatom-rich (Escutia et al., 2011) rather than a pure pelagic component).

Unpublished XRF data of Ba/Al composition was carried out by Francisco Jimenez-Espejo (JAMSTEC), and is incorporated into this thesis to demonstrate reliability in the biogenic opal weight percent data. The bulk major element composition was measured through-out cores Site U1361A-6H to 11H using an Aavatech TMX-ray fluorescence (XRF-Scanner) core scanner at the IODP-Core Respository/A&T Texas University laboratories (USA). Non-destructive XRF core-scanning measurements were performed at 10 kV in order to measure the relative content of elements ranging from aluminum (Al) to barium (Ba). Measurements were acquired every 5cm. Therefore, Ba and Al were obtained by X-Ray Fluorescence (XRF) using pressed pellets prepared by pressing about 5 g of ground, bulk sediment into a briquet with boric acid backing. The quality of the analysis was monitored with reference materials showing high precision with 1 sigma 1.0e3.4% on 16 data-sets at the 95% confidence level. For XRF 42 samples were selected in a 20 mts representative interval (47 to 67 mbsf) each 40-60 cms. Compared Ba and Al trends using both techniques are virtually identical and indicate that obtained XRF-Scanner data are robust and reliable.

2.2.4. Identification of Iceberg rafted debris versus lag deposits

In order to make the distinction between enrichments in the %CS due to current winnowing of the fine fraction, the sorting parameter defined by Folk and Ward (1957) was determined on fine grain terrigenous sediment (i.e., biogenic component removed), following the methodology of previous studies recovered from sediment drifts on the continental rise around the Antarctic margin (see Appendix A) (Passchier et al., 2011). IBRD peaks coinciding with well sorted terrigenous material are likely to be a concentration of coarse material following winnowing of fine-grained sediments by higher energy bottom currents. Whereas, IBRD peaks correlating with poorly to very poorly sorted material reflect actual IBRD events superimposed onto the background hemipelagic sedimentation. Furthermore, peaks of well-sorted terrigenous material also serve to identify potential hiatuses between the chronostratigraphic tiepoints (i.e., magnetic reversals) in our record related to current winnowing. There is a complete absence of well-sorted material in all samples anaylsed, further supporting the assumption of no major hiatuses in our studied interval. All IBRD peaks coincide with poorly to very-poorly sorted sediment, indicating IBRD events are not the product of lag deposits and the lack of moderately- to well-sorted terrigenous sediment indicates bottom current energy was never high enough energy for erosion to dominate over deposition (Figure 2.6). Along-slope or contour currents are also unlikely to have been a major erosive control, as mean modern-day bottom currents flow eastward across the drill site at a velocity of 1.8 to 6.6 cms^{-1} (Bindoff et al., 2000), which is well-below the current strength required for the onset of selective deposition (10-12cms^{-1}) or extensive winnowing of the fine fraction (>20cm s^{-1}) (McCave and Hall 2006). Downslope currents, resulting from HSSW passing down the continental rise, are also inferred to have been low-energy throughout the Pliocene-Plesitocene in these distal levee environments along the Wilkesland margin (Escutia et al., 2005; Caburlotto et al., 2010).

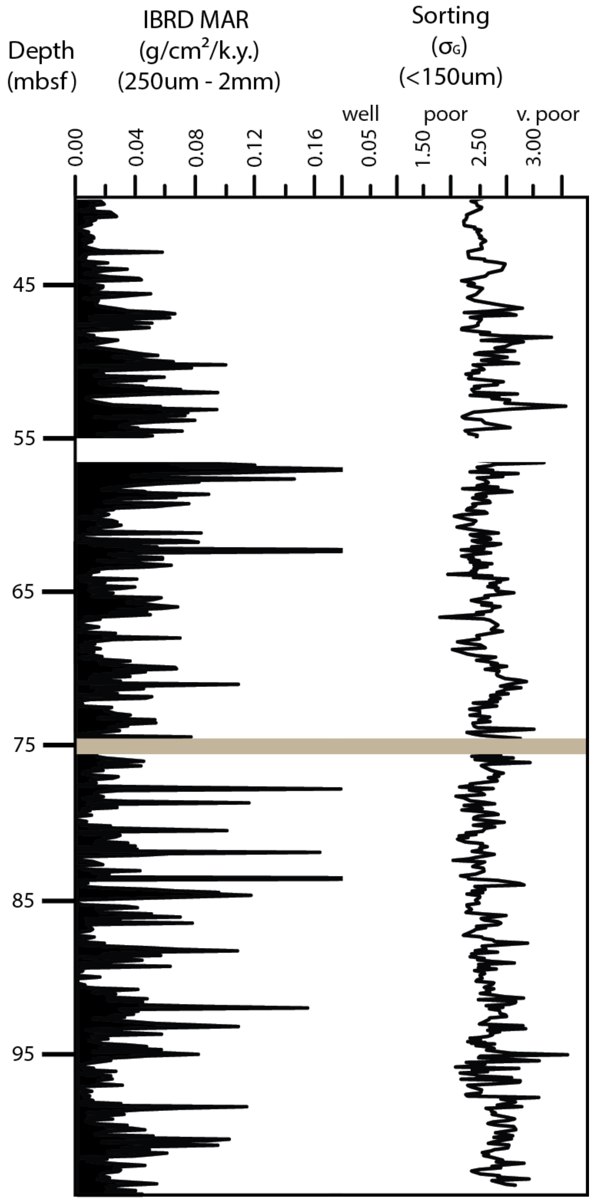

Figure 2.6. Site U1361 IBRD MAR compared to sorting of fine grained (<150 µm) terrigenous material. Sorting measurements follow parameters defined by (Folk and Ward, 1957). All samples are classified as being very poorly (2-4 σ) sorted. Grey/brown bar indicates core break.

2.2.5. Distribution of laminae

The distribution of every sub-mm to cm- scale silt and sand laminae in the Site U1361 core was determined using high-resolution, line-scan images of the split core face. The thickness and stratigraphic depth of each laminae was accurately mapped through the use of a purpose built image analysis script in Matlab©. In some cases, laminae may have been discontinuous and had been obscured by bioturbation and these were included in this analysis as they provide insight into initial processes of sediment delivery to the drill site.

2.3. RESULTS

The Site U1361 lithofacies scheme follows that of the shipboard scientific party (Escutia et al., 2011), with each facies representing specific environments of deposition. Two primary lithofacies are identified. (1) Massive mudstones containing intervals with packages of mm- to cm-scale silt/sand laminations, and (2) bioturbated diatom-rich/bearing mudstone. The grainsize data collected in this study (see Appendix A) confirm the initial sediment texture and lithological descriptions (Figure 2.7) as well as highlighting a dramatic decrease in IBRD coinciding with an overall increasing trend of silt during the Early Pleistocene (Figure 2.8c). The interbedding of these two facies form repetitive lithological cycles at the m-scale throughout the Pliocene, but become less obvious in Early Pleistocene sediments. IBRD MAR demonstrates a cyclical characteristic in which Early Pliocene sediments consists of peak events of equal amplitude and variability between lithofacies, while peak IBRD events in Late Pliocene sediments occur more regularly at lithofacies boundaries.

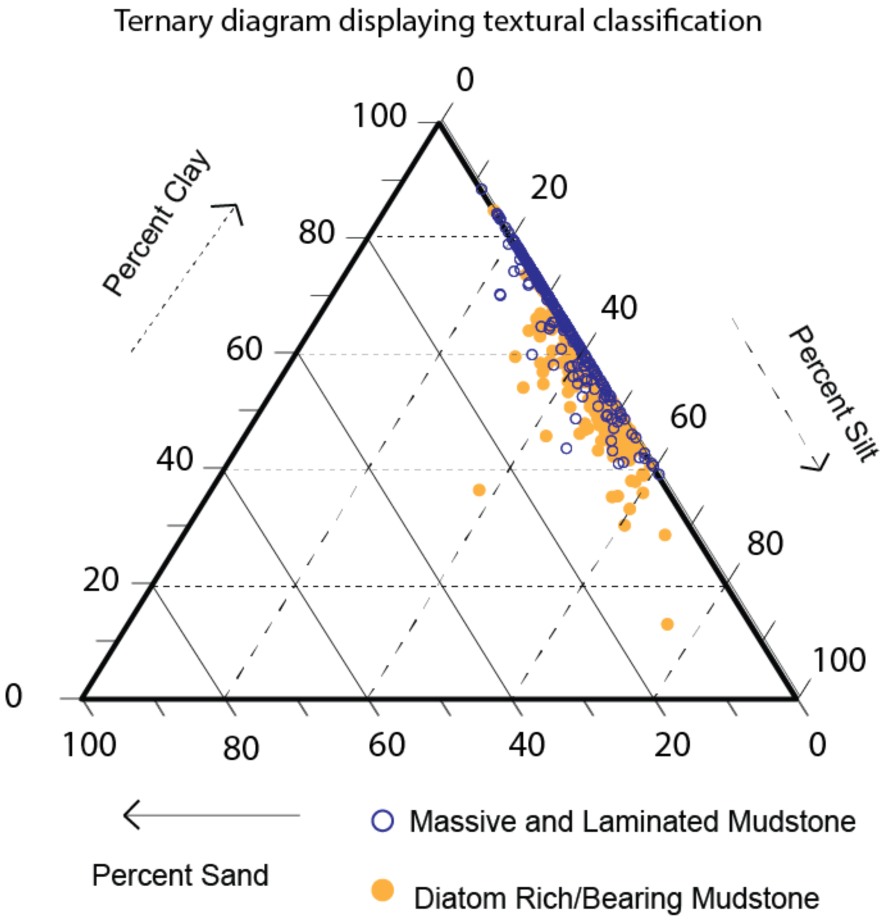

Figure 2.7. Ternary diagram displaying textural variability between Massive and Laminated Mudstone facies and Diatom-Rich/Bearing Mudstone facies (Graham and Midgley, 2000).

2.3.1. Lithofacies

The diatom-rich/bearing mudstone lithofacies is directly equivalent to Facies D from the initial report volume of IODP Exp. 318 Site U1361 (Escutia et al., 2011) (Figure 2.8 and 2.9a). This facies is light greenish grey in colour, contains >25 wt% biogenic opal (>25% diatoms in smear slides from lithological descriptions) and is strong to moderate bioturbation that obscures any primary sedimentary structures. IBRD is common throughout, and this facies is characterized by high Ba/Al values, a surface productivity indicator (Figure 2.10) (Dymond et al., 1992). Above 48 mbsf, this facies is coarser (silty) in texture (negative grading) (Figure 2.9c), IBRD MAR is lower, and silt mottles and lenses (rather than continuous laminae) are common with an irregular horizontal alignment. Variation in diatom content and grainsize occur in this interval, but this bedding is characterised by gradational/indistinct contacts relative to the facies contacts in underlying sections (Figure 2.8).

The massive and laminated mudstone lithofacies is equivalent to Facies E from the initial report volume of IODP Exp. 318 Site U1361 (Escutia et al., 2011) (Figure 2.9c). This facies appears olive grey in colour and is characterised by mudstone with packages of mm- and cm-scale silt and fine sand laminae/beds, that grade up into massive mudstones with variable degrees of bioturbation (absent to common). Of the 305 identified laminations, only 13 (4%) exceeded 1 cm (i.e., a bed rather a lamina) in thickness. These packages of laminae are generally characterised by mm- to cm-scale couplets of mud and silt, with thicker silt laminae at the base of the package, gradually passing up into thinner laminae and eventually into discontinuous mm-size silt lenses, and then massive/bioturbated mudstone (Figure 2.9). The silt laminae/beds are internally massive, have sharp bases and range from 1.3 mm to 2.5 cm in thickness, but the mean thickness is 4.5 mm and those exceeding 1 cm in thickness are rare. Diatom content is relatively poor throughout (<25wt% biogenic opal) and contains low Ba/Al values (Figure 2.10). IBRD is common throughout.

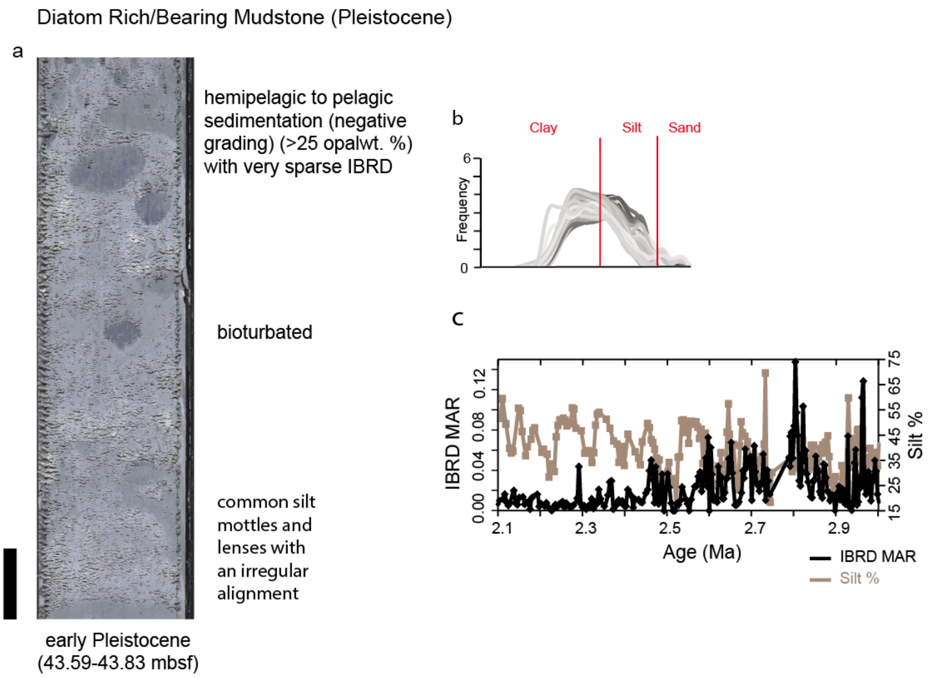

Figure. 2.8. Representative photo highlighting distinct sediment characteristics of Early Pleistocene diatom-rich/bearing Mudstone lithofacies (a). Black scale bar represents 3 cm. Grain size frequencies of representative samples are displayed with sampled intervals (b). Draw down in Early Pleistocene IBRD coinciding with an overall increase in silt content (c).

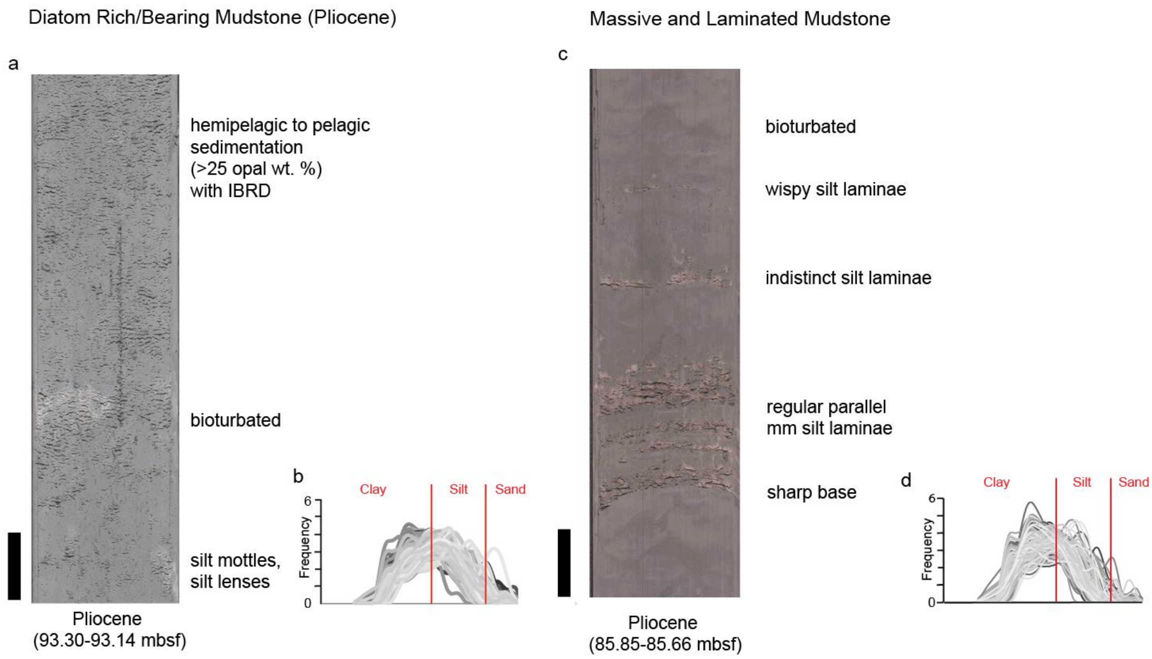

Figure 2.9. Representative photo highlighting distinct sediment characteristics of diatom-rich/bearing Mudstone (a) and the Massive and Laminated Mudstone (c) lithofacies for the Pliocene. Black scale bar represents 3 cm. Grain size frequencies demonstrate textural variability between lithofacies (b and c).

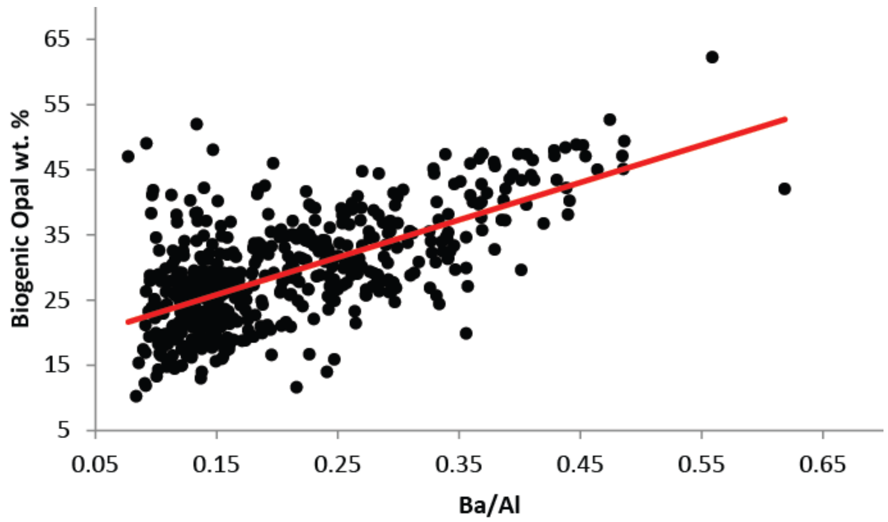

Figure 2.10. Cross plot of Site U1361 biogenic opal wt. % and Ba/Al. Linear interpolated at 3 kyr resolution of biogenic opal wt. % and Ba/Al with r = 0.65 and p value of 0.00.

2.4. DISCUSSION

2.4.1. Facies interpretation

The facies assemblages in the Pliocene-Early Pleistocene of Site U1361 are consistent with pre-existing facies models of sedimentation in distal channel-leeve systems on the lower continental rise from other regions globally (Stow and Piper, 1984) and from the Antarctic margin (Table 2.2) (Gilbert et al., 1998; Pudsey and Camerlenghi, 1998; Pudsey, 2000; Lucchi et al., 2002; Busetti et al., 2003; Hepp et al., 2006; Lucchi and Rebesco, 2007; Caburlotto et al., 2010). The presence of normally graded well sorted mm-scale silt laminae to lenses in otherwise massive mudstones, with sharp bases but no internal structures or IBRD is consistent with deposition by non-erosive spill-over of low density turbidites deposits onto a channel leeve in a distal lower continental rise setting (Figure 2.5b) (e.g. Stow and Piper 1984; Lucchi et al., 2002; Caburlotto et al., 2010). The laminae themselves lack IBRD and bioturbation, indicating relatively rapid deposition. Thus, the characteristics of these laminae argue against a traction current origin of deposition (Stow and Piper 1984; Lucchi et al., 2002; Caburlotto et al., 2010). It is also noted that the relationship between these laminaeted intervals of mudstones are identical in nature to the mud turbidite facies “T3” to “T7” beds of Stow and Piper (1984), representing base-cut-out sequences and deposition by or from low-density turbidity current by overflow on the distal levee setting –i.e. a non-erosional depositional setting compared to more proximal settings (Stow and Piper, 1984; Caburlotto et al., 2010). The presence of IBRD and bioturbation within intervals of the massive mudstone facies, suggests that turbidite intervals were deposited by numerous events over a relatively prolonged period, rather than a single event.

A lull or reduction in persistent turbidity current activity is represented by the bioturbated diatom-rich/bearing mudstone, consistent with the Pelagite/Hemipelagite “F” beds (Stow and Piper 1984). Grain size analysis reveals that the bioturbated diatom-rich/bearing mudstone facies are coarser (i.e. silty clays) than the massive mudstone intervals (clays; n.b. distinct silt laminae were excluded from analysis). The coarse nature of the bioturbated diatom-rich/bearing facies deposits suggest that pre-exisiting turbidites (Escutia et al., 2005) (i.e. silts laminae and clays) have been reworked and homogenized to a silty clay texture as a result of sediment reworking from bioturbation and moderate bottom current processes during a relative lull in turbidite activity. The lack of erosional surfaces or coarse sands/gravel layers (i.e. lag surfaces) suggests that although low-energy bottom currents or bioturbation acted to remobilize fine-grained sediment, depositional processes dominated over erosional events.

However, in the Early Pleistocene (e.g. above 48 mbsf) the bioturbated diatom-rich mudstones are distinguished from Pliocene intervals by an overall decrease in IBRD, and an increase in overall silt abundance displaying a gradual coarsing upwards (i.e. negative grading) at the m-scale (Figure 2.8c). There is also a slight decrease in the long-term sedimentation rate (~2.33 cm/k.y.) as compared to the Pliocene section (~3.10 cm/k.y.). Furthermore, although distinct continuous laminae are lacking, silt lenses and silt mottles are common and often display an irregular alignment (Figure 2.8a). Combined, the textural characteristics, negative grading, and the sedimentary structures are comparable to silty-sandy contourite facies (Stow and Piper 1984 Figure 9). In areas influenced by active polynyas, glacial contourites are highly bioturbated with irregularly aligned silt lenses and mottles in which boundaries between different sediment layers become difficult to distinguish (Lucchi and Rebesco, 2007). This is interpreted to be consequence of the low-energy downslope delivery of highly oxygenated and nutrient-rich waters formed off the margin within active polynya systems resulting in sediments containing high biogenic content and benthic activity. Such a situation is in contrast to other regions in Antarctica not influenced by an active polynya system, where anoxic conditions result in glacial bottom currents are characterised by hemipelagic grey muds with well-defined laminae that are rhythmic in nature, continuous, lack bioturbation, contain low biogenic content, and contain sparse IBRD or pebbly layers (Lucchi and Rebesco, 2007; Carbolotto et al., 2010). Thus, negative grading above ~48 mbsf, sparse IBRD, highly bioturbated sediment with irregular alignment of silt lenses and mottles suggest distinctly colder glacial conditions in which sediment-laden iceberg discharge becomes rare and downslope currents are enhanced. The latter process is the possible consequence of enhanced polynya mixing off the Wilkes Land margin increasing the delivery of oxygenated nutrient-rich water to the lower continental rise, increasing both bioturbation and bottom current strength (Lucchi and Rebesco, 2007; Carbulotto et al, 2010).

Seismic stratigraphic interpretation of existing multichannel reflection seismic profiles crossing Site U1361 (Figure 2.2) provide further evidence that the dominant sedimentary processes building these low-relief, distal levees (i.e. lowermost continental rise) are turbidity flows traveling through the channel (where erosion occurs) and from inter- and over-flow depositing sediment as a hemipelagic drapes. Although, sediment waves are observed locally in seismic lines from the lower rise that are perpendicular to the margin (downslope processes), these are within the overbank deposits and are smooth (i.e., very low-relief) indicating that bottom-currents are not a dominant process at this distal site. In contrast, sediment waves are well-developed in older sequences (i.e., phase 2 of Escutia et al., (1997), of upper Oligocene-Miocence age (Escutia et al., 2011) on the lower continental rise and in more proximal continental rise areas (i.e., where Site U1359 is located) and suggest deposition by mixed turbidite and bottom-current deposition (Escutia et al., 1997; 2002; Donda et al., 2003). The change from mixed turbidite and bottom-current deposition (Phase 2) to turbidite and hemipelagic dominated deposition (section containing sediments considered in this study) coincides with a shift in sedimentary depocenters from the continental rise to the continetal shelf (Escutia et al., 2002). Instead of large levee deposits, low-relief overbank deposits spilling from the channels are commonly observed on-lapping the previous levees and ridges during Pliocene sequences (Escutia et al., 1997; Escutia et al., 2002).

2.4.2. Identification of glacial to interglacial sedimentation processes

Massive/laminated mudstone facies are interpreted as being predominately deposited during periods of glacial maxima (Figure 2.11a), during which large volumes of unconsolidated sediment were being delivered to the continental shelf edge either through the deposition of till deltas or via bedload rich turbid glacial melt water plumes as glaciers advance (Eittreim et al., 1995; Hesse et al., 1997; Lucchi et al., 2002; Escutia et al., 2005; Beaman et al., 2011) with turbidity current initiation due to slope failures on oversteepen foreset strata potentially from a mixture of processes related to extended ice sheets (i.e., sediment-rich melt water plumes and or from hypersaline density flows). This interpretation is supported by seismic profiles that indicate glacial advances occurred regularly since the Early Pliocene, as evidenced by the onset of steeply dipping foresets and the development of the modern progradational wedge above seismic unconformity WL-U8 which can be traced from the continental shelf to rise and dated at 4.2 Ma (~100 mbsf) in Site U1361 (Figure 2.2) (Escutia et al., 2005; Tauxe et al., 2012). Steeply dipping foresets are commonly found around the margin of the Antarctic and are interpreted as being deposited in a proglacial setting at the grounding line of ice streams, and are therefore a direct result of glacial advances to the shelf edge (Cooper et al., 1991; Eittreim et al., 1995; Anderson 1999; Rebesco and Camerlenghi, 2008). Major deglaciation events (Figure 2.11b) are associated with peaks in IBRD as a consequence of accelerated calving during glacial termination from marine terminating outlet glaciers along the Wilkes Land coastline as well as a contribution from EAIS outlet glaciers entering the western Ross Sea. This interpretation is consistent with both lithofacies models from the Antarctic (Table 2.2) as well as model simulations and paleo-observations, which imply the most rapid mass loss of the EAIS marine margin during the last glacial termination occurred between 12-7 ka, and was primarily the consequence of oceanic warming (Mackintosh et al., 2011).

Diatom-rich/bearing mudstone facies with IBRD and pervasive bioturbation throughout are interpreted to be predominately deposited during glacial minima (Figure 2.11c). This interpretation is supported by recent isotopic Nd and Sr provenance studies of the fine-grained fraction in the Pliocene interval of Site U1361 which indicate that the eroding margin of the EAIS had receded up to several 100 kms inland to the central portion of the Wilkes Subglacial Basin (Cook et al., 2013). The interplay of bioturbation and downslope currents results in an overall increase in the silt component, most likely due to homogenization of sediment texture and removal of primary sedimentary structures (i.e., silt laminae) within these intervals. Turbidity currents and slope failures may have still been delivering sediment during these intervals, perhaps as the consequence of isostatic adjustments during postglacial retreats (Escutia et al., 2005) or initiated by hypersaline density flows of high salinity shelf waters passing down the continental rise. However, the homogenization of these sediments suggests that turbidity current activity may have been less frequent. Reduced turbidity current activity does not explain these facies alone, as changes in biogenic opal weight percent covary with Ba/Al measurements within these diatom-rich intervals (Figure 2.10). Thus, we interpret these intervals as representing intervals of enhanced biogenic activity in the surface waters above the drill site, accompanied by a reduction in turbidity current activity. We also note that during the Holocene, most fine grained sediment is advected towards the inner continental shelf in the Mertz-Ninnis tough rather than towards the shelf edge (Presti et al., 2003), due to the reverse slope morphology of the continental shelf that began to developed in the Early Pliocene (i.e. above WL-U8) (Figure 2.2), and thus it is likely this was also the situation for Late Pliocene-Pleistocene glacial minima.

The modern day position of the Southern Boundary of the ACC is ~200 km to the north of Site U1361 (Orsi et al., 1995), and is the location of the Antarctic Divergence where relatively warm UCDW currently upwells and biological productivity is high. Sea surface temperature (SST) reconstructions indicate that the Southern Ocean was up to +4°C warmer (Dowsett et al., 2012) with a significantly reduced sea ice field during the warmest Pliocene in the Ross Sea (McKay et al., 2012), Prydz Bay (Whitehead and Bohaty, 2003) and Antarctic Peninsula (Hillenbrand and Cortese, 2006) regions. A number of studies outline cyrosphere connections between zonal shifts in the intensity or location of southern westerlies influence on ocean fronts (e.g., Toggweiler and Russell, 2008; Anderson et al., 2009; Martinez-Garcia et al., 2011). Such changes in turn may regulate incursions of CDW (or modified CDW when mixing with Antarctic waters has occurred) onto the continental shelves around Antarctica and thus leading to melting of the marine margins of the ice sheets (Toggweiler et al., 2006; Anderson et al., 2009; Naish et al., 2009; Denton et al., 2010; McKay et al., 2012; Pritchard et al., 2012). The main dynamical barrier for CDW (or MCDW) in Wilkes Land is the Antarctic Slope Front (at the shelf break/upper continental rise) which creates a “V-shaped” isopycnal that extends into intermediate water depths and restricts CDW incursions onto the continental shelf (Bindoff et al., 2000). Thus, changes in the location, intensity or vigour of this current, related to the strength or location of the zonal polar winds (i.e., polar easterlies and the subpolar westerlies), directly regulates CDW incursion, more so than a direct bathymetric control (Williams et al. 2008).

Early Pleistocene diatom-rich/bearing intervals above ~48 mbsf, while containing similarities to Pliocene intervals, are distinctively different in IBRD content, arrangement of silt lenses and mottles, and an apparent overall negative grading as displayed in the grain size data (Figure 2.12). The Early Pleistocene intervals reflecting some reworking by bottom currents in which enhanced delivery of oxygenated and nutrient rich waters formed in the Mertz Polynya promoting productivity and bioturbation. Silt lenses and mottles appear more irregularly aligned suggesting more highly energised bottom current remobilization of fine grain clay sediments. Sparse IBRD suggests lulls in iceberg calving as disintegration events become less frequent as the ice sheet stabilised and begain to fluctuate at the same extent as the Late Pleistocene glacial cycles. These bottom currents appear to be related to low energy downslope (rather than alongslope currents), due to seismic data and modern oceanographic current data (discussed earlier). Continental rise channels (like the Jussieu channel) act as conduits for the delivery of cascading HSSW to the rise, however, these currents remain at low-energy and appear non-erosived in this distal low-relief levee setting (William and Bindoff, 2003; Carbulotto et al., 2010).

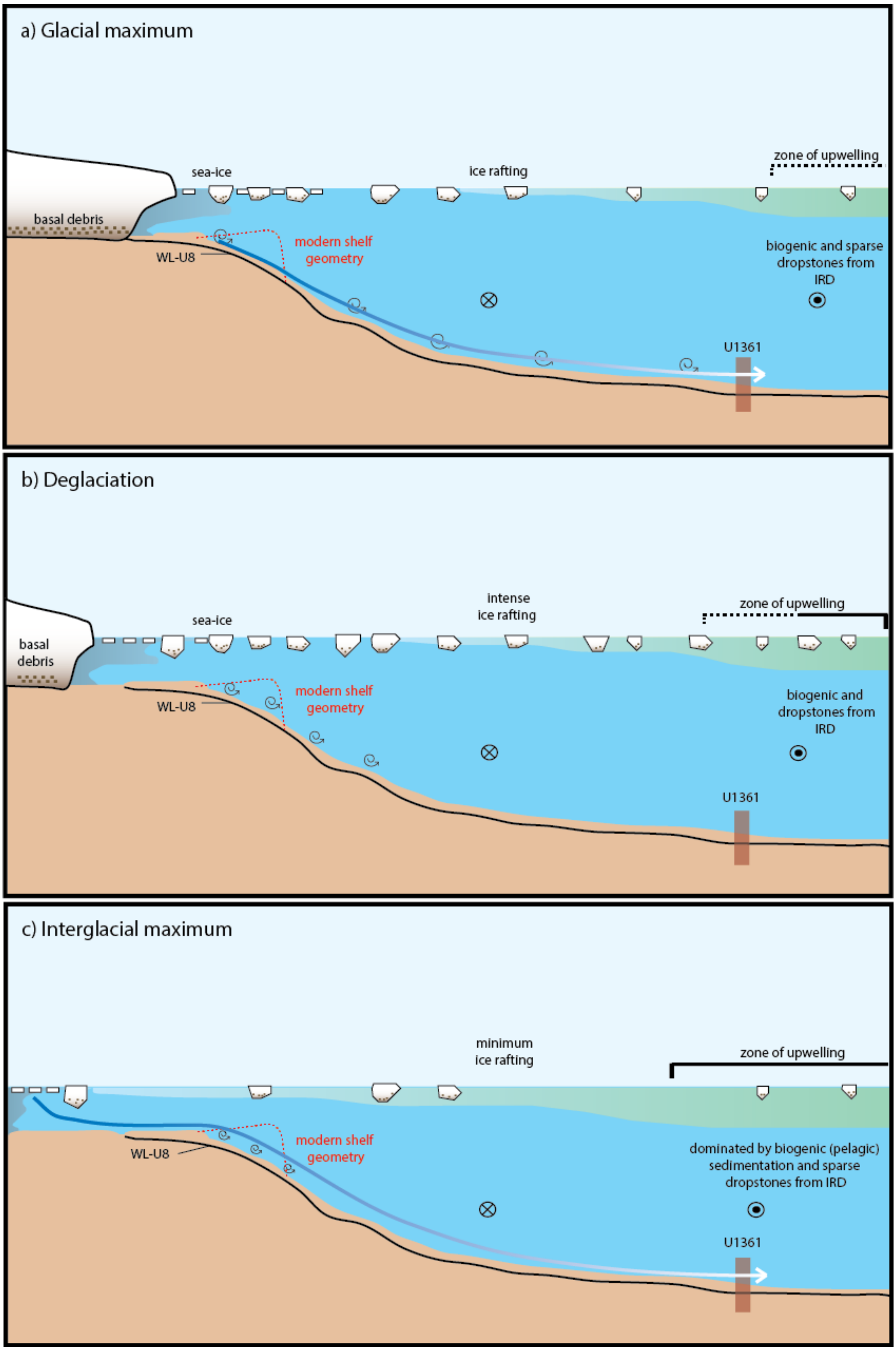

Figure 2.11. Schematic diagram displaying our interpreted climate stages influence on sedimentation at Site U1361. The red dotted line is an interpreted representation of the modern shelf edge. The Antarctic Coastal Current is represented by the black "x" with a flow direction into the diagram, while the ACC is represented by the black dot with a flow

direction coming out of the diagram. Adélie Land sourced AABW is distinguished by the blue to white arrow.

2.4.3. Stratigraphic Framework

The Pliocene-Early Pleistocene record of Site U1361 contains 18 lithological cycles. Individual cycles are identified by a single interbedding of biotubated diatom-rich mudstone facies and massive/laminated mudstones. However, lithological cycles for the Early Pleistocene (cycles 1-4) are based on diatom richness observed in visual observations and constrained by opal weight percent values. However, it is worth noting boundaries between these “more” diatom-rich/bearing to “less” diatom-rich/bearing intervals become more difficult to distinguish compared to cycles 5-18. While facies appear to have lasted for extended glacial-interglacial periods, glacial maxima are represented by massive and laminated mudstones, with peaks in IBRD associated with ice sheet disintegration events whereas diatom-rich/bearing mudstones are associated with a retreated ice sheet margin (Figure 2.12).

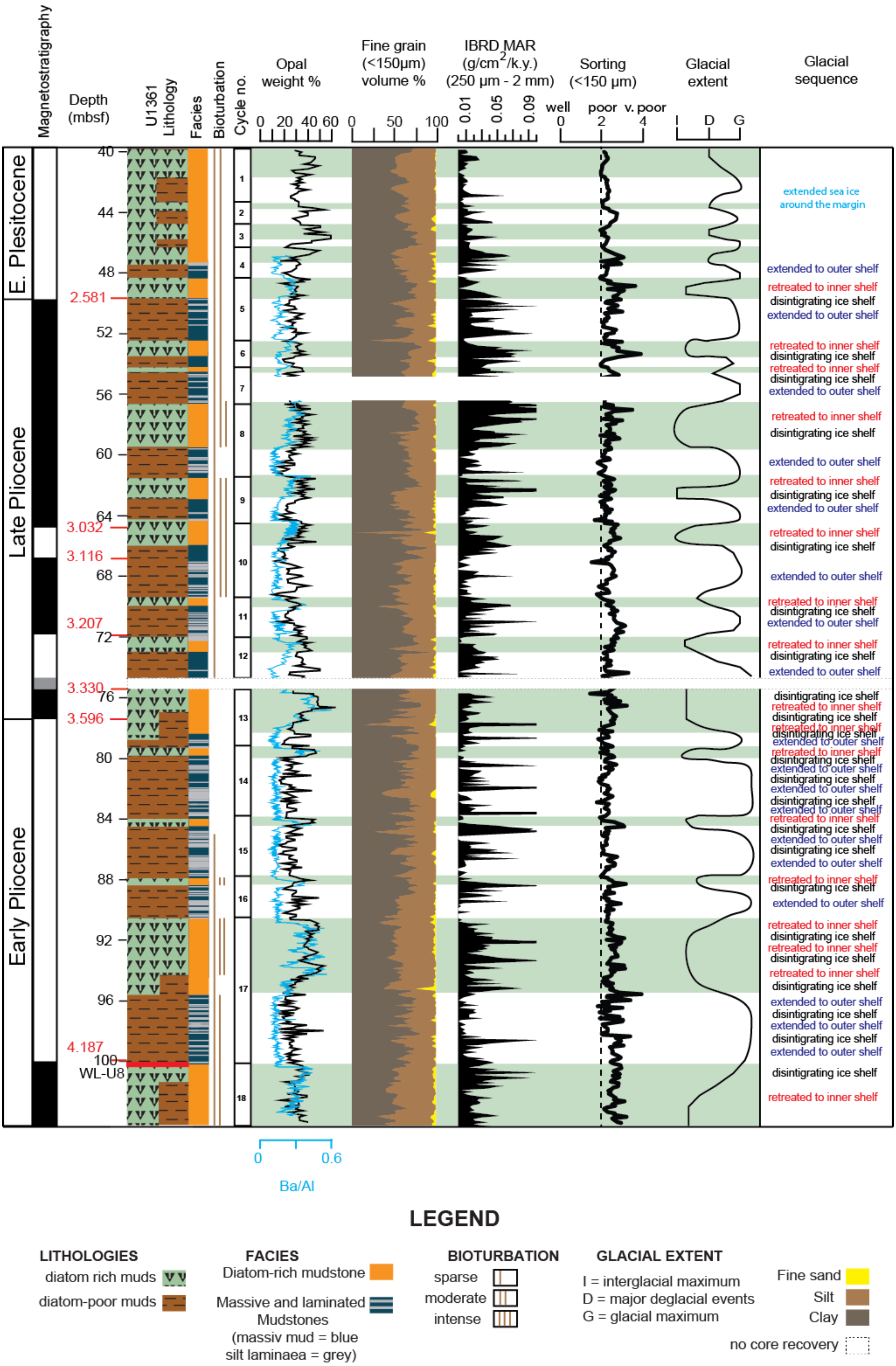

Magnetostratigraphy
Depth (mbsf)
U1361 Lithology
Facies
Bioturbation
Cycle no.
Opal weight %
Fine grain (<150µm) volume %
IBRD MAR (g/cm2/k.y.) (250 µm - 2 mm)
Sorting (<150 µm)
well poor v. poor
Glacial extent
I D G
Glacial sequence
E. Plesitocene
Late Pliocene
Early Pliocene
2.581
3.032
3.116
3.207
3.330
3.596
4.187
WL-U8
Ba/Al
extended sea ice around the margin
extended to outer shelf
retreated to inner shelf
disintigrating ice shelf
LEGEND
LITHOLOGIES
diatom rich muds
diatom-poor muds
FACIES
Diatom-rich mudstone
Massive and laminated Mudstones (massiv mud = blue silt laminaea = grey)
BIOTURBATION
sparse
moderate
intense
GLACIAL EXTENT
I = interglacial maximum
D = major deglacial events
G = glacial maximum
Fine sand
Silt
Clay
no core recovery

Figure. 2.12. Stratigraphic log with lithology, facies, bioturbation, lithostratigraphic cycles and grain size data. Diatom abundance is based on initial scientific results (Escutia et al., 2011) as well as quantitative estimates of biogenic opal (opal weight % and Ba/Al). Age intervals are based on magnetostratigraphy from Tauxe et al., (2012). Glacial extent (I = interglacial, D = deglaciation, G = glaciation) and sequence are based on lithofacies associations.

2.4.4. Diatom-rich/bearing mudstone during Late Pliocene-Early Pleistocene cooling (3.3 to 2.0 Ma)

While the Early Pleistocene diatom-rich/bearing mudstones are structurally and textural similar to those deposted in the Pliocene, there are some subtle but important differences. After 2.8 Ma, silt laminae become less frequent and when present are disturbed by bioturbation. Additionally, IBRD substantially decreases in comparison with the entire Pliocene record, coinciding with the lower sedimentation rates than the Pliocene, as well as a gradual overall increase in silt content. Furthermore, lithological cycles become less obvious to visually distinguish (Figure 2.12).

Sedimentologic and seismic records recovered around the Antarctic margin document a period of major ice sheet expansion from 3.0 to 2.0 Ma (Kennett and Barker, 1990; Barrett and Hambrey, 1992; De Santis et al., 2003; Escutia et al., 2005; Whitehead et al., 2006; Rebesco and Camerlenghi, 2008; Cowan et al., 2008; Escutia et al., 2009; Naish et al., 2009; Levy et al., 2012; Passchier, 2011; McKay et al., 2012). This cooling trend has also been associated with extended sea ice cover in Antarctica's coastal regions (i.e., Antarctic Peninsula, Ross Sea and Prydz Bay) (Hillenbrand and Cortese, 2006; Whitehead et al., 2006; Cowan et al., 2008; Escutia et al., 2009; Naish et al., 2009; McKay et al., 2012). Coupled atmosphere-ocean general circulation models have demonstrated the important role that ice sheet growth and stability has on the development of sea ice, with the latter being a requirement in the development of the extended Antarctic sea ice field (DeConto et al., 2007). Ice sheet and sea ice growth along the margin coincide with a drawdown in atmospheric CO_2 to pre-industrial levels (Seki et al., 2010), as well as a decline in the relative flux of NADW, or its precursor, into the Atlantic (Billups et al., 1997; Hodell and Venz-Curtis, 2006), and an associated decrease in Southern Ocean ventilation (Hodell and Venz-Curtis, 2006). The expansion of the sea ice field and inherent 5°C cooling of Southern Ocean SST between 3.3 and 2.5 Ma have been suggested to cause the expansion of the westerly winds and promote a northward migration of ocean fronts, which restricts upwelling of CDW along the Antarctic margin (McKay et al., 2012). Such a situation would promote a reduction in ocean induced melting of marine-based ice.

Of particular importance is the increase in polynya style activity in the Ross Sea region as indicated by sea ice diatom assemblages and bulk sediment stable isotopes between 3.3 and 2.5 Ma (McKay et al., 2012). Polynyas around the Antarctic margin are regions where the rate of sea-ice formation may be up to 10 times greater than in the surrounding sea-ice zone, allowing for enhanced brine rejection, an important process in the formation of AABW (Bindoff et al., 2000). Polynya activity in the Ross Sea during this time is important as Site U1361 is bathed by AABW sourced from the Ross Sea via the alongslope, Antarctic Slope Current, as well as AABW sourced from within the Adélie depression along the Wilkes Land margin, which also interacts with the drill site through downslope currents (Williams et al., 2008; Escutia et al., 2011). Enhanced delivery of bottom water across Site U1361 has two consequences; (1) an increase in oxygenated water allowing for an increase in benthic productivity, and (2) enhanced current winnowing of sediment. The overall increasing trend in silt content and lack of primary sediment features (i.e., lamina) after 2.6 Ma potentially highlight the enhanced interaction between the reworking of turbidites by bioturbation as well as both downslope and alongslope bottom current winnowing. This assumption is based on the observation that AABW/ALBW is currently forming in the Adélie depression during the present interglacial, and that interglacial stages after ~2.8 Ma reach Holocene benthic $\delta^{18}O$ values suggesting similar ice volume configurations to the modern interglacial (Lisiecki and Raymo, 2005; Escutia et al., 2005; Pollard and DeConto, 2009). Cyclicity within the percent silt data and reverse grading infers the processes explained above including increased bioturbation and current winnowing becomes enhanced through time as the overall climate cools and ice sheet developes to Late Pleistocene extent. Furthermore, glacial erosion and over deepening of the continental shelf during the larger ice volume fluctuations of the Late Pliocene-Early Pleistocene, provided accommodation space in which the depocenter of terrigenous material moved southward instead of extending to the shelf edge, resulting in less terrigenous sediment delivery to the rise. This is reflected in both a relative decrease in packages of silt lamina compared to the Early Pliocene record of Site U1361, and lower sedimentation rates during the Early Pleistocene, in addition to seismic data (Eittriem et al., 1995; Presti et al., 2003; Escutia et al., 2005; Escutia et al., 2011; Tauxe et al., 2012). The increase in silt content is accompanied by a dramatic decrease in IBRD MAR. The decrease in IBRD deposition is potentially related to a number of factors concerning Late Pliocene-

Early Pleistocene cooling. (1) Reduced rates of ice calving along the margin as a result of changes in the thermal glacier regime (i.e., less direct ice sheet/ocean interaction via sea ice production), (2) changes in the melt rate of bergs as a function cooler SST, and (3) ice-bergs start to become grounded along the shelf edge allowing for most basal debris to melt out before reaching the continental rise.

2.5. CONCLUSIONS

The Pliocene-Early Pleistocene record of Site U1361 consists of two dominant lithofacies that are consistent with times of peak glacial extent as well as prolonged warming with a retreated ice sheet margin. Although there are some site-specific considerations, sediment deposition at Site U1361 closely aligns with established models of non-erosive overbank turbidite depositional model in a lower continental rise "distal" levee setting from the Antarctic margin (i.e., Lucchi et al., 2002). Massive and laminated mudstones are interpreted as periods of extended ice sheet advances across the continental shelf even during peak Pliocene warmth. Peaks in IBRD are interpreted as major deglaciation events. Diatom-rich/bearing mudstones highlight periods of enhanced ocean upwelling over the core site during times of a reduced sea ice field during interglacial maxima. A major change occurs during the Early Pleistocene cooling (2.7 to 2.0 Ma) and is reflected in diatom-rich/bearing mudstones that show distinct differences (i.e., decrease in IBRD and increase in silt content) compared to the Pliocene. Such differences in lithological characteristics infer enhanced delivery of highly oxygenated shelf waters by downslope currents as a result of an increased in polynya-style mixing along the Wilkes Land margin as sea ice became more extensive and the continental shelf continued to become over steepened from Pleistocene glaciations.

CHAPTER 3

ORBITAL RESPONSE OF THE EAST ANTARCTIC ICE SHEET DURING THE PLIOCENE-EARLY PLEISTOCENE: IMPLICATIONS FOR GLOBAL SEA LEVEL CHANGES

Geological reconstructions of global ice volume (Lisiecki and Raymo, 2005) and sea-level (Miller et al., 2012) during the Pliocene and Early Pleistocene (5 to 2 Ma) display regular glacial-interglacial cycles occurring every 40-kyr, paced by variations in Earth's axial tilt (obliquity). The absence of a strong ~20-kyr precession signal challenges our fundamental understanding of how ice sheets respond to orbital forcing because precession should impart the greatest influence on high-latitude summer insolation intensity, and therefore polar ice volume (Milanković, 1941; Raymo et al., 2006). While a number of hypotheses have been proposed (Raymo et al., 2006; Raymo and Huybers, 2008; Huybersand Tziperman, 2008), reconciliation of this conundrum remains hampered by a lack of observational evidence from the Antarctic ice sheet. Here, we present an orbital-scale time-series of ice-berg rafted debris and continental rise sedimentation from a well-dated sediment core (Integrated Ocean Drilling Program Site U1361) adjacent to the Wilkes Land margin of the East Antarctic Ice Sheet (EAIS). Our data reveal ~40-kyr cyclic variations in the extent of the EAIS paced by obliquity between 4.3 to 3.3 Ma during the warmer-than-present climate of the Pliocene, as has previously been demonstrated for the West Antarctic Ice Sheet (WAIS) (Naish et al., 2009; Pollard and DeConto, 2009). Under a warmer climate state, mean annual insolation (paced by obliquity) had more influence on Antarctic ice volume, than insolation intensity modulated by precession (Huybers and Tziperman, 2008). However, a transition to 20-kyr precession cycle dominance at 3.3 Ma preceded the development of a more stable EAIS marine margin at ~ 2.5 Ma, reflecting the declining influence of oceanic forcing as the high latitude Southern Ocean cooled and a perennial summer sea-ice field developed (McKay et al., 2012). Our data shows that precession-paced EAIS variability occurs during cold climate states, even when the obliquity signal dominates globally-integrated proxy records.

3.1. INTRODUCTION

The dominance of the 41-kyr variability during the Pliocene-Early Pleistocene is evident in sea-level reconstructions (Miller et al., 2012), sea surface temperature reconstructions based on proxy records (Dowsett et al., 2012), WAIS sediment records (Naish et al., 2009), as well as Southern Ocean and Northern Hemisphere mineral dust aerosol records (Martínez-Garcia et al., 2011; Naafs et al., 2012). This suggests a close coupling in the climate system between ice volume/sea-level, temperature, and atmospheric circulation in response to obliquity forcing. The absence of a strong precession influence on ice volume has been explained by two different hypotheses. Raymo et al. (2006) using a non-dimensional ice sheet-climate model, demonstrated that (10-30 m sea level equivalent) changes in the Antarctic ice volume driven by local insolation could counter balance Northern Hemisphere ice volume changes also paced by local insolation, as precession is out-of-phase between hemispheres. Such a scenario would enhance the 40-kyr obliquity component reflected in the benthic $\delta^{18}O$ ice volume record. However, this hypothesis does not account for the lack of a strong precession signal prior to the onset of Northern Hemisphere glaciation at ~3.3 Ma (e.g., Lisiecki and Raymo, 2005; Naish et al., 2009; Martínez-Garcia et al., 2011; Naafs et al., 2012). An alternative hypothesis that suggests long term variations in mean annual insolation controlled by obliquity may have more influence on polar temperatures than peak seasonal insolation modulated by precession, provided the surface temperature remains above 0°C for a significant part of the summer season (Huybers, 2006). In this case, integrated summer insolation (summer energy) has been shown in one model to control the melting of Northern Hemisphere ice sheets at the obliquity period during the Early Pleistocene (Huybers and Tziperman, 2008). Although this condition is not currently met by the Antarctic Ice Sheet, its summer melt threshold may have been exceeded during the Early and mid-Pliocene (5-3 Ma) (Naish et al., 2009; Pollard and DeConto, 2009) when atmospheric CO_2 was ~400 ppm (Seki et al., 2010) and global surface temperature was 2-3°C warmer (Haywood et al., 2013).

Sub-ice bedrock topography reveals extensive regions where the EAIS is grounded below sea level (Fretwell et al., 2012), and may be vulnerable to the same process of ocean induced melt that caused retreat of WAIS during the Pliocene (Naish et al., 2009; Pollard and DeConto, 2009), and indeed, is influencing its present mass loss (Pritchard et al., 2012). Recent geophysical surveys along the Wilkes Land continental margin of the EAIS show the presence of landward deepening reverse slope troughs that can be traced southward where they reach depths of up 2 km below sea-level in the Wilkes subglacial basin (Fretwell et al., 2012). Such bed geometries heighten the vulnerability of this sector of the EAIS to marine ice sheet instability. Reconstructions of Pliocene sea-level (~3.6-3.0 Ma) based on far-field geological evidence suggest global mean sea-level was up to +20 m higher than present during the warmest 41-kyr, interglacial high stands (Miller et al., 2012), requiring near deglaciation of West Antarctica (+4 m) and Greenland (+7 m), as well as a significant contribution from the low elevation marine margins of the EAIS.

The marine sediment core Site U1361, recovered by IODP from ~3000 m water depth on the continental rise adjacent to the Wilkes Land sector of Antarctica, provides a well-dated and continuous geological archive of Pliocene and Early Pleistocene orbital scale variability of the marine margin of the EAIS. Sediment deposition at this site is controlled by the interplay between: (i) downslope marine sediment gravity flows triggered by the buildup of sediment on the edge of the continental shelf during glacial advance; (ii) the rainout of biogenic detritus from surface water plankton; and (iii) iceberg rafting of terrigenous sediments (see Chapter 2 for detailed discussion).

3.2. METHODS

Methodology concerning grain size (i.e., IBRD MAR) and productivity indicators are described in Chapter 2 (section 2.2). This section will focus on the methodology of spectra analysis as it is unique to this chapter in regards to the Site U1361 data being presented.

3.2.1. Frequency analysis

Using the age model of Tauxe et al. (2012; Table 2.1 and Figure 2.4), evolutionary spectral analysis was performed in Matlab© using a spectrogram function developed by Peter Huybers and is available at his website (http://www.people.fas.harvard.edu/~phuybers/). This allows for the detection of non-stationary spectra variability within the time series. Power spectral analysis using the SSA-MTM toolkit for the Multi-Taper method (MTM) analysis (Ghil et al., 2002) with five data tapers for the untuned IBRD MAR and biogenic opal weight percent time series at 3 kyr resolution for the Early Pliocene and 4 kyr resolution for the Late Pliocene-Early Pleistocene. Equal time spacing was achieved by linear interpolation based on average temporal sample spacing of time series segments as there is a gap in our data exceeding 100 kyr that predates 3.33 Ma. The statistical significance of spectral peaks was tested relative to the null hypothesis of a robust red noise background, AR(1) modelling of median smoothing, at a confidence level of 90% and 95% (Mann and Lees, 1996). We have also applied a Raw (AR1) model, and with a harmonic reshape set to a 90% threshold to test the comparative variance in obliquity versus precession.

Tuning of the IBRD MAR record and bandpass filtering were conducted in Analyseries (Paillard et al., 1996), with filters for obliquity (central frequency of 0.25, bandwidth of 0.03) and precession (central frequency of 0.45, bandwidth of 0.05) being applied. Tuning, power spectra was carried out using the same parameters with the SSA-MTM toolkit as the untuned data.

3.2.2. Theoretical background to frequency analysis

While cyclostratigraphy is the study of interpreting observational data obtained from a stratigraphic record and placing it into the context of environmental cycles (e.g., orbital cycles). Spectral analysis allows for the identification of cyclicity within a given time series using Fast Fourier Transforms. Fourier's theorem suggests that any time series can be recreated by adding together sine and consine waves having the correct wavelength and amplitude (Weedon, 2003). Power spectra analysis assesses the frequency (1/period) in which periodic and quasi-periodic (regular to near regular) oscillations in a given time series occur which get reflected through peaks in periodograms.

In order to access for statistical significance of spectral peaks, time series need to be tested against an appropriate background "noise" (null hypothesis) that considers the natural physical variability within the climate system and depositional system dynamics. Time series commonly used in paleoclimate studies, produce spectra that drop off towards high frequencies (e.g., 23 and 19-kyr) suggesting there is a red noise component embedded into the data set, as red light is dominated by low frequency (Weedon, 2003). Commonly used autoregressive "red noise" models (e.g., AR1) are mathematically defined (Gilman et al., 1963; Mann and Lees, 1996), where n=1, …, N is the time increment, r_n is the red noise sequence, $0 \leq \rho < 1$ is the lag-1 autocorrelation coefficient , and ω_n is a Gaussian white noise sequence. In summary, these models account for simple stochastic process that occur in the physical climate system as well as in depositional systems and white noise (e.g., weather) component integrated with a slower response time represented in the Earth System (e.g., oceans) (Meyers, 2012).

Another important consideration for spectra analysis is that time series data stops abruptly at either side which produces discontinuities during Fourier transformation that introduces additional power in the spectrum. This produces a bias in that power spectra as it is weakens the significance of real peaks while raising the power elsewhere. Spectral leakage, as it is referred to, is reduced through data tapering and allows for the detection of small-amplitude high frequency events. Tapering is described by Weedon (2003) as "… multiplying the time series by a series of values, window weights, that start at one in the centre of the data (i.e., no tapering) and drop to zero at the edges."

The MTM method used for spectral estimation is non-parametric as it does not use an a priori parameter dependent model (Thomson, 1982; Ghil et al., 2002). A series of special data windows are used to taper (number of tapers is usually 4 to 8) the time series and suppress spectral leakage. The tapers allow for different weighting for different sections of the data providing well-suppressed side lobes (small bias), good smoothing and high frequency resolution (Ghil et al., 2002; Weedon et al., 2003).

3.3. RESULTS

Spectra analysis on our IBRD MAR and biogenic opal time-series data sets highlight significant Milankovitch style frequency events at obliquity and precession frequencies suggesting lithofacies cycles, discussed in Chapter 2, last for multiple glacial to interglacial cycles (Figure 3.1 - 3.3). The IBRD MAR record is dominated by 40-kyr-duration cycles related to obliquity during the Early Pliocene while the Late Pliocene-Early Pleistocene is dominated by the 23 and 19-kyr-duration cycles related to precession (Figure 3.1b). While not significant at 90%, spectrogram analysis highlights strong 100-kyr eccentricity during the Late Pliocene-Early Pleistocene. Early Pliocene biogenic opal is significant at 90% for both obliquity and precession frequencies while the Late Pliocene-Early Pleistocene is significant at 95% for both frequencies. Evolutionary spectra analysis highlights a strong onset 40-kyr cyclicity of biogenic silica around ~2.8 Ma (Figure 3.1c).

Due to the strong orbital signature in our IBRD MAR record we have tuned the IBRD MAR data to obliquity and the precession influenced local insolation at 65°S based on visual correlations made from peak events (Figure 3.3) and applied band-pass filters at obliquity and precession frequencies. This demonstrates that long-term minima in IBRD MAR are associated with (eccentricity-modulated) nodes in precession after 3.3 Ma, and the obliquity node at 4.1 Ma (Figure 3.4).

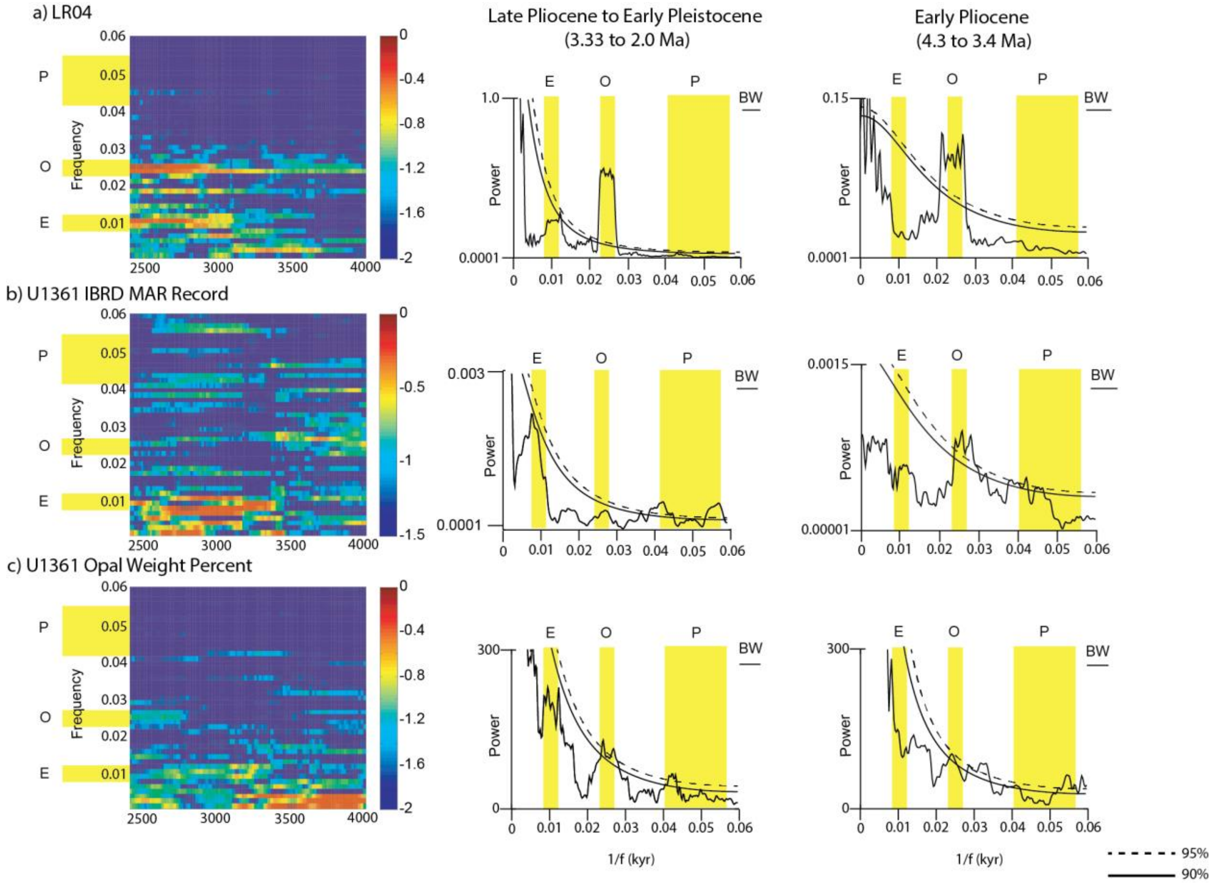

Figure 3.1. Evolutionary and power spectra of time steps for LR04 (Lisiecki and Raymo, 2005) (a), and Site U1361 IBRD MAR (untuned) (b) and Site U1361 opal weight percent (untuned) (c). Bandwidth is indicated by black horizontal line in the top right of individual periodograms (BW).

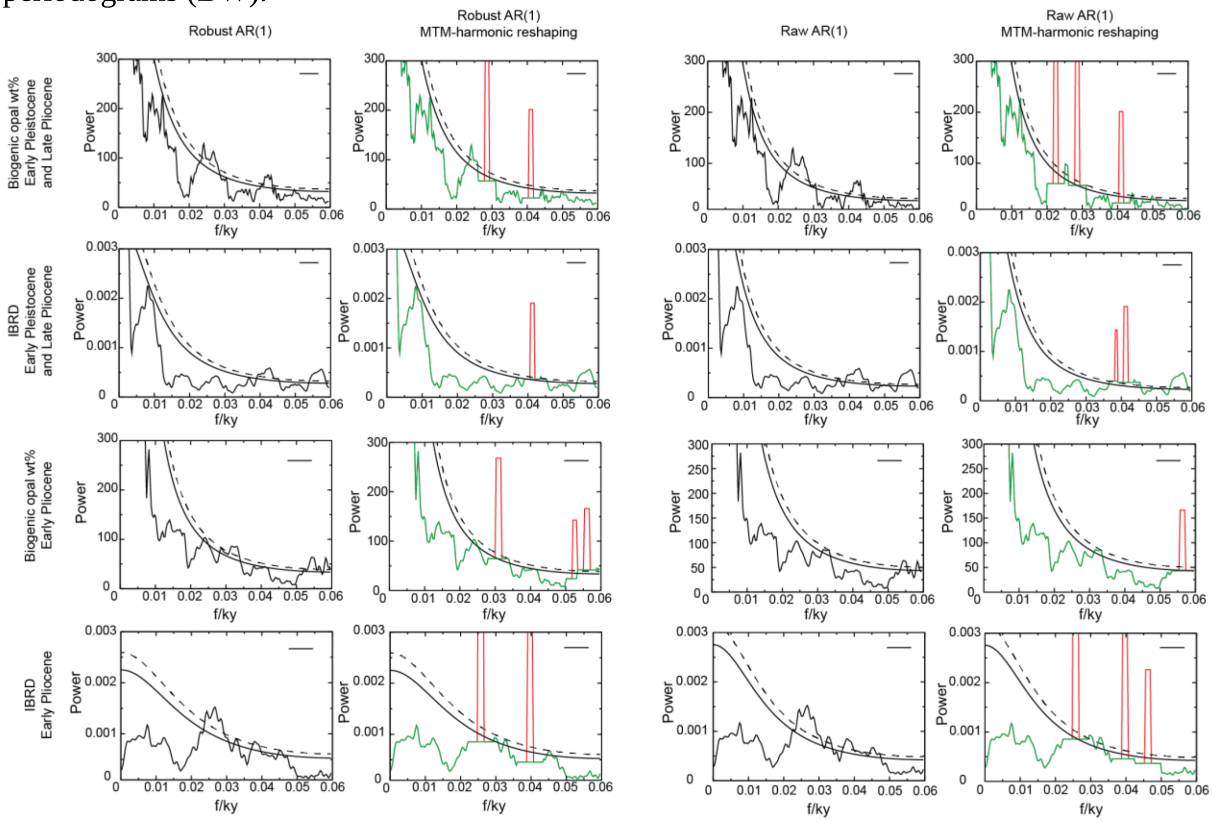

Figure 3.2. Power spectra using Robust and Raw AR(1) red noise background. Raw data output is represented in black lines, while harmonic reshaping data output set to a 90% threshold is represented with green lines in which red lines highlight harmonics. Statistical significance is noted at 90% (solid black line) and 95% (dashed black line).

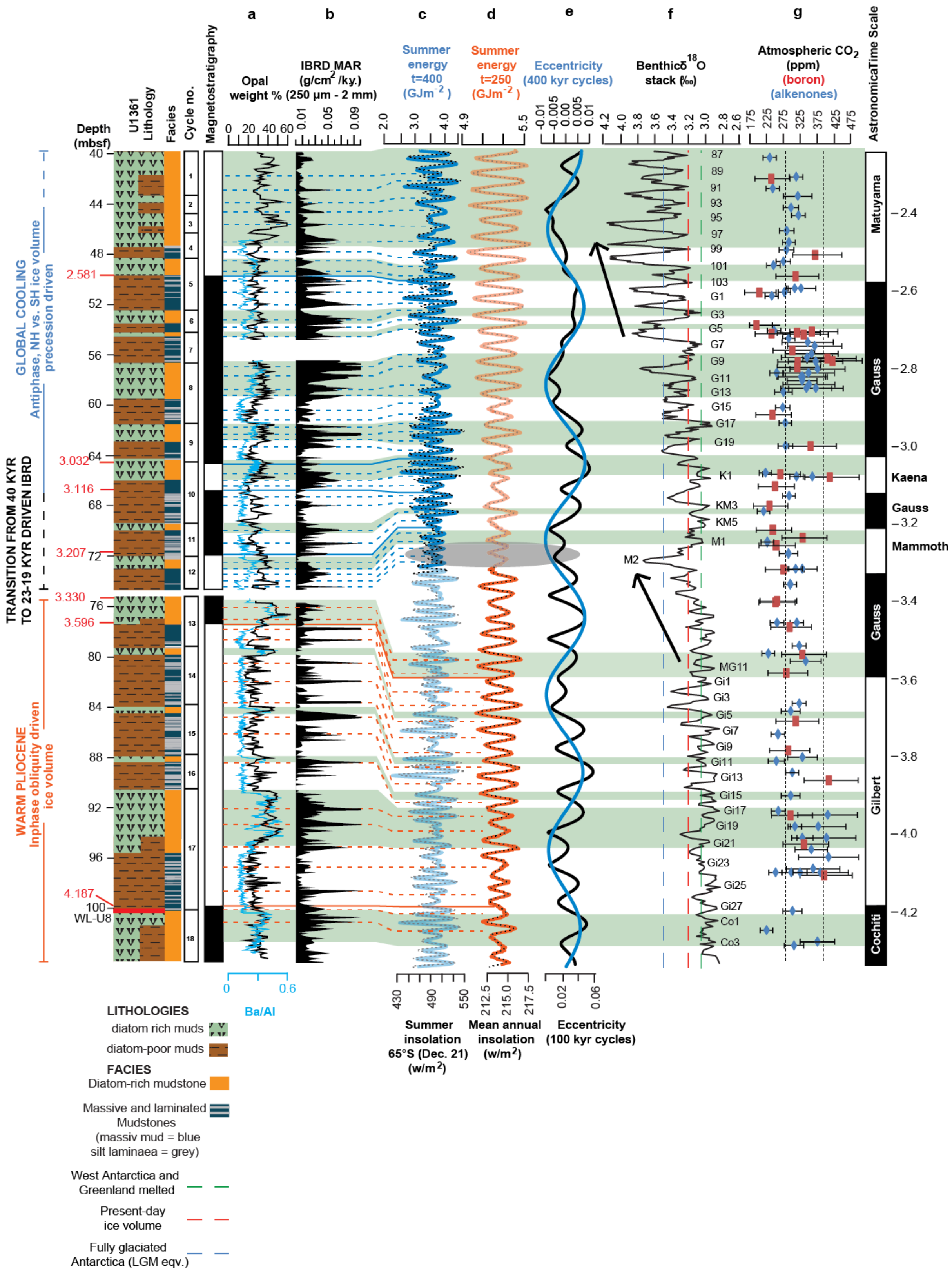

Figure 3.3. Depth series developed for IODP Site U1361 sediment core between 4.4-2.2 Ma of (a) opal percent, (b) IBRD MAR correlated with time series of (c) January insolation and total integrated summer energy (where melt threshold [t]=400GJm^{-2}) , (d) mean annual insolation and total integrated summer energy (where melt threshold [t]=250GJm^{-2}), (e) eccentricity, and (f) the stacked benthic δ^{18}O record (Lisiecki and Raymo, 2005). Also shown is the down core distribution of lithofacies, lithological cycles and magnetic polarity stratigraphy (Tauxe et al., 2012). Maxima in productivity estimates of biogenic opal weight percent and Ba/Al covary with bioturbated/diatom-rich mudstone facies. Grey shaded elipse denotes alignment between a 1.2 Ma node in (d) obliquity modulated mean annual insolation and (e) a 400-kyr minimum in eccentricity which favours polar ice sheet growth and corresponds to (f) a 1‰ glacial δ^{18}O excursion culminating with MIS M2 (arrow). A significant increase in (f) δ^{18}O glacial values from 2.7 Ma (arrow) corresponds with a marked decline in the amplitude of (a) IBRD and a 100ppm decrease in (g) reconstructed atmospheric CO_2 concentration (Seki et al., 2010; Pagani et al., 2010; Bartoli et al., 2011). An (h) evolutive spectrogram of IBRD MAR time series and frequency spectra of (i) late Pliocene to Early Pleistocene (3.3-2.2Ma) and (j) Early Pliocene (4.3-3.4Ma) IBRD MAR time series show transferral of spectral power from ~40-kyr frequency dominance prior to 3.3 Ma to the 100-kyr and 23-19-kyr frequency bands after 3.3 Ma.

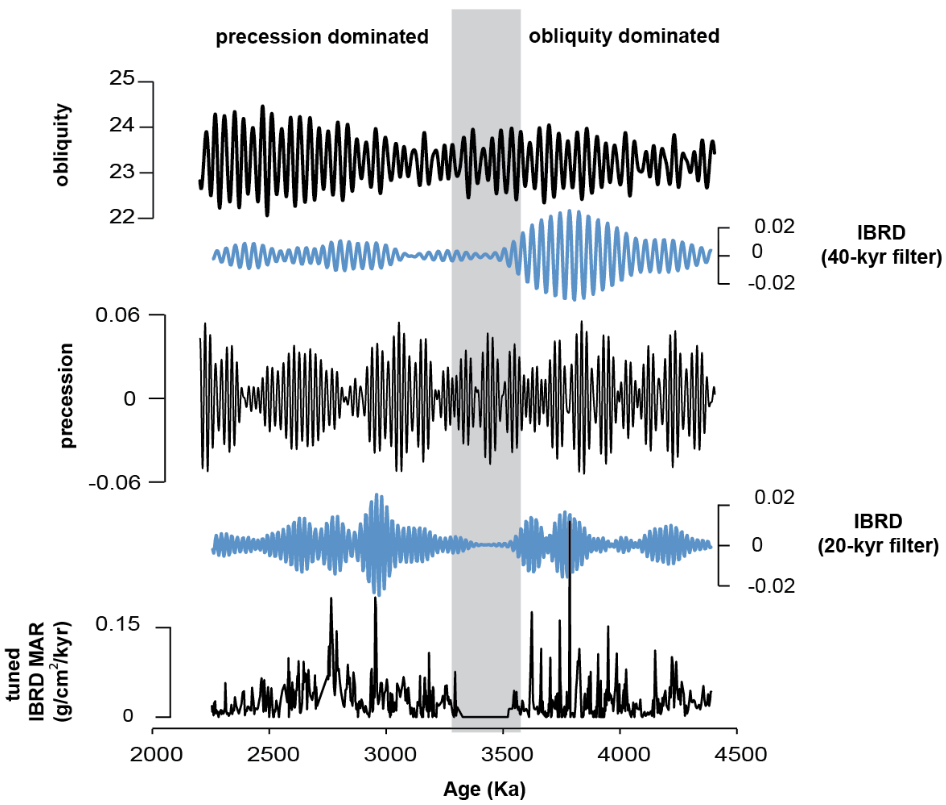

Figure 3.4. Tuned IBRD MAR time series for Site U1361 record with output from band-pass filters at precession (20-kyr) as well as obliquity (40-kyr) frequencies. Grey shading represents a time gap missing from the Site U1361 record followed by IBRD minima at ~3.3 Ma associated with a 1.2 Ma node in obliquity and 400-kyr eccentricity-modulated node in precession.

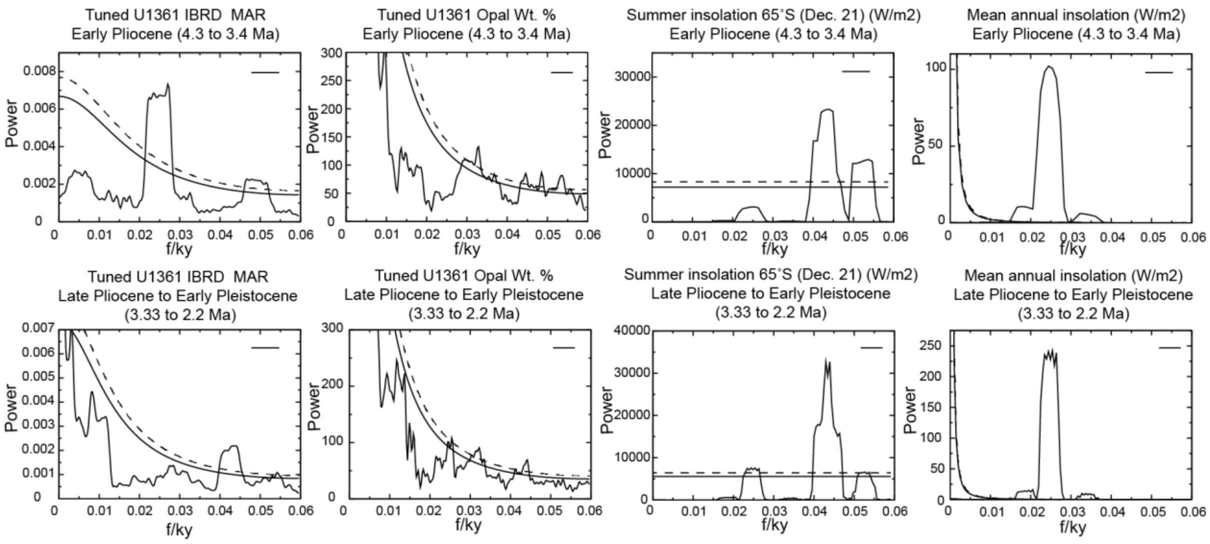

Figure 3.5. Power spectra using the IBRD MAR tuned age model. Early Pliocene IBRD MAR and mean annual insolation display strong 40-kyr cycles of obliquity while biogenic opal does not display Milankovitch frequencies. Late Pliocene-Early Pleistocene IBRD MAR and summer insolation display strong 23- and 19-kyr cycles of precession while biogenic opal wt. % only contains less distinct precession frequencies with 40-kyr obliquity significance. Statistical significance is noted at 90% (solid black line) and 95% (dashed black line).

3.4 DISCUSSION

3.4.1. Iceberg rafted debris as a proxy

As the Antarctic Ice Sheets lose 50-80% of their mass from iceberg calving (Depoorter et al., 2013), IBRD records (i.e., IBRD MAR) provide direct physical evidence of ice sheet calving events along the marine margins of the ice sheets. These calving events are related to the release of ice from fast-flowing ice outlets (outlet glaciers), major deglacial events, and or ice sheet collapse. While the exact physical understanding of calving events is complex, ice sheets and glaciers in contact with the ocean and grounded below sea level are susceptible to rapid iceberg discharge (Bassis and Jacobs, 2013). Distal glacimarine sediment records offer the opportunity to measure such variability of iceberg discharge without being hindered by hiatuses from Neogene and Quaternary ice grounding events that continental shelf sites are subject to. That said, IBRD records need to be interpreted with caution as calving can occur during both glacial and interglacial maximums as well as being heavily influenced by the glacial regime at the time (e.g., Anderson, 1999; Williams et al., 2010). For instance, the thermal regime of Antarctica's small ice shelves, as well as ice tongues, are more favourable to basal freezing, when compared to larger ice shelves that lack basal debris and in which subglacial debris is deposited before major calving events through basal melting (i.e., Ross Ice Shelf). As a result, small ice shelves and ice tongues source sediment-laden icebergs containing abundant basal debris layers (Anderson, 1999). Furthermore, iceberg drift patterns are complex and are under the influence of sea ice conditions, ocean currents and wind around the Antarctic margin (Anderson, 1999).

At present, icebergs get entrained in the westward flowing Antarctic coastal current as well as local gyres and as they flow northward are then influenced by the eastward flowing Antarctic Circumpolar Current (ACC) (Stuart and Long, 2011). The location of Site U1361, south of the ACC boundary front results in IBRD sourced from ice calving along the Ross Sea region as well as the Wilkes Land margin and highlights the advantage of using IBRD records to understand broad geographical scale periodicities in ice calving events along the margin. However, according to geochemical provenance analysis, the majority of modern IBRD is deposited adjacent to its source region (Roy et al., 2007).

Changes in surface ocean currents are unlikely to influence iceberg drift patterns at Site U1361. The dominant westerly flow over the site (Antarctic Coastal Current and its associated front - Antarctic Slope Front) is unlikely to have changed direction, due to bathymetric (i.e., the continental rise/shelf break) and geostrophic considerations, as demonstrated under the scenarios of a greatly reduced EAIS (DeConto et al., 2007). IBRD peaks from the Southern Ocean (e.g., Polar Front) may represent glacial maxima as icebergs can survive for longer time periods in the colder glacial period waters. However, Site U1361 is proximal enough to outlet glaciers of the Antarctic margin for smaller “dirty” icebergs derived from these sources to survive moderate levels of SST warming (as inferred for the Pliocene) (Williams et al., 2010; Cook et al., 2013), but not so close as to be influenced by a single outlet glacier, or a single iceberg dumping (Stuart and Long, 2011). The 3500 m water depth and open ocean location of Site U1361 (with only seasonal winter sea) means icebergs would never be “locked in” place over the drill site, and would pass over the drill site very rapidly (i.e., minutes as they do today).

While previous Pliocene and Quaternary IBRD records recovered from the Antarctic margin display similar characteristics between glacial to interglacial stages (e.g., Ó’Cofaigh et al., 2001; Lucchi et al., 2002; Williams et al., 2010; Passchier, 2011), changes in local sedimentation rates and current winnowing can falsify the magnitude of IBRD events. It is unlikely that changes in sedimentation rates amplifies IBRD events in Site U1361 for the following reasons. Firstly, the peak amplitude of IBRD in the Early Pliocene record is similar between facies. Geochemical provenance studies spanning the Early Pliocene highlight the release of icebergs sourced from the Wilkes Land margin during both sustained warm and cold intervals (Williams et al., 2010; Cook et al., 2013). Secondly, during the Late Pliocene portion of the record the greatest amplitude in change occurs largely at facies transitions. While there is the exception within lithological cycle 8 when obliquity is high and atmospheric CO_2 concentrations straddle levels higher than pre-industrial levels, suggesting the potential for obliquity to have a greater role in iceberg discharge during this time, similar to the Early Pliocene record. Lastly, IBRD during the Early Pleistocene begins to decrease after ~2.5 to the top of the core at ~2.0 Ma (Figure 3.3) suggesting that neither a reduction in background sedimentation rate nor current winnowing have an amplifying affect. This is significant as the Early Pleistocene, based on lithofacies characteristics, is the time most likely to have had the greatest interactions with bottom currents (see Chapter 2). Furthermore, sorting of terrigenous material suggest no such correlation between bottom current winnowing and IBRD to suggest the presence of lag deposits (see Chapter 2 Figure 2.6). Thus, an alternative explanation for the decrease in IBRD MAR after 2.5 Ma, or during nodes in precession and obliquity, may be due to the increased persistence or duration of large fringing ice shelf (and thus “cleaner” icebergs) during these colder intervals, which in turn lead to reduced dynamical ice discharge. Finally, the overall characteristics driving iceberg discharge and calving events appear to change more with major transitions in Southern Hemisphere climate occurring at ~3.3 Ma and ~2.6 to 2.5 Ma (e.g., McKay et al., 2012).

Moreover, it has been demonstrated that the untuned IBRD data contain a statistically significant signal at orbital periodicities throughout our record (Figure 3.1 and 3.2), which suggests iceberg calving is not a random process. Orbital pacing has been also subjectively demonstrated by previous studies along the EAIS margin, but these studies could not statistically identify the frequencies of this pacing as well as the relative power between the 40-kyr and 20-kyr cycles (Escutia et al., 2009; Passchier, 2011).

3.4.2. Cyclostratigraphy framework

The core consists of eighteen sedimentary cycles spanning 4.3 to 2.0 Ma, and comprising alternating terrigenous massive to laminated clay and diatom-rich/bearing silty clay units (cycles 1-18 Figure 3.3). As discussed in Chapter 2, the muds contain packages of well-defined laminae and are consistent with well-established models of non-erosive overbank hemipelagic deposition onto a channel levee setting via mass debris flow (i.e., turbidity currents) on the lowermost Antarctic continental rise (Lucchi et al., 2002). The turbidite units are associated with periods of glacial advance to the Wilkes Land continental shelf edge, whereas bioturbated, diatom-rich/bearing facies represent warm interglacial periods of relatively ice-free ocean and increased primary productivity when the grounding line had migrated landward away from the shelf edge. Increased productivity during interglacial warmth may be associated with enhanced upwelling of nutrient-rich CDW (Anderson et al., 2009), which has been linked to southward expansion of the westerly wind field in response to a reduced pole-equator temperature gradient during past warm periods (Toggweiler et al., 2006; Anderson et al., 2009). Presently this relatively warm, nutrient-rich CDW upwells to the surface north of the Southern Boundary Front of the ACC and is marked by areas of enhanced productivity (the Antarctic Divergence) immediately to the north of Site U1361.

In general, the highest intensity of IBRD occurs during transitions from glacial terrigenous clay facies to interglacial diatom-rich/beraing sediments up-core until ~47 mbsf, with most IBRD peaks immediately preceding opal peaks (Figure 3.3). Isotopic Nd and Sr provenance indicators suggest that these diatom-rich/bearing intervals are associated with periods of deglacial retreat of the ice margin across the continental shelf and into the central portion of the Wilkes Land subglacial basin (Cook et al., 2013) during the Early Pliocene. As the Antarctic Ice Sheet loses the majority of its mass via icebergs (Depoorter et al., 2013), it is interpreted that maximum in IBRD MAR are the consequence of accelerated calving during glacial termination from marine terminating outlet glaciers along the Wilkes Land coastline as well as a contribution from EAIS outlet glaciers entering the western Ross Sea (Naish et al., 2009; Williams et al., 2010; Cook et al., 2013). This interpretation is consistent with models and paleo-observations, which imply the most rapid mass loss of the EAIS marine margin during the last glacial termination occurred between 12 to 7 ka, and was primarily the consequence of oceanic warming (Mackintosh et al., 2011).

The top of the Early Pliocene ~40-kyr-dominated interval is marked by a ~300 to 100-kyr-long condensed section between ~3.6 to 3.3 Ma, and corresponds to a +1‰ glacial $\delta^{18}O$ excursion spanning Marine Isotope Stage (MIS) MG9 and MIS M2. Indeed, this glacial excursion has also been associated with southern high-latitude climate cooling and the re-establishment of grounded ice on middle to outer continental shelf in the Ross Sea following a ~200-kyr period of warm open ocean conditions (Naish et al., 2009; McKay et al., 2012). Previous studies of older Oligocene and Miocene $\delta^{18}O$ glacial excursions have proposed a relationship between intervals of increased glacial amplitude in the $\delta^{18}O$ record with a coincidence of 1.2 Ma nodes in obliquity and 400-kyr minima in long period eccentricity (Zachos et al., 2001; Pälike et al., 2006). This orbital configuration, which favours extended periods of cold summers and low seasonality, is considered optimal for Antarctic ice sheet expansion, and occurs at ~3.3 Ma - the time of the transition from ~40-yr to ~20-kyr dominance in the IBRD MAR times series from Site U1361 (Figure 3.3).

Observed ~20-kyr-duration IBRD cycles are correlated with summer insolation calculated for 65°S for the interval of the core between 3.3 to 2.2 Ma (Figure 3.3). This orbital-tuning strategy is based on the strong orbital signal in our un-tuned IBRD MAR record, and clear link between peaks and trough in austral summer insolation and opal content which are synchronous across the top and bottom Kaena Subchron paleomagnetic reversals, respectively. Band-pass filters at obliquity and precession frequencies applied to the IBRD MAR confirm visual observations that long-term minima are associated with (eccentricity-modulated) nodes in precession after 3.3 Ma, and the obliquity node at 4.1 Ma (Figure 3.4). Furthermore while these IBRD cycles are embedded within longer period 100-kyr IBRD cycles (Figure 3.3e), broad peaks of IBRD maxima are clearly associated with transitions between laminated mudstones to diatom-rich/bearing mudstones. Although this lithological variability is also evident in frequency spectra of opal percentage, it is not significant at 90% (Figure 3.1 and 3.5), which is the likely consequence of a lower signal-to-noise ratio in the opal data. A dramatic decrease in the amplitude of ~20-kyr IBRD peaks, and a change to lithofacies associated with non-erosive low-energy bottom currents in the core from ~2.5 Ma is broadly coincident with the intensification of global high-latitude cooling and onset of major Northern Hemisphere glaciations (Kleiven et al., 2002; McKay et al., 2012). This is attributed to the progressive reduction in calving intensity to cooling and a relative stabilization of the EAIS ice margin. Homogenization of the turbidite sediments during glacial maxima by enhanced bioturbation and bottom current activity is most likely due to the observed increase of Antarctic sea ice and polynya-style mixing at this time (McKay et al., 2012) producing cold high salinity shelf water, in which oxygenated waters may be transferred downslope over Site U1361 to form AABW(Williams et al., 2008).

In summary, correlation of variations in IBRD and opal content with the benthic $\delta^{18}O$ stack and orbital parameters identify up to sixteen ~40-kyr-duration cycles within six major lithological cycles during the Early Pliocene (4.3 to 3.3 Ma) (cycles 13-18 Figure 3.3). This is followed by forty-two ~20-kyr-duration cycles, within twelve longer-duration lithological cycles (cycles 1-12 Figure 3.3).

3.4.3. Implications for an East Antarctic contribution to sea level during the warm Early Pliocene

Diatom-rich mud deposition at Site U1361 typically occurs during Early Pliocene interglacials when benthic $\delta^{18}O$ values are at or below Holocene levels. Moreover, prolonged intervals of diatom-rich mud deposition combined with a lack of turbidity current activity correlate with successive isotopically-depleted 40-kyr cycles of low amplitude variance in benthic $\delta^{18}O$ values, representing extended periods of reduced EAIS volume, associated with global mean sea-level >+10 m above Holocene. Such an interpretation is supported by geochemical provenance analysis of detrital material from Site U1361 (Cook et al., 2013), geological reconstructions of Pliocene ice volume and global sea-level based on backstripping of shallow-marine sedimentary sequences in New Zealand and Virginia (Miller et al., 2012) as well as a calibration of the benthic $\delta^{18}O$ record (Naish and Wilson, 2009), that estimate global mean sea-levels were up to ~+20 m with amplitudes of 5-10 m during the warmest and least variable glacial-interglacial $\delta^{18}O$ cycles between 4.3 to 3.2 Ma. Given, (1) geochemical provenance of detrital material along the Wilkes Land margin documenting retreats several hundred kilometres inland with the release of ice-berg armadas (Williams et al., 2010; Cook et al., 2013), (2) the AND-1B sediment core indicates SST of ~4°C and an ice free Ross-Sea (Naish et al., 2009) with significantly reduced WAIS (i.e. <3 m sea-level equivalent (Pollard and DeConto, 2009), (3) a lack of geologic evidence for major continental glaciation in the Northern Hemisphere (Jansen et al., 1996; Haug et al., 1999; Brigham-Grette et al., 2013), and (4) that models imply Greenland deglaciation (i.e. <7 m sea-level equivalent) (Dolan et al., 2011), this thesis data support orbitally-induced oscillations in the EAIS contributed up to +10 m sea-level equivalent ice volume during the Pliocene.

3.4.4. Significance of the Site U1361 iceberg rafted debris orbital signature

Although, the marine sediment core recovered by the ANDRILL Program from the Ross Sea region provided the first direct evidence that the WAIS periodically advanced and retreated across the continental shelf was paced by obliquity during the Pliocene prior to ~3 Ma (Naish et al., 2009), sub-glacial erosion surfaces in the ANDRILL core associated with ice advance have raised the possibility of missing cycles, particularly after 3.1 Ma. The continuous Site U1361 record presented here confirms the dynamic response, not only of the WAIS but also the marine margins of the EAIS, to obliquity forcing during the warm Pliocene prior to the onset of southern high-latitude cooling at 3.3 Ma.

Geological records (Naish et al., 2009; McKay et al., 2012; Cook et al., 2013) and model simulations (Pollard and DeConto, 2009) of recent and past warm climates highlight the sensitivity of the marine-based portions of the Antarctic ice sheets to ocean warming. However, the mechanism by which the coastal ocean warms and destabilises marine grounding lines in response to obliquity forcing remains elusive. It has been proposed that changes in the intensity and the meridional distribution of mean annual insolation controlled by obliquity may have a profound influence on the position and strength of the Southern Hemisphere zonal westerly winds (Naish et al., 2009). Indeed, an aerosolic dust record from the Southern Ocean is dominated by ~40-kyr cycles in iron and leaf-wax biomarkers prior to ~0.8 Ma (Martínez-Garcia, et al. 2011). Moreover, prior to ~3.3 Ma the southward expansion of the westerly wind-field over the Antarctic circumpolar convergence zone under a reduced meriodional temperature gradient, has been associated with a reduced sea-ice field (McKay et al., 2012), and the upwelling of warm, CO_2-rich CDW (Toggweiler et al., 2006; Martinson et al., 2008) onto the continental shelf with consequences for the stability of marine grounding-lines (Pritchard et al., 2012). The dominance of precession-paced variability and the corresponding reduction in obliquity influence revealed by IBRD data after ~3.3 Ma is interpreted to reflect a declining influence of oceanic forcing on EAIS stability and extent, as the southern high latitudes cooled. Both model and geological reconstructions imply that past Antarctic Ice Sheet expansion is closely linked with development of the sea-ice field (DeConto et al., 2007) potentially resulting in northward migration of westerly winds and Southern Ocean fronts (McKay et al., 2012). In addition, sea ice expansion after 3.3 Ma likely restricted upwelling and ventilation of warm CO_2 rich CDW at the Antarctic margin acting to further enhance climate cooling, which has been linked in models to a change in frequency of the orbital response of polar ice sheets (Huybers and Denton, 2008). Under such a scenario, a warmer climate state during the Early to mid-Pliocene with higher atmospheric CO_2 concentration (Seki et al., 2010), required less insolation to melt sea ice, thus extending the austral summer with its duration more strongly influenced by mean annual insolation controlled by obliquity (Figure 3.3d and 3.3.1.5), rather than seasonal insolation intensity controlled by precession (Huybers and Tziperman, 2008). Late Pliocene cooling raised the melt threshold such that the duration of the melt season was restricted to times of austral summer insolation maxima controlled by precession (Figure. 3.3c and 3.5), with extensive sea-ice cover for much of the summer season limiting the influence of CDW on marine grounding line instability. This supports the notion that the length of the summer melt season is controlled by the overall climate state, and is the primary influence on the frequency response of the EAIS to orbital forcing (Naish et al., 2009).

The precession and eccentricity signal observed in the IBRD data is consistent with a reduction of obliquity variance in the benthic $\delta^{18}O$ LR04 stack at ~3.5 Ma (Meyers and Hinnov, 2010 Figure 1.C), which coincides with an obliquity node in the astronomical solution (Meyers and Hinnov, 2010 Figure 1.D). This is followed by a gradual reemergence of a 40-kyr signal at ~3.0 Ma in the benthic $\delta^{18}O$ LR04 stack, which most likely reflects a similar re-emergence of strong obliquity forcing in the orbital records and possibly also a direct response of the developing Northern Hemisphere continental ice sheets to obliquity forcing. Thus, it is possible that precession-driven, anti-phase oscillations in both hemispheric ice volumes may have cancelled out in globally integrated proxy records after 3.3-2.8 Ma (e.g., Raymo et al., 2006). However, the mechanistic argument of Raymo et al., (2006) that the intensity of summer insolation was a direct control on surface melt of a dynamic EAIS with a terrestrial ablation margin, is not supported by this study. The geometry of strata on the Wilkes Land continental shelf indicate that the EAIS periodically expanded towards the continental shelf edge during glacial maxima in the Pliocene (Eittreim et al., 1995) and suggests most Antarctic ice volume variance at this time was growth and retreat of the marine-based ice sheets. Indeed, iceberg calving appears to be associated with sea-ice melt as evidenced by the covariance of IBRD peaks with facies transitions going from relatively colder glacial maxima conditions to warmer interglacial minima conditions as implied by open ocean primary productivity (opal) in our data. This is particularly true for the Late Pliocene from 3.3 to 2.5 Ma, but during the Early Pliocene, when the sea ice field was reduced and the ice sheet was in more direct contact with oceanic influences, (1) iceberg calving occurred more regularly within both glacial and interglacial facies. Based on the significant decrease in IBRD after 2.5 Ma (Figure 3.3 and 3.4) and (2) Southern Ocean records inferring colder SSTs (Escutia et al., 2009; McKay et al., 2012), it is also inferred that the EAIS started to stabilize and became less sensitive to ocean induced melting compared to the WAIS (Pritchard et al., 2012). Furthermore, the fully-glaciated East Antarctic ice volume potentially fluctuating by a similar magnitude to that of Late Pleistocene glacial cycles (e.g. 15-20 m ice volume equivalent sea level) (Pollard and DeConto, 2009).

Notwithstanding this relative stability of the EAIS, model results suggest that ~20-kyr-duration fluctuations in the total Antarctic ice volume (i.e., including WAIS) may have contributed up to 15 m of the total amplitude during Late Pleistocene glacial-interglacial cycles (Pollard and DeConto, 2009). Given the $\delta^{18}O$ composition of Antarctic ice, that contribution could have offset a larger out-of-phase precessional change in Northern Hemisphere ice volume (e.g. 20-40m) resulting in an enhanced obliquity signal in the globally integrated sea-level and ice volume proxy records after 3.0-2.8 Ma (e.g., Raymo et al., 2006). Alternatively, direct obliquity forcing of the Northern Hemisphere ice sheet is supported by proxy evidence including ice rafted debris records (Martínez-Garcia et al., 2011) and a recent dust flux record (Naafs et al., 2012), suggesting that Northern Hemisphere ice sheet variability (marine-based margins) and climate primarily responded to obliquity under a relatively warm Northern Hemisphere climate state. Northern Hemisphere cooling and ice sheet growth across the mid-Pleistocene transition ~0.8 Ma has been implicated in a similar switch to precession and eccentricity-paced glaciations, albeit by different mass balance forcing mechanisms (Huybers, 2008). In contrast, our results imply that Southern Ocean sea-ice feedbacks caused a fundamentally different response of the marine-based sectors of the EAIS under a cooler Late Pliocene/Early Pleistocene climate state, characterized by a dominance of precession-paced variability.

3.5. CONCLUSIONS

In summary, the data presented in this chapter reveals ~40-kyr cyclic variations in the extent of the EAIS paced by obliquity during the warmer-than-present climate of the Pliocene between 4.3 to 3.3 Ma. However, after 3.3 Ma a transition to 20-kyr precession cyclicity dominates the EAIS. Stabilization of the marine-based margin of the EAIS between 2.8 and 2.5 Ma suggests a declining influence of oceanic forcing as the high latitude Southern Ocean cooled and a perennial summer sea-ice field developed to limiting basal melting of the marine-based margins of the EAIS.

With atmospheric CO_2 concentrations and global surface temperatures projected to remain above 400 ppm and >+2°C beyond 2100 (Meinshausen et al., 2009), the results suggest that the marine margins of EAIS ice sheet, as well as the marine-based WAIS, will become increasingly susceptible to ocean-forced melting providing the potential for widespread mass loss raising sea-level by meters over the coming centuries.

CHAPTER 4

BOTTOM WATER INFLOW INTO THE SOUTHWEST PACIFIC OCEAN DURING THE PLIOCENE-EARLY PLEISTOCENE

Benthic stable isotope (oxygen, carbon) and grain size (sortable silt) records spanning the Pliocene to Early Pleistocene from Ocean Drilling Program (ODP) Site 1123, located in the southwest Pacific Ocean, are presented in this chapter. The benthic $\delta^{18}O$ and $\delta^{13}C$ records display similar long-term transitions at 3.33 Ma and 2.6 Ma that coincide with the major climate transition in both the Southern and Northern Hemispheres. Site 1123 benthic $\delta^{18}O$ record is consistent with the globally integrated stack, LR04, but also demonstrates a temperature component which is consistent with previously established stable isotope records recovered from other Southern Ocean sites. Size sorting of silt (sortable silt) implies a potential increase in deep water inflow into the Pacific after 3.3 Ma as a consequence of sea ice development around the Antarctic margin that is characterised by relatively low $\delta^{13}C$ composition, reflecting the enhanced contribution of Circumpolar Deepwater (CDW) with a relatively stronger southern sourced signature. This coincides with invigorated zonal circulation patterns in mid latitudes suggesting enhanced interaction of the westerly winds over the northern limb of the Antarctic Circumpolar Current (ACC). After 2.6 Ma benthic $\delta^{13}C$ was lowest (0.044‰) with deep water gradients between the equatorial and southwest Pacific reduced, and together with sortable silt values imply an overall decrease in Southern Ocean ventilation. This decrease in Southern Ocean ventilation coincides with a decrease in atmospheric CO_2 levels to consistently reaching pre-industrial values, and with associated climate feedbacks driven from the southern high-latitudes potentially pre-conditioned the onset of major Northern Hemisphere glaciation.

4.1. INTRODUCTION

Deep ocean circulation of waters originating in high latitudes has important consequences for Earth's meridional distribution and transport of heat, salt, gases and nutrients. Integral to this circulation system are deep western boundary currents (DWBC) that transport water formed in high latitudes towards the equator. Ocean Drilling Program (ODP) Site 1123 sits in the path of the southwest Pacific DWBC through which deep water enters the Pacific Ocean Basin from the Southern Ocean. It serves as the largest inflow of deep Antarctic sourced bottom water into the global ocean. The intensity of inflow into the southwest Pacific has been demonstrated to conicinde with glacial-interglacial cycles, inferred to be in response to changing AABW production and ice sheet expansion during the Miocene and Late Pleistocene (Hall et al., 2001; Hall et al., 2003). A prominent feature of global climate during the warm Early Pliocene from ~4.4 to 3.0 Ma is a reduced Equator-to-pole surface temperature gradient in both the Pacific and Atlantic Ocean basins, which was significantly smaller than present day (Pliocene Pacific, <10°, Atlantic, ~5°; modern Pacific, 16°, Atlantic, 8-10°) (Chandler et al., 1994; Crowley, 1996; Fedorov et al., 2013). North Atlantic records imply a close coupling between deep ocean changes and SST during this time (Ballantyne et al., 2010). Therefore, observing changes in the flow regime entering the southwest Pacific across ODP Site 1123 may provide insights concerning the role that high latitude/Antarctic climate forcing has on mid to low-latitude climate.

In the Southern Ocean today, upwelling of Circumpolar Deep Water (CDW) along the Antarctic divergence ventilates the deep ocean by releasing dissolved CO_2 from depth to the atmosphere (Jacobs, 1991). Ventilation of the deep ocean also requires the production of oxygen-rich, cold saline bottom waters from around the Antarctic margin and the Arctic associated with sea-ice fields and polynya formation. During glacial periods, extended sea ice cover is thought to promote the formation of dense, cold water, that enhances stratification of the surface ocean and decreases upwelling and ventilation of the deep ocean (Jacobs, 1991; Bostock et al., 2013). While such processes have been demonstrated to have occurred on glacial-interglacial time scales (e.g., Anderson et al., 2009; Skinner et al., 2010), long-term changes in Antarctic surface conditions in regards to its icescape (configuration of ice sheets, ice shelves, sea ice, etc.) have potentially played an important role in the global trend of Late Pliocene-Early Pleistocene cooling by altering oceanic circulation and ventilation and setting the stage of large-scale Northern Hemisphere glaciation during the Late Pleistocene (McKay et al., 2012).

In this chapter, benthic foraminiferal stable isotope records ($\delta^{18}O$ and $\delta^{13}C$) and sedimentary data from ODP Site 1123 (Figure 4.2a) are investigated to help identify if changes in Antarctic ice volume (such as the discussed in Chapter 3 of this thesis) had implications for Southern Ocean ventilation and deep water inflow into the Pacific Ocean basin during the Early Pliocene to Early Pleistocene.

4.1.1. ODP Site 1123 and bottom water inflow into the southwest Pacific Ocean

In the southwest Pacific Ocean, the Campbell Plateau and the Chatham Rise serve as important topographic control on the positioning of two major surface ocean boundary fronts, the Subantarctic Front (SAF) and the Subtroptical Front (STF) (Figure 4.1a). The STF is commonly defined as the northern boundary of the Southern Ocean as it acts as the boundary between (1) Subtropical Surface Waters to the north that are characterized as warm, salty, and nutrient-poor and (2) cool, relatively less salty, nutrient-rich Subantarctic Surface Waters to the south (Deacon, 1937; Orsi et al., 1995; Belkin and Gordon, 1996; Nodder and Northcote, 2001). The SAF marks the northern boundary of the eastward flowing (ACC) and is constrained by the southwest margin of the Campbell Plataeu (Orsi et al., 1995). Flowing along and around south eastern margin of New Zealand, the “cold” Southland Current (SC) is separated from the “warm” East Cape Current (ECC), east of New Zealand by the Chatham Rise east at which of which point they merge to form the South Pacific Current (SPC) (Stramma et al., 1995). It is this flow pattern North and South of the Chatham Rise that constrains the STF to the rise crest. There, seasonal movement of the STF are only up to 2° latitude, whereas, in the open ocean seasonal migrations of up to 6° of latitude are observed (Chriswell, 1994; Kawahata, 2002; McCave et al., 2008). Minimal latitudinal variability of the STF in the Chatham Rise region appears to also hold true over longer-term climate cycles (Fenner et al., 1992; Nelson et al., 1993; Weaver et al., 1998; McCave et al., 2008).

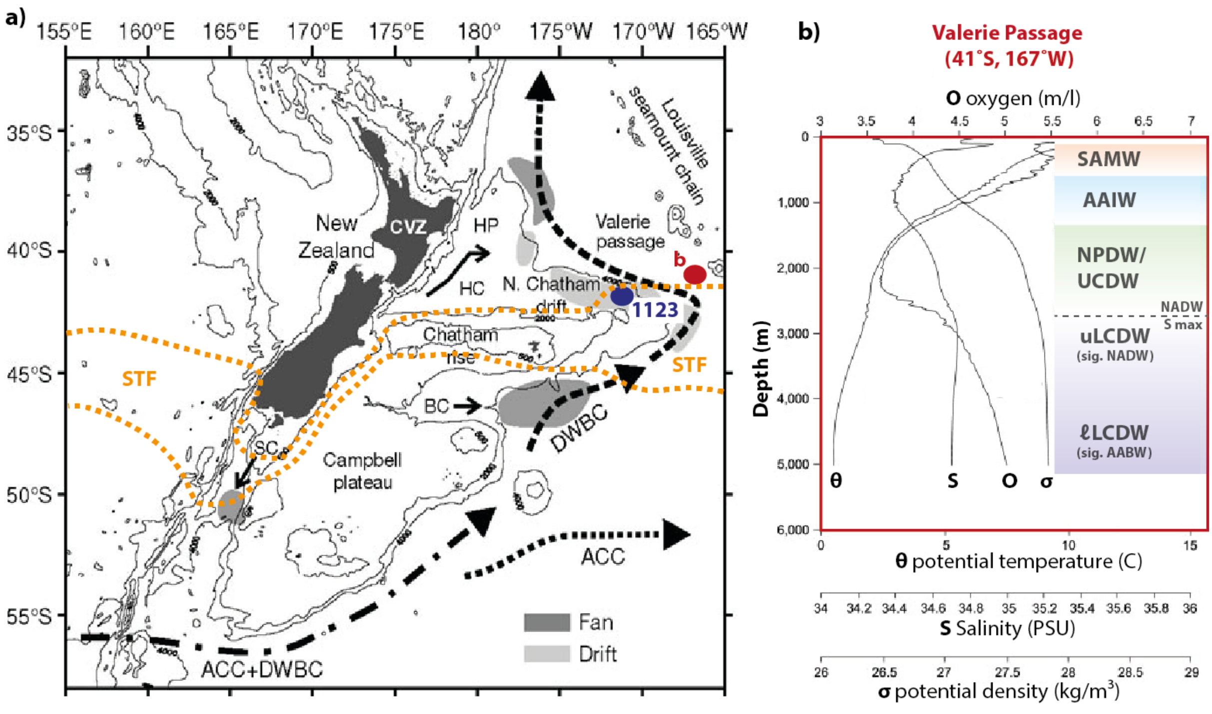

Figure 4.1. Location of Site 1123 on the North Chatham drift and in the path of the DWBC (a) (after Hall et al., 2001). The orange dotted line infers the general location of the

Subtropical Front (STF). Other notable sediment transport and depositional features are the Solander Channel/Fan complex (SC), the Bounty Channel/Fan complex (BC) and Hikurangi Plateau (HP) and Chennel (HC). Hydrographic profile from the Valerie Passage (station R631, 41°S, 167°W) showing features of the main water masses including Antarctic Intermediate Water (AAIW), North Pacific Deep Water/Upper Circumpolar Deep Water (NPDW/UCDW), Lower Circumpolar Deep Water (LCDW) with the salinity maximum a signature of North Atlantic Deep Water (NADW) and oxygen maximum a signature of Antarctic Bottom Water (AABW) (b) (after McCave et al., 2008).

Site 1123 at 3290 m water depth is located just north of the Chatham Rise in the path of the DWBC (Figure 4.1a). Since the early Miocene, near continuous deposition has occurred as the DWBC has been re-depositing sediment as drifts derived from the Solander Fan/Complex, eastern side of the Campbell Plateau, Bounty Fan, and southern Chatham Rise along the eastern and northern side of the Rise (Carter et al., 2004). Comparisons of sediment flux between the Bounty Fan (ODP Site 1122) and Site 1123 suggests that the shallower depth of Site 1123 prevents a direct sediment pathway connection with the Bounty Fan (Carter et al., 1999). A significant volume of sediment from the North Island is suggested to be transported via the subtropical inflow of the ECC with additional aeolian input from westerly winds depositing dust derived from New Zealand and Australia (Hall et al., 2001). It is along the pathway of the southwest Pacific DWBC and at depth between 1200 m to 4800 m, 35-40% of cold bottom water formed in high latitudes enters the Pacific Ocean (Warren, 1973; Schmitz, 1995), making this the largest volume transport of bottom water into any of the three ocean basins (Warren, 1973; Orsi et al., 1995; Carter et al., 1996; Rintoul et al., 2001). Site 1123 is currently situated at a depth shallow enough to not undergo erosive current winnowing by intense bottom current flow (K_E are < 1 to 2 $cm^2 s^{-2}$) while also above the critical threshold of bed sheer stress threshold (K_E 0.32 $cm^2 s^{-2}$) for deposition of particle sizes >10µm (McCave and Hall, 2006), and positioned well northward of the high eddy turbulence associated with the modern ACC in this region (K_E up to 80 $cm^2 s^{-2}$) (Carter and Wilkin, 1999).

Due to lateral mixing in the water column, the abyssal current entering the southwest Pacific is a hybrid of AABW and LCDW, a variety of CDW (Kroopnick, 1985; Carter et al., 2004b: McCave et al., 2008). The signature of LCDW is a salinity maximum (34.70-34.75 psu) (Orsi et al., 1999; Carter et al., 2009) reflecting the NADW component that enters the Southern Ocean in the Atlantic sector. The hybrid AABW component of bottom water entering the Pacific Ocean via the DWBC is sourced from a mixture of Ross Sea Bottom Water (RSBW) and Adélie Land Bottom Water (ALBW) (Orsi et al., 1999; McCartney and Donohue, 2007;

McCave et al., 2008; Williams et al., 2008) (Figure 4.1b). This delivery of bottom water into the Pacific Ocean is mainly through the transport of CDW by the wind-driven and bathymetrically steered ACC (Orsi et al., 1995; Rintoul et al., 2001). North of the Chatham Rise, extending south of the Equator and at shallower depths (~140-2900 m), low-oxygen/high-nutrient waters that originate in the North Pacific (PDW) mix with southern-sourced CDW. UCDW, in part, is created along this southward flow path from the mixing of PDW and CDW (Callahan, 1972; Rintoul and Bullister, 1999; Bostock et al., 2011). Site 1123 presently sits at 3290 m water depth, near the base of UCDW/PDW water masses, straddling the upper boundary of the deeper LCDW (McCave et al., 2008).

In general, benthic isotopic depth profiles spanning the last 160 kyr years demonstrate oxygen and carbon isotopic values have retained a constant structure of LCDW-UCDW/NPDW-Antarctic Intermediate Water (AAIW) (Figure 4.1b) (McCave et al., 2008). Modern and Holocene values of benthic ^{13}C at Site 1123 (~0.8‰) reflect nutrient-depleted UCDW/PDW whereas, relatively low ^{13}C LGM (-0.6‰) values are more nutrient-enriched Southern Ocean sourced and reflect CDW values (McCave et al., 2008).

4.1.2. Using stable carbon isotopes to identify changes in deepwater circulation

Stable isotopes derived from benthic foraminifera are widely used to reconstruct global ice volume and deep sea temperatures using δ^{18}O, while circulation of deep water masses can be traced using δ^{13}C values. The carbon isotopic distribution through the modern ocean has been largely identified through the GEOSECS program (Kroopnick, 1985). Three main factors control the δ^{13}C of dissolved inorganic carbon (DIC) in deep water. Firstly, the preformed δ^{13}C value in the source region is determined by the mixed layer properties in high-latitude surface waters, i.e., the main deep water production regions, which are influenced by numerous processes include upwelling, surface water productivity (e.g., sea ice cover), ocean and atmospheric gas exchange, and mixing of intermediate and deep water (Broecker et al., 1982; Charles and Fairbanks, 1990; Hodell and Venz-Curtis, 2006).

Secondly, organic matter is remineralized (oxidized) by respiration along its flow path (accumulating ^{12}C) resulting in a decrease in δ^{13}C (nutrient enriched) value compared to the preformed δ^{13}C. This ageing processes is considered to be much more important for the Pacific Ocean than compared to the Atlantic and Indian oceans (Raymo et al., 1997) as the North Pacific contains the most depleted values anywhere in the world oceans (Kroopnick, 1985). The low $\delta^{13}C$ water (nutrient enriched) of the North Pacific is due to nutrient trapping of southern sourced Lower Circumpolar Deep Water (LCDW) upwelling at mid-depth (2000 to 4000 m) where it warms and freshens while returning southward as Pacific Deep Water (PDW), at which point, it continues to accumulate nutrients along it flow path (Schmitz, 1996; Matsumoto et al., 2002). Thirdly, $\delta^{13}C$ values can be affected by mixing with other water masses (e.g., Oppo and Fairbanks, 1987). For example, as PDW continues to flow southward towards the equator, whereby it mixes with LCDW, providing the oxygen minimum, nutrient, and CO_2 maximum signature of UCDW (Figure 4.1.b) (Callahan, 1972; Rintoul and Bullister, 1999).

Additional influences on $\delta^{13}C$ are known to occur in areas with high productivity in surface waters which can lower the $\delta^{13}C$ through the decomposition of ^{13}C-depleted organic matter in phytodetritus layer (Mackensen et al., 2001). This situation has been associated with epifaunal benthic foraminifera (i.e., *Cibicidoides wuellerstorfi* and *Planulina wuellerstorfi*) in the South Atlantic sector of the Antarctic Polar Front (Mackensen et al., 1993, 2001).

In general, the highly saline and nutrient-depleted bottom waters that largely form around the Labrador and Greenland seas, North Atlantic Deep Water (NADW), contain relatively high $\delta^{13}C$ values due to long exposure time in surface waters prior to sinking. Whereas, nutrient-enriched Antarctic bottom waters (AABW) sourced around the Antarctic margin, AABW, largely formed in the Weddell and Ross Seas as well as in the Adélie depression along the Wilkes Land margin, and have relatively low $\delta^{13}C$ values (e.g., Hodell and Venz-Curtis, 2006). The lower values for AABW are generally related to the recirculation of old deep water (i.e., NADW) and limited equilibration with the atmospheric due to processes related to sea ice cover and ice sheets – i.e., reduced ventilation in the Southern Ocean (Hodell and Venz-Curtis, 2006).

4.1.3. Southern Ocean ventilation and the G-I cycle

The ocean is the world's largest carbon reservoir and plays an integral role in determining atmospheric CO_2 content (Sharp, 2007). Simplistically, the deep ocean becomes enriched in CO_2 through the respiration of organic matter. Upwelling of these CO_2 rich deep waters in the Southern Ocean along the southern boundary of the ACC allows for ventilation of CO_2 into the atmosphere. Ventilation of the Southern Ocean can best be described through a series of positive feedbacks involving the mid-latitude westerly winds, atmospheric temperatures and overturning of CO_2 rich deep water in the Southern Ocean. Such feedbacks are commonly suggested to explain the lead of Antarctic temperatures over CO_2 at terminations (Petit et al., 1999; Jouzel et al., 2007) and shifts to $\delta^{13}C$ minimum in the deep ocean (Toggweiler et al., 2006).

The pathway of ACC is strongly coupled to the ocean's bathymetry and constrained at its northern limit by the tip of South America (56°S) and Campbell Plateau (56°S). However, the Southern Hemisphere westerly winds, which can shift due to changes in the thermal contrast in the middle of the atmosphere, drive the ACC vigour and thus influences Southern Ocean overturning. During glacial periods lower atmospheric CO_2 levels (Petit et al., 1999; Jouzel et al., 2007) allow for contrast between the upper troposphere (pocket of warm air near the surface) and the cold air of the stratosphere to be relatively smaller when compared to interglacial times containing higher atmospheric CO_2 and increasing the temperature gradient (Toggweiler et al., 2006). The lower contrast in temperature (during glacials) between the upper troposphere and stratosphere results in a weakened wind field. Therefore, the strongest westerly winds in the Southern Hemisphere are hypothesized to have been located in a more northward position (7-10°) during glacials, and thus interacting less directly over the ACC, which is effectively locked in placed by bathymetric constraints, potentially resulting in less overturning in circulation of CO_2 rich deep water (Toggweiler et al., 2006; Toggweiler and Russell, 2008). Such a situation of less overturning may allow for more sequestering of CO_2 as upwelling in the Southern Ocean reduces and the intensity of NADW slows as the Northern Hemisphere cools. In the high latitudes, the production of sea ice is also considered to have acted as a physical cap reducing ventilation (Figure 4.1a) (Stephens and Keeling, 2000; Toggweiler et al., 2006; Hodell and Venz-Curtis, 2006).

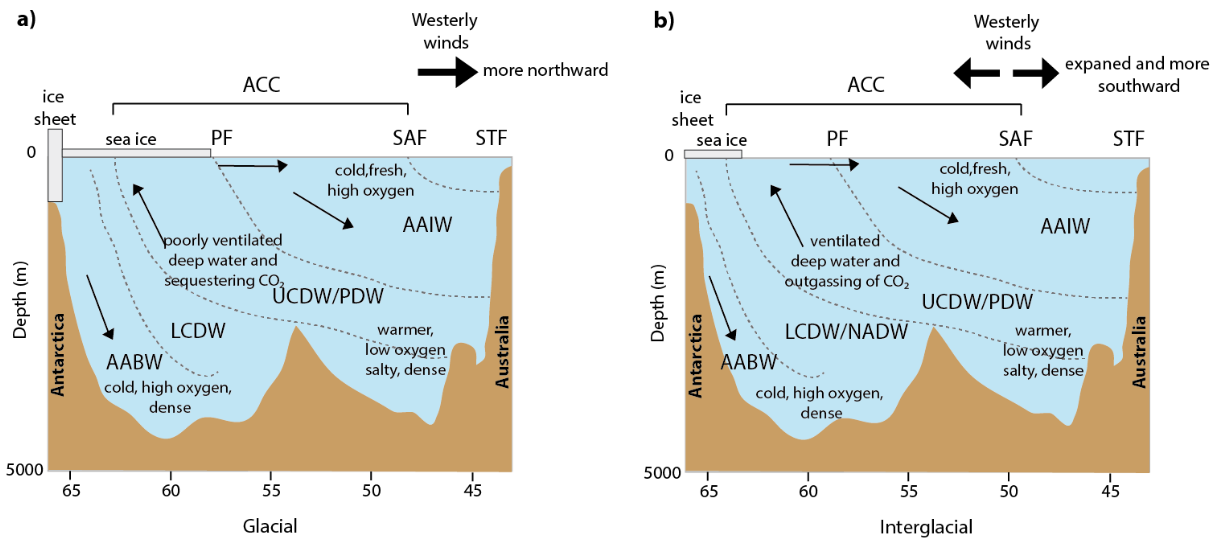

Figure 4.2. Schematic diagrams of deep ocean ventilation in the Pacific sector of the Southern Ocean during (a) glacial and (b) interglacial periods (after Toggweiler and Russel1, 2008; Bostock et al., 2013).

Conversely, higher CO_2 during interglacial periods increases the temperature gradient between the upper troposphere and stratosphere. In which case, the westerlies intensify and the wind field migrates southerwards into the latitudes of the ACC displacing ocean fronts polaward as well as enhancing circulation and overturning of CO_2 rich deep waters. This situation, in addition to enhanced production of relatively warm saline NADW and reduced sea ice fields, amplifies the warming by ventilating the deep ocean (Figure 4.1b) (Toggweiler et al., 2006; Toggweiler and Russell, 2008). Geological evidence from deep sea sediment records since the LGM from both the Southern Ocean and around the Antarctica margin supports increased Southern Ocean ventilation during termination events (Anderson et al., 2009; Skinner et al., 2010; Bostock et al., 2013). The recent WAIS Divide ice core infers a close coupling of a warming WAIS during times of increased wind stress over the Southern Ocean and ventilation as the sea ice field was reduced during austral summer warming (WAIS Divide Project Members, 2013). Furthermore, a decrease in benthic $\delta^{13}C$ in marine sediment cores spanning the past 9 myr associates the overall reduction of Northern Component Waters (NCW) (NADW precursor) on longer term time scales (multiple glacial and interglacial periods) with reduced ventilation of the Southern Ocean and acting as a positive feedback to drive a gradual cooling climate trend reflected in the benthic $\delta^{18}O$ ice volume record (Hodell and Venz-Curtis, 2006). However, it is worth noting the complexity and limited undertstanding of these systems as some studies employing sensitivity experiemnets using an Earth system model with a fully coupled marine carbon cycle model demonstrate shifts in both the position and intensity of the Southern Hemisphere westerlies only account for a minor compoenent of the large scale glacial to interglacial variations in atmospheric CO_2 (Menziel et al., 2008). These studies suggest changes in terrestrial vegetation may play a stronger role in the large scale variations in atmospheric CO_2 on glacial to interglacial time scales (Menziel et al., 2008).

4.1.4. LITHOSTRATIGRAPHY

Pliocene-Pleistocene age sediments presented in this study (~157.6 to 98.4 mbsf) correspond to Unit 1A and consist of successive alternations of light greenish grey to greenish grey and white clayey nannofossil oozes with tephra layers at 124.03 mbsf (4 cm thick), 117.15 mbsf (6 cm thick), and 104.7 mbsf (3 cm thick) (Carter et al., 1999). Lithological beds (1-1.5 m thick) are distinguishable by colour but contain minimal terrigenous compositional differences with gradational contacts. Tephras have sharp bases with normal grading and below ~90 mbsf are darker in colour due to increased diagenetic pyrite (Carter et al., 1999). Down core measurements of color reflectance have also been demonstrated to be a reliable proxy for carbonate percentage (Carter et al., 1999; Millwood et al., 2002).

4.2. METHODS

The gradual cooling trend extending from the warm Early Pliocene at 4.3 Ma through the reestablishment of major Antarctic ice sheet expansion during the MIS M2 glaciation (3.3 Ma) (e.g., Zachos et al., 2001; Naish et al., 2009; Escutia et al., 2009; McKay et al., 2009; Chapter 3 of this thesis) and into the Late Pliocene cooling after 3.33 Ma is the time interval that has been the focus of the sampling strategy from Site 1123 Hole B. Sediment samples were taken for every 5-10 cm between 142 to 98.40 mbsf (~4.3 to 3.0 Ma) giving a temporal resolution between 3-4 kyr (unpublished age model of Wilson et al., personal communications). Whereas, a coarser resolution of sampling with an average temporal spacing of ~6 kyr was included from 157.6 to 142 mbsf in order to extend the grain size record further back in time. Due to time constraints isotope data has not yet been obtained from 157.6 to 142 mbsf. Grain size analysis of the sortable silt fraction was carried out on sediment samples in order to understand variability of paleocurrent intensity across the core site and extends from ~4.7 to 3.0 Ma (e.g., Hall et al., 2001; Hall et al., 2003; McCave et al, 2008). The carbonate fraction was derived from a colour reflectance regression against carbonate measurement on discrete samples (Carter et al., 1999; Millwood et al., 2002).

Benthic foraminifera *Uvigerina* spp. and *Cibicides* spp. were recovered when possible in order to construct a benthic stable isotope stratigraphy from 142 to 98.40 mbsf. However, there are two intervals in where neither species were recoverable (and or other calcareous species) are between 112.00 to 111.60 mbsf and 111.60 to 110.60 mbsf lasting ~12-kyr and ~30-kyr respectively. The benthic stable isotope records (oxygen and carbon) obtained in this study temporally extend previously published, younger data set from Site 1123, that extends from 3.0 to present day (Hall et al., 2001; Harris, 2002). This expanded time series allows for the assessment of orbital-scale and longer-term trends in ice volume as well as Pacific Ocean and interbasinal $\delta^{13}C$ gradients extending from the warm Early Pliocene (4.3 Ma) into the bipolar Pleistocene (~1.24 Ma), in particular the mid-Pliocene cooling of the EAIS (Chapter 3) and the WAIS (Naish et al., 2009; McKay et al., 2012)

4.2.1. Age model

The age model used in this study comes from revised unpublished magnetostratigraphic interpretations summarized in Table 4.1 (Wilson et al., unpublished data), with additional tuning of the benthic $\delta^{18}O$ stratigraphy from Site 1123 to the LR04 $\delta^{18}O$ benthic stack with Analyseries software (Paillard et al., 1996; Lisiecki and Raymo, 2005). The revised metres composite depth scale of Hall et al., (2001) and Harris (2002) was employed. Visual comparison between the benthic $\delta^{18}O$ record from Site 1123 to the LR04 stack infers that the oxygen isotope record at Site 1123 is in good agreement with other Pacific Ocean records, ODP sites 677, 846 and 849, sites that served as three of the seven high-resolution initial alignment targets during compilation of LR04. Magnetostratgiraphy, according to the rMCD depth scale, suggests near-continuous deposition and relatively uniform depositional rate with an average sedimentation rate of 3.47 cm/k.y (Figure 4.3; Table 4.1).

Table 4.1. Unpublished age/depth tie points from magnetostratigraphic interpretations for Site 1123 (courtesy of Gary Wilson) and following rMCD corrections by Hall (2002). Magnetic polarity reversal ages of Lisiecki and Raymo (2005) (i.e., LR04) are provided with linear sedimentation rate (LSR) (ΔrMCD/ΔMa).

Chron (base)	Core	Core/Secton/ Depth (cm)	MBSF (m)	MCD (m)	rMCD (m)	Age (Ma) LR04	LSR (cm/k.y.)
C1r.1r (MATUYAMA)	U1123C	1123C-5H3-145	41.95	44.85	47.57	1.075	
C2n (Olduvai)	u1123B	1123B-8H4102	71.52	74.62	77.34	1.968	3.334
C2r.2r (MATUYAMA)	u1123B	1123B-10H 4-112	85.02	89.84	92.56	2.608	2.378
C2An.1n (GAUSS)	u1123B	1123B-12H 4-0	102.90	109.84	112.56	3.045	4.577
C2An.1r (Kaena)	u1123B	1123B-12H 4-120	104.10	111.04	113.76	3.127	1.463
C2An.2n (GAUSS)	s1123B	1123B-13H 1-118	109.08	116.24	118.96	3.210	6.265
C2An.2r (Mammoth)	s1123B	1123B-13H 4-38	112.78	119.94	122.66	3.319	3.394
C2An.3n (GAUSS)	s1123B	1123B-14H 3-59	120.99	129.59	132.31	3.588	3.587
C2Ar (GILBERT)	s1123Bs	1123B-16H 2-59	138.49	150.51	153.23	4.174	3.570
C3n.1n (Cochiti)	s1123Bs	1123B-16H 4-65	141.55	153.57	156.29	4.306	2.318
C3n.1r (GILBERT)	s1123Bs	1123B-17H 5-32	152.22	164.16	166.88	4.478	6.157
C3n.2n (Nunivak)	s1123Bs	1123B-17H7-35	155.25	167.19	169.91	4.642	1.848
C3n.2r (GILBERT)	S1123Bs	1123B-18x3-144	159.84	171.78	174.50	4.807	2.782

* Metres Below Sea Floor (MBSF)
*Metres Composite Depth (MCD)
*revised Metres Composite Depth (rMCD)

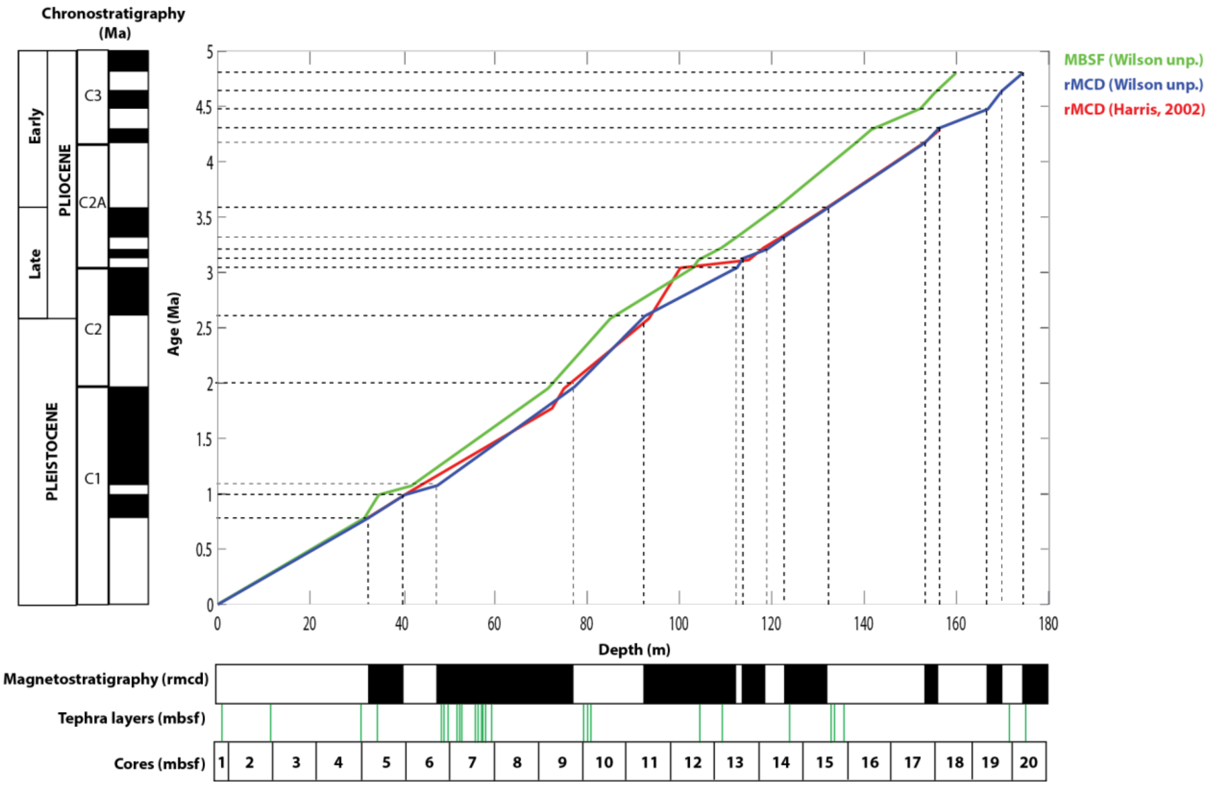

Figure 4.3. Age-depth plot and magnetostratigraphy tie points from unpublished age model (Table 4.1) and the previously published age model of Harris (2002).

4.2.2. Stable isotopes

Approximately 20g of samples from 394 intervals were processed for stable isotope analysis on benthic foraminifera. Data was collected at Stanford University's Stable Isotope Biogeochemistry Lab using a Thermo Finnigan Kiel III Carbonate Device with a typical precision of measurement <0.05‰ for oxygen and <0.03‰ for carbon. Foraminifera were hand-picked from the >63 µm size fraction, brushed clean and manually crushed. Primary calibration to PDB standard was obtained through NBS-19, assuming $\delta^{18}O$ = -2.20‰ and $\delta^{13}C$ = +1.95‰.

Previous oxygen and carbon stable isotope analyses from Site 1123 were obtained predominantly on the shallow infaunal *Uvigerina* in addition to epifaunal *Cibicides* (Hall et al., 2001; Harris, 2002; Hall et al., 2003; Russon et al., 2009; Elderfield et al., 2010). *Cibicides* does not appear continuously through our sampled intervals while *Uvigerina* does, providing a more complete isotope stratigraphy record. However, some authors have suggested the potential for *Cibicides* to form its tests closer to the oxygen isotopic equilibrium compared to *Uvigerina*. In order to determine if there is an isotopic difference between species from the same sampled interval, 125 samples were analysed in which isotopes for both species were measured.

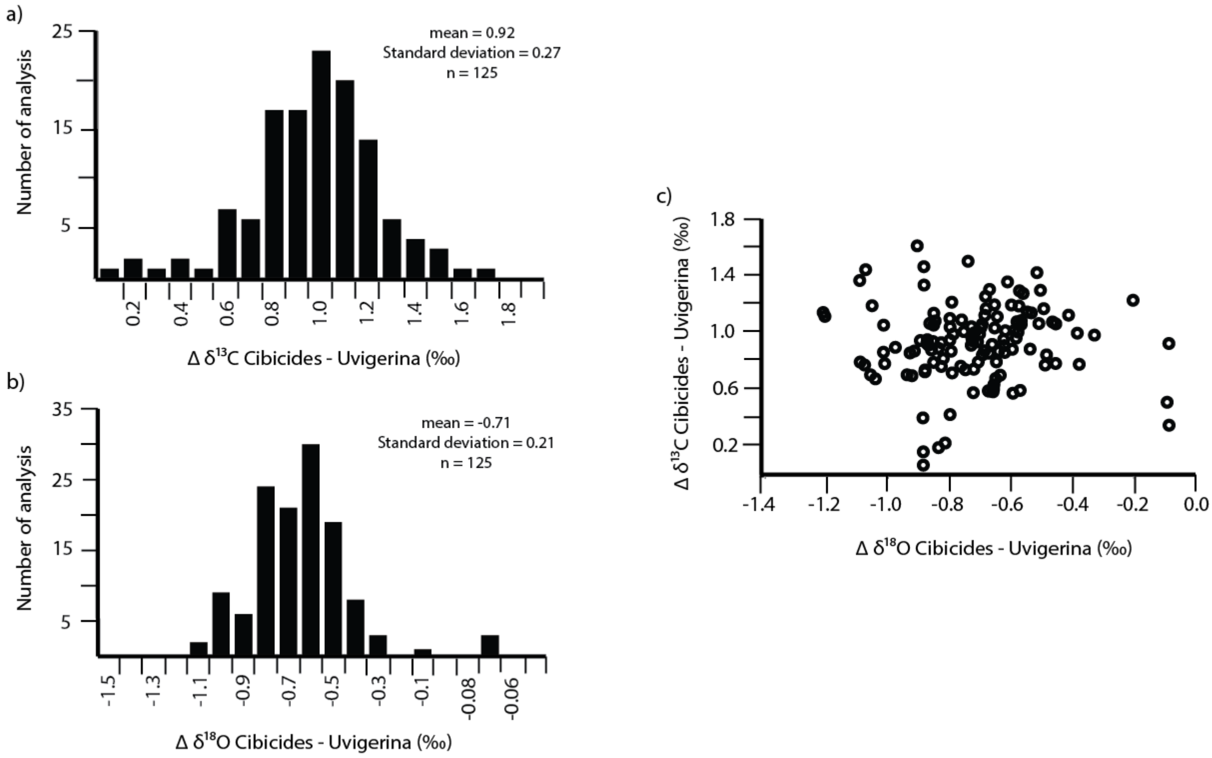

Figure 4.4. Isotopic offsets between paired analyses of *Cibicides* and *Uvigerina* at Site 1123. (a) Histogram of $\Delta\delta^{13}C$ *Cibicides-Uvigerina* (mean = 0.92‰ ± 0.27‰). (b) Histogram of $\Delta\delta^{18}O$ *Cibicides-Uvigerina* (mean = -0.71‰ ± 0.21‰). (c) Scatter plot of individual paired analysis of $\Delta\delta^{13}C$ *Cibicides-Uvigerina* vs. $\Delta\delta^{18}O$ *Cibicides-Uvigerina*, showing that variations in the carbon and oxygen isotopic offsets between species are not related to each other.

The mean isotopic differences (*Cibicides – Uvigerina*) are -0.71‰ ± 0.21‰ for $\delta^{18}O$ and 0.92‰ ± 0.27 for $\delta^{13}C$ (Figure 4.4a and b). Precision of *Uvigerina* samples is ± 0.075‰ for $\delta^{18}O$ and ± 0.12‰ for $\delta^{13}C$ (n = 42). Precision of *Cibicides* samples is ± 0.075‰ for $\delta^{18}O$ and ± 0.19‰ for $\delta^{13}C$ (n = 17). Therefore, most of this scatter in between species offsets is the result of analytical error with additional error from a combination of true variability in the isotopic difference between species, as well as individual specimen, impurities within the test and the possibility of bioturbation having mixed together specimens from different times. However, cross plots indicate that there is no evidence for a systematic relationship of oxygen and carbon isotopic offsets between species (Figure 4.4c). The constants -0.64‰ was added to the $\delta^{18}O$ and 0.90‰ for $\delta^{13}C$ data as these values are consistent with those previously used widely in paleoceanographic studies (e.g., Shackleton, 1974; Duplessy et al., 1984; Mix et al., 1995; Elderfield et al., 2012) and with measured offsets (Figure 4.4). Figure 4.4 displays a crossplot of the data that fits the equation *Uvigerina* $\delta^{13}C$ = *Cibicides* $\delta^{13}C$-0.86 (r^2 = 0.56) which is consistent with an offset of 0.90‰ between species (green), and where 0.90‰ added to *Cibicides* $\delta^{13}C$ acts in agreement with *Uvigerina* $\delta^{13}C$ = *Cibicides* $\delta^{13}C$ +

0.04 (r^2 = 0.56) (blue). In keeping with previously published data sets (e.g., Mix et al., 1995; Harris, 2002) $\delta^{18}O$ is expressed in *Uvigerina* equivalent while the $\delta^{13}C$ is expressed to approximate values from *Cibicides*. Furthermore, all replicated samples have been averaged.

4.2.3. Comparison to pre-existing stable isotope records

This newly compiled benthic stable isotope records obtained from Site 1123 in this study can be compared to pre-existing benthic stable isotope records in order to observe interbasinal changes in benthic $\delta^{13}C$. Several sites exist that have continuous records extending from the warm Early Pliocene and into the Early Pleistocene (4.3 to 1.24 Ma). These include records recovered from the North Atlantic (ODP Site 607), South Atlantic (ODP sites 704 and 1090), South Pacific (MV0502-AJC), and equatorial Pacific (ODP Site 849). Stable isotope values from all sites are interpolated/smoothed to an equal time step of 10-kyr, consistent with previously published compilations of Hodell and Venz-Curtis (2006) and Waddell et al., (2009).

The geographic location of isotope records discussed in this chapter are shown in Figure 4.5. North Atlantic Site 607 is located on the western flank of the Mid-Atlantic Ridge and is bathed by lower NADW (Raymo et al., 1990). South Atlantic ODP sites 704 and 1090 were combined to create a single record inferring change in the CDW composition. ODP Site 704 is located on the Meteor Rise while ODP Site 1090 is on the Agulhas Ridge (Hodell and Venz, 1992; Venz and Hodell, 2002). Bathed by PDW, equatorial Pacific ODP Site 849 is located on the eastern flank of the East Pacific Rise (Mix et al., 1995). Core MV0502-4JC was recovered from the southern edge of the southwest Pacific Basin near the Eltanin Fracture Zone within the subantartic at depth in which lower CDW contains an AABW signature (Waddell et al., 2009). Core site locations, depths and dominant water masses at each site are summarized in Table 4.2.

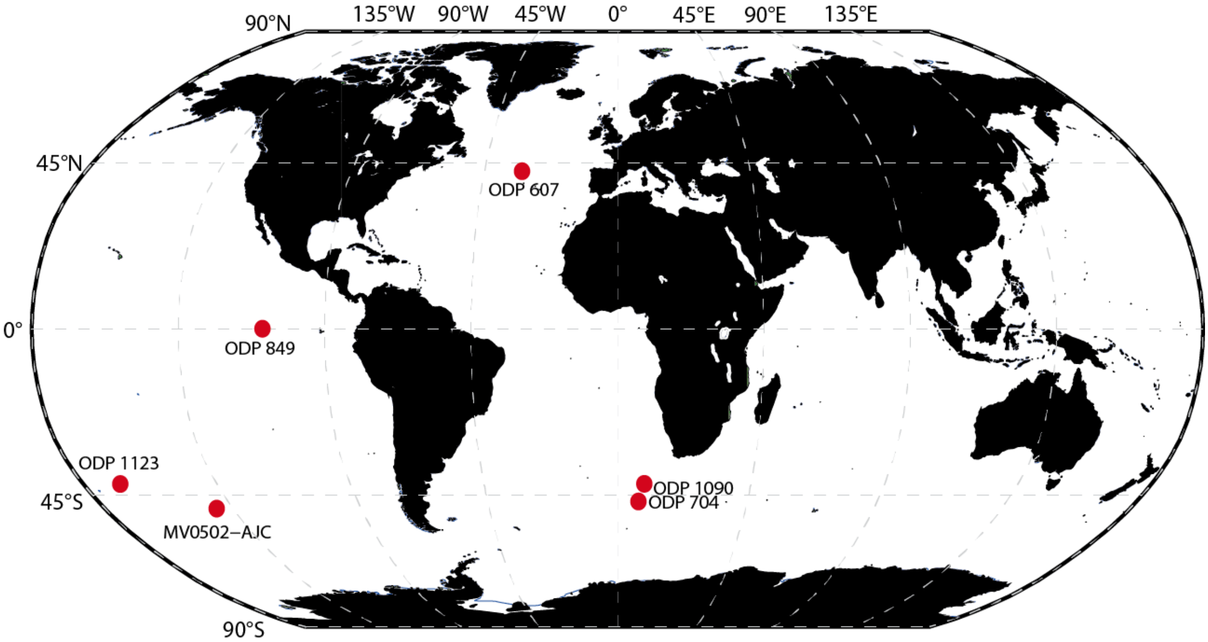

Figure 4.5. Map showing the locations of existing benthic isotope records that are compared to Site 1123.

Table 4.2. Location, water depth and water mass association of stable isotope records discussed in this study.

Site/Core	Location	Water Depth	Water Mass	Reference
ODP 607	41°00'N, 33°37'W (North Atlantic)	3427 m	lower NADW	Raymo et al., (1990)
ODP 704	46°53'S, 7°25'E (South Atlantic)	2532 m	CDW	Hodell and Venz (1992)
ODP 1090	42°55'S, 8°54'E (South Atlantic)	3702 m	lower CDW	Venz and Hodell (2002)
ODP 1123	41°47.2'S, 171°29.9'W (Southwest Pacific)	3290 m	upper CDW	Harris (2002) (2.0 to 2.9 Ma) this study (2.9 to 4.3 Ma)
ODP 849	0°11'N, 110°31'W (equatorial Pacific)	3850 m	PDW	Mix et al., (1995)
MV0502-AJC	50°20'S, 148°08'W (South Pacific)	4286 m	lower CDW	Waddell et al., (2009)

4.2.4. Sortable silt analysis

The percentage of terrigenous mean grain size between 10-63 µm from 529 samples is used as a proxy for near-bottom paleocurrent activity and referred to as sortable silt (McCave et al., 1995). Silt coarser than 10 µm has been shown to display size sorting in response to hydrodynamic processes, while terrigenous silt <10 µm acts in a cohesive behaviour

(McCave et al., 1995). Miocene and Pleistocene age sediments from Site 1123 have demonstrated that increases in sortable silt covary with glacial periods, and has been interpreted as representing increases in paleocurrent intensity during glacial maxima (Hall et al., 2001; Hall et al., 2003).

Following the methodology of McCave et al., (1995) and Bianchi et al., (1999) sample preparation consisted of the removal of carbonate material ($CaCO_3$) with a diluted acetic acid (1M) while organic matter was removed with 10% H_2O_2. Microscopic examination by smear slide demonstrated biogenic silica to be an insignificant component consisting of only a few percent. Samples were analysed for particle size using the Coulter Counter Multisizer^{tm}3 at Victoria University of Wellington. A representative ~0.01 g of subsamples was diluted with 20 mL of calgon solution (1%), stirred and sonicated for 10 minutes. Using a pipette, samples were diluted into a particle-free electrolyte (NaCl) to concentrations low enough to minimize coincidence in the aperture tube. A 100 µm aperture tube was used obtaining data in the range of 1.87-62.9 µm. Each sample was run three times at a preset of 90 second intervals and with a precision of the sortable silt fraction of 0.93%. While data output is reflected in volume percent, Bianchi et al., (1999) considered it to be identical to the diameter of a sphere. However, in order to correct for an over estimation of coarse grain particles sizes, all three runs per sample were averaged to give a single representative grain size distribution. The data were than smoothed using the rloess (a robust version of local regression) function in MATLAB©. The calculation of mean particle size for the 10-63 µm fraction was carried out in GRADISTAT according to Folk and Ward (1957) (Blott and Pye, 2001).

4.2.5. Frequency analysis

All data was detrended and interpolated to a 4-kyr equal time step in order to carry out frequency analysis. Evolutionary spectral analysis was performed in Matlab© (using a spectrogram function developed by Peter Huybers and available at his website http://www.people.fas.harvard.edu/~phuybers/Mfiles/index.html) for isotope data using a 300 ka moving window with a 10 ka increment . This was followed by power spectral analysis using the SSA-MTM toolkit for the Multi-Taper method (MTM) analysis (Ghil et al., 2002). Five data tapers were used for oxygen and carbon isotope data sets. All data were detrended and a linear interpolation at 4-kyr resolution was applied in order to achieve equal time spacing. The statistical significance of spectral peaks was tested relative to the null hypothesis of a robust red noise background, AR (1) model, with a harmonic reshape set to a 90% threshold to test the comparative variance in Milankovitch frequencies. This method is consistent with frequency analysis on benthic isotopes spanning the Pleistocene from Site 1123 (Hall et al., 2001). Coherency and phasing of ODP Site 1123 $\delta^{18}O$ and $\delta^{13}C$ was carried out using the Arand software package (Howell et al., 2006).

4.3. RESULTS

The revised unpublished magnetostratigraphy is presented in Figure 4.6 with down core measurements of colour reflectance used as a carbonate proxy (Carter et al., 1999; Millwood et al., 2002) presented with new raw data of grain size (sortable silt and silt/clay) and stable isotopes (carbon and oxygen) for Site 1123 Hole B. Grain size data extends from within the reversed polarity event, Chron C3n.2r (Gilbert) at 157.60 mbsf to within normal polarity event, Chron C2An.1n (Gauss) at 98.50 mbsf, whereas stable isotope data only extends from reversed polarity event, Chron C3n.1r (Gilbert) at 142.00 mbsf to within normal polarity event, Chron C2An.1n (Gauss). The establishment of this new benthic oxygen and carbon isotope record for Site 1123, extending from the warm Early Pliocene (4.3 Ma) to the Late Pliocene (2.9 Ma), allows for the assessment of changes in $\delta^{13}C$ from the Pacific Ocean as well as longer term trends of interbasinal $\delta^{13}C$ gradients during the Pliocene and into the Pleistocene (4.3 to 2.0 Ma), with an emphasis on investigating far-field oceanographic response to Late Pliocene cooling in the Antarctic and Southern Ocean (Hodell and Venz-Curtis, 2006; Naish et al., 2009; Waddell et al., 2009; McKay et al., 2012; Chapter 3). Sortable silt analysis is used here in conjunction with stable isotope analysis to assess if southern high latitude cooling during the Late Pliocene affected the vigor in which bottom water entered the southwest Pacific Ocean via the ACC and the DWBC.

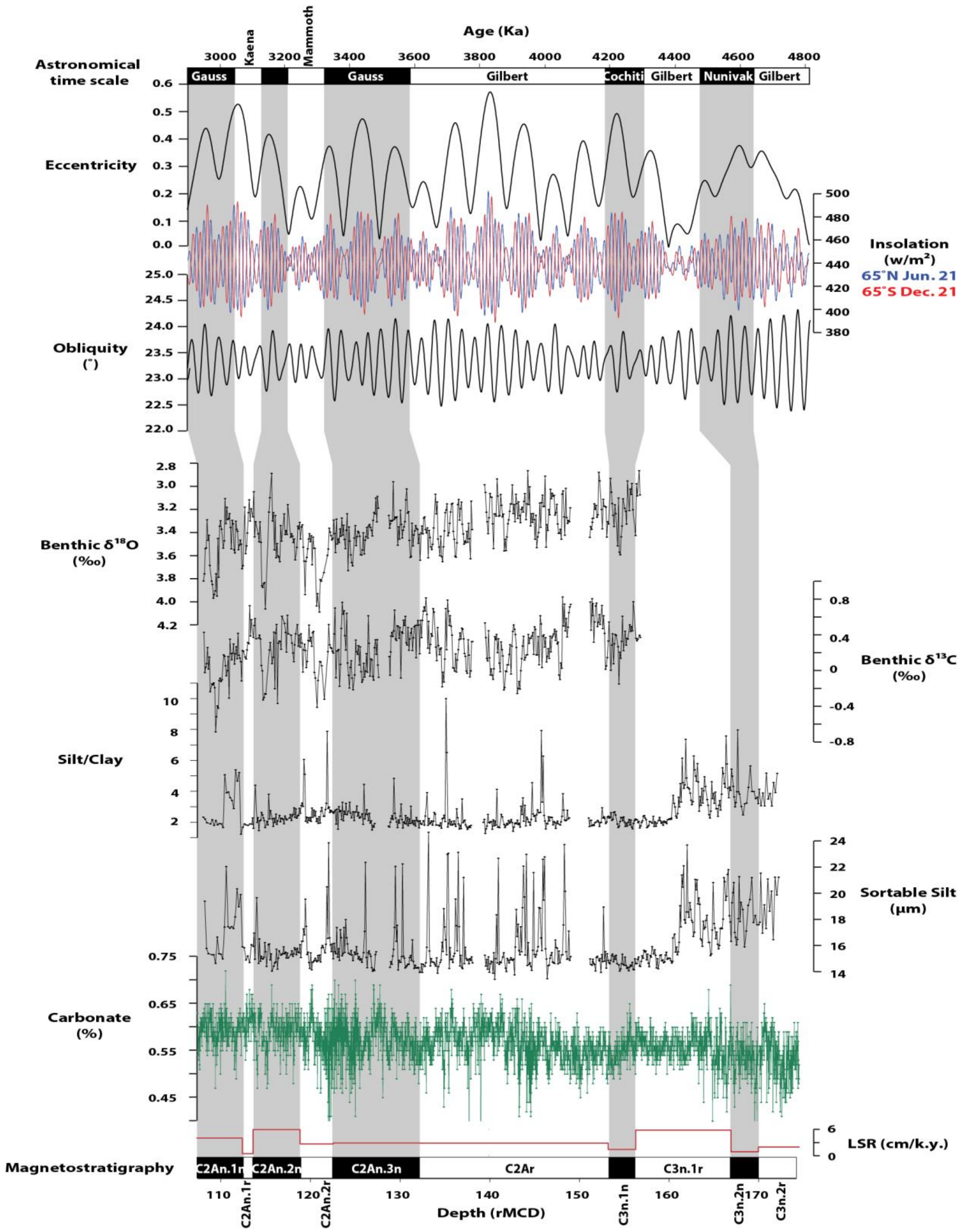

Figure 4.6. Comparison of linear sedimentation rates (LSR) according to magnetostratigraphy tie points, colour reflectance-based carbonate (%) (Millwood et al., 2002), sortable silt, silt/clay, benthic $\delta^{13}C$, benthic $\delta^{18}O$ and orbital parameters of obliquity, insolation and 100-kyr eccentricity for Site 1123.

4.3.1. Stable isotopes

The new benthic $\delta^{18}O$ record was tuned to the global composite LR04 benthic $\delta^{18}O$ stack (Lisiecki and Raymo, 2005) using the Analyseries software (Paillard et al., 1996). Orbital frequencies in the untuned Early Pliocene (4.3 to 3.0 Ma) benthic $\delta^{18}O$ record are relatively subdued and are just significant at 90% (Figure 4.6b) and is potentially due to a combination of factors. Firstly, the LR04 stack has a significant eccentricity component between 3.5 and 3.0 Ma (Meyers and Hinnov, 2010; Chapter 3), which is also recognized in the Site 1123, $\delta^{18}O$ (Figure 4.13a). Secondly, because I wanted to minimise any potential splicing errors (Lisiecki and Herbet, 2007) in this study my sampling was exclusively from Hole 1123B, and this appears to contain three stratigraphic gaps of ~40-kyr, relative to the splice record, potentially introducing some bias towards lower frequency events and reducing spectral significance at higher frequencies (i.e., 40-kyr). Future sampling of Hole C will target these intervals, based on the spliced composite depth, but with some overlap between the 1123B data points. Finally, the Early Pliocene is a time of low amplitude obliquity cycles in the LR04, and consequently there is a lower signal to noise ratio during this part of the time series. To assess these influences, I have run spectra for each discrete section of core where there is continuous stratigraphy (4.4-4.2 Ma, 4.2-3.8 Ma, 3.8-3.1 Ma) (Figure 4.8). The power spectra indicates a significant 40-kyr component that is within band width error at 95% for the younger splices, 4.2-3.8 Ma and 3.8-3.1 Ma (Figure 4.8a and b), while also highlighting the significant 100-kyr component between 3.8-3.1 also observed in the LR04 stack (Meyers and Hinnov, 2010). The oldest section which consists of lowest amplitude and least amount of time is only significant at 90% while containing a strong white noise background (Figure 4.8c). Comparison of $\delta^{18}O$ to $\delta^{13}C$ demonstrates coherency at 40-kyr with a near in-phase relationship in which $\delta^{18}O$ slightly leads $\delta^{13}C$ by 2-5 kyr.

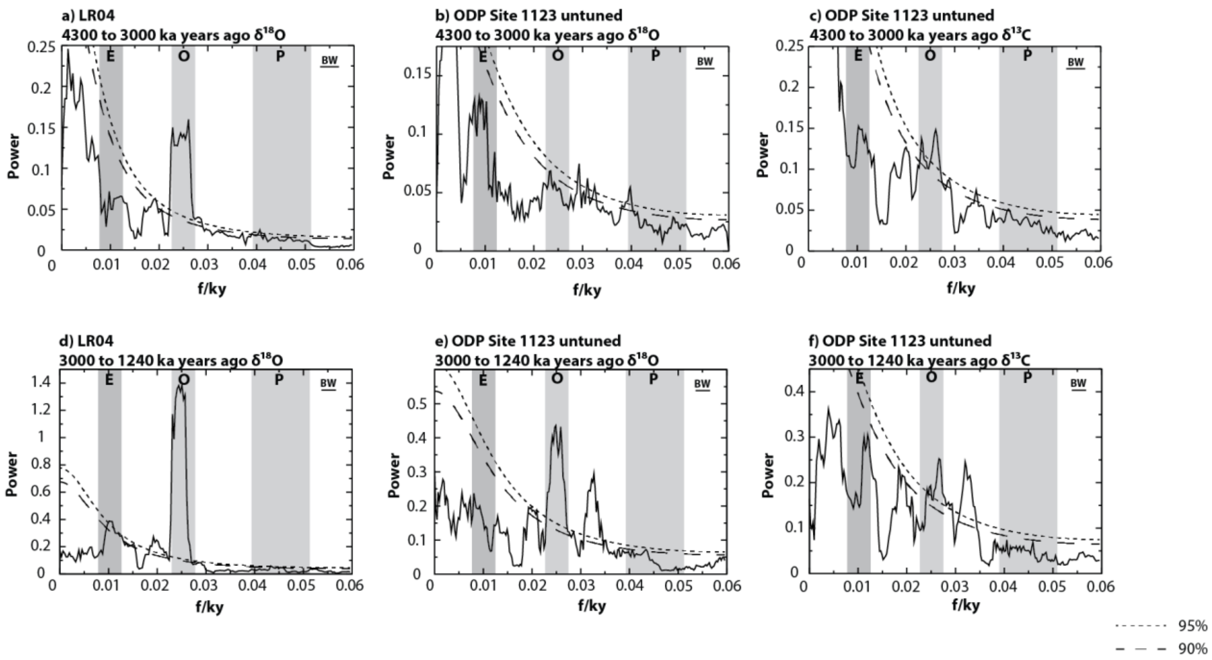

Figure 4.7. Power spectra for untuned stable isotopes for new data presented in this thesis from 4.3 to 3.0 Ma (b,c), and previously published data spanning 3.0 to 1.24 Ma (Harris, 2002) (e,f). The LR04 benthic stack is provided for comparision (a,d). Grey shaded areas highlights the 100-kyr eccentricity (E), 40-kyr obliquity (O) and 20-kyr precession (P) frequencies.

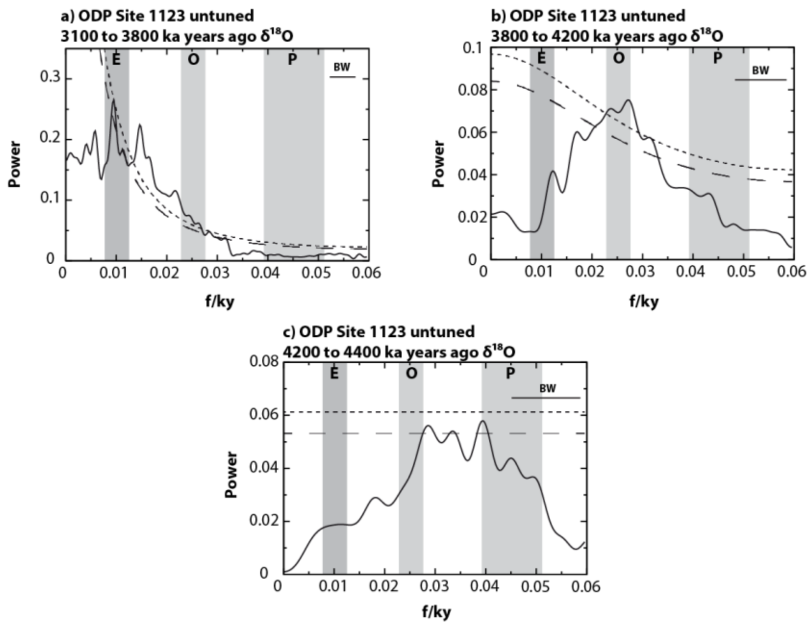

Figure 4.8. Power spectra for untuned splice sections for Hole 1123B.

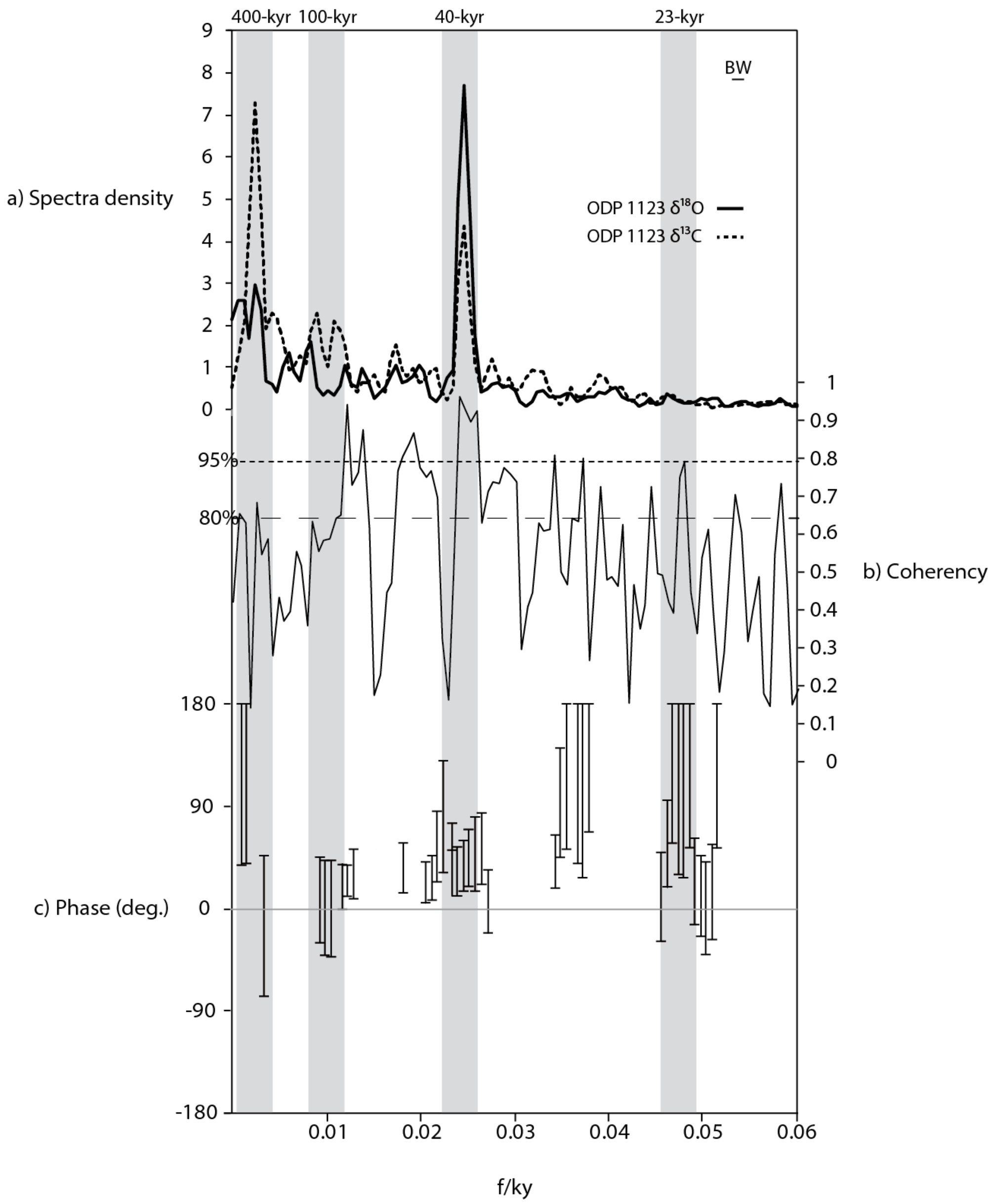

Figure 4.9. (a) Spectral density, (b) coherency, and (c) phase of untuned Site 1123 $\delta^{18}O$ and $\delta^{13}C$.

Using paleomagnetic reversals as absolute tie points during tuning, there are obvious correlations in the amplitude and over all shape of the LR04 and Site 1123 $\delta^{18}O$ cycles (Figure 4.10). Additionally, the overlying trends in the data are also highly consistent with LR04 and other benthic $\delta^{18}O$ records globally, with three major transitions apparent between 3.33 Ma and 2.5 Ma. In general, Site 1123 benthic $\delta^{18}O$ values are heavier (0.16‰) compared to the LR04 stack, which is a similar offset to that between other Southern Ocean sites (e.g., ODP sites 704/1090) (0.15‰) and North Atlantic sites (e.g., ODP Site 607) (-0.11‰), which is likely due to temperature and salinity differences in the water masses feeding these sites, suggesting a Southern Ocean influence. Tuning to the LR04 stack enhances the 40-kyr signal in the Site 1123 $\delta^{18}O$ and $\delta^{13}C$ records for both time steps (Figure 4.11).

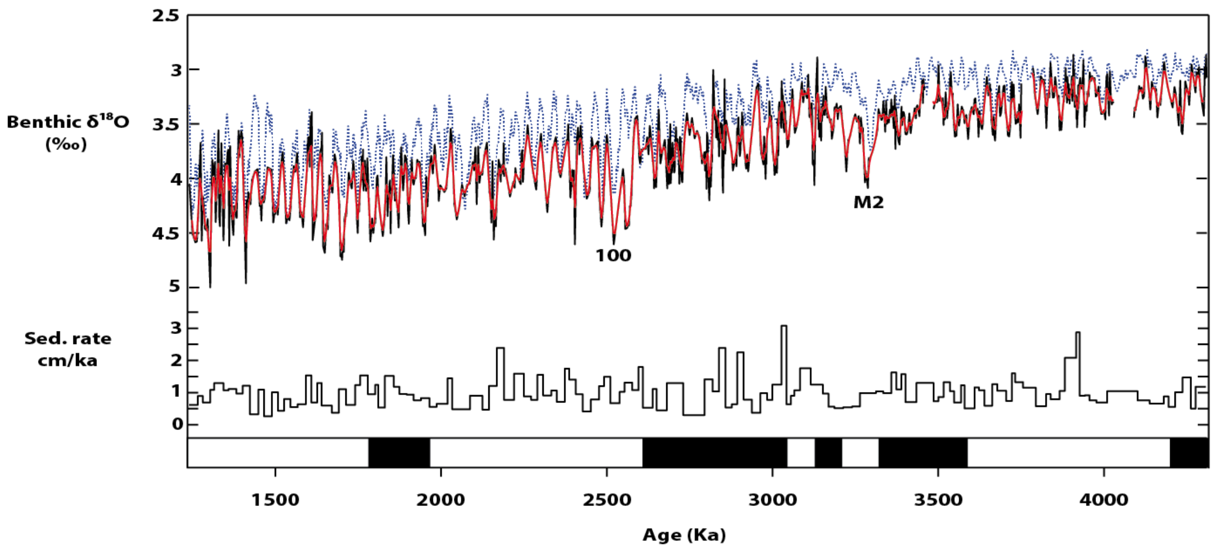

Figure 4.10. Tuned Site 1123 benthic oxygen isotopes (black line with red smoothed line) to LR04 (blue dotted line). Red line is a smoothed 12-kyr Gaussian filter at 4-kyr resolution of Site 1123 benthic oxygen isotopes. Also displayed is the sedimentation rate based on tuning.

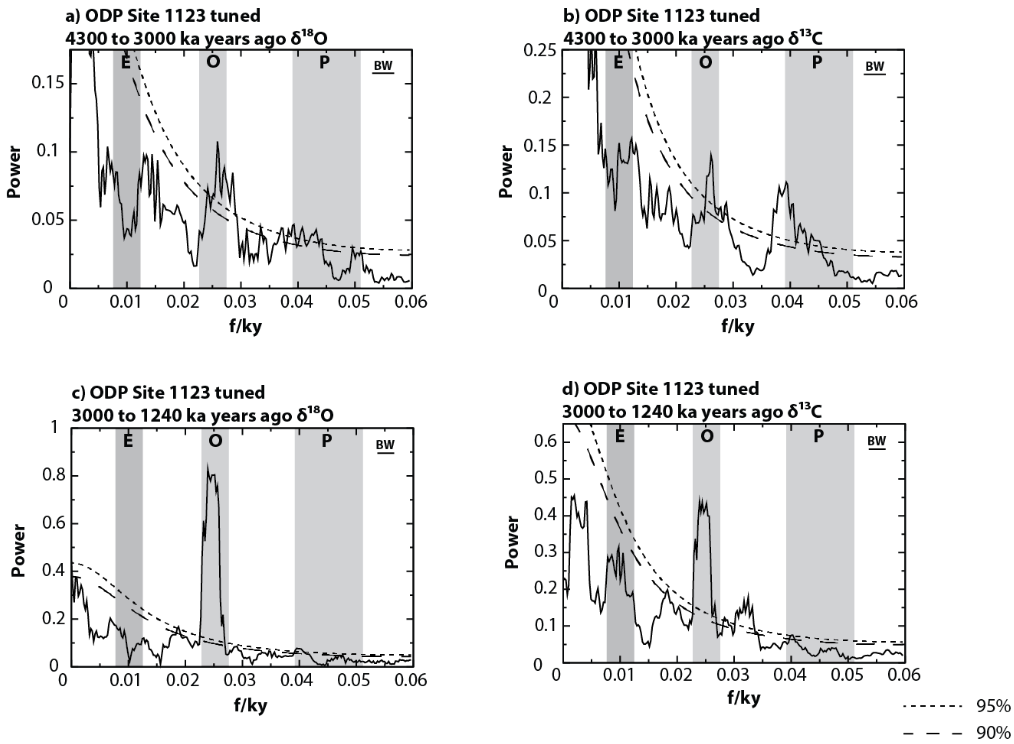

Figure 4.11. Power spectra for tuned stable isotopes for new data presented in this thesis from 4.3 to 3.0 Ma (a,b), and previously published data spanning 3.0 to 1.24 Ma (Harris, 2002) (c,d).

Benthic $\delta^{18}O$ values at Site 1123 during the Early Pliocene (4.3 to 3.33 Ma) are the lowest and least variable over all, averaging 3.30‰ (maximum, 3.69‰; minimum, 2.87‰). The prominent positive excursion associated with the M2 glaciation at 3.33 Ma marks the onset of more enriched benthic $\delta^{18}O$ values than for any other time prior. Average $\delta^{18}O$ values between 3.33 to 2.5 Ma is 3.64‰ (maximum, 4.61‰; minimum, 3.00‰), while interglacial $\delta^{18}O$ values after 3.33 Ma are still within the range of the more depleted Early Pliocene values. After 2.5 Ma, both interglacial and glacial values become gradually more enriched over time with interglacial $\delta^{18}O$ values never as depleted as the Early Pliocene values. After 2.5 Ma benthic $\delta^{18}O$ values average 4.06‰ (maximum, 4.96‰; minimum, 3.43‰) (Figure 4.12). While power spectra analysis highlights the significance of the 40-kyr frequency component within the tuned data, evolutionary spectra analysis demonstrates that the 40-kyr frequency is subdued prior to 3.0 Ma ago (Figure 4.13). Gaussian band-pass filtering applied to isolate variance associated with the lower frequency 400- and 100-kyr eccentricity cycles demonstrates increased variance of the 100-kyr frequency from 3.5 to 2.7 Ma (Figure 4.12).

Benthic $\delta^{13}C$ values from Site 1123 also demonstrate a significant 40-kyr glacial to interglacial pacing (Figure 4.13), in which glacial periods are associated with lower values towards more LGM equivalent (-0.60‰). They also demonstrate extended periods of time reflecting higher values towards Holocene equivalent values (0.80‰). The glacial to interglacial cyclicity helps rule out the existence of a significant surface water productivity overprint that would possible result in a negative offset in $\delta^{13}C$ values (Mackensen et al., 2001; Ninnemann and Charles, 2002). Similarly to the $\delta^{18}O$ record, transitions in long-term trends of the $\delta^{13}C$ record occur at 3.33 Ma and 2.5 Ma. From 4.3 to 3.33 Ma $\delta^{13}C$ values are high averaging 0.29‰ (maximum, 0.82‰; minimum, -0.26‰). A shift to lower values occurs during the M2 glaciation at 3.33 Ma with values averaging 0.21‰ (maximum, 0.73‰; minimum, -0.69‰) between 3.33 and 2.5 Ma. After 2.5 Ma the amplitude of variance in the $\delta^{13}C$ values increases (prior to 2.5 Ma, 0.068‰; after 2.5 Ma, 0.091‰) as well as an overall decrease in values (averaging 0.044‰) reaching LGM equivalent values (Figure 4.12). This long-term trend is punctuated by 400-kyr long period eccentricity pacing that is evident in both evolutionary spectra analysis (Figure 4.13). Furthermore, power spectra analysis demonstrates the significance of the 400-kyr frequency at 95% (Figure 4.13).

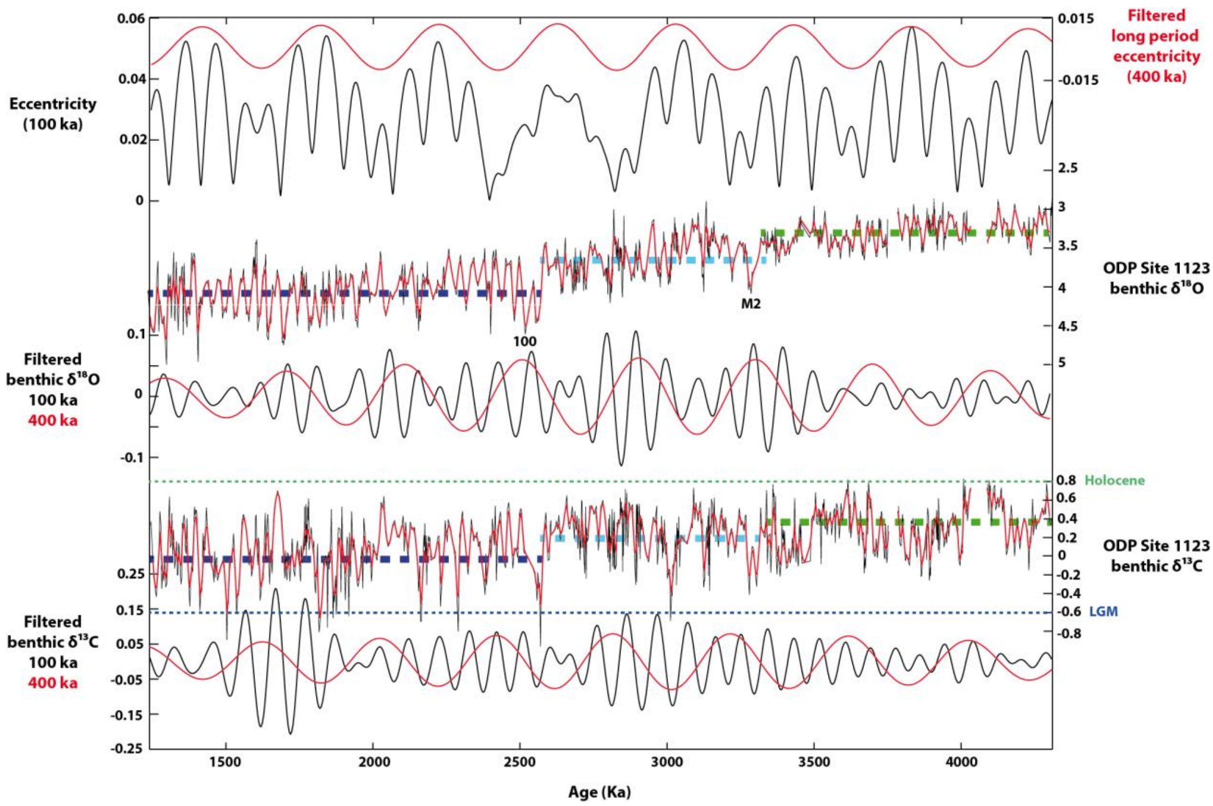

Figure 4.12. Long period (400-kyr) and short period (100-kyr) orbital eccentricity compared to Site 1123 benthic $\delta^{18}O$ and $\delta^{13}C$ records with overlain red lines showing a smoothed 12-kyr Gaussian filter at 4-kyr resolution. Dashed lines are stable isotope averages for time steps at 4.3 to 3.33 Ma (green), 3.33 to 2.5 Ma (light blue), and 2.5 to 1.24 Ma (dark blue). Holocene (0.8‰) and LGM (-0.6‰) equivalent benthic $\delta^{13}C$ values at Site 1123 are plotted following McCave et al., (2008). Gaussian band-pass filters are used to isolated variance associated with the 400- and 100-kyr eccentricity cycles for both $\delta^{18}O$ and $\delta^{13}C$ records. The 400-kyr filter has a central frequency = 0.0025 and a bandwidth = 0.0002; the 100-kyr central frequency = 0.01 and bandwidth = 0.002.

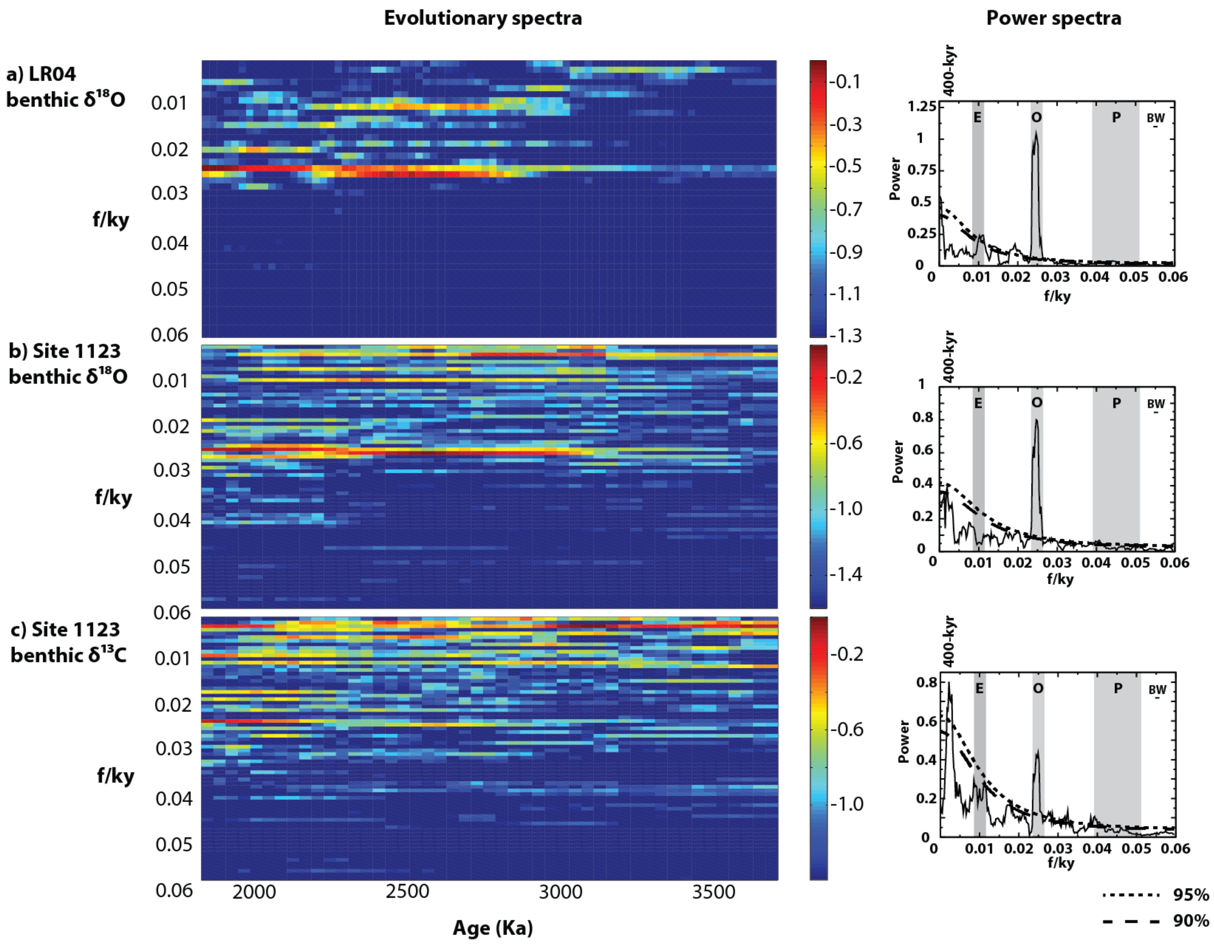

Figure 4.13. Evolutionary and power spectra analysis of tuned Site 1123 stable isotopes compared to the LR04 stack.

4.3.2. Interbasinal stable isotope gradients

The benthic $\delta^{18}O$ record from Site 1123 appears to be most similar to the South Atlantic (ODP sites 704/1090) records and is on average heavier when compared to North Atlantic (ODP Site 607) and equatorial Pacific (ODP Site 849) records. During the Early Pliocene to Late Pliocene (4.3 to 3.33 Ma), Site 1123 $\delta^{18}O$ values (3.29‰) resemble those of the South Atlantic (ODP sites 704/1090) (3.33‰). However, the two records diverge at 3.33 to 2.8 Ma with an increasing gradient between the two sites with the South Atlantic (ODP sites 704/1090) records attaining heavier values than those from Site 1123 (Figure 4.14). This is followed by a re-convergence of the two records after 2.8 Ma, albeit with Site 1123 overall reflecting slightly heavier values. After 2.8 Ma, Site 1123 becomes on average heavier (4.02‰) than South Atlantic sites (ODP sites 704/1090) (3.86‰) but it never gets as heavy as the South Pacific (MV0502-AJC) (4.48‰) (Figure 4.14).

Benthic $\delta^{13}C$ values at Sites 1123 are more negative compared to the North Atlantic (ODP Site 607) values that are generally more positive. Whereas, benthic $\delta^{13}C$ values at Site 1123 are never as low as those observed in the equatorial Pacific (ODP Site 849) and South Pacific (MV0502-AJC) records. A major shift in $\delta^{13}C$ gradients between the South Atlantic (ODP Sites 704/1090) and Site 1123 occur at two time steps at 3.6 Ma and 2.8 Ma. From 4.3 to 3.6 Ma the gradient difference between the South Atlantic sites (ODP sites 704/1090) and Site 1123 is minimal, averaging 0.35‰ and 0.36‰, respectively. At 3.6 Ma this gradient increases with the South Atlantic sites (ODP sites 704/1090) displaying higher values and Site 1123 reflecting lower values (3.6 to 2.8 Ma ODP sites 704/1090, 0.60‰; Site 1123, 0.23‰). A re-convergence between $\delta^{13}C$ values for South Atlantic sites (ODP sites 704/1090) and Site 1123 occurs after 2.8 Ma, albeit with average values for the South Atlantic becoming slightly lower than at Site 1123 (ODP sites 704/1090, -0.13‰; Site 1123, 0.08‰) (Figure 4.14).

In general, the $\delta^{13}C$ gradient between the equatorial Pacific (ODP Site 849) and Site 1123 increased when the $\delta^{13}C$ values at Site 1123 are higher (i.e., more nutrient depleted) and "Holocene like", whereas negative gradients correlate to extended periods of time when Site 1123 $\delta^{13}C$ values are lower (Figure 4.14d). An exception is the interval spanning 3.319 to 3.210 Ma (the Mammoth Subchron). Both Sites 1123 and 849 contain more nutrient depleted (high) $\delta^{13}C$ values. While the gradient between the southwest Pacific and equatorial Pacific reached modern values in the Early Pliocene, two noticeable trends are apparent: 1) From 4.3 to 1.24 Ma the gradient decreases over time while more consistently reaching modern values as ice volume increases (Figure 4.14): and 2) nodes in long period (400-kyr) eccentricity coincide with times in which the gradient increases (Figure 4.14d and e).

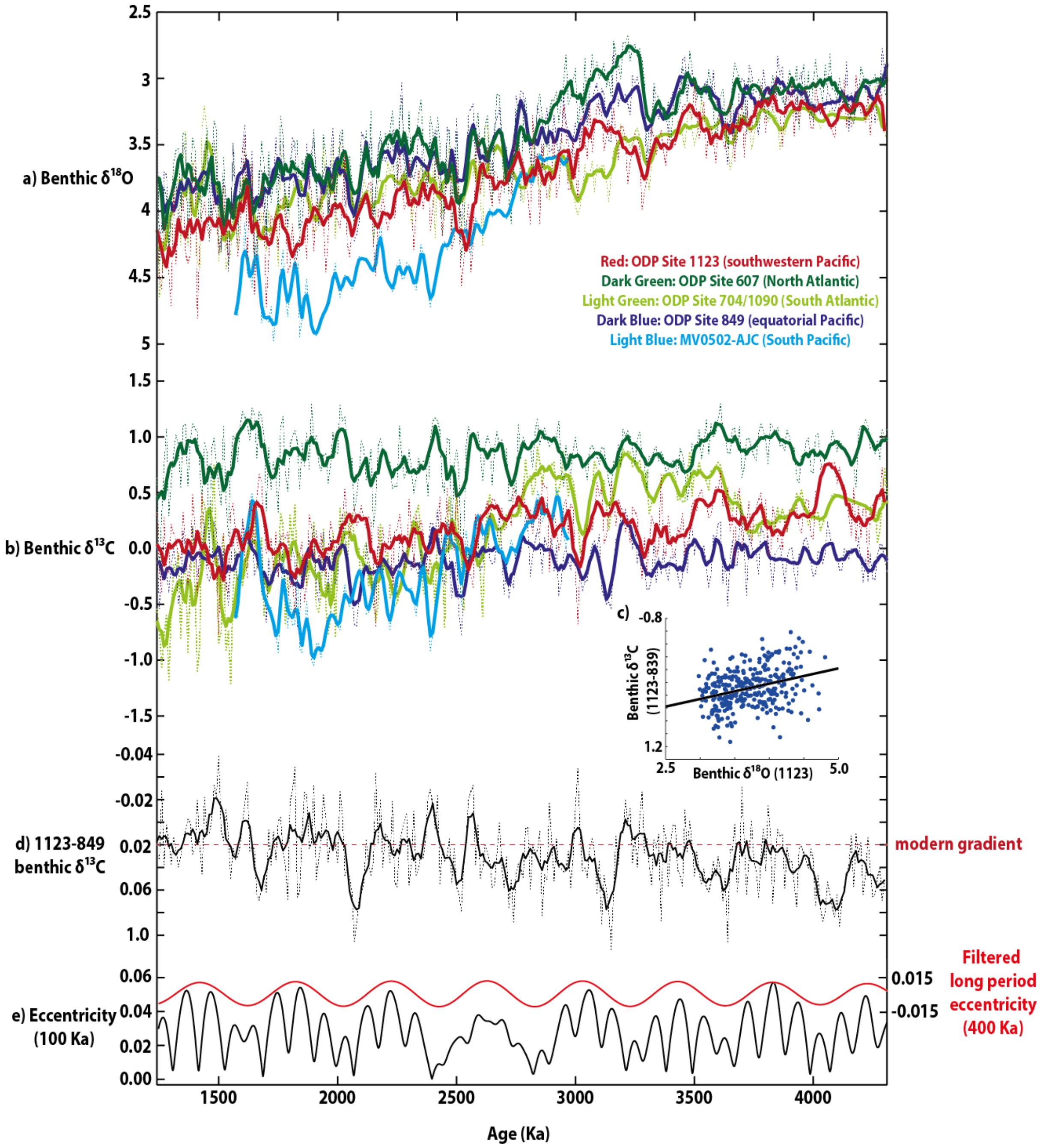

Figure 4.14. Comparison of Site 1123 (red) benthic $\delta^{18}O$ (a) and $\delta^{13}C$ (b) records spanning 4.31 to 1.24 Ma to records from the North Atlantic (dark green), South Atlantic (light green), equatorial Pacific (dark blue), and South Pacific (light blue). Dotted lines expresses data as smooth 10-kyr equivalent presented in Waddell et al., (2009; Figure 5) with thick dark lines representing a 5 pt. moving average. c) Scatter plot of the Δ $\delta^{13}C$ from Sites 1123 to 849 against the benthic $\delta^{18}O$ from Site 1123. (d) Gradient between Site 1123 and 849 with the modern gradient value represented by the red dashed line. (e) The 100-kyr eccentricity cycles with the band-passed filtered long period 400-kyr eccentricity signal in red.

4.3.3. Sedimentological parameters

The sedimentological parameters shown against depth (rMCD) (Figure 4.6) and age (Figure. 4.15) display both long-term gradual changes as well as some high-frequency variability. The carbonate fraction demonstrates an inverse relationship to magnetic susceptibility (Figure 4.15; note axes scales), with higher values in the latter reflecting increased terrestrial material (Carter et al., 1999). Spectra analysis using the tuned aged model infers a complete lack of Milankovitch pacing within the sortable silt and sily/clay records. However, carbonate fraction of the sediment demonstrates a 40-kyr variability significant at 95% (Figure 4.16). An additional peak at 30-kyr is observed that is also significant at 95% in the carbonate spectra. This frequency is commonly observed in paleo-oceanographic timeseries (e.g., Mix et al., 1995) and is considered a consequence of weakly non-linear interactions between obliquity and other orbital frequencies – in particular eccentricity (Huybers and Wunsch, 2004).

A noticeable aspect to the grain size data is that during the oldest part of the record prior to 4.7 to 4.35 Ma, both sortable silt and silt/clay values display distinct coarse grained values inferring an overall increase in silt abundance compared to the younger part of the record. This increase in coarse grained silt content coincides with an increasing trend of magnetic susceptibility and the lowest carbonate values. Furthermore, linear sedimentation rates calculated from paleomagentic reversals indicates this portion of the record contains elevated sedimentation (6.157 cm/kyr) during the late part of this interval. After ~4.35 Ma, background values for both sortable silt and silt/clay decreases significantly, but quasi-periodic short-duration/high frequency excursions back to the elevated values are seen prior (i.e., pre-4.3 Ma) (Figure 4.15). Magnetic susceptibility also decreases after ~4.35 Ma with carbonate increasing. At ~3.75 Ma, around MIS Gi8, both sortable silt and silt/clay gradually increase while magnetic susceptibility generally decreases and carbonate increases. An exception to this long-term trend is centered on the MIS M2 glacial excursion in the $\delta^{18}O$ data, where magnetic susceptibility increases and carbonate decreases (Figure 4.15).

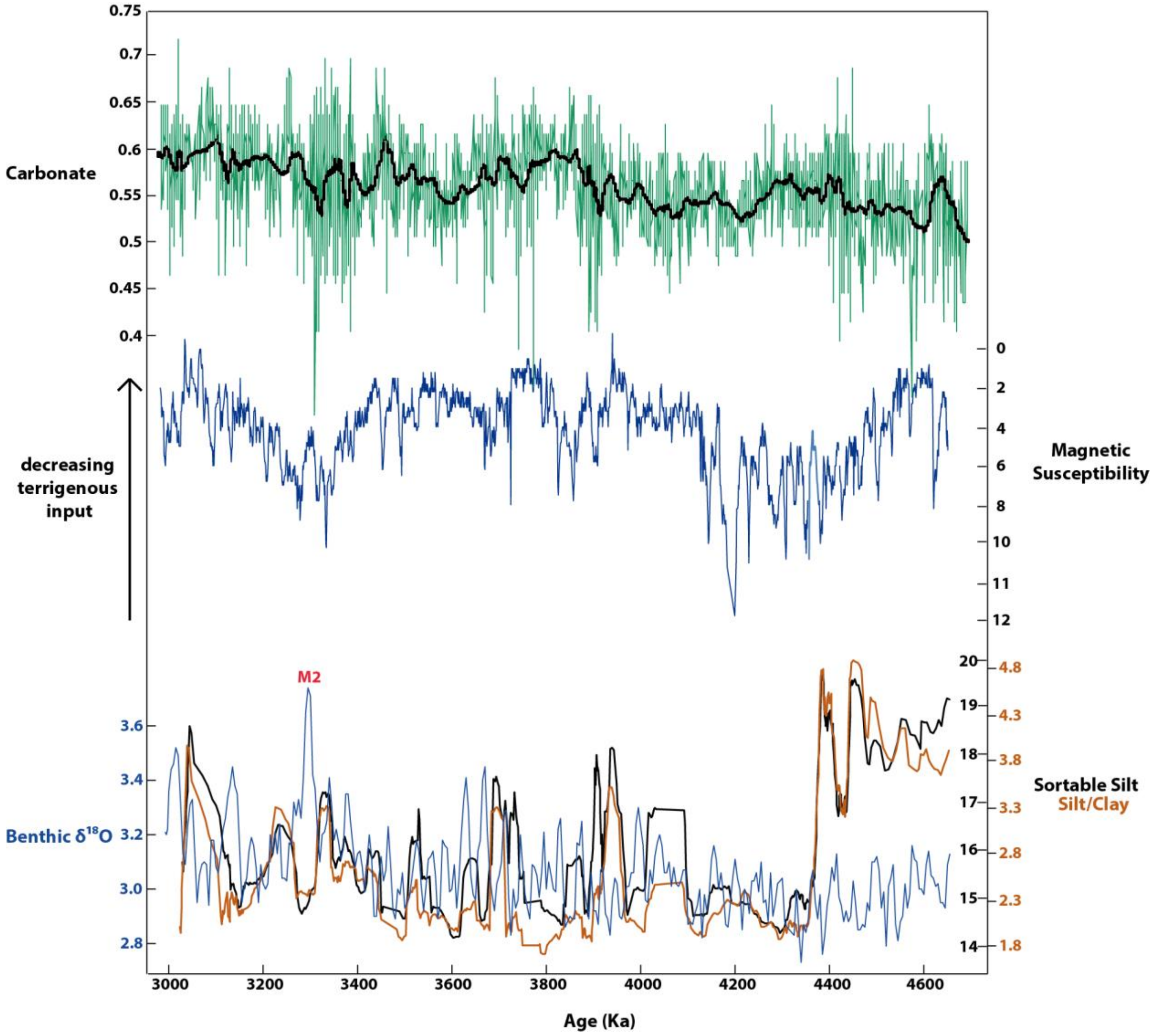

Figure 4.15. Sedimentological data for Site 1123 versus age. Displayed is the LR04 benthic $\delta^{18}O$ stack (Lisiecki and Raymo, 2005) (light blue), sortable silt (black), silt/clay (orange), downcore magnetic susceptibility measurements (Carter et al., 1999) and carbonate fraction as determined from color reflectance with a 50 pt. moving average (Millwood et al., 2002).

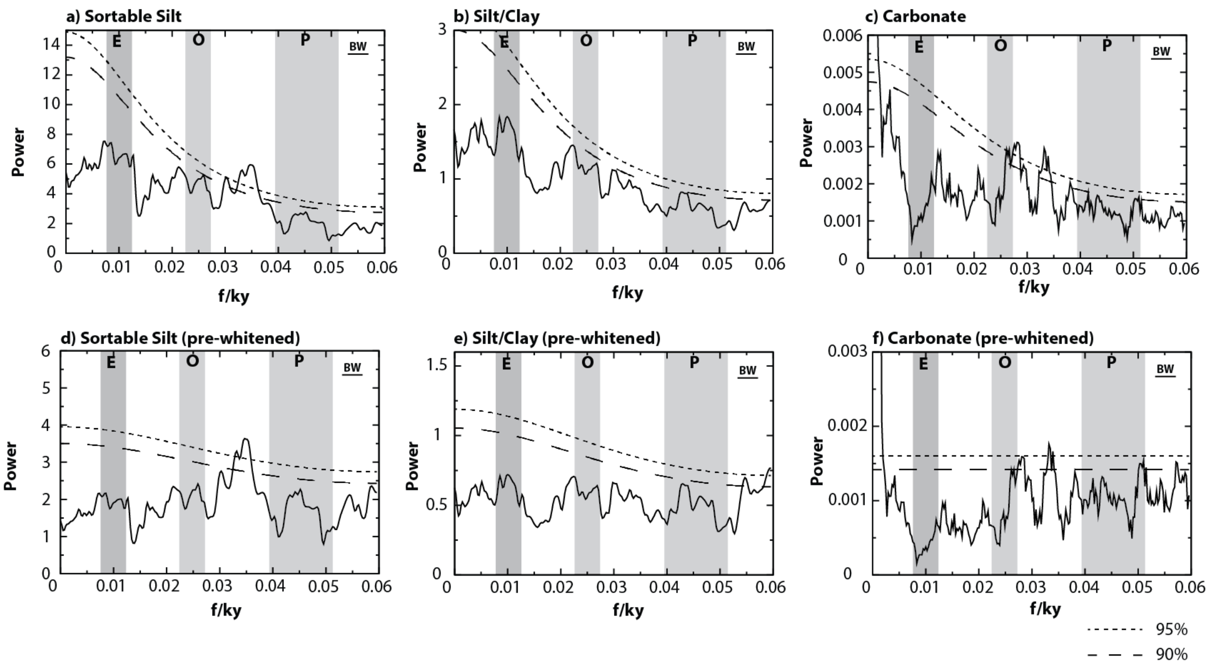

Figure 4.16. Power spectra analysis of sortable silt, silt/clay and carbonate (a-c). d-f is power spectra applied following a pre-whitening data processing step (Weedon, 2003) to test whether higher frequency events surround the ~20-kyr precessional (p) frequency were significant.

4.4. DISCUSSION

4.4.1. The deposition of terrigenous material and the vigor of Pacific abyssal in-flow during the warm Early to mid-Pliocene

The apparent lack of significant Milankovitch frequencies within sedimentological data could be the consequence of large-scale changes in sediment delivery to Site 1123 – i.e., the deposition and size sorting of terrigenous material did not solely respond to processes related to Southern Ocean circulation regulated by ice volume variability. On the basis of coherency and phase testing of the sortable silt proxy with $\delta^{18}O$ and $\delta^{13}C$, Hall et al., (2001) demonstrated that Pleistocene age sediments from Site 1123 were deposited as a result of changes in in-flow controlled by increased production of bottom water during glacial periods. Similar orbital variability in the deep water circulation patterns have also been inferred to have occurred with the development of the EAIS during the middle Miocene (~15.5 to 12.5 myr), by Hall et al., (2003) although they were more speculative as they did not have an independently tuned age scale (i.e., $\delta^{18}O$) to constrain the frequencies at which sortable silt varied. However, the lack of any significant Milankovitch pacing in the sortable silt data in this thesis, particularly the 40-kyr obliquity signal, implies that either no orbital signal is present, or that it is potentially masked by other processes influencing sediment supply. A visual examination of these data between 4.0 to 3.0 Ma suggest that large peaks in the silt/clay and sortable silt data occur in quasi-100 kyr cycles (Figure 4.17). Power spectra estimation using the multi-taper method at 3 tapers displays sortable silt and silt/clay to be significant at 90% while also demonstrating significance of the 50-kyr harmonic (quasi periodic frequency) of the 100-kyr frequency and the 23-kyr signal of precession. Greater smoothing (higher degrees of freedom) results from using five tapers and displays both sortable silt and silt/clay to not be significant at 90%.

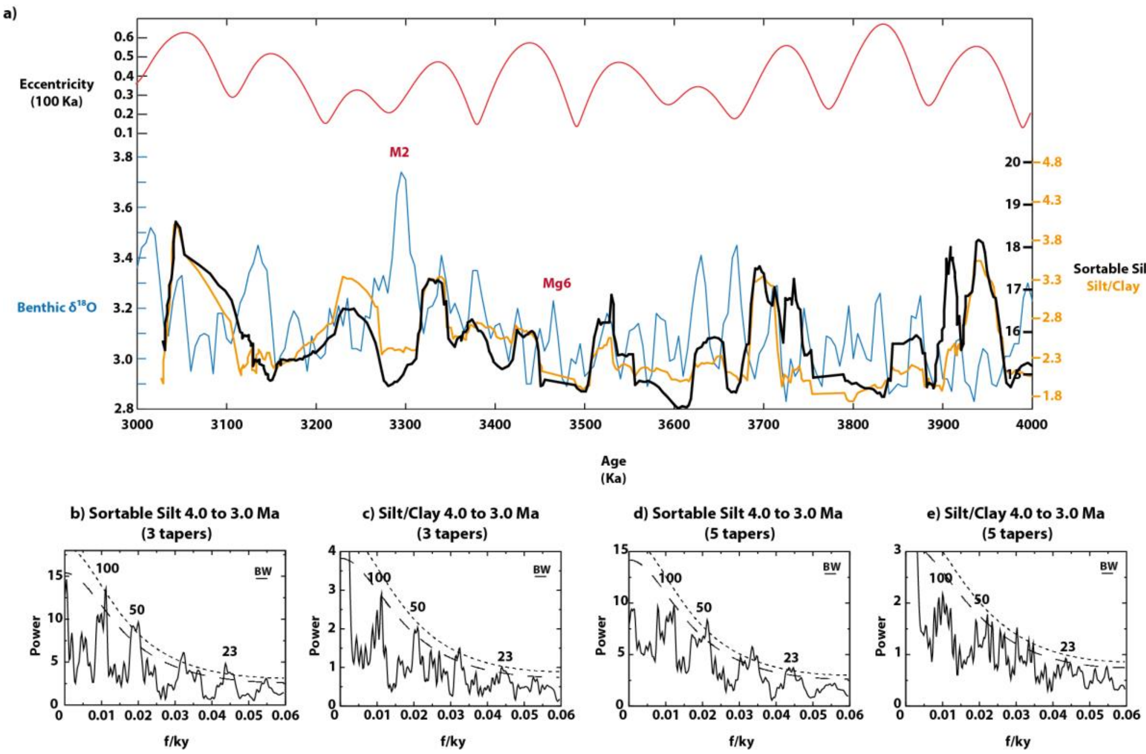

Figure 4.17. Quasi 100-kyr cycles in sortable silt and silt/clay between 4.0 to 3.0 Ma. Power spectra using the multi-taper method using 3 (b and c) and 5 (d and e) tapers.

Major changes in topographic development and regional shifts in New Zealand climate took place during the Early Pliocene (e.g., Chamberlain et al., 1999; Salzmann et al., 2008). Such events potentially had a major influence on the influx of terrigenous material delivered to the deep ocean. Traditionally, the established sedimentary model of the Eastern New Zealand Oceanic Sedimentary System (ENZOSS) infers the terrigenous flux to the deep ocean varies with eustatic sea level and terrestrial New Zealand glaciation on orbital timescales (Carter et al., 2004), whereby sea level lowstands during periods of Southern Alps glaciation are associated with an increase in the terrigenous flux to the continental margin and adjacent ocean basins due to increased erosion of a denuded landscape and river discharge occurring closer to the continental shelf edge (Carter et al., 2004). However, this is complicated by more recent studies suggesting that during interglacial highstands, surface waters become less mixed and rising temperatures are accompanied by increased precipitation rates, increasing the influx of terrigenous material delivered to the deep ocean via high fluvial discharge rates (Carter and Manighetti, 2006). Such a scenario could potentially allow for a significant volume of sediment from the North Island to be transported in suspended load via the south and then eastward subtropical inflow of the ECC to the Chatham Rise towards ODP Site 1123 (Hall et al., 2001; Carter and Manighetti, 2006). ODP Site 1124 located just north of ODP Site 1123 on the Rekohu sediment drift also demonstrates increased terrigenous input from the North Island during the late Neogene (after 9 Ma.) (Joseph et al., 2004). Additionally, orbitally paced 100-kyr and 20-kyr (eccentricity and precession) aeolian input from westerly winds are suggested to deposit dust derived from New Zealand and Australia based on the presence of North Island Pollen (Mildenhall et al., 2004; Sniderman et al., 2007).

During the warm Early Pliocene, sea level highstands were up to 20+/-10 m higher than today (e.g., Miller et al., 2012), surface-land temperatures were 2-3°C warmer globally, there was increased precipitation rates, with warm-temperate vegetation and forests systems greatly expanded (Sniderman et al., 2007; Salzmann et al., 2008; Dowsett et al., 2012). Furthermore, a warm moist climate system prevailed along the eastern portion of New Zealand's South Island, and this is suggested to have persisted through the Early Pliocene (Salzmann et al., 2008; Salzmann et al., 2011). This regional climate was likely significantly altered by increased rates of convergence across the Pacific Australia plate boundary intensifying rock uplift and denudation rates in the Southern Alps (after ~6 Ma) and the resultant rain shadow effect it currently has on the east coast of the South Island, while ultimately effecting sediment input along the continental shelf and to the deep ocean (Walcott, 1985; Chamberlain et al., 1999; Carter et al., 2004).

A notable long-term decrease in the baseline terrigenous silt/clay ratio and sortable silt values at Site 1123 occurs at 4.35 Ma, and is associated with an increase in carbonate percentage and MAR which also coincides with some of the highest linear sedimentation rates in the Plio-Plesitocene (6.157 cm/k.y.). Mica tracer work of Carter and Mitchell (1987) suggest that at least part of the terrigenous component of the North Chatham drift was derived from sediments transported in suspended load from the Bounty Fan region via the DWBC. However, terrigenous sediment did not reach the head of the Bounty Fan region until the

Early Pliocene around ~4.0 Ma, with a marked increase after 2.5 Ma (Carter et al., 2004). Sediment records from ODP Site 1122 infer a ~5 myr hiatus separating the middle Miocene from the Early Pliocene potentially related to injection of sediment input from enhanced uplift and erosion of the Southern Alps (Carter et al., 1999), while the Solander Channel/Fan complex is suggested to have grown at least 700 km south of the New Zealand continental margin during the late Miocene to Pleistocene (Schuur et al., 1998). While the increase in terrigenous material observed at Site 1123 predates the eastward extension of the Bounty Fan into the path of the DWBC at 3.5 Ma, the increase in terrigenous material may have been sourced from a mixture of sediment sourced from older deposits along the continental apron at the base of the Campbell Plateau (ODP Site 1121) or southern flank of the Chatham Rise (Shuur et al., 1998; Carter et al., 2004). Thus, the higher amount of terrigenous silt deposition prior to 4.35 Ma may reflect increased sediment delivery during the earliest onset of rapid Southern Alps uplift, when the resultant rain shadow effect was still weak and a warm wet climate added in erosion. Alternatively, the increased silt component of the fine fraction may reflect a prolonged period of winnowing of clays via an enhanced ACC, although determining the exact cause for either scenario is difficult within the scope of this thesis.

Regardless of the exact mechanistic cause, after 4.35 Ma there is a major change in sediment delivery and/or erosion to Site 1123. Silt/clay ratio and linear sedimentation rate decrease until around 4.0 Ma (Figure 4.17). Although the spikey nature, and background/baseline shifts in the grain size data compromises the ability to easily identify Milankovitch frequencies in frequency analysis, after 4.0 Ma there appears to be an enhanced correlation between the LR04 benthic $\delta^{18}O$ stack, sortable silt and silt/clay ratio after 4.0 Ma. Such a relationship infers long-term (i.e., >100 kyr) increases in grain size coincide with periods of larger variance in greater values of $\delta^{18}O$ in the LR04 stack (Figure 4.17). The increase of coherency also coincides with the eastward expansion of the Bounty Fan system as the Southern Alps continue to develop and erode material off the continent (Carter et al., 2004). An exception to this relationship is the large M2 glacial excursion in the $\delta^{18}O$ (Lisiecki and Raymo, 2006). The Marine Isotope Stage (MIS) M2 glacial is the first large glacial excursion of the Pliocene and has been documented from Antarctic records to represent a major cooling trend that initiated at 3.5 Ma, characterised by a 0.7‰ enrichment $\delta^{18}O$ between MIS Mg6 (~3.5 Ma) and M2 (3.3 Ma; Figure 4.17). This cooling would have resulted in a ~20-30 m lowering of sea level (Miller et al., 2012) and is the first major sea level lowstand of the Pliocene (Naish and Wilson 2009; Miller et al., 2012). The silt/clay and sortable silt increases in tandem with the enrichment of $\delta^{18}O$ during the first part of this cooling (Mg6 to Mg2), but this trend reverses abruptly during the M2 event. The cause of such a departure from the generally coherent pattern of increased silt abundance and size during glacial periods is difficult to explain, except to say that this first rapid and large sea level drop may have perturbed the standard mode of sediment delivery during this glacial cycle. Such a perturbation is reflected in the magnetic susceptibility data and may be more consistent with the traditional ENZOSS deposition model in which exposure of the continental shelf during sea level lowstands (glacial periods) allows for the increased input of terrigenous material to the deep ocean via the ECC (Figure 4.15). However, despite this complication, the general pattern of higher silt/clay ratios and sortable silt values during $\delta^{18}O$ enrichments (i.e., glacial periods is consistent with Late Pleistocene records inferring enhanced bottom currents associated with an invigorated ACC, and thereby enhanced inflow related to an increase in bottom water formation during glacial periods in response to ice sheet development (e.g., Hall et al., 2001; Hall et al., 2003).

4.4.2. Pliocene-Early Pleistocene orbital forcing of ice volume and the carbon cycle

As expected from a globally integrated proxy data set, the benthic $\delta^{18}O$ record at Site 1123 displays the signature 40-kyr variability associated with Pliocene and Early Pleistocene glacial to interglacial cycles reflected in the globally integrated benthic LR04 stack. Meyers and Hinnov (2010) identified non-linear climate dynamics during the Late Pliocene and Early Pleistocene in which long (400-kyr) and short (100-kyr) period eccentricity dominate the globally integrated signal of the LR04 stack rather than the 40-kyr obliquity signal from ~3.5 to 2.7 myr. Evolutionary spectra analysis carried out in this study on both the LR04 stack and Site 1123 $\delta^{18}O$ record exhibit the emergence of a 400-kyr signal and lack of strong obliquity pacing from ~3.5 to 2.7 myr. After ~3.0 and 2.7 Ma, and similar to the LR04 Site 1123 $\delta^{18}O$ record displays the strong 40-kyr pacing and long period eccentricity is replaced by the shorter 100-kyr signal until about 2.0 Ma when the 100-kyr signal begins to disappear (Figure 4.13). While the 40-kyr and 100-kyr pacing after ~2.7 Ma is also evident in the benthic $\delta^{18}O$ record of Site 1123, so is the long period 400-kyr eccentricity signal. Power spectra analysis infers the long period eccentricity is significant at almost 95% throughout 4.3 to 1.24 myr (Figure 4.13) and band-pass filtering of the 100-kyr frequency on the Site 1123 $\delta^{18}O$ record highlights strong 100-kyr influence between ~3.5 and 2.7 myr (Figure 4.12).

Of the 57 records included in the benthic stack less than a 1/4 comes from the Pacific Ocean. As stated earlier, LCDW entering the Pacific Ocean Basin across Site 1123 is sourced from the Ross Sea and Wilkes Land margin of Antarctica. When compared to South Atlantic sites 1090/704, South Pacific Site MV0502-AJC and Site 1123 benthic $\delta^{18}O$ values are on average heavier (Figure 4.14), implying deep bottom water entering the Pacific Ocean sector carries more of a abyssal Southern Ocean sourced temperature and salinity signature signature compared to South Atlantic sites where there is more mixing with NCW (Hodell and Venz-Curtis, 2006; Waddell et al., 2009). A major change in the glacial regime in the Antarctic Ice Sheet occurs between 3.33 Ma and ~2.7 Ma (McKay et al., 2012; Chapter 3 this thesis). During this time, there is inferred to have been a step wise transition into more persistent cold polar ice sheet over West Antarctica with enhanced polynya style mixing in the Ross Sea (McKay et al., 2012) and potentially along the Wilkes Land margin with the EAIS responding to the 400 and 100-kyr eccentricity modulated changes in precession (Chapter 2 and 3 of this thesis). The higher $\delta^{18}O$ values observed in South Pacific sites (Site 1123 and MV0502-AJC) and the significant long period (400-kyr) eccentricity signal persistent within the Site 1123 benthic $\delta^{18}O$ is potentially a temperature signal associated with AABW/LCDW formation, and may have been regulated by the long term response of the Antarctic Ice Sheet and Southern Ocean sea-ice belt after ~3.5 to 3.33 myr to precessional forcing.

The benthic $\delta^{13}C$ record of Site 1123 displays the strong 400-kyr frequency significant at 95% while the 40-kyr obliquity signal becomes more persistent after ~2.7 Ma (Figure 4.13). Band-pass filtering at long period 400-kyr eccentricity and power spectra analysis demonstrates the relationship between the benthic $\delta^{13}C$ record at Site 1123 and the long period 400-kyr eccentricity cycle. This is also demonstrated in the $\Delta\delta^{13}C$ gradient from Site 1123 to ODP Site 849 in the equatorial Pacific, whereby a lower gradient is associated with minima in the 400-kyr eccentricity cycle (Figure 4.13d). Such a strong signal of the 400-eccentricity cycle is consistent with the box modelling study of Palike et al., (2006) demonstrating the interaction between the carbon cycle, solar forcing and Antarctic ice volume modulated changes in deep ocean acidity as well as the production and burial of biomass.

4.4.3. Southern Ocean ventilation during the Late Pliocene cooling and the onset of the bipolar world

Hodell and Venz-Curtis (2006) compiled benthic foraminifera $\delta^{13}C$ records (e.g., ODP sites 607, 704/1090 and 849) in order to trace the ventilation history of intermediate and deep water masses for the last 9 myr. That study highlighted the influence of surface water processes in the Southern Ocean on deep water ventilation during major transitions in Earth's climate system. Waddell et al., (2009) added to this compilation with stable isotope records from the Pacific sector of the Southern Ocean (subantarctic Pacific). The addition of the South Pacific records provided a circum-Antarctic perspective for carbon isotopic shifts during the late Miocene carbon shift (~7 Ma) and the stepwise Late Pliocene cooling (3.1, 2.7, 2.6 and 2.4 Ma). However, the record of Waddell et al., (2009) does not contain data spanning the Early to mid-Pliocene (4.3 to 3.0 Ma). Therefore, when combining the data sets presented in those two studies, no South Pacific record is represented during the transition from the warm Early Pliocene into the Late Pliocene cooling. The newly developed $\delta^{13}C$ record from Site 1123 provides a South Pacific representation during this important transition in southern high latitude climate.

Currently, deep water in the Southern Ocean is well mixed between high $\delta^{13}C$ North Atlantic values and low $\delta^{13}C$ Pacific "like" with an average $\delta^{13}C$ of 0.4‰ (Hodell and Venz-Curtis, 2006). However, records from the Atlantic and Pacific sectors spanning 4.3 to 12.4 myr infer homogeneity did not always exist (Hodell and Venz-Curtis, 2006). During the Early Pliocene from 4.3 to ~3.6 myr, South Atlantic $\delta^{13}C$ values closely match those of Site 1123 (Figure 4.14). Continuous and strong outflow of Northern Component Water (NCW), including NADW, is inferred to have taken place during this time based on higher values in benthic $\delta^{13}C$ records, Nd and Pb isotopes in ferromanganese records inferring source region of bottom water, and lowering of the calcite-lysocline in the equatorial western Atlantic from $CaCO_3$ records (Billups et al., 1997; King et al., 1997; Kwiek and Ravelo, 1999; Ravelo and Andreasen, 2000; Frank et al., 2002).

The preformed $\delta^{13}C$ values in high southern latitudes are largely controlled by surface water productivity, and ocean-atmosphere gas exchange – e.g., wind mixing (Villinski et al., 2000; Hodell and Venz Curtis, 2006). During the Early Pliocene, both of the source regions of AABW/LCDW (Ross Sea and Wilkes Land margin) that ultimately feed the deep Pacific inflow at Site 1123, are characterised by minimal summer sea ice extent with periods in which the winter sea ice margin was much farther south than today (McCartney and Donohue, 2007; Williams et al., 2008; McKay et al., 2012; Cook et al., 2013; Chapter 2 and 3 of this thesis). Consequently there must have been much larger areas of highly-productive seasonally open marine conditions (see Naish et al., 2009) on the continental shelves in these two regions, and this would result in a high preformed $\delta^{13}C$, compared to times in the Late Pliocene and more recent ice sheets/shelves and perennial sea ice restricted productivity on the continental shelves, and expanded sea ice covered in the Southern Ocean restricted ventilation of upwelling deep waters.

The mixture of higher-preformed values of $\delta^{13}C$ NADW entering the Southern Ocean, and higher-preformed $\delta^{13}C$ sourced from the Southern Ocean would cause bottom waters in both the South Atlantic and South Pacific sectors to have a higher benthic $\delta^{13}C$ value. In the South Pacific, the water mass feeding Site 1123 is a hybrid of Southern (AABW) and Northern component deep water with a NADW signature. The highest $\delta^{13}C$ values in the core occur between 4.3 to 3.5 Ma (averaging 0.29‰). Stratigraphic and geochemical evidence from the ANDRILL-1B core in the Ross Sea indicates that this time interval coincides with a largely deglaciated WAIS throughout much of this time, reduced extent and duration of summer sea ice, and sea surface temperatures in the Ross Sea 4-6°C warmer than present (McKay et al., 2012). Between 3.5 and 2.5 Ma, the benthic $\delta^{13}C$ values at Site 1123 decreased to an average value of 0.21‰, coinciding with more regular obliquity paced readvances of the WAIS, increasing the duration and extent of summer sea ice, cooling sea surface temperatures in the Ross Sea (Naish et al., 2009; McKay et al., 2012), and a major shift in the glacial dynamics of the EAIS inferred to represent a major cooling event (Chapter 3 of this thesis). After 2.5 Ma, there is another stepped decrease in the average $\delta^{13}C$ value (0.04‰), coinciding with a stepped increase in Ross Sea sea ice extent, and greatly reduced IBRD at the Wilkes Land IODP Site U1361 interpreted as a stabilisation of the marine margin of the EAIS (Figure 4.18) (Chapter 3).

The deep water $\delta^{13}C$ gradient in the Pacific Ocean ($\Delta\delta^{13}C_{(1123\text{-}849)}$) is a measure of the aging of water masses as they pass through the Pacific. The Site 1123 $\delta^{13}C$ record highlights that this gradient was consistently increased during the Pliocene when compared to modern (Figure 4.18). Hall et al., (2001) noted that for the Late Pleistocene, a higher $\delta^{13}C_{(1123\text{-}849)}$ values occur during interglacial conditions (or warm intervals) was a consequence of substantial input of high $\delta^{13}C$ NADW entering the Southern Ocean when sortable silt values indicate a slowdown of the DWBC when compared to glacial periods. The high Pacific carbon gradient ($\Delta\delta^{13}C_{(1123\text{-}849)}$) during the Pliocene (4.3 to 2.7 Ma; Figure 4.18) thus can be explained by the enhanced outflow of NADW and reaching deeper depths during a stronger period of Atlantic Meriodal Overturning Circulation (AMOC), until ~2.7 Ma, which coincided with the build-up of the Northern Hemisphere ice sheet and enhanced production of Glacial North Atlantic Intermediate Water (GNAIW) (Boyle and Keigwin, 1987; de Menocal et al., 1993; Oppo and Lehman, 1995; Billups et al., 1997; Oppo et al., 1997; Marchitto et al., 1998; Oppo and Horowitz, 2000; Ravelo and Andreasen, 2000; Frank et al., 2002). This coincided with a more diminished pole to equator temperature gradient leading to reduced zonal circulation (Brieley et al., 2009), and ultimately reduced ACC vigor which drives the DWBC along the Campbell Plateau (e.g., Hall et al., 2001). This interpretation for the Pliocene is consistent with a reduced meridonal temperature gradient in the Pacific at this time until ~2.7 Ma (Figure 4.18h) (Federov et al., 2013), reduced dust MARs in the South Atlantic (Figure 4.18e) (Martínez-Garcia et al., 2010), and reduced Antarctic ice sheet and sea ice extent (Figure 4.18b) (McKay et al., 2012). Model simulations indicate ice sheet and sea ice expansion can have a significant effect on the global Hadley circulation potentially resulting in latitudinal shifts in the positioning of the Intertropical Convergence Zone, trade winds and southern mid-latitude westerlies (Chian and Bitz, 2005). Such an effect on atmospheric circulation would have a consequence on wind driven upwelling of cold deep waters sourced from high latitudes as well as the latitudinal position of ocean fronts. While the mid-Pliocene, ~3.6 to ~2.8 Ma, zonal equatorial Pacific SST gradients barely differ to that of the Early Pliocene's "permanent El Niño like state", meridional SST gradients gradually increase during this time of increased Southern Hemisphere ice volume and southern sourced water entering the Pacific Ocean (Figure 4.18h). However, shifts in the Southern Hemisphere westerlies as a mechanism to explain deep ocean ventilation and large scale changes in atmospheric CO_2 is of debate (e.g., Bonining et al., 2008; Menviel et al., 2008), and hightlights the complexity of Earth's climate system feedbacks and uncertaintity of the proposed mechanism of Toggweiler and Russell (2008).

After ~2.5 Ma, there is a baseline shift in the $\Delta\delta^{13}C_{(1123\text{-}849)}$ reflecting a more reduced gradient as well as over all lower $\delta^{13}C$ values at Site 1123. This coincides with the expansion of ice sheet/sea ice around the Antarctic margin (McKay et al., 2012; Chapter 2 and 3 of this thesis), thus promoting the formation of AABW and reduced deep ocean ventilation in the Southern Ocean ventilation while most likely further enhancing the delivery of cold southern sourced AABW/LCDW into the Pacific Ocean. This is also supported by reeduced opal MAR from the Antarctic Peninsula region during this time due to restricted light availability or nutrient upwelling on account of increased summer sea ice cover (Hillenbrand and Cortese, 2006).

While the benthic $\delta^{18}O$ records from the North Atlantic, South Atlantic, South Pacific and equatorial Pacific were almost equal in value during the Early Pliocene, after ~3.6 Ma North Atlantic records become much lighter in comparison to Southern Ocean sites (South Atlantic and South Pacific). This marked increase in Southern Ocean benthic $\delta^{18}O$ records coincides with a decrease in atmospheric CO_2 concentrations and transition of the EAIS into a more "cold climate state" in which the Southern Hemisphere ice sheet becomes more sensitive to precessional forcing and summer sea ice extent begins to develop along the margin providing a stabilising effect (Chapter 3 this thesis). Southern Hemisphere cooling during this time coincides with a marked increased in the zonal gradient between the South Atlantic and South Pacific $\delta^{13}C$ records as well as a slight increase in mid-latitude Southern Hemisphere dust records inferring stronger atmospheric circulation. The increase in the benthic $\delta^{13}C$ gradient between the South Atlantic and South Pacific probably reflects the enhanced delivery of NADW with higher preformed $\delta^{13}C$ into the Atlantic sector of the Southern Ocean until ~3.0 Ma and in particular until 2.7 Ma (Boyle and Keigwin, 1987; de Menocal et al., 1993; Oppo and Lehman, 1995; Billups et al., 1997; Oppo et al., 1997; Marchitto et al., 1998; Oppo and Horowitz, 2000; Ravelo and Andreasen, 2000; Frank et al., 2002).

During the Late Pliocene to Early Pleistocene (~2.8 to ~2.6 myr) atmospheric CO_2 dramatically decreases and more consistently reaches pre-industrial values (~200 ppm) while interbasinal benthic $\delta^{18}O$ records converge to similar values with the exception of the South Pacific site (MV0502-AJC) which is significantly heavier (Figure 4.18). This persistent cooling trend is evident in the Wilkes Land sector of the EAIS by a dramatic decrease in iceberg discharging from the EAIS margin, and with the inferred the increased duration and extent of summer sea ice along the margin provides a stabilising effect on the ice sheet (DeConto et al., 2007; Chapter 2 and 3 of this thesis). Such a transition to a more persistent and extended summer sea ice extent is also inferred from lower bulk sediment $\delta^{13}C$ values in the Ross Sea Embayment reflecting enhanced polynya-style, deep water mixing of the surface similar to modern values (McKay et al., 2012) and a dramatic drop in opal production in the Antarctic Peninsula region (Hillenbrand and Cortese, 2006).

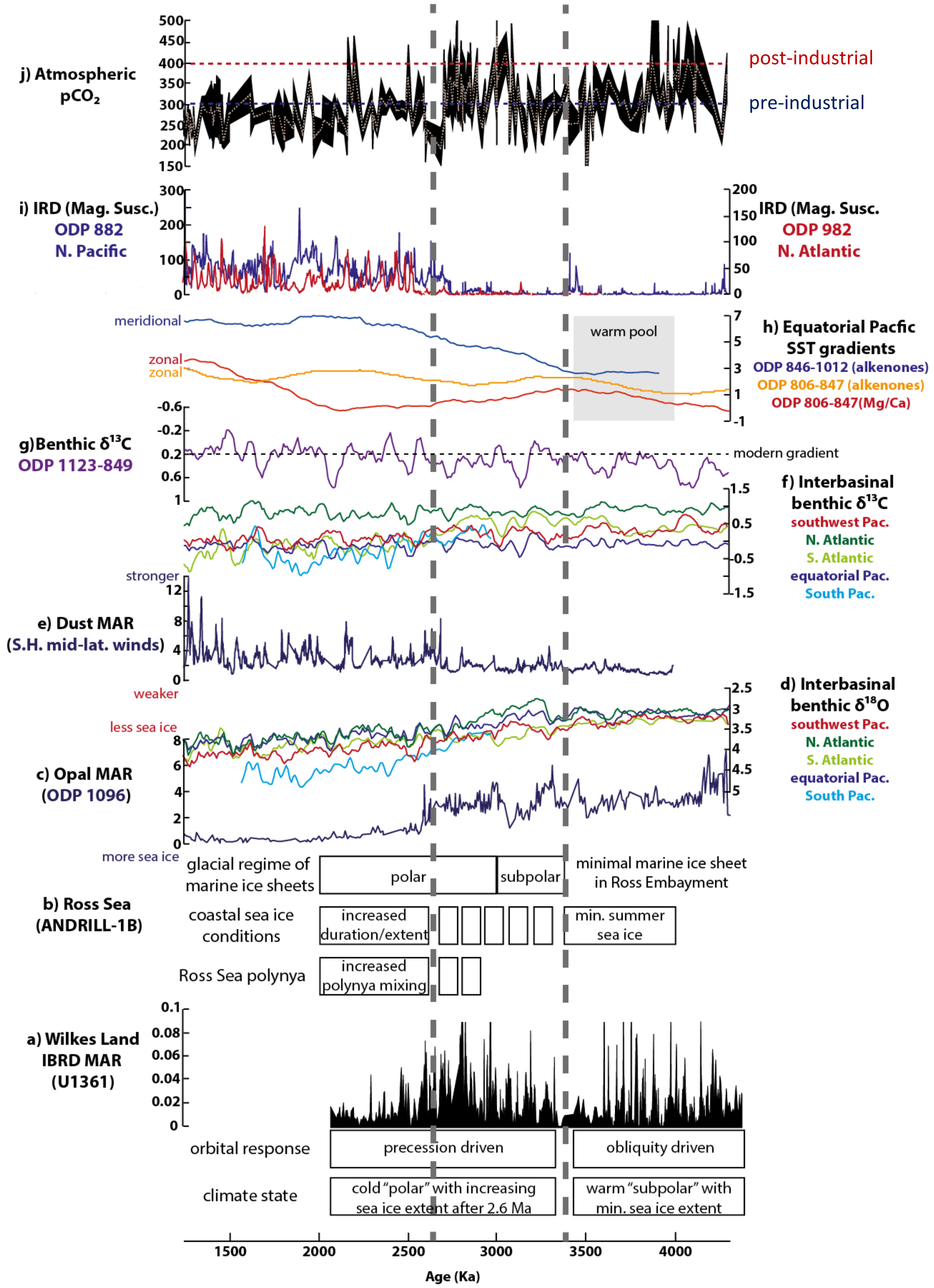

Figure 4.18. Southern and Northern Hemisphere climate transition based on proxy evidence concerning climate system feedbacks between 4.3 to 1.24 Ma. Transitions occur after 3.5 Ma and ~2.6 Ma and are noted by grey dashed lines. a) Wilkes Land IBRD MAR record from Site (U1361) (g/cm^2/k.y.) (Chapter 3 of this thesis). b) Summary of ocean, sea ice, and ice sheet evolution in the Ross Sea Embayment based on the AND-1B record (McKay et al., 2012). c) Opal MAR from ODP Site 1096 (g/cm^2/k.y.) (Hillenbrand and Cortese, 2006). d)

Interbasinal $\delta^{18}O$ gradients (‰) (Hodell and Venz-Curtis, 2006; Waddell et al., 2009). e) Southern mid-latitude dust record inferring wind strength (g/m/k.y) (Martínez-Garcia et al., 2010). f) Interbasinal $\delta^{13}C$ gradients (‰) (Hodell and Venz-Curtis, 2006; Waddell et al., 2009). g) Benthic $\delta^{13}C$ gradient between Site 1123 and Site 849 (‰). h) Meridional and zonal SST from the Pacific Ocean (°C) (Fedorov et al., 2013). i) IRD records (Mag. Susc.) from the North Pacific (Haug et al., 2005) and North Atlantic (Jansen et al., 1996). j) Atmospheric CO_2 (ppm) with pre-indsutrial (blue) and post-industrial (red) values noted with dashed lines (IPCC, 2014).

4.5. SUMMARY

In summary, a new stable isotope ($\delta^{18}O$ and $\delta^{13}C$) stratigraphy for ODP Site 1123 allows for astronomically tuned timescale for this site to extend back to 4.3 Ma. The benthic $\delta^{18}O$ record from Site 1123 compares well to the globally integrated LR04 stack, and the major Marine Isotope Stages can be easily identified even during the lower amplitude glacial-interglacial cycles of the Early Pliocene. The benthic $\delta^{13}C$ record from Site 1123 contains the significant long period eccentricity signal, potentially highlighting the role of the Antarctic Ice Sheet and Southern Ocean has on the global carbon cycle, and has implications for the ventilation of the abyssal ocean as the world transitioned from the warm Early Pliocene into the bipolar Early Pleistocene world.

The intensification of southern sourced bottom water inflow into the southwest Pacific Ocean can be reconstructed by the benthic $\delta^{13}C$ gradient in the Pacific ($\Delta\delta^{13}C_{(1123\text{-}849)}$), with higher benthic $\delta^{13}C$ at ODP Site 1123 and increased $\Delta\delta^{13}C_{(1123\text{-}849)}$ indicating increased NADW input into the southwest Pacific during the Pliocene. This is interpreted to be a consequence of enhanced circulation or Southern Ocean ventilationg during an enhanced ACC, potentially as the westerlies wind field was most likely positioned at a more southern latitude at this time. A Decrease in Southern Ocean ventilation occurs in conjunction with ice sheet/sea ice development around the Atlantic margin between 3.5 to 3.33 myr. The intensification of southern sourced bottom water inflow into the southwest Pacific after this time coincides with a decrease in preformed values of $\delta^{13}C$, interpreted to be the consequence of increased productiong of AABW in the two main formation regions in the Ross Sea and Wilkes Land margin due to ice sheet and sea ice expansion in the Southern Ocean. Thus, this led to a reduction in the ocean-gas exchange of upwelling deep waters at the southern margin of the ACC, and a shift of the major productivity zone to more northerly regions in the ACC, (i.e., north of the major AABW formation zones). However, invigorated zonal circulation also occurred at this time (Martínez-Garcia et al., 2010), and this study indicates this resulted in an increase in deep water inflow into the Pacific Ocean, as the $\Delta\delta^{13}C_{(1123\text{-}849)}$ gradient decreased, which occurred in tandem with proxy evidence for the expansion of the marine margins of the Antarctic Ice Sheet, Southern Ocean sea ice (Hillenbrand and Cortese, 2006; McKay et al., 2012; Chapter 3 of this thesis) and enhanced westerly wind over the ACC (Martínez-Garcia et al., 2011). Thus changes in the extent of Southern Hemisphere Ice Sheets and sea ice lead to reduced ventilation of the abyssal ocean, and may have played a role in decreasing atmospheric CO_2 concentrations over this major climatic transition (Pagani et al., 2010), that ultimately led to the initiation of large scale glaciations in the Northern Hemisphere (Lunt et al., 2009).

CHAPTER 5

IDENTIFYING ORBTIAL PACING OF ANTARCTIC ICE VOLME VARIATIONS FROM MID-PLIOCENE SEA LEVEL FLUCTUATIONS RECORDED IN A FAR-FIELD SHALLOW-MARINE CONTINENTAL MARGIN SEDIMENT RECORD: THE WANGANUI BASIN, NEW ZEALAND

Eleven outcrop exposures along the Turakina River in Wanganui Basin, North Island, New Zealand, just west of Taihape, have been described and sampled in order to assess the role of orbital pacing as well as the frequency variability of mid-Pliocene sea level changes. Sedimentary exposures consist of blue-grey concretionary sandy to fine sandy mudstones of the Utiku Subgroup. Detailed paleomagnetic studies, previously carried out along this river section, provide time constraints for two ~100-kyr sedimentary cycles extending from ~3.2 to 3.0 Ma. Detailed grain size analyses highlight changes in percent mud that range from up to 55% during lowstands to 90% during highstands. By employing modern analogue studies carried out along the Manawatu coast, changes in grain size reflect bathymetric changes of up to ~20 m amplitude. While higher frequency events are also observed, these ~100-kyr-duration sequences occur during a time in which the Laskar et al., (2004) orbital solution demonstrates low-amplitude obliquity (40-kyr) and eccentricity (100-kyr-duration) modulated high-amplitude precession (20-kyr) cycles. Although these changes of ~20 m in local water depth contain tectonic contributions, they are in good agreement with global eustatic sea-level estimates for peak interglacial periods of ~22 m higher than present with a deglaciated Greenland Ice Sheet up to (+7 m sea level equivalent) and West Antarctic Ice Sheet (+3 m sea level equivalent) as well as a significant contribution between +2-15 m from the East Antarctic Ice Sheet. As described elsewhere in this thesis (Chapter 3), geological evidence from the EAIS margin infer ice marginal retreats during this time extended several 100's km inland and provided a ~10 m contribution with the greatest amount of ice volume loss paced by the 100-kyr eccentricity modulations of precession.

5.1. INTRODUCTION

Over eighty years after the orbital theory of the ice ages was first proposed by Milankovitch (Milanković, 1936), the mechanistic link between variations in polar ice sheet volume and orbital forcing is still not well understood (e.g., Huybers, 2006; Raymo et al., 2006; Raymo and Huybers, 2008). While the 100-kyr cycles that pace Late Pleistocene global ice volume are consistent with a non-linear response to strong influence of Northern Hemisphere influence on local insolation (i.e., precession), the 40-kyr cycles of the Pliocene to Early Pleistocene (5.3 to 0.8 myr) challenge the classical understanding of Milankovitch's theory, in that there is an apparent lack of significant precessional power in the globally integrated proxy records of ice volume (i.e. $\delta^{18}O$) (Lisiecki and Raymo, 2005) and sequence stratigraphic sea level records (Naish, 1997; Naish and Wilson, 2009; Miller et al., 2012).

This apparent lack of precession has sparked several models that explain how orbital forcing mechanisms may drive ice volume changes during the Late Pliocene and Early Pleistocene. Raymo et al., (2006) suggest that because the influence of precession on seasonal insolation is out-of-phase between hemispheres, ice volume variance at precessional frequencies (23 and 18-kyr) is cancelled out in global integrated proxy records, leaving the residual obliquity (40-kyr) signal to dominate (i.e., benthic $\delta^{18}O$ and sea level records). While Raymo's hypothesis implies an explicit response of ice sheet variance to precessional forcing, Huybers (2006) argues that under certain climate states, precession may have minimal influence. This is due to Kepler's Second Law of Planetary Motion, whereby the Earth travels fastest when it is closest to the sun (in perihelion), resulting in intense, but short, Northern Hemisphere summers and longer cooler Northern Hemisphere winter, when situated at aphelion. Thus, because the mass balance of Northern Hemisphere ice sheets is controlled by surface melt, and therefore the number of positive degree days, the threshold at which ice sheets melt is forced by the duration or total amount of summer insolation, and consequently the overall climate state. During the warmer climate state of the Early Pliocene to Early Pleistocene, the enhanced radiative forcing due to elevated atmospheric CO_2 concentrations lowered the insolation threshold required to initiate surface ice sheet melt, and thus increasing the melt season. The implication is that increasing the duration of the summer melt season results in enhanced obliquity (40-kyr) control on ice sheet ablation. As polar regions receive no sunlight in winter, increasing the duration of the "summer melt season" skews the total summer insolation towards the mean annual insolation value - which is directly modulated by obliquity as the influence of precession on insolation always cancels out seasonally. Conversely, as climate cooled during the Late Pleistocene, the insolation threshold for ice sheet melt increased and the summer melt season became more sensitive to precession (23 and 18-kyr), with internal mass balance feedback (e.g. height mass balance, albedo) potentially allowing for the ice sheets to build up over multiple forcing cycles (i.e. the 100-kyr cycle of eccentricity modulation of precession).

Raised coastal terraces and Pacific atolls provide independent evidence that mid-Pliocene sea-level was globally higher (Dowsett and Cronin, 1990; Wardlaw and Quinn, 1991). Sequence stratigraphic reconstructions of Pliocene global mean sea-level have been used to calibrate the benthic foraminiferal $\delta^{18}O$ record in order to demonstrate that eustatic sea level may have been ~22 higher than present, with sea level variance having amplitudes of 5-10 m during the warmest and least variable glacial-interglacial $\delta^{18}O$ cycles between 4.3 and 3.2 myr (Naish, 1997; Naish and Wilson, 2009; Miller et al., 2012). Shallow marine cyclothems apparent in outcrop exposures from Wanganui Basin, New Zealand, have demonstrated that these variations occurred at a 40-kyr pacing through most of this interval (Naish et al, 1998).

The Wanganui Basin in New Zealand contains one of the best-dated Neogene shallow-marine sedimentary strata exposures in the world recording unconformity-bound sequences (cyclotherms) of glacio-eustatic changes in sea level. Previous studies, using grain size texture and microfossil assemblages have been able to link the sea level cycles identified in these cyclothems to the glacial-interglacial cycles in the benthic oxygen isotope record, with up to 60 cyclotherms identified since 3.6 Ma (Journeaux et al., 1996; Naish, 1997; Kamp et al., 1998; Naish et al., 1998; Naish et al., 2005; Naish and Wilson, 2009). These studies have also identified higher frequency water depth and facies cycles within individual cyclothems, but were unable to identify if they correspond to precessional forcing or autocycles. Moreover, in the pre-Pleistocene part of the Wanganui succession, where independent age-control from tephra and paleomagnetic stratigraphy is less frequent, the frequency of orbital-pacing of the Wanganui cyclothems is more ambiguous. Of particular interest is the Pliocene orbital record between 3.15 to 3.05 myr (Kaena Subchron) characterised by high-amplitude precession and low-amplitude obliquity (e.g. a 1.2 Ma node) (Laskar, 2004), implying that global sea-level change should be controlled either by: (1) out of phase precessional and weak obliquity forcing of the Antarctic and a small Northern Hemisphere ice sheet, or (2) local precessional forcing and weak obliquity forcing of the Antarctic ice sheet preceding the development of a Northern Hemisphere ice sheet (Figure 5.1) (c.f. Raymo et al., 2006). In the case of the former eccentricity may also be significant in driving global sea-level variability as obliquity is extremely weak and the precession signal should cancel out, which in the case of the latter precession and/or eccentricity should dominate global sea-level change over weak obliquity forcing. The well-dated mid-Pliocene shallow-marine strata exposed in Wanganui Basin provide an opportunity to reconstruct high-resolution (sampling interval of

1-2 kyr) water depth changes controlled by orbitally-forced, glacio-eustatic sea-level changes through this time interval. Previous studies have described the tectonic evolution of the Wanganui Basin during the Pliocene (Saul et al., 1999), which is characterized by linear long-term flexural subsidence due to plate boundary processes (e.g. Stern et al. 1992; Fig. 2). Changes in subsidence rate due to more localised active faulting cycles are on the order of 0.5-1.0 Ma. Therefore, while there is a tectonic imprint on the stratigraphic architecture of the Wanganui Basin succession (Saul et al., 1999), the primary frequency of sedimentary cyclicity is on the order of 10^4-10^5 years, and most likely, orbital in origin.

High resolution paleomagnetic studies (i.e., McGuire, 1989; Turner et al., 2005) have laid a foundation to accurately date strata belonging to the Utiku Group exposed along the Turakina River spanning the Kaena Subchron (3.116 to 3.032 myr). The mid-Pliocene Turakina River Section is ideal, from a sedimentological perspective to capture water depth variations of ~+20 m above present (Miller et al., 2012), with glacial-interglacial amplitudes of up to 30 m (Naish and Wilson, 2009) due to global sea level changes. This is because deposition occurred on shallower inner-mid shelf (McGuire, 1989) water-depths, which are sensitive to depth-related sediment grain-size variability (Dunbar and Barrett, 2005) and depth-related changes in benthic foraminiferal assemblages (i.e., Naish and Kamp, 1995), yet deep enough not to have been subaerially exposed or eroded during sea-level lowstands.

This study develops a well-dated, high resolution (~2 kyr sample distribution) grain size record that enables correlation of local changes in sea level to a global ice volume record (i.e. deep sea benthic δ^{18}O records) and orbital parameters in order to assess the role orbital-forcing has on the frequency of water-depth changes during this key interval. It is important to note that the amplitude of these water-depth changes reflects the combined influence of eustatic sea-level, tectonic overprint, long term subsidence, compaction and sediment supply. Therefore, while this study aims to capture the frequency of eustatic change, it will not resolve the absolute magnitude. That is the aim of a recently funded Marsden project, led by Professor Tim Naish (VUW), which will employ 2-dimensional backstripping for 2 drill holes to extract the eustatic amplitudes. Additionally, the benthic foraminiferal assemblage analysis is currently been undertaken by Hugh Morgan (GNS Science) in order to provide an additional supporting data set for the result in this chapter – in particular to better constrain the paleowater water depth estimates from the stand-alone grain size results in this chapter.

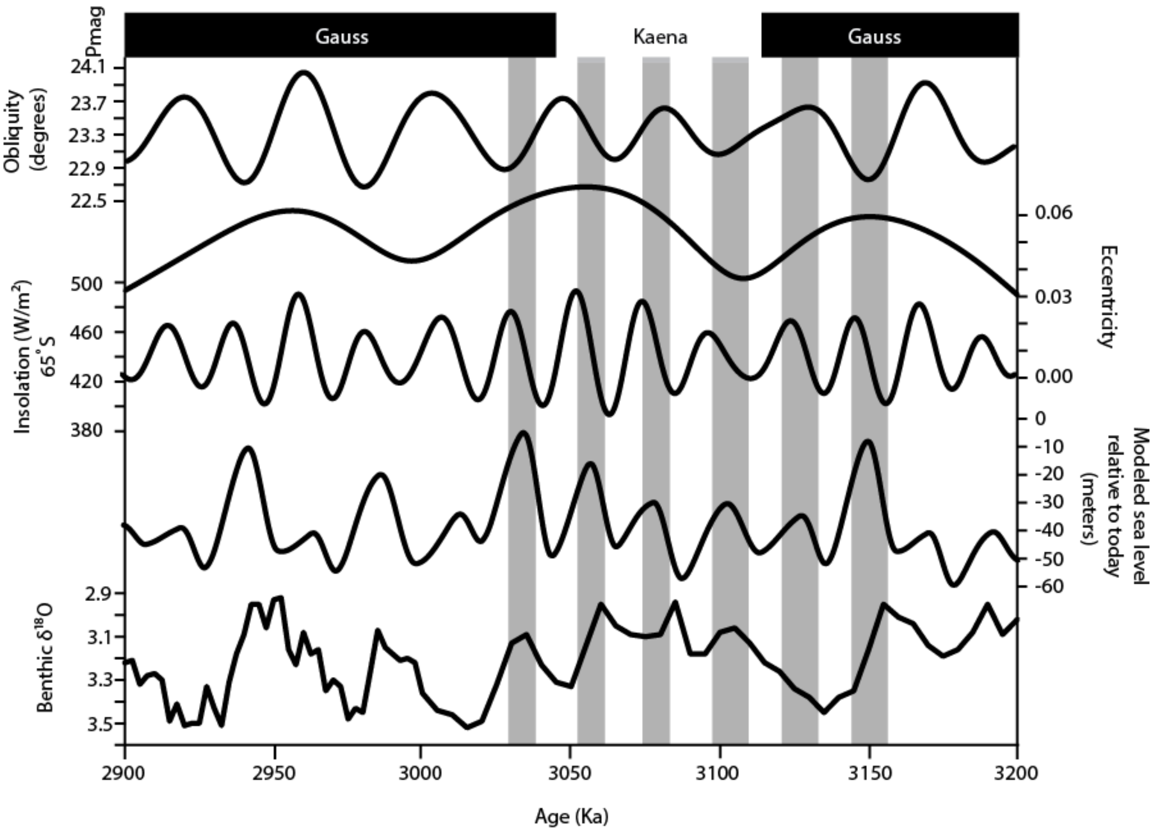

Figure 5.1. Records of benthic $\delta^{18}O$ (Lisiecki and Raymo, 2005), modeled sea level relative to today (Raymo et al., 2006), high-latitude southern insolation, eccentricity, and obliquity with potential precession-paced ice volume changes (Raymo et al., 2006) highlighted in grey, within the target interval for this is study based on outcrop exposures in Wanganui Basin, New Zealand.

5.1.1. Geological Setting and Paleogeography

The Wanganui Basin of New Zealand's North Island is an sedimentary basin (200 x 200 km) that formed in response to subduction along the Australian and Pacific plate boundary (Figure 2) (Stern et al., 1992; 2006). Eastward of the North Island along the Hikurangi Trough, the Pacific Plate subducts under the overriding Australian Plate and continues westward resulting in lithospheric loading and compressional downwarping for back-arc basin formation (Figure 5.2) (Stern et al., 1992; 2006). A southward migration of the depocentre and uplift associated with the axial ranges to the east during the Early Pleistocene have resulted in on-land exposure of Pliocene and Pleistocene shallow marine sedimentary sequences (Pillans, 1983; Stern et al., 1992; Abbott and Carter, 1994; Naish and Kemp, 1995; Journeaux et al., 1996).

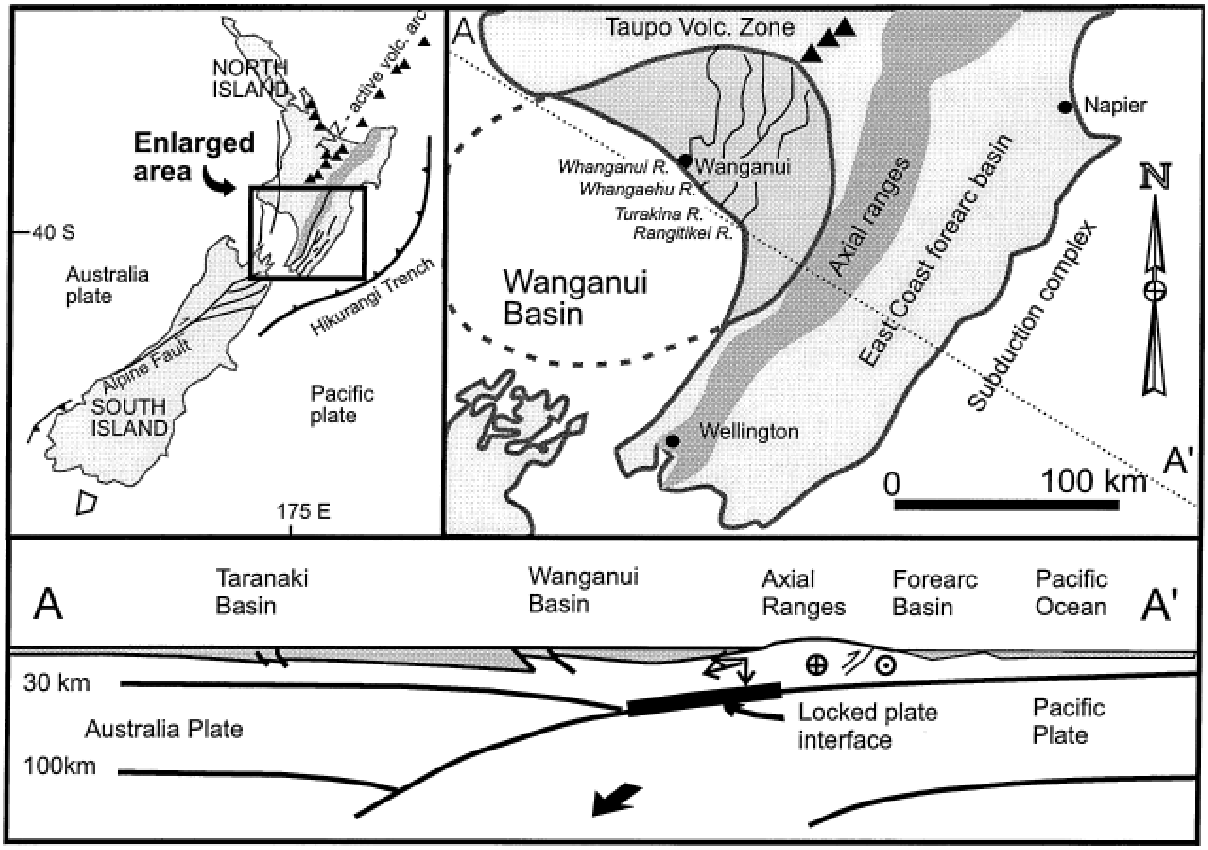

Figure 5.2. Location of Wanganui Basin, North Island, New Zealand and tectonic setting of North Island proposed by Stern et al., (1992) (from Naish et al., 1998).

Palaeogeographic reconstruction of New Zealand does not contain a major seaway through the North and South islands during the Early Pliocene ~4-3 myr (Trewick and Bland, 2012). However, a narrow and shallow connection across the modern Kaweka Range ("Manawatu Strait" in Figure 5.3) is thought to have existed from rapid subsidence in the Wanganui and Manawatu area at ~3 Ma that caused local sea level rise (or regional subsidence) of up to 600 m over ~200 Ka (Figure 5.3) (Browne, 2004; Kamp et al., 2004; Bland et al., 2008; Trewick and Bland, 2012). Subsidence in the back-arc Wanganui basin resulted in an arcuate westward facing shoreline defined as a broad embayment from south Taranaki to northern Marlborough. While the modern axial ranges were generally at or above sea level at 3 Ma, the region that includes Wanganui City and south Taranaki were 200-400 m water-depth below sea level with the Manawatu area occupying shelfal water depths (0-200 m) (Trewick and Bland, 2012). By ~2 Ma, the Wanganui basin depocentre moved south east with sediment supply largely the consequence of drainage by river systems. The Wanganui and Manawatu regions occupied shelf to marginal marine settings (Trewick and Bland, 2012). By 1 Ma subsidence in the Wanganui area ceased and uplift began, resulting in on land exposures of marine terraces that are preserved in the Wanganui and south Taranaki regions

(Pillans, 1983; Trewick and Bland, 2012). Today, the north-east and south-west orientated river valleys and coastal cliffs provide well exposed outcrops of sediment successions which are part of a regional monocline with strata dipping to the south and south-west at 3-4° (Kamp et al., 2004; Turner et al., 2005).

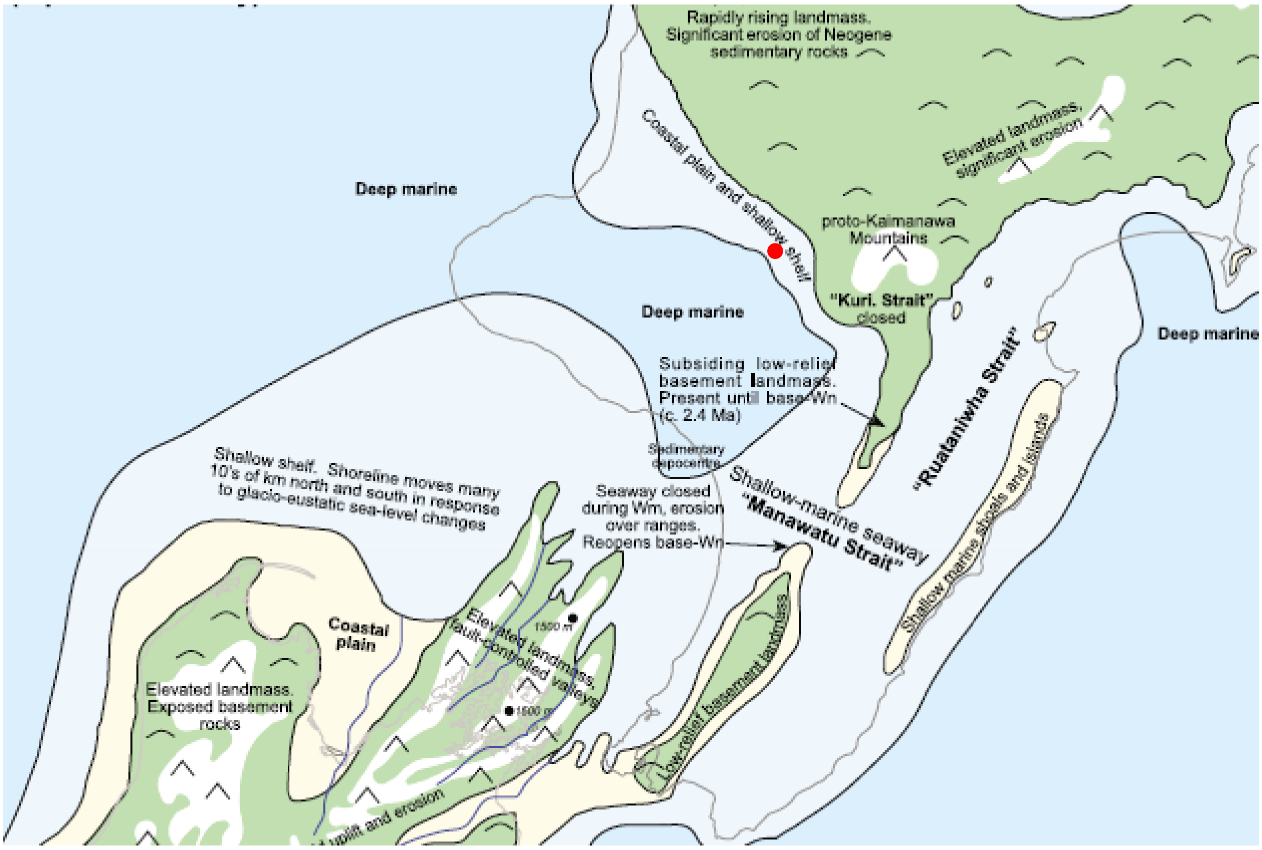

Figure 5.3. Paleogeographic map of the Wanganui Basin area 3 Ma years ago (from Trewick and Bland, 2012), relative to modern New Zealand (grey outline) deep marine environments (>200 meters) = dark blue, shelfal water depths (< 200 m) = light blue, coastal land = light yellow, with land areas = green and mountainous areas > 1000 m = white. Red circle infers the location of the stratigraphic sections presented in this study.

5.1.2. Pliocene-Pleistocene sea level records and cyclostratigraphy from Wanganui Basin, New Zealand

Outcrop exposures of shallow-marine sedimentary cycles from Wanganui Basin, New Zealand contain one of the most complete Pliocene-Pleistocene stratigraphic records in the world recording sea level fluctuations in response to glacio-eustasy (i.e., Kamp, 1978; Beu and Edwards, 1984; Naish and Kemp, 1995; Naish et al., 1998; Naish et al., 2005; Turner et al., 2005; Naish and Wilson, 2009). These exposures are unique as most Quaternary continental margins remain flooded (i.e., Gulf of Mexico). Early work in the 1950's by Sir

Charles Fleming recognised that depositional cycles were related to sea level changes (Fleming, 1953). However, his observations predated the orbital theory of ice ages, deep ocean climate proxies (i.e., benthic $\delta^{18}O$) and modern geochronologic techniques (i.e., magnetostratigraphy and radiometric ash dating). Therefore, Fleming explained the occurrence of depositional cycles as a result of tectonic influence by local crustal movements (Fleming, 1953). Approximately forty years later, these Pliocene-Pleistocene sedimentary cycles were correlated to glaciations reflected in the deep-sea ice volume records (i.e., Kamp, 1978; Pillans, 1983; Beu and Edwards, 1984; Naish and Kamp, 1995; Naish et al., 2005; Naish and Wilson, 2009).

Kamp (1978) was one of the first to correlate Pleistocene outcrop exposures at Cape Kidnappers to oxygen isotope stages. Pillans (1983) dated 12 Quaternary marine terraces in the South Taranaki region representing marine transgression events between 680 and 60 kyr. Beu and Edwards (1984) demonstrated Pleistocene (~2.2 to 0.1 myr) glacio-eustatic sea-level cycles represented in terrestrial stratigraphic sections described by Fleming (1953), Vella (1963), Vella and Briggs (1971) and Lillie (1953) (Castlecliff Section, Mangaopari Stream Section and Hawkes Bay Nukumaruan Section) exposed on land could be correlated to Pillans' (1983) marine terraces as well as the oxygen isotope stages identified from the marine-based records of Shackleton and Opdyke (1976) and Gardner (1982).

Following the original descriptive sedimentological work of Fleming (1953), detailed sequence stratigraphy was carried out along the southern Taranaki coast, southern Wanganui coast and within Rangitikei River valley by numerous workers (Abbott and Carter., 1994; Naish and Kamp, 1997; Journeaux et al., 1996; Naish et al., 2005). The substantial number of silicic tephra from North Island arc volcanoes deposited during the Plio-Pleistocene, has provided a precise chronostratigraphy also constrained by magnestratigraphy (Naish et al., 2005b; Pillans et al., 2005). The preservation of tephra deposits within the basin, as well as those recorded in ODP Leg 181 (includes Site 1123) off eastern New Zealand, from single eruptive events have provided direct chronostratigraphic ties between the Wanganui cyclothems and the $\delta^{18}O$ ice volume record (i.e., Naish, 1997; Carter et al., 2003; Lisiecki and Raymo, 2005; Alloway et al., 2005; Naish and Wilson, 2009).

The ability to integrate the sedimentological record with accurately constrained chronostratigraphy has resulted in the identification of sedimentary cyclothems representing transgressive and regressive cycles responding at Milankovitch-frequency for the last 3.6 myr (Abbott and Carter., 1994; Naish and Kamp, 1997; Naish et al., 1998; Journeaux et al., 1996; Naish et al., 2005). Chronostratigraphy of these cyclothemic records has allowed for one-to-one correlation to single Milankovitch driven events responding to 40-kyr and 100-kyr cycles related to glacio-eustatice sea-level changes (Abbott and Carter, 1994; Naish, 1997; Kamp et al., 1998; Naish et al., 2005b). By reconstructing water depth changes using extant benthic formainiferal depth associations, and placing first-order constraints on total subsidence and sediment decompaction, Naish (1997) and Naish and Wilson (2009) were able to estimate changes in the amplitude of eustatic sea-level inferred from Wanganui cyclothemic records. By mapping these chronologically constrained, eustatic changes to global benthic $\delta^{18}O$ records Naish and Wilson (2009) were able to independently calibrate the ice volume/sea-level component of the $\delta^{18}O$ records. Their estimates inferred from the Wanganui cyclothems are consistent with (1) ice volume changes implied by the $\delta^{18}O$ records (Lisiecki and Raymo, 2005), and (2) numerical ice sheet models suggesting near-complete deglaciation of Greenland (+7 m sea-level rise) (e.g Hill et al., 2010; Dolan et al., 2011), with the WAIS contributing +3 m (Pollard and DeConto, 2009), and <+10 m from the EAIS (Pollard and DeConto, 2009; Hill et al., 2010). Other estimates based on uplifted shorelines and backstripping from far-field sites suggest global mean sea level was ~+20 m during peak Pliocene interglacial (Miller et al., 2012). However, large uncertainties in these estimates are a result of glacio-hydro isostatic adjustment, resulting in regionally-uneven sea-level changes ranging from 5 to 30 m (Raymo et al., 2011).

5.1.3. The Turakina River Section of Wanganui Basin

The Turakina River valley section is located in the central part of the Wanganui Basin where Pliocene-Pleistocene sediments are finer grained reflecting deep water (mid-shelf) compared to the thicker corresponding stratigraphic units further to the east in the basin such as the Rangitikei River Section which consists of shelf to coastal plain setting (Figure 5.2) (McGuire, 1989; Turner et al., 2005; Naish and Wilson, 2009). Following the work done by Superior Oil workers, McGuire (1989) identified five formations within the Waitotaran New Zealand Superstage (mid-Pliocene) exposed along the Turakina River that span the Tangahoe Mudstone to the base of the Nukumaruan strata (Figure 5.4), which McGuire (1989) refers to as; Reef-Bearing Sands Formation, Taihape Mudstone, Utiku Sandstone, Mangaweka Mudstone and the lower portion of the Nukumaruan Formation (Figure 5.5).

Following the work of McGuire (1989), Turner et al., (2005) defined the base of the Turakina Section, to consist of the Tangahoe Mudstone (760 m), a mid-Pliocene continental slope succession, that is overlain by Late Pliocene-Pleistocene shelf successions (Okiwa Group and younger units). The Utiku Subgroup (200 m) directly overlies the Tangahoe Mudstone and is characterized by a blue-grey fine grained, concretionary sandstones and sandy siltstones. According to McGuire (1989), the Utiku Sand is not mappable to the west. The Utiku Subgroup passes upwards into the Mangaweka Mudstone (840 m), which is predominantly a massive-blue-grey mudstone with occasional concretionary bands that increase in abundance at the top of the section (Figure 5.4) (McGuire, 1989; Turner et al., 2005). The Utiku Subgroup strata have a simple post-depositional structure with a strike of 110° and dip 6 to 4° towards the south.

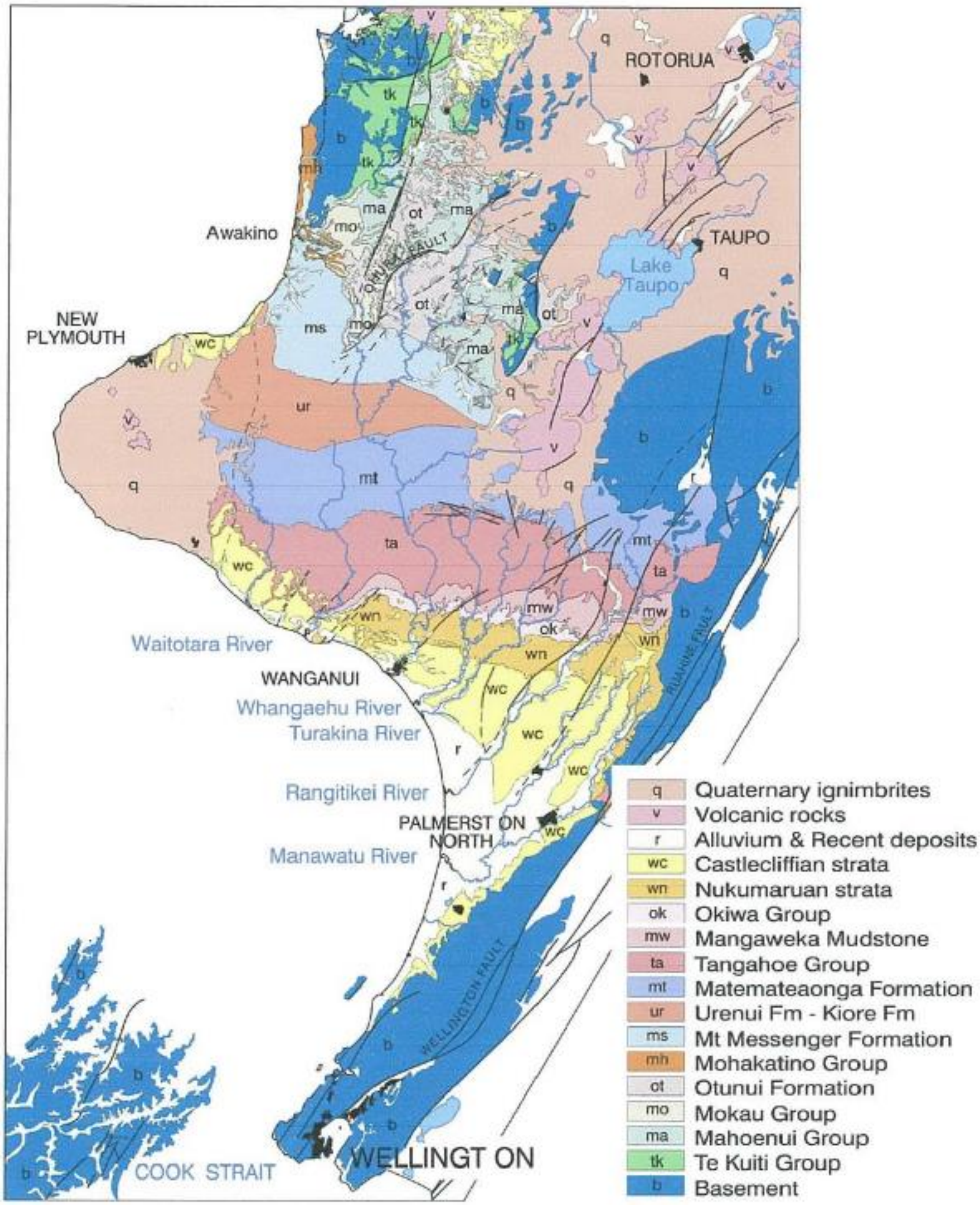

Figure 5.4. Geological map of the Wanganui Basin showing the location of the Turakina River.

An estimated sediment accumulation rate for the Turakina River Section is 1.5 m/k.y. (Turner et al., 2005). Detailed sampling used to erect a magnetostratigraphy for this river section was carried out by McGuire (1989) and Turner et al., (2005), which is constrained by tephrochronology and biostratigraphy (Turner et al., 2005). This study employs stratigraphic dating from Turner et al., (2005) of the lower and upper boundaries of the Kaena Subchron in order to make correlations between the local expression of eustatic (global) sea level oscillations observed in the Turakina River Section to that of MISs reflected in the benthic $\delta^{18}O$ record (Lisiecki and Raymo, 2005).

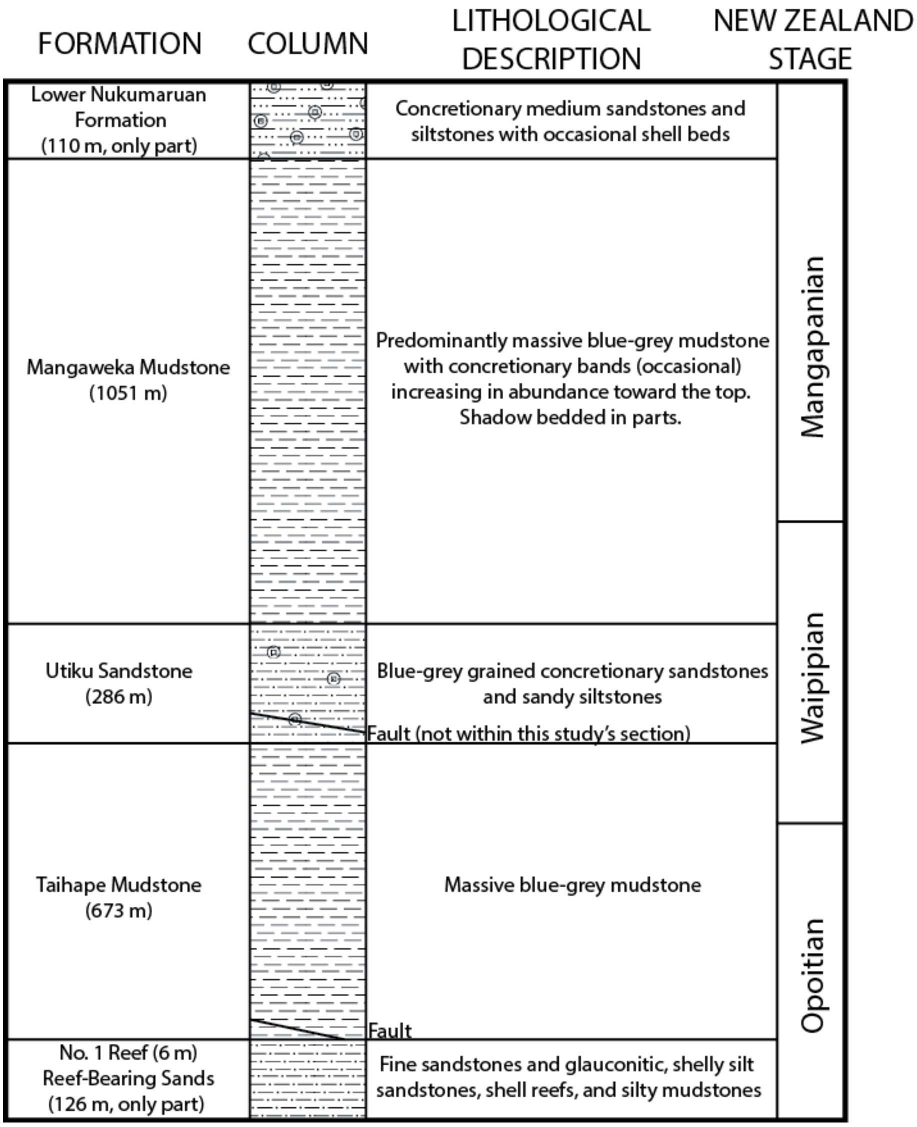

Figure 5.5. Stratigraphic column of Pliocene sediments exposed along the Turakina River as described by McGuire (1989). Note stratigraphic thickness of sections differs from that of Turner et al., (2005) measurements (paragraph 2; section 5.1.3). Note the Reef-Bearing Sands, Taihape Mudstone, and Utiku Sandstone are displayed on the geological map Figure 5.4 as the Tangahoe Group.

5.2. METHODOLOGY

Seventy nine samples were obtained from 11 outcrop sections along the Turakina River, in the vicinity of Siberia Station for grain size and benthic foraminiferal assemblage analysis extending from ~3.2 to 3.0 Ma, spanning the Kaena Subchron (Figure 5.6). In this study detailed lithological descriptions are made for individual sections and compiled into a composite stratigraphic section based on careful elevation and position measurements (by GPS and barometric altimeter), geological mapping and dip projections. Grain size analysis of sampled intervals at ~1.5 to 2-kyr resolution (1.5 to 2 meter intervals), has been carried out to estimate water-depth variations. The eleven outcrops display a regional strike of 110° and dip of 5° to the southwest, which is consistent with both McGuire (1989) and Turner et al., (2005). These structural measurements, in addition to altimeter measurements, allowed for construction of a geological cross section (Figure 5.7) and the ability to correlate individual sections into a single composite stratigraphic section.

The grain size-based proxy used for paleobathmetric reconstructions is based on modern analogue studies along the Manawatu coast, New Zealand, that have subsequently been applied to mid-Pliocene cyclothems exposed in Wanganui records (Figure 5.8) (Dunbar and Barrett, 2005). Assuming a depositional setting of a wave-graded coast system (shelf and shoreline) in hydrodynamic equilibrium with an analogous wave climate, the percent mud of the sea-floor sediments is a function of the shear stress imparted on the sea-bed by the contemporary wave climate, which is in turn a function of water depth. For sedimentary strata deposited near fair-weather wave base and below fair-weather wave base on the inner to mid-shelf (20-100 m) the grain-size proxy may provide higher fidelity water depth estimates (+/-5 m error) than other methods (e.g., foraminifera) (Dunbar and Barrett, 2005).

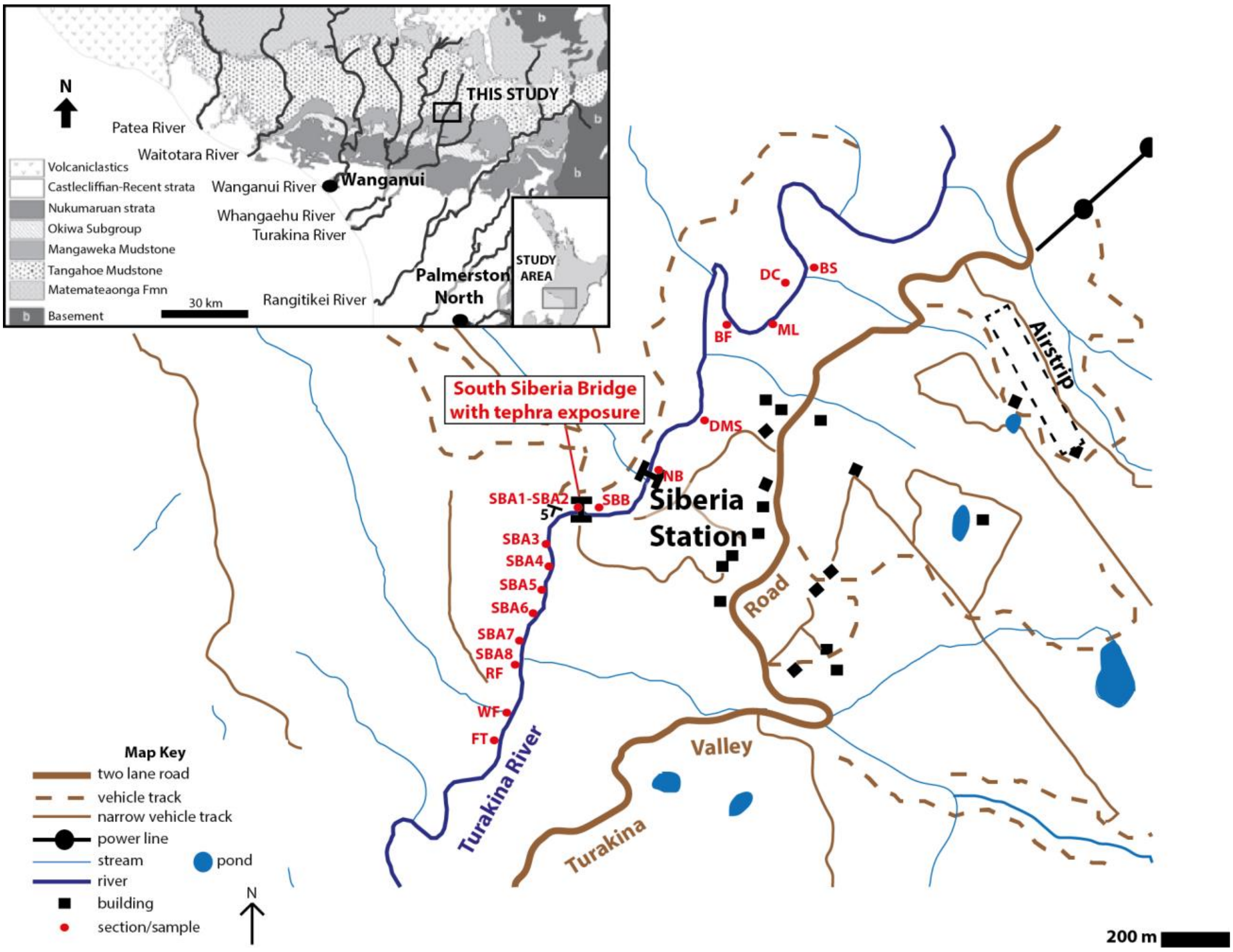

Figure 5.6. Base map of measured sections within the Turakina River Valley near Siberia Station adjacent to the Turakina Valley Road and just south of Papanui Junction (NZMS 260 grid reference) (after Turner et al., 2005). Exposures along the river bed are noted; BS = Base of Section, DC = Dead Cow Section, ML = Missing Link Section, BF = Big Face Section, DMS = Dutch Man's Stairs Section, NB = North Bridge Section, SBB = South Bridge Section (below tephra), SBA = South Bridge Section and individual samples obtained from river bed (above tephra), RF = Rob's Face Section (note: SBA8 is recovered at the base of Rob's Face Section), WF = Gillian's Waterfall Section =, and FT = Falling Tim Section.

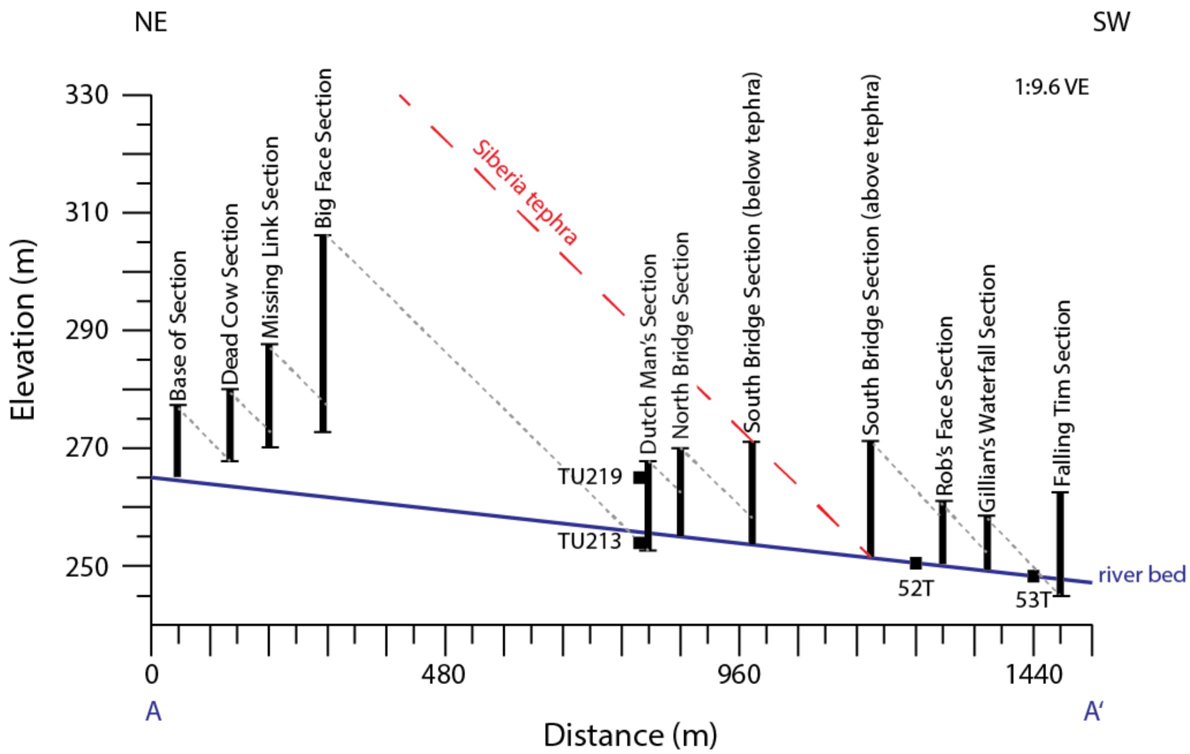

Figure 5.7. Cross section of measured sections along the Turakina River using bedding dip to demonstrate how each section is projected into the next. Also included are the magnetostratigraphic reversal constraints for the bottom (lower; TU213 [last normal] and upper; TU219 [first reversed]) and top (lower; 52T [last reverse] and upper; 53T [first normal]) of the Kaena Subchron.

Grain size sample preparations included gentle physical disaggregation of a (~0.25g) representative sub-sample with wooden spatula, followed by the removal of both organic and carbonate material. Organic material was removed with H_2O_2 (hydrogen peroxide), followed by digestion in 10% HCl (Hydrogen chloride) to dissolve carbonate material. Samples were washed three times in between treatments. Prior to analysis, sub-samples were diluted with 0.1g/l Calgon solution (1%), and sonicated with a stirrer for ~30 minutes. This allowed for optimal concentrations for grain size measurements using a LS 13 320 Laser Diffraction Particle Size Analyzer with a precision of 2.52% for the calculated percentage of mud (<63 µm).

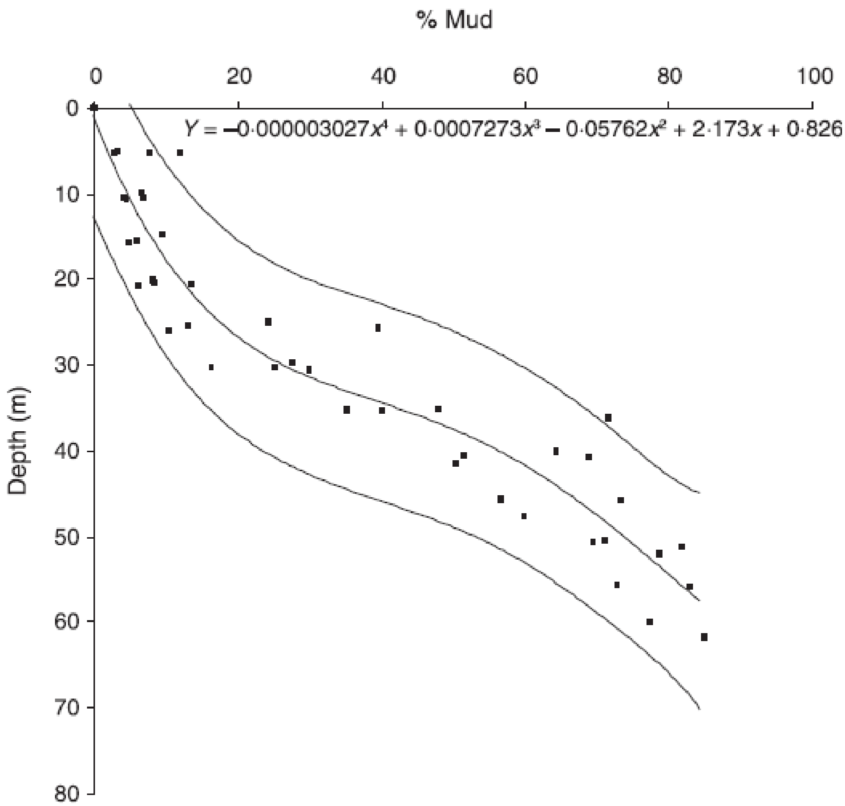

Figure 5.8. Interpolated fourth-order polynomial curve relating percent mud to water depth from various transects off the Manawatu coast and used in this study to derive paleobathymetric trends (from Dunbar and Barrett, 2005).

5.3. RESULTS/DISCUSSION

5.3.1. Lithostratigraphy

Exact locations of outcrop exposures and sampled locations are provided in Appendix C. Similar to that observed by McGuire (1989) and Turner et al., (2005), lithologic sections characteristically comprised of massive-blue-grey mudstones. However, textural variability ranged from sandy mudstone to mudstone. Detailed grain size analysis results are provided in Appendix C. Obvious concretionary layers punctuate textural boundary layers between fine to coarser grain sediment. Overall, the sequences are sparsely fossiliferous, and where present consist of in-situ articulated and disarticulated thin walled bivalves, gastropods and shell fragments. The sediment is moderately to intensely bioturbated with occasional moderate to weak horizontal stratification. A 1 m-thick reworked silicic tephra, Siberia Tephra (after McGuire et al., 1989) was observed (Figure 5.6; 5.7; 5.17).

Individual stratigraphic sections were compiled using standard field mapping and measuring techniques. Each section was measured using a barometric altimeter for accurate elevation readings and normalized to the the river bed, with individual sections measured from the base of each section to the top. Altimeter measurements were calibrated by re-occupying a base-station of known height several times a day and at South Siberia Bridge (Figure 5.6) to account for barometric pressure changes throughout the day. A meter stick and tape measure were used to accurately measure sample spacing of 1.5 to 2 m.

The base of the composite section consists of the sandiest (almost 50 %) interval in which three well defined concretionary layers are observed. Above the concretionary layers the strata fines upwards into siltstone between 12 and 36 m, before coarsening again upwards to fine sandy siltstone by 40 m. A second larger fining-coarsening cycle occurs between 40 and 69 m above which more concretionary layers appear and highlight an extended interval of fine sandy siltstone with almost 40% sand (~60% mud) up to ~85 m. Above this, the succession progressively fines up into siltstone at 135 m. The Siberia Tephra occurs at ~96 m. The tephra layer is characterized by massive to mm-scale lamination and bedding with a combination cross- and planar-stratification, possibly from reworking by tidal currents or emplacement as a sediment gravity flow onto the shelf. Above this tephra layer sediment continues to fine upward into almost 90% mud.

Outcrop exposures are individually named: Base of Section, Dead Cow Section, Missing Link Section, Big Face Section, Dutch Man's Stairs Section, North Bridge Section, South Bridge Section-below tephra, South Bridge Section-above tephra, Rob's Face Section, Gillian's Waterfall Section, Falling Tim Section. Descriptions are organized starting from the base of the river section (Base of Section) to the top (Falling Tim Section) (Figures 5.9 to 5.20). A composite stratigraphic section is defined for the Turakina River Section (Figure 5.21) based on structural and height measurements of individual sections.

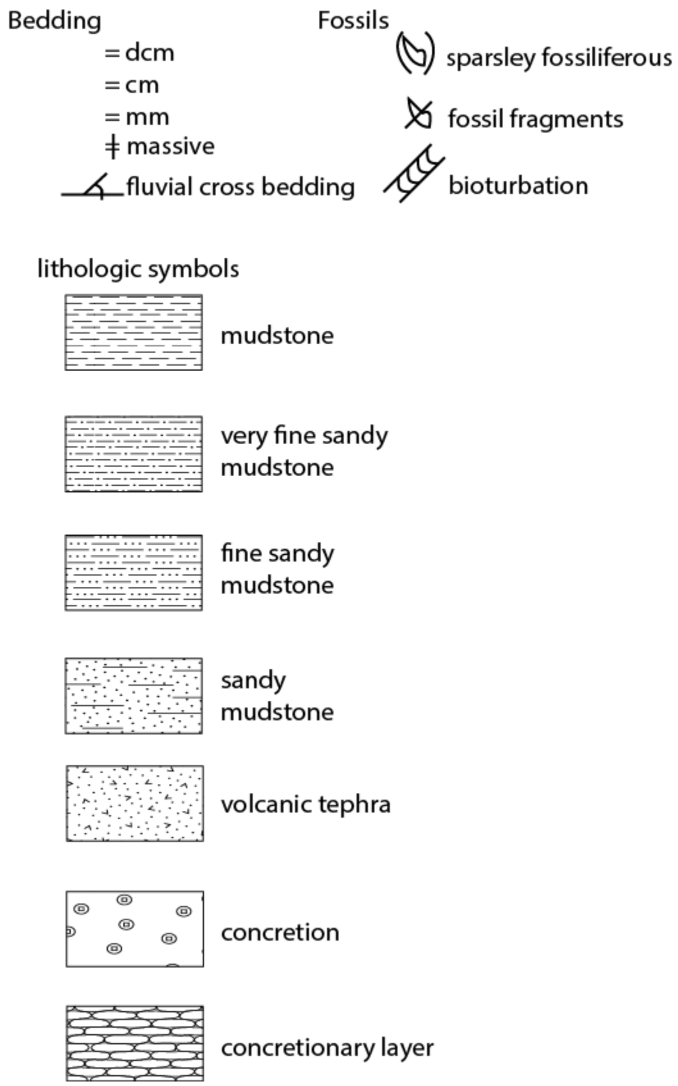

Figure 5.9. Outcrop description key following those of Andrews (1982).

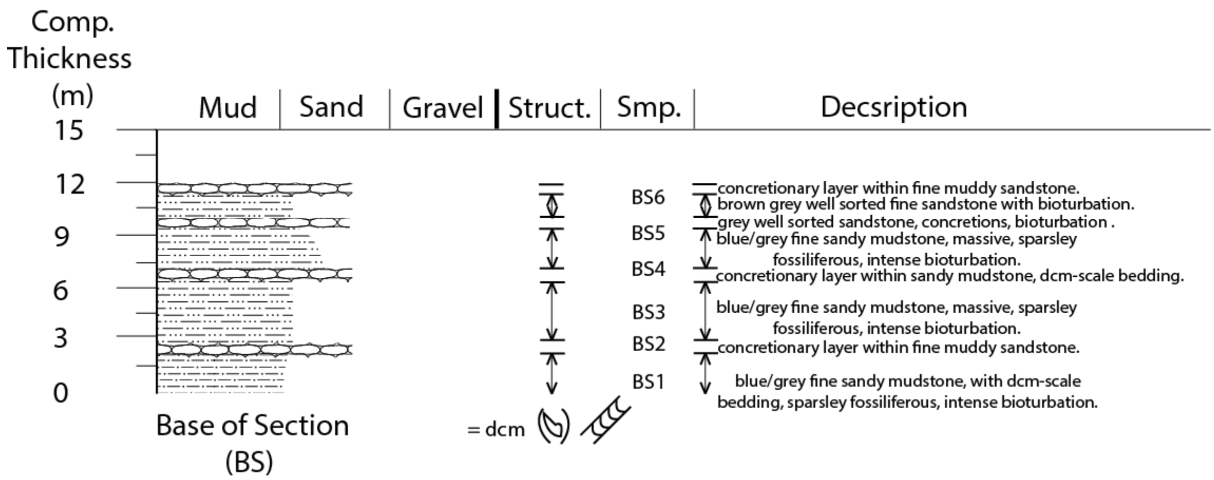

Figure 5.10. Outcrop description of Base of Section.

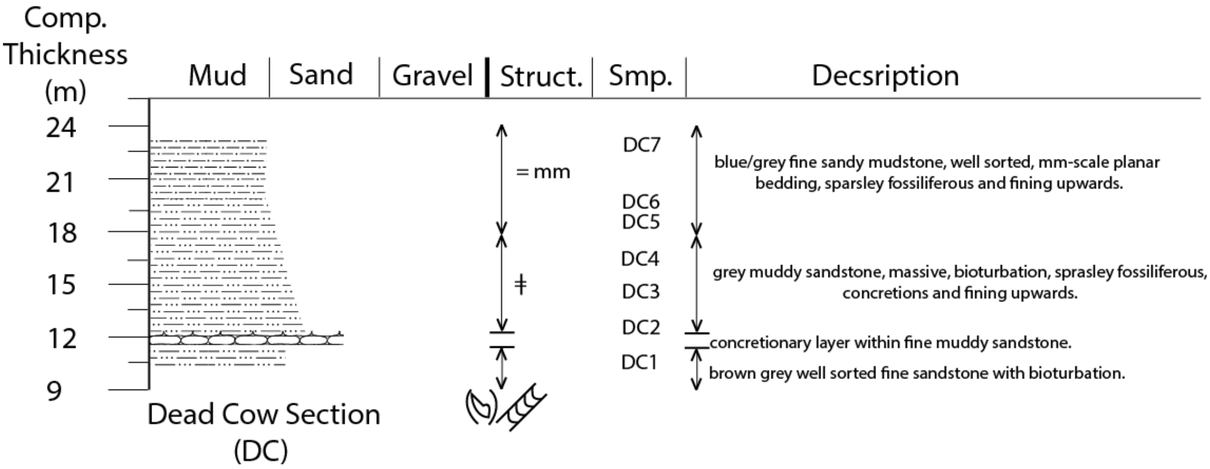

Figure 5.11. Outcrop description of Dead Cow Section.

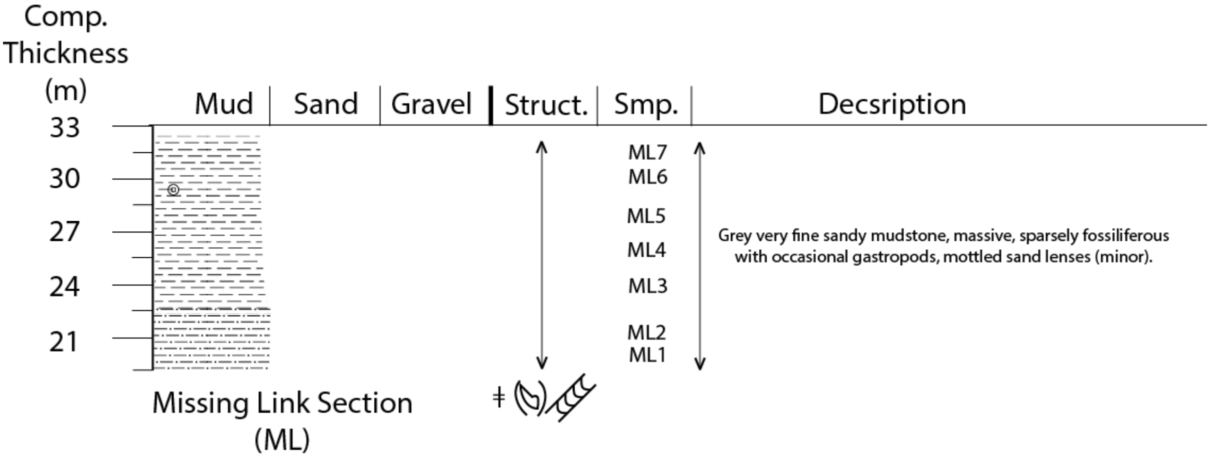

Figure 5.12. Outcrop description of Missing Link Section.

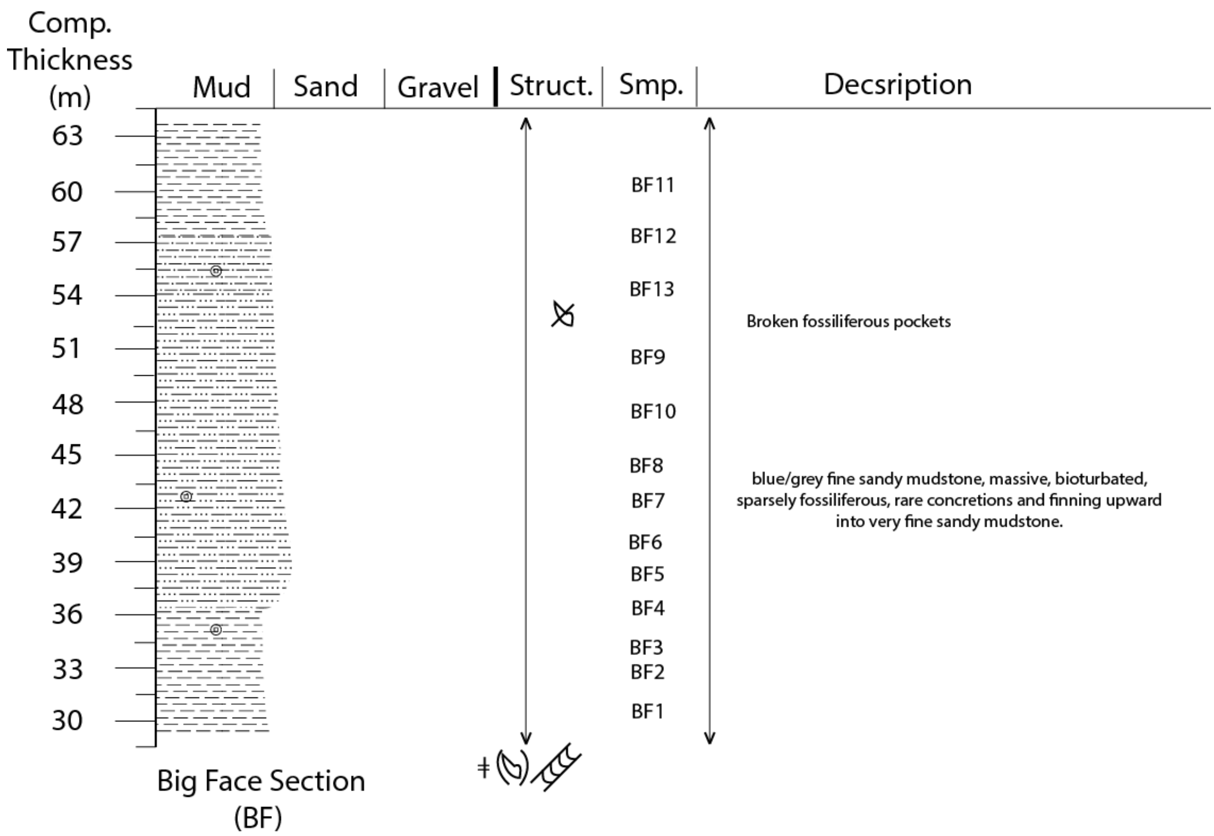

Figure 5.13. Outcrop description of Big Face Section.

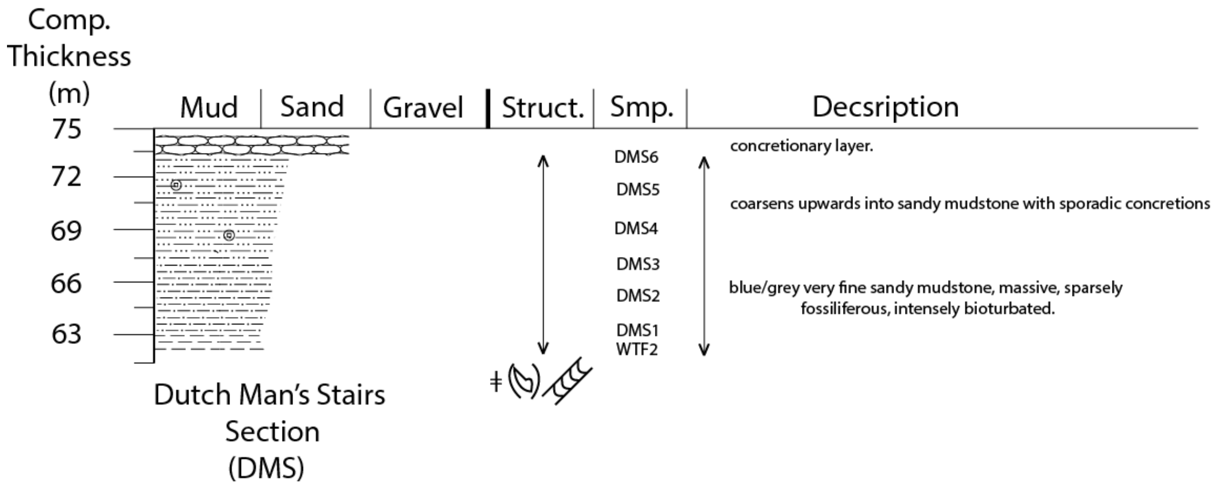

Figure 5.14. Outcrop description of Dutch Man's Stairs Section.

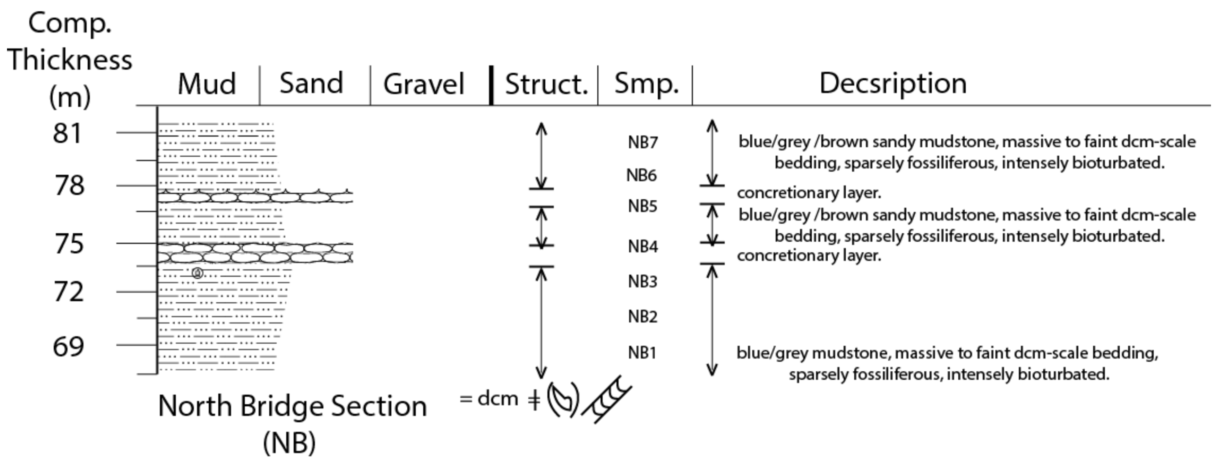

Figure 5.15. Outcrop description of North Bridge Section.

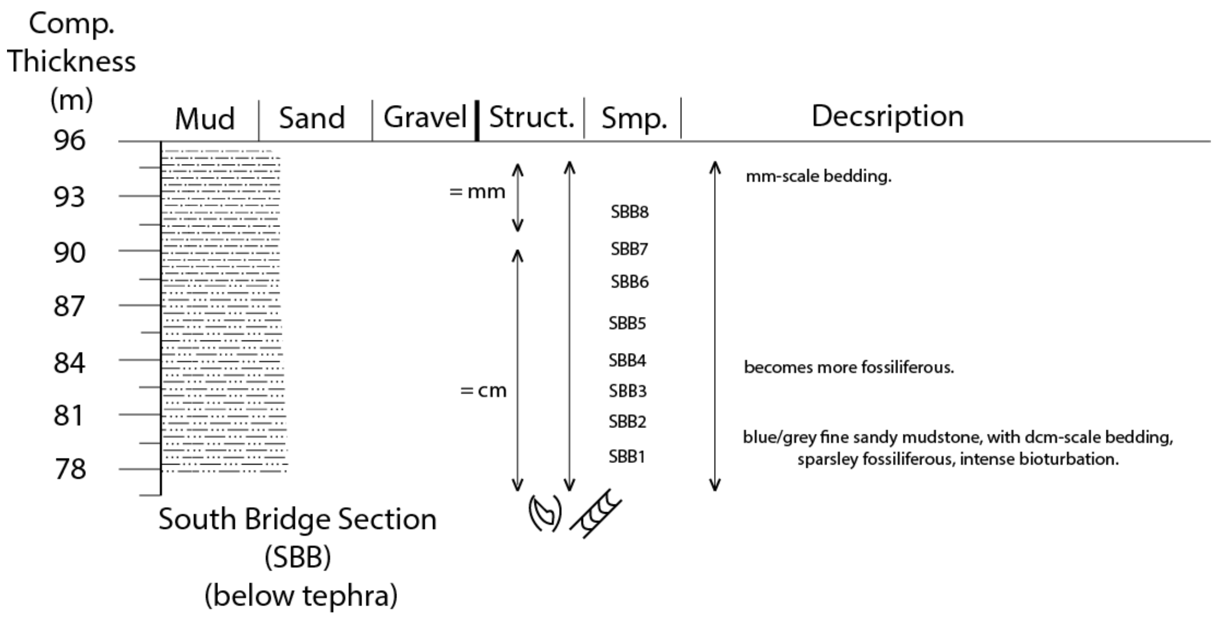

Figure 5.16. Outcrop description of South Bridge Section (below tephra).

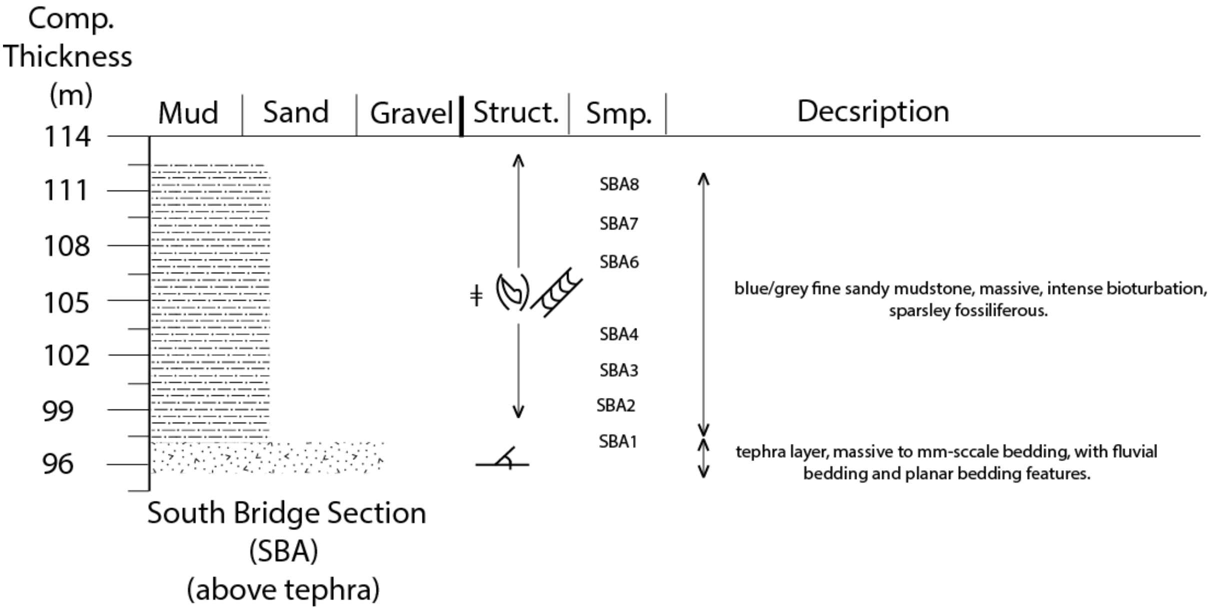

Figure 5.17. Outcrop description of South Bridge Section (above tephra). Compiled from strata exposed along the river bed.

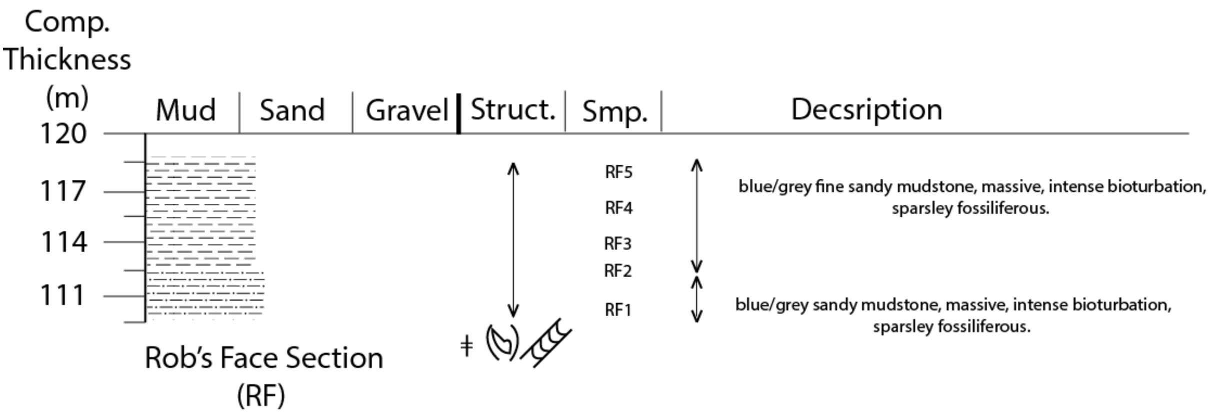

Figure 5.18. Outcrop description of Rob's Face Section.

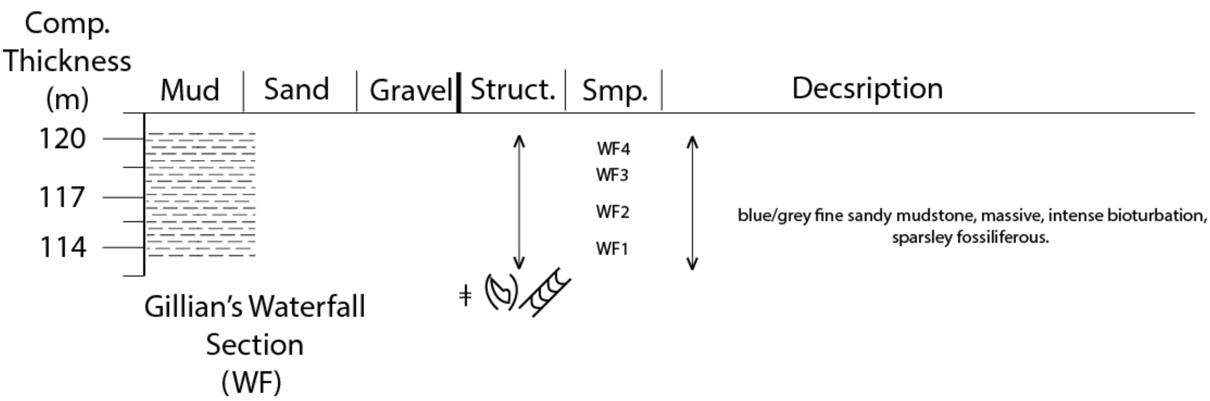

Figure 5.19. Outcrop description of Gillian's Waterfall Section.

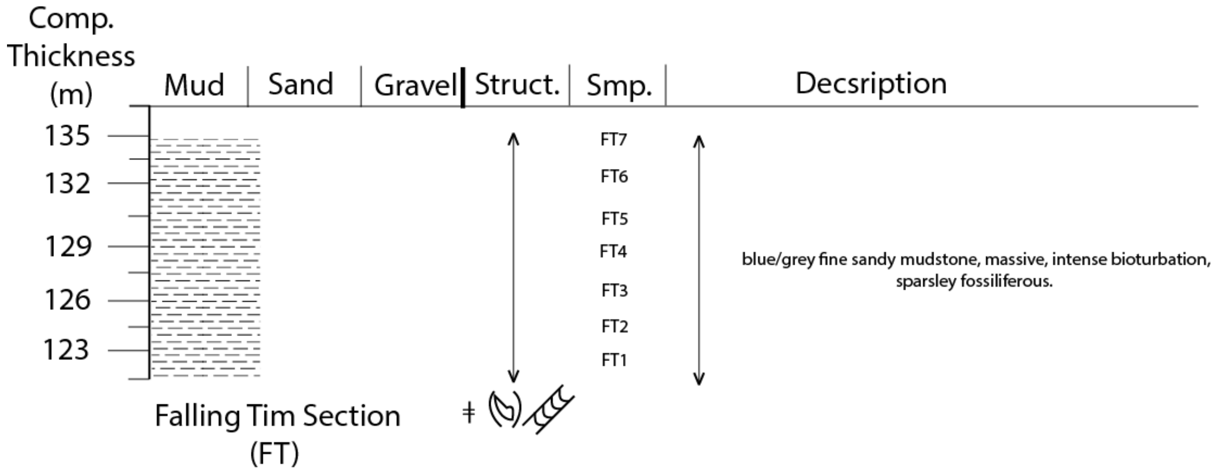

Figure 5.20. Outcrop description of Falling Tim Section.

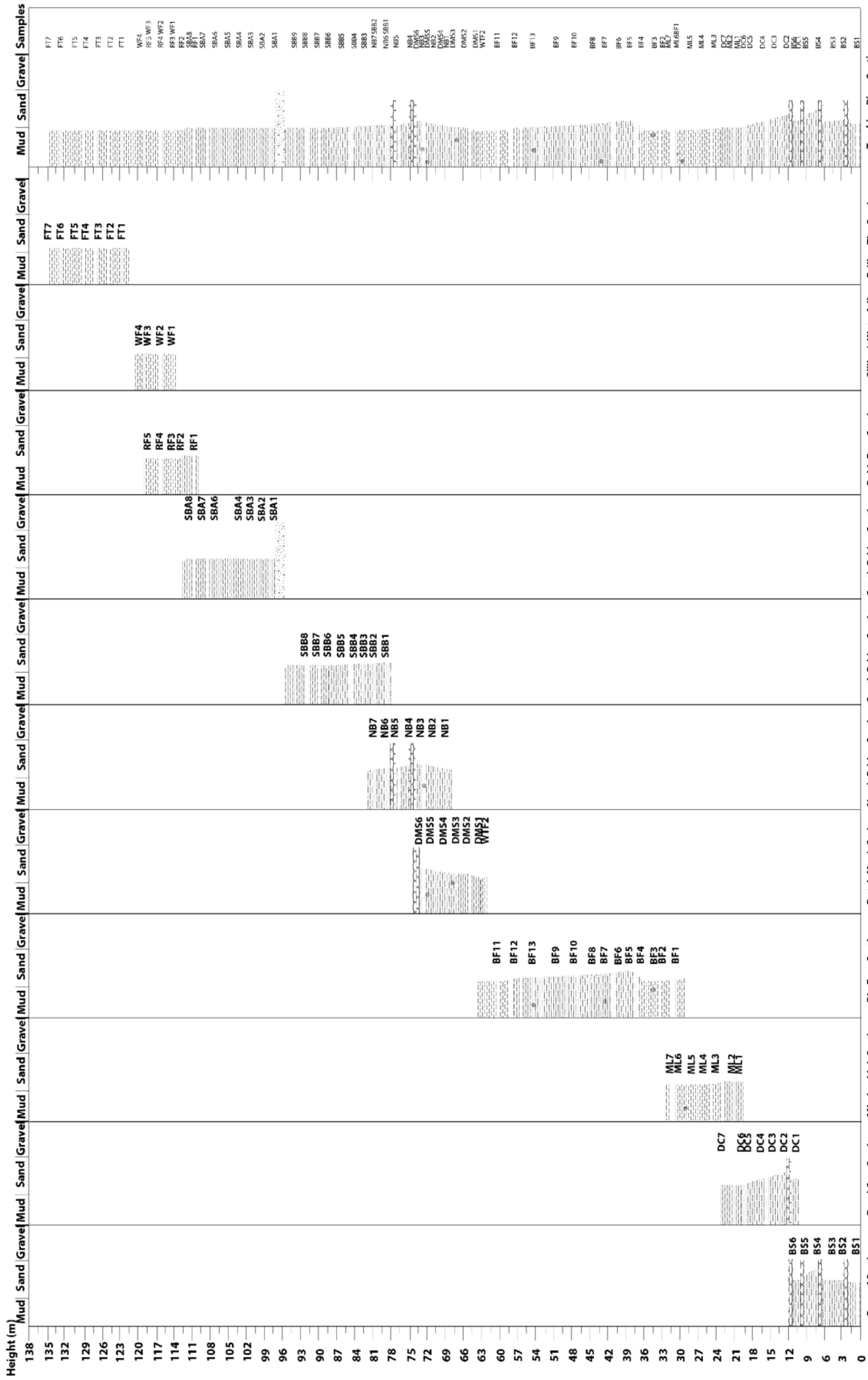

Figure 5.21. Individual measured sections and correlation into composite section.

5.3.2. Cyclostratigraphy

Using the base and top of the 82-kyr-duration Kaena Subchron (Lisecki and Raymo 2005; Turner et al., 2005) as absolute age tie points, there is one broad 60 m thick cycle in the sand to mud ratio (cycle 1). Immediately below the Kaena/Gauss boundary there is a peak of ~ 90% mud before passing up into ~70% by the middle of the Kaena Subchron, before grading normally to 80% mud just above the top of the Kaena Subchron (cycle 2) (Figure 5.22).

Within the uncertainties constraining the paleomagnetic boundaries in this sequence, these cycles exceed 80-kyr in duration and are consistent with a 100-kyr duration cycle of eccentricity. This interpretation is supported by the high mud values, which appear to correspond directly to maxima in eccentricity, while the increased sand abundance in the middle of the Kaena corresponds with a mimima in eccentricity (Figure 5.22). Using the Dunbar and Barrett (2005) grainsize-water depth calibration in Figure 5.8, the variations in percent mud are consistent with local water-depth variation of 20-15 m (+/-5 m) associated with these ~100 cycles, with the sea level highstands (i.e., high mud percentage) being associated with a maximum in eccentricity forcing. Paleobathymetric estimates during these cycles ranged from inner (~39+/-5 meters below sea level) to mid-shelf (56+/-5 meters below sea level) depths, although the forthcoming benthic foraminifera census will help to refine this estimate.

Superimposed on these long duration (~100-kyr) cycles are thinner (~10 m thick), lower amplitude variations (5-10%) in the mud abundance. Below the uncertaintiy of the base of the Kaena Subchron three distinct low amplitude events, in which there are excursions in grain size data associated with peaks in mud abundance occur at 24-33, 45 and 61 m, whereas within the Kaena Subchron, there are peaks at ~80, 91, and 100 m. As peaks within the Kaena Subchron are situated well within the zones that span the paleolmagnetic reversals, and within the 82-kyr duration of the Kaena Subchron itself, the frequency of these cycles must be less than 27 kyr. When the higher amplitude peaks at 61 and 116 m are included, it implies at least 5 cycles of relatively smaller scale sea level variations over the duration of the lower frequency "~100-kyr eccentricity" (top of cycle 1 to cycle 2), implying that a precession component is present in the grain size-based sea level proxies. Furthermore, the higher amplitude peak at ~61 m lies within the uncertainty of the base of the Kaena Subchron. Thus, if the base of the Kaena Subchron falls stratigraphically within the lower estimate of the paleomagentic reversal, than the peak in percent mud would correlate to a peak in Southern Hemisphere insolation.

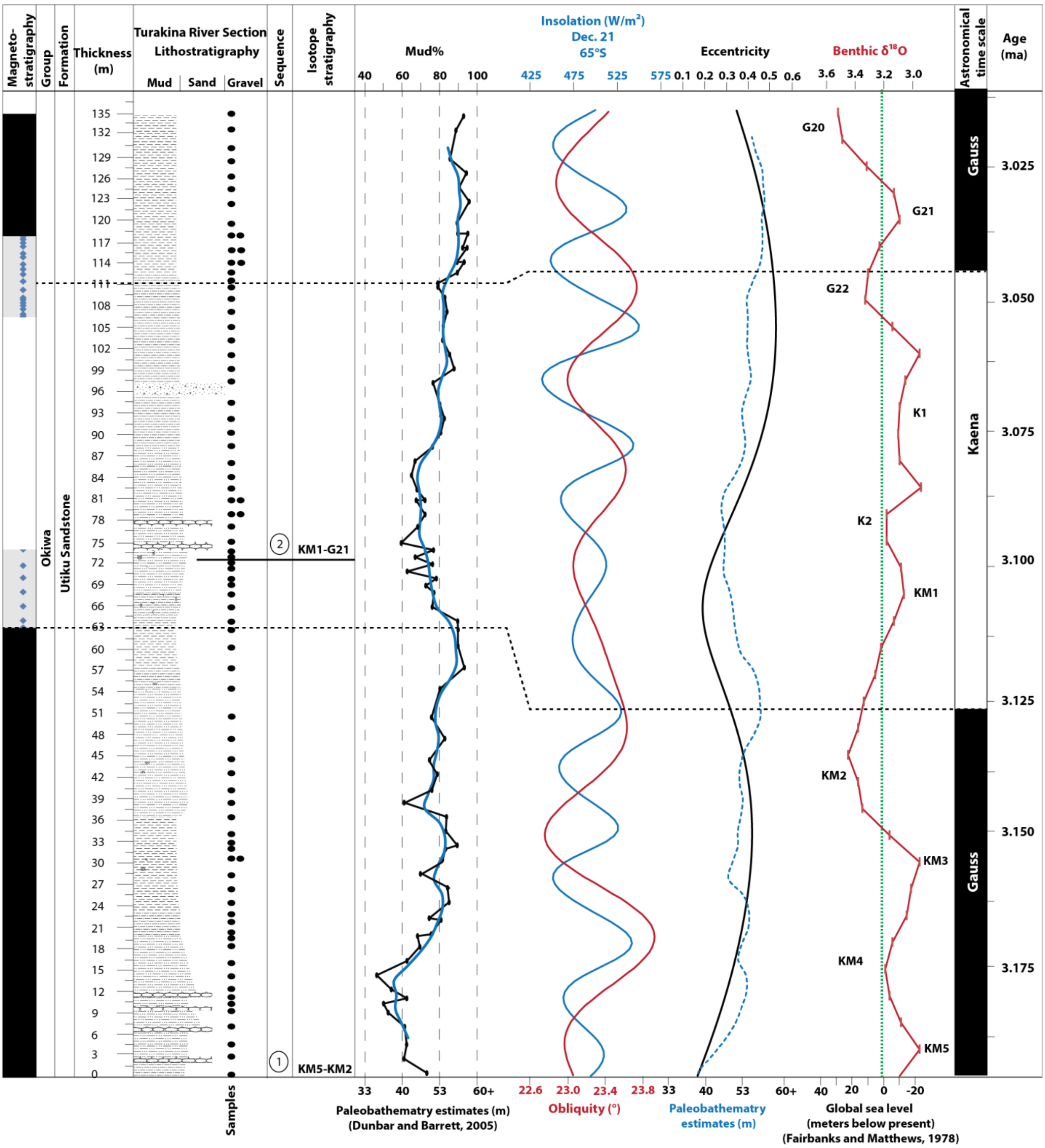

Figure 5.22. Stratigraphic column and percent mud of the mid-Pliocene Turakina River Section correlated to benthic $\delta^{18}O$ LR04 stack (‰) (Lisiecki and Raymo, 2005) and orbital parameters with polarity reversal stratigraphy constrained by tephrochronology and biostratigraphy (Turner et al., 2005). Blue diamonds in grey shading highlight sampled intervals for magnetostratigraphy since Turner et al., (2005) that were recovered in order to more tightly constrain stratigraphical polarity reversals of the top and bottom of the Kaena Subchron (Turner correspondence). Blue dotted line over laying eccentricity is percent mud interpolated using tie points within the uncertainty of paleomagnetic reversals.

5.3.3. Implications of the Turakina River Section cyclostratigraphy

Figure 5.22 demonstrates the greatest amplitude of water depth variability in the studied interval approximately corresponding with the 100-kyr eccentricity cycle. However, this interpretation would be significantly strengthened by further work to constrain the stratigraphic position of Kaena Subchron polarity reversals, as well as the forminiferal paleobathymetric estimates. Therefore, the discussion below outlines a preliminary interpretation.

Similar to what has already been demonstrated from sedimentary sequences observed in Wanganui Basin (Naish 1997; Naish and Wilson, 2009), this study infers sedimentary cycles in the Turakina River Section have formed in response to the interplay of subsidence, sediment supply and glacio-eustatic sea level fluctuations driven by the orbital variability of the ice sheets. While geological records, spanning a range of depositional processes and environments in both hemispheres during the Late Pliocene and Early Pleistocene, are dominated by obliquity (e.g., Shackleton et al., 1984; Dwyer et al., 1995; Naish, 1997; Hall et al., 2001; Ding et al., 2002; Kleiven et al., 2002; Lisiecki and Raymo, 2005; Crundwell et al., 2008; Naish et al., 2009; Martínez-Garcia et al., 2011; Passchier et al., 2011; Naafs et al., 2012), recent studies using detailed spectra analysis on the LR04 benthic $\delta^{18}O$ stack inferring ice volume changes, demonstrate the presence of strong precessional and eccentricity (short 100-kyr and long 400-kyr period) forcing from 3.5 to 2.5 myr (Lisiecki, 2010; Meyers and Hinnov, 2010).

Meyers and Hinnov (2010) showed through evolutionary spectral analysis of the benthic $\delta^{18}O$ LR04 Stack an emergence in the power of long period (400-kyr) eccentricity at ~3.5 Ma, which transitions into short period (100-kyr) eccentricity between ~3.3 to 3.0 Ma until ~2.6 Ma. Furthermore, they identify the disappearance of the 40-kyr obliquity signal at 3.5 Ma and its slight re-emergence around 3.2 Ma with an increase in power after 3.0 Ma (Figure 1C Meyers and Hinnov, 2010). This coeval emergence of increased 100-kyr eccentricity and decline in 40-kyr obliquity power in the LR04 Stack between 3.2 to 3.0 myr provides some support to the notion that grain size data presented in this study demonstrates a larger scale variability is potentially paced by 100-ky eccentricity. Furthermore, the lack of an apparent 40-kyr signal within the grain size data is not surprising when considering the lack of a strong 40-kyr signal and low amplitude variance in the Laskar et al., (2004) orbital solution, indicating the occurrence of a 1.2 million year node in obliquity during the mid-Pliocene (Meyers and Hinnov, 2010).

Chapter 3 of this thesis documents a direct response of the EAIS during the Late Pliocene to precession that is modulated by the longer 100-kyr eccentricity cycle using an ice-berg rafted debris (IBRD) record. The modulation of the 100-kyr eccentricity forcing can be observed also in lithological cycles in which the most rapid amount of ice loss occurs during lithofacies transitions paced by eccentricity. Cook et al., (2013) used radiogenic isotopes from the same Site U1361 record to identify provenance signatures from detrital material in which highly productive diatom-rich intervals, representing "warm" periods, consists of sediments sourced from the central portion of the Wilkes Subglacial Basin and were deposited during multiple erosional events when the ice margin would have retreated 100's of km inland. While the smallest estimates based on numerical ice sheet models imply 3 m of Pliocene glacio-eustatic sea level rise could have come from the EAIS (Pollard and DeConto, 2009), Cook et al., (2013) suggest the ice margin retreated several 100's of km inland are in better agreement with the larger estimates inferring a contribution of ~10 m (Miller et al., 2012).

The ANDRILL AND-1B drill core, recovered from the Ross Sea Embayment, record spanning the length of the Kaena Subchron, demonstrates multiple higher frequency events (4) that are associated with relatively smaller retreats along the WAIS margin lasting multiple glacial to interglacial cycles (KM2 to G21). These smaller cycles are superimposed over a longer term lithological cycle where the core transitions from subglacial, at the base of the Kaena, into an open marine setting associated with the G21 interglacial. Assuming this open marine setting infers near retreat and or collapse of the WAIS, a maximum contribution of 3 m from the WAIS (Miller et al., 2012) and ~10 m from the EAIS is in line with the 20-15 m of sea level change inferred from the percent mud estimates from the Turakina River Section.

The results of this study are important as they provide complimentary far-field evidence of precession forcing via eccentricity modulation that is observed in the deep ocean records (Lisiecki and Raymo, 2005; Meyers and Hinnov, 2010) and from the Antarctic ice sheet margin (Naish et al., 2009; Cook et al., 2013; Chapter 3 this thesis) during the mid-Pliocene. In regards to hypotheses of orbital forcing of Pliocene-Early Pleistocene ice volume, this study lends support to the notion that following the 40-kyr obliquity dominance on Antarctic ice volume during the Early warm Pliocene (prior to 3.3 Ma) (e.g., Naish et al., 2009; Chapter

3 this thesis), cooling during the Late Pliocene (after 3.3 Ma) allowed the ice sheet to begin to stabilize and become more sensitive to eccentricity modulated changes in precession. Whereas, by the Early Pleistocene the Antarctic ice volume contribution identified in ice volume and sea level records is minimal and records become dominated by changes in the Northern Hemisphere ice sheets with ice volume changes paced by obliquity until the 100-kyr cycles following the mid-Pleistocene transition between 1 Ma and 800 Ka years ago.

5.3.4. Future work

This study needs to be taken as a stepping stone in which future work is required to be done in order to better constrain the timing of paleobathymetic changes that can be used to infer changes in ice volume with an influence on local sea level and ultimately eustatic sea level. Four main areas of focus should be: 1.) more tightly constrained polarity reversal boundaries: 2.) benthic foraminifera assemblage analysis: 3.) benthic oxygen isotope analysis and 4.) geochemical analysis of Siberia tephra layer.

Constraining the stratigraphic position of polarity reversals of the Kaena Subchron and correlating the geochemical signature of the Siberia tephra to a deep ocean record for dating purposes, such as ODP Site 1123 (Chapter 4 of this thesis), will more tightly constrain the timing of regression and high stands with respect to orbital forcing. High resolution benthic foraminifera assemblage analysis would provide an additional proxy for interpreting paleobathymetric changes and serve as a constraint on changes in water depth inferred from percent mud. This technique has been proven to reveal cyclical water depth changes in Wanganui Basin marines Pliocene-Pleistocene deposits (e.g., Naish and Kamp, 1997). However, while this study only observes changes of ~20 meters (according to percent mud estimates), within depth limits of species, which may serve useful for changes particularly between inner to mid-shelf depths. Furthermore, oxygen isotope analysis should be carried out on benthic foraminifera in order to demonstrate whether precessional changes in grain size correspond to those observed in the $\delta^{18}O$ record from ODP Site 1123 inferring ice volume and sea level.

CHAPTER 6
SUMMARY AND CONCLUDING REMARKS

6.1. RECONSTRCUTING SOUTHERN HIGH LATITUDE EARTH SYSTEM RESPONSES DURING THE WARM EARLY PLIOCENE CLIMATE (5.3 to 3.3 Ma)

This thesis presents, a reconstruction of southern high-latitude ice-sheet and Southern Ocean response during the warm Early Pliocene. A time when atmospheric CO_2 levels were 400 ppm (Pagani et al., 2009; Seki et al., 2010) and globally averaged surface temperatures were 2-3°C higher than modern (Haywood et al., 2013).

Alternating lithofacies consisting of massive to laminated mudstones and diatom-rich/bearing mudstones are identified in IODP Site U1361, recovered from the continental rise adjacent to the Wilkes Land margin of the EAIS. These lithofacies are thought to represent variations in the extent of the marine-based margins of the EAIS. Massive mudstones with discrete packages of silt laminae are consistent with a base-cut-out turbidite facies model and combined with seismic profiles, indicate turbidite deposition occured in an non-erosive, overbank levee/distal continental rise setting. It is suggested these coincide with extended periods of time in when the ice sheet expanded to the continental shelf edge. Large volumes of unconsolidated sediment were delivered to the continental shelf edge either through the deposition of till deltas or from bedload-rich turbid glacial melt water plumes (Eittreim et al., 1995; Hesse et al., 1997; Lucchi et al., 2002; Escutia et al., 2005; Beaman et al., 2011). Seismic profiles for stratigraphic packages on the continental shelf support this interpretation, with the onset of steeply dipping foresets and the development of the modern progradational wedge that commenced during the Early Pliocene around 4.2 Ma, coincident with turbidite deposition (Escutia et al., 2005; Tauxe et al., 2012).

In contrast, diatom-rich/bearing mudstone facies represent extended periods of enhanced biogenic productivity over the drill site, and a corresponding lull in turbidite deposition (Figure 2.9) (Chapter 2). During the Early Pliocene, these lulls in turbidite deposition (5.3 to 3.3 Ma) reflect a retreated ice sheet margin. This is supported by independent studies of these diatom-rich facies using Nb and Sr provenance signatures of fine grained terrigenous material, which indicate the margin of the EAIS was eroding sediments within the Wilkes Subglacial Basin with the ice sheet retreated by as much as 100 km to the south of its present margin (Cook et al., 2013).

The facies assemblages presented in Chapter 2 appear to be the consequence of marine-based EAIS expansions and retreats near the continental shelf edge. The IBRD MAR record from Site U1361 infers the orbital sensitivity in which these major advances and retreats of the ice sheet responded to (Chapter 3). The facies assemblages combined with the IBRD MAR data suggests, the greatest amount of ice discharge during this time was associated with deglacial phases of ice margin retreat. Spectral anaylsis indicates a highly significant pacing by 40-kyr obliquity cycles during between 4.2 and 3.5 Ma. Obliquity pacing has been previously qualitatively demonstrated for the WAIS during this time from the semi-continuous ANDRILL-1B record (Naish et al., 2009; Pollard and DeConto, 2009). The statistically-significant orbital pacing within the IBRD record allows for near one-to-one correlations with the benthic $\delta^{18}O$ LR04 stack to be made (Lisiecki and Raymo, 2005). This correlation indicates that the deposition of the diatom-rich/bearing mudstones typically occurs during multiple low amplitude cycles when interglacial $\delta^{18}O$ values are consistently lower than Holocene levels (Figure 3.3) (Chapter 3). Thus, the facies analysis from Site U1361 confirm the presence of orbitally-induced oscillations in the EAIS with prolonged periods of reduced ice sheet extent coinciding with the warmest and least variable glacial to interglacial $\delta^{18}O$ cycles at this time. This is consistent with inferences from the $\delta^{18}O$ and sequence stratigraphic records of a significant (~10m) EAIS contribution to peak Pliocene eustatic sea-levels of ~+20 m above present levels – i.e. assuming a +3 m contribution from the marine-based WAIS and +7 m from the Greenland ice sheet.

During the Early Pliocene, SST reconstructions based on diatom assemblage proxy data in both the Ross Sea Embayment and Prydz Bay regions are dominated by subantarctic species and infer persistent open ocean conditions with a southward retraction of the winter sea ice limit (Whitehead et al., 2005; McKay et al., 2012). Furthermore, TEX^{L}_{86} (tetraether index of lipids biomarkers consisting of 86 carbon atoms) data from the Ross Sea Embayment supports diatom assemblage reconstructions inferring SST estimates between 2 to 5°C during peak Pliocene warmth when bulk stable isotopes ($\delta^{13}C$ and $\delta^{15}N$) infer polynya style mixing was decreased compared to modern (McKay et al., 2012). Such a reduction in sea ice extent is accompanied by a reduced production of AABW with a southward migration of the westerly winds and the Southern Boundary front (McKay et al., 2012). The reduced production of AABW, reduced sea ice field extent with extended seasonal duration (extended summers), was accompanied by enhanced supply of NADW entering the Southern Ocean during a stronger AMOC (Ravelo and Andreasen, 2000; Hodell and Venz-Curtis, 2006;

Chapter 4). This allowed for the upwelling of CDW, driven by Ekman-pumping (Toggweiler et al., 2006) along the margin and promoting the basal melting of marine based margins of the Antarctic Ice Sheet (Naish et al., 2009; McKay et al., 2012; Chapter 3; Chapter 4).

6.2. SOUTHERN HIGH LATITUDE EARTH SYSTEM RESPONSES AND FEEDBACKS THROUGH THE GLOBAL LATE PLIOCENE COOLING EVENT (3.3 to 2.7 Ma).

The Site U1361 IBRD MAR record displays a transition from the 40-kyr obliquity-paced ice rafting events to 20-kyr precession dominated events around 3.33 Ma (Chapter 3). This transition coincides with the MIS M2 event, a +1‰ glacial $\delta^{18}O$ excursion in which modelled Antarctic ice volume reaches LGM equivalent (Pollard and DeConto, 2009; Chapter 3). The orbital configuration surrounding the M2 glaciation is optimal for Antarctic ice sheet growth as it coincides with a 1.2 Ma node in obliquity and 400-kyr minima in long period (400-kyr) eccentricity, favouring cold summers and low seasonality (Zachos et al., 2001; Pälike et al., 2006). The significant 20-kyr precessional pacing in the IBRD record after 3.3 Ma is modulated by the 100-kyr cycle of eccentricity in which the greatest amount of ice rafting occurs during facies transitions from massive/laminated mudstones to diatom-rich/bearing mudstones. Peak diatom-rich/bearing mudstones loosely coincide with peaks in 100-kyr eccentricity (Figure 3.3) (Chapter 3). This eccentricity modulated imprint on Antarctic ice volume is also evident in benthic stable isotope records from the southwest Pacific and in far field sea level records presented in Chapters 4 and 5 of this thesis.

The M2 glacial excursion has been associated with southern high latitude cooling when grounded ice re-established on the middle to outer continental shelf following an extended warm period lasting ~200-kyr of open water conditions is observed in the ANDRILL-1B drill core record (Naish et al., 2009). While that record provided the first direct evidence of the WAIS oscillating at 40-kyr obliquity frequencies prior to 3.3 Ma (Naish et al., 2009), sub-glacial erosion surfaces from ice sheet advances cannot rule out the possibility of missing cycles. Frequency analysis quantifying the deterministic orbital forcing/pacing reflected in the benthic $\delta^{18}O$ LR04 stack (inferring ice volume) indicates the emergence of significant long period 400-kyr eccentricity at ~3.6 Ma, followed by a transfer in power to short period 100-kyr eccentricity from ~3.3 to 2.5 Ma (Meyers and Hinnov, 2010; Figure 1C). Deep water sourced from the Southern Ocean (Ross Sea and Wilkes Land margin) entering the southwest Pacific Ocean during the Late Pliocene and into the Early Pleistocene also carries this orbital signature with a significant and persistent long-period (400-kyr) and short-period (100-kyr) eccentricity signal in benthic $\delta^{18}O$ and $\delta^{13}C$ records from ODP Site 1123 present in Chapter 4 (Figure 4.13). This is in contrast to the globally integrated LR04 stack in which records are biased toward the Atlantic sector. The eccentricity modulated precessional variability of the Antarctic Ice Sheet during the Late Pliocene plays an important role in long-term reorganisation of circulation in Southern Ocean regulating the formation of AABW and the ventilation of CDW with a profound impact on the global carbon cycle after ~3.6 Ma. Furthermore, the 100-kyr eccentricity pacing of EAIS also may be reflected in the sea level record from the Wanganui Basin present in Chapter 5. These mid-Pliocene (3.2 to 3.0 Ma) shallow marine outcrop exposures in Wanganui Basin, New Zealand infer the maximum amount of sea level change of up to ~20 m sea level equivalent is modulated by the 100-kyr eccentricity cycle (Figure 5.22).

The switch from obliquity to precession-pacing in the Site U1361 IBRD MAR record after ~3.3 Ma is interpreted to reflect a declining influence of oceanic warming via the development of persistent summer sea ice around the margin (Chapter 3). It is suggested that expanded and more persistent summer sea ice fields after 3.3 Ma, combined with a northward migration of the Southern Hemisphere subpolar westerlies, reduced the upwelling of CO_2 rich CDW at the Antarctic margin. Thus, the basal melting of marine based margins of the EAIS was regulated by periods of reduced sea ice extent during peaks in austral summer insolation maxima, which is controlled by precession (Chapter 3).

In the Ross Sea, diatom assemblages and bulk stable isotope ($\delta^{13}C$ and $\delta^{15}N$) data infer a shift to more polar open ocean/seasonal sea ice assemblages and enhanced polynya style mixing after ~3.3 Ma, inferred to have resulted in increase AABW formation. Chapter 4 presents size sorting data of terrigenous silt material for Site 1123, located in the path of the DWBC. It infers the initiation of enhanced bottom current winnowing in the southwest Pacific Ocean from an invigorated ACC as both the production of AABW increased and zonal winds in the Southern Ocean intensified (Martínez Garcia et al., 2012; Chapter 4). The enhanced delivery of bottom water with a southern-sourced deepwater signature (i.e., AABW) entering the Pacific Ocean basin decreases the deep water $\delta^{13}C$ gradient between the southwest Pacific and equatorial Pacific. This shift in the Pacific deepwater gradient is interpreted to reflect reduced deep ocean ventilation of CDW in the Southern Ocean around Antarctic due to stratification (Chapter 4), and enhanced delivery of southern sourced bottom waters with an overall reduction of NADW entering the Pacific basin.

After ~2.6 Ma IBRD at Site U1361's begins to dramatically decreases (Figure 3.3 Ma), inferring the ice sheet margin begins to fully stabilise and also the EAIS begins fluctuate by a similar magnitude to that of the Late Pleistocene glacial cycles (Chapter 3). Primary sediment features become increasing more reworked from the interplay between bioturbation and downslope currents delivery of highly oxygenated water, inferring enhanced polynya style mixing in the Adélie depression (Chapter 2). At Site 1123, deep water $\delta^{13}C$ values are lower than modern for the Pliocene (5.3 to 2.6 Ma) interval, and is interpreted to be a consequence of a decrease in preformed $\delta^{13}C$ values due to decreased productivity in the main AABW regions and enhanced delivery of Lower Circumpolar Deep Water with a southern sourced signature (i.e., LCDW/AABW) rather than NADW entering the Pacific Ocean basin (McKay et al., 2012; Chapter 4). This maxima in ice volume and reduced deep ocean ventilation coincides with a draw down in atmospheric CO_2 concentrations to being consistently at pre-industrial levels (Seki et al., 2010), a critical precondition for the development of the Northern Hemisphere ice sheet expansion (Lunt et al., 2008).

REFERENCES

Abbott, S. T., and Carter, R. M., 1994. The sequence architecture of mid-Pleistocene (ca. 1.1–0.4 Ma) cyclothems from New Zealand: facies development during a period of orbital control on sea level cyclicity, *In* de Boer PL, Smith DG ed. Orbital forcing and cyclic sequences. International Association of Sedimentologists, Special Publication 19, p. 367–394.

Abelmann, A., Gersonde, R., and Spiess, V., 1990. Pliocene—pleistocene paleoceanography in the Weddell Sea—siliceous microfossil evidence, *In* Geological History of the Polar Oceans: Arctic Versus Antarctic, Springer Netherlands, p. 729-759.

Alloway, B. V., Pillans, B. J., Carter, L., Naish, T. R., and Westgate, J. A., 2005. Onshore–offshore correlation of Pleistocene rhyolitic eruptions from New Zealand: implications for TVZ eruptive history and paleoenvironmental construction. *Quaternary Science Reviews* v. 24(14), p. 1601-1622.

Anderson, J. B., Kurtz, D. D., Domack, E. W., and Balshaw, K. M., 1980. Glacial and glacial marine sediments of the Antarctic continental shelf. *The Journal of Geology* v. 88(4), p. 399-414.

Anderson, J. B., 1999. *Antarctic marine geology*. Cambridge University Press.

Anderson, R. F., Ali, S., Bradtmiller, L. I., Nielsen, S. H. H., Fleisher, M. Q., Anderson, B. E., and Burckle, L. H., 2009. Wind-driven upwelling in the Southern Ocean and the deglacial rise in atmospheric CO2. *Science* v. 323(5920), p. 1443-1448.

Bailey, I., Hole, G. M., Foster, G. L., Wilson, P. A., Storey, C. D., Trueman, C. N., and Raymo, M. E., 2013. An alternative suggestion for the Pliocene onset of major northern hemisphere glaciation based on the geochemical provenance of North Atlantic Ocean ice-rafted debris. *Quaternary Science Reviews* v. 75, p. 181-194.

Baines, Peter G., and Scott Condie., 1998. "Observations and modelling of Antarctic downslope flows: A review." *Ocean, Ice, and atmosphere: Interactions at the Antarctic continental margin*, p. 29-49.

Balco, G., and Rovey, C. W., 2010. Absolute chronology for major Pleistocene advances of the Laurentide Ice Sheet. *Geology* v. 38(9), p. 795-798.

Ballantyne, A. P., Greenwood, D. R., Damsté, J. S., Csank, A. Z., Eberle, J. J., and Rybczynski, N., 2010. Significantly warmer Arctic surface temperatures during the Pliocene indicated by multiple independent proxies. *Geology* v. 38(7), p. 603-606.

Ballantyne, A. P., Axford, Y., Miller, G. H., Otto-Bliesner, B. L., Rosenbloom, N., and White, J. W., 2013. The amplification of Arctic terrestrial surface temperatures by reduced sea-ice extent during the Pliocene. *Palaeogeography, Palaeoclimatology, Palaeoecology* v. 386, p. 59-67.

Barker, P. F., and Camerlenghi, A., 2002. Glacial history of the Antarctic Peninsula from Pacific margin sediments. *Proceedings of the ocean drilling program, scientific results* v. 178, p. 1-40.

Barreiro, M., and Philander, S. G., 2008. Response of the tropical Pacific to changes in extratropical clouds. *Climate dynamics* v. 31(6), p. 713-729.

Barrett, P. J., 1989. *Antarctic Cenozoic history from the CIROS-1 drillhole, McMurdo Sound*. DRIS Publishing.

Barrett, P. J., and Hambrey, M. J., 1992. Plio-Pleistocene sedimentation in Ferrar Fiord, Antarctica. *Sedimentology* v. 39(1), p. 109-123.

Barrett, P. J., 2013. Resolving views on Antarctic Neogene glacial history–the Sirius debate. *Earth and Environmental Science Transactions of the Royal Society of Edinburgh* v. 104(01), p. 31-53.

Bart, P.J., DeBatist, M., and Jokat,W., 1999. Interglacial collapse off Crary Trough Mouth Fan, Weddell Sea, Antarctica: implications for Antarctic Glacial History. *Journal of Sedimentary Research* v. 69, p. 1276–1289.

Bartoli, G., Hönisch, B., and Zeebe, R. E., 2011. Atmospheric CO2 decline during the Pliocene intensification of Northern Hemisphere glaciations. *Paleoceanography* v. 26(4).

Bassis, J. N., and Jacobs, S., 2013. Diverse calving patterns linked to glacier geometry. *Nature Geoscience* v. 6(10), p. 833-836.

Beaman, R. J., O'Brien, P. E., Post, A. L., and De Santis, L., 2011. A new high-resolution bathymetry model for the Terre Adélie and George V continental margin, East Antarctica. *Antarctic Science* v. *23*(01), p. 95-103.

Belkin, I. M., and Gordon, A. L., 1996. Southern Ocean fronts from the Greenwich meridian to Tasmania. *Journal of Geophysical Research: Oceans (1978–2012)* v. 101(C2), p. 3675-3696.

Berger, A., Li, X. S., and Loutre, M. F., 1999. Modelling northern hemisphere ice volume over the last 3Ma. *Quaternary Science Reviews* v. 18(1), p. 1-11.

Beu, A. G., and Edwards, A. R., 1984. New Zealand Pleistocene and late Pliocene glacio-eustatic cycles. *Palaeogeography, Palaeoclimatology, Palaeoecology* v. 46(1), p. 119-142.

Bianchi, G. G., Hall, I. R., McCave, I. N., and Joseph, L., 1999. Measurement of the sortable silt current speed proxy using the Sedigraph 5100 and Coulter Multisizer IIe: Precision and accuracy. *Sedimentology* v. 46(6), p. 1001-1014.

Billups, K., Ravelo, A. C., and Zachos, J. C., 1997. Early Pliocene deep-water circulation: stable isotope evidence for enhanced northern component deep water. *Proceedings of Ocean Driling Program Scientific Results* v. 154, p. 319-330.

Bindoff, N. L., Rosenberg, M. A., and Warner, M. J., 2000. On the circulation and water masses over the Antarctic continental slope and rise between 80 and 1503E. *Deep-Sea Research II* v. 27, p. 2299-2326.

Bland, K. J., Kamp, P. J., and Nelson, C. S., 2008. Late Miocene–Early Pleistocene paleogeography of the onshore central Hawke's Bay sector of the forearc basin, eastern North Island, New Zealand, and some implications for hydrocarbon prospectivity. *New Zealand Petroleum Conference Proceedings*.

Blott, S. J., and Pye, K., 2001. GRADISTAT: a grain size distribution and statistics package for the analysis of unconsolidated sediments. *Earth surface processes and Landforms* v. 26(11), 1237-1248.

Bohaty, S. M., and Harwood, D. M., 1998. Southern Ocean Pliocene paleotemperature variation from high-resolution silicoflagellate biostratigraphy. *Marine Micropaleontology* v. 33(3), p. 241-272.

Bonham, S. G., Haywood, A. M., Lunt, D. J., Collins, M., and Salzmann, U., 2008. El Nińo–Southern Oscillation, Pliocene climate and equifinality. *Philosophical Transactions of the Royal Society A: Mathematical, Physical and Engineering Sciences* v. 367(1886), p. 127-156.

Böning, C. W., Dispert, A., Visbeck, M., Rintoul, S. R., and Schwarzkopf, F. U., 2008. The response of the Antarctic Circumpolar Current to recent climate change. *Nature Geoscience* v.1.12, p. 864-869.

Bostock, H. C., Hayward, B. W., Neil, H. L., Currie, K. I., and Dunbar, G. B., 2011. Deep-water carbonate concentrations in the southwest Pacific. *Deep Sea Research Part I: Oceanographic Research Papers* v. 58(1), p. 72-85.

Bostock, H. C., Barrows, T. T., Carter, L., Chase, Z., Cortese, G., Dunbar, G. B., Ellwood, M., Hayward, B., Howard, W., Neil, H. L., Noble, T. L., Mackintosh, A., Moss, P. T., Moy, A. D., White, D., Williams, M. J. M., and Armand, L. K., 2013. A review of the Australian–New Zealand sector of the Southern Ocean over the last 30 ka (Aus-INTIMATE project). *Quaternary Science Reviews* v. 74, p. 35-57.

Boyle, E. A., and Keigwin L. D., 1987. North Atlantic thermohaline circulation during the past 20,000 years linked to high-latitude surface temperature. *Nature* v. 330, p. 35–40.

Brigham-Grette, J., Melles, M., Minyuk, P., Andreev, A., Tarasov, P., DeConto, R., Koening, S., Nowaczyk, N., Wennrich, V., Rosén, P., Haltia, E., Cook, T., Gebhardt, C., Meyer_Jacob, C., Snyder, C., and Herzschuh, U., 2013, Pliocene Warmth, Polar Amplification, and Stepped Pleistocene Cooling Recorded in NE Arctic Russia. *Science* v. 340(6139), p. 1421-1427.

Broecker, W. S., Peng, T. H., and Beng, Z., 1982. *Tracers in the Sea*. Lamont-Doherty Geological Observatory, Columbia University.

Broecker, W. S., and Denton, G. H., 1989. The role of ocean-atmosphere reorganizations in glacial cycles. *Geochimica et Cosmochimica Acta* v. 53(10), p. 2465-2501.

Browne, G. H., 2004. Late Neogene sedimentation adjacent to the tectonically evolving North Island axial ranges: Insights from Kuripapango, western Hawke's Bay. *New Zealand Journal of Geology and Geophysics* v. 47, p. 663-674.

Busetti, M., Caburlotto, A., Armand, L., Damian, D., Giorgetti, G., Lucchi, R. G., Quilty, P. G., and Villa, G., 2003. Plio-Quaternary sedimentation on the Wilkes land continental rise: preliminary results. *Deep Sea Research Part II: Topical Studies in Oceanography* v. 50(8-9), p. 1529-1562.

Butt, F. A., Drange, H., Elverhøi, A., Otterå, O. H., and Solheim, A., 2002. Modelling Late Cenozoic isostatic elevation changes in the Barents Sea and their implications for oceanic and climatic regimes: preliminary results. *Quaternary Science Reviews* v. 21(14), p. 1643-1660.
Caburlotto, A., Lucchi, R. G., De Santis, L., Macrì, P., and Tolotti, R., 2010. Sedimentary processes on the Wilkes Land continental rise reflect changes in glacial dynamic and bottom water flow. *International Journal of Earth Sciences* v. 99(4), p. 909-926.
Callahan, J. E., 1972. The structure and circulation of deep water in the Antarctic. In *Deep Sea Research and Oceanographic Abstracts* v. 19(8), p. 563-575.
Cane, M. A., and Molnar, P., 2001. Closing of the Indonesian seaway as a precursor to east African aridification around 3–4 million years ago. *Nature* v. 411(6834), p. 157-162.
Carter, L., and Mitchell, J. S., 1987. Late Quaternary sediment pathways through the deep ocean, east of New Zealand. *Paleoceanography* v. 2(4), p. 409-422.
Carter, L., and Wilkin, J., 1999. Abyssal circulation around New Zealand—A comparison between observations and a global circulation model. *Marine Geology* v. 159(1), p. 221-239.
Carter, R. M., Carter, L., and McCave, I. N., 1996. Current controlled sediment deposition from the shelf to the deep ocean: the Cenozoic evolution of circulation the SW Pacific gateway. *Geol Rundsch* v. 85, p. 438-451.
Carter, R. M., McCave, I. N., Richer, C., Carter, L., and Shipboard Scientific Party., 1999. Leg 181 Summary: Southwest Pacific Paleoceanography. *Proceedings of the Ocean Drilling Program, Initial Reports* v. 181, p. 1-80.
Carter, L., Shane, P., Alloway, B., Hall, I.R., Harris, S., 2003. Demise of one volcanic zone and birth of another - a 12 m.y. marine record of major rhyolitic eruptions from New Zealand. *Geology* v. 31, p. 493-496.
Carter, R. M., McCave, I. N., and Carter, L., 2004, Leg 181 Synthesis: fronts, flows, drifts, volcanoes, and the evolution of the southwestern gateway to the Pacific Ocean, eastern New Zealand. *Proceedings of the Ocean Drilling Program, Scientific Results* v. 181, p. 1-111.
Carter, L., Carter, R. M., and McCave, I. N., 2004b. Evolution of the sedimentary system beneath the deep Pacific inflow off eastern New Zealand. *Marine Geology* v. 205, p. 9-27.
Carter, L., and Manighetti, B., 2006. Glacial/interglacial control of terrigenous and biogenic fluxes in the deep ocean off a high input, collisional margin: A 139 kyr-record from New Zealand. *Marine geology* v. 226(3), p. 307-322.
Carter, L., McCave, I. N., and Williams, M. J., 2009. Circulation and water masses of the Southern Ocean: a review. *Developments in Earth and Environmental Sciences* v. 8, p. 85-114.
Chamberlain, C. P., Poage, M. A., Craw, D., and Reynolds, R. C., 1999. Topographic development of the Southern Alps recorded by the isotopic composition of authigenic clay minerals, South Island, New Zealand. *Chemical Geology* v. 155(3), p. 279-294.
Chandler, M., Rind, D., and Thompson, R., 1994. Joint investigation of the Middle Pliocene climate: II. GISS GCM Northern Hemisphere results. *Global Planetary Change* v. 9, p. 198-219.
Charles, C. D., and Fairbanks, R. G., 1990. Glacial to interglacial changes in the isotopic gradients of Southern Ocean surface water. In *Geological History of the Polar Oceans: Arctic Versus Antarctic* . Springer Netherlands, p. 519-538.
Chiang, J. C. H., and Bitz, C. M., 2005. Influence of high latitude ice cover on the marine Intertropical Convergence Zone. *Climate Dynamics* v. 25, p. 477-496.
Chiswell, S. M., 1994. Variability in sea surface temperature around New Zealand from AVHRR images. *New Zealand journal of marine and freshwater research* v. 28(2), p. 179-192.
Ciesielski, P. F., and Weaver, F. M., 1974. Early Pliocene temperature changes in the Antarctic seas. *Geology* v. 2(10), p. 511-515.
Clark, P. U., and Pollard, D., 1998. Origin of the middle Pleistocene transition by ice sheet erosion of regolith. *Paleoceanography* v. 13(1), p. 1-9.
Cook, C. P., van de Flierdt, T., Williams, T., Hemming, S. R., Iwai, M., Kobayashi, M., Jimenez-Espejo, F., Francisco, J., Escutia, C., González, J. J., Khim, B. K., McKay, R. M., Passchier, S., Bohaty, S. M., Riesselman, C. R., Tauxe, L., Sugisaki, S., Galindo, A. L., Patterson, M. O., Sangiorgi, F., Pierce, E. L., Brinkhuis, H., Klaus, A., Fehr, A., Bendle, J. A. P., Bijil, P. K., Carr, S. A., Dunbar, R. B., Flores, J. A., Hayden, T. G., Katsuki, K., Kong, G. S., Nakai, M., Olney, M. P., Pekar, S. F., Pross, J., Röhl, U., Sakai, T., Shrivastava, P. K., Stickley, C. E., Tuo,

S., Welsh, K., and Yamane, M., 2013. Dynamic behaviour of the East Antarctic ice sheet during Pliocene warmth. *Nature Geoscience* v. 6(9), p. 765-769.

Cooper, A. K., Barrett, P. J., Hinz, K., Traube, V., Letichenkov, G., and Stagg, H. M., 1991. Cenozoic prograding sequences of the Antarctic continental margin: a record of glacio-eustatic and tectonic events. *Marine Geology* v. 102(1), p. 175-213.

Cooper, A. K., and O'Brien, P. E., 2004, Leg 188 synthesis: transitions in the glacial history of the Prydz Bay Region, East Antarctica, from ODP drilling. *Proceedings of the Ocean Drilling Program, Scientific Results* v. 188, p. 1-42.

Cowan, E. A., Hillenbrand, C. D., Hassler, L. E., and Ake, M. T., 2008. Coarse-grained terrigenous sediment deposition on continental rise drifts: A record of Plio-Pleistocene glaciation on the Antarctic Peninsula. *Palaeogeography, Palaeoclimatology, Palaeoecology* v. 265(3), p. 275-291.

Croll, J., 1867. On the eccentricity of the Earth's orbit, and its physical relations to the glacial epochs. *Philosophical Magazine* v. 33, p. 119–131.

Cronin, T. M., Whatley, R., Wood, A., Tsukagoshi, A., Ikeya, N., Brouwers, E. M., and Briggs, W. M., 1993. Microfaunal evidence for elevated Pliocene temperatures in the Arctic Ocean. *Paleoceanography* v. 8(2), p. 161-173.

Cronin, T. M., Kitamura, A., Ikeya, N., Watanabe, M., and Kamiya, T., 1994. Late Pliocene climate change 3.4-2.3 Ma: paleoceanographic record from the Yabuta Formation, Sea of Japan. *Palaeogeography, Palaeoclimatology, Palaeoecology* v. 108(3), p. 437-455.

Crowley, T. J., 1996. Pliocene climates: the nature of the problem. *Marine Micropaleontology* v. *27*(1), p. 3-12.

Crundwell, M., Scott, G., Naish, T., and Carter, L., 2008. Glacial–interglacial ocean climate variability from planktonic foraminifera during the Mid-Pleistocene transition in the temperate Southwest Pacific, ODP Site 1123. *Palaeogeography, Palaeoclimatology, Palaeoecology* v. 260(1), p. 202-229.

Darby, D. A., 2008. Arctic perennial ice cover over the last 14 million years. *Paleoceanography* v. 23(1).

D'Asaro, E. A., 2003. The ocean boundary layer below Hurricane Dennis. *Journal of Physical* v. 33, p. 561-579.

Deacon, G. E. R., 1937. The hydrology of the Southern Ocean. *Discovery Report* v. 15, p. 1-124.

DeConto, R., Pollard, D., and Harwood, D., 2007. Sea ice feedback and Cenozoic evolution of Antarctic climate and ice sheets. *Paleoceanography* v. 22(3).

Dekens, P. S., Ravelo, A. C., and McCarthy, M. D., 2007. Warm upwelling regions in the Pliocene warm period. *Paleoceanography* v. 22(3).

Denton, G. H., Sugden, D. E., Marchant, D. R., Hall, B. L., and Wilch, T. I., 1993. East Antarctic Ice Sheet sensitivity to Pliocene climatic change from a Dry Valleys perspective. *Geografiska Annaler. Series A. Physical Geography* p. 155-204.

Denton, G. H., Anderson, R. F., Toggweiler, J. R., Edwards, R. L., Schaefer, J. M., and Putnam, A. E., 2010. The last glacial termination. *Science* v. 328(5986), p. 1652-1656.

Demenocal, P. B., Ruddiman, W. F., and Pokras, E. M., 1993. Influences of High-and Low-Latitude Processes on African Terrestrial Climate: Pleistocene Eolian Records from Equatorial Atlantic Ocean Drilling Program Site 663. *Paleoceanography* v. 8(2), p. 209-242.

Depoorter, M. A., Bamber, J. L., Griggs, J. A., Lenaerts, J. T. M., Ligtenberg, S. R. M., van den Broeke, M. R., and Moholdt, G., 2013. Calving fluxes and basal melt rates of Antarctic ice shelves. *Nature* v. 502, p. 89-92.

Santis, L. D., Brancolini, G., and Donda, F., 2003. Seismo-stratigraphic analysis of the Wilkes Land continental margin (East Antarctica): influence of glacially driven processes on the Cenozoic deposition. *Deep Sea Research Part II: Topical Studies in Oceanography* v. 50(8), p. 1563-1594.

Dickinson, W. R.., 2004. Evolution of the North American cordillera. *Annu. Rev. Earth Planet. Sci.* v. 32, p. 13-45.

Ding, Z. L., Derbyshire, E., Yang, S. L., Yu, Z. W., Xiong, S. F., and Liu, T. S., 2002. Stacked 2.6-Ma grain size record from the Chinese loess based on five sections and correlation with the deep-sea δ18O record. *Paleoceanography* v. 17(3), 5-1.

Dolan, A. M., Haywood, A. M., Hill, D. J., Dowsett, H. J., Hunter, S. J., Lunt, D. J., and Pickering, S. J., 2011. Sensitivity of Pliocene ice sheets to orbital forcing. *Palaeogeography, Palaeoclimatolog, Palaeoecology* v. 309, no. 1-2, p. 98–110.

Domack, E. W., 1982. Sedimentology of glacial and glacial marine deposits on the George V-Adelie continental shelf, East Antarctica. *Boreas* v. 11(1), p. 79-97.

Donda, F., Brancolini, G., Santis, L. D., and Trincardi, F., 2003. Seismic facies and sedimentary processes on the continental rise off Wilkes Land (East Antarctica): evidence of bottom current activity. *Deep Sea Research Part II: Topical Studies in Oceanography* v. 50(8), p. 1509-1527.

Dowsett, H. J., and Cronin, T. M., 1990. High eustatic sea level during the middle Pliocene: Evidence from the southeastern US Atlantic Coastal Plain. *Geology* v.18(5), p. 435-438.

Dowsett, H., 2007. Faunal re-evaluation of Mid-Pliocene conditions in the western equatorial Pacific. *Micropaleontology* v. 53(6), p. 447-456.

Dowsett, H. J., Haywood, A. M., Valdes, P. J., Robinson, M. M., Lunt, D. J., Hill, D. J., Stoll, D. K., and Foley, K. M., 2011. Sea surface temperatures of the mid-Piacenzian Warm Period: A comparison of PRISM3 and HadCM3. *Palaeogeography, Palaeoclimatology, Palaeoecology* v. 309(1), p. 83-91.

Dowsett, H. J., Robinson, M. M., Haywood, A. M., Hill, D. J., Dolan, A. M., Stoll, D. K., Chan, L-W., Abe-Ouchi, A., Chandler, M. A., Rosenbloom, N. A., Otto-Bliesner, B. L., Bragg, F. J., Lunt, D. J., Foley, K. M., and Riesselman, C. R., 2012. Assessing confidence in Pliocene sea surface temperatures to evaluate predictive models. *Nature Climate Change* v. 2(5), p. 365-371.

Dunbar, G. B., and Barrett, P. J., 2005. Estimating palaeobathymetry of wave-graded continental shelves from sediment texture. *Sedimentology* v. *52*(2), p. 253-269.

Duplessy, J. C., Shackleton, N. J., Matthews, R. K., Prell, W., Ruddiman, W. F., Caralp, M., and Hendy, C. H., 1984. C^{13} record of benthic foraminifera in the last interglacial ocean: implications for the carbon cycle and global deep water circulation. *Quaternary Research* v. 21, p. 225-243.

Dwyer, G. S., Cronin, T. M., Baker, P. A., Raymo, M. E., Buzas, J. S., and Correge, T., 1995, North Atlantic Deepwater Temperature Change During Late Pliocene and Late Quaternary Climatic Cycles. *Science* v. 270, p. 1347-1350.

Dwyer, G. S., and Chandler, M. A., 2008. Mid-Pliocene sea level and continental ice volume based on coupled benthic Mg/Ca palaeotemperatures and oxygen isotopes. *Philosophical Transactions of the Royal Society A: Mathematical, Physical and Engineering Sciences* v. 367(1886), p. 157-168.

Drewry, D.J., ed., 1983, Antarctica: giaciological and geophysical folio. Cambridge, University of Cambridge. Scott Polar Research Institute.

Eittreim, S. L., Cooper, A. K., and Wannesson, J., 1995. Seismic stratigraphic evidence of ice-sheet advances on the Wilkes Land margin of Antarctica. *Sedimentary Geology* v. 96(1), p. 131-156.

Elderfield, H., Greaves, M., Barker, S., Hall, I. R., Tripati, A., Ferretti, P., Crwhurst, S., Booth, L., and Daunt, C., 2010. A record of bottom water temperature and seawater $\delta^{18}O$ for the Southern Ocean over the past 440 kyr based on Mg/Ca of benthic foraminiferal *Uvigerina* spp. *Quaternary Science Reviews* v. 29(1), p. 160-169.

Elderfield, H., Ferretti, P., Greaves, M., Crowhurst, S., McCave, I. N., Hodell, D., and Piotrowski, A. M., 2012. Evolution of ocean temperature and ice volume through the Mid-Pleistocene climate transition. *Science* v. 337(6095), p. 704-709.

Emiliani, C., 1966. Paleotemperature analysis of Caribbean cores P6304-8 and P6304-9 and a generalized temperature curve for the past 425,000 years. *The Journal of Geology* p. 109-124.

Escutia, C., Eittreim, S.L., and Cooper, A.K., 1997. Cenozoic glaciomarine sequences on the Wilkes Land continental rise, Antarctica. *VII International Symposium on Antarctic Earth Sciences, Proceedings Volume*, p. 791–795.

Escutia, C., Eittreim, S. L., Cooper, A. K., and Nelson, C. H., 2000. Morphology and acoustic character of the Antarctic Wilkes Land turbidite systems: ice-sheet-sourced versus river-sourced fans. *Journal of Sedimentary Research* v. 70(1).

Escutia, C., Nelson, C. H., Acton, G. D., Eittreim, S. L., Cooper, A. K., Warnke, D. A., and Jaramillo, J. M., 2002. Current controlled deposition on the Wilkes Land continental rise, Antarctica. *Geological Society, London, Memoirs* v. 22(1), p. 373-384.

Escutia, C., Warnke, D., Acton, G. D., Barcena, A., Burckle, L., Canals, M., and Frazee, C. S., 2003. Sediment distribution and sedimentary processes across the Antarctic Wilkes Land margin during the Quaternary. *Deep Sea Research Part II: Topical Studies in Oceanography* v. 50(8), p. 1481-1508.

Escutia, C., De Santis, L., Donda, F., Dunbar, R. B., Cooper, A. K., Brancolini, G., and Eittreim, S. L., 2005. Cenozoic ice sheet history from East Antarctic Wilkes Land continental margin sediments. *Global and Planetary Change* v. 45(1), p. 51-81.

Escutia, C., Bárcena, M. A., Lucchi, R. G., Romero, O., Ballegeer, A. M., Gonzalez, J. J., and Harwood, D. M., 2009. Circum-Antarctic warming events between 4 and 3.5 Ma recorded in marine sediments from the Prydz Bay (ODP Leg 188) and the Antarctic Peninsula (ODP Leg 178) margins. *Global and Planetary Change* v. 69(3), p. 170-184.

Escutia, C., Brinkhuis, H., Klaus, A., and the Expedition 318 Scientists., 2011. Site U1361. *Proceedings of the Integrated Ocean Drilling Program* v. 318, p. 1-57.

Fairbanks, R. G., and Matthews, R. K., 1978. The marine oxygen isotope record in Pleistocene coral, Barbados, West Indies. *Quaternary Research* v. 10(2), p. 181-196.

Fedorov, A. V., Brierley, C. M., and Emanuel, K., 2010. Tropical cyclones and permanent El Niño in the early Pliocene epoch. *Nature* v. 463(7284), p. 1066-1070.

Fedorov, A. V., Brierley, C. M., Lawrence, K. T., Liu, Z., Dekens, P. S., and Ravelo, A. C., 2013. Patterns and mechanisms of early Pliocene warmth. *Nature* v. 496(7443), p. 43-49.

Fenner, J., Carter, L., and Stewart, R., 1992. Late Quaternary paleoclimatic and paleoceanographic change over northern Chatham Rise, New Zealand. *Marine Geology* v. 108(3), p. 383-404.

Ferraccioli, F., Armadillo, E., Jordan, T., Bozzo, E., and Corr, H., 2009. Aeromagnetic exploration over the East Antarctic Ice Sheet: a new view of the Wilkes Subglacial Basin. *Tectonophysics* v. 478(1), p. 62-77.

Fleming, C. A., 1953. The geology of Wanganui Subdivision. *New Zealand Geological Survey bulletin* 52.

Florindo, F., Bohaty, S. M., Erwin, P. S., Richter, C., Roberts, A. P., Whalen, P. A., and Whitehead, J. M., 2003. Magnetobiostratigraphic chronology and palaeoenvironmental history of Cenozoic sequences from ODP sites 1165 and 1166, Prydz Bay, Antarctica. *Palaeogeography, Palaeoclimatology, Palaeoecology* v. 198(1), p. 69-100.

Folk, R. L., and Ward, W. C., 1957. Brazos River bar: a study in the significance of grain size parameters. *Journal of Sedimentary Research* v. 27(1).

Francis, J. E., and Hill, R. S., 1996. Fossil plants from the Pliocene Sirius Group, Transantarctic Mountains; evidence for climate from growth rings and fossil leaves. *Palaios* v. 11(4), p. 389-396.

Frank, M., Whiteley, N., Kasten, S., Hein, J. R., and O'Nions, K., 2002. North Atlantic Deep Water export to the Southern Ocean over the past 14 Myr: Evidence from Nd and Pb isotopes in ferromanganese crusts. *Paleoceanography* v. 17(2), p. 12-1.

Fretwell, P., Pritchard, H. D., Vaughan, D. G., Bamber, J. L., Barrand, N. E., Bell, R., Bianchi, C., Bingham, R. G., Blankenship, D. D., Casassa, G., Catania, G., Callens, D., Conway, H., Cook, A. J., Corr, H. F. J., Damaske, D., Damm, V., Ferraccioli, F., Forsberg, R., Fujita, S., Gogineni, P., Griggs, J. A., Hindmarsh, R. C. A., Holmlund, P., Holt, J. W., Jacobel, R. W., Jenkins, A., Jokat, W., Jordan, T., King, E. C., Kohler, J., Krabill, W., Riger-Kusk, M., Langley, K. A., Leitchenkov, G., Leuschen, C., Luyendyk, B. P., Matsuoka, K., Nogi, Y., Nost, O. A., Popov, S. V., Rignot, E., Rippin, D. M., Riviera, A., Roberts, J., Ross, N., Siegert, M. J., Smith, A. M., Steinhage, D., Studinger, M., Sun, B., Tinto, B. K., Welch, B. C., Young, D. A., Xiangbin, C., and Zirizzotti, A., 2012. Bedmap2: improved ice bed, surface and thickness datasets for Antarctica. *The Cryosphere Discussions* v. 6(5), p. 4305-4361.

Fronval, T., and Jansen, E., 1996. Late Neogene paleoclimates and paleoceanography in the Iceland-Norwegian Sea: evidence from the Iceland and Vøring Plateaus. In *Proceedings of the Ocean Drilling Program. Scientific Results* v. 151, p. 455-468.

Gardner, J. V., 1982. High-resolution carbonate and organic-carbon stratigraphies for the late Neogene and Quaternary from the western Caribbean and eastern equatorial Pacific. *Initial Reports Deep Sea Driling. Project* v. 68, p. 347-364.

Ghil, M., Allen, M. R., Dettinger, M. D., Ide, K., Kondrashov, D., Mann, M. E., Robertson, A. W., Saunders, A., Tian, Y., Varadi, F., and Yiou, P., 2002. Advanced spectral methods for climatic time series. *Reviews of geophysics* v. 40(1), p. 3-1.

Gilbert, I. M., Pudsey, C. J., and Murray, J. W., 1998. A sediment record of cyclic bottom-current variability from the northwest Weddell Sea. *Sedimentary geology* v. 115(1), p. 185-214.

Gilman, D. L., Fuglister, F. J., and Mitchell Jr, J. M., 1963. On the power spectrum of "red noise". *Journal of the Atmospheric Sciences* v. 20(2), p. 182-184.

Gladenkov, A. Y., 2006. Neogene diatoms from the Sandy Ridge section, Alaska Peninsula: significance for stratigraphic and paleogeographic reconstructions. *Stratigraphy and Geological Correlation* v. 14(1), p. 73-90.

Gradstein, F. M., Ogg, J. G., Smith, A. G., Bleeker, W., and Lourens, L. J., 2004. A new geologic time scale, with special reference to Precambrian and Neogene. *Episodes* v. 27(2), p. 83-100.

Graham, D. J., and Midgley, N. G., 2000. TECHNICAL COMMUNICATION-Graphical Representation of Particle Shape using Triangular Diagrams: An Excel Spreadsheet Method. *Earth Surface Processes and Landforms* v. 25(13), p. 1473-1478.

Groeneveld, J., Steph, S., Tiedemann, R., Garbe-Schönberg, C., Nürnberg, D., and Sturm, A., 2006. Pliocene mixed-layer oceanography for Site 1241, using combined Mg/Ca and δ 18 O analyses of *Globigerinoides sacculifer*. In *Proceedings of the Ocean Drilling Program: Scientific Results* v. 202, p. 1-27.

Haley, B. A., Frank, M., Spielhagen, R. F., and Eisenhauer, A., 2008. Influence of brine formation on Arctic Ocean circulation over the past 15 million years. *Nature Geoscience* v. 1(1), p. 68-72.

Hall, I. R., McCave, I. N., Shackleton, N. J., Weedon, G. P., and Harris, S. E., 2001. Intensified deep Pacific inflow and ventilation in Pleistocene glacial times. *Nature* v. 412(6849), p. 809-812.

Hall, I. R., McCave, I. N., Zahn, R., Carter, L., Knutz, P. C., and Weedon, G. P., 2003. Paleocurrent reconstruction of the deep Pacific inflow during the middle Miocene: Reflections of East Antarctic Ice Sheet growth. *Paleoceanography* v. 18(2).

Hambrey, M. J., Ehrmann, W., and Larsen, B., 1991, Cenozoic glacial record of the Prydz Bay continental shelf, East Antarctica. In: Barron, J; Larsen, B, et al.(eds.), *Proceedings of Ocean Drilling Program Scientific Results, College Station, TX.(Ocean Drilling Program)* v. 119, p. 77-132.

Hambrey, M. J., and McKelvey, B., 2000. Major Neogene fluctuations of the East Antarctic ice sheet: Stratigraphic evidence from the Lambert Glacier region. *Geology* v. 28(10), p. 887-890.

Hansen, J., Sato, M., Ruedy, R., Lo, K., Lea, D. W., and Medina-Elizade, M., 2006. Global temperature change. *Proceedings of the National Academy of Sciences* v. 103(39), 14288-14293.

Harris, S. E., 2002. Data Report: Late Pliocene-Pleistocene carbon and oxygen stable isotopes from benthic foraminifers at ocean drilling program Site 1123. *Proceedings of the Ocean Drilling Program, Scientific Results* v. 181, p. 1-4.

Harrison, T. M., Copeland, P., Kidd, W. S. F., and Yin, A., 1992. Raising Tibet. *Science* v. 255(5052), p. 1663-1670.

Hartley, A., 2003. Andean uplift and climate change. *Journal of the Geological Society* v. 160(1), p. 7-10.

Harwood, D. M., 1983. Diatoms from the Sirius Formation, Transantarctic Mountains. *Antarctic Journal of the US* v. 18, no. 5, p. 98-100.

Haug, G. H., and Tiedemann, R., 1998. Effect of the formation of the Isthmus of Panama on Atlantic Ocean thermohaline circulation. *Nature* v. 393(6686), p. 673-676.

Haug, G. H., Sigman, D. M., Tiedemann, R., Pedersen, T. F., and Sarnthein, M., 1999. Onset of permanent stratification in the subarctic Pacific Ocean. *Nature* v. 401(6755), p. 779-782.

Haug, G. H., Tiedemann, R., Zahn, R., and Ravelo, A. C., 2001. Role of Panama uplift on oceanic freshwater balance. *Geology* v. 29(3), p. 207-210.

Haug, G. H., Ganopolski, A., Sigman, D. M., Rosell-Mele, A., Swann, G. E., Tiedemann, R., Jaccard, S. L., Bollmann, J., Maslin, M. A., Leng, M. J., and Eglinton, G., 2005. North Pacific seasonality and the glaciation of North America 2.7 million years ago. *Nature* v. 433(7028), p. 821-825.

Hayes, D. E., and Frakes, L. A., 1975. General synthesis, deep sea drilling project leg 28. *Initial Reports of the Deep Sea Drilling Project* v. 28, p. 919-942.
Hays, J. D., Imbrie, J., and Shackleton, N. J., 1976. Variations in the Earth's Orbit: Pacemaker of the Ice Ages. *Science* v. 194(4270), p. 1121-1132.
Haywood, A. M., Hill, D. J., Dolan, A. M., Otto-Bliesner, B. L., Bragg, F., Chan, W. L., Chandler, M. A., Contoux, C., Dowsett, H. J., Jost, A., Kamae, Y., Lohmann, G., Lunt, D. J., Abe-Ouchi, A., Pickering, S. J., Ramstein, G., Rosenbloom, N. A., Salzmann, U., Sohl, L., Stepanek, C., Ueda, H., Yan, Q., and Zhang, Z., 2013. Large-scale features of Pliocene climate: results from the Pliocene Model Intercomparison Project. *Climate of the Past* v. 9(1).
Henrich, R., Wolf, T., Bohrmann, G., and Thiede, J., 1989. Cenozoic paleoclimatic and Paleoceanographic changes in the northern hemisphere revealed by variability of coarse-fraction composition in sediments from the Vøring Plateau - ODP Leg 104 Drill Sites. *Proceedings of the Ocean Drilling Program, Scientific Results* v. 104, p. 75-188.
Hepp, D. A., Mörz, T., and Grützner, J., 2006. Pliocene glacial cyclicity in a deep-sea sediment drift (Antarctic Peninsula Pacific Margin). *Palaeogeography, Palaeoclimatology, Palaeoecology* v. 231(1), p. 181-198.
Hesse, R., Khodabakhsh, S., Klaucke, I., and Ryan, W. B., 1997. Asymmetrical turbid surface-plume deposition near ice-outlets of the Pleistocene Laurentide ice sheet in the Labrador Sea. *Geo-Marine Letters* v. 17(3), p. 179-187.
Hill, D. J., Haywood, A. M., Hindmarsh, R. C. A., and Valdes, P. J., 2007. Characterizing ice sheets during the Pliocene: evidence from data and models. In: Williams, M.; Haywood, A.M.; Gregory, F.J.; Schmidt, D.N., (eds.) *Deep-time perspectives on climate change: marrying the signal from computer models and biological proxies.* London, Geological Society of London, p. 517-538. (Micropalaeontological Society special publications)
Hill, D. J., Dolan, A. M., Haywood, A. M., Hunter, S. J., and Stoll, D. K., 2010. Sensitivity of the Greenland Ice Sheet to Pliocene sea surface temperatures. *Stratigraphy* v. 7(2-3), p. 111-121.
Hillenbrand, C-D and Futterer, D. K., 2002. Neogene to Quaternary Deposition of opal on the continental rise west of the Antarctic Peninsula, ODP Leg 178, Sites 1095, 1096, and 1101. *Proceedings of the Ocean Drilling Program, Scientific Results* v. 178, p. 1-33.
Hillenbrand, C. D., and Cortese, G., 2006. Polar stratification: a critical view from the Southern Ocean. *Palaeogeography, Palaeoclimatology, Palaeoecology* v. 242(3), p. 240-252.
Hodell, D. A., and Venz, K. A., 1992, Toward a high-resolution stable isotopic record of the Southern Ocean during the Plio-Pleistocene (4.8 to 0.8 Ma), *In* The Antarctic Paleoenvironment: A Perspective on Global Change, Part I, Antarct. Res. Ser., vol. 56, edited by J. P. Kennett and D. A. Warnke, pp. 265–310, AGU, Washington, D. C.
Hodell, D. A., and Venz-Curtis, K. A., 2006. Late Neogene history of deepwater ventilation in the Southern Ocean. *Geochemistry, Geophysics, Geosystems* v. 7(9).
Howell, P., Pisias, N., Balance, J., Baughman, J., and Ochs, L., 2006. ARAND Time-Series Analysis Software. Brown University, Providence RI.
Huybers, P., and Wunsch, C., 2004. A depth-derived Pleistocene age model: Uncertainty estimates, sedimentation variability, and nonlinear climate change. *Paleoceanography* v. 19(1).
Huybers, P., 2006. Early Pleistocene glacial cycles and the integrated summer insolation forcing. *Science* v. 313, p. 508-511.
Huybers, P., 2007. Glacial variability over the last two million years: an extended depth-derived agemodel, continuous obliquity pacing, and the Pleistocene progression. *Quaternary Science Reviews* v. 26(1), p. 37-55.
Huybers, P., and Denton, G., 2008. Antarctic temperature at orbital timescales controlled by local summer duration. *Nature Geoscience* v. 1(11), p. 787-792.
Huybers, P., and Tziperman, E., 2008. Integrated summer insolation forcing and 40,000-year glacial cycles: The perspective from an ice-sheet/energy-balance model. *Paleoceanography* v. 23(1).
Huybers, P., 2011. Combined obliquity and precession pacing of late Pleistocene deglaciations. *Nature* v. 480(7376), p. 229-232.
Imbrie, J., and Imbrie, J. Z., 1980, Modeling the climatic Response to orbital variations. *Science* v. 207, p. 943-953.

Ishman, S. E., and Reick, H. J., 1992. A late Neogene Antarctic glacio-eustatic record, Victoria Land Basin Margin, Antarctica. *Antarctic Research Series* v. 56, p. 327-347.

Jacobs, S. S., 1991. On the nature and significance of the Antarctic Slope Front. *Marine Chemistry* v. 35(1), 9-24.

Jacobs, B. F., 2004. Palaeobotanical studies from tropical Africa: relevance to the evolution of forest, woodland and savannah biomes. *Philosophical Transactions of the Royal Society of London. Series B: Biological Sciences* v. 359(1450), p. 1573-1583.

Jansen, E., Raymo, M. E., Blum, P., et al., 1996. Proceedings of the Ocean Drilling Program, Initial Reports, 162. College Station, TX.

Jansen, E., Overpeck, J., Briffa, K.R., Duplessy, J.-C., Joos, F., Masson-Delmotte, V., Olago D., Otto-Bliesner, B., Peltier, W.R., Rahmstorf, S., Ramesh, R., Raynaud, D., Rind, D., Solomina, O., Villalba R., and Zhang D., 2007. Palaeoclimate. In: *Climate Change 2007: The Physical Science Basis. Contribution of Working Group I to the Fourth Assessment Report of the Intergovernmental Panel on Climate Change* [Solomon, S., D. Qin, M. Manning, Z. Chen, M. Marquis, K.B. Averyt, M. Tignor and H.L. Miller (eds.)]. Cambridge University Press, Cambridge, United Kingdom and New York, NY, USA.

Joseph, L. H., David K. R., and van der Pluijm, B. A.., 2004. Neogene history of the deep western boundary current at Rekohu Sediment Drift, Southwest Pacific (ODP Site 1124). *Marine Geology* v. 205.1, p. 185-206.

Journeaux, T. D., Kamp, P. J., and Naish, T., 1996. Middle Pliocene cyclothems, Mangaweka region, Wanganui Basin, New Zealand: a lithostratigraphic framework. *New Zealand Journal of Geology and Geophysics* v. 39(1), p. 135-149.

Jouzel, J., Masson-Delmotte, V., Cattani, O., Dreyfus, G., Falourd, S., Hoffmann, G., Minster, B., Nouet, J., Barnola, J. M., Chappellaz, J., Fischer, H., Gallet, J. C., Johnsen, S., Leuenberger, M., Loulergue, L., Luethi, D., Oerter, H., Parrenin, F., Raisbeck, G., Raynaud, D., Schilt, A., Schwander, J., Selmp, E., Souchez, R., Spahni, R., Stauffer, B., Steffensen, J. P., Stenni, B., Stocker, T. F., Tison, J. L., Werner, M., and Wolff, E. W., 2007. Orbital and millennial Antarctic climate variability over the past 800,000 years. *Science* v. 317(5839), p. 793-796.

Kamp, P. J., 1978. Stratigraphy and sedimentology of conglomerates in the Kidnappers Bay. Thesis, Library, University of Waikoto, Hamilotn, p. 1-276 (unpublished).

Kamp, P. J., Journeaux, T. D., and Morgans, H. E., 1998. Cyclostratigraphy of middle Pliocene mid shelf to upper slope strata, eastern Wanganui Basin (New Zealand): correlations to the deep sea isotope record. *Sedimentary geology* v. 117(3), p. 165-192.

Kamp, P. J., Vonk, A. J., Bland, K. J., Hansen, R. J., Hendy, A. J., McIntyre, A. P., Ngatai, M., Cartwright, S. J., Hayton, S., and Nelson, C. S., 2004. Neogene stratigraphic architecture and tectonic evolution of Wanganui, King Country, and eastern Taranaki Basins, New Zealand. *New Zealand Journal of Geology and Geophysics* v. 47(4), p. 625-644.

Kawamura, K., Parrenin, F., Lisiecki, L., Uemura, R., Vimeux, F., Severinghaus, J. P., Hutterli, M. A., Nakazawa, T., Aoki, S., Jouzel, J., Raymo, M. E., Matsumoto, K., Nakata, H., Motoyama, H., Fujita, S., Goto-Azuma, K., Fujii, Y., and Watanabe, O., 2007. Northern Hemisphere forcing of climatic cycles in Antarctica over the past 360,000 years. *Nature* v. 448(7156), p. 912-916.

Keigwin, L. D., 1978. Pliocene closing of the Isthmus of Panama, based on biostratigraphic evidence from nearby Pacific Ocean and Caribbean Sea cores. *Geology* v. 6(10), p. 630-634.

Keigwin, L., 1982. Isotopic paleoceanography of the Caribbean and East Pacific: role of Panama uplift in late Neogene time. *Science* v. 217(4557), p. 350-353.

Keller, G., Zenker, C. E., and Stone, S. M., 1989. Late Neogene history of the Pacific-Caribbean gateway. *Journal of South American Earth Sciences* v. 2(1), p. 73-108.

Kennett, J. P., and Barker, P. F., 1990. Latest Cretaceous to Cenozoic climate and oceanographic developments in the Weddell Sea, Antarctica: an ocean-drilling perspective. *Proceedings of Ocean Driling. Program Scientific Results* v. 113, p. 937-960.

Kennett, J. P., and Hodell, D. A., 1993. Evidence for relative climatic stability of Antarctica during the early Pliocene: a marine perspective. *Geografiska Annaler. Series A. Physical Geography* p. 205-220.

King, T. A., Ellis, W. G., Murray, D. W., Shackleton, N. J., and Harris, S., 1997. Miocene evolution of carbonate sedimentation at the Ceara Rise: A multivariate data/proxy approach. *Proceedings of the Ocean Drilling Program. Scientific results* v. 154, p. 349-365.

Kleiven, H. F., Jansen, E., Fronval, T., and Smith, T. M., 2002. Intensification of Northern Hemisphere glaciations in the circum Atlantic region (3.5–2.4 Ma)–ice-rafted detritus evidence. *Palaeogeography, Palaeoclimatology, Palaeoecology* v. 184(3), p. 213-223.

Knies, J., Matthiessen, J., Vogt, C., Laberg J. S., Hjelstuen, B. O., Smelror, M., Larsen, E., Andreassen, K., Eidvin, T., and Vorren, T. O., 2009, The Plio-Pleistocene glaciation of the Barents Sea–Svalbard region: a new model based on revised chronostratigraphy. *Quaternary Science Reviews* v. 28(9), p. 812-829

Korty, R. L., Emanuel, K. A., and Scott J. R.., 2008. Tropical cyclone-induced upper-ocean mixing and climate: Application to equable climates. *Journal of Climate* v. 21(4), p. 638-654.

Krissek, L. A., 1995. Late Cenozoic ice-rafting records from Leg 145 sites in the North Pacific: Late Miocene onset, Late Pliocene intensification and Pliocene-Pleistocene events. *Proceedings of the Ocean Drilling Program, Scientific Results* v. 145, p. 179-194.

Kroopnick, P. M., 1985. The distribution of ^{13}C of ΣCO_2 in the world oceans. *Deep Sea Research Part A. Oceanographic Research Papers* v. 32(1), p. 57-84.

Krylov, A. A., Andreeva, I. A., Vogt, C., Backman, J., Krupskaya, V. V., Grikurov, G. E., Moran, K., and Shoji, H., 2008. A shift in heavy and clay mineral provenance indicates a middle Miocene onset of a perennial sea ice cover in the Arctic Ocean. *Paleoceanography* v. *23*(1).

Kwiek, P. B., and Ravelo, A. C., 1999. Pacific Ocean intermediate and deep water circulation during the Pliocene. *Palaeogeography, Palaeoclimatology, Palaeoecology* v. 154(3), p. 191-217.

Lagoe, M. B., and Zellers, S. D., 1996. Depositional and microfaunal response to Pliocene climate change and tectonics in the eastern Gulf of Alaska. *Marine Micropaleontology* v. 27(1), p. 121-140.

Larsen, H. C., Saunders, A. D., Clift, P. D., Beget, J., Wei, W., Spezzaferri, S., Ali, J., Cambray, H., Demant, A., Fitton, G., Fram, M. S., Fukuma, K., Gieskes, J., Holmes, M. A., Hunt J., Lacasse, C., Larsen, L. M., Lykke-Andersen, H., Meltser, A., Morrison, M. L., Nemoto, N., Okay, N., Saito, S., Sinton, C., Stax, R., Vallier, T. L., Vandamme, D., and Werner, R., 1994. Seven million years of glaciation in Greenland.

Larter, R. D., and Barker, P. F., 2009. Neogene interaction of tectonic and glacial processes at the Pacific margin of the Antarctic Peninsula. *Sedimentation, Tectonics, and Eustasy: Special Publication 12 of the IAS* v. 12, p.165-186

Laskar, J., Robutel, P., Joutel, F., Gastineau, M., Correia, A. C. M., and Levrard, B., 2004. A long-term numerical solution for the insolation quantities of the Earth. *Astronomy & Astrophysics* v. 428(1), p. 261-285.

Lawrence, K. T., Liu, Z., and Herbert, T. D., 2006. Evolution of the eastern tropical Pacific through Plio-Pleistocene glaciation. *Science* v. 312(5770), p. 79-83.

Lee, S. Y., and Poulsen, C. J., 2006. Sea ice control of Plio–Pleistocene tropical Pacific climate evolution. *Earth and Planetary Science Letters* v. *248*(1), p. 253-262.

Levy, R., Cody, R., Crampton, J., Fielding, C., Golledge, N., Harwood, D., Henrys, S., McKay, R., Naish, T., Ohneiser, C., Wilson, G., Wilson, T., and Winter, D., 2012. Late Neogene climate and glacial history of the Southern Victoria Land coast from integrated drill core, seismic and outcrop data. *Global and Planetary Change* v. *80*, p. 61-84.

Lewis, A. R., Marchant, D. R., Kowalewski, D. E., Baldwin, S. L., and Webb, L. E., 2006. The age and origin of the Labyrinth, western Dry Valleys, Antarctica: Evidence for extensive middle Miocene subglacial floods and freshwater discharge to the Southern Ocean. *Geology* v. 34(7), p. 513-516.

Lewis, A. R., Marchant, D. R., Ashworth, A. C., Hemming, S. R., and Machlus, M. L., 2007. Major middle Miocene global climate change: Evidence from East Antarctica and the Transantarctic Mountains. *Geological Society of America Bulletin* v. 119(11-12), p. 1449-1461.

Lewis, A. R., Marchant, D. R., Ashworth, A. C., Hedenäs, L., Hemming, S. R., Johnson, J. V., Leng, M. J., Machlus, M. L., Newton, A. E., Raine, I., Willenbring, J. K., Williams, M., and Wolfe, A. P., 2008. Mid-Miocene cooling and the extinction of tundra in continental Antarctica. *Proceedings of the National Academy of Sciences* v. 105(31), p. 10676-10680.

Lillie, A. R., 1953. The geology of the Dannevirke Subdivision. *New Zealand Geological Survey Bulletin* v. 46, p. 156.
Lisiecki, L. E., and Raymo, M. E., 2005. A Pliocene-Pleistocene stack of 57 globally distributed benthic $\delta^{18}O$ records. *Paleoceanography* v. 20(1).
Lisiecki, L. E., Raymo, M. E., and Curry, W. B., 2008. Atlantic overturning responses to Late Pleistocene climate forcings. *Nature* v. 456(7218), p. 85-88.
Lisiecki, L. E., 2010. Links between eccentricity forcing and the 100,000-year glacial cycle. *Nature geosciences* v. 3(5), p. 349-352.
Lourens, L. J., Becker, J., Bintanja, R., Hilgen, F. J., Tuenter, E., van de Wal, R. S., and Ziegler, M., 2010. Linear and non-linear response of late Neogene glacial cycles to obliquity forcing and implications for the Milankovitch theory. *Quaternary Science Reviews* v. 29(1), p. 352-365.
Lucchi, R. G., Rebesco, M., Camerlenghi, A., Busetti, M., Tomadin, L., Villa, G., Persico, D., Morigi, C., Bonci, M. C., and Giorgetti, G., 2002. Mid-late Pleistocene glacimarine sedimentary processes of a high-latitude, deep-sea sediment drift (Antarctic Peninsula Pacific margin). *Marine Geology* v. 189(3), p. 343-370.
Lucchi, R. G., and Rebesco, M., 2007. Glacial contourites on the Antarctic Peninsula margin: insight for palaeoenvironmental and palaeoclimatic conditions. *Geological Society, London, Special Publications* v. 276(1), p. 111-127.
Lunt, D. J., Foster, G. L., Haywood, A. M., and Stone, E. J., 2008. Late Pliocene Greenland glaciation controlled by a decline in atmospheric CO_2 leverls. *Nature* v. 454, p. 1102-1105
Lunt, D. J., Haywood, A. M., Schmidt, G. A., Salzmann, U., Valdes, P. J., and Dowsett, H. J., 2009. Earth system sensitivity inferred from Pliocene modelling and data. *Nature Geoscience* v. 3, p. 60-64.
Lunt, D. J., Haywood, A. M., Schmidt, G. A., Salzmann, U., Valdes, P. J., and Dowsett, H. J., 2010. Earth system sensitivity inferred from Pliocene modelling and data. *Nature Geoscience* v. 3(1), p. 60-64.
Mackensen, A., Hubberten, H.-W., Bickert, T., Fischer, G., and Fu¨ tterer, D. K., 1993, The $\delta^{13}C$ in benthic foraminiferal tests of Fantbotia wuellerstorfi (Schwager) relative to the $\delta^{13}C$ of dissolved inorganic carbon in Southern Ocean deep water: Implications for glacial ocean circulation models. *Paleoceanography* v. 8(5), p. 587– 610.
Mackensen, A., Rudolph, M., and Kuhn, G., 2001, Late Pleistocene deep-water circulation in the subantarctic eastern Atlantic. *Global Planetary Change* v. 30, p. 197 – 229.
Mackintosh, A., Golledge, N., Domack, E., Dunbar, R., Leventer, A., White, D., Pollard, d., DeConto, R., Fink, D., Zwart, D., Gore, D., and Lavoie, C., 2011. Retreat of the East Antarctic ice sheet during the last glacial termination. *Nature Geoscience* v. 4(3), p. 195-202.
Mann, M. E., and Lees, J. M., 1996. Robust estimation of background noise and signal detection in climatic time series. *Climatic Change* v. 33(3), p. 409-445.
Marchitto, T. M., Curry, W. B., and Oppo, D. W., 1998. Millennial-scale changes in North Atlantic circulation since the last glaciation. *Nature* v. 393(6685), p. 557-561.
Marlow, J. R., Lange, C. B., Wefer, G., and Rosell-Melé, A., 2000. Upwelling intensification as part of the Pliocene-Pleistocene climate transition. *Science* v. 290(5500), p. 2288-2291.
Martin, J. H., 1990. Glacial-interglacial CO_2 change: The iron hypothesis. *Paleoceanography* v. 5(1), p. 1-13.
Martinson, D. G., Stammerjohn, S. E., Iannuzzi, R. A., Smith, R. C., and Vernet, M., 2008. Western Antarctic Peninsula physical oceanography and spatio–temporal variability. *Deep Sea Research Part II: Topical Studies in Oceanography* v. 55(18), p. 1964-1987.
Martínez-Garcia, A., Rosell-Melé, A., McClymont, E. L., Gersonde, R., and Haug, G. H., 2010. Subpolar link to the emergence of the modern equatorial Pacific cold tongue. *Science* v. 328(5985), p. 1550-1553.
Martínez-Garcia, A., Rosell-Melé, A., Jaccard, S. L., Geibert, W., Sigman, D. M., and Haug, G. H., 2011. Southern Ocean dust-climate coupling over the past four million years. *Nature* v. 476(7360), p. 312-315.
Maslin, M. A., Li, X. S., Loutre, M. F., and Berger, A., 1998. The contribution of orbital forcing to the progressive intensification of Northern Hemisphere glaciation. *Quaternary Science Reviews* v. 17(4), 411-426.

Masson, V., Braconnot, P., Jouzel, J., de Noblet, N., Cheddadi, R., and Marchal, O., 2000. Simulation of intense monsoons under glacial conditions.*Geophysical Research Letters* v. 27(12), p. 1747-1750.

Masson-Delmotte, V., M. Schulz, A. Abe-Ouchi, J. Beer, A. Ganopolski, J.F. González Rouco, E. Jansen, K. Lambeck, J. Luterbacher, T. Naish, T. Osborn, B. Otto-Bliesner, T. Quinn, R. Ramesh, M. Rojas, X. Shao and A. Timmermann, 2013: Information from Paleoclimate Archives. In: Climate Change 2013: The Physical Science Basis. Contribution of Working Group I to the Fifth Assessment Report of the Intergovernmental Panel on Climate Change [Stocker, T.F., D. Qin, G.-K. Plattner, M. Tignor, S.K. Allen, J. Boschung, A. Nauels, Y. Xia, V. Bex and P.M. Midgley (eds.)]. Cambridge University Press, Cambridge, United Kingdom and New York, NY, USA.

Matsumoto, K., Oba, T., Lynch-Stieglitz, J., and Yamamoto, H., 2002. Interior hydrography and circulation of the glacial Pacific Ocean. *Quaternary Science Reviews* v. 21(14), p. 1693-1704.

Matthiessen, J., Knies, J., Vogt, C., and Stein, R., 2009. Pliocene palaeoceanography of the Arctic Ocean and subarctic seas. *Philosophical Transactions of the Royal Society A: Mathematical, Physical and Engineering Sciences* v. 367(1886), p. 21-48.

McCartney, M. S., and Donohue, K. A., 2007. A deep cyclonic gyre in the Australian–Antarctic Basin. *Progress in Oceanography* v. 75(4), p. 675-750.

McCave, I. N., Manighetti, B., & Robinson, S. G. (1995). Sortable silt and fine sediment size/composition slicing: parameters for palaeocurrent speed and palaeoceanography. *Paleoceanography* v. 10(3), p. 593-610.

McCave, I. N., and Hall, I. R., 2006. Size sorting in marine muds: Processes, pitfalls, and prospects for paleoflow-speed proxies. *Geochemistry, Geophysics, Geosystems* v. 7(10).

McCave, I. N., Hall, I. R., and Bianchi, G. G., 2006. Laser vs. settling velocity differences in silt grainsize measurements: estimation of palaeocurrent vigour. *Sedimentology* v. 53(4), p. 919-928.

McCave, I. N., Carter, L., and Hall, I. R., 2008. Glacial–interglacial changes in water mass structure and flow in the SW Pacific Ocean. *Quaternary Science Reviews* v. 27(19), p. 1886-1908.

McGuire, D. M., 1989. *Paleomagnetic stratigraphy and magnetic properties of Pliocene strata, Turakina River, North Island, New Zealand* (Doctoral dissertation, Victoria University of Wellington).

McKay, R. M., Barrett, P. J., Harper, M. A., and Hannah, M. J., 2008. Atmospheric transport and concentration of diatoms in surficial and glacial sediments of the Allan Hills, Transantarctic Mountains. *Palaeogeography, Palaeoclimatology, Palaeoecology* v. 260(1), p. 168-183.

McKay, R., Browne, G., Carter, L., Cowan, E., Dunbar, G., Krissek, L., Naish, T., Powell, R., Reed, J., Talarico, F., and Wilch, T., 2009. The stratigraphic signature of the late Cenozoic Antarctic Ice Sheets in the Ross Embayment. *Geological Society of America Bulletin* v. 121(11-12), p. 1537-1561.

McKay, R., Naish, T., Carter, L., Riesselman, C., Sjunneskog, C., Winter, D., Dunbar, R., Sangiorgi, F., Warren, C., Pagani, M., Schouten, S., Willmott, V., Levy, R., DeConto, R., and Powell, R., 2012. Antarctic and Southern Ocean influences on Late Pliocene global cooling. *Proceedings of the National Academy of Sciences* v. 109, p. 6423-6428.

McKay, R., Naish, T., Powell, R., Barrett, P., Scherer, R., Talarico, F., Monien, D., Kuhn, G., Jackolski, C., and Williams, T., 2012. Pleistocene variability of Antarctic ice sheet extent in the Ross embayment. *Quaternary Science Reviews* v. 34, p. 93-112.

McKelvey, B. C., 1981. The lithologic logs of DVDP cores 10 and 11, eastern Taylor Valley. *Antarctic Research Series* v. 33, p. 63-94.

McKelvey, B. C., 1982. Late Cenozoic marine and terrestrial glacial sedimentation in eastern Taylor Valley, Southern Victoria Land. *Antarctic geoscience. Series B* v. 4, p. 1109-1116.

Meinshausen, M., Meinshausen, H., Hare, W., Raper, S. B., Frieler, K., Knutti, R., Fram, D., and Allen, M. R., 2009. Greenhouse gas emission targets for limiting global warming to 2°C. *Nature* v. 458, p. 1158-1163.

Menviel, L., Timmermann, A., Mouchet, A., and Timm, O., 2008. Climate and marine carbon cycle response to changes in the strength of the Southern Hemispheric westerlies. *Paleoceanography* v. 23(4).

Meyers, S. R., and Hinnov, L. A., 2010. Northern Hemisphere glaciation and the evolution of Plio-Pleistocene climate noise. *Paleoceanography* v. 25(3).
Meyers, S. R., 2012. Seeing red in cyclic stratigraphy: Spectral noise estimation for astrochronology. *Paleoceanography* v. 27(3).
Melles, M., Brigham-Grette, J., Minyuk, P. S., Nowaczyk, N. R., Wennrich, V., DeConto, R. M., Anderson, P. M., Andreev, A. A., Coletti, A., Cook, T. L., Haltia-Hovi, E., Kukkonen, M., Lozhkin, A. V., Rosén, P., Tarasov, P., Vogel, H., and Wagner, B., 2012. 2.8 million years of Arctic climate change from Lake El'gygytgyn, NE Russia. *Science* v. 337, no. 6092, p. 315-320.
Milanković, M., 1936. *Durch ferne Welten und Zeiten: Briefe eines Weltallbummlers*. Koehler and Amelang.
Milankovitch, M. M., 1941, Canon of Insolation and Ice Age problem: Royal Serbian Academy Special Publication.
Miller, K. G., Kominz, M. A., Browning, J. V., Wright, J. D., Mountain, G. S., Katz, M. E., Sugarman, P. J., Cramer, B. S., Christie-Blick, N., and Pekar, S. F., 2005. The Phanerozoic record of global sea-level change. *Science* v. 310(5752), p. 1293-1298.
Miller, K. G., Wright, J. D., Browning, J. V., Kulpecz, A., Kominz, M., Naish, T. R., Cramer, B. S., Rosenthal, Y., Peltier, W. R., and Sosdian, S., 2012. High tide of the warm Pliocene: Implications of global sea level for Antarctic deglaciation. *Geology* v. 40(5), p. 407-410.
Millwood, L. D., Hawkins Jr, D. L., and Wells, S. M., 2002. Data report: Utilizing color reflectance analysis as a carbonate concentration proxy. *Proceedings of the Ocean Drilling Program, Scientific Results, Ocean Drilling Program, College Station, TX* v. 181.
Mix, A. C., Pisias, N. G., Rugh, W., Wilson, J., Morey, A., and Hagelberg, T. K., 1995. Benthic foraminifer stable isotope record from Site 849 (0-5 Ma): local and global climate changes. *Proceedings of the Ocean Drilling Program, Scientific Results* v. 138.
Molnar, P., England, P., and Martinod, J.,1993. Mantle dynamics, uplift of the Tibetan Plateau, and the Indian monsoon. *Reviews of Geophysics* v. 31(4), p. 357-396.
Molnar, P., 2008. Closing of the Central American Seaway and the Ice Age: A critical review. *Paleoceanography* v. 23(2).
Mudelsee, M., and Raymo, M. E., 2005. Slow dynamics of the Northern Hemisphere glaciation. *Paleoceanography* v. 20(4).
Naish, T., and Kamp, P. J., 1995. Pliocene-Pleistocene marine cyclothems, Wanganui Basin, New Zealand: A lithostratigraphic framework. *New Zealand journal of geology and geophysics* v. 38(2), p. 223-243.
Naish, T., and Kamp, P. J., 1997. Sequence stratigraphy of sixth-order (41 ky) Pliocene–Pleistocene cyclothems, Wanganui Basin, New Zealand: a case for the regressive systems tract. *Geological Society of America Bulletin* v. 109(8), p. 978-999.
Naish, T., 1997. Constraints on the amplitude of late Pliocene eustatic sea-level fluctuations: new evidence from the New Zealand shallow-marine sediment record. *Geology* v. 25(12), p. 1139-1142.
Naish, T. R., Abbott, S. T., Alloway, V., Beu, A. G., Carter, R. M., Edwards, A. R., Journeaux, T. D., Kamp, P. J. J., Pillians, B. J., Saul, G., and Woolfe, K. J., 1998. Astronomical calibration of a southern hemisphere Plio-Pleistocene reference section, Wanganui Basin, New Zealand. *Quaternary Science Reviews* v. 17(8), p. 695-710.
Naish, T. R., Woolfe, K. J., Barrett, P. J., Wilson, G. S., Atkins, C., Bohaty, S. M., Bücker, J., Claps, M., Davey, F. J., Dunbar, G. B., Dunn, A. G., Fielding, C. R., Florindo, F., Hannah, M. J., Harwood, D. M., Henrys, S. A., Krissek, L. A., Lavelle, M., van der Meer, J., McIntosh, W. C., Niessen, F., Passchier, S., Powell, R. D., Roberts, A. P., Sagnottie, L., Scherer, R. P., Strong, C. P., Talarico, F., Verosub, K. L., Villa, G., Watkins, D. K., Webb, P. N., and Wonik, T., 2001. Orbitally induced oscillations in the East Antarctic ice sheet at the Oligocene/Miocene boundary. *Nature* v. 413(6857), p. 719-723.
Naish, T. R., Wehland, F., Wilson, G. S., Browne, G. H., Cook, R. A., Morgans, H. E., Rosenberg, M., King, P. R., Smale, D., Nelson, C. S., Kamp, P. J. J., and Ricketts, B., 2005. An integrated sequence stratigraphic, palaeoenvironmental, and chronostratigraphic analysis of the Tangahoe Formation, southern Taranaki coast, with implications for mid-Pliocene (c. 3.4–3.0 Ma) glacio-eustatic sea-level changes. *Journal of the Royal Society of New Zealand* v. 35(1-2), p. 151-196.

Naish, T. R., 2007. Constraints on the amplitude of late Pliocene eustatic sea-level fluctuations: new evidence from the New Zealand shallow-marine sediment record. *Geology* v. 25, p. 1139-1142.

Naish, T. R., Powell, R. D., Barrett, P. J., Levy, R., Henrys, S. A., Wilson, G. S., Krissek, L. A., Niessen, F., Pompilio, M., Ross, J., Scherer, R., Talarico, F., Pyne, A., and the ANDRILL-MIS Science team., 2008. Late Cenozoic climate history of the Ross Embayment from the AND-1B drill hole: Culmination of three decades of Antarctic margin drilling. *Antarctica: A keystone in a Changing World* v. 4.

Naish, T., Powell, R., Levy, R., Wilson, G., Scherer, R., Talarico, F., Krissek, L., Niessen, F., Pompilio, M., Wilson, T., Carter, L., DeConto, R., Huybers, P., McKay, R., Pollard, D., Ross, J., Winter, D., Barrett, P., Browne, G., Cody, R., Cowan, E., Crampton, J., Dunbar, G., Dunbar, N., Florindo, F., Gebhardt, C., Graham, I., Hannah, M., Hansaraj, D., Harwood, D., Helling, D., Henry, S., Hinnov, L., Kuhn, G., Kyle, P., Läufer, A., Mafioli, P., Magens, D., Mandernack, K., McIntosh, W., Millan, C., Morin, R., Ohneiser, C., Paulsen, T., Persico, D., Raine, I., Reed, J., Riesselman, C., Sagnotti, L., Schmitt, D., Sjunneskog, C., Strong, P., Taviani, M., Vogel, S., Wilch, T., and Williams, T., 2009, Obliquity-paced Pliocene West Antarctic ice sheet oscillations: Nature, v. 458(7236), p. 322-328.

Naish, T. R., and Wilson, G. S., 2009. Constraints on the amplitude of Mid-Pliocene (3.6–2.4 Ma) eustatic sea-level fluctuations from the New Zealand shallow-marine sediment record. *Philosophical Transactions of the Royal Society A: Mathematical, Physical and Engineering Sciences* v. 367(1886), p. 169-187.

Naafs, B. D. A., Hefter, J., Acton, G., Haug, G. H., Martínez-Garcia, A., Pancost, R., and Stein, R., 2012. Strengthening of North American dust sources during the late Pliocene (2.7 Ma). *Earth and Planetary Science Letters* v. 317, p. 8-19.

Naish, T., and Zwartz, D., 2012. Palaeoclimate: looking back to the future. *Nature Climate Change* v. 2(5), p. 317-318.

Nelson, C. S., Cooke, P. J., Hendy, C. H., and Cuthbertson, A. M., 1993. Oceanographic and climatic changes over the past 160,000 years at Deep Sea Drilling Project Site 594 off southeastern New Zealand, southwest Pacific Ocean. *Paleoceanography* v. 8(4), p. 435-458.

Ninnemann, U. S., and Charles, C. D., 2002. Changes in the mode of Southern Ocean circulation over the last glacial cycle revealed by foraminiferal stable isotopic variability. *Earth and Planetary Science Letters* v. 201(2), p. 383-396.

Nodder, S. D., and Northcote, L. C., 2001. Episodic particulate fluxes at southern temperate mid-latitudes (42–45 S) in the Subtropical Front region, east of New Zealand. *Deep Sea Research Part I: Oceanographic Research Papers* v. 48(3), p. 833-864.

O'Brien, P. E., Goodwin, I., Forsberg, C. F., Cooper, A. K., and Whitehead, J., 2007. Late Neogene ice drainage changes in Prydz Bay, East Antarctica and the interaction of Antarctic ice sheet evolution and climate. *Palaeogeography, Palaeoclimatology, Palaeoecology* v. 245(3), p. 390-410.

Ó Cofaigh, C., Dowdeswell, J. A., and Pudsey, C. J., 2001. Late Quaternary iceberg rafting along the Antarctic Peninsula continental rise and in the Weddell and Scotia Seas. *Quaternary Research* v. 56(3), p. 308-321.

Oppo, D. W., and Fairbanks, R. G., 1987. Variability in the deep and intermediate water circulation of the Atlantic Ocean during the past 25,000 years: Northern Hemisphere modulation of the Southern Ocean. *Earth and Planetary Science Letters* v. 86(1), p. 1-15.

Oppo, D. W., and Lehman, S. J., 1995. Suborbital timescale variability of North Atlantic Deep Water during the past 200,000 years. *Paleoceanography* v.10(5), p. 901-910.

Oppo, D. W., Horowitz, M., and Lehman, S. J., 1997. Marine core evidence for reduced deep water production during Termination II followed by a relatively stable substage 5e (Eemian). *Paleoceanography* v. 12(1), p. 51-63.

Oppo, D. W., and Horowitz, M., 2000. Glacial deep water geometry: South Atlantic benthic foraminiferal Cd/Ca and δ13C evidence. *Paleoceanography* v. 15(2), p. 147-160.

Orsi, A. H., Whitworth III, T., and Nowlin Jr, W. D., 1995. On the meridional extent and fronts of the Antarctic Circumpolar Current. *Deep Sea Research Part I: Oceanographic Research Papers* v. 42(5), p. 641-673.

Orsi, A. H., Johnson, G. C., and Bullister, J. L., 1999. Circulation, mixing, and production of Antarctic Bottom Water. *Progress in Oceanography* v. 43(1), p. 55-109.

Pagani, M., Liu, Z., LaRiviere, J., and Ravelo, A. C., 2010. High Earth-system climate sensitivity determined from Pliocene carbon dioxide concentrations. *Nature Geoscience* v. 3(1), p. 27-30.

Pälike, H., Norris, R. D., Herrle, J. O., Wilson, P. A., Coxall, H. K., Lear, C. H., Shackleton, N. J., Tripati, A. K., and Wade, B. S., 2006. The heartbeat of the Oligocene climate system. *Science* v. 314(5807), p. 1894-1898.

Paillard, D., Labeyrie, L., and Yiou, P., 1996. Macintosh program performs time-series analysis. *Eos, Transactions, Am. Geophys. Union* v. 77, p. 379

Paillard, D., 2010. Climate and the orbital parameters of the Earth. *Comptes Rendus Geoscience*. v. 342(4), p. 273-285.

Passchier, S., 2011. Linkages between East Antarctic Ice Sheet extent and Southern Ocean temperatures based on a Pliocene high-resolution record of ice-rafted debris off Prydz Bay, East Antarctica. *Paleoceanography* v. 26(4).

Payne, R. R., Conolly, J. R., and Abbott, W. H., 1972. Turbidite muds within diatom ooze off Antarctica: Pleistocene sediment variation defined by closely spaced piston cores. *Geological Society of America Bulletin* v. 83(2), p. 481-486.

Petit, J. R., Jouzel, J., Raynaud, D., Barkov, N. I., Barnola, J. M., Basile, I., Bender, M., Chappellaz, J., Davis, M., Delaygue, G., Delmotte, M., Kotlyakov, V. M., Legrand, M., Lipenkov, V. Y., Lorius, C., Pépin, L., Ritz, C., Saltzman, E., and Stievenard, M., 1999. Climate and atmospheric history of the past 420,000 years from the Vostok ice core, Antarctica. *Nature* v. 399(6735), p. 429-436.

Peucat, J. J., Ménot, R. P., Monnier, O., and Fanning, C. M., 1999. The Terre Adélie basement in the East-Antarctica Shield: geological and isotopic evidence for a major 1.7 Ga thermal event; comparison with the Gawler Craton in South Australia. *Precambrian Research* v. 94(3), p. 205-224.

Pillans, B., 1983. Upper Quaternary marine terrace chronology and deformation, south Taranaki, New Zealand. *Geology* v. 11(5), p. 292-297.

Pillans, B., and Naish, T., 2004. Defining the quaternary. *Quaternary Science Reviews* v. 23(23), p. 2271-2282.

Pillans, B., Alloway, B., Naish, T., Westgate, J., Abbott, S., and Palmer, A., 2005. Silicic tephras in Pleistocene shallow-marine sediments of Wanganui Basin, New Zealand. *Journal of the royal Society of New Zealand* v. 35(1-2), p. 43-90.

Pollard, D., and DeConto, R. M., 2009. Modelling West Antarctic ice sheet growth and collapse through the past five million years. *Nature* v. 458(7236), p. 329-332.

Poore, H. R., Samworth, R., White, N. J., Jones, S. M., and McCave, I. N., 2006. Neogene overflow of Northern Component Water at the Greenland-Scotland Ridge. *Geochemistry, Geophysics, Geosystems* v. 7(6).

Pillans, B., Chappell, J., and Naish, T. R., 1998. A review of the Milankovitch climatic beat: template for Plio–Pleistocene sea-level changes and sequence stratigraphy. *Sedimentary Geology* v. 122(1), p. 5-21.

Powell, R.D., 1981. Sedimentation conditions in Taylor Valley, Antarctica, inferred from textural analysis of DVDP cores. In: McGinnis, L.D. (Ed.), Dry Valley Drilling Project. American Geophysical Union, Washington, p. 331–349.

Powell, R.D., 1984. Glacimarine processes and inductive lithofacies modelling of ice shelf and tidewater glacier sediments based on Quaternary examples. *Marine Geology* v. 57, p. 1-52.

Presti, M., De Santis, L., Busetti, M., and Harris, P. T., 2003. Late Pleistocene and Holocene sedimentation on the George V continental shelf, East Antarctica. *Deep Sea Research Part II: Topical Studies in Oceanography* v. 50(8), p. 1441-1461.

Pritchard, H. D., Ligtenberg, S. R. M., Fricker, H. A., Vaughan, D. G., Van den Broeke, M. R., and Padman, L., 2012. Antarctic ice-sheet loss driven by basal melting of ice shelves. *Nature* v. 484(7395), p. 502-505.

Pudsey, C. J., and Camerlenghi, A., 1998. Glacial–interglacial deposition on a sediment drift on the Pacific margin of the Antarctic Peninsula. *Antarctic Science* v. 10(03), p. 286-308.

Pudsey, C. J., 2000. Sedimentation on the continental rise west of the Antarctic Peninsula over the last three glacial cycles. *Marine Geology* v. 167(3), p. 313-338.

Pollard, D., and DeConto, R. M., 2009. Modelling West Antarctic ice sheet growth and collapse through the past five million years. *Nature* v. 458(7236), p. 329-332.

Quilty, P.G., Lirio, J.M. and Jillett, D., 2000. Stratigraphy of the Pliocene Sørsdal Formation, Marine Plain, Vestfold Hills, East Antarctica. *Antarctic Science* v. 12(02), p.205–216.

Ravelo, A. C., and Andreasen, D. H., 2000. Enhanced circulation during a warm period. *Geophysical Research Letters* v. 27(7), p. 1001-1004.

Ravelo, A. C., Andreasen, D. H., Lyle, M., Lyle, A. O., and Wara, M. W., 2004. Regional climate shifts caused by gradual global cooling in the Pliocene epoch. *Nature* v. 429(6989), p. 263-267.

Ravelo, A. C., and Wara, M. W., 2004. The role of the tropical oceans on global climate during a warm period and a major climate transition. *Oceanography-Washington DC Oceanography Society* v. 17, p. 32-41.

Raymo, M. E., Ruddiman, W. F., Shackleton, N. J., and Oppo, D. W., 1990. Evolution of Atlantic-Pacific δ^{13}C gradients over the last 2.5 my.*Earth and Planetary Science Letters* v. 97(3), p. 353-368.

Raymo, M. E., 1994. The initiation of Northern Hemisphere glaciation. *Annual Review of Earth and Planetary Sciences* v. 22, p. 353-383.

Raymo, M. E., Oppo, D. W., and Curry, W., 1997. The Mid-Pleistocene climate transition: A deep sea carbon isotopic perspective. *Paleoceanography* v. 12(4), p. 546-559.

Raymo, M.E., 1997b. The timing of major climate terminations. *Paleoceanography* v. 12, p. 577-585.

Raymo, M. E., Lisiecki, L. E., and Nisancioglu, K. H., 2006. Plio-Pleistocene ice volume, Antarctic climate, and the global δ18O record. *Science* v. 313(5786), p. 492-495.

Raymo, M. E., and Huybers, P., 2008. Unlocking the mysteries of the ice ages. *Nature* v. 451(7176), p. 284-285.

Raymo, M. E., Mitrovica, J. X., O'Leary, M. J., DeConto, R. M., and Hearty, P. J., 2011. Departures from eustasy in Pliocene sea-level records. *Nature Geoscience* v. 4(5), p. 328-332.

Rea, D. K., and Snoeckx, H., 1995. Sediment fluxes in the Gulf of Alaska; paleoceanographic record from Site 887 on the Patton-Murray Seamont Platform, *In* Rea, D. K., Basov, I. A., Scholl, D. W., and Allan, J. F., (eds), *Proceedings of the Ocean Drilling Program, Scientific Results, Ocean Drilling Program*, College Station, TX, p. 247-256.

Rea, D. K., Snoeckx, H., and Joseph, L. H., 1998. Late Cenozoic eolian deposition in the North Pacific: Asian drying, Tibetan uplift, and cooling of the northern hemisphere. *Paleoceanography* v. 13(3), p. 215-224.

Rebesco, M., and Camerlenghi, A., 2008. Late Pliocene margin development and mega debris flow deposits on the Antarctic continental margins: Evidence of the onset of the modern Antarctic Ice Sheet?. *Palaeogeography, Palaeoclimatology, Palaeoecology* v. 260(1), p. 149-167.

Rial, J. A., Oh, J., and Reischmann, E., 2013. Synchronization of the climate system to eccentricity forcing and the 100,000-year problem. *Nature Geoscience* v. 6(4), p. 289-293.

Rignot, E., Jacobs, S., Mouginot, J., and Scheuchl, B., 2013. Ice-shelf melting around Antarctica. *Science* v. 341(6143), p. 266-270.

Rintoul, S. R., 1998. On the origin and influence of Adélie Land Bottom Water.*Antarctic Research Series* v. 75, p. 151-171.

Rintoul, S. R., and Bullister, J. L., 1999. A late winter hydrographic section from Tasmania to Antarctica. *Deep Sea Research Part I: Oceanographic Research Papers* v. 46(8), p. 1417-1454.

Rintoul, S., Hughes, C., and Olbers, D., 2001. The Antarctic circumpolar current system. *In: Ocean Circulation and Climate/G. Siedler, J. Church and J. Gould, eds. New York: Academic Press.* p. 271-302.

Robinson, M. M., Valdes, P. J., Haywood, A. M., Dowsett, H. J., Hill, D. J., and Jones, S. M., 2011. Bathymetric controls on Pliocene North Atlantic and Arctic sea surface temperature and deepwater production. *Palaeogeography, Palaeoclimatology, Palaeoecology* v. 309(1), p. 92-97.

Ross, N., Bingham, R. G., Corr, H. F., Ferraccioli, F., Jordan, T. A., Le Brocq, A., Rippin, D. M., Young, D., Blankenship, D. D., and Siegert, M. J., 2012. Steep reverse bed slope at the grounding line of the Weddell Sea sector in West Antarctica. *Nature Geoscience* v. 5(6), p. 393-396.

Roy, M., van de Flierdt, T., Hemming, S. R., and Goldstein, S. L., 2007. $^{40}Ar/^{39}Ar$ ages of hornblende grains and bulk Sm/Nd isotopes of circum-Antarctic glacio-marine sediments: Implications for sediment provenance in the southern ocean. *Chemical Geology* v. 244(3), p. 507-519.

Russon, T., Elliot, M., Kissel, C., Cabioch, G., De Deckker, P., and Correge, T., 2009. Middle-late Pleistocene deep water circulation in the southwest subtropical Pacific. *Paleoceanography* v. 24(4).

Salzmann, U., Haywood, A. M., Lunt, D. J., Valdes, P. J., and Hill, D. J., 2008. A new global biome reconstruction and data-model comparison for the middle Pliocene. *Global Ecology and Biogeography* v. 17(3), p. 432-447.

Salzmann, U., Williams, M., Haywood, A. M., Johnson, A. L., Kender, S., and Zalasiewicz, J., 2011. Climate and environment of a Pliocene warm world. *Palaeogeography, Palaeoclimatology, Palaeoecology* v. 309(1), p. 1-8.

Sandroni, S., and Talarico, F.M., 2006. Analysis of clast lithologies from CIROS-2 core, New Harbour, Antarctica — implications for ice flow directions during Plio–Pleistocene time. *Palaeogeography Palaeoclimatology Palaeoecology* v. 231(1–2), p. 215–232.

Saul, G., Naish, T. R., Abbott, S. T., and Carter, R. M., 1999. Sedimentary cyclicity in the marine Pliocene-Pleistocene of the Wanganui basin (New Zealand): Sequence stratigraphic motifs characteristic of the past 2.5 my. *Geological Society of America Bulletin* v. 111(4), p. 524-537.

Scherer, R. P., Bohaty, S. M., Dunbar, R. B., Esper, O., Flores, J. A., Gersonde, R., Harwood, D. M., Roberts, A. P., and Taviani, M., 2008. Antarctic records of precession-paced insolation-driven warming during early Pleistocene Marine Isotope Stage 31.*Geophysical Research Letters* v. 35(3).

Schmitz, W. J., 1995. On the interbasin-scale thermohaline circulation.*Reviews of Geophysics* v. 33(2), p. 151-173.

Schmitz, W. J., 1996. *On the world ocean circulation. Volume II, the Pacific and Indian Oceans/a global update*. Woods Hole Oceanographic Institution.

Schuur, C. L., Coffin, M. F., Frohlich, C., Massell, C. G., Karner, G. D., Ramsay, D., and Caress, D. W., 1998. Sedimentary regimes at the Macquarie Ridge Complex: Interaction of Southern Ocean circulation and plate boundary bathymetry. *Paleoceanography* v. 13(6), p. 646-670.

Seki, O., Foster, G. L., Schmidt, D. N., Mackensen, A., Kawamura, K., and Pancost, R. D., 2010. Alkenone and boron-based Pliocene pCO_2 records. *Earth and Planetary Science Letters* v. 292(1), p. 201-211.

Shackleton, N. J., 1974. Attainment of isotopic equilibrium between ocean water and the benthonic foraminifera genus Uvigerina: Isotopic changes in the ocean during the last glacial. *Les Meth. Quant. D'etude Var. Clim. Au Cours du Pleist, Coll. Int. C.N.R.S.* v. 219, p. 203-209.

Shackleton, N. J., and Opdyke, N. D., 1973. Oxygen isotope and palaeomagnetic stratigraphy of Equatorial Pacific core V28-238: Oxygen isotope temperatures and ice volumes on a 10^5 year and 10^6 year scale. *Quaternary research* v. 3(1), p. 39-55.

Shackleton, N. J., and Opdyke, N. D., 1976. Oxygen-isotope and paleomagnetic stratigraphy of Pacific core V28-239 late Pliocene to latest Pleistocene. *Geoogical Society of America Memoir* v. 145, p. 449-464.

Shackleton, N. J., and Cita, M. B., 1979. Oxygen and carbon isotope stratigraphy of benthic foraminifers at Site 397: Detailed history of climatic change during the late Neogene. *Initial Reports Deep Sea Drilling Project* v. 47, p. 433-445.

Shackleton, N. J., Backman, J., Zimmerman, H., Kent, D. V., Hall, M. A., Roberts, D. G., Schnitker, D., Baldauf, J. G., Desprairies, A., Homrighausen, R., Huddlestun, P., Keene, J. B., Kaltenback, A. J., Krumsiek, K. A. O., Morton, A. C., Murray, J. W., and Westberg-Smith, J., 1984. Oxygen isotope calibration of the onset of ice-rafting and history of glaciation in the North Atlantic region. *Nature* v. 307(5952), p. 620-623.

Shackleton, N. J., 1995. Pliocene stable isotope stratigraphy of Site 846. *Proceeding of Ocean Drilling Program, Scientific Results* v. 138, p. 337-355.

Shackleton, N. J., Hagelberg, T. K., and Crowhurst, S. J., 1995. Evaluating the success of astronomical tuning: Pitfalls of using coherence as a criterion for assessing pre-Pleistocene timescales. *Paleoceanography* v. 10(4), p. 693-697.

Shackleton, N. J., 2000. The 100,000-year ice-age cycle identified and found to lag temperature, carbon dioxide, and orbital eccentricity. *Science* v. 289(5486), p. 1897-1902.

Shevenell, A. E., Kennett, J. P., and Lea, D. W., 2004. Middle Miocene southern ocean cooling and Antarctic cryosphere expansion. *Science* v. 305(5691), p. 1766-1770.

Shipboard Scientific Party, 2001. Leg 188 summary: Prydz Bay-Cooperation Sea, Antarctica.O'Brien, PE, Cooper, AK, Richter, C., et al. *Proceedings of Ocean Drilling Program Initial Report* 188, 1-65.

Skinner, L. C., Fallon, S., Waelbroeck, C., Michel, E., and Barker, S., 2010. Ventilation of the deep Southern Ocean and deglacial CO_2 rise. *Science* v. 328(5982), p. 1147-1151.

Sloan, L.C., Crowley, T., and Pollard, D., 1996. Modelling of Middle Pliocene climate with the NCAR GENESIS general circulation mode. *Marine Micropaleontology* v. 27, p. 51-61.

Smellie, J. L., Haywood, A. M., Hillenbrand, C. D., Lunt, D. J., and Valdes, P. J., 2009. Nature of the Antarctic Peninsula Ice Sheet during the Pliocene: Geological evidence and modelling results compared. *Earth-Science Reviews* v. 94(1), p. 79-94.

Sniderman, J. K., Pillans, B., O'Sullivan, P. B., and Kershaw, A. P., 2007. Climate and vegetation in southeastern Australia respond to Southern Hemisphere insolation forcing in the late Pliocene–early Pleistocene. *Geology* v. 35(1), p. 41-44.

Solheim, A., Faleide, J. I., Andersen, E. S., Elverhøi, A., Forsberg, C. F., Vanneste, K., Uenzelmann-Neben, G., and Channell, J. E., 1998. Late Cenozoic seismic stratigraphy and glacial geological development of the East Greenland and Svalbard–Barents Sea continental margins. *Quaternary Science Reviews* v. 17(1-3), p. 155-184.

Sperazza, M., Moore, J. N., and Hendrix, M. S., 2004. High-Resolution Particle Size Analysis of Naturally Occurring Very Fine-Grained Sediment Through Laser Diffractometry: RESEARCH METHODS PAPERS. *Journal of Sedimentary Research* v. 74(5), p. 736-743.

Srinivasan, M. S., and Sinha, D. K., 1998. Early Pliocene closing of the Indonesian Seaway: evidence from north-east Indian Ocean and Tropical Pacific deep sea cores. *Journal of Asian Earth Sciences*, v. 16(1), p. 29-44.

Staiger, J. W., Marchant, D. R., Schaefer, J. M., Oberholzer, P., Johnson, J. V., Lewis, A. R., and Swanger, K. M., 2006. Plio-Pleistocene history of Ferrar Glacier, Antarctica: Implications for climate and ice sheet stability. *Earth and Planetary Science Letters* v. 243(3), p. 489-503.

Steph, S., Tiedemann, R., Groeneveld, J., Sturm, A., and Nürnberg, D., 2006. Pliocene changes in tropical east Pacific upper ocean stratification: response to tropical gateways?. In *Proceedings of the Ocean Drilling Program: Scientific Results* v. 202, p. 1-51.

Steph, S., Tiedemann, R., Prange, M., Groeneveld, J., Schulz, M., Timmermann, A., Nürnberg, D., Rühlemann, C., Saukel, C., and Haug, G. H., 2010. Early Pliocene increase in thermohaline overturning: A precondition for the development of the modern equatorial Pacific cold tongue. *Paleoceanography* v. 25(2).

Stephens, B. B., and Keeling, R. F., 2000. The influence of Antarctic sea ice on glacial–interglacial CO_2 variations. *Nature* v. 404(6774), p. 171-174.

Stern, T. A., Quinlan, G. M., and Holt, W. E., 1992. Basin formation behind an active subduction zone: three-dimensional flexural modelling of Wanganui Basin, New Zealand. *Basin research* v. 4(3-4), p. 197-214.

Stern, T. A., Stratford, W. R., and Salmon, M. L., 2006. Subduction evolution and mantle dynamics at a continental margin: Central North Island, New Zealand. *Reviews of Geophysics* v. 44(4).

John, K. E. S., and Krissek, L. A., 2002. The late Miocene to Pleistocene ice-rafting history of southeast Greenland. *Boreas* v. 31(1), p. 28-35.

John, K. S., 2008. Cenozoic ice-rafting history of the central Arctic Ocean: Terrigenous sands on the Lomonosov Ridge. *Paleoceanography* v. 23(1).

Stickley, C. E., St John, K., Koç, N., Jordan, R. W., Passchier, S., Pearce, R. B., and Kearns, L. E., 2009. Evidence for middle Eocene Arctic sea ice from diatoms and ice-rafted debris. *Nature* v. 460(7253), p. 376-379.

Stow, D. A., and Piper, D. J. W., 1984. Deep-water fine-grained sediments: facies models. *Geological Society, London, Special Publications* v. 15(1), p. 611-646.
Stramma, L., Peterson, R. G., and Tomczak, M., 1995. The south Pacific current. *Journal of physical oceanography* v. 25(1), p. 77-91.
Stuart, K. M., and Long, D. G., 2011. Tracking large tabular icebergs using the SeaWinds Ku-band microwave scatterometer. *Deep Sea Research Part II: Topical Studies in Oceanography* v. 58(11), p. 1285-1300.
Stroeven, A. P., Prentice, M. L., and Kleman, J., 1996. On marine microfossil transport and pathways in Antarctica during the late Neogene: Evidence from the Sirius Group at Mount Fleming. *Geology* v. 24(8), p. 727-730.
Tauxe, L., Stickley, C. E., Sugisaki, S., Bijl, P. K., Bohaty, S. M., Brinkhuis, H., Escutia, C., Flores, J. A., Houben, A. J. P., Iwai, M., Jiménez-Espejo, F., McKay et al., R., Passchier, S., Pross, J., Riesselman, C. R., Röhl, U., Sangiorgi, F., Welsh, K., Klaus, A., Fehr, A., Bendle, J. A. P., Dunbar, R., Gonzàlez, J., Hayden, T., Katsuki, K., Olney, M. P., Pekar, S. F., Shrivastava, P. K., van de Flierdt, T., Williams, T., and Yamane, M., 2012. Chronostratigraphic framework for the IODP Expedition 318 cores from the Wilkes Land Margin: Constraints for paleoceanographic reconstruction. *Paleoceanography* v. 27(2).
Tiedemann, R., Sarnthein, M., and Shackleton, N. J., 1994. Astronomic timescale for the Pliocene Atlantic δ^{18}O and dust flux records of Ocean Drilling Program site 659. *Paleoceanography* v. 9(4), p. 619-638.
Theissen, K. M., Dunbar, R. B., Cooper, A. K., Mucciarone, D. A., and Hoffmann, D., 2003. The Pleistocene evolution of the East Antarctic Ice Sheet in the Prydz Bay region: stable isotopic evidence from ODP Site 1167. *Global and Planetary Change* v. 39(3), p. 227-256.
Thomson, D. J., 1982. Spectrum estimation and harmonic analysis. *Proceedings of the IEEE* v. 70(9), p. 1055-1096.
Toggweiler, J. R., Russell, J. L., and Carson, S. R., 2006. Midlatitude westerlies, atmospheric CO_2, and climate change during the ice ages. *Paleoceanography* v. 21(2).
Toggweiler, J. R., and Russell, J., 2008. Ocean circulation in a warming climate. *Nature* v. 451(7176), p. 286-288.
Trewick, S. A., and Bland, K. J., 2012. Fire and slice: palaeogeography for biogeography at New Zealand's North Island/South Island juncture. *Journal of the Royal Society of New Zealand* v. 42(3), p. 153-183.
Turner, G. M., Kamp, P. J., McIntyre, A. P., Hayton, S., McGuire, D. M., and Wilson, G. S., 2005. A coherent middle Pliocene magnetostratigraphy, Wanganui Basin, New Zealand. *Journal of the Royal Society of New Zealand* v. 35(1-2), p. 197-227.
Vella, P., 1963. Plio-Pleistocene cyclothems, Wairarapa, New Zealand. *Transactiona of the Royal Society of New Zealand Geology* v. 2, p. 15-50.
Vella, P., and Briggs, W. M., 1971. Lithostratigraphic names, upper Miocene to lower Pleistocene, northern Aorangi Range, Wairarapa. *New Zealand Journal of Geology and Geophysics* v. 14, p. 253-274.
Venz, K. A., & Hodell, D. A. (2002). New evidence for changes in Plio–Pleistocene deep water circulation from Southern Ocean ODP Leg 177 Site 1090. *Palaeogeography, Palaeoclimatology, Palaeoecology* v. 182(3), p. 197-220.
Villinski, J. C, Dunbar R. B, Mucciarone D. A., 2000. Carbon 13/Carbon 12 ratios of sedimentary organic matter from the Ross Sea, Antarctica: A record of phytoplankton bloom dynamics. *Journal of Geophysical Research* v. 105, p. 14163–14172.
Waddell, L. M., Hendy, I. L., Moore, T. C., and Lyle, M. W., 2009. Ventilation of the abyssal Southern Ocean during the late Neogene: A new perspective from the subantarctic Pacific. *Paleoceanography* v. 24(3).
WAIS Divide Project Members., 2013. Onset of deglacial warming in West Antarctica driven by local orbital forcing. *Nature* v. 500(7463), p. 440-444.
Walcott, R. I., 1998. Modes of oblique compression: Late Cenozoic tectonics of the South Island of New Zealand. *Reviews of Geophysics* v. 36(1), p. 1-26.

Wan, S., Tian, J., Steinke, S., Li, A., and Li, T., 2010. Evolution and variability of the East Asian summer monsoon during the Pliocene: Evidence from clay mineral records of the South China Sea. *Palaeogeography, Palaeoclimatology, Palaeoecology* v. 293(1), 237-247.
Wara, M. W., Ravelo, A. C., and Delaney, M. L., 2005. Permanent El Niño-like conditions during the Pliocene warm period. *Science* v. 309(5735), p. 758-761.
Wardlaw, B. R., and Quinn, T. M., 1991. The record of Pliocene sea-level change at Enewetak Atoll. *Quaternary Science Reviews* v. 10(2), p. 247-258.
Warren, B. A., 1973. Transpacific hydrographic sections at Lats 437S and 287S: the SCORPIO expedition. *II Deep water: Deep-Sea Research* v. 20, p. 9–38.
Weaver, A. J., Eby, M., Fanning, A. F., and Wiebe, E. C., 1998. Simulated influence of carbon dioxide, orbital forcing and ice sheets on the climate of the Last Glacial Maximum. *Nature* v. 394(6696), p. 847-853.
Webb, P. N., 1974. Micropaleontology, paleoecology and correlation of the Pecten Gravels, Wright Valley, Antarctica, and description of *Trochoelphidiella onyxi* n. gen., n. sp. *The Journal of Foraminiferal Research* v. 4(4), p. 185-199.
Webb, P. N., Harwood, D. M., McKelvey, B. C., Mercer, J. H., and Stott, L. D., 1984. Cenozoic marine sedimentation and ice-volume variation on the East Antarctic craton. *Geology* v. 12(5), p. 287-291.
Weber, M. E., Clark, P. U., Ricken, W., Mitrovica, J. X., Hostetler, S. W., and Kuhn, G., 2011. Interhemispheric ice-sheet synchronicity during the Last Glacial Maximum. *Science* v. 334(6060), p. 1265-1269.
Weedon, G. P., 2003. *Time-series analysis and cyclostratigraphy: examining stratigraphic records of environmental cycles*. Cambridge University Press.
Whitehead, J. M., and Bohaty, S. M., 2003. Pliocene summer sea surface temperature reconstruction using silicoflagellates from Southern Ocean ODP Site 1165. *Paleoceanography* v. 18(3).
Whitehead, J. M., Wotherspoon, S., and Bohaty, S. M., 2005. Minimal Antarctic sea ice during the Pliocene. *Geology* v. 33(2), p. 137-140.
Whitehead, J. M., Quilty, P. G., McKelvey, B. C., and O'Brien, P. E., 2006. A review of the Cenozoic stratigraphy and glacial history of the Lambert Graben—Prydz Bay region, East Antarctica. *Antarctic Science* v. 18(01), p. 83-99.
Williams, G. D., and Bindoff, N. L., 2003. Wintertime oceanography of the Adélie Depression. *Deep Sea Research Part II: Topical Studies in Oceanography* v. 50(8), p. 1373-1392.
Williams, G. D., Bindoff, N. L., Marsland, S. J., and Rintoul, S. R., 2008. Formation and export of dense shelf water from the Adélie Depression, East Antarctica. *Journal of Geophysical Research: Oceans* v. 113(C4), p. 1978–2012.
Williams, T., van de Flierdt, T., Hemming, S. R., Chung, E., Roy, M., and Goldstein, S. L., 2010. Evidence for iceberg armadas from East Antarctica in the Southern Ocean during the late Miocene and early Pliocene. *Earth and Planetary Science Letters* v. 290(3), p. 351-361.
Wright, D., and Miller, K. G., 1996. Control of North Atlantic deep water circulation by the Greenland-Scotland Ridge. *Paleoceanography* v. 11, p. 157–170.
Zachos, J., Pagani, M., Sloan, L., Thomas, E., and Billups, K., 2001. Trends, rhythms, and aberrations in global climate 65 Ma to present. *Science* v. 292(5517), p. 686-693.
Zhang, R., Zhang, Z. S., Jiang, D., Otto-Bliesner, B. L., Haywood, A. M., Hill, D. J., Dolan, A. M., Stepanek, C., Lohmann, G., Contoux, C., Bragg, F., Chan, W. –L., Chandler, M. A., Jost, A., Kamae, Y., Abe-Ouchi, A., Ramstein, G., Rosenbloom, N. A., Sohl, L., and Ueda, H., 2013. East Asian monsoon climate simulated in the PlioMIP. *Climate of the Past Discussions* v. 9(1).

ABBREVIATION INDEX

AABW – Antarctic Bottom Water

ACC – Antarctic Circumpolar Current

ALBW – Adélie Land Bottom Water

ANDRILL – Antarctic Gelogical DRILLing program

AMOC – Atlantic Meridional Overturning Circulation

CAS – Central American Seaway

CDW – Circumpolar Deep Water

DSDP - Deep Sea Drilling Project

DVDP – Dry Valley Drilling Project

DWBC – Deep Western Boundary Current

EAIS – East Antarctic Ice Sheet

ECC – East Cape Current

ENZOSS – Eastern New Zealand Oceanic Sedimentary System

GIS – Greenland Ice Sheet

GNAIW – Glacial North Atlantic Intermediate Water

HSSW – High Salinity Shelf Water

IBRD MAR – Ice-Berg Rafted Debris Mass Accumulation Rate

IODP – Integrated Ocean Drilling Program

IRD – Ice Rafted Debris

ISRD – Ice Shelf-Rafted Debris

ITCZ – Intertropical Convergence Zone

LCDW – Lower Circumpolar Deep Water

LGM – Last Glacial Maximum

MBSF – Meters Below Sea Floor

MCD – Meters Composite Depth
MCDW – Modified Circumpolar Deep Water
MIS – Marine Isotope Stage

NADW – North Atlantic Deep Water
NCW – Northern Component Water

ODP – Ocean Drilling Program

PDW – Pacific Deep Water
PFZ – Polar Front Zone
PRISM – Pliocene Interpretation and Synoptic Mapping

rMCD – revised Meters Composite Depth
RSBW – Ross Sea Bottom Water

SAF – Subantarctic Front
SC – Southland Current
SCW – Southern Component Water
SIRD – Sea Ice-Rafted Debris
SPC – South Pacific Current
SST – Sea Surface Temperatures
STF – Subtropical Front

UCDW – Upper Circumpolar Deep Water

WAIS – West Antarctic Ice Sheet
WSBW – Weddell Sea Bottom Water

APPENDIX A

IODP Site U1361 IBRD MAR and biogenic opal weight percent

Core, section, interval (cm)	Depth (mbsf)	Age (Ma)	CS (wt%)	DBD (g/cm3)	LSR (cm/k.y.)	IBRD MAR (g/cm2/k.y.)	Biogenic opal (wt%)
5H 2W 85-87	39.85	2.159	0.377	1.54	2.33	0.014	28.24
5H 2W 95-97	39.95	2.163	0.175	1.54	2.33	0.006	33.53
5H 2W 105-107	40.05	2.168	0.220	1.54	2.33	0.008	31.58
5H 2W 115-117	40.15	2.172	0.232	1.54	2.33	0.008	31.58
5H 2W 125-127	40.25	2.176	0.039	1.54	2.33	0.001	44.89
5H 2W 135-137	40.35	2.181	0.351	1.54	2.33	0.013	44.89
5H 3W 15-17	40.65	2.193	0.439	1.56	2.33	0.016	41.24
5H 3W 25-27	40.75	2.198	0.108	1.56	2.33	0.004	35.71
5H 3W 35-37	40.85	2.202	0.189	1.56	2.33	0.007	48.02
5H 3W 55-57	41.05	2.211	0.123	1.56	2.33	0.004	38.85
5H 3W 65-67	41.15	2.215	0.211	1.56	2.33	0.008	25.47
5H 3W 85-87	41.35	2.223	0.052	1.56	2.33	0.002	28.14
5H 3W 95-97	41.45	2.228	0.000	1.56	2.33	0.000	41.24
5H 3W 105-107	41.55	2.232	0.072	1.56	2.33	0.003	35.19
5H 3W 115-117	41.65	2.236	0.163	1.56	2.33	0.006	30.18
5H 3W 125-127	41.75	2.241	0.102	1.56	2.33	0.004	33.54
5H 3W 135-137	41.85	2.245	0.168	1.56	2.33	0.006	29.65
5H 3W 145-147	41.95	2.249	0.219	1.48	2.33	0.008	34.52
5H 4W 5-7	42.05	2.253	0.253	1.48	2.33	0.009	26.16
5H 4W 15-17	42.15	2.258	0.091	1.48	2.33	0.003	31.41
5H 4W 25-27	42.25	2.262	0.214	1.48	2.33	0.007	30.72
5H 4W 35-37	42.35	2.266	0.149	1.48	2.33	0.005	29.17
5H 4W 45-47	42.45	2.270	0.109	1.48	2.33	0.004	38.71
5H 4W 55-57	42.55	2.275	0.111	1.48	2.33	0.004	31.14
5H 4W 65-67	42.65	2.279	0.156	1.48	2.33	0.005	30.12
5H 4W 85-87	42.85	2.288	0.352	1.48	2.33	0.012	24.40
5H 4W 95-97	42.95	2.292	1.262	1.48	2.33	0.044	24.40
5H 4W 105-107	43.05	2.296	0.206	1.48	2.33	0.007	27.98
5H 4W 115-117	43.15	2.300	0.098	1.48	2.33	0.003	27.98
5H 4W 125-127	43.25	2.305	0.134	1.48	2.33	0.005	31.18
5H 4W 135-137	43.35	2.309	0.044	1.48	2.33	0.002	31.18
5H 4W 145-147	43.45	2.313	0.124	1.48	2.33	0.004	31.10
5H 5W 5-7	43.55	2.318	0.141	1.51	2.33	0.005	31.10
5H 5W 15-17	43.65	2.322	0.331	1.51	2.33	0.012	44.79
5H 5W 25-27	43.75	2.326	0.063	1.51	2.33	0.002	52.76
5H 5W 35-37	43.85	2.330	0.236	1.51	2.33	0.008	33.97
5H 5W 45-47	43.95	2.335	0.196	1.51	2.33	0.007	38.76
5H 5W 55-57	44.05	2.339	0.595	1.51	2.33	0.021	38.76
5H 5W 65-67	44.15	2.343	0.333	1.51	2.33	0.012	38.76
5H 5W 85-87	44.35	2.352	0.122	1.51	2.33	0.004	26.49
5H 5W 105-107	44.55	2.360	0.432	1.51	2.33	0.015	31.71
5H 5W 115-117	44.65	2.365	0.802	1.51	2.33	0.028	32.74
5H 5W 125-127	44.75	2.369	0.836	1.51	2.33	0.030	32.74
5H 5W 135-137	44.85	2.373	0.038	1.51	2.33	0.001	49.40
5H 5W 145-147	44.95	2.378	0.206	1.31	2.33	0.006	49.40
5H 6W 5-7	45.05	2.382	0.199	1.31	2.33	0.006	37.21

5H 6W 15-17	45.15	2.386	0.340	1.31	2.33	0.010	42.58
5H 6W 25-27	45.25	2.390	0.282	1.31	2.33	0.009	51.90
5H 6W 35-37	45.35	2.395	0.314	1.31	2.33	0.010	35.09
5H 6W 45-47	45.45	2.399	0.164	1.31	2.33	0.005	58.13
5H 6W 55-57	45.55	2.403	0.148	1.31	2.33	0.005	58.13
5H 6W 65-67	45.65	2.408	0.686	1.31	2.33	0.021	58.13
5H 6W 85-87	45.85	2.416	0.477	1.31	2.33	0.015	42.01
5H 6W 95-97	45.95	2.420	0.100	1.31	2.33	0.003	42.01
5H 6W 105-107	46.05	2.425	0.371	1.31	2.33	0.011	25.00
5H 6W 125-127	46.25	2.433	0.304	1.54	2.33	0.011	20.00
5H 6W 135-137	46.35	2.438	0.239	1.54	2.33	0.009	35.54
5H 6W 145-147	46.45	2.442	0.225	1.54	2.33	0.008	48.19
5H 7W 15-17	46.65	2.450	0.483	1.54	2.33	0.017	42.53
5H 7W 25-27	46.75	2.455	0.581	1.54	2.33	0.021	40.12
5H 7W 35-37	46.85	2.459	1.105	1.54	2.33	0.040	32.08
5H 7W 45-47	46.95	2.463	1.393	1.54	2.33	0.050	24.55
5H 7W 55-57	47.05	2.468	0.847	1.54	2.33	0.030	29.94
5H 7W 63-65	47.13	2.471	0.218	1.54	2.33	0.008	15.59
6H 1W 15-17	47.15	2.472	0.446	1.54	2.33	0.016	28.85
5H CC 5-7	47.2	2.474	1.214	1.54	2.33	0.044	30.64
6H 1W 35-37	47.35	2.480	0.174	1.61	2.33	0.007	32.54
6H 1W 45-47	47.45	2.485	0.526	1.61	2.33	0.020	29.22
6H 1W 55-57	47.55	2.489	0.955	1.61	2.33	0.036	29.22
6H 1W 65-67	47.65	2.493	0.000	1.61	2.33	0.000	29.22
6H 1W 85-87	47.85	2.502	0.975	1.61	2.33	0.037	25.12
6H 1W 95-97	47.95	2.506	0.615	1.61	2.33	0.023	18.42
6H 1W 105-107	48.05	2.510	0.197	1.61	2.33	0.007	22.59
6H 1W 115-117	48.15	2.515	0.000	1.61	2.33	0.000	24.85
6H 1W 125-127	48.25	2.519	0.000	1.61	2.33	0.000	28.84
6H 1W 135-137	48.35	2.523	0.186	1.61	2.33	0.007	41.25
6H 1W 145-147	48.45	2.527	0.155	1.61	2.33	0.006	32.00
6H 2W 5-7	48.55	2.532	0.282	1.50	2.33	0.010	34.86
6H 2W 15-17	48.65	2.536	0.663	1.50	2.33	0.023	16.67
6H 2W 35-37	48.85	2.545	0.321	1.50	2.33	0.011	30.43
6H 2W 45-47	48.95	2.549	0.192	1.50	2.33	0.007	29.10
6H 2W 55-57	49.05	2.553	0.000	1.50	2.33	0.000	27.68
6H 2W 65-67	49.15	2.557	0.313	1.50	2.33	0.011	29.00
6H 2W 85-87	49.35	2.566	0.682	1.50	2.33	0.024	25.15
6H 2W 95-97	49.45	2.570	0.690	1.50	2.33	0.024	35.50
6H 2W 105-107	49.55	2.575	0.968	1.50	2.33	0.034	24.66
6H 2W 115-117	49.65	2.579	1.090	1.50	2.33	0.038	30.12
6H 2W 125-127	49.75	2.583	0.386	1.50	3.29	0.019	23.38
6H 2W 135-137	49.85	2.586	0.628	1.50	3.29	0.031	23.24
6H 2W 145-147	49.95	2.589	0.746	1.50	3.29	0.037	23.24
6H 3W 5-7	50.05	2.592	1.047	1.51	3.29	0.052	19.89
6H 3W 15-17	50.15	2.595	0.487	1.51	3.29	0.024	27.75
6H 3W 25-27	50.25	2.598	1.455	1.51	3.29	0.073	27.75
6H 3W 35-37	50.35	2.601	0.000	1.51	3.29	0.000	29.03
6H 3W 45-47	50.45	2.604	1.256	1.51	3.29	0.063	19.14
6H 3W 55-57	50.55	2.607	0.718	1.51	3.29	0.036	22.78
6H 3W 65-67	50.65	2.610	0.211	1.51	3.29	0.011	34.78
6H 3W 85-87	50.85	2.616	0.269	1.51	3.29	0.013	28.04
6H 3W 95-97	50.95	2.619	0.168	1.51	3.29	0.008	32.30
6H 3W 105-107	51.05	2.622	0.877	1.51	3.29	0.044	26.06

6H 3W 115-117	51.15	2.625	0.572	1.51	3.29	0.029	21.43
6H 3W 125-127	51.25	2.628	0.679	1.51	3.29	0.034	27.87
6H 3W 135-137	51.35	2.631	0.249	1.51	3.29	0.012	25.64
6H 3W 145-147	51.45	2.634	0.235	1.51	3.29	0.012	26.10
6H 4W 5-7	51.55	2.637	0.358	1.51	3.29	0.018	18.86
6H 4W 15-17	51.65	2.640	0.640	1.51	3.29	0.032	28.91
6H 4W 25-27	51.75	2.643	0.656	1.49	3.29	0.032	28.86
6H 4W 35-37	51.85	2.646	1.051	1.49	3.29	0.051	26.60
6H 4W 45-47	51.95	2.649	0.792	1.49	3.29	0.039	36.30
6H 4W 55-57	52.05	2.652	1.380	1.49	3.29	0.068	28.99
6H 4W 65-67	52.15	2.655	0.764	1.49	3.29	0.037	28.96
6H 4W 85-87	52.35	2.661	0.117	1.49	3.29	0.006	25.08
6H 4W 95-97	52.45	2.665	0.111	1.49	3.29	0.005	19.34
6H 4W 105-107	52.55	2.668	0.138	1.49	3.29	0.007	28.93
6H 4W 115-117	52.65	2.671	0.180	1.49	3.29	0.009	33.33
6H 4W 135-137	52.85	2.677	0.362	1.49	3.29	0.018	28.80
6H 4W 145-147	52.95	2.680	0.807	1.49	3.29	0.039	30.11
6H 5W 5-7	53.05	2.683	0.658	1.49	3.29	0.032	29.88
6H 5W 15-17	53.15	2.686	1.249	1.49	3.29	0.061	35.25
6H 5W 25-27	53.25	2.689	0.867	1.49	3.29	0.042	27.60
6H 5W 35-37	53.35	2.692	0.924	1.55	3.29	0.047	37.13
6H 5W 45-47	53.45	2.695	0.938	1.55	3.29	0.048	28.32
6H 5W 55-57	53.55	2.698	1.051	1.55	3.29	0.054	26.60
6H 5W 65-67	53.65	2.701	0.202	1.55	3.29	0.010	17.85
6H 5W 85-87	53.85	2.707	1.260	1.55	3.29	0.064	19.33
6H 5W 95-97	53.95	2.710	0.755	1.55	3.29	0.039	27.04
6H 5W 105-107	54.05	2.713	0.534	1.55	3.29	0.027	26.01
6H 5W 115-117	54.15	2.716	0.487	1.55	3.29	0.025	25.04
6H 5W 125-127	54.25	2.719	0.380	1.55	3.29	0.019	34.13
6H 5W 135-137	54.35	2.722	0.537	1.55	3.29	0.027	34.13
6H 5W 145-147	54.45	2.725	0.501	1.61	3.29	0.027	35.06
6H 6W 5-7	54.55	2.728	1.053	1.61	3.29	0.056	21.44
6H 6W 15-17	54.65	2.731	0.586	1.61	3.29	0.031	19.16
6H 6W 25-27	54.75	2.734	0.194	1.61	3.29	0.010	28.66
6H 6W 35-37	54.85	2.737	0.757	1.61	3.29	0.040	21.52
6H 6W 45-47	54.95	2.740	0.557	1.61	3.29	0.030	22.13
6H 6W 55-57	55.05	2.743	0.305	1.61	3.29	0.016	15.99
6H CC 5-7	56.555	2.789	1.023	1.56	3.29	0.053	24.40
7H 1W 15-17	56.65	2.792	0.853	1.56	3.29	0.044	31.32
6H CC 15-17	56.655	2.792	1.476	1.52	3.29	0.074	19.08
7H 1W 25-27	56.75	2.795	1.551	1.52	3.29	0.078	35.24
7H 1W 35-37	56.85	2.798	1.039	1.52	3.29	0.052	26.12
7H 1W 45-47	56.95	2.801	1.677	1.52	3.29	0.084	41.40
7H 1W 55-57	57.05	2.804	2.946	1.52	3.29	0.148	26.83
7H 1W 65-67	57.15	2.807	1.943	1.52	3.29	0.097	33.70
7H 1W 75-77	57.25	2.810	1.487	1.52	3.29	0.074	31.85
7H 1W 85-87	57.35	2.813	0.594	1.52	3.29	0.030	42.77
7H 1W 95-97	57.45	2.816	0.490	1.52	3.29	0.025	33.78
7H 1W 105-107	57.55	2.819	0.792	1.52	3.29	0.040	34.62
7H 1W 115-117	57.65	2.822	2.066	1.52	3.29	0.103	29.33
7H 1W 125-127	57.75	2.825	0.993	1.52	3.29	0.050	37.22
7H 1W 135-137	57.85	2.829	1.188	1.52	3.29	0.059	27.79
7H 1W 145-147	57.95	2.832	0.725	1.52	3.29	0.036	39.07
7H 2W 5-7	58.05	2.835	0.568	1.52	3.29	0.028	34.14

7H 2W 25-27	58.25	2.841	0.282	1.48	3.29	0.014	35.20
7H 2W 35-37	58.35	2.844	0.262	1.48	3.29	0.013	25.55
7H 2W 45-47	58.45	2.847	0.593	1.48	3.29	0.029	36.78
7H 2W 55-57	58.55	2.850	0.634	1.48	3.29	0.031	35.02
7H 2W 65-67	58.65	2.853	1.108	1.48	3.29	0.054	39.24
7H 2W 75-77	58.75	2.856	0.848	1.48	3.29	0.041	26.62
7H 2W 85-87	58.85	2.859	0.790	1.48	3.29	0.039	42.50
7H 2W 95-97	58.95	2.862	0.385	1.48	3.29	0.019	32.76
7H 2W 105-107	59.05	2.865	0.323	1.48	3.29	0.016	41.98
7H 2W 115-117	59.15	2.868	0.259	1.48	3.29	0.013	34.19
7H 2W 125-127	59.25	2.871	0.948	1.48	3.29	0.046	38.89
7H 2W 135-137	59.35	2.874	0.928	1.48	3.29	0.045	27.59
7H 2W 145-147	59.45	2.877	0.670	1.48	3.29	0.033	39.02
7H 3W 5-7	59.55	2.880	0.400	1.48	3.29	0.019	25.74
7H 3W 15-17	59.65	2.883	0.368	1.48	3.29	0.018	27.93
7H 3W 25-27	59.75	2.886	0.202	1.48	3.29	0.010	21.89
7H 3W 35-37	59.85	2.889	0.247	1.48	3.29	0.012	25.73
7H 3W 45-47	59.95	2.892	0.316	1.48	3.29	0.015	30.13
7H 3W 55-57	60.05	2.895	0.280	1.53	3.29	0.014	23.03
7H 3W 65-67	60.15	2.898	0.000	1.53	3.29	0.000	23.03
7H 3W 85-87	60.35	2.904	0.356	1.53	3.29	0.018	25.80
7H 3W 95-97	60.45	2.907	0.478	1.53	3.29	0.024	12.20
7H 3W 105-107	60.55	2.911	0.213	1.53	3.29	0.011	27.78
7H 3W 115-117	60.65	2.914	0.433	1.53	3.29	0.022	27.78
7H 3W 125-127	60.75	2.917	0.421	1.53	3.29	0.021	12.97
7H 3W 135-137	60.85	2.920	0.178	1.53	3.29	0.009	16.88
7H 3W 145-147	60.95	2.923	0.128	1.53	3.29	0.006	22.80
7H 4W 5-7	61.05	2.926	0.337	1.53	3.29	0.017	20.25
7H 4W 25-27	61.25	2.932	0.080	1.55	3.29	0.004	17.44
7H 4W 35-37	61.35	2.935	0.087	1.55	3.29	0.004	17.44
7H 4W 45-47	61.45	2.938	0.000	1.55	3.29	0.000	23.60
7H 4W 55-57	61.55	2.941	0.169	1.55	3.29	0.009	45.51
7H 4W 65-67	61.65	2.944	0.928	1.55	3.29	0.047	35.50
7H 4W 75-77	61.75	2.947	1.182	1.55	3.29	0.060	26.22
7H 4W 85-87	61.85	2.950	0.111	1.55	3.29	0.006	36.77
7H 4W 95-97	61.95	2.953	0.171	1.55	3.29	0.009	30.92
7H 4W 105-107	62.05	2.956	0.658	1.55	3.29	0.034	38.01
7H 4W 115-117	62.15	2.959	0.452	1.55	3.29	0.023	30.83
7H 4W 125-127	62.25	2.962	2.196	1.55	3.29	0.112	44.72
7H 4W 135-137	62.35	2.965	2.512	1.55	3.29	0.128	31.51
7H 4W 145-147	62.45	2.968	0.565	1.55	3.29	0.029	35.47
7H 5W 5-7	62.55	2.971	0.311	1.59	3.29	0.016	26.58
7H 5W 15-17	62.65	2.974	0.376	1.59	3.29	0.020	35.80
7H 5W 25-27	62.75	2.977	0.738	1.59	3.29	0.039	33.48
7H 5W 35-37	62.85	2.980	0.668	1.59	3.29	0.035	39.63
7H 5W 45-47	62.95	2.983	0.187	1.59	3.29	0.010	31.59
7H 5W 55-57	63.05	2.986	0.544	1.59	3.29	0.028	27.96
7H 5W 65-67	63.15	2.989	0.624	1.59	3.29	0.033	27.96
7H 5W 75-77	63.25	2.993	0.952	1.59	3.29	0.050	21.89
7H 5W 85-87	63.35	2.996	0.750	1.59	3.29	0.039	20.80
7H 5W 95-97	63.45	2.999	0.311	1.59	3.29	0.016	21.93
7H 5W 105-107	63.55	3.002	0.162	1.59	3.29	0.008	21.93
7H 5W 115-117	63.65	3.005	0.232	1.59	3.29	0.012	20.11
7H 5W 125-127	63.75	3.008	0.126	1.59	3.29	0.007	21.99

7H 5W 135-137	63.85	3.011	0.140	1.59	3.29	0.007	26.28
7H 5W 145-147	63.95	3.014	0.102	1.49	3.29	0.005	14.29
7H 6W 5-7	64.05	3.017	0.000	1.49	3.29	0.000	18.64
7H 6W 15-17	64.15	3.020	0.635	1.49	3.29	0.031	23.36
7H 6W 25-27	64.25	3.023	0.053	1.49	3.29	0.003	15.89
7H 6W 35-37	64.35	3.026	0.278	1.49	3.29	0.014	29.22
7H 6W 45-47	64.45	3.029	0.214	1.49	3.29	0.011	33.44
7H 6W 55-57	64.55	3.032	0.122	1.49	3.29	0.006	33.44
7H 6W 65-67	64.65	3.034	0.610	1.49	2.56	0.023	40.91
7H 6W 75-77	64.75	3.037	0.525	1.49	2.56	0.020	33.04
7H 6W 85-87	64.85	3.039	0.144	1.49	2.56	0.005	36.85
7H 6W 95-97	64.95	3.042	0.191	1.49	2.56	0.007	25.73
7H 6W 105-107	65.05	3.044	0.403	1.52	2.56	0.016	36.59
7H 6W 115-117	65.15	3.047	0.335	1.52	2.56	0.013	29.51
7H 6W 125-127	65.25	3.049	0.187	1.52	2.56	0.007	32.26
7H 6W 135-137	65.35	3.052	1.040	1.52	2.56	0.041	28.92
7H 6W 145-147	65.45	3.054	0.896	1.52	2.56	0.035	33.91
7H 7W 8-10	65.58	3.057	0.927	1.52	2.56	0.036	17.04
7H 7W 15-17	65.65	3.059	0.617	1.52	2.56	0.024	29.14
7H 7W 25-27	65.75	3.061	0.622	1.52	2.56	0.024	45.95
7H 7W 35-37	65.85	3.064	1.092	1.52	2.56	0.043	21.98
7H 7W 45-47	65.95	3.066	1.365	1.52	2.56	0.053	21.98
7H 7W 55-57	66.05	3.069	1.075	1.52	2.56	0.042	26.79
8H 1W 15-17	66.15	3.071	0.517	1.56	2.56	0.021	25.32
8H 1W 25-27	66.25	3.074	1.021	1.56	2.56	0.041	13.95
7H CC 20-22	66.35	3.076	0.501	1.56	2.56	0.020	13.95
8H 1W 45-47	66.45	3.079	1.011	1.56	2.56	0.040	18.71
8H 1W 65-67	66.65	3.084	0.110	1.56	2.56	0.004	19.88
8H 1W 75-77	66.75	3.086	0.155	1.56	5.46	0.013	17.47
8H 1W 85-87	66.85	3.089	0.062	1.56	5.46	0.005	20.69
8H 1W 105-107	67.05	3.093	0.000	1.56	5.46	0.000	11.61
8H 1W 125-127	67.25	3.098	0.131	1.59	5.46	0.011	24.34
8h 1W 145-147	67.45	3.103	0.000	1.59	5.46	0.000	32.56
8H 2W 5-7	67.56	3.106	0.000	1.59	5.46	0.000	21.35
8H 2W 15-17	67.66	3.108	0.233	1.59	5.46	0.020	23.08
8H 2W 35-37	67.86	3.113	0.168	1.59	5.46	0.015	21.43
8H 2W 45-47	67.96	3.116	0.535	1.59	5.46	0.047	33.13
8H 2W 55-57	68.06	3.118	0.189	1.59	5.46	0.016	34.12
8H 2W 75-77	68.26	3.123	0.054	1.59	5.46	0.005	21.57
8H 2W 85-87	68.36	3.126	0.112	1.59	5.46	0.010	22.10
8H 2W 95-97	68.46	3.128	0.026	1.59	5.46	0.002	22.10
8H 2W 115-117	68.66	3.133	0.113	1.59	5.46	0.010	39.20
8H 2W 125-127	68.76	3.135	0.000	1.59	5.46	0.000	29.49
8H 2W 135-137	68.86	3.138	0.104	1.47	5.46	0.008	29.49
8H 3W 5-7	69.06	3.143	0.097	1.47	5.46	0.008	27.86
8H 3W 15-17	69.16	3.145	0.183	1.47	5.46	0.015	15.21
8H 3W 25-27	69.26	3.148	0.000	1.47	5.46	0.000	9.67
8H 3W 45-47	69.46	3.153	0.322	1.47	5.46	0.026	28.61
8H 3W 55-57	69.56	3.155	0.157	1.47	5.46	0.013	20.50
8H 3W 65-67	69.66	3.158	0.165	1.47	5.46	0.013	22.41
8H 3W 85-87	69.86	3.163	0.568	1.47	5.46	0.046	31.20
8H 3W 95-97	69.96	3.165	0.563	1.47	5.46	0.045	32.92
8H 3W 107-109	70.08	3.168	0.239	1.47	5.46	0.019	25.10
8H 3W 115-117	70.16	3.170	0.415	1.47	5.46	0.033	28.26

8H 3W 125-127	70.26	3.172	0.299	1.47	5.46	0.024	26.67
8H 3W 135-137	70.36	3.175	0.116	1.47	5.46	0.009	22.19
8H 3W 145-147	70.46	3.177	0.332	1.55	5.46	0.028	22.19
8H 4W 5-7	70.56	3.180	0.090	1.55	5.46	0.008	19.88
8H 4W 15-17	70.66	3.182	0.086	1.55	5.46	0.007	19.75
8H 4W 25-27	70.76	3.185	0.282	1.55	5.46	0.024	19.75
8H 4W 35-37	70.86	3.187	0.000	1.55	5.46	0.000	23.26
8H 4W 45-47	70.96	3.190	0.959	1.55	5.46	0.081	25.53
8H 4W 55-57	71.06	3.192	0.573	1.55	5.46	0.048	15.14
8H 4W 65-67	71.16	3.194	0.087	1.55	5.46	0.007	27.27
8H 4W 75-77	71.26	3.197	0.388	1.55	5.46	0.033	27.27
8H 4W 85-87	71.36	3.199	0.123	1.55	5.46	0.010	34.38
8H 4W 95-97	71.46	3.202	0.115	1.55	5.46	0.010	27.78
8H 4W 105-107	71.56	3.204	0.237	1.55	5.46	0.020	27.15
8H 4W 115-117	71.66	3.207	0.000	1.55	5.46	0.000	33.55
8H 4W 125-127	71.76	3.211	0.985	1.55	2.32	0.035	30.34
8H 4W 135-137	71.86	3.215	0.903	1.49	2.32	0.031	33.12
8H 4W 145-147	71.96	3.220	0.200	1.49	2.32	0.007	26.64
8H 5W 5-7	72.06	3.224	0.027	1.49	2.32	0.001	38.10
8H 5W 15-17	72.16	3.228	0.062	1.49	2.32	0.002	38.32
8H 5W 25-27	72.26	3.232	0.088	1.49	2.32	0.003	32.96
8H 5W 35-37	72.36	3.237	0.000	1.49	2.32	0.000	30.36
8H 5W 45-47	72.46	3.241	0.408	1.49	2.32	0.014	40.88
8H 5W 55-57	72.56	3.245	0.366	1.49	2.32	0.013	33.77
8H 5W 65-67	72.66	3.250	0.357	1.49	2.32	0.012	37.58
8H 5W 75-77	72.76	3.254	0.433	1.49	2.32	0.015	35.91
8H 5W 85-87	72.86	3.258	0.462	1.49	2.32	0.016	39.47
8H 5W 95-97	72.96	3.263	0.612	1.49	2.32	0.021	41.85
8H 5W 105-107	73.06	3.267	0.669	1.49	2.32	0.023	29.64
8H 5W 115-117	73.16	3.271	0.301	1.49	2.32	0.010	29.64
8H 5W 125-127	73.26	3.276	1.091	1.49	2.32	0.038	28.59
8H 5W 135-137	73.36	3.280	0.919	1.49	2.32	0.032	28.59
8H 5W 145-147	73.46	3.284	1.025	1.49	2.32	0.035	33.73
8H 6W 5-7	73.57	3.289	0.534	1.49	2.32	0.018	34.70
8H 6W 15-17	73.67	3.293	0.656	1.49	2.32	0.023	34.32
8H 6W 25-27	73.77	3.298	0.422	1.49	2.32	0.015	33.54
8H 6W 35-37	73.87	3.302	0.406	1.49	2.32	0.014	35.90
8H 6W 45-47	73.97	3.306	0.597	1.49	2.32	0.021	28.83
8H 6W 65-67	74.17	3.315	0.076	1.49	2.32	0.003	49.02
8H 6W 75-77	74.27	3.319	0.000	1.49	2.32	0.000	49.02
8H 6W 85-87	74.37	3.324	1.694	1.49	2.32	0.059	23.90
8H 6W 95-97	74.47	3.328	0.055	1.49	2.32	0.002	23.90
8H 7W 5-7	74.58	3.335	0.789	1.49	1.10	0.013	23.03
8H 7W 15-17	74.68	3.345	0.000	1.49	1.10	0.000	35.46
8H 7W 25-27	74.78	3.354	0.000	1.49	1.10	0.000	34.13
8H 7W 35-37	74.88	3.363	0.000	1.49	1.10	0.000	40.15
8H 7W 45-47	74.98	3.372	0.380	1.49	1.10	0.006	40.15
8H 7W 55-57	75.08	3.381	0.577	1.40	1.10	0.009	33.92
9H 1W 15-17	75.65	3.433	0.655	1.40	1.10	0.010	26.49
9H 1W 25-27	75.75	3.442	0.960	1.40	1.10	0.015	26.49
9H 1W 35-37	75.85	3.451	1.207	1.40	1.10	0.019	43.42
9H 1W 45-47	75.95	3.460	1.656	1.40	1.10	0.026	43.42
9H 1W 55-57	76.05	3.469	0.518	1.40	1.10	0.008	47.37
9H 1W 65-67	76.15	3.478	0.876	1.40	1.10	0.014	47.33

9H 1W 75-77	76.25	3.487	1.479	1.40	1.10	0.023	47.34
9H 1W 85-87	76.35	3.496	0.559	1.40	1.10	0.009	46.45
9H 1W 95-97	76.45	3.505	0.394	1.40	1.10	0.006	47.37
9H 1W 105-107	76.55	3.514	0.618	1.40	1.10	0.010	47.03
9H 1W 115-117	76.65	3.523	0.190	1.40	1.10	0.003	48.73
9H 1W 125-127	76.75	3.532	0.104	1.40	1.10	0.002	62.21
9H 1W 135-137	76.85	3.542	0.416	1.40	1.10	0.006	42.05
9H 1W 145-147	76.95	3.551	1.018	1.46	1.10	0.016	42.05
9H 2W 5-7	77.05	3.560	0.993	1.46	1.10	0.016	

9H 5W 45-47	81.95	3.714	0.762	1.64	3.81	0.048	23.51
9H 5W 55-57	82.05	3.717	0.501	1.64	3.81	0.031	27.17
9H 5W 65-67	82.15	3.719	0.000	1.64	3.81	0.000	23.44
9H 5W 75-77	82.25	3.722	0.000	1.64	3.81	0.000	42.17
9H 5W 85-87	82.35	3.724	0.032	1.64	3.81	0.002	17.37
9H 5W 95-97	82.45	3.727	0.141	1.64	3.81	0.009	21.59
9H 5W 115-117	82.65	3.732	0.204	1.64	3.81	0.013	28.48
9H 5W 125-127	82.75	3.735	0.000	1.64	3.81	0.000	19.23
9H 5W 135-137	82.85	3.738	0.042	1.64	3.81	0.003	26.01
9H 5W 145-147	82.95	3.740	0.061	1.64	3.81	0.004	15.34
9H 6W 5-7	83.05	3.743	0.486	1.64	3.81	0.030	28.99
9H 6W 15-17	83.15	3.745	0.141	1.64	3.81	0.009	21.38
9H 6W 25-27	83.25	3.748	0.278	1.64	3.81	0.017	21.46
9H 6W 35-37	83.35	3.751	0.217	1.64	3.81	0.014	21.46
9H 6W 45-47	83.45	3.753	0.170	1.64	3.81	0.011	29.12
9H 6W 55-57	83.55	3.756	3.750	1.64	3.81	0.235	29.12
9H 6W 65-67	83.65	3.759	0.000	1.64	3.81	0.000	21.05
9H 6W 75-77	83.75	3.761	0.073	1.64	3.81	0.005	21.05
9H 6W 95-97	83.95	3.766	0.085	1.64	3.81	0.005	20.86
9H 6W 105-107	84.05	3.769	0.000	1.64	3.81	0.000	20.25
9H 6W 115-117	84.15	3.772	0.000	1.64	3.81	0.000	44.38
9H 6W 125-127	84.25	3.774	0.150	1.64	3.81	0.009	41.88
9H 6W 135-137	84.35	3.777	0.424	1.64	3.81	0.027	44.13
9H 6W 145-147	84.45	3.780	0.702	1.64	3.81	0.044	32.45
9H 7W 5-7	84.55	3.782	1.197	1.64	3.81	0.075	20.73
9H 7W 15-17	84.65	3.785	1.054	1.63	3.81	0.066	26.92
9H 7W 25-27	84.75	3.787	1.259	1.63	3.81	0.078	32.58
9H 7W 55-57	85.05	3.795	0.000	1.63	3.81	0.000	21.69
10H 1W 15-17	85.15	3.798	0.000	1.63	3.81	0.000	34.83
10H 1W 25-27	85.25	3.801	0.000	1.63	3.81	0.000	20.77
10H 1W 35-37	85.35	3.803	0.039	1.63	3.81	0.002	20.77
10H 1W 45-47	85.45	3.806	0.370	1.63	3.81	0.023	27.85
10H 1W 55-57	85.55	3.808	0.465	1.63	3.81	0.029	27.85
10H 1W 65-67	85.65	3.811	0.163	1.63	3.81	0.010	21.51
10H 1W 75-77	85.75	3.814	0.209	1.63	3.81	0.013	20.34
10H 1W 85-87	85.85	3.816	0.201	1.63	3.81	0.012	14.94
10H 1W 95-97	85.95	3.819	0.656	1.63	3.81	0.041	17.42
10H 1W 105-107	86.05	3.821	0.414	1.63	3.81	0.026	29.14
10H 1W 115-117	86.15	3.824	0.785	1.63	3.81	0.049	28.90
10H 1W 125-127	86.25	3.827	0.075	1.58	3.81	0.005	18.23
10H 1W 135-137	86.35	3.829	0.386	1.58	3.81	0.023	18.23
10H 1W 145-147	86.45	3.832	0.092	1.58	3.81	0.006	15.56
10H 2W 5-7	86.55	3.835	0.952	1.58	3.81	0.057	25.56
10H 2W 15-17	86.65	3.837	0.080	1.58	3.81	0.005	22.99
10H 2W 25-27	86.75	3.840	0.111	1.58	3.81	0.007	22.99
10H 2W 35-37	86.85	3.842	0.103	1.58	3.81	0.006	29.48
10H 2W 45-47	86.95	3.845	0.118	1.58	3.81	0.007	29.48
10H 2W 55-57	87.05	3.848	0.108	1.58	3.81	0.006	17.65
10H 2W 65-67	87.15	3.850	0.000	1.58	3.81	0.000	27.81
10H 2W 75-77	87.25	3.853	0.000	1.58	3.81	0.000	26.04
10H 2W 85-87	87.35	3.856	0.000	1.58	3.81	0.000	34.08
10H 2W 95-97	87.45	3.858	0.149	1.58	3.81	0.009	18.63
10H 2W 105-107	87.55	3.861	0.080	1.58	3.81	0.005	24.44
10H 2W 125-127	87.75	3.866	0.000	1.61	3.81	0.000	23.33

10H 2W 135-137	87.85	3.869	0.222	1.61	3.81	0.014	23.46
10H 2W 145-147	87.95	3.871	0.000	1.61	3.81	0.000	28.66
10H 3W 5-7	88.05	3.874	0.275	1.61	3.81	0.017	32.45
10H 3W 15-17	88.15	3.877	0.457	1.61	3.81	0.028	41.40
10H 3W 25-27	88.25	3.879	0.740	1.61	3.81	0.045	33.33
10H 3W 35-37	88.35	3.882	1.274	1.61	3.81	0.078	27.06
10H 3W 45-47	88.45	3.884	0.391	1.61	3.81	0.024	26.14
10H 3W 55-57	88.55	3.887	0.211	1.61	3.81	0.013	26.14
10H 3W 65-67	88.65	3.890	0.717	1.61	3.81	0.044	20.96
10H 3W 75-77	88.75	3.892	0.000	1.61	3.81	0.000	18.50
10H 3W 85-87	88.85	3.895	0.329	1.61	3.81	0.020	28.99
10H 3W 95-97	88.95	3.898	0.499	1.61	3.81	0.031	28.99
10H 3W 115-117	89.15	3.903	0.045	1.61	3.81	0.003	25.58
10H 3W 125-127	89.25	3.905	0.000	1.61	3.81	0.000	25.58
10H 3W 135-137	89.35	3.908	0.525	1.61	3.81	0.032	48.02
10H 3W 145-147	89.45	3.911	0.076	1.58	3.81	0.005	24.86
10H 4W 5-7	89.55	3.913	0.000	1.58	3.81	0.000	34.57
10H 4W 15-17	89.65	3.916	0.043	1.58	3.81	0.003	24.29
10h 4W 25-27	89.75	3.919	0.000	1.58	3.81	0.000	37.11
10H 4W 35-37	89.85	3.921	0.000	1.58	3.81	0.000	27.67
10H 4W 45-47	89.95	3.924	0.000	1.58	3.81	0.000	32.08
10H 4W 55-57	90.05	3.926	0.168	1.58	3.81	0.010	32.08
10H 4W 65-67	90.15	3.929	0.000	1.58	3.81	0.000	27.59
10H 4W 75-77	90.25	3.932	0.000	1.58	3.81	0.000	22.70
10H 4W 85-87	90.35	3.934	0.000	1.58	3.81	0.000	18.93
10H 4W 95-97	90.45	3.937	0.000	1.58	3.81	0.000	28.85
10H 4W 105-107	90.55	3.939	0.057	1.58	3.81	0.003	28.85
10H 4W 115-117	90.65	3.942	0.000	1.58	3.81	0.000	23.72
10H 4W 125-127	90.75	3.945	0.149	1.58	3.81	0.009	24.20
10H 4W 135-137	90.85	3.947	0.397	1.58	3.81	0.024	40.74
10H 4W 145-147	90.95	3.950	0.179	1.58	3.81	0.011	44.25
10H 5W 5-7	91.05	3.953	0.099	1.42	3.81	0.005	47.40
10H 5W 15-17	91.15	3.955	0.259	1.42	3.81	0.014	44.97
10H 5W 25-27	91.25	3.958	0.187	1.42	3.81	0.010	48.37
10H 5W 35-37	91.35	3.960	0.203	1.42	3.81	0.011	47.09
10H 5W 45-47	91.45	3.963	0.447	1.42	3.81	0.024	47.93
10H 5W 55-57	91.55	3.966	0.233	1.42	3.81	0.013	37.28
10H 5W 65-67	91.65	3.968	0.485	1.42	3.81	0.026	39.53
10H 5W 75-77	91.75	3.971	0.455	1.42	3.81	0.025	43.14
10H 5W 85-87	91.85	3.974	0.468	1.42	3.81	0.025	39.63
10H 5W 95-97	91.95	3.976	0.916	1.42	3.81	0.050	42.17
10H 5W 105-107	92.05	3.979	1.786	1.42	3.81	0.097	37.27
10H 5W 115-117	92.15	3.981	0.311	1.42	3.81	0.017	40.25
10H 5W 125-127	92.25	3.984	0.464	1.42	3.81	0.025	38.10
10H 5W 135-137	92.35	3.987	0.368	1.42	3.81	0.020	37.21
10H 5W 145-147	92.45	3.989	0.444	1.42	3.81	0.024	35.54
10H 6W 5-7	92.55	3.992	0.274	1.40	3.81	0.015	35.54
10H 6W 15-17	92.65	3.995	0.360	1.40	3.81	0.019	38.71
10H 6W 25-27	92.75	3.997	0.113	1.40	3.81	0.006	39.66
10H 6W 45-47	92.95	4.002	0.385	1.40	3.81	0.021	47.10
10H 6W 55-57	93.05	4.005	0.536	1.40	3.81	0.029	45.06
10H 6W 75-77	93.25	4.010	1.303	1.40	3.81	0.070	35.33
10H 6W 85-87	93.35	4.013	0.572	1.40	3.81	0.031	38.04
10H 6W 95-97	93.45	4.016	0.073	1.40	3.81	0.004	31.61

10H 6W 105-107	93.55	4.018	0.132	1.40	3.81	0.007	32.69
10H 6W 125-127	93.75	4.023	0.644	1.30	3.81	0.032	43.56
10H 6W 135-137	93.85	4.026	0.094	1.30	3.81	0.005	52.63
10H 6W 145-147	93.95	4.029	0.176	1.30	3.81	0.009	48.81
10H 7W 5-7	94.05	4.031	0.222	1.30	3.81	0.011	46.15
10H 7W 15-17	94.15	4.034	0.077	1.30	3.81	0.004	49.38
10H 7W 25-27	94.25	4.036	0.131	1.30	3.81	0.006	46.71
10H 7W 35-37	94.35	4.039	0.196	1.30	3.81	0.010	42.77
10H 7W 45-47	94.45	4.042	0.402	1.30	3.81	0.020	41.04
10H 7W 55-57	94.55	4.044	0.637	1.30	3.81	0.031	31.76
11H 1W 7-9	94.57	4.045	0.324	1.30	3.81	0.016	30.52
11H 1W 15-17	94.65	4.047	0.204	1.30	3.81	0.010	34.71
10H 7W 67-69	94.67	4.048	0.384	1.30	3.81	0.019	39.51
11H 1W 25-27	94.75	4.050	0.859	1.30	3.81	0.042	24.26
10H CC 5-7	94.8	4.051	0.306	1.70	3.81	0.020	31.49
11H 1W 35-37	94.85	4.052	0.125	1.70	3.81	0.008	33.33
10H CC 15-17	94.9	4.054	0.110	1.70	3.81	0.007	29.65
11H 1W 45-47	94.95	4.055	0.634	1.70	3.81	0.041	28.30
11H 1W 55-57	95.05	4.057	0.895	1.70	3.81	0.058	28.29
11H 1W 65-67	95.15	4.060	0.572	1.70	3.81	0.037	22.08
11H 1W 75-77	95.25	4.063	0.344	1.70	3.81	0.022	27.27
11H 1W 85-87	95.35	4.065	0.128	1.70	3.81	0.008	24.85
11H 1W 95-96	95.45	4.068	0.257	1.70	3.81	0.017	24.85
11H 1W 105-107	95.55	4.071	0.177	1.70	3.81	0.011	20.90
11H 1W 115-117	95.65	4.073	0.079	1.70	3.81	0.005	19.05
11H 1W 125-127	95.75	4.076	0.027	1.70	3.81	0.002	37.13
11H 1W 135-137	95.85	4.078	0.000	1.70	3.81	0.000	20.21
11H 1W 145-147	95.95	4.081	0.137	1.62	3.81	0.008	20.21
11H 2W 5-7	96.05	4.084	0.067	1.62	3.81	0.004	19.62
11H 2W 15-17	96.15	4.086	0.304	1.62	3.81	0.019	26.22
11H 2W 25-27	96.25	4.089	0.087	1.62	3.81	0.005	18.90
11H 2W 35-37	96.35	4.092	0.000	1.62	3.81	0.000	24.85
11H 2W 45-47	96.45	4.094	0.305	1.62	3.81	0.019	14.72
11H 2W 55-57	96.55	4.097	0.218	1.62	3.81	0.013	26.70
11H 2W 65-67	96.65	4.099	0.257	1.62	3.81	0.016	31.10
11H 2W 75-77	96.75	4.102	0.158	1.62	3.81	0.010	28.22
11H 2W 85-87	96.85	4.105	0.194	1.62	3.81	0.012	13.26
11H 2W 95-97	96.95	4.107	0.157	1.62	3.81	0.010	27.53
11H 2W 105-107	97.05	4.110	0.404	1.62	3.81	0.025	16.48
11H 2W 115-117	97.15	4.113	0.029	1.62	3.81	0.002	24.01
11H 2W 125-127	97.25	4.115	0.000	1.62	3.81	0.000	17.71
11H 2W 145-147	97.45	4.120	0.118	1.66	3.81	0.007	20.00
11H 3W 5-7	97.55	4.123	0.024	1.66	3.81	0.002	23.60
11H 3W 15-17	97.65	4.126	0.054	1.66	3.81	0.003	18.01
11H 3W 25-27	97.75	4.128	0.080	1.66	3.81	0.005	38.04
11H 3W 35-37	97.85	4.131	0.051	1.66	3.81	0.003	27.90
11H 3W 45-47	97.95	4.134	0.080	1.66	3.81	0.005	27.90
11H 3W 55-57	98.05	4.136	0.137	1.66	3.81	0.009	14.46
11H 3W 65-67	98.15	4.139	0.018	1.66	3.81	0.001	51.98
11H 3W 75-77	98.25	4.141	0.388	1.66	3.81	0.025	15.38
11H 3W 85-87	98.35	4.144	0.000	1.66	3.81	0.000	38.29
11H 3W 95-97	98.45	4.147	1.401	1.66	3.81	0.089	21.71
11H 3W 105-107	98.55	4.149	0.769	1.66	3.81	0.049	28.21
11H 3W 115-117	98.65	4.152	0.527	1.66	3.81	0.033	19.21

11H 3W 125-127	98.75	4.154	0.297	1.66	3.81	0.019	26.83
11H 3W 135-137	98.85	4.157	0.075	1.66	3.81	0.005	26.93
11H 3W 145-147	98.95	4.160	0.376	1.66	3.81	0.024	23.46
11H 4W 5-7	99.05	4.162	0.195	1.66	3.81	0.012	23.46
11H 4W 15-17	99.15	4.165	0.086	1.64	3.81	0.005	25.54
11H 4W 25-27	99.25	4.168	0.285	1.64	3.81	0.018	24.00
11H 4W 35-37	99.35	4.170	0.058	1.64	3.81	0.004	31.21
11H 4W 45-47	99.45	4.173	0.090	1.64	3.81	0.006	25.61
11H 4W 55-57	99.55	4.175	0.149	1.64	3.81	0.009	25.18
11H 4W 65-67	99.65	4.178	0.418	1.64	3.81	0.026	21.12
11H 4W 75-77	99.75	4.181	0.219	1.64	3.81	0.014	28.81
11H 4W 85-87	99.85	4.183	0.459	1.64	3.81	0.029	21.55
11H 4W 95-97	99.95	4.186	0.547	1.64	3.81	0.034	24.15
11H 4W 105-107	100.05	4.190	0.429	1.64	2.18	0.015	22.16
11H 4W 115-117	100.15	4.194	0.299	1.64	2.18	0.011	31.61
11H 4W 125-127	100.25	4.199	0.252	1.64	2.18	0.009	23.23
11H 4W 135-137	100.35	4.203	0.998	1.64	2.18	0.036	29.58
11H 4W 145-147	100.45	4.208	0.605	1.64	2.18	0.022	34.37
11H 5W 5-7	100.55	4.213	1.829	1.64	2.18	0.065	35.67
11H 5W 15-17	100.65	4.217	1.731	1.46	2.18	0.055	36.71
11H 5W 25-27	100.75	4.222	0.355	1.46	2.18	0.011	29.86
11H 5W 35-37	100.85	4.226	1.124	1.46	2.18	0.036	33.92
11H 5W 45-47	100.95	4.231	1.764	1.46	2.18	0.056	40.00
11H 5W 55-57	101.05	4.236	0.834	1.46	2.18	0.027	40.00
11H 5W 65-67	101.15	4.240	0.653	1.46	2.18	0.021	29.61
11H 5W 75-77	101.25	4.245	0.975	1.46	2.18	0.031	35.22
11H 5W 85-87	101.35	4.249	0.428	1.46	2.18	0.014	33.33
11H 5W 95-97	101.45	4.254	1.333	1.46	2.18	0.043	28.74
11H 5W 105-107	101.55	4.258	1.229	1.46	2.18	0.039	19.85
11H 5W 115-117	101.65	4.263	0.865	1.46	2.18	0.028	27.61
11H 5W 125-127	101.75	4.268	0.045	1.46	2.18	0.001	27.61
11H 5W 135-137	101.85	4.272	0.443	1.46	2.18	0.014	28.09
11H 5W 145-147	101.95	4.277	0.144	1.46	2.18	0.005	28.09
11H 6W 5-7	102.05	4.281	0.284	1.48	2.18	0.009	27.93
11H 6W 15-17	102.15	4.286	0.580	1.48	2.18	0.019	30.82
11H 6W 25-27	102.25	4.291	0.987	1.48	2.18	0.032	29.14
11H 6W 35-37	102.35	4.295	0.638	1.48	2.18	0.021	21.43
11H 6W 45-47	102.45	4.300	0.470	1.48	2.18	0.015	38.15
11H 6W 55-57	102.55	4.304	0.551	1.48	2.18	0.018	38.15
11H 6W 65-67	102.65	4.309	0.628	1.48	2.18	0.020	25.70
11H 6W 75-77	102.75	4.313	0.457	1.48	2.18	0.015	15.86
11H 6W 85-87	102.85	4.318	0.328	1.48	2.18	0.011	30.39
11H 6W 95-97	102.95	4.323	0.372	1.48	2.18	0.012	31.36
11H 6W 105-105	103.05	4.327	0.451	1.48	2.18	0.015	31.36
11H 6W 115-117	103.15	4.332	0.330	1.48	2.18	0.011	19.35
11H 6W 125-127	103.25	4.336	0.461	1.48	2.18	0.015	30.49
11H 6W 135-137	103.35	4.341	0.845	1.48	2.18	0.027	28.66
11H 6W 145-147	103.45	4.346	1.063	1.48	2.18	0.034	34.97
11H 7W 5-7	103.55	4.350	0.684	1.48	2.18	0.022	23.66
11H 7W 15-17	103.65	4.355	0.423	1.48	2.18	0.014	28.90
11H 7W 28-30	103.78	4.361	0.431	1.48	2.18	0.014	36.00
11H 7W 38-40	103.88	4.365	0.822	1.48	2.18	0.027	31.37
11H 7W 48-50	103.98	4.370	0.394	1.48	2.18	0.013	31.84
11H 7W 58-60	104.08	4.374	0.643	1.48	2.18	0.021	31.84

11H CC 2-4	104.12	4.376	0.870	1.48	2.18	0.028	34.86
11H CC 8-10	104.18	4.379	0.823	1.48	2.18	0.027	38.36

Percent of fine grain material (<150μm) (see methods for silt clay μm boundary discussion), sorting (Folk and Ward, 1957) (very well sorted = < 1.27, well sorted = 1.27-1.41, moderately sorted = 1.41-2.00, poorly sorted = 2.00-4.00, very poorly sorted = 4.00-16.00), and lithofacies (D = diatom-rich/bearing mudstone; LC = massive to laminated mudstone)

Core, section, interval (cm)	Depth (mbsf)	Age (Ma)	Clay <8μm (vol. %)	Silt 8-63μm (vol. %)	Fine Sand 63-150μm (vol. %)	Sorting σ_G	Lithofacies
5H 1W 95-97	38.45	2.099	46.88	51.71	1.41	2.603	D
5H 1W 105-107	38.55	2.103	40.45	59.38	0.18	2.606	D
5H 1W 125-127	38.75	2.112	50.33	49.41	0.26	2.432	D
5H 1W 145-147	38.95	2.121	60.19	39.81	0.00	2.325	D
5H 2W 5-7	39.05	2.125	60.65	37.98	1.37	2.330	D
5H 2W 15-17	39.15	2.129	61.39	38.61	0.00	2.307	D
5H 2W 45-47	39.45	2.142	42.41	55.67	1.92	2.693	D
5H 2W 55-57	39.55	2.146	45.33	54.66	0.01	2.614	D
5H 2W 65-67	39.65	2.151	51.63	46.37	2.00	2.575	D
5H 2W 85-87	39.85	2.159	60.87	36.87	2.26	2.356	D
5H 2W 95-97	39.95	2.163	57.72	40.34	1.94	2.452	D
5H 2W 115-117	40.15	2.172	55.75	43.43	0.82	2.476	D
5H 2W 125-127	40.25	2.176	53.16	46.73	0.11	2.553	D
5H 2W 135-137	40.35	2.181	52.15	47.82	0.03	2.538	D
5H 3W 25-27	40.75	2.198	61.83	38.17	0.00	2.273	D
5H 3W 35-37	40.85	2.202	60.64	39.36	0.00	2.286	D
5H 3W 55-57	41.05	2.211	62.56	37.44	0.00	2.263	D
5H 3W 65-67	41.15	2.215	71.45	28.41	0.14	2.223	D
5H 3W 85-87	41.35	2.223	66.43	33.57	0.00	2.228	D
5H 3W 95-97	41.45	2.228	69.45	30.55	0.00	2.239	D
5H 3W 105-107	41.55	2.232	54.55	44.26	1.19	2.429	D
5H 3W 115-117	41.65	2.236	51.20	48.80	0.00	2.422	D
5H 3W 125-127	41.75	2.241	47.38	51.08	1.54	2.542	D
5H 3W 135-137	41.85	2.245	48.68	50.28	1.04	2.465	D
5H 3W 145-147	41.95	2.249	48.30	51.70	0.00	2.498	D
5H 4W 5-7	42.05	2.253	49.01	50.99	0.00	2.497	D
5H 4W 15-17	42.15	2.258	51.32	48.66	0.02	2.550	D
5H 4W 25-27	42.25	2.262	49.77	49.80	0.43	2.513	D
5H 4W 35-37	42.35	2.266	49.83	49.52	0.65	2.586	D
5H 4W 45-47	42.45	2.270	42.18	55.73	2.09	2.629	D
5H 4W 55-57	42.55	2.275	44.29	55.35	0.37	2.571	D
5H 4W 65-67	42.65	2.279	52.19	47.74	0.07	2.534	D
5H 4W 95-97	42.95	2.292	52.26	46.65	1.09	2.561	D
5H 4W 115-117	43.15	2.300	61.62	37.90	0.48	2.301	D
5H 4W 135-137	43.35	2.309	61.15	38.85	0.00	2.306	D
5H 5W 5-7	43.55	2.318	65.84	34.15	0.01	2.323	D
5H 5W 15-17	43.65	2.322	61.81	38.04	0.15	2.606	D
5H 5W 25-27	43.75	2.326	51.12	48.87	0.02	2.608	D

5H 5W 35-37	43.85	2.330	44.96	53.36	1.68	2.821	D
5H 5W 45-47	43.95	2.335	43.45	53.99	2.56	2.986	D
5H 5W 85-87	44.35	2.352	48.70	51.27	0.03	2.922	D
5H 5W 105-107	44.55	2.360	51.78	47.65	0.57	2.680	D
5H 5W 125-127	44.75	2.369	57.39	42.61	0.00	2.622	D
5H 5W 145-147	44.95	2.378	58.52	41.48	0.00	2.359	D
5H 6W 5-7	45.05	2.382	65.79	34.21	0.00	2.184	D
5H 6W 15-17	45.15	2.386	61.77	38.23	0.00	2.339	D
5H 6W 25-27	45.25	2.390	58.98	40.43	0.59	2.419	D
5H 6W 35-37	45.35	2.395	66.98	33.02	0.00	2.299	D
5H 6W 55-57	45.55	2.403	54.58	45.39	0.04	2.570	D
5H 6W 95-97	45.95	2.420	60.86	38.34	0.80	2.447	D
5H 6W 115-117	46.15	2.429	64.13	35.84	0.02	2.287	D
5H 6W 125-127	46.25	2.433	66.32	33.24	0.44	2.360	D
5H 6W 135-137	46.35	2.438	57.73	42.27	0.00	2.423	D
5H 7W 15-17	46.65	2.450	49.58	49.58	0.84	2.911	D
5H 7W 25-27	46.75	2.455	48.52	47.93	3.56	3.115	D
5H 7W 35-37	46.85	2.459	50.44	43.15	6.41	3.302	D
5H 7W 45-47	46.95	2.463	54.04	41.92	4.05	3.002	D
5H 7W 55-57	47.05	2.468	58.79	39.38	1.84	2.652	D
5H 7W 63-65	47.13	2.471	70.46	29.52	0.02	2.234	D
6H 1W 15-17	47.15	2.472	63.48	35.97	0.55	2.749	D
5H CC 5-7	47.2	2.474	63.72	30.78	5.50	3.068	D
5H CC 15-17	47.3	2.478	58.14	35.15	6.71	3.182	D
6H 1W 35-37	47.35	2.480	74.06	25.94	0.00	2.580	D
6H 1W 45-47	47.45	2.485	76.63	23.37	0.00	2.344	D
6H 1W 55-57	47.55	2.489	70.92	29.08	0.00	2.551	D
6H 1W 85-87	47.85	2.502	65.88	34.12	0.00	2.477	D
6H 1W 95-97	47.95	2.506	74.73	25.27	0.00	2.487	D
6H 1W 105-107	48.05	2.510	72.97	27.02	0.01	2.408	D
6H 1W 115-117	48.15	2.515	72.30	27.70	0.00	2.191	D
6H 1W 125-127	48.25	2.519	83.77	16.23	0.00	2.183	D
6H 1W 135-137	48.35	2.523	63.80	36.19	0.01	2.412	D
6H 1W 145-147	48.45	2.527	63.62	36.39	0.00	2.698	D
6H 2W 5-7	48.55	2.532	49.18	50.74	0.08	2.535	D
6H 2W 15-17	48.65	2.536	48.63	51.01	0.35	2.925	D
6H 2W 25-27	48.75	2.540	43.29	46.04	10.67	3.836	D
6H 2W 35-37	48.85	2.545	50.47	49.22	0.31	3.054	D
6H 2W 45-47	48.95	2.549	58.27	41.73	0.00	2.547	D
6H 2W 55-57	49.05	2.553	44.64	50.44	4.92	3.319	D
6H 2W 65-67	49.15	2.557	47.72	49.23	3.05	3.113	D
6H 2W 85-87	49.35	2.566	47.56	50.27	2.17	2.993	D
6H 2W 95-97	49.45	2.570	49.26	48.17	2.57	2.793	D
6H 2W 105-107	49.55	2.575	56.28	43.64	0.08	2.874	D
6H 2W 115-117	49.65	2.579	46.55	47.23	6.21	3.160	D
6H 2W 125-127	49.75	2.583	66.18	33.73	0.09	2.511	D

6H 2W 135-137	49.85	2.586	59.12	40.88	0.00	2.427	D
6H 2W 145-147	49.95	2.589	52.63	45.78	1.59	2.788	D
6H 3W 5-7	50.05	2.592	64.28	31.55	4.17	3.022	LC
6H 3W 25-27	50.25	2.598	60.76	38.30	0.94	2.551	LC
6H 3W 35-37	50.35	2.601	66.22	33.77	0.01	2.880	LC
6H 3W 45-47	50.45	2.604	59.20	31.13	9.67	3.230	LC
6H 3W 55-57	50.55	2.607	75.03	24.97	0.00	2.396	LC
6H 3W 65-67	50.65	2.610	74.62	25.38	0.00	2.495	LC
6H 3W 85-87	50.85	2.616	74.19	25.80	0.01	2.599	LC
6H 3W 95-97	50.95	2.619	67.27	32.73	0.00	2.387	LC
6H 3W 105-107	51.05	2.622	69.12	30.49	0.39	2.501	LC
6H 3W 115-117	51.15	2.625	61.93	37.97	0.10	2.263	LC
6H 3W 125-127	51.25	2.628	74.71	25.29	0.00	2.364	LC
6H 3W 135-137	51.35	2.631	70.56	29.44	0.00	2.353	LC
6H 3W 145-147	51.45	2.634	76.67	23.33	0.00	2.309	LC
6H 4W 5-7	51.55	2.637	64.07	33.28	2.65	2.638	LC
6H 4W 15-17	51.65	2.640	53.85	46.13	0.03	2.948	LC
6H 4W 25-27	51.75	2.643	42.51	57.35	0.13	2.776	LC
6H 4W 35-37	51.85	2.646	54.67	45.30	0.02	2.843	LC
6H 4W 45-47	51.95	2.649	58.74	40.54	0.71	2.421	LC
6H 4W 55-57	52.05	2.652	68.76	31.24	0.00	2.517	LC
6H 4W 65-67	52.15	2.655	57.71	41.31	0.98	2.370	LC
6H 4W 85-87	52.35	2.661	72.37	27.63	0.00	2.419	LC
6H 4W 95-97	52.45	2.665	70.08	23.36	6.56	3.212	LC
6H 4W 105-107	52.55	2.668	74.51	25.47	0.02	2.344	LC
6H 4W 115-117	52.65	2.671	55.77	40.80	3.43	2.867	LC
6H 4W 125-127	52.75	2.674	49.09	50.30	0.61	2.742	LC
6H 4W 135-137	52.85	2.677	50.55	45.89	3.56	3.071	LC
6H 5W 5-7	53.05	2.683	54.77	44.48	0.75	2.976	D
6H 5W 25-27	53.25	2.689	45.45	42.32	12.23	4.100	D
6H 5W 45-47	53.45	2.695	64.25	35.33	0.42	3.052	D
6H 5W 65-67	53.65	2.701	73.59	26.41	0.00	2.403	LC
6H 5W 95-97	53.95	2.710	65.72	34.04	0.24	2.192	LC
6H 5W 105-107	54.05	2.713	71.15	28.61	0.23	2.245	LC
6H 5W 115-117	54.15	2.716	64.97	35.03	0.00	2.550	LC
6H 5W 135-137	54.35	2.722	63.45	36.55	0.00	2.614	LC
6H 6W 5-7	54.55	2.728	55.86	41.45	2.69	2.920	LC
6H 6W 15-17	54.65	2.731	20.12	69.61	10.28	3.074	LC
6H 6W 25-27	54.75	2.734	71.50	28.50	0.00	2.598	LC
6H 6W 35-37	54.85	2.737	71.15	28.61	0.23	2.245	LC
6H 6W 45-47	54.95	2.740	79.43	20.57	0.00	2.320	LC
6H 6W 55-57	55.05	2.743	81.58	18.42	0.00	2.314	LC
6H 6W 65-67	55.15	2.747	69.86	30.14	0.00	2.468	LC
6H CC 5-7	56.555	2.789	64.09	35.58	0.33	2.395	D
7H 1W 15-17	56.65	2.792	63.85	35.41	0.74	2.790	D
6H CC 15-17	56.66	2.792	65.15	33.46	1.40	2.793	D

7H 1W 25-27	56.75	2.795	69.35	30.65	0.00	2.344	D
7H 1W 35-37	56.85	2.798	66.73	33.14	0.14	2.668	D
7H 1W 45-47	56.95	2.801	53.87	34.89	11.25	3.698	D
7H 1W 55-57	57.05	2.804	66.26	31.99	1.75	2.797	D
7H 1W 65-67	57.15	2.807	64.88	32.57	2.55	2.707	D
7H 1W 75-77	57.25	2.810	66.67	33.33	0.00	2.464	D
7H 1W 85-87	57.35	2.813	63.99	35.97	0.04	2.518	D
7H 1W 95-97	57.45	2.816	61.23	37.81	0.96	2.756	D
7H 1W 105-107	57.55	2.819	54.78	43.11	2.11	2.341	D
7H 1W 115-117	57.65	2.822	58.48	36.37	5.15	3.223	D
7H 1W 125-127	57.75	2.825	60.27	35.80	3.93	2.738	D
7H 1W 135-137	57.85	2.829	64.41	32.51	3.09	2.939	D
7H 1W 145-147	57.95	2.832	68.74	31.24	0.02	2.474	D
7H 2W 5-7	58.05	2.835	68.57	31.40	0.02	2.596	D
7H 2W 25-27	58.25	2.841	58.16	40.89	0.95	2.675	D
7H 2W 35-37	58.35	2.844	67.87	32.13	0.00	2.606	D
7H 2W 45-47	58.45	2.847	59.13	40.85	0.02	2.472	D
7H 2W 55-57	58.55	2.850	62.76	32.80	4.44	2.851	D
7H 2W 65-67	58.65	2.853	69.08	30.92	0.00	2.204	D
7H 2W 75-77	58.75	2.856	65.81	30.75	3.44	2.919	D
7H 2W 85-87	58.85	2.859	56.61	36.27	7.12	3.107	D
7H 2W 95-97	58.95	2.862	60.39	39.61	0.00	2.572	D
7H 2W 105-107	59.05	2.865	62.02	37.85	0.14	2.452	D
7H 2W 115-117	59.15	2.868	58.86	41.14	0.00	2.633	D
7H 2W 125-127	59.25	2.871	61.04	38.96	0.00	2.386	D
7H 2W 135-137	59.35	2.874	57.73	42.15	0.12	2.527	D
7H 2W 145-147	59.45	2.877	58.18	38.04	3.79	2.688	D
7H 3W 5-7	59.55	2.880	55.25	44.70	0.05	2.710	D
7H 3W 15-17	59.65	2.883	63.56	36.43	0.01	2.384	D
7H 3W 25-27	59.75	2.886	72.30	27.70	0.00	2.446	LC
7H 3W 35-37	59.85	2.889	73.99	26.01	0.00	2.393	LC
7H 3W 45-47	59.95	2.892	77.47	22.53	0.00	2.297	LC
7H 3W 55-57	60.05	2.895	73.08	26.92	0.00	2.272	LC
7H 3W 65-67	60.15	2.898	71.37	28.52	0.12	2.603	LC
7H 3W 75-77	60.25	2.901	74.02	23.36	2.61	2.656	LC
7H 3W 85-87	60.35	2.904	75.34	24.66	0.00	2.194	LC
7H 3W 95-97	60.45	2.907	78.77	20.23	1.00	2.052	LC
7H 3W 115-117	60.65	2.914	67.08	32.92	0.00	2.311	LC
7H 3W 125-127	60.75	2.917	75.68	24.32	0.00	2.451	LC
7H 3W 135-137	60.85	2.920	77.85	22.15	0.00	2.407	LC
7H 3W 145-147	60.95	2.923	71.26	28.74	0.00	2.398	LC
7H 4W 15-17	61.15	2.929	40.28	59.72	0.00	2.100	LC
7H 4W 35-37	61.35	2.935	67.84	32.16	0.00	2.424	LC
7H 4W 55-57	61.55	2.941	54.59	41.97	3.44	2.858	D
7H 4W 65-67	61.65	2.944	55.26	43.58	1.16	2.338	D
7H 4W 75-77	61.75	2.947	70.19	29.81	0.00	2.409	D

7H 4W 85-87	61.85	2.950	52.58	46.86	0.57	2.690	D
7H 4W 95-97	61.95	2.953	52.19	47.30	0.51	2.721	D
7H 4W 105-107	62.05	2.956	59.25	40.75	0.00	2.378	D
7H 4W 115-117	62.15	2.959	65.75	34.25	0.00	2.469	D
7H 4W 125-127	62.25	2.962	57.76	36.32	5.93	2.902	D
7H 4W 135-137	62.35	2.965	63.94	33.82	2.24	2.781	D
7H 4W 145-147	62.45	2.968	64.19	35.81	0.00	2.370	D
7H 5W 5-7	62.55	2.971	64.49	35.51	0.00	2.595	LC
7H 5W 15-17	62.65	2.974	63.84	36.16	0.00	2.178	LC
7H 5W 25-27	62.75	2.977	71.31	28.69	0.00	2.498	LC
7H 5W 35-37	62.85	2.980	56.70	39.79	3.51	2.717	LC
7H 5W 45-47	62.95	2.983	63.58	36.18	0.24	2.385	LC
7H 5W 55-57	63.05	2.986	65.22	34.78	0.00	2.187	LC
7H 5W 65-67	63.15	2.989	70.70	29.30	0.00	2.401	LC
7H 5W 75-77	63.25	2.993	61.73	38.16	0.11	2.316	LC
7H 5W 85-87	63.35	2.996	62.84	37.16	0.00	2.508	LC
7H 5W 95-97	63.45	2.999	67.16	32.84	0.00	2.346	LC
7H 5W 105-107	63.55	3.002	58.47	41.42	0.10	2.740	LC
7H 5W 115-117	63.65	3.005	64.45	35.55	0.00	2.413	LC
7H 5W 125-127	63.75	3.008	65.14	34.86	0.00	2.653	LC
7H 5W 135-137	63.85	3.011	72.39	27.61	0.00	2.407	LC
7H 5W 145-147	63.95	3.014	73.00	27.00	0.00	2.468	LC
7H 6W 5-7	64.05	3.017	79.25	20.75	0.00	2.359	LC
7H 6W 15-17	64.15	3.020	73.79	26.21	0.00	2.446	LC
7H 6W 25-27	64.25	3.023	83.08	16.92	0.00	1.934	LC
7H 6W 35-37	64.35	3.026	58.51	41.49	0.00	2.743	D
7H 6W 45-47	64.45	3.029	65.89	33.99	0.12	2.402	D
7H 6W 55-57	64.55	3.032	45.90	51.88	2.22	3.029	D
7H 6W 65-67	64.65	3.036	42.95	55.85	1.19	2.835	D
7H 6W 75-77	64.75	3.040	51.77	46.29	1.94	2.898	D
7H 6W 85-87	64.85	3.044	46.33	51.82	1.85	2.707	D
7H 6W 95-97	64.95	3.048	46.97	52.86	0.18	2.819	D
7H 6W 105-107	65.05	3.052	46.63	50.47	2.90	2.666	D
7H 6W 115-117	65.15	3.055	56.14	43.84	0.02	2.861	D
7H 6W 125-127	65.25	3.059	41.57	55.74	2.69	2.808	D
7H 6W 135-137	65.35	3.063	57.93	41.80	0.27	2.844	D
7H 6W 145-147	65.45	3.067	46.77	47.51	5.73	3.145	D
7H 7W 8-10	65.58	3.072	65.68	32.53	1.78	2.810	LC
7H 7W 15-17	65.65	3.075	66.73	30.89	2.38	2.609	LC
7H 7W 25-27	65.75	3.079	62.53	36.41	1.06	2.673	LC
7H 7W 45-47	65.95	3.087	66.74	32.43	0.83	2.365	LC
7H 7W 55-57	66.05	3.091	75.54	24.46	0.00	2.498	LC
8H 1W 15-17	66.15	3.095	52.29	43.78	3.93	2.734	LC
8H 1W 25-27	66.25	3.098	67.66	32.34	0.00	2.556	LC
8H 1W 35-37	66.35	3.102	71.68	26.54	1.78	2.893	LC
8H 1W 45-47	66.45	3.106	60.58	36.67	2.75	2.759	LC

8H 1W 65-67	66.65	3.114	57.42	39.46	3.12	2.730	LC
8H 1W 75-77	66.75	3.117	79.16	20.84	0.00	2.461	LC
8H 1W 85-87	66.85	3.119	83.60	16.33	0.07	2.582	LC
8H 1W 105-107	67.05	3.122	5.44	74.22	20.34	1.784	LC
8H 1W 115-117	67.15	3.124	71.91	27.91	0.17	2.587	LC
8H 1W 125-127	67.25	3.126	67.10	32.90	0.00	2.703	LC
8H 2W 5-7	67.56	3.132	41.55	57.89	0.56	2.854	LC
8H 2W 35-37	67.86	3.137	64.31	35.69	0.00	2.726	LC
8H 2W 45-47	67.96	3.139	55.37	42.63	2.00	2.936	LC
8H 2W 75-77	68.26	3.145	57.17	42.83	0.00	2.459	LC
8H 2W 95-97	68.46	3.148	63.80	36.20	0.00	2.513	LC
8H 2W 115-117	68.66	3.152	88.31	11.69	0.00	2.108	LC
8H 2W 125-127	68.76	3.154	84.01	15.99	0.00	2.275	LC
8H 2W 135-137	68.86	3.156	62.02	37.98	0.00	2.525	LC
8H 3W 5-7	69.06	3.159	59.54	40.46	0.00	2.622	LC
8H 3W 15-17	69.16	3.161	73.16	26.84	0.00	2.015	LC
8H 3W 25-27	69.26	3.163	79.65	20.35	0.00	2.120	LC
8H 3W 45-47	69.46	3.167	83.18	16.82	0.00	2.295	LC
8H 3W 55-57	69.56	3.168	60.28	39.72	0.00	2.465	LC
8H 3W 65-67	69.66	3.170	55.73	44.24	0.03	2.809	LC
8H 3W 75-77	69.76	3.172	43.81	54.28	1.91	2.657	LC
8H 3W 85-87	69.86	3.174	56.42	43.58	0.00	2.461	D
8H 3W 95-97	69.96	3.176	57.13	40.98	1.89	2.671	D
8H 3W 107-109	70.08	3.178	54.99	43.22	1.79	2.840	D
8H 3W 115-117	70.16	3.179	51.41	45.82	2.77	2.727	D
8H 3W 125-127	70.26	3.181	49.51	47.97	2.52	3.012	D
8H 3W 145-147	70.46	3.185	69.86	30.14	0.00	2.618	LC
8H 4W 5-7	70.56	3.187	66.55	33.45	0.00	2.873	LC
8H 4W 25-27	70.76	3.190	57.93	40.32	1.75	2.823	LC
8H 4W 35-37	70.86	3.192	61.19	38.71	0.10	2.844	LC
8H 4W 55-57	71.06	3.196	69.53	30.41	0.06	2.983	LC
8H 4W 65-67	71.16	3.198	65.19	33.13	1.67	3.244	LC
8H 4W 75-77	71.26	3.199	40.89	55.24	3.87	3.376	LC
8H 4W 85-87	71.36	3.201	50.58	46.86	2.56	3.164	LC
8H 4W 95-97	71.46	3.203	53.78	43.48	2.74	3.020	LC
8H 4W 105-107	71.56	3.205	55.10	44.90	0.00	2.900	LC
8H 4W 115-117	71.66	3.207	44.64	51.67	3.69	3.274	LC
8H 4W 125-127	71.76	3.211	51.56	48.10	0.34	2.983	LC
8H 4W 135-137	71.86	3.215	57.55	41.46	0.98	2.954	LC
8H 4W 145-147	71.96	3.220	47.92	50.85	1.23	2.837	LC
8H 5W 5-7	72.06	3.224	50.74	48.69	0.57	3.039	D
8H 5W 15-17	72.16	3.228	61.37	38.54	0.09	2.718	D
8H 5W 25-27	72.26	3.232	67.33	32.67	0.00	2.722	D
8H 5W 35-37	72.36	3.237	28.30	67.52	4.18	2.892	D
8H 5W 45-47	72.46	3.241	50.35	47.33	2.33	2.701	D
8H 5W 55-57	72.56	3.245	56.21	42.26	1.53	2.840	D

8H 5W 65-67	72.66	3.250	59.49	39.97	0.54	2.401	D
8H 5W 75-77	72.76	3.254	65.46	34.48	0.07	2.672	D
8H 5W 85-87	72.86	3.258	54.77	42.08	3.15	2.830	D
8H 5W 95-97	72.96	3.263	68.34	31.66	0.00	2.541	LC
8H 5W 105-107	73.06	3.267	70.82	29.18	0.00	2.332	LC
8H 5W 115-117	73.16	3.271	65.81	34.19	0.00	2.514	LC
8H 5W 135-137	73.36	3.280	65.20	34.80	0.00	2.518	LC
8H 5W 145-147	73.46	3.284	61.80	37.78	0.42	2.339	LC
8H 6W 5-7	73.57	3.289	56.63	43.37	0.00	2.704	LC
8H 6W 15-17	73.67	3.293	60.38	39.62	0.00	2.627	LC
8H 6W 25-27	73.77	3.298	58.31	41.31	0.38	2.500	LC
8H 6W 35-37	73.87	3.302	56.53	43.32	0.16	2.705	LC
8H 6W 45-47	73.97	3.306	65.40	34.33	0.27	2.389	LC
8H 6W 65-67	74.17	3.315	76.73	23.23	0.03	2.416	LC
8H 6W 75-77	74.27	3.319	69.87	30.13	0.00	2.476	LC
8H 6W 85-87	74.37	3.324	69.86	23.57	6.57	3.514	LC
8H 7W 5-7	74.58	3.335	70.85	29.14	0.01	2.284	D
8H 7W 15-17	74.68	3.345	78.33	21.67	0.00	2.400	D
8H 7W 25-27	74.78	3.354	73.25	26.75	0.00	2.553	D
8H 7W 45-47	74.98	3.372	57.63	39.69	2.68	3.262	D
8H 7W 55-57	75.08	3.381	40.68	54.65	4.67	3.150	D
9H 1W 15-17	75.65	3.433	68.65	31.35	0.00	2.550	D
9H 1W 25-27	75.75	3.442	100.00	0.00	0.00	1.713	D
9H 1W 35-37	75.85	3.451	53.57	46.43	0.00	2.736	D
9H 1W 45-47	75.95	3.460	59.32	38.36	2.32	2.558	D
9H 1W 55-57	76.05	3.469	50.61	46.97	2.42	2.902	D
9H 1W 65-67	76.15	3.478	54.56	44.09	1.34	2.373	D
9H 1W 75-77	76.25	3.487	55.01	40.54	4.45	3.134	D
9H 1W 85-87	76.35	3.496	65.14	34.83	0.02	2.434	D
9H 1W 95-97	76.45	3.505	58.97	39.24	1.79	2.715	D
9H 1W 105-107	76.55	3.514	54.51	37.40	8.09	3.441	D
9H 1W 115-117	76.65	3.523	57.35	41.04	1.60	2.694	D
9H 1W 125-127	76.75	3.532	56.45	43.55	0.00	2.543	D
9H 2W 5-7	77.05	3.560	52.02	47.98	0.00	2.720	D
9H 2W 15-17	77.15	3.569	46.06	50.22	3.72	2.821	D
9H 2W 25-27	77.25	3.578	42.26	53.97	3.77	2.949	D
9H 2W 35-37	77.35	3.587	50.02	48.57	1.41	2.780	D
9H 2W 45-47	77.45	3.596	49.10	48.70	2.21	2.872	D
9H 2W 55-57	77.55	3.599	45.19	51.83	2.98	2.675	D
9H 2W 65-67	77.65	3.601	43.48	53.63	2.89	2.812	D
9H 2W 75-77	77.75	3.604	53.14	41.54	5.32	2.840	D
9H 2W 85-87	77.85	3.606	51.02	48.98	0.00	2.594	D
9H 2W 95-97	77.95	3.609	60.86	39.14	0.00	2.337	LC
9H 2W 105-107	78.05	3.612	65.76	34.24	0.00	2.381	LC
9H 2W 115-117	78.15	3.614	63.81	36.19	0.00	2.149	LC
9H 2W 125-127	78.25	3.617	52.31	47.69	0.00	2.764	LC

9H 2W 135-137	78.35	3.620	54.46	45.54	0.00	2.329	LC
9H 2W 145-147	78.45	3.622	69.06	30.94	0.00	2.503	LC
9H 3W 15-17	78.65	3.627	50.67	49.33	0.00	2.606	LC
9H 3W 25-27	78.75	3.630	77.83	22.17	0.00	2.081	LC
9H 3W 35-37	78.85	3.633	78.40	21.60	0.00	2.223	LC
9H 3W 55-57	79.05	3.638	80.84	19.16	0.00	2.345	LC
9H 3W 65-67	79.15	3.641	74.19	25.74	0.07	2.599	LC
9H 3W 75-77	79.25	3.643	43.04	56.75	0.21	2.789	LC
9H 3W 85-87	79.35	3.646	66.31	33.69	0.00	2.232	LC
9H 3W 95-97	79.45	3.648	60.21	39.79	0.00	2.481	LC
9H 3W 105-107	79.55	3.651	45.67	52.73	1.60	2.565	D
9H 3W 115-117	79.65	3.654	84.56	15.44	0.00	2.189	D
9H 3W 12-127	79.75	3.656	38.85	59.07	2.08	2.520	D
9H 3W 135-137	79.85	3.659	44.18	54.08	1.74	2.772	D
9H 3W 145-147	79.95	3.662	41.92	53.48	4.60	2.855	D
9H 4W 5-7	80.05	3.664	12.80	75.59	11.61	2.491	LC
9H 4W 15-17	80.15	3.667	69.37	30.63	0.00	2.409	LC
9H 4W 25-27	80.25	3.669	71.81	28.18	0.00	2.407	LC
9H 4W 45-47	80.45	3.675	57.96	42.04	0.00	2.967	LC
9H 4AW 55-57	80.55	3.677	75.08	24.92	0.00	2.623	LC
9H 4W 65-67	80.65	3.680	78.20	21.80	0.00	2.404	LC
9H 4W 75-77	80.75	3.683	41.74	57.02	1.24	2.793	LC
9H 4W 85-87	80.85	3.685	56.20	43.78	0.03	2.621	LC
9H 4W 105-107	81.05	3.690	60.61	39.39	0.00	2.568	LC
9H 4W 115-117	81.15	3.693	62.42	37.58	0.00	2.269	LC
9H 4W 125-127	81.25	3.696	60.45	39.55	0.00	2.448	LC
9H 4W 135-137	81.35	3.698	74.54	25.46	0.00	2.139	LC
9H 4W 145-147	81.45	3.701	77.37	22.63	0.00	2.302	LC
9H 5W 5-7	81.55	3.704	76.28	23.72	0.00	2.105	LC
9H 5W 25-27	81.75	3.709	75.34	24.66	0.00	2.262	LC
9H 5W 35-37	81.85	3.711	66.42	33.58	0.00	2.569	LC
9H 5W 45-47	81.95	3.714	71.88	28.09	0.02	2.532	LC
9H 5W 55-57	82.05	3.717	63.73	36.27	0.00	2.654	LC
9H 5W 65-67	82.15	3.719	79.10	20.90	0.00	2.514	LC
9H 5W 75-77	82.25	3.722	72.10	27.90	0.00	2.552	LC
9H 5W 85-87	82.35	3.724	45.19	54.81	0.00	2.378	LC
9H 5W 95-97	82.45	3.727	65.69	34.31	0.00	2.578	LC
9H 5W 105-107	82.55	3.730	57.93	41.95	0.12	2.783	LC
9H 5W 115-117	82.65	3.732	57.02	42.98	0.00	2.624	LC
9H 5W 125-127	82.75	3.735	79.33	20.67	0.00	2.457	LC
9H 5W 135-137	82.85	3.738	49.61	50.39	0.00	2.312	LC
9H 5W 145-147	82.95	3.740	74.87	25.13	0.00	2.028	LC
9H 6W 5-7	83.05	3.743	54.21	45.79	0.00	2.608	LC
9H 6W 25-27	83.25	3.748	68.41	31.59	0.00	2.453	LC
9H 6W 35-37	83.35	3.751	72.54	27.44	0.01	2.384	LC
9H 6W 45-47	83.45	3.753	52.55	47.44	0.01	2.586	LC

9H 6W 65-67	83.65	3.759	61.97	38.03	0.00	2.595	LC
9H 6W 85-87	83.85	3.764	58.92	41.07	0.01	2.440	LC
9H 6W 95-97	83.95	3.766	53.36	46.60	0.04	2.167	LC
9H 6W 105-107	84.05	3.769	71.89	28.11	0.00	2.313	LC
9H 6W 115-117	84.15	3.772	46.47	53.53	0.00	2.309	D
9H 6W 125-127	84.25	3.774	37.58	58.70	3.72	2.845	D
9H 6W 135-137	84.35	3.777	32.82	60.33	6.85	3.031	D
9H 6W 145-147	84.45	3.780	35.01	57.56	7.43	3.250	D
9H 7W 5-7	84.55	3.782	45.87	46.79	7.34	3.331	LC
9H 7W 15-17	84.65	3.785	69.39	30.61	0.00	2.430	LC
9H 7W 35-37	84.85	3.790	64.27	35.73	0.00	2.617	LC
9H 7W 45-47	84.95	3.793	68.22	31.78	0.00	2.380	LC
9H 7W 55-57	85.05	3.795	64.80	35.20	0.00	2.574	LC
9H 7W 65-67	85.15	3.798	83.60	16.40	0.00	2.282	LC
10H 1W 25-27	85.25	3.801	64.75	35.25	0.00	2.507	LC
10H 1W 35-37	85.35	3.803	67.34	32.66	0.00	2.522	LC
10H 1W 55-57	85.55	3.808	75.75	24.25	0.00	2.438	LC
10H 1W 75-77	85.75	3.814	40.69	59.31	0.00	2.508	LC
10H 1W 85-87	85.85	3.816	58.10	41.90	0.00	2.279	LC
10H 1W 95-97	85.95	3.819	68.62	31.38	0.00	2.288	LC
10H 1W 115-117	86.15	3.824	69.76	30.24	0.00	2.366	LC
10H 1W 135-137	86.35	3.829	74.10	25.90	0.00	2.261	LC
10H 1W 145-147	86.45	3.832	48.84	48.90	2.26	2.597	LC
10H 2W 5-7	86.55	3.835	49.13	48.90	1.97	2.999	LC
10H 2W 25-27	86.75	3.840	74.01	25.99	0.00	2.540	LC
10H 2W 35-37	86.85	3.842	54.99	43.08	1.94	2.600	LC
10H 2W 45-47	86.95	3.845	52.16	46.87	0.97	2.846	LC
10H 2W 55-57	87.05	3.848	24.86	70.36	4.77	2.909	LC
10H 2W 65-67	87.15	3.850	48.39	51.61	0.00	2.844	LC
10H 2W 75-77	87.25	3.853	72.40	27.60	0.00	2.461	LC
10H 2W 85-87	87.35	3.856	72.52	27.48	0.00	2.624	LC
10H 2W 95-97	87.45	3.858	58.13	41.69	0.19	2.448	LC
10H 2W 105-107	87.55	3.861	71.63	28.37	0.00	2.405	LC
10H 2W 125-127	87.75	3.866	77.54	22.46	0.00	2.277	LC
10H 2W 135-137	87.85	3.869	61.38	38.62	0.00	2.214	LC
10H 2W 145-147	87.95	3.871	73.36	26.64	0.00	2.551	LC
10H 3W 5-7	88.05	3.874	49.52	50.36	0.12	2.583	D
10H 3W 15-17	88.15	3.877	47.78	51.91	0.31	2.762	D
10H 3W 25-27	88.25	3.879	43.96	52.33	3.70	2.790	D
10H 3W 35-37	88.35	3.882	42.97	50.84	6.19	3.395	LC
10H 3W 55-57	88.55	3.887	76.10	23.17	0.72	2.563	LC
10H 3W 65-67	88.65	3.890	62.24	37.76	0.00	2.603	LC
10H 3W 75-77	88.75	3.892	60.93	39.07	0.00	2.633	LC
10H 3W 85-87	88.85	3.895	64.56	33.14	2.30	2.435	LC
10H 3W 95-97	88.95	3.898	53.57	44.86	1.57	2.844	LC
10H 3W 105-107	89.05	3.900	60.92	39.08	0.00	2.362	LC

10H 3W 115-117	89.15	3.903	73.89	26.11	0.00	2.441	LC
10H 3W 125-127	89.25	3.905	73.12	26.88	0.00	2.344	LC
10H 3W 135-137	89.35	3.908	65.97	34.03	0.00	2.598	LC
10H 3W 145-147	89.45	3.911	62.89	36.84	0.27	2.482	LC
10H 4W 5-7	89.55	3.913	56.04	43.96	0.00	2.736	LC
10H 4W 15-17	89.65	3.916	45.76	54.03	0.21	3.155	LC
10h 4W 25-27	89.75	3.919	73.95	26.05	0.00	2.499	LC
10H 4W 35-37	89.85	3.921	61.67	38.33	0.00	2.684	LC
10H 4W 45-47	89.95	3.924	64.83	35.17	0.00	2.491	LC
10H 4W 55-57	90.05	3.926	64.45	31.98	3.57	2.820	LC
10H 4W 65-67	90.15	3.929	79.67	20.33	0.00	2.422	LC
10H 4W 75-77	90.25	3.932	65.58	34.37	0.05	2.576	LC
10H 4W 85-87	90.35	3.934	62.95	37.05	0.00	2.609	LC
10H 4W 95-97	90.45	3.937	69.86	30.14	0.00	2.521	LC
10H 4W 115-117	90.65	3.942	74.39	24.06	1.56	2.562	LC
10H 4W 125-127	90.75	3.945	65.38	34.34	0.28	2.475	D
10H 4W 135-137	90.85	3.947	51.94	47.10	0.95	2.447	D
10H 4W 145-147	90.95	3.950	54.79	45.19	0.02	2.779	D
10H 5W 5-7	91.05	3.953	47.74	50.74	1.52	2.749	D
10H 5W 15-17	91.15	3.955	49.73	48.82	1.45	2.688	D
10H 5W 25-27	91.25	3.958	51.07	45.98	2.95	2.597	D
10H 5W 35-37	91.35	3.960	54.94	44.34	0.72	2.775	D
10H 5W 45-47	91.45	3.963	48.97	49.72	1.31	2.641	D
10H 5W 55-57	91.55	3.966	58.32	41.68	0.00	2.703	D
10H 5W 65-67	91.65	3.968	51.65	46.60	1.76	2.529	D
10H 5W 75-77	91.75	3.971	51.19	48.24	0.57	2.767	D
10H 5W 85-87	91.85	3.974	51.11	46.45	2.44	2.961	D
10H 5W 95-97	91.95	3.976	34.90	56.82	8.28	3.323	D
10H 5W 105-107	92.05	3.979	56.56	41.34	2.10	2.493	D
10H 5W 115-117	92.15	3.981	43.79	52.40	3.81	3.182	D
10H 5W 125-127	92.25	3.984	29.99	61.00	9.01	3.174	D
10H 5W 135-137	92.35	3.987	35.57	60.78	3.65	3.067	D
10H 5W 145-147	92.45	3.989	54.28	44.51	1.21	2.637	D
10H 6W 5-7	92.55	3.992	56.42	42.26	1.32	2.942	D
10H 6W 15-17	92.65	3.995	49.59	47.09	3.33	2.698	D
10H 6W 25-27	92.75	3.997	46.85	50.82	2.33	2.878	D
10H 6W 45-47	92.95	4.002	49.11	49.18	1.71	2.893	D
10H 6W 55-57	93.05	4.005	46.23	52.62	1.15	2.993	D
10H 6W 65-67	93.15	4.008	47.45	49.86	2.69	3.011	D
10H 6W 75-77	93.25	4.010	51.85	45.03	3.12	2.700	D
10H 6W 85-87	93.35	4.013	42.91	54.52	2.57	2.688	D
10H 6W 95-97	93.45	4.016	46.68	50.13	3.19	2.626	D
10H 6W 105-107	93.55	4.018	50.63	48.75	0.61	2.576	D
10H 6W 115-117	93.65	4.021	52.58	45.30	2.12	2.508	D
10H 6W 125-127	93.75	4.023	47.37	48.76	3.86	3.312	D
10H 6W 135-137	93.85	4.026	51.90	46.43	1.68	2.703	D

10H 6W 145-147	93.95	4.029	47.61	46.67	5.72	3.359	D
10H 7W 5-7	94.05	4.031	49.48	48.26	2.26	2.664	D
10H 7W 15-17	94.15	4.034	45.58	52.94	1.48	2.883	D
10H 7W 25-27	94.25	4.036	38.65	59.34	2.01	2.713	D
10H 7W 35-37	94.35	4.039	42.99	55.32	1.69	2.753	D
10H 7W 45-47	94.45	4.042	50.82	48.72	0.47	2.669	D
10H 7W 55-57	94.55	4.044	57.34	42.66	0.00	2.441	D
11H 1W 7-9	94.57	4.045	56.75	43.25	0.00	2.339	D
11H 1W 15-17	94.65	4.047	58.78	41.18	0.05	2.450	D
10H 7W 67-69	94.67	4.048	45.13	51.98	2.89	2.529	D
11H 1W 25-27	94.75	4.050	58.37	41.63	0.00	2.456	D
10H CC 5-7	94.8	4.051	48.46	50.08	1.46	2.299	D
11H 1W 35-37	94.85	4.052	55.10	43.59	1.31	2.615	D
10H CC 15-17	94.9	4.054	54.91	44.66	0.43	2.365	D
11H 1W 45-47	94.95	4.055	51.91	47.45	0.64	2.789	D
11H 1W 55-57	95.05	4.057	58.08	39.28	2.64	2.449	D
11H 1W 65-67	95.15	4.060	50.88	47.75	1.37	2.676	D
11H 1W 75-77	95.25	4.063	41.32	56.06	2.62	2.788	D
11H 1W 85-87	95.35	4.065	43.03	55.37	1.60	2.644	D
11H 1W 105-107	95.55	4.071	37.71	58.11	4.18	3.091	D
11H 1W 115-117	95.65	4.073	36.06	37.62	26.32	4.133	D
11H 1W 125-127	95.75	4.076	73.44	25.52	1.04	2.525	D
11H 1W 135-137	95.85	4.078	61.79	38.21	0.00	2.494	LC
11H 1W 145-147	95.95	4.081	51.80	45.27	2.93	3.108	LC
11H 2W 5-7	96.05	4.084	57.77	37.04	5.19	3.610	LC
11H 2W 15-17	96.15	4.086	74.73	25.27	0.00	2.271	LC
11H 2W 25-27	96.25	4.089	72.05	26.43	1.52	2.620	LC
11H 2W 35-37	96.35	4.092	67.70	32.24	0.06	2.564	LC
11H 2W 45-47	96.45	4.094	73.27	26.73	0.00	2.074	LC
11H 2W 55-57	96.55	4.097	48.49	49.79	1.72	3.233	LC
11H 2W 65-67	96.65	4.099	77.14	22.86	0.00	2.383	LC
11H 2W 75-77	96.75	4.102	59.95	39.87	0.18	2.662	LC
11H 2W 85-87	96.85	4.105	72.08	27.59	0.33	2.158	LC
11H 2W 95-97	96.95	4.107	65.85	34.15	0.00	2.434	LC
11H 2W 105-107	97.05	4.110	59.56	40.44	0.01	2.491	LC
11H 2W 115-117	97.15	4.113	46.77	50.94	2.29	3.102	LC
11H 2W 125-127	97.25	4.115	68.58	31.42	0.00	2.175	LC
11H 2W 135-137	97.35	4.118	59.55	33.15	7.30	3.262	LC
11H 2W 145-147	97.45	4.120	60.79	39.21	0.00	3.253	LC
11H 3W 5-7	97.55	4.123	66.24	33.70	0.05	2.813	LC
11H 3W 15-17	97.65	4.126	38.78	61.22	0.00	2.291	LC
11H 3W 25-27	97.75	4.128	73.82	26.15	0.03	2.359	LC
11H 3W 45-47	97.95	4.134	65.19	34.81	0.00	2.549	LC
11H 3W 65-67	98.15	4.139	69.56	30.44	0.00	2.536	LC
11H 3W 75-77	98.25	4.141	77.13	22.87	0.00	2.257	LC
11H 3W 85-87	98.35	4.144	79.01	20.99	0.00	2.289	LC

11H 3W 95-97	98.45	4.147	48.44	44.76	6.80	3.600	LC
11H 3W 105-107	98.55	4.149	65.43	34.55	0.02	2.907	LC
11H 3W 115-117	98.65	4.152	42.90	52.69	4.41	3.085	LC
11H 3W 125-127	98.75	4.154	49.07	49.82	1.11	3.179	LC
11H 3W 145-147	98.95	4.160	61.78	38.22	0.00	2.841	LC
11H 4W 5-7	99.05	4.162	59.71	35.52	4.78	3.289	LC
11H 4W 15-17	99.15	4.165	70.40	29.60	0.00	2.634	LC
11H 4W 25-27	99.25	4.168	72.39	27.60	0.02	2.740	LC
11H 4W 35-37	99.35	4.170	60.53	39.47	0.00	2.733	LC
11H 4W 45-47	99.45	4.173	71.45	28.10	0.45	2.809	LC
11H 4W 55-57	99.55	4.175	60.65	39.35	0.00	2.742	LC
11H 4W 75-77	99.75	4.181	57.75	42.06	0.19	3.045	LC
11H 4W 85-87	99.85	4.183	50.35	46.61	3.05	3.164	LC
11H 4W 95-97	99.95	4.186	63.00	35.79	1.21	3.035	LC
11H 4W 105-107	100.05	4.190	70.91	29.06	0.02	2.765	LC
11H 4W 115-117	100.15	4.194	57.68	42.32	0.00	2.663	LC
11H 4W 125-127	100.25	4.199	65.26	34.44	0.30	2.816	LC
11H 4W 135-137	100.35	4.203	48.61	47.14	4.25	3.143	D
11H 5W 5-7	100.55	4.213	44.07	51.55	4.38	3.184	D
11H 5W 25-27	100.75	4.222	51.93	45.97	2.10	2.807	D
11H 5W 45-47	100.95	4.231	52.79	43.02	4.19	3.125	D
11H 5W 55-57	101.05	4.236	53.29	42.76	3.95	2.779	D
11H 5W 65-67	101.15	4.240	47.07	49.15	3.78	3.100	D
11H 5W 85-87	101.35	4.249	46.17	52.05	1.77	2.765	D
11H 5W 95-97	101.45	4.254	60.93	37.76	1.31	2.676	D
11H 5W 105-107	101.55	4.258	40.99	55.37	3.64	3.054	D
11H 5W 125-127	101.75	4.268	47.99	49.72	2.28	3.034	D
11H 5W 135-137	101.85	4.272	42.25	54.06	3.69	2.792	D
11H 5W 145-147	101.95	4.277	37.96	60.42	1.61	2.720	D
11H 6W 5-7	102.05	4.281	37.36	61.31	1.33	2.565	D
11H 6W 15-17	102.15	4.286	37.64	61.73	0.63	2.682	D
11H 6W 25-27	102.25	4.291	52.64	47.33	0.03	2.585	D
11H 6W 35-37	102.35	4.295	50.44	47.68	1.88	2.732	D
11H 6W 55-57	102.55	4.304	49.39	48.16	2.45	2.944	D
11H 6W 65-67	102.65	4.309	46.06	51.06	2.89	2.824	D
11H 6W 75-77	102.75	4.313	46.97	48.20	4.83	3.332	D
11H 6W 85-87	102.85	4.318	44.37	51.65	3.98	2.980	D
11H 6W 95-97	102.95	4.323	50.48	49.40	0.12	2.741	D
11H 6W 105-105	103.05	4.327	57.05	42.24	0.71	2.901	D
11H 6W 115-117	103.15	4.332	62.05	37.95	0.00	2.516	D
11H 6W 125-127	103.25	4.336	47.30	50.95	1.75	2.363	D
11H 6W 145-147	103.45	4.346	49.11	48.75	2.15	2.538	D
11H 7W 5-7	103.55	4.350	47.24	50.29	2.47	2.882	D
11H 7W 15-17	103.65	4.355	27.79	65.01	7.19	2.844	D
11H 7W 28-30	103.78	4.361	37.46	55.30	7.24	3.425	D
11H 7W 38-40	103.88	4.365	49.33	47.14	3.53	2.743	D

11H 7W 58-60	104.08	4.374	49.09	48.64	2.28	2.956	D
11H CC 2-4	104.12	4.376	35.99	58.63	5.38	2.998	D
11H CC 8-10	104.18	4.379	42.87	51.82	5.32	3.169	D

APPENDIX B

ODP Site 1123 stable isotope data

Core, section, interval (cm)	Depth (mbsf)	rMCD	Age (Ka)	Species	$\delta^{18}O_{PDB}$	$\delta^{13}C_{PDB}$
12H 1W 0-2	98.40	108.06	3006	*Uvigerina* spp.	3.820	-0.473
12H 1W 20-22	98.50	108.16	3009	*Uvigerina* spp.	3.758	-0.922
12H 1W 40-42	98.60	108.26	3011	*Uvigerina* spp.	3.539	-0.863
12H 1 30-32	98.70	108.36	3014	*Uvigerina* spp.	3.534	-0.822
12H 1W 40-42	98.80	108.46	3017	*Uvigerina* spp.	3.290	-0.642
12H 1W 50-52	98.90	108.56	3019	*Uvigerina* spp.	3.468	-0.883
12H 1W 60-62	99.00	108.66	3022	*Uvigerina* spp.	3.425	-0.750
12H 1W 70-72	99.10	108.76	3025	*Uvigerina* spp.	3.685	-1.137
12H 1W 90-92	99.30	108.96	3030	*Uvigerina* spp.	3.821	-1.049
12H 1W 98-100	99.40	109.06	3033	*Uvigerina* spp.	3.850	-1.061
12H 1W 110-112	99.50	109.16	3036	*Uvigerina* spp.	3.969	-1.039
12H 1W 120-122	99.60	109.26	3038	*Uvigerina* spp.	3.936	-1.093
12H 1W 130-132	99.70	109.36	3041	*Uvigerina* spp.	3.905	-1.587
12H 1W 140-142	99.80	109.46	3044	*Uvigerina* spp.	3.758	-1.417
12H 2W 0-2	99.90	109.56	3049	*Uvigerina* spp.	3.950	-1.296
12H 2W 10-12	100.00	109.66	3056	*Uvigerina* spp.	3.452	-1.322
12H 2W 20-22	100.10	109.76	3063	*Uvigerina* spp.	3.788	-1.012
12H 2W 30-32	100.20	109.86	3070	*Uvigerina* spp.	3.346	-0.984
12H 2W 40-42	100.30	109.96	3076	*Uvigerina* spp.	3.299	-1.023
12H 2W 50-52	100.40	110.06	3083	*Uvigerina* spp.	3.371	-1.004
12H 2W 70-72	100.60	110.26	3097	*Uvigerina* spp.	3.535	-0.724
12H 2W 80-82	100.70	110.36	3104	*Uvigerina* spp.	3.472	-0.739
12H 2W 90-92	100.80	110.46	3111	*Uvigerina* spp.	3.107	-0.846
12H 2W 100-102	100.90	110.56	3117	*Uvigerina* spp.	3.323	-0.958
12H 2W 110-112	101.00	110.66	3124	*Uvigerina* spp.	3.182	-0.901
12H 2W 120-122	101.10	110.76	3128	*Uvigerina* spp.	3.288	-0.743
12H 2W 130-132	101.20	110.86	3130	*Uvigerina* spp.	3.279	-1.208
12H 2W 140-142	101.30	110.96	3131	*Uvigerina* spp.	3.237	-0.548
12H 3W 0-2	101.40	111.06	3133	*Uvigerina* spp.	3.357	-0.711
12H 3W 10-12	101.50	111.16	3134	*Uvigerina* spp.	3.541	-0.780
12H 3W 20-22	101.60	111.26	3136	*Uvigerina* spp.	3.295	-0.706
12H 3W 30-32	101.70	111.36	3138	*Uvigerina* spp.	3.325	-0.602
12H 3W 40-42	101.80	111.46	3139	*Uvigerina* spp.	3.550	-0.827
12H 3W 50-52	101.90	111.56	3141	*Uvigerina* spp.	3.577	-0.713
12H 3W 50-52	101.9	111.56	3141	*Cibicides* spp.	2.887	0.376
12H 3W 60-62	102.00	111.66	3142	*Uvigerina* spp.	3.303	-0.634
12H 3W 70-72	102.10	111.76	3144	*Uvigerina* spp.	3.373	-0.768
12H 3W 80-82	102.20	111.86	3146	*Uvigerina* spp.	3.389	-0.483
12H 3W 90-92	102.30	111.96	3147	*Uvigerina* spp.	3.549	-0.729
12H 3W 100-102	102.40	112.06	3149	*Uvigerina* spp.	3.509	-0.760
12H 3W 110-112	102.50	112.16	3150	*Uvigerina* spp.	3.466	-0.801
12H 3W 120-122	102.60	112.26	3152	*Uvigerina* spp.	3.501	-1.016
12H 3W 130-132	102.70	112.36	3153	*Uvigerina* spp.	3.714	-0.677
12H 3W 140-142	102.80	112.46	3155	*Uvigerina* spp.	3.688	-0.684
12H 4W 10-12	103.00	112.66	3158	*Uvigerina* spp.	3.181	-0.749
12H 4W 20-22	103.10	112.76	3160	*Uvigerina* spp.	3.583	-0.771
12H 4W 30-32	103.20	112.86	3161	*Uvigerina* spp.	3.516	-0.669

12H 4W 40-42	103.30	112.96	3163	*Uvigerina* spp.	3.405	-0.586
12H 4W 50-52	103.40	113.06	3165	*Uvigerina* spp.	3.228	-0.599
12H 4W 60-62	103.50	113.16	3166	*Uvigerina* spp.	3.155	-0.297
12H 4W 60-62	103.50	113.16	3166	*Uvigerina* spp.	3.080	-0.051
12H 4W 70-72	103.60	113.26	3168	*Uvigerina* spp.	3.301	-0.512
12H 4W 70-72	103.6	113.26	3168	*Cibicides* spp.	2.733	0.637
12H 4W 80-82	103.70	113.36	3169	*Uvigerina* spp.	3.180	-0.318
12H 4W 80-82	103.70	113.36	3169	*Uvigerina* spp.	3.209	-0.344
12H 4W 100-102	103.90	113.56	3173	*Uvigerina* spp.	3.252	-0.622
12H 4W 100-102	103.90	113.56	3173	*Uvigerina* spp.	3.277	-0.435
12H 4W 110-112	104.00	113.66	3174	*Uvigerina* spp.	3.047	-0.396
12H 4W 120-122	104.10	113.76	3176	*Uvigerina* spp.	3.351	-0.366
12H 4W 120-122	104.10	113.76	3176	*Uvigerina* spp.	3.525	-0.272
12H 4W 130-132	104.20	113.86	3177	*Uvigerina* spp.	3.307	-0.544
12H 5W 10-12	104.50	114.16	3182	*Uvigerina* spp.	3.418	-0.415
12H 5W 10-12	104.50	114.16	3182	*Uvigerina* spp.	3.405	-0.657
12H 5W 20-22	104.60	114.26	3184	*Uvigerina* spp.	3.480	-0.503
12H 5W 30-32	104.70	114.36	3185	*Uvigerina* spp.	3.309	-0.547
12H 5W 40-42	104.80	114.46	3187	*Uvigerina* spp.	3.485	-0.843
12H 5W 50-52	104.90	114.56	3189	*Uvigerina* spp.	3.861	-0.903
12H 5W 60-62	105.00	114.66	3190	*Uvigerina* spp.	3.876	-1.229
12H 5W 70-72	105.10	114.76	3192	*Uvigerina* spp.	3.844	-1.203
12H 5W 80-82	105.20	114.86	3193	*Uvigerina* spp.	3.834	-1.159
12H 5W 90-92	105.30	114.96	3195	*Uvigerina* spp.	4.062	-1.165
12H 5W 130-132	105.70	115.36	3201	*Uvigerina* spp.	3.227	-0.600
12H 5W 130-132	105.70	115.36	3201	*Uvigerina* spp.	3.220	-0.742
12H 5W 140-142	105.80	115.46	3203	*Uvigerina* spp.	3.099	-0.587
12H 6W 10-12	106.00	115.66	3206	*Uvigerina* spp.	2.888	-0.822
12H 6W 20-22	106.10	115.76	3208	*Uvigerina* spp.	3.301	-0.751
12H 6W 30-32	106.20	115.86	3209	*Uvigerina* spp.	3.108	-0.652
12H 6W 30-32	106.20	117.52	3258	*Cibicides* spp.	2.709	0.611
12H 6W 40-42	106.30	115.96	3212	*Uvigerina* spp.	3.550	-1.105
12H 6W 50-52	106.40	116.06	3215	*Uvigerina* spp.	3.253	-0.482
12H 6W 50-52	106.4	116.06	3215	*Cibicides* spp.	2.800	0.333
12H 6W 60-62	106.50	116.16	3218	*Uvigerina* spp.	3.618	-0.384
12H 6W 70-72	106.60	116.26	3221	*Uvigerina* spp.	3.496	-1.268
12H 6W 80-82	106.70	116.36	3224	*Uvigerina* spp.	3.602	-0.593
12H 6W 90-92	106.80	116.46	3226	*Uvigerina* spp.	3.613	-0.571
12H 6W 100-102	106.90	116.56	3229	*Uvigerina* spp.	3.653	-0.573
12H 6W 110-112	107.00	116.66	3232	*Uvigerina* spp.	3.453	-0.573
12H 6W 110-112	107.00	116.66	3232	*Cibicides* spp.	2.586	0.149
12H 6W 120-122	107.10	116.76	3235	*Uvigerina* spp.	3.655	-0.272
12H 6W 120-122	107.10	116.76	3235	*Cibicides* spp.	2.653	0.588
12H 7W 0-2	107.40	117.06	3244	*Uvigerina* spp.	3.240	-0.373
12H 7W 10-12	107.50	117.16	3247	*Uvigerina* spp.	3.417	-0.474
12H 7W 20-22	107.60	117.26	3250	*Uvigerina* spp.	3.384	-0.693
12H 7W 30-32	107.70	117.36	3253	*Uvigerina* spp.	3.401	-0.285
12H 7W 30-32	107.70	117.36	3253	*Cibicides* spp.	2.792	0.622
12H 7W 40-42	107.80	117.46	3256	*Uvigerina* spp.	3.159	-0.488
13H 1W 0-2	107.90	117.78	3265	*Uvigerina* spp.	3.450	-0.480
13H 1W 0-2	107.90	117.78	3265	*Cibicides* spp.	2.793	0.372
13H 1W 10-12	108.00	117.88	3268	*Uvigerina* spp.	3.411	-0.593
13H 1W 20-22	108.10	117.98	3271	*Uvigerina* spp.	3.557	-1.059
13H 1W 20-22	108.10	117.98	3271	*Cibicides* spp.	2.666	0.551

13H 1W 30-32	108.20	118.08	3274	*Uvigerina* spp.	3.766	-0.921
13H 1W 30-32	108.20	118.08	3274	*Cibicides* spp.	2.568	0.220
13H 1W 40-42	108.30	118.18	3277	*Uvigerina* spp.	3.566	-0.637
13H 1W 40-42	108.30	118.18	3277	*Cibicides* spp.	2.708	0.312
13H 1W 50-52	108.40	118.28	3280	*Uvigerina* spp.	3.637	-0.488
13H 1W 70-72	108.60	118.48	3286	*Uvigerina* spp.	3.805	-0.493
13H 1W 70-72	108.60	118.48	3286	*Cibicides* spp.	2.613	0.621
13H 1W 80-82	108.70	118.58	3289	*Uvigerina* spp.	3.346	-0.625
13H 1W 90-92	108.80	118.68	3292	*Uvigerina* spp.	3.296	-0.585
13H 1W 90-92	108.80	118.68	3292	*Cibicides* spp.	2.800	0.478
13H 1W 100-102	108.90	118.78	3295	*Uvigerina* spp.	3.211	-0.713
13H 1W 100-102	108.90	118.78	3295	*Uvigerina* spp.	3.312	-0.668
13H 1W 100-102	108.90	118.78	3295	*Cibicides* spp.	2.736	0.056
13H 1W 100-102	108.90	118.78	3295	*Cibicides* spp.	2.711	0.577
13H 1W 110-112	109.00	118.88	3298	*Uvigerina* spp.	3.456	-0.488
13H 1W 120-122	109.10	118.98	3301	*Uvigerina* spp.	3.190	-0.632
13H 1W 120-122	109.10	118.98	3301	*Cibicides* spp.	2.875	0.349
13H 1W 120-122	109.20	119.08	3304	*Uvigerina* spp.	3.451	-0.665
13H 1W 120-122	109.20	119.08	3304	*Cibicides* spp.	2.578	-0.268
13H 1W 140-142	109.30	119.18	3307	*Uvigerina* spp.	3.484	-0.747
13H 1W 140-142	109.30	119.18	3307	*Cibicides* spp.	2.930	0.309
13H 2W 0-2	109.40	119.28	3310	*Uvigerina* spp.	3.730	-0.573
13H 2W 0-2	109.40	119.28	3310	*Cibicides* spp.	2.849	0.370
13H 2W 0-2	109.40	119.28	3310	*Cibicides* spp.	3.082	0.189
13H 2W 10-12	109.50	119.38	3313	*Uvigerina* spp.	3.937	-0.677
13H 2W 20-22	109.60	119.48	3315	*Uvigerina* spp.	3.651	-0.868
13H 2W 30-32	109.70	119.58	3318	*Uvigerina* spp.	3.615	-0.798
13H 2W 40-42	109.80	119.68	3321	*Uvigerina* spp.	3.654	-0.480
13H 2W 40-42	109.80	119.68	3321	*Cibicides* spp.	2.788	0.255
13H 2W 50-52	109.90	119.78	3324	*Uvigerina* spp.	3.556	-0.467
13H 2W 50-52	109.90	119.78	3324	*Cibicides* spp.	2.718	0.584
13H 2W 50-52	110.00	119.88	3327	*Uvigerina* spp.	3.411	-0.572
13H 2W 70-72	110.10	119.98	3330	*Uvigerina* spp.	3.463	-0.509
13H 2W 70-72	110.10	119.98	3330	*Cibicides* spp.	2.856	0.350
13H 2W 80-82	110.20	120.08	3332	*Uvigerina* spp.	3.428	-0.629
13H 2W 90-92	110.30	120.18	3335	*Cibicides* spp.	3.040	0.423
13H 2W 100-102	110.40	120.28	3338	*Cibicides* spp.	2.801	0.439
13H 2W 110-112	110.50	120.38	3341	*Uvigerina* spp.	3.537	-0.921
13H 2W 120-122	110.60	120.48	3344	*Uvigerina* spp.	3.559	-1.046
13H 2W 120-122	110.60	120.48	3344	*Uvigerina* spp.	3.514	-0.920
13H 2W 140-142	110.80	120.68	3349	*Cibicides* spp.	3.359	-0.767
13H 2W 140-142	110.80	120.68	3349	*Cibicides* spp.	3.435	-0.056
13H 3W 0-2	110.90	120.78	3352	*Cibicides* spp.	3.290	-0.112
13H 3W 20-22	111.10	120.98	3357	*Cibicides* spp.	3.448	0.102
13H 3W 30-32	111.20	121.08	3360	*Cibicides* spp.	3.168	0.096
13H 3W 40-42	111.30	121.18	3363	*Cibicides* spp.	3.181	0.054
13H 3W 70-72	111.60	121.48	3371	*Uvigerina* spp.	3.748	-1.222
13H 3W 110-112	112.00	121.88	3383	*Uvigerina* spp.	3.681	-0.645
13H 3W 110-112	112.00	121.88	3383	*Cibicides* spp.	2.875	0.170
13H 3W 120-122	112.10	121.98	3385	*Uvigerina* spp.	3.543	-0.385
13H 3W 130-132	112.20	122.08	3388	*Uvigerina* spp.	3.263	-0.692
13H 3W 130-132	112.20	122.08	3388	*Cibicides* spp.	2.823	0.368
13H 3W 140-142	112.30	122.18	3391	*Uvigerina* spp.	3.358	-0.785
13H 3W 140-142	112.30	122.18	3391	*Cibicides* spp.	2.797	0.401

13H 4W 0-2	112.40	122.28	3394	*Uvigerina* spp.	3.447	-0.730
13H 4W 0-2	112.40	122.28	3394	*Cibicides* spp.	2.767	0.327
13H 4W 10-12	112.50	122.38	3396	*Uvigerina* spp.	3.437	-0.831
13H 4W 10-12	112.50	122.38	3396	*Cibicides* spp.	2.852	0.362
13H 4W 20-22	112.60	122.48	3399	*Uvigerina* spp.	3.516	-1.135
13H 4W 20-22	112.60	122.48	3399	*Uvigerina* spp.	3.412	-0.667
13H 4W 20-22	112.60	122.48	3399	*Cibicides* spp.	2.790	0.366
13H 4W 20-22	112.60	122.48	3399	*Cibicides* spp.	2.806	0.419
13H 4W 30-32	112.70	122.58	3402	*Uvigerina* spp.	3.292	-0.490
13H 4W 40-42	112.80	122.68	3405	*Uvigerina* spp.	3.445	-0.220
13H 4W 40-42	112.80	122.68	3405	*Cibicides* spp.	2.734	0.720
13H 4W 50-52	112.90	122.78	3408	*Uvigerina* spp.	3.573	-0.981
13H 4W 60-62	113.00	122.88	3410	*Uvigerina* spp.	3.227	-0.672
13H 4W 60-62	113.00	122.88	3410	*Cibicides* spp.	2.703	0.211
13H 4W 70-72	113.10	122.98	3413	*Uvigerina* spp.	3.710	-0.949
13H 4W 70-72	113.10	122.98	3413	*Cibicides* spp.	2.650	0.493
13H 4W 80-82	113.20	123.08	3416	*Uvigerina* spp.	3.546	-0.689
13H 4W 80-82	113.20	123.08	3416	*Cibicides* spp.	2.841	0.310
13H 4W 80-82	113.20	123.08	3416	*Cibicides* spp.	2.700	0.187
13H 4W 90-92	113.30	123.18	3419	*Uvigerina* spp.	3.487	-1.076
13H 4W 100-102	113.40	123.28	3422	*Uvigerina* spp.	3.303	-0.343
13H 4W 100-102	113.40	123.28	3422	*Uvigerina* spp.	3.440	-1.106
13H 4W 100-102	113.40	123.28	3422	*Cibicides* spp.	2.727	-0.148
13H 4W 110-112	113.50	123.38	3424	*Uvigerina* spp.	3.488	-0.359
13H 4W 110-112	113.50	123.38	3424	*Cibicides* spp.	2.738	0.403
13H 4W 120-122	113.60	123.48	3427	*Uvigerina* spp.	3.277	0.023
13H 4W 120-122	113.60	123.48	3427	*Cibicides* spp.	2.633	0.605
13H 4W 130-132	113.70	123.58	3430	*Uvigerina* spp.	3.522	-0.285
13H 4W 130-132	113.70	123.58	3430	*Cibicides* spp.	2.683	0.650
13H 4W 140-142	113.80	123.68	3433	*Uvigerina* spp.	3.373	-0.269
13H 4W 140-142	113.80	123.68	3433	*Cibicides* spp.	2.663	0.707
13H 5W 0-2	113.90	123.78	3436	*Uvigerina* spp.	3.603	-0.410
13H 5W 0-2	113.90	123.78	3436	*Cibicides* spp.	2.678	0.291
13H 5W 10-12	114.00	123.88	3438	*Uvigerina* spp.	3.502	-0.575
13H 5W 10-12	114.00	123.88	3438	*Uvigerina* spp.	3.531	-0.556
13H 5W 10-12	114.00	123.88	3438	*Cibicides* spp.	2.945	0.017
13H 5W 20-22	114.10	123.98	3441	*Uvigerina* spp.	3.381	-0.260
13H 5W 30-32	114.20	124.08	3444	*Uvigerina* spp.	3.015	-0.623
13H 5W 30-32	114.20	124.08	3444	*Uvigerina* spp.	3.187	-0.914
13H 5W 30-32	114.20	124.08	3444	*Cibicides* spp.	2.724	0.210
13H 5W 30-32	114.20	124.08	3444	*Cibicides* spp.	2.746	-0.134
13H 5W 40-42	114.30	124.18	3447	*Cibicides* spp.	3.090	-0.054
13H 5W 50-52	114.40	124.28	3449	*Uvigerina* spp.	3.353	-1.095
13H 5W 60-62	114.50	124.38	3452	*Uvigerina* spp.	3.590	-0.568
13H 5W 60-62	114.50	124.38	3452	*Uvigerina* spp.	3.481	-0.706
13H 5W 60-62	114.50	124.38	3452	*Cibicides* spp.	2.718	-0.410
13H 5W 60-62	114.50	124.38	3452	*Cibicides* spp.	2.829	0.021
13H 5W 70-72	114.60	124.48	3455	*Uvigerina* spp.	3.552	-0.830
13H 5W 70-72	114.60	124.48	3455	*Cibicides* spp.	2.961	0.085
13H 5W 70-72	114.60	124.48	3455	*Cibicides* spp.	2.989	0.172
13H 5W 80-82	114.70	124.58	3458	*Uvigerina* spp.	3.660	-0.984
13H 5W 90-92	114.80	124.68	3461	*Uvigerina* spp.	3.689	-1.115
13H 5W 110-112	115.00	124.88	3466	*Uvigerina* spp.	3.448	-0.949
13H 5W 120-122	115.10	124.98	3469	*Uvigerina* spp.	3.556	-0.409

13H 5W 120-122	115.10	124.98	3469	*Uvigerina* spp.	3.335	-0.728
13H 5W 120-122	115.10	124.98	3469	*Cibicides* spp.	2.493	0.361
13H 5W 130-132	115.20	125.08	3472	*Uvigerina* spp.	3.628	-0.907
13H 5W 130-132	115.20	125.08	3472	*Cibicides* spp.	2.759	0.427
13H 5W 140-142	115.30	125.18	3475	*Uvigerina* spp.	3.437	-0.719
13H 6W 0-2	115.40	125.28	3477	*Uvigerina* spp.	3.391	-0.472
13H 6W 0-2	115.40	125.28	3477	*Cibicides* spp.	2.748	0.129
13H 6W 10-12	115.50	125.38	3480	*Uvigerina* spp.	3.424	-0.904
13H 6W 10-12	115.50	125.38	3480	*Cibicides* spp.	2.739	0.129
13H 6W 20-22	115.60	125.48	3483	*Uvigerina* spp.	3.432	-0.635
13H 6W 30-32	115.70	125.58	3486	*Uvigerina* spp.	3.550	-1.005
13H 6W 30-32	115.70	125.58	3486	*Cibicides* spp.	2.997	0.079
13H 6W 40-42	115.80	125.68	3488	*Uvigerina* spp.	3.596	-1.032
13H 6W 50-52	115.90	125.78	3491	*Uvigerina* spp.	3.551	-1.005
13H 6W 60-62	116.00	125.88	3494	*Cibicides* spp.	2.763	0.081
13H 6W 70-72	116.10	125.98	3497	*Uvigerina* spp.	3.525	-1.092
13H 6W 70-72	116.10	125.98	3497	*Cibicides* spp.	3.005	0.046
13H 6W 80-82	116.20	126.08	3500	*Cibicides* spp.	2.827	-0.006
13H 6W 90-92	116.30	126.18	3502	*Cibicides* spp.	2.796	0.189
13H 6W 100-102	116.40	126.28	3505	*Uvigerina* spp.	3.356	-0.918
13H 6W 110-112	116.50	126.38	3508	*Uvigerina* spp.	3.449	-0.287
13H 6W 120-122	116.60	126.48	3511	*Uvigerina* spp.	3.475	-0.579
13H 6W 120-122	116.60	126.48	3511	*Cibicides* spp.	2.574	0.290
13H 6W 130-132	116.70	126.58	3514	*Uvigerina* spp.	3.445	-1.244
13H 6W 130-132	116.70	126.58	3514	*Cibicides* spp.	2.575	0.219
13H 6W 140-142	116.80	126.68	3516	*Uvigerina* spp.	3.442	-0.877
13H 6W 140-142	116.80	126.68	3516	*Uvigerina* spp.	3.395	-0.724
13H 6W 140-142	116.80	126.68	3516	*Cibicides* spp.	2.591	0.188
13H 7W 0-2	116.90	126.78	3519	*Uvigerina* spp.	3.316	-0.910
13H 7W 0-2	116.90	126.78	3519	*Cibicides* spp.	2.710	0.101
13H 7W 0-2	116.90	126.78	3519	*Cibicides* spp.	2.835	0.266
13H 7W 10-12	117.00	126.88	3522	*Uvigerina* spp.	3.430	-0.966
13H 7W 20-22	117.10	126.98	3525	*Uvigerina* spp.	3.386	-0.651
13H 7W 20-22	117.10	126.98	3525	*Cibicides* spp.	2.564	-0.464
13H 7W 30-32	117.20	127.08	3528	*Uvigerina* spp.	3.227	-0.644
13H 7W 40-42	117.30	127.18	3530	*Uvigerina* spp.	3.311	-0.624
13H 7W 40-42	117.30	127.18	3530	*Cibicides* spp.	2.527	0.413
14H 1W 0-2	117.40	128.72	3573	*Uvigerina* spp.	3.252	-0.742
13H 7W 40-42	117.40	127.28	3533	*Uvigerina* spp.	3.110	-0.696
13H 7W 40-42	117.40	127.28	3533	*Uvigerina* spp.	3.151	-0.622
13H 7W 40-42	117.40	127.28	3533	*Cibicides* spp.	2.456	0.196
13H 7W 40-42	117.40	127.28	3533	*Cibicides* spp.	2.414	0.046
13H 7W 60-62	117.50	127.38	3536	*Uvigerina* spp.	3.293	-0.610
13H 7W 60-62	117.50	127.38	3536	*Uvigerina* spp.	3.293	-0.410
14H IW 10-12	117.50	128.82	3576	*Uvigerina* spp.	3.363	-0.952
13H 7W 60-62	117.50	127.38	3536	*Cibicides* spp.	2.698	0.255
13H CC 0-2	117.57	127.45	3538	*Uvigerina* spp.	3.079	-0.810
13H CC 0-2	117.57	127.45	3538	*Uvigerina* spp.	3.097	-0.867
14H 1W 20-22	117.60	128.92	3579	*Uvigerina* spp.	3.382	-0.479
14H 1W 20-22	117.60	128.92	3579	*Uvigerina* spp.	3.209	-0.548
13H CC 10-12	117.67	127.55	3541	*Uvigerina* spp.	3.232	-0.923
13H CC 10-12	117.67	127.55	3541	*Uvigerina* spp.	3.149	-1.029
14H 1W 30-32	117.70	129.02	3582	*Uvigerina* spp.	3.313	-0.412
14H 1W 30-32	117.70	129.02	3582	*Uvigerina* spp.	3.292	-0.536

14H 1W 40-42	117.80	129.12	3584	*Uvigerina* spp.	3.332	-0.357
14H 1W 40-42	117.80	129.12	3584	*Cibicides* spp.	2.623	0.218
14H 1W 50-52	117.90	129.22	3587	*Uvigerina* spp.	3.118	-0.035
14H 1W 50-52	117.90	129.22	3587	*Uvigerina* spp.	3.111	-0.499
14H 1W 50-52	117.90	129.22	3587	*Cibicides* spp.	2.246	0.030
14H 1W 50-52	117.90	129.22	3587	*Cibicides* spp.	2.091	0.478
14H 1W 60-62	118.00	129.32	3590	*Uvigerina* spp.	3.257	-0.328
14H 1W 60-62	118.00	129.32	3590	*Uvigerina* spp.	3.318	-0.119
14H 1W 70-72	118.10	129.42	3593	*Uvigerina* spp.	3.266	-0.546
14H 1W 80-82	118.20	129.52	3596	*Uvigerina* spp.	3.275	-0.563
14H 1W 90-92	118.30	129.62	3598	*Uvigerina* spp.	3.461	-0.249
14H 1W 90-92	118.30	129.62	3598	*Uvigerina* spp.	3.183	-0.255
14H 1W 90-92	118.30	129.62	3598	*Cibicides* spp.	2.533	0.032
14H 1W 90-92	118.30	129.62	3598	*Cibicides* spp.	2.601	0.674
14H 1W 100-102	118.40	129.72	3601	*Uvigerina* spp.	3.510	-0.404
14H 1W 110-112	118.50	129.82	3604	*Uvigerina* spp.	3.556	-0.427
14H 1W 110-112	118.50	129.82	3604	*Uvigerina* spp.	3.354	-0.556
14H 1W 110-112	118.50	129.82	3604	*Cibicides* spp.	2.479	0.364
14H 1W 110-112	118.50	129.82	3604	*Cibicides* spp.	2.738	0.266
14H 1W 120-122	118.60	129.92	3607	*Uvigerina* spp.	3.560	-0.406
14H 1W 120-122	118.60	129.92	3607	*Cibicides* spp.	2.715	0.470
14H 1W 130-132	118.70	130.02	3610	*Uvigerina* spp.	3.208	-0.983
14H 1W 140-142	118.80	130.12	3612	*Uvigerina* spp.	3.402	-0.490
14H 1W 140-142	118.80	130.12	3612	*Cibicides* spp.	2.617	0.455
14H 2W 0-2	118.90	130.22	3615	*Uvigerina* spp.	3.546	-0.599
14H 2W 0-2	118.90	130.22	3615	*Cibicides* spp.	2.708	0.536
14H 2W 10-12	119.00	130.32	3618	*Uvigerina* spp.	3.381	-0.337
14H 2W 20-22	119.10	130.42	3621	*Uvigerina* spp.	3.348	-0.341
14H 2W 20-22	119.10	130.42	3621	*Cibicides* spp.	2.714	0.452
14H 2W 30-32	119.20	130.52	3624	*Uvigerina* spp.	3.306	-0.293
14H 2W 30-32	119.2	130.52	3624	*Cibicides* spp.	2.460	0.275
14H 2W 40-42	119.30	130.62	3626	*Uvigerina* spp.	3.156	-0.595
14H 2W 40-42	119.30	130.62	3626	*Cibicides* spp.	2.440	0.315
14H 2W 50-52	119.40	130.72	3629	*Uvigerina* spp.	3.023	-0.615
14H 2W 60-62	119.50	130.82	3632	*Uvigerina* spp.	3.232	-0.417
14H 2W 70-72	119.60	130.92	3635	*Uvigerina* spp.	3.311	-0.666
14H 2W 70-72	119.60	130.92	3635	*Cibicides* spp.	2.488	0.221
14H 2W 80-82	119.70	131.02	3638	*Uvigerina* spp.	3.479	-0.661
14H 2W 80-82	119.70	131.02	3638	*Cibicides* spp.	2.903	0.353
14H 2W 80-82	119.70	131.02	3638	*Cibicides* spp.	2.743	0.469
14H 2W 90-92	119.80	131.12	3640	*Uvigerina* spp.	3.616	-0.478
14H 2W 100-102	119.90	131.22	3643	*Uvigerina* spp.	3.565	-0.406
14H 2W 100-102	119.90	131.22	3643	*Uvigerina* spp.	3.590	-0.419
14H 2W 100-102	119.90	131.22	3643	*Uvigerina* spp.	3.666	-0.463
14H 2W 100-102	119.9	131.22	3643	*Cibicides* spp.	2.626	0.276
14H 2W 110-112	120.00	131.32	3646	*Uvigerina* spp.	3.482	-0.512
14H 2W 110-112	120.00	131.32	3646	*Uvigerina* spp.	3.381	-0.680
14H 2W 110-112	120.00	131.32	3646	*Cibicides* spp.	2.454	0.161
14H 2W 110-112	120.00	131.32	3646	*Cibicides* spp.	2.684	0.132
14H 2W 120-122	120.10	131.42	3649	*Uvigerina* spp.	3.516	-0.534
14H 2W 130-132	120.20	131.52	3652	*Uvigerina* spp.	3.559	-0.386
14H 2W 130-132	120.20	131.52	3652	*Cibicides* spp.	2.644	0.469
14H 2W 1340-142	120.30	131.62	3654	*Uvigerina* spp.	3.451	-0.319
14H 2W 1340-142	120.30	131.62	3654	*Uvigerina* spp.	3.428	-0.406

14H 2W 1340-142	120.30	131.62	3654	*Cibicides* spp.	2.638	0.441
14H 3W 0-2	120.40	131.72	3657	*Cibicides* spp.	2.701	0.144
14H 3W 10-12	120.50	131.82	3660	*Uvigerina* spp.	3.432	-0.443
14H 3W 10-12	120.50	131.82	3660	*Uvigerina* spp.	3.300	-0.345
14H 3W 20-22	120.60	131.92	3663	*Uvigerina* spp.	3.374	-0.339
14H 3W 30-32	120.70	132.02	3666	*Uvigerina* spp.	3.493	-0.390
14H 3W 40-42	120.80	132.12	3668	*Uvigerina* spp.	3.497	-0.372
14H 3W 40-42	120.80	132.12	3668	*Cibicides* spp.	2.696	-0.152
14H 3W 50-52	120.90	132.22	3671	*Uvigerina* spp.	3.640	-0.338
14H 3W 60-62	121.00	132.32	3674	*Uvigerina* spp.	3.477	-0.292
14H 3W 60-62	121.00	132.32	3674	*Cibicides* spp.	2.693	0.129
14H 3W 70-72	121.10	132.42	3677	*Uvigerina* spp.	3.344	-0.338
14H 3W 80-82	121.20	132.52	3680	*Uvigerina* spp.	3.412	-0.235
14H 3W 90-92	121.30	132.62	3682	*Uvigerina* spp.	3.277	-0.054
14H 3W 90-92	121.30	132.62	3682	*Cibicides* spp.	2.635	0.578
14H 3W 100-102	121.40	132.72	3685	*Uvigerina* spp.	3.236	-0.224
14H 3W 100-102	121.40	132.72	3685	*Cibicides* spp.	2.654	0.658
14H 3W 110-112	121.50	132.82	3688	*Uvigerina* spp.	3.375	-0.087
14H 3W 120-122	121.60	132.92	3691	*Uvigerina* spp.	3.584	-0.347
14H 3W 120-122	121.60	132.92	3691	*Cibicides* spp.	2.583	0.704
14H 3W 120-122	121.6	132.92	3691	*Cibicides* spp.	2.727	0.402
14H 3W 130-132	121.70	133.02	3694	*Uvigerina* spp.	3.539	-0.590
14H 3W 130-132	121.70	133.02	3694	*Cibicides* spp.	2.541	0.190
14H 3W 140-142	121.80	133.12	3696	*Uvigerina* spp.	3.620	-0.349
14H 4W 0-2	121.90	133.22	3699	*Uvigerina* spp.	3.451	-0.612
14H 4W 0-2	121.90	133.22	3699	*Cibicides* spp.	2.673	0.103
14H 4W 10-12	122.00	133.32	3702	*Uvigerina* spp.	3.444	-0.608
14H 4W 20-22	122.10	133.42	3705	*Uvigerina* spp.	3.651	-0.328
14H 4W 20-22	122.10	133.42	3705	*Uvigerina* spp.	3.672	-0.260
14H 4W 20-22	122.10	133.42	3705	*Cibicides* spp.	2.609	0.025
14H 4W 30-32	122.20	133.52	3708	*Uvigerina* spp.	3.777	-0.633
14H 4W 30-32	122.20	133.52	3708	*Uvigerina* spp.	3.530	-0.746
14H 4W 30-32	122.20	133.52	3708	*Cibicides* spp.	2.698	0.733
14H 4W 40-42	122.30	133.62	3710	*Uvigerina* spp.	3.502	-0.206
14H 4W 50-52	122.40	133.72	3713	*Uvigerina* spp.	3.361	-0.246
14H 4W 70-72	122.60	133.92	3719	*Cibicides* spp.	2.429	0.263
14H 4W 80-82	122.70	135.3	3757	*Uvigerina* spp.	3.239	-0.790
14H 4W 90-92	122.80	134.12	3724	*Uvigerina* spp.	3.136	-0.419
14H 4W 100-102	122.90	134.22	3727	*Uvigerina* spp.	3.422	-0.442
14H 4W 100-102	122.90	134.22	3727	*Uvigerina* spp.	3.250	-0.606
14H 4W 100-102	122.90	134.22	3727	*Cibicides* spp.	3.058	0.088
14H 4W 110-112	123.00	134.32	3730	*Uvigerina* spp.	3.526	-0.723
14H 4W 120-122	123.10	134.42	3733	*Uvigerina* spp.	3.600	-0.660
14H 4W 130-132	123.20	134.52	3736	*Uvigerina* spp.	3.665	-0.921
14H 4W 130-132	123.20	134.52	3736	*Cibicides* spp.	2.561	0.527
14H 4W 140-142	123.30	134.62	3738	*Uvigerina* spp.	3.609	-1.082
14H 4W 140-142	123.3	134.62	3738	*Cibicides* spp.	2.721	-0.103
14H 5W 0-2	123.40	134.72	3741	*Uvigerina* spp.	3.757	-1.064
14H 5W 0-2	123.40	134.72	3741	*Cibicides* spp.	2.999	0.092
14H 5W 0-2	123.40	134.72	3741	*Cibicides* spp.	2.924	0.017
14H 5W 10-12	123.50	134.82	3744	*Uvigerina* spp.	3.478	-0.916
14H 5W 10-12	123.50	134.82	3744	*Cibicides* spp.	2.929	-0.240
14H 5W 20-22	123.60	134.92	3747	*Uvigerina* spp.	3.302	-0.714
14H 5W 20-22	123.60	134.92	3747	*Uvigerina* spp.	3.470	-0.830

14H 5W 30-32	123.70	135.02	3750	*Uvigerina* spp.	3.170	-0.101
14H 5W 30-32	123.70	135.02	3750	*Cibicides* spp.	2.646	0.589
14H 5W 40-42	123.80	135.12	3752	*Uvigerina* spp.	2.921	-0.389
14H 5W 40-42	123.80	135.12	3752	*Cibicides* spp.	2.849	-0.043
14H 5W 50-52	123.90	135.22	3755	*Uvigerina* spp.	3.152	-0.111
14H 5W 60-62	124.00	135.32	3758	*Cibicides* spp.	2.788	0.664
14H 5W 70-72	124.10	135.42	3761	*Uvigerina* spp.	3.462	-0.357
14H 5W 70-72	124.10	135.42	3761	*Uvigerina* spp.	3.341	-0.433
14H 5W 80-82	124.20	135.52	3764	*Uvigerina* spp.	3.357	-0.306
14H 5W 80-82	124.20	135.52	3764	*Cibicides* spp.	2.644	0.635
14H 5W 90-92	124.30	135.62	3766	*Uvigerina* spp.	3.387	-0.253
14H 5W 90-92	124.30	135.62	3766	*Cibicides* spp.	2.419	0.344
14H 5W 90-92	124.3	135.62	3766	*Cibicides* spp.	2.575	0.260
14H 5W 100-102	124.40	135.72	3769	*Uvigerina* spp.	3.154	-0.504
14H 5W 110-112	124.50	135.82	3772	*Uvigerina* spp.	3.194	-1.125
14H 5W 110-112	124.50	135.82	3772	*Cibicides* spp.	2.460	0.287
14H 5W 120-122	124.60	135.92	3775	*Uvigerina* spp.	3.390	-0.873
14H 5W 130-132	124.70	136.02	3778	*Uvigerina* spp.	3.534	-0.934
14H 5W 130-132	124.70	136.02	3778	*Uvigerina* spp.	3.585	-0.998
14H 5W 130-132	124.70	136.02	3778	*Cibicides* spp.	2.616	0.116
14H 5W 140-142	124.80	136.12	3780	*Uvigerina* spp.	3.606	-0.714
14H 6W 0-2	124.90	136.22	3783	*Uvigerina* spp.	3.630	-1.027
14H 6W 0-2	124.90	136.22	3783	*Cibicides* spp.	2.959	0.093
14H 6W 10-12	125.00	136.32	3786	*Uvigerina* spp.	3.441	-0.690
14H 6W 10-12	125.00	136.32	3786	*Cibicides* spp.	2.898	0.027
14H 6W 20-22	125.10	136.42	3789	*Uvigerina* spp.	3.278	-0.571
14H 6W 20-22	125.10	136.42	3789	*Uvigerina* spp.	3.038	-0.761
14H 6W 30-32	125.20	136.52	3792	*Uvigerina* spp.	3.168	-0.649
14H 6W 30-32	125.20	136.52	3792	*Cibicides* spp.	2.420	0.439
14H 6W 40-42	125.30	136.62	3794	*Uvigerina* spp.	3.293	-0.479
14H 6W 50-52	125.40	136.72	3797	*Uvigerina* spp.	3.366	-0.407
14H 6W 50-52	125.40	136.72	3797	*Cibicides* spp.	2.384	0.215
14H 6W 60-62	125.50	136.82	3800	*Uvigerina* spp.	3.231	-0.437
14H 6W 60-62	125.50	136.82	3800	*Cibicides* spp.	2.403	0.488
14H 6W 70-72	125.60	136.92	3803	*Uvigerina* spp.	3.324	-0.543
14H 6W 70-72	125.60	136.92	3803	*Cibicides* spp.	2.693	0.568
14H 6W 80-82	125.70	137.02	3806	*Uvigerina* spp.	3.413	-0.546
14H 6W 90-92	125.80	137.12	3808	*Uvigerina* spp.	3.501	-0.709
14H 6W 100-102	125.90	137.22	3811	*Uvigerina* spp.	3.548	-0.879
14H 6W 100-102	125.90	137.22	3811	*Cibicides* spp.	2.761	0.297
14H 6W 110-112	126.00	137.32	3814	*Uvigerina* spp.	3.489	-0.906
14H 6W 120-122	126.10	137.42	3817	*Uvigerina* spp.	3.391	-0.931
14H 6W 130-132	126.20	137.52	3820	*Cibicides* spp.	2.844	0.344
14H 6W 140-142	126.30	137.62	3822	*Uvigerina* spp.	3.320	-0.728
14H 7W 0-2	126.40	137.72	3825	*Uvigerina* spp.	3.455	-0.971
14H 7W 0-2	126.4	137.72	3825	*Cibicides* spp.	2.796	0.377
14H 7W 10-12	126.50	137.82	3828	*Uvigerina* spp.	3.628	-0.903
14H 7W 20-22	126.60	137.92	3831	*Uvigerina* spp.	3.279	-0.456
14H 7W 20-22	126.60	137.92	3831	*Uvigerina* spp.	3.166	-0.599
14H 7W 20-22	126.60	137.92	3831	*Uvigerina* spp.	3.005	-0.804
14H 7W 20-22	126.60	137.92	3831	*Cibicides* spp.	2.424	0.456
14H 7W 30-32	126.70	138.02	3834	*Uvigerina* spp.	3.390	-0.709
14H 7W 30-32	126.70	138.02	3834	*Cibicides* spp.	2.722	0.458
14H 7W 40-42	126.80	139.4	3872	*Uvigerina* spp.	2.986	-0.367

15H 1W 0-2	126.90	139.5	3875	*Uvigerina* spp.	3.053	-0.531
15H 1W 10-12	127.00	139.6	3878	*Uvigerina* spp.	3.225	-0.765
15H 1W 20-22	127.10	139.7	3881	*Uvigerina* spp.	3.307	-0.792
15H 1W 30-32	127.20	139.8	3884	*Uvigerina* spp.	3.353	-0.383
15H 1W 30-32	127.20	139.8	3884	*Cibicides* spp.	2.828	0.375
15H 1W 40-42	127.30	139.9	3886	*Uvigerina* spp.	3.212	-0.822
15H 1W 40-42	127.30	139.9	3886	*Cibicides* spp.	2.693	0.206
15H 1W 50-52	127.40	140	3889	*Uvigerina* spp.	3.062	-0.950
15H 1W 60-62	127.50	140.1	3892	*Uvigerina* spp.	3.126	-0.945
15H 1W 60-62	127.50	140.1	3892	*Cibicides* spp.	2.422	0.081
15H 1W 70-72	127.60	140.2	3895	*Uvigerina* spp.	3.094	-0.952
15H 1W 80-82	127.70	140.3	3898	*Uvigerina* spp.	3.604	-1.134
15H 1W 80-82	127.70	140.3	3898	*Cibicides* spp.	2.405	0.038
15H 1W 90-92	127.80	140.4	3900	*Uvigerina* spp.	3.539	-0.880
15H 1W 100-102	127.90	140.5	3903	*Uvigerina* spp.	3.240	-0.520
15H 1W 110-112	128.00	140.6	3906	*Uvigerina* spp.	3.239	-0.555
15H 1W 120-122	128.10	140.7	3909	*Uvigerina* spp.	3.205	-0.497
15H 1W 120-122	128.10	140.7	3909	*Cibicides* spp.	2.670	0.404
15H 1W 130-132	128.20	140.8	3912	*Uvigerina* spp.	2.937	-0.699
15H 1W 140-142	128.30	140.9	3914	*Uvigerina* spp.	3.084	-0.544
15H 2W 0-2	128.40	141	3917	*Uvigerina* spp.	3.259	-0.817
15H 2W 10-12	128.50	141.1	3920	*Uvigerina* spp.	3.254	-0.913
15H 2W 20-22	128.60	141.2	3923	*Uvigerina* spp.	3.071	-0.579
15H 2W 30-32	128.70	141.3	3926	*Uvigerina* spp.	3.240	-0.552
15H 2W 30-32	128.70	141.3	3926	*Cibicides* spp.	2.450	0.120
15H 2W 40-42	128.80	141.4	3928	*Uvigerina* spp.	3.277	-0.888
15H 2W 40-42	128.80	141.4	3928	*Cibicides* spp.	2.613	0.315
15H 2W 50-52	128.90	141.5	3931	*Uvigerina* spp.	3.241	-1.118
15H 2W 60-62	129.00	141.6	3934	*Uvigerina* spp.	3.560	-1.091
15H 2W 70-72	129.10	141.7	3937	*Uvigerina* spp.	3.277	-1.113
15H 2W 70-72	129.10	141.7	3937	*Cibicides* spp.	3.001	0.202
15H 2W 80-82	129.20	141.8	3940	*Uvigerina* spp.	3.556	-0.912
15H 2W 90-92	129.30	141.9	3942	*Uvigerina* spp.	3.439	-0.836
15H 2W 100-102	129.40	142	3945	*Uvigerina* spp.	3.324	-0.836
15H 2W 110-112	129.50	142.1	3948	*Uvigerina* spp.	3.257	-0.898
15H 2W 110-112	129.50	142.1	3948	*Cibicides* spp.	2.684	0.358
15H 2W 120-122	129.60	142.2	3951	*Uvigerina* spp.	3.205	-0.676
15H 2W 120-122	129.60	142.2	3951	*Cibicides* spp.	2.588	0.355
15H 2W 130-132	129.70	142.3	3954	*Uvigerina* spp.	3.152	-0.939
15H 2W 140-142	129.80	142.4	3956	*Uvigerina* spp.	3.112	-0.771
15H 2W 140-142	129.80	142.4	3956	*Cibicides* spp.	2.555	0.416
15H 3W 0-2	129.90	142.5	3959	*Uvigerina* spp.	2.988	-0.461
15H 3W 10-12	130.00	142.6	3962	*Uvigerina* spp.	3.236	-0.388
15H 3W 20-22	130.10	142.7	3965	*Uvigerina* spp.	3.134	-0.523
15H 3W 20-22	130.10	142.7	3965	*Cibicides* spp.	2.541	0.547
15H 3W 30-32	130.20	142.8	3968	*Uvigerina* spp.	3.309	-0.413
15H 3W 30-32	130.20	142.8	3968	*Cibicides* spp.	2.663	0.318
15H 3W 40-42	130.30	142.9	3970	*Uvigerina* spp.	2.924	-0.704
15H 3W 40-42	130.30	142.9	3970	*Cibicides* spp.	2.575	0.323
15H 3W 50-52	130.40	143	3973	*Uvigerina* spp.	3.150	-1.157
15H 3W 60-62	130.50	143.1	3976	*Uvigerina* spp.	3.278	-1.098
15H 3W 70-72	130.60	143.2	3979	*Uvigerina* spp.	3.131	-1.261
15H 3W 70-72	130.60	143.2	3979	*Cibicides* spp.	2.499	0.115
15H 3W 80-82	130.70	143.3	3982	*Uvigerina* spp.	3.227	-1.353

15H 3W 80-82	130.70	143.3	3982	*Cibicides* spp.	2.640	0.037
15H 3W 90-92	130.80	143.4	3984	*Uvigerina* spp.	3.264	-0.971
15H 3W 90-92	130.80	143.4	3984	*Cibicides* spp.	2.725	0.068
15H 3W 100-102	130.90	143.5	3987	*Uvigerina* spp.	3.201	-0.767
15H 3W 110-122	131.00	143.6	3990	*Uvigerina* spp.	3.056	-0.727
15H 3W 110-122	131.00	143.6	3990	*Cibicides* spp.	2.668	0.377
15H 3W 120-122	131.10	143.7	3993	*Uvigerina* spp.	3.121	-0.401
15H 3W 120-122	131.10	143.7	3993	*Cibicides* spp.	2.686	0.268
15H 3W 130-132	131.20	143.8	3996	*Uvigerina* spp.	3.082	-0.836
15H 3W 130-132	131.20	143.8	3996	*Cibicides* spp.	2.541	0.171
15H 3W 140-142	131.30	143.9	3998	*Uvigerina* spp.	2.969	-0.841
15H 3W 140-142	131.30	143.9	3998	*Cibicides* spp.	2.517	0.233
15H 4W 0-2	131.43	144.03	4002	*Uvigerina* spp.	3.289	-0.726
15H 4W 10-12	131.53	144.13	4005	*Uvigerina* spp.	3.152	-0.722
15H 4W 20-22	131.63	144.23	4008	*Uvigerina* spp.	2.865	-0.496
15H 4W 30-32	131.73	144.33	4010	*Uvigerina* spp.	2.883	-0.718
15H 4W 30-32	131.73	144.33	4010	*Cibicides* spp.	2.792	0.426
15H 4W 40-42	131.83	144.43	4013	*Uvigerina* spp.	3.004	-0.535
15H 4W 50-52	131.93	144.53	4016	*Uvigerina* spp.	3.343	-0.540
15H 4W 60-62	132.03	144.63	4019	*Uvigerina* spp.	3.238	-0.514
15H 4W 70-72	132.13	144.73	4022	*Uvigerina* spp.	3.355	-0.487
15H 4W 70-72	132.13	144.73	4022	*Cibicides* spp.	2.629	0.437
15H 4W 80-82	132.23	144.83	4024	*Uvigerina* spp.	3.236	-0.719
15H 4W 90-92	132.33	144.93	4027	*Uvigerina* spp.	2.891	-0.429
15H 4W 90-92	132.33	144.93	4027	*Cibicides* spp.	3.047	0.508
15H 4W 100-102	132.43	145.03	4030	*Uvigerina* spp.	3.458	-0.439
15H 4W 110-112	132.53	145.13	4033	*Uvigerina* spp.	3.251	-0.725
15H 4W 120-122	132.63	145.23	4036	*Uvigerina* spp.	3.531	-0.725
15H 4W 130-132	132.73	145.33	4038	*Uvigerina* spp.	3.421	-0.455
15H 4W 130-132	132.73	145.33	4038	*Cibicides* spp.	2.816	0.316
15H 4W 140-142	132.83	145.43	4041	*Uvigerina* spp.	3.399	-0.901
15H 4W 140-142	132.83	145.43	4041	*Cibicides* spp.	2.762	0.132
15H 5W 0-2	132.96	145.56	4045	*Uvigerina* spp.	3.145	-0.287
15H 5W 10-12	133.06	145.66	4048	*Uvigerina* spp.	3.355	-0.379
15H 5W 20-22	133.16	145.76	4050	*Uvigerina* spp.	3.142	-0.867
15H 5W 30-32	133.26	145.86	4053	*Uvigerina* spp.	3.077	-0.515
15H 5W 40-42	133.36	145.96	4056	*Uvigerina* spp.	3.175	-0.501
15H 5W 50-52	133.46	146.06	4059	*Uvigerina* spp.	3.175	-0.636
15H 5W 60-62	133.56	146.16	4062	*Uvigerina* spp.	2.903	-0.431
15H 5W 60-62	133.56	146.16	4062	*Uvigerina* spp.	2.921	-0.633
15H 5W 70-72	133.66	146.26	4064	*Uvigerina* spp.	3.528	-0.803
15H 5W 80-82	133.76	146.36	4067	*Uvigerina* spp.	3.311	-0.709
15H 5W 80-82	133.76	146.36	4067	*Cibicides* spp.	2.714	0.126
15H 5 90-92	133.86	146.46	4070	*Uvigerina* spp.	3.382	-0.655
15H 5W 100-102	133.96	146.56	4073	*Uvigerina* spp.	3.202	-0.764
15H 5W 110-112	134.06	146.66	4076	*Uvigerina* spp.	3.247	-0.516
15H 5W 120-122	134.16	146.76	4078	*Uvigerina* spp.	3.026	-0.691
15H 5W 130-132	134.26	146.86	4081	*Uvigerina* spp.	3.107	-0.533
15H 5W 140-142	134.36	146.96	4084	*Uvigerina* spp.	3.049	-0.464
15H 5W 140-142	134.36	146.96	4084	*Cibicides* spp.	2.434	0.338
15H 6W 0-2	134.46	147.06	4087	*Uvigerina* spp.	3.087	-0.492
15H 6W 10-12	134.56	147.16	4090	*Uvigerina* spp.	3.078	-0.439
15H 6W 20-22	134.66	147.26	4092	*Uvigerina* spp.	3.249	-0.562
15H 6W 30-32	134.76	147.36	4095	*Uvigerina* spp.	3.229	-0.460

15H 6W 40-42	134.86	147.46	4098	*Uvigerina* spp.	3.157	-0.602
15H 6W 50-52	134.96	147.56	4101	*Uvigerina* spp.	3.326	-0.583
15H 6W 60-62	135.06	147.66	4104	*Uvigerina* spp.	3.408	-0.951
15H 6W 70-72	135.16	147.76	4106	*Uvigerina* spp.	3.406	-1.000
15H 6W 80-82	135.26	147.86	4109	*Uvigerina* spp.	3.485	-0.828
15H 6W 80-82	135.26	147.86	4109	*Cibicides* spp.	2.620	0.098
15H 6W 90-92	135.36	147.96	4112	*Uvigerina* spp.	3.459	-0.874
15H 6W 100-102	135.46	148.06	4115	*Uvigerina* spp.	3.068	-0.076
15H 6W 100-102	135.56	148.16	4118	*Uvigerina* spp.	3.040	-0.401
15H 6W 120-122	135.66	148.26	4120	*Uvigerina* spp.	3.265	-0.156
15H 6W 130-132	135.76	148.36	4123	*Uvigerina* spp.	3.424	-0.456
15H 6W 140-142	135.86	148.46	4126	*Uvigerina* spp.	3.018	-0.317
15H 7W 0-2	135.96	148.56	4129	*Uvigerina* spp.	3.271	-0.523
15H 7W 10-12	136.06	148.66	4132	*Uvigerina* spp.	3.321	-0.414
15H 7W 20-22	136.16	148.76	4135	*Uvigerina* spp.	3.296	-0.251
15H 7W 30-32	136.26	148.86	4137	*Uvigerina* spp.	3.307	-0.188
15H 7W 40-42	136.36	148.96	4140	*Uvigerina* spp.	3.186	-0.159
16H 1W 0-2	136.40	151.14	4216	*Uvigerina* spp.	3.443	-0.132
16H 1W 10-12	136.50	151.24	4220	*Uvigerina* spp.	3.382	-0.386
16H 1W 10-12	136.50	151.24	4220	*Cibicides* spp.	2.675	0.391
16H 1W 20-22	136.60	151.34	4224	*Uvigerina* spp.	3.373	-0.096
15H CC 10-12	136.68	151.42	4228	*Uvigerina* spp.	3.311	-0.285
16H 1W 30-32	136.70	151.44	4229	*Uvigerina* spp.	3.278	-0.150
16H 1W 40-42	136.80	151.54	4233	*Uvigerina* spp.	3.277	-0.582
16H 1W 50-52	136.90	151.64	4237	*Uvigerina* spp.	3.101	-0.391
16H 1W 50-52	136.90	151.64	4237	*Uvigerina* spp.	3.202	-0.321
16H 1W 60-62	137.00	151.74	4242	*Uvigerina* spp.	3.199	-0.177
16H 1W 70-72	137.10	151.84	4246	*Uvigerina* spp.	3.166	-0.145
16H 1W 80-82	137.20	151.94	4250	*Uvigerina* spp.	3.268	-0.408
16H 1W 90-92	137.30	152.04	4255	*Uvigerina* spp.	3.366	-0.281
16H 1W 90-92	137.30	152.04	4255	*Cibicides* spp.	2.487	0.460
16H 1W 100-102	137.40	152.14	4259	*Uvigerina* spp.	2.879	-0.274
16H 1W 110-112	137.50	152.24	4263	*Uvigerina* spp.	2.953	-0.383
16H 1W 130-132	137.70	152.44	4272	*Uvigerina* spp.	3.315	-0.225
16H 1W 130-132	137.70	152.44	4272	*Uvigerina* spp.	3.085	-0.118
16H 1W 140-142	137.80	152.54	4276	*Uvigerina* spp.	3.368	-0.430
16H 2W 0-2	137.90	152.64	4281	*Uvigerina* spp.	3.113	-0.286
16H 2W 10-12	138.00	152.74	4285	*Uvigerina* spp.	3.172	-0.483
16H 2W 20-22	138.10	152.84	4289	*Uvigerina* spp.	3.174	-0.886
16H 2W 30-32	138.20	152.94	4293	*Uvigerina* spp.	3.181	-0.848
16H 2W 40-42	138.30	153.04	4298	*Uvigerina* spp.	3.440	-0.755
16H 2W 50-52	138.40	153.14	4302	*Uvigerina* spp.	3.306	-0.570
16H 2W 60-62	138.50	153.24	4306	*Uvigerina* spp.	3.326	-0.357
16H 2W 80-82	138.70	153.44	4309	*Uvigerina* spp.	2.932	-0.897
16H 2W 90-92	138.80	153.54	4311	*Uvigerina* spp.	3.051	-0.616
16H 2W 100-102	138.90	153.64	4313	*Uvigerina* spp.	3.150	-0.489
16H 2W 110-112	139.00	153.74	4314	*Uvigerina* spp.	3.251	-0.824
16H 2W 120-122	139.10	153.84	4316	*Uvigerina* spp.	3.349	-0.600
16H 2W 130-132	139.20	153.94	4318	*Uvigerina* spp.	3.247	-0.707
16H 2W 130-132	139.20	153.94	4318	*Uvigerina* spp.	3.074	-0.287
16H 2W 140-142	139.30	154.04	4319	*Uvigerina* spp.	3.236	-0.505
16H 1W 110-112	139.50	154.24	4322	*Uvigerina* spp.	3.516	-0.634
16H 3W 20-22	139.60	154.34	4324	*Uvigerina* spp.	3.102	-1.050
16H 3W 30-32	139.70	154.44	4326	*Uvigerina* spp.	3.570	-0.694

16H 3W 40-42	139.80	154.54	4327	*Uvigerina* spp.	3.593	-0.762
16H 3W 50-52	139.90	154.64	4329	*Uvigerina* spp.	3.438	-0.573
16H 3W 60-62	140.00	154.74	4331	*Uvigerina* spp.	3.344	-0.292
16H 3W 70-72	140.10	154.84	4332	*Uvigerina* spp.	3.108	-0.677
16H 3W 90-92	140.30	155.04	4335	*Uvigerina* spp.	3.118	-0.395
16H 3W 90-92	140.30	155.04	4335	*Uvigerina* spp.	3.263	-0.525
16H 3W 100-102	140.40	155.14	4337	*Uvigerina* spp.	3.216	-0.616
16H 3W 110-112	140.50	155.24	4339	*Uvigerina* spp.	3.327	-0.539
16H 3W 120-122	140.60	155.34	4340	*Uvigerina* spp.	2.954	-0.547
16H 3W 140-142	140.80	155.54	4344	*Uvigerina* spp.	3.211	-0.387
16H 4W 0-2	140.90	155.64	4345	*Uvigerina* spp.	3.025	-0.462
16H 4W 10-12	141.00	155.74	4347	*Uvigerina* spp.	3.070	-0.407
16H 4W 20-22	141.10	155.84	4348	*Uvigerina* spp.	2.976	-0.455
16H 4W 30-32	141.20	155.94	4350	*Uvigerina* spp.	3.203	-0.129
16H 4W 60-62	141.50	156.24	4355	*Uvigerina* spp.	3.426	-0.539
16H 4W 70-72	141.60	156.34	4357	*Uvigerina* spp.	2.978	-0.568
16H 4W 80-82	141.70	156.44	4358	*Uvigerina* spp.	3.083	-0.548
16H 4W 100-102	141.90	156.64	4361	*Uvigerina* spp.	2.865	-0.504
16H 4W 110-112	142.00	156.74	4363	*Uvigerina* spp.	3.075	-0.529

ODP Site 1123 frequency percent of grain size analysis

Core, section, interval (cm)	Depth (mbsf)	rMCD	Age (Ka)	Clay (%) (<4µm)	Silt (%) (4-63µm)	Silt/Clay	Sortable Silt (10-63µm)
12H 1W 10-12	98.50	108.16	3009	29.89	69.94	2.34	19.36
12H 1 30-32	98.70	108.36	3014	30.87	68.49	2.22	15.75
12H 1W 50-52	98.90	108.56	3019	32.98	65.27	1.98	15.35
12H 1W 90-92	99.30	108.96	3030	34.24	65.10	1.90	15.27
12H 1W 110-112	99.50	109.16	3036	30.98	67.30	2.17	15.27
12H 1W 130-132	99.70	109.36	3041	35.35	63.72	1.80	14.61
12H 2W 0-2	99.90	109.56	3049	31.73	67.44	2.13	16.62
12H 2W 20-22	100.10	109.76	3063	34.59	63.64	1.84	15.34
12H 2W 40-42	100.30	109.96	3076	33.92	65.28	1.92	15.31
12H 2W 60-62	100.50	110.16	3090	34.31	65.39	1.91	14.95
12H 2W 80-82	100.70	110.36	3104	36.81	61.46	1.67	17.39
12H 2W 100-102	100.90	110.56	3117	16.94	86.08	5.08	22.02
12H 2W 120-122	101.10	110.76	3128	20.32	79.53	3.91	17.42
12H 2W 140-142	101.30	110.96	3131	20.01	79.39	3.97	17.30
12H 3W 10-12	101.50	111.16	3134	21.31	76.72	3.60	17.42
12H 3W 30-32	101.70	111.36	3138	22.14	75.64	3.42	17.28
12H 3W 50-52	101.90	111.56	3141	25.65	74.38	2.90	18.16
12H 3W 70-72	102.10	111.76	3144	15.84	85.57	5.40	20.31
12H 3W 90-92	102.30	111.96	3147	17.56	82.08	4.67	18.94
12H 3W 110-112	102.50	112.16	3150	16.42	85.76	5.22	19.87
12H 3W 130-132	102.70	112.36	3153	44.03	54.60	1.24	15.87
12H 4W 0-2	102.90	112.56	3157	36.67	61.85	1.69	15.81
12H 4W 20-22	103.10	112.76	3160	34.29	65.10	1.90	14.87
12H 4W 40-42	103.30	112.96	3163	35.10	64.29	1.83	15.18
12H 4W 60-62	103.50	113.16	3166	35.46	63.93	1.80	14.67
12H 4W 80-82	103.70	113.36	3169	34.41	65.52	1.90	16.04
12H 4W 100-102	103.90	113.56	3173	34.17	64.27	1.88	15.91
12H 4W 110-112	104.00	113.66	3174	30.27	69.08	2.28	16.92
12H 4W 120-122	104.10	113.76	3176	37.69	60.91	1.62	14.92
12H 4W 140-142	104.30	113.96	3179	19.08	83.99	4.40	19.63
12H 5W 10-12	104.50	114.16	3182	32.66	65.45	2.00	14.61
12H 5W 20-22	104.60	114.26	3184	30.17	69.62	2.31	16.48
12H 5W 30-32	104.70	114.36	3185	40.04	58.86	1.47	14.77
12H 5W 40-42	104.80	114.46	3187	31.96	67.00	2.10	15.15
12H 5W 50-52	104.90	114.56	3189	31.47	67.70	2.15	14.98
12H 5W 60-62	105.00	114.66	3190	27.42	72.43	2.64	14.94
12H 5W 70-72	105.10	114.76	3192	28.26	70.22	2.48	15.08
12H 5W 80-82	105.20	114.86	3193	30.23	68.91	2.28	16.20
12H 5W 90-92	105.30	114.96	3195	31.82	67.52	2.12	15.50
12H 5W 100-102	105.40	115.06	3197	37.37	62.20	1.66	14.38
12H 5W 110-113	105.60	115.26	3200	32.35	66.49	2.06	16.03
12H 5W 130-132	105.70	115.36	3201	35.17	64.70	1.84	16.10
12H 5W 140-142	105.80	115.46	3203	20.97	80.17	3.82	14.88
12H 6W 0-2	105.90	115.56	3205	30.36	67.74	2.23	15.33
12H 6W 10-12	106.00	115.66	3206	26.30	72.58	2.76	14.02
12H 6W 30-32	106.20	115.86	3209	30.57	68.27	2.23	14.40
12H 6W 40-42	106.30	115.96	3212	35.98	62.77	1.74	14.63
12H 6W 50-52	106.40	116.06	3215	30.62	69.33	2.26	14.72
12H 6W 60-62	106.50	116.16	3218	33.11	65.92	1.99	15.69
12H 6W 70-72	106.60	116.26	3221	28.05	71.04	2.53	14.17

12H 6W 80-82	106.70	116.36	3224	34.38	64.33	1.87	15.01
12H 6W 90-92	106.80	116.46	3226	32.01	67.00	2.09	15.57
12H 6W 110-112	107.00	116.66	3232	28.82	70.52	2.45	15.24
12H 6W 120-122	107.10	116.76	3235	32.12	65.41	2.04	15.29
12H 6W 130-132	107.20	116.86	3238	30.34	68.56	2.26	15.36
12H 6W 140-142	107.30	116.96	3241	30.26	68.40	2.26	15.87
12H 7W 0-2	107.40	117.06	3244	30.85	67.69	2.19	15.34
12H 7W 10-12	107.50	117.16	3247	34.10	65.21	1.91	15.46
12H 7W 20-22	107.60	117.26	3250	28.74	69.28	2.41	15.02
12H 7W 30-32	107.70	117.36	3253	30.37	68.34	2.25	15.40
12H 7W 40-42	107.80	117.46	3256	31.30	67.57	2.16	15.02
13H 1W 0-2	107.90	117.56	3259	30.01	68.66	2.29	15.28
13H 1W 10-12	108.00	117.66	3262	28.32	71.03	2.51	15.57
13H 1W 20-22	108.10	117.76	3265	31.34	66.73	2.13	15.15
13H 1W 30-32	108.20	117.86	3268	28.47	69.03	2.42	15.34
13H 1W 40-42	108.30	117.96	3271	28.20	70.92	2.51	15.80
13H 1W 50-52	108.40	118.06	3274	25.36	74.60	2.94	15.67
13H 1W 60-62	108.50	118.16	3277	29.48	68.69	2.33	15.27
13H 1W 70-72	108.60	118.26	3280	25.23	72.35	2.87	15.76
13H 1W 80-82	108.70	118.36	3282	30.13	68.59	2.28	15.47
13H 1W 90-92	108.80	118.46	3285	28.96	69.89	2.41	15.42
13H 1W 100-102	108.90	118.56	3288	28.48	70.39	2.47	16.03
13H 1W 110-112	109.00	118.66	3291	25.35	73.83	2.91	15.06
13H 1W 120-122	109.10	118.76	3294	27.28	70.61	2.59	16.31
13H 1W 120-122	109.20	118.86	3297	24.25	74.80	3.09	16.30
13H 1W 140-142	109.30	118.96	3300	23.36	75.89	3.25	17.24
13H 2W 0-2	109.40	119.06	3303	24.52	74.32	3.03	16.79
13H 2W 10-12	109.50	120.82	3353	14.45	87.74	6.07	19.52
13H 2W 20-22	109.60	119.26	3309	16.38	83.73	5.11	17.44
13H 2W 30-32	109.70	119.36	3312	31.83	65.95	2.07	15.28
13H 2W 40-42	109.80	119.46	3315	29.68	69.52	2.34	15.46
13H 2W 50-52	109.90	119.56	3318	33.22	65.82	1.98	14.67
13H 2W 50-52	110.00	119.66	3321	30.09	69.27	2.30	14.23
13H 2W 70-72	110.10	119.76	3323	31.32	66.56	2.12	15.41
13H 2W 80-82	110.20	119.86	3326	30.03	69.59	2.32	14.11
13H 2W 90-92	110.30	119.96	3329	32.53	67.00	2.06	14.68
13H 2W 100-102	110.40	120.06	3332	25.54	74.57	2.92	14.74
13H 2W 110-112	110.50	120.16	3335	29.81	69.36	2.33	14.83
13H 2W 120-122	110.60	120.26	3337	26.25	73.40	2.80	15.00
13H 2W 130-132	110.70	120.36	3340	28.94	69.95	2.42	14.83
13H 2W 140-142	110.80	120.46	3343	26.83	72.63	2.71	14.74
13H 3W 0-2	110.90	120.56	3346	31.95	65.70	2.06	15.21
13H 3W 10-12	111.00	120.66	3349	30.60	68.72	2.25	14.82
13H 3W 20-22	111.10	120.76	3351	33.93	65.59	1.93	15.25
13H 3W 30-32	111.20	120.86	3354	29.51	69.82	2.37	14.71
13H 3W 40-42	111.30	120.96	3357	33.51	65.75	1.96	15.80
13H 3W 50 -52	111.40	121.28	3366	26.61	72.45	2.72	15.98
13H 3W 60-62	111.50	121.38	3369	24.93	73.67	2.96	15.83
13H 3W 80-82	111.70	121.58	3374	29.56	70.54	2.39	15.42
13H 3W 90-92	111.80	121.68	3377	28.91	69.48	2.40	16.07
13H 3W 100-102	111.90	121.78	3380	26.50	75.00	2.83	20.46
13H 3W 110-112	112.00	121.88	3383	23.06	74.51	3.23	16.52
13H 3W 120-122	112.10	121.98	3385	10.95	86.41	7.89	23.83
13H 3W 130-132	112.20	122.08	3388	25.27	73.50	2.91	16.56

13H 3W 140-142	112.30	122.18	3391	24.88	74.50	2.99	16.02
13H 4W 0-2	112.40	122.28	3394	27.74	73.10	2.64	15.51
13H 4W 10-12	112.50	122.38	3396	26.11	72.63	2.78	16.10
13H 4W 20-22	112.60	122.48	3399	26.92	72.55	2.69	14.97
13H 4W 30-32	112.70	122.58	3402	27.09	72.67	2.68	16.14
13H 4W 40-42	112.80	122.68	3405	27.54	71.56	2.60	15.50
13H 4W 50-52	112.90	122.78	3408	26.91	72.38	2.69	15.34
13H 4W 60-62	113.00	122.88	3410	25.86	72.31	2.80	17.35
13H 4W 70-72	113.10	122.98	3413	34.21	64.76	1.89	15.09
13H 4W 80-82	113.20	123.08	3416	25.54	72.95	2.86	15.73
13H 4W 90-92	113.30	123.18	3419	38.35	59.80	1.56	14.84
13H 4W 100-102	113.40	123.28	3422	24.31	73.33	3.02	17.18
13H 4W 110-112	113.50	123.38	3424	26.67	71.84	2.69	16.58
13H 4W 120-122	113.60	123.48	3427	26.48	73.13	2.76	15.19
13H 4W 130-132	113.70	123.58	3430	30.89	67.52	2.19	15.35
13H 4W 140-142	113.80	123.68	3433	23.10	76.13	3.30	17.35
13H 5W 0-2	113.90	123.78	3436	32.07	67.55	2.11	15.45
13H 5W 10-12	114.00	123.88	3438	26.80	73.05	2.73	17.96
13H 5W 20-22	114.10	123.98	3441	27.79	70.03	2.52	16.57
13H 5W 30-32	114.20	124.08	3444	23.29	75.20	3.23	16.10
13H 5W 40-42	114.30	124.18	3447	28.52	71.15	2.49	15.39
13H 5W 60-62	114.50	124.38	3452	26.63	72.30	2.72	15.29
13H 5W 70-72	114.60	124.48	3455	23.34	76.91	3.30	15.59
13H 5W 80-82	114.70	124.58	3458	27.58	71.82	2.60	15.25
13H 5W 90-92	114.80	124.68	3461	29.92	68.72	2.30	14.82
13H 5W 110-112	115.00	124.88	3466	26.51	71.37	2.69	15.47
13H 5W 120-122	115.10	124.98	3469	31.63	67.24	2.13	15.29
13H 5W 130-132	115.20	125.08	3472	26.97	71.95	2.67	15.88
13H 5W 140-142	115.30	125.18	3475	26.88	71.88	2.67	15.35
13H 6W 0-2	115.40	125.28	3477	24.64	75.15	3.05	14.95
13H 6W 10-12	115.50	125.38	3480	29.05	69.88	2.41	15.12
13H 6W 20-22	115.60	125.48	3483	27.30	72.13	2.64	14.86
13H 6W 30-32	115.70	125.58	3486	30.11	68.59	2.28	14.96
13H 6W 40-42	115.80	125.68	3488	29.61	69.23	2.34	14.69
13H 6W 60-62	116.00	125.88	3494	27.79	70.95	2.55	15.43
13H 6W 70-72	116.10	125.98	3497	34.11	63.82	1.87	17.05
13H 6W 80-82	116.20	126.08	3500	18.56	82.75	4.46	22.33
13H 6W 90-92	116.30	126.18	3502	30.58	68.07	2.23	15.06
13H 6W 100-102	116.40	126.28	3505	28.07	71.08	2.53	14.28
13H 6W 110-112	116.50	126.38	3508	25.92	73.12	2.82	15.42
13H 6W 120-122	116.60	126.48	3511	28.14	70.62	2.51	15.56
13H 6W 130-132	116.70	126.58	3514	31.76	67.42	2.12	15.32
13H 6W 140-142	116.80	126.68	3516	27.83	71.97	2.59	15.15
13H 7W 0-2	116.90	126.78	3519	33.16	64.96	1.96	14.28
13H 7W 10-12	117.00	126.88	3522	32.05	67.38	2.10	14.01
13H 7W 20-22	117.10	126.98	3525	39.43	59.61	1.51	14.16
13H 7W 30-32	117.20	127.08	3528	35.38	63.88	1.81	14.06
13H 7W 40-42	117.30	127.18	3530	36.84	62.60	1.70	15.28
14H 1W 0-2	117.40	127.28	3533	28.39	71.15	2.51	14.91
13H 7W 50-52	117.40	127.28	3533	33.93	65.22	1.92	15.50
13H 7W 60-62	117.50	127.38	3536	28.57	70.39	2.46	14.68
14H IW 10-12	117.50	127.38	3536	35.81	62.99	1.76	14.31
14H 1W 20-22	117.60	127.48	3539	36.71	62.32	1.70	14.74
14H 1W 30-32	117.70	127.58	3541	33.13	66.54	2.01	14.54

14H 1W 40-42	117.80	127.68	3544	30.33	68.37	2.25	15.17
14H 1W 50-52	117.90	127.78	3547	28.81	69.91	2.43	15.68
14H 1W 60-62	118.00	127.88	3550	31.21	68.34	2.19	17.36
14H 1W 70-72	118.10	127.98	3553	16.99	82.35	4.85	22.03
14H 1W 80-82	118.20	128.08	3555	27.31	70.68	2.59	16.29
14H 1W 90-92	118.30	128.18	3558	29.39	67.01	2.28	17.52
14H 1W 100-102	118.40	128.28	3561	32.65	66.27	2.03	14.10
14H 1W 110-112	118.50	128.38	3564	37.22	62.00	1.67	14.85
14H 1W 120-122	118.60	128.48	3567	31.40	67.78	2.16	14.69
14H 1W 130-132	118.70	128.58	3569	33.72	65.90	1.95	14.69
14H 1W 140-142	118.80	128.68	3572	28.97	69.77	2.41	15.13
14H 2W 0-2	118.90	128.78	3575	23.32	74.22	3.18	22.21
14H 2W 10-12	119.00	128.88	3578	30.77	67.32	2.19	15.16
14H 2W 20-22	119.10	128.98	3580	37.25	60.96	1.64	15.02
14H 2W 30-32	119.20	129.08	3583	32.86	66.73	2.03	14.26
14H 2W 40-42	119.30	129.18	3586	33.83	65.40	1.93	14.35
14H 2W 50-52	119.40	129.28	3589	28.83	70.37	2.44	14.45
14H 2W 60-62	119.50	129.38	3592	34.77	65.65	1.89	14.55
14H 2W 70-72	119.60	129.48	3594	29.93	69.27	2.31	14.53
14H 2W 80-82	119.70	129.58	3597	35.77	63.96	1.79	15.05
14H 2W 90-92	119.80	129.68	3600	30.69	68.27	2.22	15.21
14H 2W 100-102	119.90	129.78	3603	34.00	65.37	1.92	14.83
14H 2W 110-112	120.00	129.88	3606	24.54	74.56	3.04	16.40
14H 2W 120-122	120.10	129.98	3608	33.75	65.88	1.95	14.75
14H 2W 130-132	120.20	130.08	3611	31.63	66.76	2.11	14.22
14H 2W 1340-142	120.30	130.18	3614	34.86	64.57	1.85	14.47
14H 3W 0-2	120.40	130.28	3617	31.77	67.51	2.13	14.27
14H 3W 10-12	120.50	130.38	3620	35.94	63.58	1.77	14.25
14H 3W 20-22	120.60	130.48	3622	29.91	69.19	2.31	14.30
14H 3W 30-32	120.70	130.58	3625	31.82	67.87	2.13	14.27
14H 3W 40-42	120.80	130.68	3628	32.26	66.30	2.05	13.92
14H 3W 50-52	120.90	130.78	3631	37.57	61.94	1.65	13.94
14H 3W 60-62	121.00	130.88	3634	32.00	67.23	2.10	14.57
14H 3W 70-72	121.10	130.98	3636	34.14	65.63	1.92	13.92
14H 3W 80-82	121.20	131.08	3639	34.70	64.79	1.87	14.54
14H 3W 100-102	121.40	131.28	3645	32.20	67.77	2.10	14.38
14H 3W 110-112	121.50	131.38	3648	35.33	64.22	1.82	14.66
14H 3W 120-122	121.60	131.48	3650	28.39	68.30	2.41	15.84
14H 3W 140-142	121.80	131.68	3656	20.49	80.38	3.92	24.63
14H 4W 0-2	121.90	131.78	3659	35.13	63.49	1.81	15.56
14H 4W 10-12	122.00	131.88	3662	30.28	68.30	2.26	14.41
14H 4W 20-22	122.10	131.98	3664	39.40	60.08	1.53	14.33
14H 4W 30-32	122.20	132.08	3667	33.16	65.90	1.99	14.71
14H 4W 50-52	122.40	132.28	3673	35.28	64.17	1.82	14.67
14H 4W 60-62	122.50	132.38	3676	32.51	67.27	2.07	14.54
14H 4W 70-72	122.60	132.48	3678	27.52	72.61	2.64	14.40
14H 4W 80-82	122.70	132.58	3681	28.09	71.32	2.54	15.03
14H 4W 90-92	122.80	132.68	3684	35.31	64.29	1.82	13.86
14H 4W 100-102	122.90	132.78	3687	35.02	63.91	1.82	14.36
14H 4W 120-122	123.10	132.98	3692	35.02	63.85	1.82	14.69
14H 4W 130-132	123.20	133.08	3695	35.63	62.67	1.76	14.87
14H 4W 140-142	123.30	133.18	3698	32.93	64.72	1.97	16.22
14H 5W 0-2	123.40	133.28	3701	37.66	61.18	1.62	15.52

14H 5W 10-12	123.50	133.38	3704	30.00	66.99	2.23	18.79
14H 5W 20-22	123.60	133.48	3706	29.65	67.43	2.27	17.40
14H 5W 30-32	123.70	133.58	3709	28.66	70.60	2.46	16.41
14H 5W 40-42	123.80	133.68	3712	32.12	65.94	2.05	15.27
14H 5W 50-52	123.90	133.78	3715	8.64	86.49	10.01	22.95
14H 5W 60-62	124.00	133.88	3718	13.14	85.68	6.52	23.03
14H 5W 70-72	124.10	133.98	3720	36.79	62.47	1.70	14.22
14H 5W 80-82	124.20	134.08	3723	33.48	64.85	1.94	15.81
14H 5W 90-92	124.30	134.18	3726	30.91	67.39	2.18	14.90
14H 5W 100-102	124.40	134.28	3729	34.98	64.37	1.84	14.93
14H 5W 110-112	124.50	134.38	3732	32.14	66.29	2.06	14.68
14H 5W 120-122	124.60	134.48	3735	35.15	63.95	1.82	15.16
14H 5W 130-132	124.70	134.58	3737	34.34	64.79	1.89	15.37
14H 5W 140-142	124.80	134.68	3740	31.91	66.74	2.09	19.53
14H 6W 0-2	124.90	134.78	3743	34.78	65.59	1.89	17.49
14H 6W 10-12	125.00	134.88	3746	36.25	63.05	1.74	15.57
14H 6W 20-22	125.10	134.98	3749	26.06	74.92	2.87	23.10
14H 6W 30-32	125.20	135.08	3751	29.12	66.95	2.30	17.42
14H 6W 40-42	125.30	135.18	3754	34.20	65.01	1.90	14.42
14H 6W 50-52	125.40	135.28	3757	38.39	60.39	1.57	15.22
14H 6W 60-62	125.50	135.38	3760	35.05	63.44	1.81	14.31
14H 6W 70-72	125.60	135.48	3763	38.06	60.83	1.60	14.21
14H 6W 80-82	125.70	135.58	3765	22.93	80.53	3.51	21.18
14H 6W 90-92	125.80	135.68	3768	33.40	65.98	1.98	14.59
14H 6W 100-102	125.90	135.78	3771	32.31	67.02	2.07	15.84
14H 6W 110-112	126.00	135.88	3774	31.26	67.14	2.15	14.99
14H 6W 120-122	126.10	135.98	3777	34.90	64.08	1.84	14.85
14H 6W 130-132	126.20	136.08	3779	36.56	62.56	1.71	14.90
14H 6W 140-142	126.30	136.18	3782	38.77	60.12	1.55	14.58
14H 7W 0-2	126.40	136.28	3785	37.11	61.49	1.66	14.97
14H 7W 10-12	126.50	136.38	3788	35.79	63.10	1.76	14.83
14H 7W 20-22	126.60	136.48	3791	36.84	61.48	1.67	15.11
14H 7W 30-32	126.70	136.58	3793	35.66	64.24	1.80	14.64
14H 7W 40-42	126.80	136.68	3796	31.43	62.97	2.00	15.23
15H 1W 0-2	126.90	136.78	3799	31.11	68.45	2.20	14.40
15H 1W 10-12	127.00	138.32	3842	43.20	55.26	1.28	14.91
15H 1W 20-22	127.10	136.98	3805	38.22	60.56	1.58	14.16
15H 1W 30-32	127.20	137.08	3807	35.55	62.83	1.77	15.11
15H 1W 40-42	127.30	137.18	3810	28.24	70.86	2.51	13.93
15H 1W 50-52	127.40	137.28	3813	32.79	65.60	2.00	14.58
15H 1W 60-62	127.50	137.38	3816	33.63	65.82	1.96	14.77
15H 1W 70-72	127.60	137.48	3819	32.74	67.00	2.05	14.70
15H 1W 80-82	127.70	139.02	3862	32.53	66.94	2.06	13.86
15H 1W 90-92	127.80	137.68	3824	38.60	59.99	1.55	15.42
15H 1W 100-102	127.90	137.78	3827	31.21	67.43	2.16	13.39
15H 1W 110-112	128.00	137.88	3830	35.05	62.16	1.77	14.98
15H 1W 120-122	128.10	139.42	3873	31.72	66.08	2.08	18.32
15H 1W 130-132	128.20	139.52	3876	35.07	63.94	1.82	14.64
15H 1W 140-142	128.30	138.18	3838	19.85	82.14	4.14	22.65
15H 2W 0-2	128.40	138.28	3841	37.14	62.46	1.68	14.53
15H 2W 10-12	128.50	139.82	3884	36.35	62.13	1.71	14.72
15H 2W 20-22	128.60	139.92	3887	37.09	61.52	1.66	14.66
15H 2W 40-42	128.80	140.12	3892	28.18	70.82	2.51	15.09
15H 2W 50-52	128.90	140.22	3895	29.68	69.81	2.35	15.42

15H 2W 70-72	129.10	140.42	3901	34.67	64.58	1.86	14.24
15H 2W 80-82	129.20	140.52	3904	37.20	62.06	1.67	13.98
15H 2W 90-92	129.30	140.62	3906	35.35	63.28	1.79	14.99
15H 2W 100-102	129.40	140.72	3909	33.53	64.67	1.93	14.85
15H 2W 110-112	129.50	140.82	3912	34.16	63.44	1.86	14.64
15H 2W 120-122	129.60	140.92	3915	31.39	66.74	2.13	14.87
15H 2W 130-132	129.70	141.02	3918	33.58	65.24	1.94	15.04
15H 2W 140-142	129.80	141.12	3920	32.36	66.21	2.05	14.90
15H 3W 0-2	129.90	141.22	3923	31.05	67.82	2.18	14.84
15H 3W 10-12	130.00	141.32	3926	33.24	66.25	1.99	14.94
15H 3W 20-22	130.10	141.42	3929	40.59	58.03	1.43	13.73
15H 3W 30-32	130.20	141.52	3932	36.55	61.79	1.69	15.85
15H 3W 40-42	130.30	141.62	3935	33.78	65.17	1.93	18.73
15H 3W 50-52	130.40	141.72	3937	33.22	65.51	1.97	16.66
15H 3W 60-62	130.50	141.82	3940	33.50	64.03	1.91	17.60
15H 3W 70-72	130.60	141.92	3943	31.43	67.40	2.14	15.59
15H 3W 80-82	130.70	142.02	3946	34.81	64.36	1.85	15.27
15H 3W 90-92	130.80	142.12	3949	33.67	65.47	1.94	17.41
15H 3W 100-102	130.90	142.22	3951	36.50	61.94	1.70	15.50
15H 3W 110-122	131.00	142.32	3954	24.39	74.30	3.05	18.87
15H 3W 120-122	131.10	142.42	3957	28.87	72.62	2.52	22.04
15H 3W 130-132	131.20	142.52	3960	21.56	77.28	3.58	19.69
15H 3W 140-142	131.30	142.62	3963	31.99	66.22	2.07	15.25
15H 4W 0-2	131.43	142.75	3966	24.36	75.52	3.10	22.95
15H 4W 10-12	131.53	142.85	3969	35.67	63.48	1.78	14.45
15H 4W 20-22	131.63	142.95	3972	29.42	68.50	2.33	16.20
15H 4W 30-32	131.73	143.05	3975	30.88	68.03	2.20	14.53
15H 4W 40-42	131.83	143.15	3977	32.80	66.26	2.02	14.65
15H 4W 50-52	131.93	143.25	3980	32.92	66.26	2.01	14.39
15H 4W 60-62	132.03	143.35	3983	34.97	63.52	1.82	14.07
15H 4W 70-72	132.13	143.45	3986	30.83	67.64	2.19	15.60
15H 4W 80-82	132.23	143.55	3989	18.00	82.22	4.57	21.55
15H 4W 90-92	132.33	143.65	3991	27.77	70.66	2.54	15.29
15H 4W 100-102	132.43	143.75	3994	29.53	70.59	2.39	15.09
15H 4W 110-112	132.53	143.85	3997	28.49	69.55	2.44	15.27
15H 4W 120-122	132.63	143.95	4000	32.08	66.70	2.08	15.55
15H 4W 130-132	132.73	144.05	4003	28.01	69.73	2.49	15.88
15H 4W 140-142	132.83	144.15	4005	25.93	72.90	2.81	18.88
15H 5W 0-2	132.96	144.28	4009	27.19	71.19	2.62	18.82
15H 5W 10-12	133.06	144.38	4012	27.11	71.70	2.64	16.55
15H 5W 20-22	133.16	144.48	4015	27.06	71.65	2.65	15.59
15H 5W 30-32	133.26	144.58	4017	10.91	86.62	7.94	22.57
15H 5W 40-42	133.36	144.68	4020	23.31	77.17	3.31	19.45
15H 5W 50-52	133.46	144.78	4023	13.71	86.14	6.28	22.75
15H 5W 60-62	133.56	144.88	4026	28.88	70.75	2.45	15.72
15H 5W 70-72	133.66	144.98	4029	32.01	66.80	2.09	14.94
15H 5W 80-82	133.76	145.08	4031	38.83	60.89	1.57	13.44
15H 5 90-92	133.86	145.18	4034	33.66	65.19	1.94	14.43
15H 5W 100-102	133.96	145.28	4037	34.16	65.05	1.90	14.48
15H 5W 110-112	134.06	145.38	4040	29.54	69.84	2.36	15.00
15H 5W 120-122	134.16	145.48	4043	31.87	66.76	2.09	15.23
15H 5W 130-132	134.26	145.58	4045	29.89	69.70	2.33	15.43
15H 5W 140-142	134.36	145.68	4048	29.74	69.34	2.33	14.71
15H 6W 0-2	134.46	145.78	4051	29.91	69.36	2.32	14.65

15H 6W 10-12	134.56	145.88	4054	34.61	63.70	1.84	14.60
15H 6W 20-22	134.66	145.98	4057	32.34	66.36	2.05	16.39
15H 6W 30-32	134.76	146.08	4059	33.14	65.98	1.99	15.82
15H 6W 40-42	134.86	146.18	4062	37.55	60.50	1.61	15.77
15H 6W 50-52	134.96	146.28	4065	33.46	65.34	1.95	14.57
15H 6W 60-62	135.06	146.38	4068	32.01	66.62	2.08	15.55
15H 6W 70-72	135.16	146.48	4071	34.21	65.13	1.90	14.66
15H 6W 90-92	135.36	146.68	4076	34.81	63.79	1.83	15.26
15H 6W 100-102	135.46	146.78	4079	32.70	66.44	2.03	15.26
15H 6W 100-102	135.56	146.88	4082	28.32	67.66	2.39	17.55
15H 6W 120-122	135.66	146.98	4085	20.08	77.32	3.85	23.70
15H 6W 130-132	135.76	147.08	4087	26.30	73.54	2.80	20.12
15H 6W 140-142	135.86	147.18	4090	31.40	67.48	2.15	15.50
15H 7W 0-2	135.96	147.28	4093	31.90	67.10	2.10	14.92
15H 7W 10-12	136.06	147.38	4096	31.51	67.67	2.15	14.95
15H 7W 20-22	136.16	147.48	4099	25.64	71.32	2.78	17.07
15H 7W 30-32	136.26	147.58	4101	30.65	68.36	2.23	14.84
15H 7W 40-42	136.36	147.68	4104	30.25	69.23	2.29	15.13
16H 1W 0-2	136.40	147.72	4105	30.13	68.68	2.28	14.95
16H 1W 10-12	136.50	147.82	4108	36.13	62.28	1.72	14.53
16H 1W 20-22	136.60	147.92	4111	31.76	67.68	2.13	14.47
15H CC 10-12	136.68	148	4113	31.44	67.26	2.14	14.73
16H 1W 30-32	136.70	148.02	4114	35.41	63.36	1.79	14.92
16H 1W 40-42	136.80	148.12	4117	35.76	63.47	1.77	14.60
16H 1W 50-52	136.90	148.22	4119	34.51	64.20	1.86	14.52
16H 1W 60-62	137.00	148.32	4122	35.28	63.48	1.80	14.03
16H 1W 70-72	137.10	148.42	4125	33.24	65.75	1.98	15.06
16H 1W 80-82	137.20	148.52	4128	32.61	65.70	2.01	15.15
16H 1W 100-102	137.40	148.72	4133	31.77	67.61	2.13	14.80
16H 1W 110-112	137.50	148.82	4136	32.68	66.20	2.03	14.99
16H 1W 120-122	137.60	148.92	4139	36.36	63.18	1.74	13.92
16H 1W 130-132	137.70	149.02	4142	32.81	64.82	1.98	15.28
16H 1W 140-142	137.80	149.12	4145	33.13	66.34	2.00	14.74
16H 2W 0-2	137.90	149.22	4147	24.84	73.15	2.94	18.92
16H 2W 10-12	138.00	150.6	4193	30.24	68.93	2.28	14.77
16H 2W 20-22	138.10	149.42	4153	29.34	69.36	2.36	15.51
16H 2W 30-32	138.20	149.52	4156	30.38	68.59	2.26	14.24
16H 2W 40-42	138.30	149.62	4159	33.84	65.10	1.92	15.34
16H 2W 50-52	138.40	149.72	4161	32.87	66.65	2.03	14.83
16H 2W 60-62	138.50	149.82	4164	29.89	70.03	2.34	14.67
16H 2W 70-72	138.60	149.92	4167	29.20	70.06	2.40	14.58
16H 2W 80-82	138.70	150.02	4170	30.25	68.78	2.27	14.84
16H 2W 90-92	138.80	150.12	4173	29.41	68.75	2.34	15.20
16H 2W 100-102	138.90	150.22	4176	27.61	72.52	2.63	15.32
16H 2W 110-112	139.00	150.32	4180	31.62	67.45	2.13	14.73
16H 2W 120-122	139.10	150.42	4185	31.05	68.32	2.20	15.16
16H 2W 130-132	139.20	150.52	4189	27.39	72.19	2.64	14.91
16H 2W 140-142	139.30	150.62	4193	27.15	72.80	2.68	15.23
16H 3W 0-2	139.40	150.72	4198	28.20	69.96	2.48	14.59
16H 3W 20-22	139.60	150.92	4206	34.43	65.21	1.89	14.49
16H 3W 30-32	139.70	151.02	4211	37.17	61.93	1.67	14.02
16H 3W 40-42	139.80	151.12	4215	36.23	63.68	1.76	14.18
16H 3W 50-52	139.90	151.22	4219	32.43	66.74	2.06	14.59
16H 3W 60-62	140.00	151.32	4224	29.75	69.09	2.32	15.31

16H 3W 70-72	140.10	151.42	4228	30.11	69.08	2.29	14.52
16H 3W 80-82	140.20	151.52	4232	31.80	67.05	2.11	14.47
16H 3W 90-92	140.30	151.62	4237	29.48	69.37	2.35	15.09
16H 3W 100-102	140.40	151.72	4241	32.83	66.12	2.01	14.45
16H 3W 110-112	140.50	151.82	4245	36.32	63.04	1.74	14.23
16H 3W 120-122	140.60	151.92	4249	34.02	66.18	1.95	14.32
16H 3W 130-132	140.70	152.02	4254	35.66	63.02	1.77	14.04
16H 3W 140-142	140.80	152.12	4258	32.72	65.73	2.01	14.33
16H 4W 0-2	140.90	152.22	4262	30.79	67.18	2.18	14.49
16H 4W 10-12	141.00	152.32	4267	34.96	64.11	1.83	14.40
16H 4W 20-22	141.10	152.42	4271	31.44	67.47	2.15	14.69
16H 4W 30-32	141.20	152.52	4275	36.86	62.54	1.70	14.16
16H 4W 40-42	141.30	152.62	4280	38.42	60.66	1.58	14.11
16H 4W 50-52	141.40	152.72	4284	33.88	65.38	1.93	14.96
16H 4W 60-62	141.50	152.82	4288	31.84	67.19	2.11	14.58
16H 4W 70-72	141.60	152.92	4293	30.95	68.62	2.22	14.59
16H 4W 80-82	141.70	153.02	4297	31.34	67.95	2.17	14.92
16H 4W 90-92	141.80	153.12	4301	31.29	68.13	2.18	15.10
16H 4W 100-102	141.90	153.22	4306	33.29	66.05	1.98	14.41
16H 4W 110-112	142.00	153.32	4307	32.63	67.19	2.06	14.38
16H 4W 120-122	142.10	153.42	4309	37.34	61.26	1.64	14.76
16H 4W 130-132	142.20	153.52	4311	35.65	63.37	1.78	15.19
16H 4W 140-142	142.30	153.62	4312	33.04	65.75	1.99	15.00
16H 5W 0-2	142.40	153.72	4314	31.97	67.15	2.10	15.61
16H 5W 10-12	142.50	153.82	4316	29.31	70.09	2.39	15.49
16H 5W 20-22	142.60	153.92	4317	28.82	70.46	2.45	15.56
16H 5W 30-32	142.70	154.02	4319	29.75	68.03	2.29	14.88
16H 5W 40-42	142.80	154.12	4320	31.48	68.51	2.18	15.31
16H 5W 50-52	142.90	154.22	4322	37.45	62.24	1.66	14.62
16H 5W 60-62	143.00	154.32	4324	36.56	62.78	1.72	14.36
16H 5W 70-72	143.10	154.42	4325	35.16	63.49	1.81	15.21
16H 5W 80-82	143.20	154.52	4327	32.56	67.03	2.06	15.09
16H 5W 90-92	143.30	154.62	4329	32.62	66.28	2.03	15.89
16H 5W 110-112	143.50	154.82	4332	33.65	65.38	1.94	15.33
16H 5W 120-122	143.60	154.92	4333	29.28	70.03	2.39	15.65
16H 5W 130-132	143.70	155.02	4335	36.01	62.64	1.74	15.22
16H 5W 140-142	143.80	155.12	4337	32.63	66.43	2.04	14.26
16H 6W 0-2	143.90	155.22	4338	36.22	63.29	1.75	14.97
16H 6W 10-12	144.00	155.32	4340	33.79	65.77	1.95	14.20
16H 6W 30-32	144.20	155.52	4343	31.94	68.05	2.13	15.22
16H 6W 40-42	144.30	155.62	4345	29.75	69.08	2.32	15.26
16H 6W 50-52	144.40	155.72	4346	31.84	67.06	2.11	14.80
16H 6W 60-62	144.50	155.82	4348	33.33	64.74	1.94	14.87
16H 6W 70-72	144.60	155.92	4350	32.97	66.90	2.03	14.66
16H 6W 80-82	144.70	156.02	4351	35.01	63.65	1.82	14.73
16H 6W 90-92	144.80	156.12	4353	32.32	67.20	2.08	15.24
16H 6W 100-102	144.90	156.22	4355	33.04	65.86	1.99	15.46
16H 6W 110-112	145.00	156.32	4356	32.76	66.94	2.04	14.92
16H 6W 120-122	145.10	156.42	4358	34.07	65.37	1.92	14.99
16H 6W 130-132	145.20	156.52	4359	31.19	67.70	2.17	15.02
16H 6W 140-142	145.30	156.62	4361	31.20	67.87	2.18	14.98
16H 7W 0-2	145.40	158	4383	30.42	67.91	2.23	14.81
16H 7W 10-12	145.50	158.1	4385	30.89	67.96	2.20	14.63
16H 7W 20-22	145.60	158.2	4387	31.19	68.49	2.20	14.75

16H 7W 30-32	145.70	158.3	4388	30.45	69.27	2.27	16.54
17H 1W 0-2	145.90	158.5	4392	21.01	78.71	3.75	16.85
17H 1W 10-12	146.00	158.6	4393	23.22	75.09	3.23	15.47
17H 1W 20-22	146.10	158.7	4395	24.68	73.90	2.99	15.85
17H 1W 30-32	146.20	158.8	4396	28.88	69.61	2.41	15.27
17H 1W 40-42	146.30	158.9	4398	30.02	68.46	2.28	15.49
17H 1W 50-52	146.40	159	4400	27.05	69.59	2.57	16.22
17H 1W 60-62	146.50	159.1	4401	21.60	78.27	3.62	19.02
17H 1W 70-72	146.60	159.2	4403	24.90	74.63	3.00	17.40
17H 1W 80-82	146.70	159.3	4405	18.52	83.60	4.51	21.36
17H 1W 90-92	146.80	159.4	4406	23.08	76.53	3.32	20.44
17H 1W 100-102	146.90	159.5	4408	13.98	85.93	6.15	22.07
17H 1W 110-112	147.00	159.6	4409	17.85	81.47	4.57	17.95
17H 1W 120-122	147.10	159.7	4411	18.92	79.47	4.20	17.69
17H 1W 130-132	147.20	159.8	4413	18.15	80.36	4.43	18.54
17H 1W 140-142	147.30	159.9	4414	11.66	86.01	7.37	23.66
17H 2W 0-2	147.40	160	4416	16.86	82.20	4.88	18.54
17H 2W 10-12	147.50	160.1	4418	18.86	80.36	4.26	18.13
17H 2W 20-22	147.60	160.2	4419	19.58	82.82	4.23	19.25
17H 2W 30-32	147.70	160.3	4421	19.34	80.50	4.16	18.72
17H 2W 40-42	147.80	160.4	4422	20.37	79.22	3.89	17.89
17H 2W 50-52	147.90	160.5	4424	22.09	75.71	3.43	17.75
17H 2W 60-62	148.00	160.6	4426	23.89	75.14	3.15	16.67
17H 2W 70-72	148.10	160.7	4427	22.65	75.69	3.34	16.99
17H 2W 80-82	148.20	160.8	4429	14.54	91.53	6.30	21.03
17H 2W 90-92	148.30	160.9	4431	15.70	84.78	5.40	20.24
17H 2W 100-102	148.40	161	4432	17.04	85.15	5.00	21.00
17H 2W 110-112	148.50	161.1	4434	17.66	82.41	4.67	19.16
17H 2W 120-122	148.60	161.2	4435	14.79	85.77	5.80	19.61
17H 2W 130-132	148.70	161.3	4437	18.22	84.21	4.62	19.12
17H 2W 140-142	148.80	161.4	4439	26.35	71.80	2.72	16.48
17H 3W 0-2	148.90	161.5	4440	21.10	77.18	3.66	16.38
17H 3W 10-12	149.00	161.6	4442	23.94	74.12	3.10	15.92
17H 3W 20-22	149.10	161.7	4444	18.66	78.26	4.19	17.83
17H 3W 30-32	149.20	161.8	4445	23.28	75.73	3.25	17.24
17H 3W 40-42	149.30	161.9	4447	19.16	77.64	4.05	17.38
17H 3W 50-52	149.40	162	4448	16.35	80.91	4.95	17.89
17H 3W 60-62	149.50	162.1	4450	18.59	80.24	4.32	18.28
17H 3W 80-82	149.70	162.3	4453	22.34	77.67	3.48	16.21
17H 3W 90-92	149.80	162.4	4455	24.36	75.70	3.11	16.22
17H 3W 100-102	149.90	162.5	4457	28.21	70.49	2.50	15.20
17H 3W 110-112	150.00	162.6	4458	30.03	68.47	2.28	15.33
17H 3W 120-122	150.10	162.7	4460	26.81	73.08	2.73	17.16
17H 3W 130-132	150.20	162.8	4461	18.17	84.19	4.63	20.79
17H 3W 140-142	150.30	162.9	4463	21.78	76.93	3.53	17.65
17H 4W 0-2	150.40	163	4465	20.47	79.15	3.87	17.31
17H 4W 10-12	150.50	163.1	4466	23.09	74.75	3.24	16.50
17H 4W 20-22	150.60	163.2	4468	20.00	79.05	3.95	17.00
17H 4W 30-32	150.70	163.3	4470	25.55	73.54	2.88	16.07
17H 4W 40-42	150.80	163.4	4471	25.51	73.88	2.90	15.72
17H 4W 50-52	150.90	163.5	4473	29.29	69.90	2.39	15.98
17H 4W 60-62	151.00	163.6	4474	24.19	75.06	3.10	17.28
17H 4W 70-72	151.10	163.7	4476	22.82	77.76	3.41	17.32
17H 4W 80-82	151.20	163.8	4478	26.25	73.49	2.80	17.26

17H 4W 90-92	151.30	163.9	4482	20.59	78.84	3.83	17.99
17H 4W 100-102	151.40	164	4488	15.85	87.66	5.53	21.17
17H 4W 110-112	151.50	164.1	4493	17.31	89.33	5.16	20.85
17H 4W 120-122	151.60	164.2	4499	17.69	79.86	4.51	19.43
17H 4W 130-132	151.70	164.3	4504	19.18	81.91	4.27	19.74
17H 4W 140-142	151.80	164.4	4509	11.72	89.01	7.59	21.41
17H 4W 0-2	151.90	164.5	4515	15.10	87.26	5.78	21.78
17H 5W 10-12	152.00	164.6	4520	18.98	79.62	4.20	18.25
17H 5W 10-12	152.10	164.7	4526	21.92	78.87	3.60	17.77
17H 5W 30-32	152.20	164.8	4531	18.54	79.48	4.29	16.29
17H 5W 40-42	152.30	164.9	4536	19.53	79.48	4.07	19.24
17H 5W 50-52	152.40	165	4542	15.92	86.62	5.44	20.02
17H 5W 60-62	152.50	165.1	4547	17.04	85.03	4.99	20.79
17H 5W 70-72	152.60	165.2	4553	18.33	79.29	4.32	16.97
17H 5W 80-82	152.70	165.3	4558	21.14	77.12	3.65	16.60
17H 5W 90-92	152.80	165.4	4564	25.04	75.20	3.00	16.02
17H 5W 100-102	152.90	165.5	4569	22.86	75.13	3.29	16.45
17H 5W 110-112	153.00	165.6	4574	19.78	78.88	3.99	18.03
17H 5W 120-122	153.10	165.7	4580	11.19	89.30	7.98	21.24
17H 5W 130-132	153.20	165.8	4585	19.76	78.48	3.97	17.81
17H 5W 140-142	153.30	165.9	4591	20.70	79.52	3.84	19.28
17H 6W 10-12	153.50	166.1	4601	24.81	75.18	3.03	18.72
17H 6W 30-32	153.70	166.3	4612	28.60	71.12	2.49	15.86
17H 6W 50-52	153.90	166.5	4623	23.45	75.15	3.20	17.07
17H 6W 70-72	154.10	166.7	4634	23.92	77.72	3.25	19.05
17H 6W 90-92	154.30	166.9	4644	19.26	82.11	4.26	19.49
17H 6W 110-112	154.50	167.1	4651	15.47	87.39	5.65	21.17
17H 6W 130-132	154.70	167.3	4658	19.85	79.40	4.00	17.73
17H 7W 0-2	154.90	167.5	4665	19.67	78.61	4.00	18.27
17H 7W 20-22	155.10	167.7	4673	21.67	76.64	3.54	17.56
17H CC 0-2	155.28	167.88	4679	21.29	77.35	3.63	17.56
18X 1W 0-2	155.40	168	4683	23.64	76.08	3.22	17.75
18X 1W 10-12	155.50	168.1	4687	20.11	83.25	4.14	21.51
18X 1W 30-32	155.70	168.3	4694	24.28	74.69	3.08	16.92
18X 1W 50-52	155.90	168.5	4701	19.95	77.84	3.90	19.08
18X 1W 70-72	156.10	168.7	4709	24.01	73.72	3.07	17.28
18X 1W 90-92	156.30	168.9	4716	16.51	85.68	5.19	21.06
18X 1W 110-112	156.50	169.1	4723	21.81	76.49	3.51	18.60
18X 1W 130-132	156.70	169.3	4730	20.76	80.36	3.87	20.13
18X 2W 0-2	156.90	169.5	4737	24.39	74.67	3.06	16.42
18X 2W 20-22	157.10	169.7	4744	17.77	81.32	4.58	21.20
18X 2W 40-42	157.30	169.9	4752	20.76	81.56	3.93	19.84
18X 2W 60-62	157.50	170.1	4759	16.83	86.94	5.17	21.20

APPENDIX C

Detailed section and sample locations

Sections	*Samples* ***Description**	Altitude	GPS coordinates (Deg)	NZ Map Grid coordinates (Northing, Easting)
Base of	*BS1 – BS6* *Located on the true left bank of river at bend with exposure facing SW.	266 m (river/base) 277 m (top)	S 39.68837 E 175.52861 (base of section)	6165459.2, 2726865.6
Dead Cow	*DC1 – DC7* *Located on the true right bank of the river.	265 m (river/base) 282 m (top)	S 39.68888 E 175.5277 (base of section)	6165399.6, 2726792.4
Missing Link	*ML1 – ML7* *Located on the true left bank of the river with exposure facing SW.	264 m (river) 274 m (base) 285 m (top)	S 39.68969 E 175.52759 (base of section)	6165307.8, 2726765.9
Big Face	*BF1 – BF11* *Located on the true left bank of the river with exposure facing NE.	264 m (river) 271 m (base) 311 m (top)	S 39.68997 E 175.52625 (base of section)	6165279.7, 2726669.8
Dutch Man's Stairs	*WTF 2,* *DMS1 – DMS2* *Located along the true right bank of the river with exposure facing into the river (SE). *WTF2 taken next to paleomag. samples 10 m (horizontal) upstream from section along river bed .	259 m (river/base) 273 m (top)	S 39.69322 E 175.52301 (base of section)	6164918.0, 2726373.5
North Bridge	*NB1 – NB7* *Located on the true left bank of the river with exposure facing into the river (NW).	258 m (river/base) 273 m (top)	S 39.69425 E 175.52151 (base of section)	6164829.6, 2726227.9
South Bridge (below tephra)	*SBB1 – SBB8* *Located on the true right bank of the river with exposure facing into the river (SE) and below the road. *Top of section is tephra layer along the road	255 m (river/base) 262 m (top)	S 39.69576 E 175.52099 (base of section)	6164645.4, 2726198.8
South Bridge (above tephra)	*SBA1 – SBA8*	SBA1 = 273.5 m SBA2 = 275.5 m	S 39.69566 E 175.52074	6164676.9, 2726175.9

	*Tephra is exposed along road cut. *SBA1 and SBA2 were taken along the road above tephra. *SBA3 – SBA8 were taken along the river (starting 2 m HIS above SBA2) on the true right bank of the river. *SBA8 is located at the base of the Rob's Face section.	 SBA3 = 2 m HIS SBA4 = 2 m HIS SBA5 = 2 m HIS SBA6 = 2 m HIS SBA7 = 2 m HIS SBA8 = 2 m HIS	(SBA1 – SBA2) S 39.69769 E 175.51959 S 39. 69777 E 175.51953 S 39.69793 E 175.51956 S 39.69808 E 175.51963 S 39.69827 E 175.51964 S 39.69449 E 175.51965	 6164433.0, 2726073.6 6164433.7, 2726049.8 6164402.9, 2726048.9 6164402.2, 2726072.7 6164371.4, 2726071.9 6164802.9, 2726084.2
Rob's Face	*RF1 – RF5* *Located on the true right bank of the river with exposure facing into the river (SE). *RF1 is 2 m above SBA8.	263 m (river/base) 273 m (top)	S 39.69849 E 175.51965 (base of section)	6164802.9, 2726084.2
Gillian's Waterfall	*WF1 – WF4* *Located on the true right bank of the river in which there is a stream entering the river. *WF 4 taken 1.5 m (horizontal) downstream from base of section	267 m (river) 268 m (base) 274 m (top) 265 m (WF 4)	S 39.6952 E 175.51927 (base of section)	6164711.8, 2726033.9
Falling Tim	*FT1 – FT7* *Located on the true right bank of the river with exposure facing into the river (SE).	258 m (river) 259 m (base) 271 m (top)	S 39.70030 E 175.51892 (base of section)	6163880.2, 2725986.4

Grain size frequency data with Phi ϕ scale for Turakina River Section

Sample	FT7	FT6	FT5	FT4	FT3	FT2	FT1	WF4	RF5	WF3
Height	**134.5**	**132.5**	**130.5**	**128.5**	**126.5**	**124.5**	**122.5**	**119.5**	**118**	**118**
-1	0.000	0.000	0.000	0.000	0.000	0.000	0.000	0.000	0.000	0.000
-0.5	0.000	0.000	0.000	0.000	0.000	0.000	0.000	0.000	0.000	0.000
0	0.000	0.000	0.000	0.000	0.000	0.000	0.000	0.000	0.000	0.000
0.5	0.000	0.000	0.000	0.000	0.000	0.000	0.000	0.000	0.000	0.000
1	0.000	0.000	0.000	0.000	0.000	0.000	0.000	0.000	0.000	0.000
1.5	0.000	0.000	0.000	0.000	0.000	0.000	0.000	0.000	0.000	0.000
2	0.059	0.254	0.396	0.220	0.017	0.132	0.023	0.287	0.224	0.149
2.5	0.858	1.321	2.114	1.691	0.669	1.126	0.536	1.192	1.015	0.465
3	2.526	3.021	5.680	4.711	1.944	3.335	1.469	3.058	3.575	1.872
3.5	3.731	6.636	9.037	7.747	3.071	4.902	2.164	6.091	5.401	2.441
4	3.461	5.200	9.068	5.673	3.317	4.332	2.536	3.312	3.524	2.502
4.5	5.819	8.312	13.237	8.147	5.336	6.633	4.154	5.810	5.870	5.042
5	7.894	9.442	9.747	8.284	7.035	8.029	6.419	6.893	6.584	7.322
5.5	10.707	12.220	9.901	10.239	9.934	10.470	9.521	10.058	9.642	11.811
6	10.100	10.360	8.064	9.029	10.284	9.508	9.848	9.580	9.559	11.524
6.5	14.132	12.508	9.283	11.275	14.866	12.738	14.935	13.214	13.675	15.527
7	13.519	10.764	7.958	10.063	14.293	12.017	14.994	12.623	13.150	14.007
7.5	8.982	6.844	5.162	6.782	9.575	8.233	10.392	8.602	8.871	9.080
8	10.196	7.537	5.874	8.194	10.931	9.866	12.305	10.244	10.348	10.170
8.5	6.753	4.770	3.844	6.100	7.265	7.052	8.664	7.336	7.104	6.695
9	1.263	0.812	0.634	1.826	1.460	1.623	2.036	1.696	1.456	1.391
9.5	0.001	0.001	0.000	0.019	0.002	0.003	0.004	0.003	0.002	0.002
rest	0.000	0.000	0.000	0.000	0.000	0.000	0.000	0.000	0.000	0.000

Grain size frequency data with Phi ϕ scale for Turakina River Section continued

Sample	**RF4**	**WF2**	**RF3**	**WF1**	**RF2**	**SBA8**	**RF1**	**SBA7**	**SBA6**	**SBA5**
Height	**116**	**116**	**114.1**	**114.1**	**112.6**	**111.1**	**110.6**	**109.1**	**107.1**	**105.1**
-1	0.000	0.000	0.000	0.000	0.000	0.000	0.000	0.000	0.000	0.000
-0.5	0.000	0.000	0.000	0.000	0.000	0.000	0.000	0.000	0.000	0.000
0	0.000	0.000	0.000	0.000	0.000	0.000	0.000	0.000	0.000	0.000
0.5	0.000	0.000	0.000	0.000	0.000	0.000	0.000	0.000	0.000	0.000
1	0.000	0.000	0.000	0.000	0.000	0.000	0.000	0.000	0.000	0.000
1.5	0.000	0.000	0.000	0.000	0.000	0.000	0.000	0.000	0.000	0.000
2	0.216	0.094	0.269	0.259	0.176	0.470	0.266	0.460	0.356	0.349
2.5	0.642	0.829	1.255	0.850	1.063	2.796	2.934	2.378	1.916	2.740
3	2.199	1.034	3.090	1.406	3.980	8.354	8.424	5.737	5.482	7.135
3.5	4.613	3.374	6.043	4.351	5.276	9.278	9.225	8.582	8.241	7.732
4	3.506	2.765	3.798	2.700	4.013	4.872	5.074	4.652	4.833	4.771
4.5	6.500	4.370	6.215	5.096	6.540	6.610	6.069	5.904	7.248	5.746
5	7.417	6.491	7.457	6.551	7.444	6.131	6.396	6.175	8.884	7.437
5.5	10.420	9.830	11.636	10.232	9.900	8.620	8.541	8.547	12.049	11.917
6	9.897	10.172	10.913	10.331	9.192	8.376	8.000	8.201	9.698	10.310
6.5	13.708	15.104	13.968	14.656	12.719	11.457	10.762	11.527	11.403	12.283
7	12.961	15.053	12.292	14.081	12.244	10.653	10.199	11.328	9.857	10.395
7.5	8.744	10.207	7.833	9.482	8.437	7.087	7.043	7.927	6.455	6.567
8	10.298	11.654	8.665	10.981	10.109	8.291	8.698	9.652	7.474	7.274
8.5	7.248	7.643	5.575	7.480	7.225	5.789	6.593	7.077	5.084	4.625
9	1.628	1.379	0.990	1.543	1.679	1.214	1.765	1.845	1.019	0.718
9.5	0.003	0.001	0.001	0.002	0.003	0.002	0.011	0.010	0.001	0.000
rest	0.000	0.000	0.000	0.000	0.000	0.000	0.000	0.000	0.000	0.000

Grain size frequency data with Phi ϕ scale for Turakina River Section continued

Sample	**SBA4**	**SBA3**	**SBA2**	**SBA1**	**SBB9**	**SBB8**	**SBB7**	**SBB6**	**SBB5**	**SBB4**
Height	**103.1**	**101.1**	**99.12**	**97.13**	**94.15**	**92.15**	**90.16**	**88.17**	**86.18**	**84.18**
-1	0.000	0.000	0.000	0.000	0.000	0.000	0.000	0.000	0.000	0.000
-0.5	0.000	0.000	0.000	0.000	0.000	0.000	0.000	0.000	0.000	0.000
0	0.000	0.000	0.000	0.000	0.000	0.000	0.000	0.000	0.000	0.000
0.5	0.000	0.000	0.000	0.000	0.000	0.000	0.000	0.000	0.000	0.000
1	0.000	0.000	0.000	0.000	0.000	0.000	0.000	0.000	0.000	0.000
1.5	0.000	0.000	0.000	0.000	0.000	0.000	0.001	0.000	0.001	0.000
2	0.225	0.246	0.165	0.621	0.397	0.513	0.745	0.774	1.428	1.502
2.5	2.300	1.686	1.109	2.807	2.638	2.216	3.123	5.002	6.384	7.811
3	6.888	4.646	4.447	8.112	8.241	6.029	7.999	9.922	13.209	14.642
3.5	8.881	8.031	6.509	11.877	8.565	8.665	7.466	8.093	11.951	10.915
4	5.632	4.894	5.042	8.510	5.019	5.017	4.507	4.688	5.819	4.900
4.5	6.233	5.991	6.580	10.999	6.488	7.267	6.196	5.712	6.591	6.035
5	5.976	6.041	5.946	7.537	5.367	6.098	5.515	5.672	5.413	5.457
5.5	8.167	8.830	7.826	8.435	7.208	7.950	7.238	7.322	6.982	7.684
6	8.241	8.821	7.971	6.989	7.356	7.247	7.227	7.147	6.167	7.064
6.5	11.476	12.257	12.169	8.391	10.817	9.633	10.917	10.335	7.861	9.027
7	10.890	11.736	12.547	7.652	10.796	9.505	11.312	10.446	7.556	8.152
7.5	7.470	8.112	8.921	5.350	7.693	7.253	8.166	7.383	5.477	5.356
8	9.099	9.732	10.936	6.567	9.732	10.118	10.213	9.119	7.182	6.234
8.5	6.749	7.017	7.982	4.811	7.517	8.762	7.592	6.793	5.873	4.343
9	1.765	1.945	1.846	1.332	2.147	3.572	1.780	1.590	2.061	0.878
9.5	0.010	0.016	0.003	0.010	0.018	0.155	0.003	0.003	0.047	0.001
rest	0.000	0.000	0.000	0.000	0.000	0.000	0.000	0.000	0.000	0.000

Grain size frequency data with Phi ϕ scale for Turakina River Section continued

Sample	**SBB3**	**NB8-7**	**SBB2**	**NB6**	**SBB1**	**NB5**	**NB4**	**DMS6**	**NB3**	**DMS5**
Height	**82.19**	**80.7**	**80.7**	**78.7**	**78.7**	**76.71**	**74.72**	**73.72**	**72.73**	**71.73**
-1	0.000	0.000	0.000	0.000	0.000	0.000	0.000	0.000	0.000	0.000
-0.5	0.000	0.000	0.000	0.000	0.000	0.000	0.000	0.000	0.000	0.000
0	0.000	0.000	0.000	0.000	0.000	0.000	0.000	0.000	0.000	0.000
0.5	0.000	0.000	0.000	0.000	0.000	0.000	0.000	0.000	0.000	0.000
1	0.000	0.000	0.000	0.000	0.000	0.000	0.000	0.000	0.000	0.000
1.5	0.003	0.000	0.002	0.000	0.002	0.002	0.003	0.000	0.000	0.000
2	2.288	1.105	2.045	1.184	2.327	1.979	2.708	0.629	1.295	0.684
2.5	8.290	5.534	8.101	5.982	9.526	7.790	10.376	3.997	7.275	4.065
3	13.284	10.995	13.463	11.055	15.479	12.277	17.217	9.069	13.576	9.719
3.5	8.106	10.066	8.779	9.475	8.912	8.383	10.048	9.479	10.751	9.229
4	4.165	5.125	4.957	4.207	4.798	4.729	4.839	5.545	5.991	4.371
4.5	5.993	6.465	6.545	6.304	6.996	5.900	6.457	8.134	8.493	6.326
5	5.713	5.896	6.170	6.110	5.832	7.258	5.383	7.635	7.275	6.335
5.5	7.415	7.912	7.722	8.016	7.108	10.550	7.340	9.132	8.317	8.572
6	6.726	7.366	6.730	7.002	6.337	8.633	6.693	7.461	6.617	7.608
6.5	9.134	9.856	8.421	9.279	8.472	9.879	8.368	9.194	7.501	9.868
7	8.720	9.351	7.586	9.262	7.933	8.039	7.153	8.655	6.438	9.309
7.5	6.030	6.391	5.279	6.655	5.237	4.995	4.513	6.168	4.448	6.622
8	7.359	7.517	6.821	8.242	6.046	5.431	4.979	7.637	5.643	8.351
8.5	5.425	5.227	5.527	5.954	4.170	3.451	3.250	5.630	4.515	6.501
9	1.345	1.191	1.828	1.272	0.826	0.702	0.673	1.620	1.787	2.365
9.5	0.005	0.002	0.023	0.002	0.001	0.001	0.001	0.015	0.077	0.076
rest	0.000	0.000	0.000	0.000	0.000	0.000	0.000	0.000	0.000	0.000

Grain size frequency data with Phi ϕ scale for Turakina River Section continued

Sample	**NB2**	**DMS4**	**NB1**	**DMS3**	**DMS2**	**DMS1**	**WTF2**	**BF11**	**BF12**	**BF13**
Height	**70.73**	**69.74**	**68.74**	**67.75**	**65.75**	**63.76**	**62.77**	**60.27**	**57.29**	**54.3**
-1	0.000	0.000	0.000	0.000	0.000	0.000	0.000	0.000	0.000	0.000
-0.5	0.000	0.000	0.000	0.000	0.000	0.000	0.000	0.000	0.000	0.000
0	0.000	0.000	0.000	0.000	0.000	0.000	0.000	0.000	0.000	0.000
0.5	0.000	0.000	0.000	0.000	0.000	0.000	0.000	0.000	0.000	0.000
1	0.000	0.000	0.000	0.000	0.000	0.000	0.000	0.000	0.000	0.000
1.5	0.002	0.000	0.000	0.000	0.000	0.000	0.009	0.001	0.000	0.000
2	2.354	0.536	0.969	0.676	0.688	0.151	0.419	0.406	0.123	0.602
2.5	9.819	3.569	5.601	3.778	3.800	1.389	1.328	1.485	0.725	2.924
3	15.933	8.399	11.065	9.239	8.999	3.046	3.836	3.297	2.364	7.613
3.5	9.036	9.154	9.617	9.262	10.368	5.682	3.845	4.955	3.598	8.593
4	4.530	5.209	5.087	5.009	5.328	3.937	4.053	4.724	3.619	5.890
4.5	6.197	7.543	8.370	6.882	6.656	6.425	6.094	7.109	6.542	11.179
5	5.998	7.512	9.940	7.813	6.025	7.612	6.880	7.838	7.288	11.228
5.5	8.395	9.387	11.532	11.559	7.926	9.882	9.150	9.962	9.505	11.182
6	7.253	7.788	8.375	9.458	7.293	8.684	9.546	8.932	8.791	8.262
6.5	8.787	9.475	9.100	10.890	9.838	11.627	14.261	11.514	12.308	9.329
7	7.491	8.752	7.376	8.947	9.546	11.684	13.735	10.660	12.494	7.864
7.5	4.779	6.282	4.606	5.620	6.774	8.604	8.953	7.652	9.206	5.109
8	5.291	8.021	4.897	6.125	8.417	10.858	10.075	9.998	11.880	5.721
8.5	3.422	6.233	2.929	3.893	6.362	8.089	6.672	8.144	9.129	3.701
9	0.713	2.103	0.535	0.848	1.959	2.310	1.146	3.193	2.416	0.802
9.5	0.001	0.039	0.001	0.002	0.022	0.020	0.001	0.131	0.014	0.001
rest	0.000	0.000	0.000	0.000	0.000	0.000	0.000	0.000	0.000	0.000

Grain size frequency data with Phi ϕ scale for Turakina River Section continued

Sample	BF9	BF10	BF8	BF7	BF6	BF5	BF4	BF3	ML7	BF2
Height	**50.31**	**47.32**	**44.34**	**42.34**	**40.35**	**38.36**	**36.37**	**34.37**	**32.38**	**31.88**
-1	0.000	0.000	0.000	0.000	0.000	0.000	0.000	0.000	0.000	0.000
-0.5	0.000	0.000	0.000	0.000	0.000	0.000	0.000	0.000	0.000	0.000
0	0.000	0.000	0.000	0.000	0.000	0.000	0.000	0.000	0.000	0.000
0.5	0.000	0.000	0.000	0.000	0.000	0.000	0.000	0.000	0.000	0.000
1	0.000	0.000	0.000	0.000	0.000	0.000	0.000	0.000	0.000	0.000
1.5	0.000	0.000	0.000	0.000	0.000	0.001	0.000	0.000	0.000	0.000
2	0.679	0.483	0.801	0.639	0.681	1.878	0.231	0.417	0.286	0.616
2.5	3.867	2.945	4.780	3.693	4.008	8.519	2.601	3.070	1.975	3.296
3	9.451	7.016	10.223	8.794	8.515	16.681	6.203	6.446	4.111	6.247
3.5	10.220	6.740	9.514	8.055	10.535	11.700	7.225	6.710	4.203	6.565
4	7.937	4.733	4.279	5.433	9.314	6.560	4.672	4.677	3.231	3.793
4.5	12.108	10.046	5.388	11.340	12.511	9.146	6.014	6.919	5.927	5.897
5	9.503	12.684	5.576	11.404	8.896	6.717	6.489	9.724	10.236	7.930
5.5	9.970	12.837	8.454	11.064	9.407	7.702	8.542	12.977	14.854	12.435
6	7.614	8.900	8.088	8.127	7.429	6.229	8.263	10.021	11.828	10.774
6.5	8.511	9.822	10.757	9.162	8.353	7.090	11.708	11.524	13.541	12.839
7	7.056	8.177	10.037	7.698	7.046	5.931	11.451	9.622	10.996	10.627
7.5	4.504	5.266	6.850	4.962	4.556	3.869	7.969	6.104	6.715	6.578
8	4.920	5.826	8.105	5.471	5.050	4.394	9.675	6.662	7.103	7.054
8.5	3.056	3.714	5.706	3.447	3.150	2.913	7.090	4.217	4.289	4.430
9	0.604	0.809	1.437	0.708	0.548	0.668	1.856	0.909	0.704	0.918
9.5	0.001	0.002	0.007	0.001	0.000	0.001	0.011	0.002	0.000	0.002
rest	0.000	0.000	0.000	0.000	0.000	0.000	0.000	0.000	0.000	0.000

Grain size frequency data with Phi ϕ scale for Turakina River Section continued

Sample	**BF1**	**ML6**	**ML5**	**ML4**	**ML3**	**DC7**	**ML2**	**ML1**	**DC6**	**DC5**
Height	**30.39**	**30.39**	**28.4**	**26.4**	**24.41**	**22.17**	**21.92**	**19.93**	**19.68**	**18.18**
-1	0.000	0.000	0.000	0.000	0.000	0.000	0.000	0.000	0.000	0.000
-0.5	0.000	0.000	0.000	0.000	0.000	0.000	0.000	0.000	0.000	0.000
0	0.000	0.000	0.000	0.000	0.000	0.000	0.000	0.000	0.000	0.000
0.5	0.000	0.000	0.000	0.000	0.000	0.000	0.000	0.000	0.000	0.000
1	0.000	0.000	0.000	0.000	0.000	0.000	0.000	0.000	0.000	0.000
1.5	0.000	0.000	0.002	0.000	0.000	0.002	0.000	0.001	0.005	0.004
2	0.695	0.772	2.097	0.529	0.445	1.950	0.749	1.732	3.233	3.045
2.5	3.923	4.382	7.946	3.203	2.581	6.611	3.935	6.476	9.512	9.000
3	7.518	7.608	12.028	6.006	6.063	9.522	7.624	10.048	11.575	10.828
3.5	6.230	6.068	7.433	5.964	5.814	7.395	6.870	6.164	7.352	7.588
4	3.440	3.670	5.073	3.057	3.766	3.883	3.264	3.133	3.904	4.232
4.5	5.229	5.380	9.133	4.567	5.608	5.496	5.061	5.130	5.043	6.031
5	6.426	7.769	9.188	6.005	8.343	6.544	6.758	5.671	7.496	6.260
5.5	9.343	11.705	10.220	9.152	12.333	10.246	11.085	8.000	10.435	7.990
6	9.176	10.102	7.883	9.258	10.480	9.125	10.068	7.717	8.365	7.059
6.5	12.578	12.310	8.938	13.192	12.882	11.203	12.595	11.006	9.754	8.799
7	11.555	10.462	7.355	12.701	11.057	9.643	10.934	10.713	8.205	7.966
7.5	7.599	6.624	4.568	8.566	7.016	6.169	7.004	7.387	5.196	5.603
8	8.772	7.312	4.830	9.792	7.658	6.839	7.824	8.901	5.663	7.218
8.5	6.116	4.784	2.853	6.561	4.895	4.440	5.154	6.436	3.558	5.892
9	1.397	1.050	0.451	1.443	1.056	0.930	1.073	1.485	0.700	2.379
9.5	0.003	0.002	0.000	0.003	0.002	0.002	0.002	0.003	0.001	0.106
rest	0.000	0.000	0.000	0.000	0.000	0.000	0.000	0.000	0.000	0.000

Grain size frequency data with Phi ϕ scale for Turakina River Section continued

Sample	**DC4**	**DC3**	**DC2**	**BS6**	**DC1**	**BS5**	**BS4**	**BS3**	**BS2**	**BS1**
Height	**16.19**	**14.2**	**12.21**	**10.96**	**10.21**	**8.966**	**6.973**	**4.483**	**2.49**	**0.498**
-1	0.000	0.000	0.000	0.000	0.000	0.000	0.000	0.000	0.000	0.000
-0.5	0.000	0.000	0.000	0.000	0.000	0.000	0.000	0.000	0.000	0.000
0	0.000	0.000	0.000	0.000	0.000	0.000	0.000	0.000	0.000	0.000
0.5	0.000	0.000	0.000	0.000	0.000	0.000	0.000	0.000	0.000	0.000
1	0.000	0.000	0.000	0.000	0.000	0.000	0.000	0.000	0.000	0.000
1.5	0.061	0.058	0.025	0.002	0.141	0.005	0.002	0.001	0.002	0.000
2	6.556	8.874	6.959	2.969	11.786	4.281	2.666	1.727	1.882	0.757
2.5	12.246	19.864	16.102	10.995	19.114	14.362	10.197	7.660	8.134	4.332
3	11.729	17.776	14.476	14.890	13.111	18.423	16.011	16.119	16.785	10.924
3.5	6.668	6.776	8.047	8.537	5.579	10.228	9.640	11.952	12.043	10.726
4	3.137	3.986	4.645	4.068	3.242	5.118	4.075	5.339	6.030	4.913
4.5	5.270	4.685	6.362	5.343	4.136	6.894	5.781	6.507	7.466	6.475
5	6.420	4.536	5.852	5.630	4.893	5.951	5.240	5.365	6.294	6.457
5.5	9.249	5.375	6.959	7.647	6.313	6.865	7.313	7.076	7.415	8.665
6	7.720	4.770	5.702	6.761	5.670	5.383	6.426	6.175	6.005	7.521
6.5	9.237	5.914	6.638	8.478	6.976	6.001	8.002	7.659	6.967	9.414
7	7.822	5.149	5.633	7.566	5.891	4.960	7.002	6.765	5.931	8.574
7.5	4.902	3.462	3.714	5.078	3.808	3.283	4.718	4.631	4.031	5.977
8	5.233	4.268	4.414	6.135	4.556	3.978	5.957	5.895	5.089	7.474
8.5	3.179	3.316	3.288	4.575	3.501	3.053	4.887	4.868	4.120	5.774
9	0.572	1.161	1.152	1.313	1.248	1.169	1.993	2.113	1.719	1.974
9.5	0.001	0.028	0.032	0.012	0.035	0.048	0.090	0.147	0.086	0.042
rest	0.000	0.000	0.000	0.000	0.000	0.000	0.000	0.000	0.000	0.000

Grain size frequency data with Phi ϕ scale for Turakina River Section continued

Sample	BS3.2	BS3	DC1.2	DC1	ML4.2	ML4	BF10.2	BF10	NB1.2	NB1	SBB9.2	SBB9	SBA1.2	SBA1	FT1.2	FT1
Height	**4.483**	**4.483**	**10.21**	**10.21**	**26.4**	**26.4**	**47.32**	**47.32**	**68.74**	**68.74**	**94.15**	**94.15**	**97.13**	**97.13**	**122.5**	**122.5**
-1	0.000	0.000	0.000	0.000	0.000	0.000	0.000	0.000	0.000	0.000	0.000	0.000	0.000	0.000	0.000	0.000
-0.5	0.000	0.000	0.000	0.000	0.000	0.000	0.000	0.000	0.000	0.000	0.000	0.000	0.000	0.000	0.000	0.000
0	0.000	0.000	0.000	0.000	0.000	0.000	0.000	0.000	0.000	0.000	0.000	0.000	0.000	0.000	0.000	0.000
0.5	0.000	0.000	0.000	0.000	0.000	0.000	0.000	0.000	0.000	0.000	0.000	0.000	0.000	0.000	0.000	0.000
1	0.000	0.000	0.000	0.000	0.000	0.000	0.000	0.000	0.000	0.000	0.000	0.000	0.000	0.000	0.000	0.000
1.5	0.001	0.000	0.141	0.182	0.000	0.000	0.000	0.000	0.000	0.000	0.000	0.000	0.000	0.000	0.000	0.000
2	1.727	1.357	11.786	14.849	0.529	0.573	0.483	0.657	0.679	0.969	0.357	0.397	0.352	0.621	0.082	0.023
2.5	7.660	8.695	19.114	23.020	3.203	3.324	2.945	3.266	3.845	5.601	2.883	2.638	1.966	2.807	0.893	0.536
3	16.119	18.629	13.111	15.715	6.006	6.465	7.016	6.838	8.624	11.065	8.934	8.241	6.015	8.112	1.323	1.469
3.5	11.952	12.130	5.579	6.294	5.964	5.999	6.740	7.465	9.267	9.617	9.182	8.565	9.565	11.877	3.155	2.164
4	5.339	5.684	3.242	3.310	3.057	3.119	4.733	3.498	5.601	5.087	5.349	5.019	5.947	8.510	2.797	2.536
4.5	6.507	6.316	4.136	4.443	4.567	4.443	10.046	5.671	8.352	8.370	6.330	6.488	8.812	10.999	4.154	4.154
5	5.365	5.025	4.893	4.237	6.005	5.768	12.684	6.373	7.588	9.940	5.505	5.367	9.729	7.537	6.426	6.419
5.5	7.076	6.412	6.313	5.355	9.152	8.947	12.837	10.105	9.326	11.532	7.713	7.208	10.933	8.435	9.363	9.521
6	6.175	5.717	5.670	4.408	9.258	9.210	8.900	9.490	7.728	8.375	7.655	7.356	8.291	6.989	9.502	9.848
6.5	7.659	7.223	6.976	5.176	13.192	13.287	9.822	12.261	9.115	9.100	10.688	10.817	9.775	8.391	14.381	14.935
7	6.765	6.409	5.891	4.303	12.701	12.757	8.177	11.035	8.058	7.376	10.333	10.796	8.819	7.652	14.735	14.994
7.5	4.631	4.382	3.808	2.744	8.566	8.510	5.266	7.334	5.706	4.606	7.266	7.693	6.089	5.350	10.316	10.392
8	5.895	5.573	4.556	3.108	9.792	9.708	5.826	8.585	7.425	4.897	9.093	9.732	7.281	6.567	12.304	12.305
8.5	4.868	4.553	3.501	2.171	6.561	6.525	3.714	6.022	6.080	2.929	6.891	7.517	5.118	4.811	8.664	8.664
9	2.113	1.816	1.248	0.676	1.443	1.366	0.809	1.399	2.489	0.535	1.813	2.147	1.303	1.332	1.902	2.036
9.5	0.147	0.078	0.035	0.008	0.003	0.002	0.002	0.003	0.117	0.001	0.010	0.018	0.007	0.010	0.003	0.004
rest	0.000	0.000	0.000	0.000	0.000	0.000	0.000	0.000	0.000	0.000	0.000	0.000	0.000	0.000	0.000	0.000

Falling Tim Section grainsize statistics. (m) Method of Moments. (FW) Folk and Ward Method. (D) cumulative percentiles

Sample	Height (m)	Mode	D_{10}	D_{50}	D_{90}	(M) Mean	(M) Sort	(M) Skew	(M) Kurt	(FW) Mean	(FW) Sort	(FW) Skew	(FW) Kurt	Gr.	Sd.	St.	Cl.	Sample type	Sed. name	Text. group
FT7	134.475	6.60	4.31	6.59	8.31	6.45	1.47	-0.42	2.55	6.49	1.52	-0.14	0.97	0.00	7.40	91.60	1.00	poorly sorted	med. silt	mud
FT6	132.482	6.07	3.89	6.14	8.09	6.06	1.53	-0.16	2.27	6.06	1.60	-0.07	0.90	0.00	11.50	87.80	0.70	poorly sorted	very fine sandy med.silt	sandy mud
FT5	130.490	4.585	3.57	5.50	7.91	5.60	1.61	0.19	2.10	5.62	1.67	0.10	0.85	0.00	17.70	81.80	0.50	poorly sorted	v. f. sandy very coarse silt	sandy mud
FT4	128.497	6.07	3.69	6.14	8.28	6.05	1.67	-0.12	2.07	6.04	1.76	-0.07	0.83	0.00	14.7	83.70	1.60	poorly sorted	v. f. sandy med. silt	sandy mud
FT3	126.505	6.60	4.50	6.71	8.35	6.57	1.43	-0.48	2.67	6.60	1.47	-0.14	1.00	0.00	5.90	92.90	1.20	poorly sorted	med. silt	mud
FT2	124.513	6.33	4.03	6.47	8.34	6.33	1.57	-0.33	2.31	6.35	1.64	-0.13	0.91	0.00	9.70	89.00	1.30	poorly sorted	med. sit	mud
FT1	122.52	6.87	4.83	6.88	8.46	6.75	1.38	-0.56	2.89	6.81	1.40	-0.14	1.00	0.00	4.30	94.00	1.70	poorly sorted	fine silt	mud

Gillian's Waterfall Section grainsize statistics. (D) Cumulative percentiles. (m) Method of Moments. (FW) Folk and Ward Method

Sample	Height (m)	Mode	D_{10}	D_{50}	D_{90}	(M) Mean	(M) Sort	(M) Skew	(M) Kurt	(FW) Mean	(FW) Sort	(FW) Skew	(FW) Kurt	Gr.	Sd.	St.	Cl.	Sample type	Sed. name	Text. group
WF4	119.531	6.60	3.92	6.55	8.37	6.38	1.58	-0.41	2.39	6.40	1.65	-0.16	0.94	0.00	10.80	87.80	1.40	poorly sorted	v. f. sandy med. silt	sandy mud
WF3	118.037	6.33	4.68	6.64	8.31	6.56	1.37	-0.44	2.84	6.61	1.40	-0.08	1.03	0.00	5.00	93.90	1.10	poorly sorted	med. silt	mud
WF2	116.045	6.87	4.66	6.80	8.37	6.65	1.40	-0.56	2.86	6.70	1.43	-0.16	1.03	0.00	5.50	93.40	1.10	poorly sorted	med. silt	mud
WF1	114.052	6.60	4.44	6.70	8.37	6.56	1.46	-0.51	2.725	6.60	1.50	-0.15	1.02	0.00	7.00	91.70	1.30	poorly sorted	med. silt	mud

Rob's Face Section grainsize statistics. (D) Cumulative percentiles. (m) Method of Moments. (FW) Folk and Ward Method

Sample	**Height (m)**	**Mode**	**D_{10}**	**D_{50}**	**D_{90}**	**(M) Mean**	**(M) Sort**	**(M) Skew**	**(M) Kurt**	**(FW) Mean**	**(FW) Sort**	**(FW) Skew**	**(FW) Kurt**	**Gr.**	**Sd.**	**St.**	**Cl.**	**Sample type**	**Sed. name**	**Text. group**
RF5	118.037	6.60	3.96	6.58	8.34	6.39	1.57	-0.44	2.41	6.41	1.64	-0.18	0.95	0.00	10.40	88.40	1.20	poorly sorted	v. f. sandy med. silt	sandy mud
RF4	116.044	6.60	4.26	6.58	8.36	6.45	1.50	-0.38	2.45	6.47	1.57	-0.13	0.95	0.00	7.80	90.90	1.30	poorly sorted	med. silt	mud
RF3	114.052	6.33	3.92	6.38	8.19	6.24	1.53	-0.35	2.43	6.25	1.59	-0.13	0.97	0.00	10.90	88.30	0.80	poorly sorted	v. f. sandy med. silt	sandy mud
RF2	112.558	6.60	3.93	6.50	8.36	6.34	1.60	-0.36	2.29	6.35	1.68	-0.15	0.91	0.00	10.70	87.9	1.40	poorly sorted	v. f. sandy med. silt	sandy mud
RF1	110.565	6.60	3.35	6.16	8.32	5.95	1.81	-0.15	1.87	5.93	1.92	-0.13	0.74	0.00	21.10	77.40	1.50	poorly sorted	v. f. sandy med. silt	sandy mud

South Bridge Section above tephra grainsize statistics. (D) Cumulative percentiles. (m) Method of Moments. (FW) Folk and Ward Method

Sample	**Height (m)**	**Mode**	**D_{10}**	**D_{50}**	**D_{90}**	**(M) Mean**	**(M) Sort**	**(M) Skew**	**(M) Kurt**	**(FW) Mean**	**(FW) Sort**	**(FW) Skew**	**(FW) Kurt**	**Gr.**	**Sd.**	**St.**	**Cl.**	**Sample type**	**Sed. name**	**Text. group**
SBA8	111.075	6.60	3.35	6.14	8.22	5.90	1.78	-0.17	1.90	5.88	1.88	-0.15	0.75	0.00	21.20	77.8	1.00	poorly sorted	v. f. sandy med. silt	sandy mud
SBA7	109.082	6.87	3.53	6.37	8.36	6.13	1.76	-0.28	2.01	6.10	1.87	-0.18	0.79	0.00	17.40	81.00	1.60	poorly sorted	v. f. sandy med. silt	sandy mud
SBA6	107.090	6.07	3.59	6.04	8.13	5.94	1.63	-0.14	2.14	5.91	1.74	-0.08	0.97	0.00	16.30	82.90	0.80	poorly sorted	v. f. sandy med. silt	sandy mud
SBA5	105.098	6.07	3.43	6.08	8.06	5.90	1.66	-0.22	2.12	5.86	1.77	-0.15	0.86	0.00	18.20	81.20	0.60	poorly sorted	v. f. sandy med. silt	sandy mud
SBA4	103.105	6.60	3.48	6.28	8.33	6.05	1.77	-0.21	1.92	6.03	1.87	-0.16	0.75	0.00	18.6	79.90	1.50	poorly sorted	v. f. sandy med. silt	sandy mud
SBA3	101.113	6.60	3.68	6.44	8.36	6.22	1.70	-0.31	2.09	6.18	1.80	-0.18	0.82	0.00	14.6	83.40	1.70	poorly sorted	v. f. sandy med. silt	sandy mud
SBA2	99.120	7.28	3.80	6.60	8.41	6.34	1.67	-0.38	2.12	6.33	1.77	-0.21	0.82	0.00	12.5	86.00	1.50	poorly sorted	v. f. sandy fine silt	sandy mud
SBA1	97.128	3.64	3.36	5.42	8.10	5.56	1.76	0.22	1.94	5.57	1.83	0.12	0.77	0.00	23.90	75.00	1.10	poorly sorted	v. f. sandy v. coarse silt	sandy mud

South Bridge Section below tephra grainsize statistics. (D) Cumulative percentiles. (m) Method of Moments. (FW) Folk and Ward Method

Sample	Height (m)	Mode	D_{10}	D_{50}	D_{90}	(M) Mean	(M) Sort	(M) Skew	(M) Kurt	(FW) Mean	(FW) Sort	(FW) Skew	(FW) Kurt	Gr.	Sd.	St.	Cl.	Sample type	Sed. name	Text. group
SBB9	94.145	6.87	3.37	6.33	8.40	6.05	1.84	-0.22	1.85	6.04	1.95	-0.18	0.73	0.00	20.10	78.1	1.80	poorly sorted	v. f. sandy fine silt	sandy mud
SBB8	92.153	8.35	3.52	6.35	8.55	6.17	1.85	-0.19	1.89	6.15	1.95	-0.13	0.74	0.00	17.70	79.00	3.33	poorly sorted	v. f. sandy med. silt	sandy mud
SBB7	90.160	7.28	3.33	6.40	8.39	6.08	1.85	-0.30	1.91	6.06	1.95	-0.22	0.75	0.00	19.60	78.90	1.50	poorly sorted	v. f. sandy fine silt	sandy mud
SBB6	88.168	6.87	3.13	6.16	8.32	5.88	1.91	-0.18	1.79	5.86	2.01	-0.17	0.70	0.00	24.10	74.60	1.30	poorly sorted	v. f. sandy fine silt	sandy mud
SBB5	86.175	3.373	3.00	5.38	8.27	5.46	1.98	0.19	1.73	5.48	2.04	0.09	0.68	0.00	33.30	64.90	1.80	poorly sorted	v. f. sandy med. silt	sandy mud
SBB4	84.183	3.10	2.93	5.34	8.00	5.33	1.91	0.17	1.73	5.34	1.97	0.043	0.68	0.00	35.2	64.10	0.70	poorly sorted	v. f. sandy med. silt	sandy mud
SBB3	82.191	2.97	2.88	5.64	8.18	5.48	1.98	0.04	1.69	5.50	2.06	-0.05	0.66	0.00	32.20	66.70	1.10	poorly sorted	v. f. sandy med. silt	sandy mud
SBB2	80.696	2.97	2.90	5.45	8.21	5.43	1.98	0.14	1.75	5.44	2.06	0.03	0.68	0.00	32.70	65.70	1.60	poorly sorted	v. f. sandy med. silt	sandy mud
SBB1	78.704	2.97	2.84	5.09	7.97	5.23	1.94	0.21	1.74	5.21	1.99	0.12	0.67	0.00	36.50	62.80	0.70	poorly sorted	v. f. sandy med. silt	sandy mud

North Bridge Section grainsize statistics. (D) Cumulative percentiles. (m) Method of Moments. (FW) Folk and Ward Method

Sample	Height (m)	Mode	D_{10}	D_{50}	D_{90}	(M) Mean	(M) Sort	(M) Skew	(M) Kurt	(FW) Mean	(FW) Sort	(FW) Skew	(FW) Kurt	Gr.	Sd.	St.	Cl.	Sample type	Sed. name	Text. group
NB7	80.696	3.37	3.07	5.81	8.15	5.63	1.89	-0.01	1.76	5.64	1.96	-0.08	0.69	0.00	28.00	71.00	1.00	poorly sorted	v. f. sandy med. silt	sandy mud
NB6	78.704	6.07	3.05	5.86	8.23	5.67	1.92	-0.04	1.74	5.68	2.01	-0.09	0.68	0.00	27.90	71.10	1.00	poorly sorted	v. f. sandy med. silt	sandy mud
NB5	76.712	2.97	2.91	5.56	7.85	5.37	1.83	0.05	0.05	5.36	1.91	-0.08	0.73	0.00	30.70	68.70	0.60	poorly sorted	v. f. sandy med. silt	sandy mud
NB4	74.719	3.10	2.80	4.78	7.78	5.05	1.90	0.32	1.81	5.01	1.93	0.20	0.69	0.00	40.60	58.80	0.60	poorly sorted	v. f. sandy med. silt	sandy mud
NB3	72.727	3.10	2.96	5.10	8.07	5.29	1.89	0.30	1.93	5.27	1.96	0.15	0.74	0.00	33.20	65.20	1.60	poorly sorted	v. f. sandy v. coarse silt	sandy mud
NB2	70.734	2.97	2.83	5.12	7.83	5.16	1.90	0.22	1.78	5.16	1.94	0.08	0.68	0.00	37.40	62.00	0.60	poorly sorted	v. f. sandy med. silt	sandy mud
NB1	68.742	5.93	3.07	5.43	7.73	5.37	1.70	0.11	2.02	5.34	1.79	-0.01	0.79	0.00	27.50	72.10	0.40	poorly sorted	v. f. sandy v. coarse silt	sandy mud

Dutch Man's Stairs Section grainsize statistics. (D) Cumulative percentiles. (m) Method of Moments. (FW) Folk and Ward Method

Sample	Height (m)	Mode	D_{10}	D_{50}	D_{90}	(M) Mean	(M) Sort	(M) Skew	(M) Kurt	(FW) Mean	(FW) Sort	(FW) Skew	(FW) Kurt	Gr.	Sd.	St.	Cl.	Sample type	Sed. name	Text. group
DMS6	73.723	6.07	3.24	5.80	8.22	5.73	1.82	0.01	1.87	5.72	1.92	-0.03	0.74	0.00	23.50	75.10	1.40	poorly sorted	v. f. sandy med. silt	sandy mud
DMS5	71.731	3.37	3.12	6.04	8.35	5.85	1.89	-0.09	1.83	5.84	1.99	-0.10	0.71	0.00	23.90	74.00	2.10	poorly sorted	v. f. sandy med. silt	sandy mud
DMS4	69.738	6.07	3.30	5.93	8.31	5.83	1.83	-0.04	1.89	5.83	1.93	-0.06	0.76	0.00	21.90	76.30	1.80	poorly sorted	v. f. sandy med. silt	sandy mud
DMS3	67.746	6.07	3.25	5.82	7.95	5.66	1.72	-0.05	2.00	5.63	1.82	-0.10	0.79	0.00	23.20	76.10	0.70	poorly sorted	v. f. sandy med. silt	sandy mud
DMS2	65.754	3.64	3.26	6.01	8.31	5.83	1.87	-0.07	1.80	5.83	1.96	-0.10	0.70	0.00	24.20	74.10	1.7	poorly sorted	v. f. sandy med. silt	sandy mud
DMS1	63.761	7.28	3.96	6.55	8.44	6.39	1.63	-0.35	2.26	6.42	1.69	-0.14	0.87	0.00	10.50	87.50	2.00	poorly sorted	v. f. sandy med. silt	sandy mud
WTF2	62.765	6.74	4.04	6.59	8.29	6.37	1.56	-0.49	2.52	6.39	1.64	-0.20	0.97	0.00	9.60	89.50	0.90	poorly sorted	med. silt	mud

Big Face Section grainsize statistics. (D) Cumulative percentiles. (m) Method of Moments. (FW) Folk and Ward Method

Sample	Height (m)	Mode	D_{10}	D_{50}	D_{90}	(M) Mean	(M) Sort	(M) Skew	(M) Kurt	(FW) Mean	(FW) Sort	(FW) Skew	(FW) Kurt	Gr.	Sd.	St.	Cl.	Sample type	Sed. name	Text. group
BF11	60.274	6.33	3.97	6.46	8.50	6.35	1.67	-0.28	2.34	6.37	1.74	-0.10	0.87	0.00	10.40	86.70	2.90	poorly sorted	v. f. sandy med. silt	sandy mud
BF12	57.286	7.28	4.34	6.73	8.50	6.57	1.55	-0.42	2.40	6.60	1.61	-0.15	0.90	0.00	7.00	91.00	2.00	poorly sorted	f. silt	mud
BF13	54.297	4.85	3.37	5.56	7.90	5.60	1.64	0.11	2.14	5.57	1.73	0.03	0.88	0.00	20.00	79.30	0.70	poorly sorted	v. f. sandy coarse silt	sandy mud
BF9	50.312	4.59	3.23	5.23	7.75	5.37	1.65	0.24	2.11	5.34	1.73	0.11	0.84	0.00	24.60	74.90	0.50	poorly sorted	v. f. sandy v. coarse silt	sandy mud
BF10	47.323	5.80	3.41	5.69	7.91	5.70	1.60	0.01	2.24	5.67	1.70	-0.00	0.96	0.00	17.40	81.90	0.70	poorly sorted	v. f. sandy coarse silt	sandy mud
BF8	44.335	6.33	3.15	6.05	8.22	5.79	1.87	-0.13	1.81	5.78	1.96	-0.15	0.70	0.00	25.60	73.20	1.20	poorly sorted	v. f. sandy med. silt	sandy mud
BF7	42.342	4.85	3.26	5.49	7.85	5.53	1.65	0.11	2.13	5.49	1.76	0.03	0.88	0.00	21.40	78.00	0.60	poorly sorted	v. f. sandy coarse silt	sandy mud
BF6	40.350	4.45	3.25	5.17	7.76	5.37	1.66	0.27	2.11	5.34	1.73	0.15	0.85	0.00	24.20	75.40	0.40	poorly sorted	v. f. sandy v. coarse silt	sandy mud
BF5	38.358	3.10	2.89	4.65	7.66	4.98	1.80	0.45	2.05	4.94	1.84	0.26	0.75	0.00	39.10	60.30	0.60	poorly sorted	v. f. sandy v. coarse silt	sandy mud
BF4	36.365	6.74	3.52	6.39	8.36	6.15	1.75	-0.30	2.04	6.12	1.86	-0.19	0.82	0.00	16.50	81.90	1.60	poorly sorted	v. f. sandy med. silt	sandy mud
BF3	34.373	5.93	3.45	5.96	8.02	5.86	1.63	-0.16	2.21	5.83	1.74	-0.10	0.93	0.00	16.90	82.30	0.80	poorly sorted	v. f. sandy med. silt	sandy mud
BF2	31.882	6.07	3.43	6.12	8.05	5.94	1.65	-0.28	2.26	5.89	1.76	-0.16	0.95	0.00	16.90	82.30	0.80	poorly sorted	v. f. sandy med. silt	sandy mud
BF1	30.388	6.60	3.28	6.32	8.26	6.05	1.77	-0.35	2.11	5.99	1.90	-0.22	08.64	0.00	18.60	80.20	1.20	poorly sorted	v. f. sandy med. silt	sandy mud

Missing Link Section grain size stastics. (D) Cumulative percentiles. (m) Method of Moments. (FW) Folk and Ward Method

Sample	Height (m)	Mode	D_{10}	D_{50}	D_{90}	(M) Mean	(M) Sort	(M) Skew	(M) Kurt	(FW) Mean	(FW) Sort	(FW) Skew	(FW) Kurt	Gr.	Sd.	St.	Cl.	Sample type	Sed. name	Text. group
ML7	32.380	6.07	3.91	6.17	8.03	6.10	1.48	-0.32	2.63	6.14	1.54	-0.08	1.09	0.00	10.70	88.70	0.60	poorly sorted	v. f. sandy med. silt	sandy mud
ML6	30.387	6.07	3.23	6.10	8.10	5.90	1.72	-0.28	2.15	5.84	1.85	-0.17	0.90	0.00	19.0	80.10	0.90	poorly sorted	v. f. sandy med. silt	sandy mud
ML5	28.395	2.97	2.90	5.29	7.71	5.27	1.77	0.12	1.96	5.22	1.86	0.00	0.76	0.00	29.80	69.80	0.40	poorly sorted	v. f. sandy coarse silt	sandy mud
ML4	26.402	6.60	3.46	6.50	8.30	6.22	1.72	-0.47	2.28	6.16	1.84	-0.25	0.93	0.00	15.90	82.9	1.20	poorly sorted	v. f. sandy med. silt	sandy mud
ML3	24.410	6.07	3.52	6.20	8.12	6.04	1.63	-0.31	2.31	6.01	1.73	-0.15	0.97	0.00	15.10	84.00	0.90	poorly sorted	v. f. sandy med. silt	sandy mud
ML2	21.920	6.20	3.28	6.18	8.15	5.95	1.73	-0.31	2.13	5.88	1.86	-0.19	0.88	0.00	19.40	79.70	0.90	poorly sorted	v. f. sandy med. silt	sandy mud
ML1	19.927	6.74	2.99	6.19	8.29	5.86	1.93	-0.25	1.84	5.81	2.05	-0.21	0.71	0.00	24.60	74.20	1.20	poorly sorted	v. f. sandy med. silt	sandy mud

Dead Cow Section grainsize statistics. (D) Cumulative percentiles. (m) Method of Moments. (FW) Folk and Ward Method

Sample	Height (m)	Mode	D_{10}	D_{50}	D_{90}	(M) Mean	(M) Sort	(M) Skew	(M) Kurt	(FW) Mean	(FW) Sort	(FW) Skew	(FW) Kurt	Gr.	Sd.	St.	Cl.	Sample type	Sed. name	Text. group
DC7	22.168	6.07	2.98	5.92	8.05	5.65	1.84	-0.15	1.90	5.62	1.95	-0.16	0.75	0.00	25.70	73.50	0.80	poorly sorted	v. f. sandy med. silt	sandy mud
DC6	19.678	2.84	2.80	5.57	7.88	5.35	1.88	0.01	1.82	5.34	1.97	-0.10	0.70	0.00	31.90	67.50	0.60	poorly sorted	v. f. sandy med. silt	sandy mud
DC5	18.184	2.84	2.82	5.69	8.30	5.54	2.02	0.04	1.76	5.54	2.12	-0.05	0.69	0.00	30.70	69.30	2.20	poorly sorted	v. f. sandy med. silt	sandy mud
DC4	16.191	2.70	2.62	5.30	7.79	5.13	1.96	0.11	1.73	5.14	2.02	-0.04	0.67	0.00	37.40	62.10	0.50	v. poorly sorted	f. sandy med. silt	sandy mud
DC3	14.199	2.84	2.52	3.68	7.73	4.55	2.03	0.67	2.09	4.47	2.01	0.55	0.71	0.00	53.60	45.40	1.00	v. poorly sorted	med. silty f. sand	muddy sand
DC2	12.206	2.70	2.58	4.36	7.76	4.78	1.98	0.48	1.97	4.75	2.00	0.31	0.71	0.00	45.90	53.10	1.00	v. poorly sorted	f. sandy med. silt	sandy mud
DC1	10.214	2.70	2.45	4.01	7.81	4.68	2.09	0.49	1.85	4.60	2.08	0.41	0.67	0.00	49.90	49.00	1.10	v. poorly sorted	f. sandy med. silt	sandy mud

Base of Section grainsize statistics. (D) Cumulative percentiles. (m) Method of Moments. (FW) Folk and Ward Method

Sample	Height (m)	Mode	D_{10}	D_{50}	D_{90}	(M) Mean	(M) Sort	(M) Skew	(M) Kurt	(FW) Mean	(FW) Sort	(FW) Skew	(FW) Kurt	Gr.	Sd.	St.	Cl.	Sample type	Sed. name	Text. group
BS6	10.958	2.97	2.78	5.23	8.06	5.24	2.00	0.20	1.72	5.25	2.05	0.06	0.67	0.00	37.60	61.30	1.10	v. poorly sorted	v. f. sandy med. silt	sandy mud
BS5	8.966	2.84	2.68	4.19	7.66	4.73	1.90	0.61	2.17	4.67	1.92	0.39	0.76	0.00	47.60	53.30	1.10	poorly sorted	v. f. sandy v. coarse silt	sandy mud
BS4	6.973	2.97	2.81	5.08	8.14	5.23	2.02	0.27	1.76	5.23	2.06	0.14	0.68	0.00	38.70	59.50	1.80	v. poorly sorted	v. f. sandy med. silt	sandy mud
BS3	4.483	3.24	2.92	4.99	8.16	5.26	1.98	0.33	1.83	5.25	2.02	0.20	0.70	0.00	37.80	60.20	2.00	v. poorly sorted	v. f. sandy med. silt	sandy mud
BS2	2.490	3.10	2.90	4.75	7.99	5.10	1.91	0.44	1.98	5.08	1.96	0.26	0.74	0.00	39.20	59.20	1.60	poorly sorted	v. f. sandy v. coarse silt	sandy mud
BS1	0.498	3.51	3.17	5.82	8.26	5.68	1.88	0.03	1.80	5.70	1.97	-0.05	0.70	0.00	27.00	71.30	1.70	poorly sorted	v. f. sandy med. silt	sandy mud

Repeat sample grainsize statistics. (D) Cumulative percentiles. (M) Method of Moments. (FW) Folk and Ward Method. (R) Repeat sample

Sample	Height (m)	Mode	D_{10}	D_{50}	D_{90}	(M) Mean	(M) Sort	(M) Skew	(M) Kurt	(FW) Mean	(FW) Sort	(FW) Skew	(FW) Kurt	Gr.	Sd.	St.	Cl.	Sample type	Sed. name	Text. group
FT1	122.52	6.87	4.83	6.88	8.46	6.75	1.38	-0.56	2.89	6.81	1.40	-0.14	1.00	0.00	4.30	94.00	1.70	v. poorly sorted	v. f. sandy med. silt	mud
FT1(R)	122.52	7.01	4.65	6.86	8.45	6.70	1.43	-0.58	2.84	6.76	1.46	-0.17	1.01	0.00	5.60	92.80	1.60	v. poorly sorted	v. f. sandy med. silt	mud
SBA1	97.128	3.64	3.36	5.42	8.10	5.56	1.76	0.22	1.94	5.57	1.83	0.12	0.77	0.00	23.90	75.00	1.10	poorly sorted	v. f. sandy v. coarse silt	sandy mud
SBA(R)	97.128	5.93	3.54	5.84	8.15	5.83	1.68	0.02	2.03	5.81	1.77	-0.01	0.81	0.00	18.20	80.70	1.10	poorly sorted	v. f. sandy coarse silt	sandy mud
SBB9	94.145	6.87	3.37	6.33	8.40	6.05	1.84	-0.22	1.85	6.04	1.95	-0.18	0.73	0.00	20.10	78.10	1.80	poorly sorted	v. f. sandy f. silt	sandy mud
SBB9(R)	94.145	6.60	3.33	6.20	8.34	5.95	1.84	-0.16	1.82	5.95	1.94	-0.15	0.71	0.00	21.70	76.80	1.50	poorly sorted	v. f. sandy med. silt	sandy mud
NB1	68.742	5.93	3.07	5.43	7.73	5.37	1.70	0.11	2.02	5.34	1.79	-0.01	0.79	0.00	27.50	72.10	0.40	poorly sorted	v. f. sandy coarse silt	sandy mud
NB1(R)	68.742	6.07	3.26	5.83	8.32	5.77	1.84	0.04	1.91	5.77	1.95	-0.02	0.77	0.00	22.70	75.00	2.30	poorly sorted	v. f. sandy med. silt	sandy mud
BF10	47.323	6.33	3.39	6.26	8.25	6.03	1.74	-0.30	2.10	5.98	1.87	-0.19	0.86	0.00	18.40	80.40	1.20	poorly sorted	v. f. sandy med. silt	sandy mud
BF10(R)	47.323	5.80	3.41	5.69	7.91	5.69	1.60	0.01	2.24	5.67	1.70	-0.00	0.96	0.00	17.40	81.90	0.70	poorly sorted	v. f. sandy coarse silt	sandy mud
ML4	26.402	6.74	3.41	6.49	8.29	6.19	1.73	-0.47	2.25	6.13	1.86	-0.26	0.94	0.00	16.50	82.40	1.10	poorly sorted	v. f. sandy med. silt	sandy mud
ML4(R)	26.402	6.60	3.46	6.50	8.30	6.21	1.72	-0.47	2.28	6.16	1.84	-0.25	0.93	0.00	15.90	82.90	1.20	poorly sorted	v. f. sandy med. silt	sandy mud
DC1	10.214	2.70	2.40	3.25	7.31	4.21	1.93	0.87	2.44	4.13	1.90	0.65	0.76	0.00	60.20	39.20	0.60	poorly sorted	med. silty f. sand	muddy sand
DC1(R)	10.214	2.70	2.45	4.01	7.81	4.68	2.09	0.49	1.85	4.60	2.08	0.41	0.67	0.00	49.9	48.80	1.10	v. poorly sorted	f. sandy med. silt	sandy mud
BS3	4.483	3.10	2.90	4.67	8.08	5.12	1.97	0.42	1.86	5.09	2.00	0.31	0.70	0.00	41.10	57.20	1.70	poorly sorted	v. f. sandy med. silt	sandy mud
BS3(R)	4.483	3.24	2.92	4.99	8.16	5.26	1.98	0.33	1.83	5.25	2.02	0.20	0.70	0.00	37.80	60.20	2.00	v. poorly sorted	v. f. sandy med. silt	sandy mud